Large eddy simulation of the turbulent flow and heat transfer in tube bundles

Liang, Chunlei

LARGE EDDY SIMULATION OF TURBULENT FLOW AND HEAT TRANSFER IN TUBE BUNDLES

by

Chunlei LIANG

A thesis submitted for the Degree of

Doctor of Philosophy

to the Faculty of Engineering

University of London

Department of Mechanical Engineering

King's College London

· 2004 ·

Dedicated to my grandfather Liang ShangJun for my happy childhood with him . . .

Abstract

The objective of this thesis is to investigate the turbulent flow characteristics and heat transfer across inline and staggered tube bundles using the Large Eddy Simulation (LES) technique. The Navier-Stokes, continuity and energy equations were discretised using the Finite-Volume method in a three-dimensional, collocated, unstructured grid arrangement. For the spatial discretisation of the convection term for velocities, the second order central differencing scheme was used and for time marching, the Crank Nicolson method. Two LES subgrid-scale models were used in the simulation, namely, the standard Smagorinsky model and a dynamic model, for which the test-filtered quantities are obtained through a truncated Taylor series expansion.

In order to demonstrate the accuracy of the LES models and discretisation practises, the developed numerical approach was validated first in a turbulent channel flow at two Reynolds numbers. Then a thorough and detailed validation was also performed for steady and pulsating incoming cross-flow and heat transfer over a circular cylinder. The numerical predictions are in very good agreement with PIV measurements (especially for the pulsating incoming flow) both in terms of mean as well as turbulence quantities. The effect that the lock-on has on the vortex formation length, Strouhal number, vortex strength as well as the lift and drag coefficients was examined in detail. Computations for heat transfer revealed that the Nusselt number increases after the separation point under pulsating flow

conditions.

Several simulations were then performed for both inline and staggered tube bundles with focus on the vortex shedding phenomena occurring behind different row cylinders under steady and pulsating inlet flow conditions. New information regarding vortex interaction among multiple cylinders was obtained. The flow between the first and second cylinder in the inline tube array was found to be bistable while the interaction of the wakes in the staggered tube bundle generated two different shedding frequencies. The results were also compared with detailed experimental data at several streamwise locations inside the bundle. The enhancement of heat transfer by the external pulsation was also quantified in multiple cylinder arrays. The thesis concludes with a summary of the main findings and recommendations for future work.

Turbulence predictions in aerodynamics face two principle challenges: (I) growth and separation of the boundary layer, and (II) momentum transfer after separation...

P. R. Spalart, Boeing, Seattle

Acknowledgments

I would like to express my sincere gratitude to my first supervisor Dr George Papadakis, for his scientific and technical guidance and his essential advice and never-fading enthusiasm throughout my studies in King's College London. I am indebted to my second supervisor Prof. Michael Yianneskis for his comments and guidance.

I also want to give appreciative thanks to Drs Balabani and Konstantinidis for providing me with the PIV measurement data of the turbulent flow across the single circular cylinder and LDA measurement data for the inline tube bundle.

This research was sponsored by the Engineering and Physical Science Research Council (EPSRC) under grant no. GR/R04256/01. I was also funded by an Overseas Research Student (ORS) Award (no. 2002054034) provided by Universities UK.

I would like to express thanks to my colleagues: Lim Yeoh, Giorgos Karlatiras, Christina Giannopapa, David Basanta and Azmir Harun for studying of turbulence and computer programming and sharing of different cultures together. Many thanks also go to other office mates in ECLAT for their support in different ways.

I am very grateful to the support and encouragement from my family in China. Finally, I want to thank my girl-friend Hui Feng, for her support, love and humour.

Contents

List of Figures

List of Tables

Nomenclature

Roman Characters

Symbols		Units
A	amplitude of wave speed	-
C_D	Drag coefficient	-
C_K	Kolmogrov constant	-
C_L	Lift coefficient	-
C_p	Pressure coefficient	-
$-C_{pb}$	Base suction coefficient	-
C_s	Smagorinsky constant	-
D	Cylinder diameter	m
f	Cell face number or instantaneous variable	-
f_{bloor}	Bloor secondary frequency	Hz
f_e and f_p	Pulsating frequency	Hz
f_n	Natural vortex shedding frequency	Hz
h	Grid spacing	m
L_x	Streamwise length	m
L_y	Wall-normal length	m
L_z	Spanwise length	m
l_r	Recirculation bubble length	m

N_r^{eff}	Number of cells used in the periphery of the cylinder	-
N_z	Number of cells used in the spanwise direction	-
Nu_θ	Local Nusselt number, $\frac{q_w D}{k(\Theta_{w_\theta} - \Theta_\infty)}$	-
p	Pressure	Nm^{-2}
q_j	Subgrid scale heat flux	W/m^2
$q"_w$	Wall heat flux	W/m^2
Re_D	Reynolds number based on the cylinder diameter,	
r_{exp}	Expansion ratio for the grid cell	-
S_e	pulsating Strouhal number	-
S_n	vortex shedding Strouhal number, $S_n = \frac{f_n \times D}{u_\infty}$	-
S_L	Longitudinal spacing	m
S_T	Transverse spacing	m
u_∞	Freestream velocity	ms^{-1}
u_τ	Friction velocity	ms^{-1}
$\overline{u}$	Mean bulk velocity	ms^{-1}
U_c	Centerline velocity	ms^{-1}
y^+	Non-dimensional wall distance	-

Greek Characters

α	Streamwise wavenumber/ Ratio between test and grid filter width	-
α_f	Weighting factor	-
α_r	Coefficient of third order pressure gradient in Rhie and Chow interpolation	-

β_m	Parameter of Gamma differencing scheme	-
Γ	Diffusion coefficient	$kg \cdot m^{-1}s^{-1}$
γ	Blending factor used in Gamma differencing scheme/ CFL number	-
Δ	Grid filter width	m
$\widehat{\Delta}$	Test filter width	m
Δr	The radial thickness of the first cell on the cylinder wall	m
Δt	Time step size	s
ΔT	Normalized time step size, $\frac{\Delta t u_\infty}{D}$	-
$\Delta\Omega$	Volume of cell	m^3
Δu	The peak-to-peak amplitude	ms^{-1}
δ	Half channel width	m
δ_{ij}	Kronecker delta	-
ϵ	Dissipation rate of turbulent kinetic energy	m^2s^{-3}
η	Kolmogorov length scale	m
Θ_∞	Freestream temperature	^oC
κ	von Karman constant	-
μ	Dynamic viscosity	$kg \cdot m^{-1}s^{-1}$
ν	Kinematic viscosity	m^2s^{-1}
ξ	Unit vector connecting two neighbouring cell centroids (from P to nb)	-
ρ	density	kg m^{-3}
τ_{ij}	Component of molecular Reynolds stress tensor	Pa

τ_{ij}^{sgs}	Component of subgrid scale Reynolds stress tensor	Pa

Superscripts

i,j	Direction
t	Test filtered variable/ turbulent
*	Corrected value
n	Current time step
$n+1$	Next time step
sgs	Subgrid scale part of the variable
+	Variable in viscous units

Subscripts

bulk	Based on bulk velocity
e	East face
gap	Based on gap velocity
max	Maximum value
mean	Mean value
min	Minimum value
n	Normal
nb	Neighbouring nodes
w	West face
t	Turbulent
θ	Peripherical angle around the cylinder surface

Other

$\cdot$	Dot product
$\overline{}$	Mean value
$\|\ \|$	Magnitude
$\wedge$	Fourier transform/ test filtering
$\langle\ \rangle$	Ensemble average
$\widetilde{f}$	Grid filtering of f

Abbreviations

BICG	Bi-conjugate gradient method
CDS	Central difference scheme
CFD	Computational fluid dynamics
CFL	Courant-Friedrich-Levy
COM4	Fourth order compact differing scheme
DNS	Direct Numerical Simulation
DSGS	Dynamic subgrid scale Smagorinsky model
E	East node
LDA	Laser-Doppler anemometry
NVD	Normalised variable diagram
P	Central node
PISO	Pressure Implicit with Splitting of Operator
PIV	Particle image velocimetry
RANS	Reynolds averaged Navier-Stokes
rms/r.m.s	Root mean square
RSTM	Reynolds Stress Transport Model

SGS/sgs	Subgrid scale
SIMPLE	Semi-Implicit Method for Pressure Linked equations
UDS	upwind differencing scheme

Chapter 1

INTRODUCTION

1.1 General Background on Turbulent Flow Characteristics and Heat Transfer in Tube Bundles

Tube bundles[1] are widely employed in cross-flow[2] heat exchangers, as they combine ease of construction with good thermal and mechanical efficiency. Heat tranfer to or from a bundle of tubes is relevant to many industrial applications such as steam generators in a boiler, heating of feed water, air conditioning and refrigeration etc. The shell-and-tube exchanger is the type of heat transfer equipment most widely used in the process and power industries; it accounts for over 85% of new heat exchangers supplied to the oil refining, chemical, petrochemical and power companies in leading European countries (Butterworth et al., 1996). Therefore, efficient design and operation of such equipment can lead to significant energy savings. On the other hand, in the crossflow over tube bundles, the flow boundaries are discontinuous and the flow is forced to separate and reattach. The instability in the shear layers, the sensitivity of the separation point to pressure gradients, the vortex shedding as well as the different wake interaction mechanisms can be contributing factors to structural resonance which can induce large amplitude vibrations. Better understanding of the mutual interactions between these flow phenomena

[1]The term "tube bundles" is used to denote different arrangements (inline, staggered or asymmetric) of equal diameter circular cylinders. The terms "cylinder arrays", "tube arrays", "tube bundles" or "tube banks" are used as synonyms throughout this thesis and in the existing literature.

[2]The term "cross-flow" is used to indicate that the upstream bulk fluid flow velocity is perpendicular to the cylinders' axes.

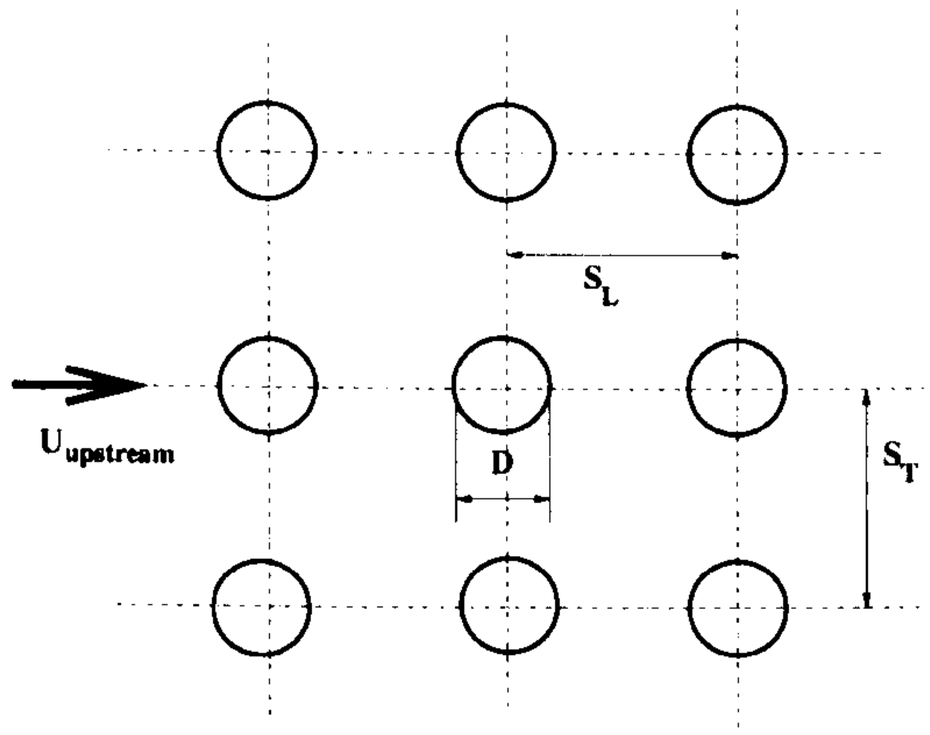

Figure 1.1: Definition of the geometric parameters for the inline arrangement.

will be very beneficial since flow-induced vibrations (FIV) of heat exchanger tube bundles often cause serious structural or thermal failure resulting in lost revenue and high repair costs.

Extensive research about flow periodicity and turbulent heat transfer inside both inline and staggered tube bundles (see figures 1.1 and 1.2 for definition of their geometric parameters) has been performed mainly experimentally. They are functions of the tube arrangements, spacings, Reynolds number and upstream flow conditions. Flow periodicity is present in tube bundles which may incite tube vibrations in liquid and acoustic resonance in gas flows. Apart from the typical inline and staggered arrangements mentioned earlier, there is a vast number of configurations used in practice; the standard configurations are shown in figure 1.3. The flow patterns can be very complicated. For instance, Sumner et al. (2000) identified nine different flow patterns (resulting from reattachment of shear layers, induced separation, vortex pairing, synchronisation and impingement) for two staggered circular cylinders in cross flow. Their study reveals that vortex shedding frequencies depend more on the characteristics of the individual shear layers rather than the location of individual cylinders.

1.1.1 Classification of cylinder arrays

When two cylinders are placed in tandem, the wake from the upstream cylinder generates velocity perturbations interacting with the downstream cylinder. The level and form depends on the tube spacing. The three-dimensional vortex structure depends on the separation distance and the Reynolds number. The flow characteristics of multiple-row inline tube bundles are similar to that of two cylin-

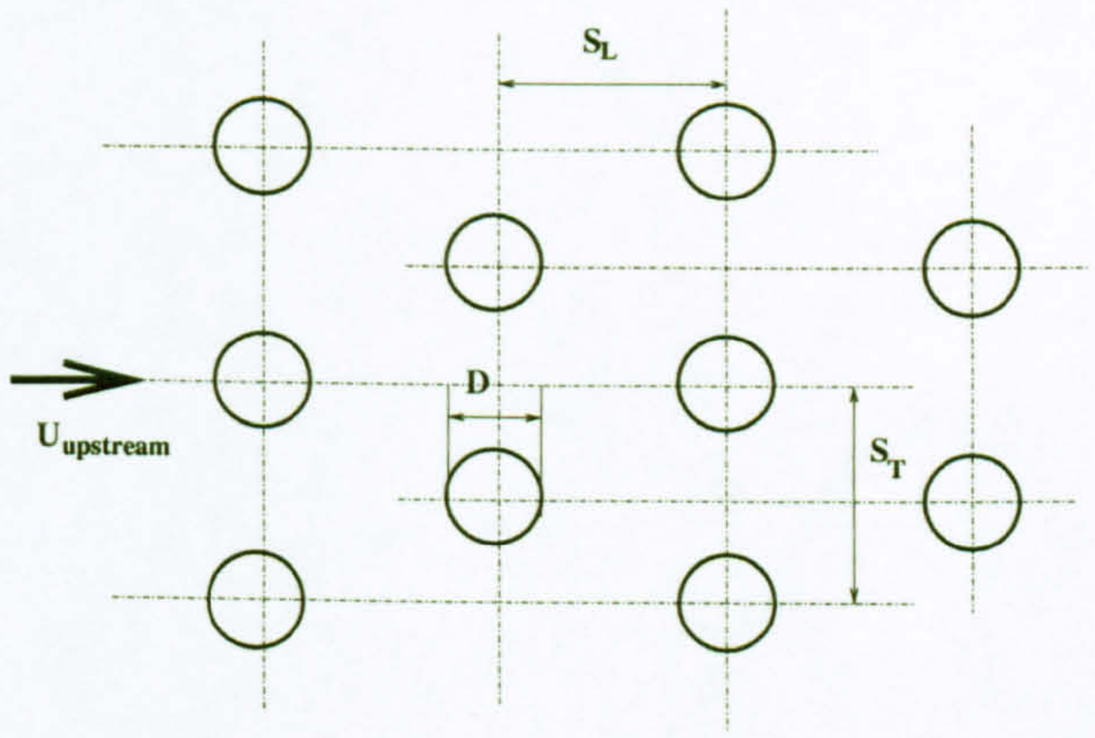

Figure 1.2: Definition of the geometric parameters for the symmetrical staggered arrangement.

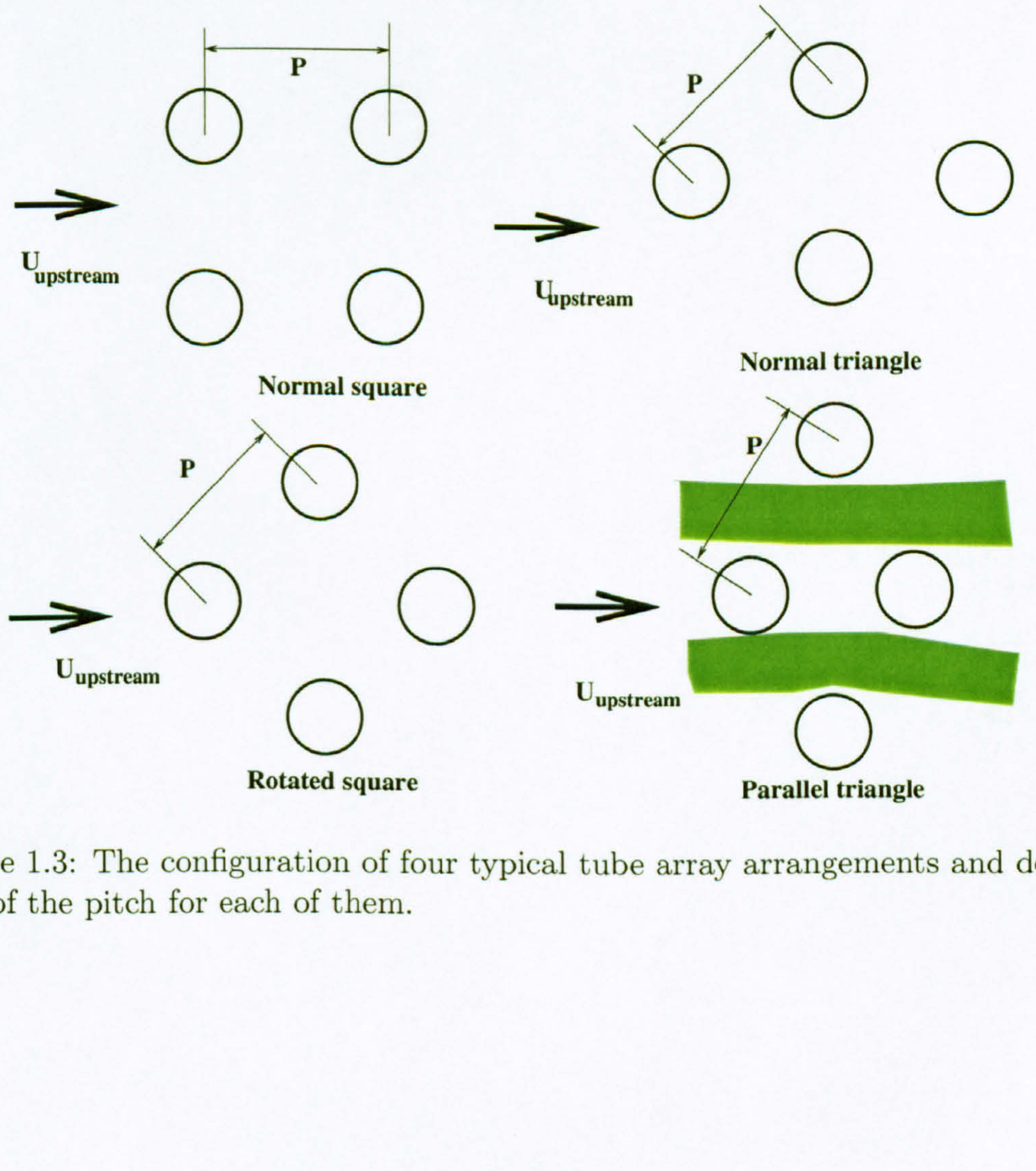

Figure 1.3: The configuration of four typical tube array arrangements and definition of the pitch for each of them.

ders in tandem, despite the higher upstream turbulence level generated in the downstream rows due to the turbulent wakes of the upstream rows. The classifications due to Zdravkovich (1977) and Ziada and Oengören (1993) for the subcritical Reynolds number range $3\times10^3 \leq Re_{gap} \leq 12\times10^3$ can be approximately described as follows:

- Small tube spacings $1 \leq S_L/D \leq 1.75$: The free shear layer that separates from the upstream cylinder does not reattach on the downstream tube. The vortex street formed behind the downstream rows is formed by the shear layer from the upstream one.

- Intermediate tube spacings $1.75 \leq S_L/D \leq 2.7$: The shear layer from the upstream tube reattaches on the downstream one, and the vorticity shedding is generated by the global jet mode [3] and persists over the whole depth of the bundle.

- Large tube spacings $2.7 < S_L/D$: The separated shear layer from the upstream tube rolls up and forms vortices in front of the downstream tube, the vorticity shedding can occur either in global jet mode or a local wake mode [4] as described by Ziada and Oengören (1993).

Nevertheless, the flow regime classification of the inline tube bundle also has to take into account the effect of Reynolds number. At Reynolds number 1.57×10^5, Okajima (1979) and Arie et al. (1983) found that a critical spacing of 3.8D lies in between the *vortex reattachement regime* and the *two vortex streets regime.* At Reynolds number around 1,000, Jester and Kallinderis (2003) found that for two cylinders in tandem with spacing 2.15D, there is a bistable transition range between the *vortex reattachement regime* and the *two vortex streets regime.* Konstantinidis et al. (2000) showed that no vortex shedding occurred behind the first cylinder in a tube bundle with streamwise tube spacings 2.1D at Reynolds number around $Re_{gap} = 3,400$. The vortex shedding at a constant frequency, however, was evident and persisted in the downstream rows. The vortex shedding patterns can be indentified indirectly through heat transfer measurements. For example, Murray (1993) measured the single-phase heat transfer over an inline tube bundle with

[3] "Global jet mode" refers to the vortex shedding mechanism that occurs with a distinct peak of vortex shedding frequency. There is a well-defined phase relation between the adjacent wakes.

[4] "Local wake mode" refers to the vortex shedding mechanism where the flow activities in adjacent wakes are not correlated. The alternate vortex shedding behind a cylinder does not seem to have any phase relationship with the wakes of neighouring tubes of the same row.

Classification of cylinder arrays		
Spacing	Inline	Normal Triangle
Small	$1 < S_L/D < 1.75$	$P/D \approx 1.61$
Intermediate	$1.75 < S_L/D < 2.7$	$P/D \approx 2.08$
Large	$2.7 < S_L/D$	$P/D \approx 3.41$

Table 1.1: Classification of the cylinder arrays based on tube spacings after Ziada and Oengören (1993) and Oengören and Ziada (1998) for inline and normal triangle tube arrays respectively.

pitch-diameter ratio 1.75 at Reynolds number $Re_{gap} = 6,000$. Murray found that the heat transfer rate in the front part of the third row is still as low as the one of the second cylinder suggesting that the separated shear layers from the second cylinder reattached to the front of the third cylinder forming two counter-rotating vortices occuping the gap between the second and third cylinders. In this thesis, computations for inline tube bundle are only performed for the arrangement used by Konstantinidis et al. (2000) which is an example of a bundle with an intermediate range of tube spacings used in power generation industry. It aims at better understanding and quantification of not only the velocity patterns, vortex shedding frequencies and their strength but also the heat transfer rate over different rows.

The classification of staggered arrays is more difficult to make because of the more complicated flow patterns. Aiba et al. (1982*b*) have shown that closely spaced staggered tube arrays are important for the design of compact heat exchangers. They observed fairly different heat transfer performance between two tube banks with spacings ($S_L/D = 1.2$; $S_T/D = 1.2$) and ($S_L/D = 1.6$; $S_T/D = 1.6$). One rough classification was also made by Oengören and Ziada (1998) for normal triangle arrays as shown in Table 1.1. Another factor that makes the classification more difficult is that the flow around tube arrays with different ranges of spacings may share common characteristics. Weaver et al. (1993) investigated rotated square arrays with spacings in the range $1.31 \leq P/D \leq 2.83$. They found that two vortex shedding frequencies coexist in the front rows. As the pitch-to-diameter ratio decreases, the frequencies fall within the range of $0.42 \leq St_1 \leq 1.85$ and $0.32 \leq St_2 \leq 1.2$ where St_1 and St_2 represent the Strouhal number based on the high and the low frequency respectively. Both are defined using the upstream velocity.

1.1.2 Heat transfer around tube bundles

Turbulent flow inside the inline tube bundle, as a whole, depends on the boundary layer seperation effects and interactions of cylinder wakes. As a consequence, heat tranfer is a function of Reynolds number, tube spacings (S_L and S_T), inlet flow conditions (e.g. freestream turbulence and pulsating flow (Sanitjai and Goldstein, 2001)) and location in the bundle. A single Strouhal frequency is often associated with vortex shedding (cf. Ziada and Oengören (1992, 1993) and Konstantinidis et al. (2000)) for the intermediate spacing inline tube bundles. On the other hand, two or three dominant frequencies could exist in the intermediate spacing staggered tube arrays (cf. Weaver et al. (1993), Polak and Weaver (1995) and Oengören and Ziada (1998)). The turbulence fluctuation level often reaches the maximum level at the 3rd-5th row and the heat transfer level is stabilised in the downstream tubes.

Aiba et al. (1982a,b) measured the pressure distribution and heat transfer around one cylinder of each row under the condition of constant heat flux for inline and staggered tube banks respectively (the largest spacings were $S_L/D = 1.6$; $S_T/D = 1.6$). The heat transfer profile shape is independent of the Reynolds number in the inline tube bank which is due to the small longitudinal spacings used in their configurations. The maximum heat transfer rate appeared at the third cylinder in the staggered tube array due to the high approaching mean velocity to the front part of the third cylinder along with its high turbulence intensity. The heat transfer rate of the first row cylinder is lower by about 45 to 50% compared to that of the other cylinders despite that nearly identical heat transfer rates exist for all the downstream rows. Murray and Fitzpatrick (1991) and Murray (1993) studied the heat transfer around the first three cylinders inside both inline and staggered tube arrays for gas-solid suspension flow under the condition of constant temperature at the cylinder wall. The circumferentially time-averaged Nusselt numbers for single-phase flow are also reported together for comparison.

Furthermore, pulsation could alter the flow structures and hence modify the heat transfer rate azimuthally around the first and second row cylinders. For instance, VandenBerghe et al. (1983) found that the pulsating incoming flow condition increased the heat transfer on the front part of the second row tube. Konstantinidis et al. (2000) found that pulsation could lead to alternate vortex shedding behind the first cylinder, which is associated with higher rate of fluid mixing particularly in front of the second cylinder. Thus the heat transfer rate in front the second cylinder is expected to increase.

This chapter is organized as follows. The experimental findings of turbulent

flow characteristics and heat transfer around a single circular cylinder as well as around inline and staggered tube bundles are generally surveyed in the first section of this chapter. Attention was paid to important issues, such as, vortex shedding, recirculation bubble zone size and regime classifications. In the second section of this chapter, a survey of the existing LES simulations about flow around a single circular cylinder and tube arrays is conducted.

1.2 Turbulent Flow Characteristics and Heat Transfer Around a Single Circular Cylinder

1.2.1 Steady approaching flow

Ideally, the uniform cross-flow over a fixed circular cylinder is a function only of the Reynolds number ($Re_D = U_\infty D/\nu$). In practice, the cross-flow is often also affected by inlet flow conditions (for example, turbulent intensity), blockage ratio, cylinder aspect ratio and cylinder vibrations. In an excellent review, Williamson (1996) reported a classification of the different flow regimes based on a plot of base suction coefficient against the Reynolds number. Table 1.2 summarises the different flow regimes due to different states of flow and transition to turbulence after Zdravkovich (1997). This thesis is focused only on the subcritical flow regime in which transition to turbulence takes place in the separating shear layers.

The flow around a circular cylinder has become the canonical problem of the flow around bluff bodies, presenting a very rich dynamic behaviour in spite of its simple geometric configuration. In the range of subcritical Reynolds numbers, the flow is a combination of laminar boundary layer, separating shear layers, small-scale turbulent wake and large-scale Kármán street vortices.

At Reynolds number about $Re_D = 1,500$, Bloor (1964) studied the instability of the shear layers separating from the cylinder, which results in the formation of secondary vortices. Wei and Smith (1986) observed the creation of high-frequency small-scale turbulent vortices as the final stage of the transition process held within the separated shear layers. These Kelvin-Helmholz vortices distort to periodic cellular structures that align themselves in the streamwise direction. Later, Prasad and Williamson (1997) confirmed that these shear layer vortices show up as important ingredients in the near wake. In particular, this Kelvin-Helmholtz instability mechanism also introduces an upstream effect, and such effect has been described by Unal and Rockwell (1988) as an 'upstream wave motion'. In this way of wave

Classification of uniform cross-flow over a circular cylinder		
STATE	REGIME	Re range
LAMINAR	No separation	0 to 4-5
	Closed wake	4-5 to 30-50
	Periodic wake	30-50 to 180-200
TRANSITION IN THE WAKE	Far wake transition	180-200 to 220-250
	Near wake transition	220-250 to 350-400
TRANSITION IN THE SHEAR LAYER (SUBCRITICAL)	Lower	350-400 to $10^3 - 2 \times 10^3$
	Intermediate	$10^3 - 2 \times 10^3$ to $2 \times 10^4 - 4 \times 10^4$
	Upper	$2 \times 10^4 - 4 \times 10^4$ to $10^5 - 2 \times 10^5$
TRANSITION IN BOUNDARY LAYERS (CRITICAL)	Precritical	$10^5 - 2 \times 10^5$ to $3 \times 10^5 - 3.4 \times 10^5$
	Single bubble	$3 - 3.4 \times 10^5$ to $3.8 \times 10^5 - 4 \times 10^5$
	Two bubble	$3.8 \times 10^5 - 4 \times 10^5$ to $5 \times 10^5 - 10^6$
	Supercritical	$5 \times 10^5 - 10^6$ to $3.5 \times 10^6 - 6 \times 10^6$
	Postcritical	$3.5 \times 10^6 - 6 \times 10^6$ to (?)

Table 1.2: Classification of flow regimes around a circular cylinder (after Zdravkovich (1997))

motion, downstream disturbances may also affect the upstream flow therefore creating more challenges for successful computer simulation.

Recently, three dimensional streamwise vortex structures were studied in depth by experimental methods. Norberg (1998) found that the mean spanwise distance between these longitudinal structures, the wavelength λ_z^B, is of the order of one cylinder diameter or slightly lower for a range of Reynolds number from 230 to 21×10^3.

Experimental investigations of heat transfer around a cylinder have concentrated on the measurement of the overall and local heat transfer coefficients, usually under the conditions of constant wall heat flux. The local Nusselt number is obtained by measuring the difference between the local static surface temperature and the bulk flow temperature. Local heat transfer from the cylinder to fluid varies azimuthally (Krall and Eckert, 1973; Scholten and Murray, 1998*b*) due to the laminar boundary layer development, separating shear layer and turbulent wake. The effect of top-bottom wall blockage as well as the aspect ratio are important mainly for the heat transfer in the rear part of the cylinder. For example, Chang and Mills (2004) found that a small aspect ratio can result in an evident increase of the local time-averaged Nusselt number on the rear part of the cylinder. Recently, the fiber-optic Bragg grating sensor technique also made possible to measure accurately the surface fluctuating temperature (Wang et al., 2003).

Norberg (1987) described in detail the effect of low intensity freestream turbulence on the velocity characteristics and pressure distribution in the subcritical regime. Free stream turbulence level also has a significant effect on the local heat transfer around the cylinder at different Reynolds numbers in the same regime. Further experimental investigations can be found in Kondjoyan and Daudin (1995), Scholten and Murray (1998*b*,*c*) and Sanitjai and Goldstein (2001). For instance, the last authors found that the characteristics of subcritical flow with high free stream turbulence appear similar to those of supercritical flow. They also found that the upstream turbulence level has smaller effect on the flow characteristics as the Reynolds number decreases. Gundappa and Diller (1991) found that the freestream turbulence results in a large increase (up to 45%) on the front side of the cylinder as well as a small decrease (up to 6%) on the back side of the cylinder at Reynolds number of 5×10^4.

1.2.2 Pulsating approaching flow

Fluid pulsation occurs in several practical situations, e.g., in flows delivered by reciprocating pumps or systems where surging might occur. It has been shown to enhance mixing (Mackley et al., 1996), heat and mass transfer (Sung et al., 1994; Kikuchi et al., 2000) and also to offer the opportunity for active flow control by tuning the frequency and amplitude of pulsation (Griffin and Hall, 1991; Papadakis and Bergeles, 2001). Pulsating approaching cross-flow at a frequency around twice the natural vortex shedding frequency introduces the phenomenon of vortex shedding lock-on. This phenomenon is accompanied by a number of changes in cylinder body forces and the wake flow and therefore it results in change of heat transfer. Experimental measurements of Barbi et al. (1986), Armstrong et al. (1986, 1987) and Konstantinidis et al. (2003*a*) revealed that lock-on modifies the near wake flow structure and increases the strength of the shed vortices. Also most of these investigations show evidence that lock-on decreases the recirculation length and increases the mean drag coefficient and r.m.s of lift coefficient. Using a flow visualization technique, Barbi et al. (1986) have shown that the vortex formed even closer to the cylinder and the shear layer had bigger amplitude of oscillation in the transverse direction. Therefore, it is generally agreed that vortex shedding lock-on modifies the flow structures leading to shorter recirculation bubble zone and stronger turbulence intensity (Konstantinidis et al., 2003*a*). It is thus expected that external pulsation can provide a means to control the local heat as well as mass transfer around the cylinder. For example, Sung et al. (1994) reported

a systematic study on the effect of different pulsating freqencies and amplitudes over the local mass transfer around a rigid cylinder at Reynolds number 4,150. It was revealed that flow pulsation has little effect on the mass transfer in the attached boundary layer region but is associated with significant increase on the mass transfer in the rear part of the cylinder, after the separation point. The effect of pulsation on the heat transfer decreases with the increase of Reynolds number. Gundappa and Diller (1991) reported that there was no or small increases in heat transfer due to flow pulsation with frequencies around the natural vortex shedding frequency at Reynolds number 5×10^4.

Several investigators have studied the effect of cylinder oscillation on the flow and heat transfer characteristics. Oscillation of the cylinder along the streamwise direction is similar to pulsating approaching flow but not identical. Nevertheless it is mentioned in this section, since it also leads to lock-on effects and similar wake characteristics. Gau et al. (2001) measured the heat transfer around a circular cylinder oscillating in streamwise direction and found the highest heat transfer coefficient when the oscillating frequency is double of the cylinder natural vortex shedding frequency. Gau et al. (1999) measured the heat transfer around a circular cylinder oscillating in the transverse direction. The local mass transfer in both the attached boundary and the rear wake region was affected due to the cylinder vibration. Park and Gharib (2001) showed an increase of heat transfer resulting from the intensification of coherent motions in the wake of a transversely oscillating cylinder.

1.3 Turbulent Flow Characteristics in Inline and Staggered Tube Bundles

Fluid-induced vibration is generally attributed to four excitation mechanisms, namely, turbulent buffeting [5], vortex shedding, acoustic resonance and fluid-elastic instability [6]. Extensive experimental reviews on these subjects can be found in

[5] "Turbulent buffeting", as the name suggests, is due to random pressure fluctuations in the turbulent flow. High levels of broadband turbulence are inevitable in tube bundle structures, and they are desirable from the heat transfer point of view. The turbulent flow field generates a pressure on a cylinder surface which randomly varies in both space and time. Therefore, each tube experiences random buffeting due to broadband turbulence.

[6] "Fluid-elastic instability" is associated with the vibration of tubes. When the incoming flow velocity exceeds a critical value, the motion of the tubes at their natural frequency is coupled with the flow and energy is transferred from the flow to the tubes to increase their vibration amplitudes (Grover and Weaver, 1978*b*,*a*).

Païdoussis (1983), Weaver and Fitzpartick (1988) and Moretti (1993). Vortex shedding (Strouhal periodicity) has received probably most of the research interest. It manifests itself as a narrow peak in the velocity and pressure spectra with a frequency that varies linearly with the flow velocity giving a constant Strouhal number over a range of Reynolds numbers. Owen (1965) attributed the widely observed resonant phenomenon to a peak in the turbulence spectrum, the frequency of which was dependent on the tube spacing and Reynolds number. He also derived a semi-empirical formula to predict the frequency of this peak. Païdoussis (1981) pointed out that other predictive formulae, which were based on the vortex shedding concept, had good agreement with Owen's model. In other words, the uncertainty of the exact nature of Strouhal periodicity still existed even at the time of the review of Paidoussis (1981). It was not until 1985, when Weaver and Abd-Rabbo (1985) performed a flow-visulization study in a fully-flexible inline tube array with pitch-to-diameter ratio of 1.5 that the periodic vortex shedding was first observed in a tube bundle.

Ziada and Oengören (1992, 1993) and Konstantinidis et al. (2000) have studied the vortex shedding phenomena inside inline tube arrays extensively. Konstantinidis et al. also studied the effect of pulsation when $f_p \approx 2f_n$ where f_p is the frequency of the external pulsation and f_n is the natural vortex shedding frequency. In a later paper, Konstantinidis et al. (2003*b*) found a symmetrical vortex formation mode when $f_p \approx 3f_n$ in the wake of the first row cylinder at Reynolds number $Re_{gap} = 1500$. Ziada and Oengören (1993) also performed a thorough flow visulization study about the asymmetric wake of the first three cylinder rows in an inline tube bundle with spacings $S_L = 3.25D$ and $S_T = 3.75D$ in the presence of low or high level of upstream turbulence. The flow visualization was made in a water channel at a range of Reynolds number $880 \leq Re_{gap} \leq 7,040$. When the upstream turbulence level was low, the global jet mode dominated. The flow structure was formed in the same mechanism as the case of intermediate tube spacings (Ziada and Oengören, 1992), i.e. the vortices formed symmetrically at both sides of the flow lanes and anti-symmetrically in the tube wakes. The vorticity shedding excitation switched to local wake mode when the upstream turbulence level was increased. Neither symmetric or anti-symmetric flow structures were found during the local wake mode oscillation, due to the lack of coherence between the flow activities in neighbouring wakes. They also found that the transition from the vorticity shedding at the second mode excitation to the broad band turbulence buffeting excitation, i.e. random fluctuating forcing, occurred deeper in the bundle

between the fifth and the seventh row.

Considering that equipment like nuclear steam generators often have large amortization periods of 20 to 40 years as mentioned by Weaver and Fitzpartick (1988), turbulence buffeting can be of significant importance in the design of tube bundles. Moretti (1993) commented that the broad band turbulence buffeting is largely one way, from fluid to solid and can incite small amplitude vibrations. In the absence of other resources of excitation, the vibrations rarely built up to large amplitudes. However, Price et al. (1995) pointed out that turbulence buffeting may be important in the sense that the small amplitude vibrations can initiate other excitation mechanisms, which can induce higher amplitude vibrations.

Flow across a staggered tube bundle is more complicated than the flow across an inline tube bundle. Fundamental differences exist in the mechanisms involved, i.e. jet instability in inline arrays and vortex shedding in staggered arrays. The vorticity in the jet shear layers in inline arrays rolls up and grows in size and strength along successive downstream tube rows (Ziada and Oengören, 1992, 1993). The feedback mechanism of the alternate vortex formation synchronizes the vorticity shedding in the successive rows to be 180^o out-of-phase. On the other hand, the vortices shed out from the shear layers in the staggered array are distorted and ultimately dissipated by turbulent buffeting in the turbulence generated by the successive downstream tube rows (Weaver et al., 1993; Polak and Weaver, 1995). Oengören and Ziada (1998) observed three vortex shedding frequencies in the normal triangle tube array. A high frequency component associated with the front rows, a low frequency component generated from the rear rows and a third component resulted from the nonlinear interaction between the high and the low frequencies. Balabani and Yianneskis (1996, 1997) studied in detail the velocity characteristics inside a staggered tube array ($S_L = 1.6D$ and $S_T = 3.6D$) at Reynolds number $Re_{gap} = 12,858$ and estimated the time- and length scales. The measurement data are accessible from the ERCOFTAC database collection (http://cfd.me.umist.ac.uk/ercoftac/). Particularly, Balabani and Yianneskis (1997) found that the shear layer associated with the vortex shedding induces a pseudo-turbulence contribution to the amplitude of rms fluctuations resulting in overestimation of the turbulence levels by up to 50% in some locations. This partly accounts for the large discrepancies between the steady-state predictions of $k - \varepsilon$ model and the measurement values.

In practice, the flow in actual heat exchangers may contain turbulent fluctuations or even disturbances at distinct frequencies, e.g. in flows delivered by

reciprocating pumps. The flow structure dominated by alternate vortex shedding behind the first row cylinder could be altered siginificantly by the external pulsation condition. A complete experimental investigation on the pulsating cross-flows over both inline and staggered tube arrays has been done by Konstantinidis (2001).

Freestream turbulence level has a high impact on the flow chacteristics inside the inline tube bundle and the effect decreases as the subcritical Reynolds number decreases (Ljungkrona et al., 1991; Ziada and Oengören, 1993). However, this effect on the flow over staggered tube bundle is much less significant due to stronger turbulent wake interaction in the front rows (Nishimura et al., 1993).

1.4 Large Eddy Simulation of a Turbulent Cross-Flow over a Single Circular Cylinder

It is evident from the survey in the previous section that although the flow configuration of the single cylinder is simple, it is very rich in fluid dynamic phenomena such as the thin developing laminar boundary layers, separating shear layers, small scales in turbulent wake and shedding of large-scale vortices (see Williamson (1996) for details). During the last decade, many LES calculations were performed for subcritical flow over a circular cylinder at $Re_D = 3900$ mainly due to the availability of the experimental results of Lourenco and Shih (1993) and Ong and Wallace (1996). The calculations have been performed in either structured mesh (Beaudan and Moin, 1994; Mittal and Moin, 1997; Kravchenko and Moin, 2000), or unstructured meshes (Fröhlich et al., 1998; Hasen and Long, 2002). Beaudan and Moin (1994) carried out calculations using the finite difference method, while several upwind schemes were used to discretize the derivative of convective flux.

Some researchers have attempted to resolve the small-scale physics using 2D simulations. But as concluded by Cantwell and Coles (1983), the production of turbulence is a 3D vortex stretching phenomenon at the intermediate scales of the global spectrum. Breuer (1998) found that the 2D simulation leads to severly short recirculation bubble zone. The large deviations between the 2D and 3D results suggested that three-dimensional structures consisting of pairs of counter-rotating streamwise vortices strongly influence the near-wake of the flow. Thus 2D LES calculations of flow around bluff bodies should be abandoned. Kravchenko and Moin (2000) also found that insufficient grid resolution can cause early transition in the shear layers separating from the cylinder which leads to inaccurate predictions of the near-wake statistics. It was indicated that a careful grid-independent study

should be performed for this particular subcritical flow case.

Mittal (1995, 1996) and Mittal and Moin (1997) concluded that high-order upwind-biased schemes were unsuitable for use in LES, due to significant numerical dissipation. The central differencing scheme damps less the higher wavenumbers of the energy spectra compared to higher-order upwind-biased schemes, and it was proved to give better results than upwind-biased schemes in the downstream wake region. Breuer (1998) tested several schemes for the nonlinear convective fluxes interpolation. He found that the 2nd order central difference scheme (CDS) and 4th order CDS are the most suitable options for LES. He concluded that low numerical dissipation produced by a scheme is more crucial for LES than its formal accuracy. As discussed by Laurence (2002) 2nd order central schemes are preferable to even higher-order hybrid scheme, presumably because dispersive errors cancel out through the statistical averaging process, whereas even-order errors introduce a systematic bias. Jordan (1999) performed LES in a generalized curvilinear coordinate system, and found that direct filtering of the transformed equations (in gereralized coordinates) in the computational space is better than either filtering the transformed equations in real space or filtering the untransformed equations in Cartesian space. Recently, Piomelli et al. (2003) performed a LES using the Lagrangian dynamic model (Meneveau et al., 1996) based on the immersed boundary method (Balaras, 2004) for finite-difference Cartesian grids applied to the cylinder.

Both Breuer (1998) and Jordan (2003) used O-type mesh in curvilinear coordinates. When comparisons were made between predictions and experiments for the mean and r.m.s. streamwise velocity transverse to the wake centerline in the near wake region, both of them over-predicted the mean and r.m.s streamwise velocity within the free shear layers due to the insufficient resolution locally within the shear layer of the O-type mesh. Breuer (1998) also proved that the dynamic Smagorinsky model gave better results than the standard Smagorinsky model using 2nd order central difference scheme. However, Jordan (2001, 2003) pointed out that the complete inability of the dynamic Smagorinsky model to capture real shear stress despite that physically there is a strong correlation between the regions of peak turbulent energy production and peak Reynolds shear stress. Jordan (2003) also argued that one can rely on the inherent dissipative element of a high-resolution upwind approximation for the resolved scales to mimic the spurious oscillations introduced by the eddy-viscosity model near cutoff. Nevertheless, in the very near wake region, the contribution of vortex shedding is very important, that is why the subgrid scale model may not be as crucial. Further downstream

in the wake, it becomes more important because the effect of vortex shedding is reduced. However, Jordan also found that low-resolution in the spanwise direction could lead to under-prediction of mean pressures in the vortex formation region and consequently result in an over-predicted mean drag coefficient although the Strouhal number could be correctly predicted.

None of the LES calculations mentioned above take into account the impact of inlet flow condition or report heat transfer predictions. Inlet flow conditions have been shown to have great impact on the wake flow structure. Inevitably, all experiments virtually contain low- or high-level freestream turbulence. Scholten and Murray (1998*b*,*c*) give much information on the effects of inlet turbulence level. Prescribing time-dependent turbulent inlet flow conditions at the upstream boundary is one important and challenging task (Lund et al., 1998). On the other hand, superimposing a small amplitude sinusoidal wave on the uniform mean bulk flow can be done in a straightforward manner in CFD. As confirmed by Konstantinidis et al. (2003*a*) and Sung et al. (1994), the vortex shedding lock-on leads to a shorter vortex formation length and higher turbulence intensity and stronger heat transfer in the recirculation bubble zone. On the contrary, the numerical simulation of Hall and Griffin (1993) found longer vortex formation length due to lock-on. The reason for this contradiction is not clear, but probably is due to the different mechanisms of vortex formation and shedding at low Reynolds numbers (less than $Re_D = 350$).

Recently Tiwari et al. (2003) performed a very coarse 3D finite-volume simulation of the heat transfer around a circular cylinder at Reynolds numbers 1,000 and 1,400 confined in a rectangular channel. Only 78,000 cells were used in their simulation which were insufficient to model the cylinder wall boundary layer. The small aspect ratio (see the experimental investigation by Chang and Mills (2004) about the influence of the aspect ratio on heat transfer) and large blockage ratio have great influence on the cylinder wake size and structure. Thus the interaction between channel wall effect and cylinder wake makes the simulation results difficult to interpret. Their results are not quantitatively compared with measurements, and thus their accuracy can not be assessed.

In summary, the subcritical flow across a cylinder remains a very challenging problem for LES models. Many LES calculations have been performed to predict the flow field. However, simulations of convective heat transfer are very rare. Also, to the best of the author's knowledge, LES has not been performed to predict the pulsated crossflow and heat transfer around a cylinder for subcritical Reynolds

numbers, although Liu and Fu (2002) performed a 2D simulation of a circular cylinder oscillating in the streamwise direction at a maximum Reynolds number 1,000 using the finite-volume method and Tutar and Holdo (2000) performed a 3D simulation of a circular cylinder oscillating in the transverse direction at a Reynolds number 2.4×10^4 using finite element method.

1.5 LES of a Turbulent Cross-Flow over Tube Arrays

The design for tube bundles is still based on empirical correlations between heat transfer and pressure drop (Kakac and Liu, 1997). There is no sound theoretical base to verify their accuracy. Turbulence in tube bundles consists of chaotic motions and very few complete solutions have been presented for large Reynolds numbers because of the complex turbulence characteristics (transitional effects and vortex shedding, etc) and the expensive computing cost. Most numerical methods at present solve the Reynolds Averaged Navier-Stokes[7] (RANS) equations in combination with a closure model for the Reynolds stresses. The cross-flow over tube bundles was considered for the ERCOFTAC workshop on turbulence modelling in UMIST in 1993 and one year later in Lisbon. RANS simulations, using the standard $k-\varepsilon$ model and Reynolds stress transport models (RSTM) were found to fail to reproduce reliable Reynolds stress profiles. Watterson et al. (1999) performed quasi- three-dimensional finite-volume calculation using the $k-\varepsilon$ model. They found that the mean velocity profiles agreed well with the measurement data despite the big discrepancy between the prediction and measurement of $\overline{v'v'}$. Bouris and Bergeles (1997) used the standard k-ϵ model to calculate the effect of deposit formation on heat transfer rates in a staggered tube bundle arrangement. A finite volume approach in a collocated orthogonal curvilinear grid system was used. Neumann conditions were employed at symmetry planes and wall functions were used at the walls. Two years later, Bouris and Bergeles (1999) reported a two-dimensional simulation of a subcriticial flow in a staggered tube bundle arrrangement. They used a subgrid scale model on the collocated orthogonal curvilinear grid. This model was strongly similar to the standard Smagorinsky model. The convection terms were discretised using the bounded second order upwind scheme. A first order fully implicit Euler scheme was used for discretisation in time. For the

[7]Reynolds averaging is based on the idea of decomposing the flow into a mean and fluctuating parts; a detailed introduction will be given in chapter 2.

discretisation of the diffusion terms the central difference scheme was used. They compared their results with the LDA measurements of Balabani and Yianneskis (1996). The simulated vortex shedding frequency agreed well with the experimental result. However, discrepancies were found in mean velocity profiles in the recirculation zones. They claimed that the discrepancies were mainly due to the fact that the subcritical flow was naturally three-dimensional. The subgrid scale model was also shown to be more suitable than the standard k-ϵ model. It should be noted that the correct prediction of turbulence levels is vital for trustworthy heat transfer predictions. Furthermore, steady RANS models cannot predict the power spectrum of the cross-flow over tube bundles, that is related to the very interesting vorticity shedding phenomenon.

Nowadays, discussion is often made on whether LES will be a reliable and real tool for industrial flows in time of one or more decades, and whether LES can replace RANS in the near future due to Moore's Law [8]. In the past few years, LES has been applied in more and more practical applications (Moin, 2002). However, only very few LES studies of the turbulent flow across tube bundles exist in the literature, and most of them are performed in two dimensions. Hassan and Ibrahim (1997) reported LES calculations of inline tube bundles with the standard Smagorinsky model. Two pitch-to-diameter ratios, 1.4 and 1.5, were examined. The results were in generally acceptable agreement with the experimental data. They attributed the discrepancies simply to the three-dimensional nature of the flow. Barsamian and Hassan (1997) performed similar calculations using the standard Smagorinsky model for both inline and staggered tube bundles. The same discrepancies appeared because the 2D simulation can not accurately simulate 3D flow. Two years later, Hassan and Barsamian (1999) performed the simulation of inline tube bundle using the Dynamic Subgrid Scale (DSGS) model but the results were not improved much. Bouris and Bergeles (1999) also performed two-dimensional LES for the staggered tube bundle measured by Balabani and Yianneskis (1996). Since turbulence is inherently three dimensional, 2D LES cannot capture fully the turbulence phenomena correctly. For instance, the three-dimensional patterns of streamwise vorticity in the turbulent near-wake of a single cylinder have a lifetime of the order of half the period of the large-scale Karman vortices and an order of magnitude larger than the period of the small-scale Kelvin-Helmholtz vortices initially formed in the separating shear layer and

[8] Over a quarter of a century ago, Intel co-founder Gordon Moore observed that the number of transistors on a given piece of silicon would double every couple of years.

thus can not be neglected. The streamwise vortices also have a constant spanwise wavelength (λ_z) which is approximately equal to the cylinder diameter (Lin et al., 1995). Rollet-Miet et al. (1999) pointed out the superiority of 3D LES predictions because LES is better suited to flows where the size of the eddies (integral length scale of the turbulence) is comparable to the size of the obstacles of the flow. Alternatively, Sweeney and Meskell (2003) simulated the flow through a normal triangular array with pitch ratio 1.6 at Reynolds number 2,200 using a discrete vortex method and predicted accurately the vortex shedding Strouhal numbers. This method can be very fast, however, their simulation was also performed in two dimensions. A more detailed comparison with existing experimental results is needed to assess the accuracy of the discrete vortex method.

Recently fully three-dimensional Large Eddy Simulation calculations have appeared as a suitable tool to study the separation, transition and the large, unsteady, turbulent structures. Benhamadouche and Laurence (2003) recently performed both LES and a transient Reynolds Stress Transport Model (RSTM) simulations using the finite-volume method for the staggered tube bundle with two levels of grid refinement. They found that the 2D unsteady RSTM produced a severe over-prediction of the total Reynolds stresses. On the other hand, LES produced satisfactory results even on the coarse 3D mesh while the type of subgrid scale models (the standard or the dynamic Smagorinsky model) does not affect much the results. However, they only focused on a subdomain surrounding a tube in the fifth row where the flow appeared to have reached a periodic state. Less attention was paid on the vortex shedding phenomena, perhaps due to the small spacing between the cylinders ($S_L \approx 1D$, $S_T \approx 2D$).

Experimental investigations have confirmed different interesting vortex shedding patterns in larger spaced inline and staggered tube arrays. A numerical simulation of the laminar unsteady fluid flow in inline and staggered tube bundles with a few rows had been performed by Beale and Spalding (1999) only at a low Reynolds number ($Re_{bulk} = 300$). The vortex shedding was reported along with the lift and drag forces. Hassan and Barsamian (2004) performed three-dimensional LES of a staggered tube bundle with pitch-to-diameter ratio 1.58 on a curvilinear coordinate. The turbulent flow developed in depth of five rows. The wall modelling took into account the effect of ejection and sweep[9] (Hassan and Barsamian,

[9]Kline et al. (1967) have shown an organized trend among the elongated streaks in the region very near to the wall of the turbulent boundary layer. Streaks containing low-momentum fluid was found to rise slowly, and break up in a process called 'bursting'. 'Ejection' is the motion of the low-momentum fluid away from the wall and 'sweep' is the motion of high-momentum fluid

2001) was used with the dynamic Smagorinsky sgs model. Good agreement between prediction and measurement for $\overline{v'v'}$ were obtained. The improvement over the predictions of turbulence quantities can also be clearly seen compared to the prediction of Watterson et al. (1999). However, the important vortex shedding parameters, for example the dominant vortex shedding frequencies and recirculation bubble length behind each cylinder are not clearly reported, because the cylinders are closely arranged.

The simulations of turbulent flows across inline and staggered tube bundles in this thesis aim to provide information on mean velocity, Reynolds stresses, vortex shedding frequency of each cylinder's shear layer as well as lift and drag coefficients of each cylinder. These results are compared to existing experimental results and provide new information for the design of heat exchangers.

1.6 LES of Forced Convection Heat Transfer around Cylinders

Turbulent flow is characterised by chaotic motion features. Heat transfer is strongly correlated with the velocity fluctuations and is affected by the physical transport processes of turbulence. Reynolds (1976) pointed out that there must exist an intimate relation between the local shearing stress and the local heat flux since both depend on the same basic mechanism.

The computational accuracy of turbulent heat transfer predictions still heavily relies on the modelling accuracy of turbulence correlations. The computational results presented in this thesis about the turbulent convective heat transfer around tube bundles are particularly novel. The main reason is that the fully 3D turbulence modelling for tube bundles is still in the preliminary stage, and there are few highly-accurate experimental measurements for the intermediate-spacing inline and staggered tube arrays considered in this thesis. Most of computational works still aim at improving the predictions of the flow field, without paying much attention to heat tranfer.

Two types of boundary conditions, namely, constant temperature and constant heat flux wall are widely used for the simulations of the heat transfer across tube arrays, in order to match the different measurement conditions. Tiselj et al. (2001) tested both boundary conditions in a direct numerical simulation for a turbulent

towards the wall.

channel flow. They found that the mean temperature profile does not depend on the type of wall boundary condition. Furthermore, the temperature rms fluctuations were found to attain a non-zero value on the wall for constant heat flux boundary condition. In contrast, the constant temperature boundary condition gave a zero value on the wall as expected. The correlation between the temperature and streamwise velocity was found to be weaker for the constant heat flux condition. Karniadakis et al. (1986) and Karniadakis (1988) performed DNS calculations of the convective heat transfer of a circular cylinder in a laminar crossflow at Reynolds numbers of 100 and 200. Constant temperature and constant heat flux wall boundary conditions were used. It can be shown that the mean Nusselt number profiles in the wake region are different for these two boundary conditions. Buyruk et al. (1998) performed a numerical and experimental study of the flow and heat transfer around a circular cylinder at maximum Reynolds number 390. The heat transfer distribution in the rear of the cylinder was not accurately predicted because of the difficulty of predicting accurately the separation point. Gowda et al. (1998) have simulated the heat transfer past inline tube bundles at Reynolds number 100 and Prandtl number of 0.7. Two pitch-to-diameter ratios were examined, and a higher pressure drop across the closely-spaced tube bundle was found. The decrease in the values of averaged Nusselt numbers was found to be dependent on the pitch-to-diameter ratio and were higher for the closely-spaced tube bundle. Papadakis and Bergeles (2001) simulated the convective heat transfer around a single cylinder at low Reynolds number under different pulsating conditions. They found that the vortex shedding lock-on can enhance heat transfer.

Mathey et al. (1999) simulated the convective heat transfer over a wall-mounted matrix of cubes using LES (both Smagorinsky and dynamic SGS models were tested). Structured collocated finite-volume grids were used. Both LES models did not improve much over the results obtained with no subgrid model. They also concluded that improving the SGS heat-flux model is not expected to improve the heat transfer distribution. This work is also included in this section, although it does not refer to circular cylinders, because of the information it provides on the effect of subgrid scale models and also because the same numerical methodology is used with the present study.

In summary, the simplest eddy-diffusivity type SGS heat flux model has not been employed in simulating the turbulent heat transfer around either an inline or a staggered tube bundle. Information on the local time-averaged Nusselt number

distribution around each cylinder in the tube arrays as well as in the temperature profiles in different locations inside the bundles is still very scarce in literature.

1.7 Major Findings of This Survey

The main findings of the preceding literature review can be summarised as follows:

- The flow and heat transfer characteristics around a circular cylinder at the subcritical flow regime have been studied extensively using experimental methodologies. Recently, there is a growing number of Large Eddy Simulation calculations performed for the cross-flow over a single cylinder. The majority of these used structured grids in curvilinear coordinates and focus mainly on the flow field.

- Most of these 3D LES simulations could predict correctly the vortex shedding Strouhal number. However, accurate resolution of the turbulent wake requires sufficient grid resolution as well as higher-order non-dissipative numerical schemes. The grid cells near the cylinder body typically have aspect ratios much higher than those further downstream. Low-order differencing schemes under-resolve the inertial subrange in the spanwise direction leading to under-prediction of mean pressures in the vortex formation region and consequently the mean drag coefficient is usually over-predicted.

- For a staggered tube bundle, RANS models generally fail to predict accurately the Reynolds stresses, although the prediction of the mean profiles is more accurate. 2D unsteady RSTM produced a severe over-prediction of the total Reynolds stresses.

- There are a few fully 3D LES calculations for a closely spaced staggered tube array. The results obtained are satisfactory in terms of industrial interests even using a fairly coarse mesh. To the best of the author's knowledge, fully 3D LES calculations of the turbulent flow over a number of rows of inline tube array has not yet appeared in the literature.

- Vortex shedding and turbulent buffeting inside an array of rigid cylinders are still not well understood, although these are important mechanisms that can excite flow-induced vibrations.

- Experimental investigations found that the effect of pulsation on the vortex formation kinematics and heat transfer in the rear part of the cylinder is significant. LES calculations that take into account the effect of inlet pulsating flow on the near wake flow structures, are not available for a single circular cylinder, let alone for an inline or a staggered tube array.

- LES investigations about the heat transfer around a single cylinder are very few. Fully 3D LES computations of heat transfer at subcritical Reynolds numbers are even fewer in the literature. The effect of variation of inlet frequency on heat transfer has still not been investigated via computer simulation.

- Information about pressure distribution, lift and drag forces around cylinders in the tube array is still very scarce in the existing literature.

- To the best of the author's knowledge, detailed numerical simulations of heat transfer for tube arrays have not appeared so far in the literature.

1.8 Objectives

The objectives of this thesis are:

- to assess the suitability and accuracy of the LES technique in modelling the turbulent cross-flow and heat transfer inside both inline and staggered tube arrays, using a Finite-Volume method in collocated unstructured grid arrangement. To this end, a detailed comparison with measurement data is performed.

- to improve the understanding of boundary layer separation, wake interaction and vortex shedding phenomena occurring inside the tube arrays.

- to quantify the vortex-induced forces on the individual rigid cylinders.

- to explore in detail the relationships among velocity and vorticity patterns, pressure distribution and convective heat transfer.

- to clarify the effect of pulsation on the flow and heat transfer over a single cylinder as well as tube arrays by comparing with the steady approaching flow and existing measurement data.

1.9 Thesis Outline

The rest of this thesis is arranged as follows: The second chapter will present the turbulence modelling techniques used for all simulations performed for this thesis. Chapter 3 is devoted to the description of the numerical approaches used to solve the Navier-Stokes equations and the thermal energy equation in detail. The validation cases of the turbulent channel flow as well as cross-flow and heat transfer over a single circular cylinder will be presented in the fourth and fifth chapter respectively. Chapters six and seven describe the numerical results of the LES simulation of cross-flow and heat transfer across inline and staggered tube arrays respectively. Finally, the last chapter will present a summary of the thesis along with the main conclusions and will make some recommendations for future work.

Chapter 2

GOVERNING EQUATIONS OF TURBULENT INCOMPRESSIBLE FLOW AND SUBGRID-SCALE MODELS

2.1 Introduction

Application of the LES technique to an incompressible turbulent flow in complex geometries consists of three main steps. First a filtering operation is performed on the incompressible Navier-Stokes equations to remove the small spatial scales which are less than the filter size. The filtered equations then only contain the subgrid scale (sgs) stress tensor that describes the effect of the unresolved small scales on the resolved scales. In the second step, the sgs stresses are expressed in terms of the resolved scales using models which may or may not contain some adjustable parameters, such as eddy viscosity type sgs model (Smagorinsky, 1963; Germano et al., 1991; Chester et al., 2001), scale-similar model (Sarghini et al., 1999) or mixed model (Meneveau and Katz, 2000). The final step is the numerical solution of the 'closed' large-scale transport equations on a grid fine enough to resolve the large and energy-containing eddies, but still much coarser than the small-scale structures at the Kolmogorov length (at this level, DNS is performed).

Complex geometries, like tube bundles, introduce complexities in all three

steps. For instance, in the first step, construction of a class of commutative and cost-effective discrete nonuniform filters to precisely separate the large and small scales is extremely challenging (see Ghosal and Moin (1995) and Vasilyev et al. (1998) for an understanding of the complexity of this issue). On the other hand, evidence has shown that increasing the filter-grid ratio can effectively reduce both the finite-difference discretization error and the aliasing error[1] (see Ghosal (1996) and Chow and Moin (2003)). However, Ghosal concludes that the magnitude of the aliasing error of the nonlinear term is always larger than the subgrid scale force, while, Chow and Moin argue that increasing the filter-grid ratio can reduce the aliasing error level to be smaller than the subgrid scale force. Nowadays, most of the turbulence research is focused on the second step (see relevant reviews by Lesieur and Metais (1996) and Meneveau and Katz (2000)). The performance of different subgrid scale models can be very difficult to assess, although there is a general agreement that the Germano-type dynamic model is more sensitive to the local state of the flow, and thus predicts more accurately transition or re-laminarization as well as the near-wall behaviour than the constant-cofficient Smagorinsky model. However, sgs modelling is often required to be able to deal with mesh anisotropy for a complex geometry (see Scotti et al. (1993, 1997) for application to anisotropic grids of Smagorinsky model and dynamic model respectively), a priori and a posteriori studies have to be performed in a case-independent manner, while there is extremely limited understanding of the interplay between numerical and modeling errors. A more flexible grid arrangement is generally required for complex geometries where higher-order discretization schemes are difficult to implement. The body-fitted type grid is often used in the commercial packages in collocated arrangement (Muzaferija and Gosman, 1997). The immersed boundary methods have appeared recently for Finite-Volume and Finite-Difference methods and can handle irregular body shapes up to second-order accuracy (Kim et al., 2001; Balaras, 2004).

Among other things, consistency among all steps is also very crucial. Piomelli et al. (1988) provide a discussion on the consistency of all steps, i.e., between the numerical technique, the sgs models and the filter type. Furthermore, different discretization schemes may be required when different type of flows are considered. For instance, Park et al. (2004) showed that there exists an optimal amount of dissipation that minimizes the total discretization error when compact upwind schemes were used for isotropic turbulence and channel flow. However, the central

[1]See Appendix A for details.

difference schemes gave much better results than the optimal compact upwind schemes for the flow over a circular cylinder at subcritical Reynolds numbers.

This chapter will focus on the first two steps. The most common filters will be briefly introduced, followed by a detailed desciption of the sgs turbulence models used throughout this thesis. The final step, the solution approach using the finite-volume method, will be discussed in the next Chapter 3. The rest of this chapter is arranged as follows: firstly, the governing equations will be presented; secondly, the filtering operations for LES will be introduced; and finally the LES sgs models used in this thesis will be described in detail.

2.2 Continuity, Navier-Stokes and energy equations

The starting point for a computational investigation is the identification of the equations that govern the phenomena under study. In this thesis, the fluid is assumed to be Newtonian and incompressible. Body forces are assumed negligible. Under these conditions, the Navier-Stokes equations that govern the motion of the fluid can be written in Cartesian coordinates as follows:

Mass conservation:

$$\frac{\partial(\rho u_i)}{\partial x_i} = 0, \tag{2.1}$$

where u_i denotes velocity in the i direction and ρ is the fluid density.

Newton's second law (momentum equations):

$$\underbrace{\frac{\partial(\rho u_i)}{\partial t}}_{Transient} + \underbrace{\frac{\partial(\rho u_i u_j)}{\partial x_j}}_{Convection} = - \underbrace{\frac{\partial p}{\partial x_i}}_{Pressure} + \underbrace{\frac{\partial}{\partial x_j}\left\{\mu\left(\frac{\partial u_i}{\partial x_j} + \frac{\partial u_j}{\partial x_i}\right)\right\}}_{Viscous}. \tag{2.2}$$

Throughout this thesis, Einstein's summation convention is applied unless stated otherwise.

The passive scalar transport equation for temperature is given by

$$\frac{\partial \Theta}{\partial t} + u_j \frac{\partial \Theta}{\partial x_j} = \alpha \frac{\partial^2 \Theta}{\partial x_j \partial x_j} \tag{2.3}$$

where Θ denotes the scalar variable of temperature and α is its diffusivity.

2.3 Filtering Operations

2.3.1 Time-averaging and space filtering

In CFD, time averaging of the Navier-Stokes equations results in equations that describe the behaviour of time-mean quantities. This is called Reynolds time averaging and is defined by:

$$\langle \Phi \rangle = \underbrace{lim}_{T \to \infty} \frac{1}{2T} \int_{-T}^{T} \Phi(t) dt. \tag{2.4}$$

The general variable Φ is decomposed into a mean part and a fluctuation part as $\Phi = \langle \Phi \rangle + \Phi'$. The resulting set of equations is called the Reynolds-averaged Navier-Stokes equations (RANS). In RANS, if a variable is time averaged twice, the result is the same. In addition, time average of the fluctuating part of the flow is always zero by definition, i.e.

$$\langle \Phi' \rangle = \underbrace{lim}_{T \to \infty} \frac{1}{2T} \int_{-T}^{T} \Phi'(t) dt \equiv 0 \tag{2.5}$$

On the other hand, in LES the space filtering method is used as a means of defining the large-scale part $\widetilde{f(x_i, t)}$ of the variable $f(x_i, t)$. The filtered variables are functions of space and time.

The most general continuous filtering operation in physical space is written as

$$\widetilde{f(x_i, t)} = \int_D G(x_i - x_i^{'}) f(x_i^{'}, t) dx_i^{'} \tag{2.6}$$

where D denotes the entire domain and G is a space-dependent 3-dimensional filter function. The reader can refer to Sagaut (2002) for the different filtering functions. Nevertheless, three filters, namely top-hat, Gaussian and Fourier cut-off filter are the ones most widely used and are presented in Table 2.1.

The top-hat and Gaussian filtering functions are shown in figures 2.1 and 2.2. Generally, if the spatial filtering operator is performed twice, the result will not be the same. As shown in figure 2.3, if a second filtering operation is performed for $\overline{u}_I$, the double filtered value will be

$$\overline{\overline{u}}_I = \frac{1}{\Delta x} \int_{-\Delta x/2}^{\Delta x/2} \overline{u}(\xi) d\xi \cong \frac{1}{\Delta x} \left(\frac{\Delta x}{2} \overline{u}_A + \frac{\Delta x}{2} \overline{u}_B \right) \tag{2.7}$$

where, the second order trapezoidal rule is used to evaluate the integral. $\overline{u}_A$ and

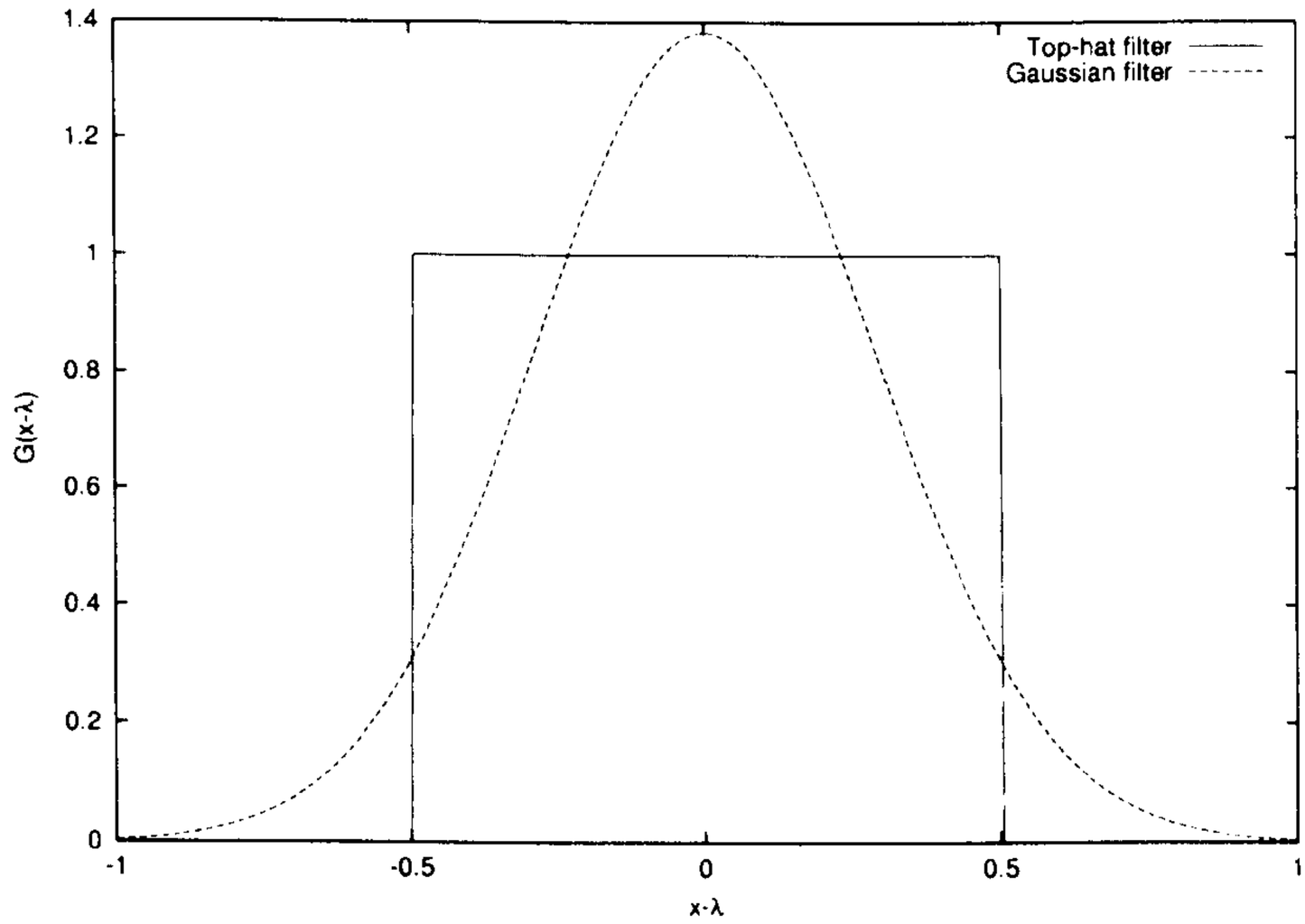

Figure 2.1: Convolution kernel in the physical space of the top-hat and Gaussian filters

Three spatial filters		
Filter name	Filter function $G(x-x')$	Fourier transform $\widehat{G}(k)$
Top-hat	$\begin{cases} \frac{1}{\Delta}, & \text{if } \lvert x-x'\rvert \le \frac{\Delta}{2} \\ 0, & \text{otherwise.} \end{cases}$	$\frac{sin(\Delta k/2)}{\Delta k/2}$
Gaussian	$\left(\frac{6}{\pi\Delta^2}\right)^{1/2} exp\left(\frac{-6\lvert x-x'\rvert^2}{\Delta^2}\right)$	$exp\left(\frac{-(\Delta k)^2}{24}\right)$
Fourier cut-off	$\frac{sin(k_c(x-x'))}{\pi(x-x')}$, $k_c = \frac{\pi}{\Delta}$	$\begin{cases} 1, & \text{if } k \le k_c \\ 0, & \text{otherwise.} \end{cases}$

Table 2.1: Filter functions $G(x-x')$ and their Fourier transforms $\widehat{G}(k)$

$\overline{u}_B$ in figure 2.3 can be estimated by linear interpolation, which eventually gives

$$\overline{\overline{u}}_I = \frac{1}{8}(\overline{u}_{I-1} + 6\overline{u}_I + \overline{u}_{I+1}) \tag{2.8}$$

2.3.2 Energy spectrum

It is well known that the generation of turbulent energy is essentially the result of the action of the large scales. The energy is then transferred in a cascade manner to the smaller and even smaller scales and is eventually dissipated by the smallest eddy structures at Kolmogorov scale (see figure 2.4).

The Kolmogorov scale is the smallest scale in turbulent flow, with length scale, η, velocity scale, υ, and the time scale, τ, given by

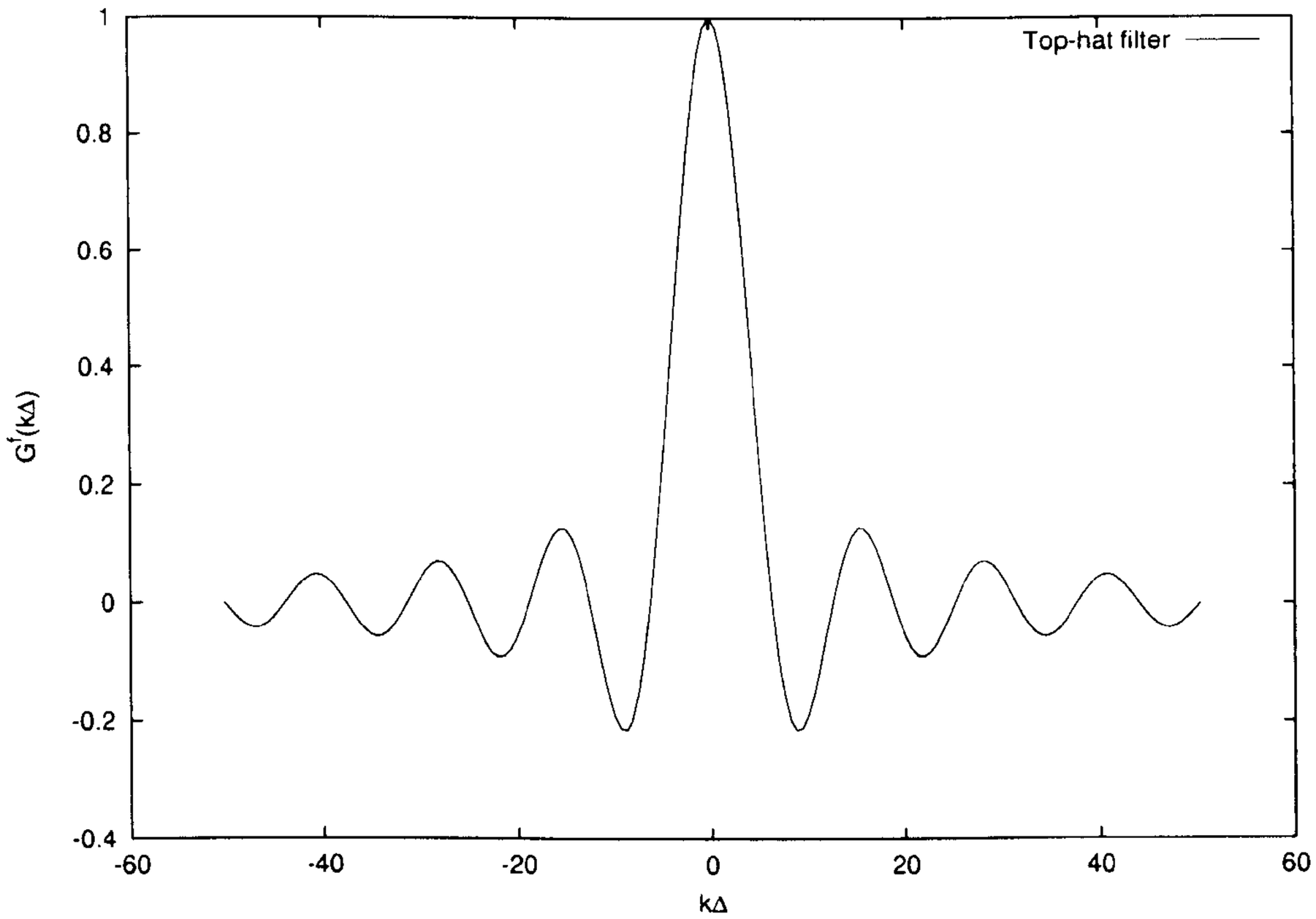

(a) Top-hat filter

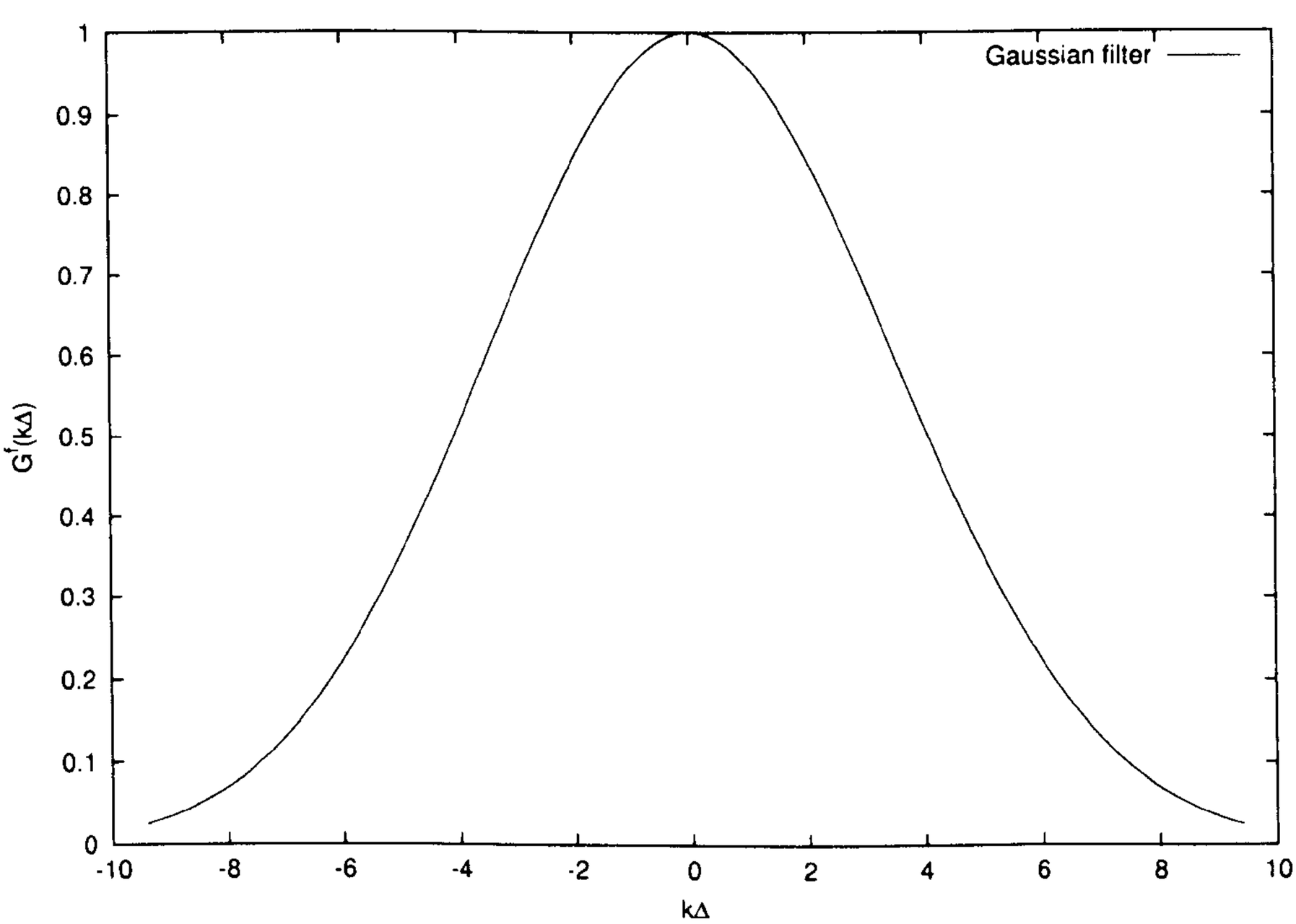

(b) Gaussian filter

Figure 2.2: Associated transfer function of the top-hat and Gaussian filter

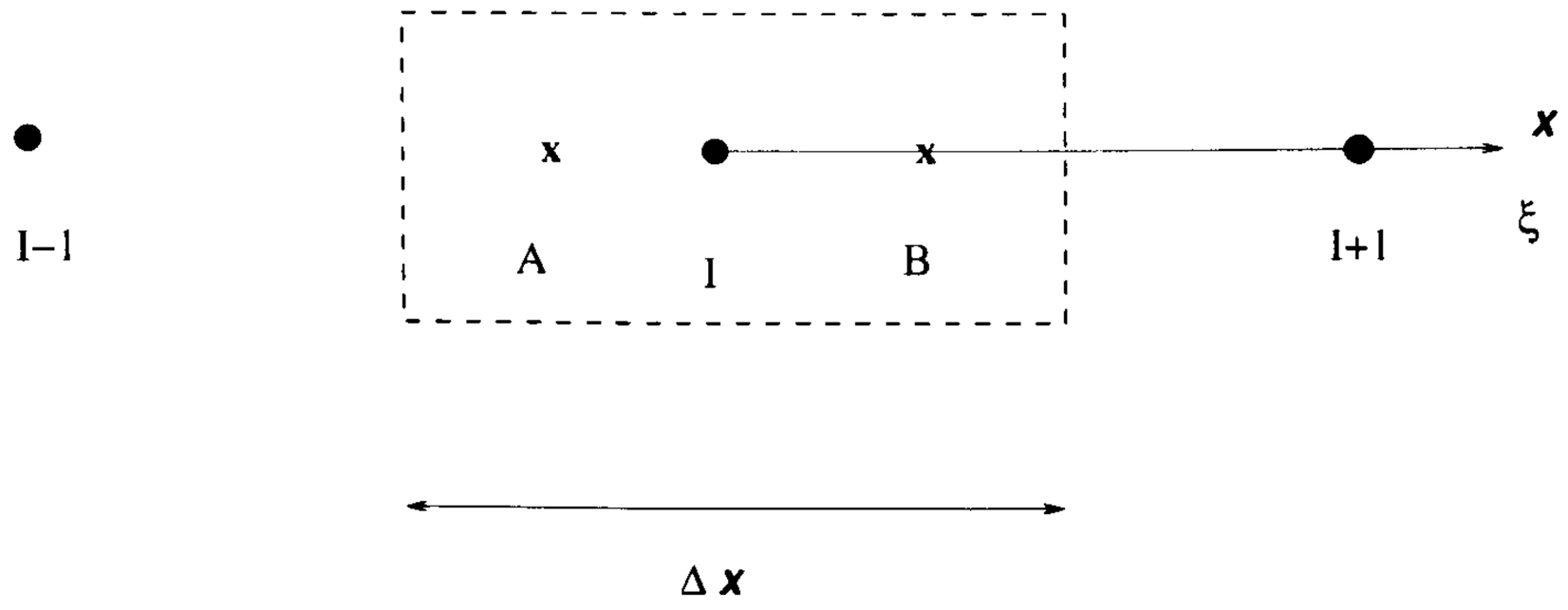

Figure 2.3: Illustration of 1D spatial filtering operation

$$\eta \equiv \left(\nu^3/\varepsilon\right)^{1/4} \quad v \equiv (\nu\varepsilon)^{1/4} \quad \tau \equiv (\nu/\varepsilon)^{1/2} \tag{2.9}$$

In the steady form of the Reynolds Averaged Navier Stokes (RANS) equations, all scales are modelled using the Reynolds time-averaging technique during which the effect of all fluctuations is averaged out and spectra effects are lost. On the other hand, Direct Numerical Simulation (DNS) solves all the scales directly, i.e. from the largest scales to the Kolmogorov length scales. The DNS resolution increases with increasing Reynolds number because the structure of the turbulence becomes finer and finer as the Reynolds number ($Re_l = ul/\nu$) increases. If the largest length scales are of the order of l in a DNS calculation, the required grid number, in one direction, will be proportional to l/η ($= Re_l^{3/4}$). The total grid cell number will be proportional to $Re_l^{9/4}$ which leads to very expensive calculations even for relatively low Reynolds numbers for the current level of computer power. The LES technique lies in between RANS and DNS. The basic philosophy of LES is to explicitly simulate the large-scale motion and only the effect of small scales is modelled. A spatial filtering operation as described is used to decompose the flow variables into large (energy-carrying) scales and small (energy-dissipative) scales. In this way, the Navier-Stokes equations and the thermal energy equation are tranformed to the governing equations for the large-scale momentum and energy transport. Ideally, the filtering cutoff shall be operated at the inertial subrange of the energy spectra. The SGS model itself would neither generate nor destroy energy but only transfer the correct amount of turbulent kinetic energy from the large to the small scales.

LES is usually much cheaper than DNS in computer time. However, the situation is different for the flow in the near wall region, where the decrease of the

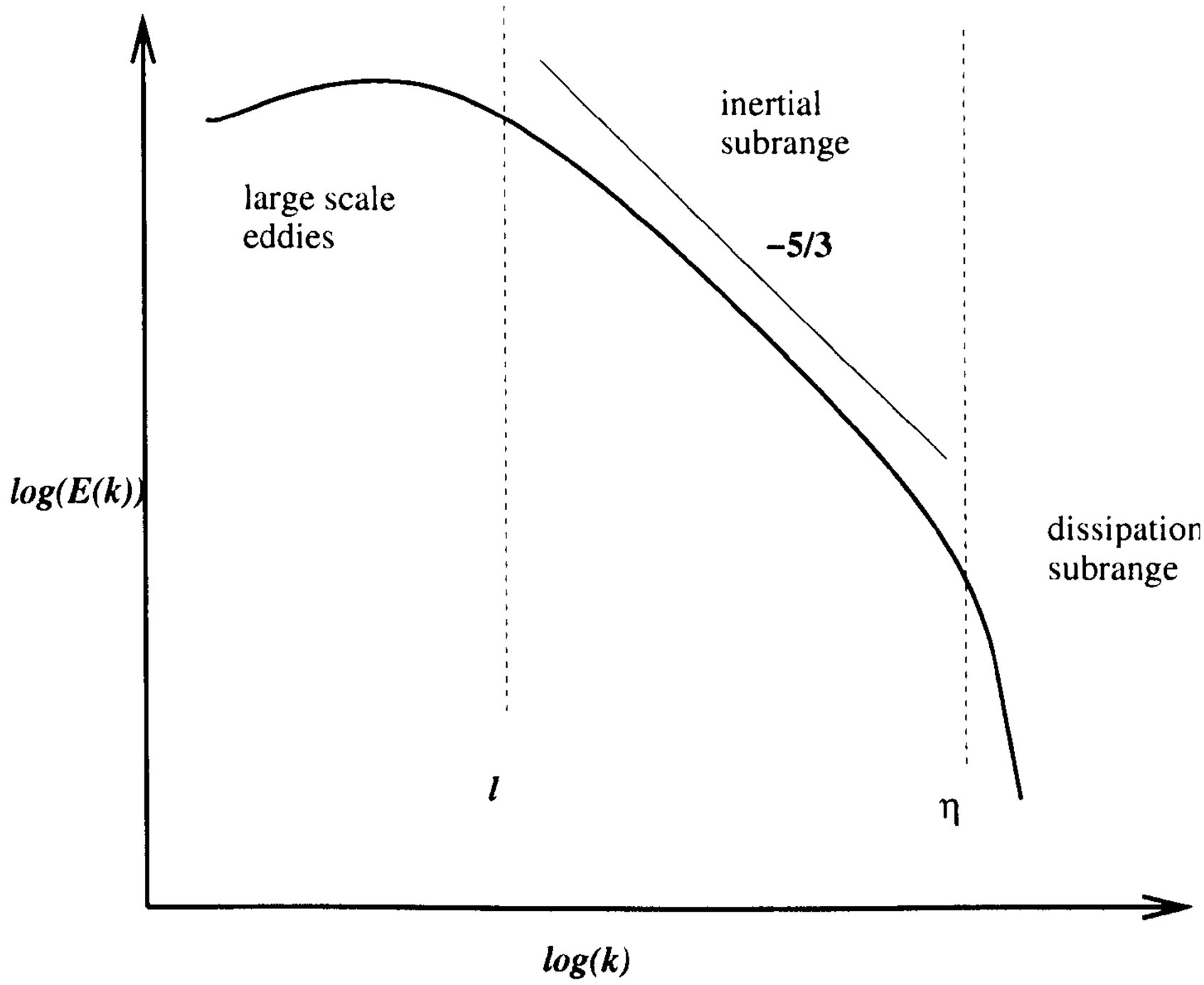

Figure 2.4: A sketch of the Kolmogorov turbulent energy spectrum of homogeneous turbulence.

integral scales in the wall normal direction results in a number of anisotropic modes which increase with Reynolds number. As a consequence, the resolution requirements for LES will heavily depend on the Reynolds number and are the main limitation for the simulation of flows in presence of wall as shown by Chapman (1979).

2.4 Formulations of LES Models

The filtered Navier-Stokes equation can be obtained:

$$\frac{\partial(\rho\widetilde{u}_i)}{\partial x_i} = 0, \tag{2.10}$$

$$\frac{\partial(\rho\widetilde{u}_i)}{\partial t} + \frac{\partial(\rho\widetilde{u}_i\ \widetilde{u}_j)}{\partial x_j} = -\frac{\partial\widetilde{p}}{\partial x_i} + \frac{\partial\tau_{ij}^{sgs}}{\partial x_j} + \frac{\partial}{\partial x_j}\left\{\mu\left(\frac{\partial\widetilde{u}_i}{\partial x_j} + \frac{\partial\widetilde{u}_j}{\partial x_i}\right)\right\}. \tag{2.11}$$

where τ_{ij}^{sgs} is the subgrid scale Reynolds stress.

The corresponding value of τ_{ij}^{sgs} is

$$\tau_{ij}^{sgs} = -\rho\left(\widetilde{u_i u_j} - \widetilde{u}_i \widetilde{u}_j\right). \tag{2.12}$$

This term has to be closed using a LES model. It is generally recognized that Smagorinsky (1963) was the first to propose a turbulence modelling technique in which the averaging is performed over space instead of time. This technique was later defined as Large Eddy Simulation (LES).

2.4.1 The Smagorinsky model

An eddy viscosity model is usually applied to model the deviatoric part of the subgrid scale stresses τ_{ij}^{sgs} as follows:

$$\tau_{ij}^{sgs} - \frac{\delta_{ij}}{3}\tau_{kk}^{sgs} = 2\mu_t \widetilde{S_{ij}}. \tag{2.13}$$

The eddy viscosity μ_t is defined using the Smagorinsky model (Smagorinsky, 1963) as follows:

$$\mu_t = \rho(C_s\Delta)^2 \left|\widetilde{S_{ij}}\right|. \tag{2.14}$$

where $\left|\widetilde{S_{ij}}\right|$ is the magnitude of the strain rate tensor and is defined as follows:

$$\left|\widetilde{S_{ij}}\right| = \left(2\widetilde{S_{ij}}\ \widetilde{S_{ij}}\right)^{\frac{1}{2}}. \tag{2.15}$$

The filter width Δ is defined as $\Delta = (\Delta x \Delta y \Delta z)^{\frac{1}{3}}$ (Piomelli, 1997), and the strain rate tensor is denoted as follows

$$\widetilde{S_{ij}} = \frac{1}{2}\left(\frac{\partial \widetilde{u}_i}{\partial x_j} + \frac{\partial \widetilde{u}_j}{\partial x_i}\right). \tag{2.16}$$

Therefore, substituting the subgrid scale stress τ_{ij}^{sgs} in (2.11) using (2.13), the following equation is obtained:

$$\frac{\partial(\rho\widetilde{u}_i)}{\partial t} + \frac{\partial(\rho\widetilde{u}_i\ \widetilde{u}_j)}{\partial x_j} = -\frac{\partial \widetilde{p}}{\partial x_i} + \frac{\partial}{\partial x_j}\left(2\mu_t\widetilde{S_{ij}} + \frac{\delta_{ij}}{3}\tau_{kk}^{sgs}\right) + \frac{\partial}{\partial x_j}\left\{\mu\left(\frac{\partial \widetilde{u}_i}{\partial x_j} + \frac{\partial \widetilde{u}_j}{\partial x_i}\right)\right\}. \tag{2.17}$$

Substituting equation (2.16) into (2.17) and incorporating $\frac{\partial}{\partial x_j}\left(\frac{\delta_{ij}}{3}\tau_{kk}^{sgs}\right)$ into the pressure term, the new form of the filtered momentum equation is obtained:

$$\frac{\partial(\rho\widetilde{u}_i)}{\partial t} + \frac{\partial(\rho\widetilde{u}_i\ \widetilde{u}_j)}{\partial x_j} = -\frac{\partial \breve{P}_{smag}}{\partial x_i} + \frac{\partial}{\partial x_j}\left\{(\mu+\mu_t)\left(\frac{\partial\widetilde{u}_i}{\partial x_j} + \frac{\partial\widetilde{u}_j}{\partial x_i}\right)\right\}. \tag{2.18}$$

where the new pressure term is

$$\breve{P}_{smag} = \widetilde{p} - \frac{\delta_{ij}}{3}\tau_{kk}^{sgs}. \tag{2.19}$$

The basic Smagorinsky model often fails to simulate the transition in a boundary layer on a channel flow that starts from a laminar profile to which small perturbations are added. This is due to the excessive eddy viscosity predicted coming from mean shear. Therefore, for channel flow, the basic Smagorinsky model is often used with the van Driest damping function to reduce the eddy viscosity in the near-wall region. The eddy viscosity is calculated as follows:

$$\mu_T = \rho\left[C_s\Delta(1-exp(-y^+/A^+))\right]^2\left|\widetilde{S_{ij}}\right| \tag{2.20}$$

where the nondimensional distance from the wall is $y^+ = (\delta - |y|)u_\tau/\nu$ and the constant A^+ is often taken equal to 25.

Fureby et al. (1997) simulated the turbulent channel flow using various type of turbulence models and they found that the van Driest damping function did not necessarily improve the overall predictions. In fact the van Driest damping function is not capable of producing the correct near-wall asymptotic behaviour (Sagaut, 2002).

The filtering operation with the function G does not appear explicitly in the standard Smagorinsky model, as the filter width is given by the cubic root of the cell volume ($\Delta = (\Delta x\Delta y\Delta z)^{1/3}$) or twice that. There exists an equivalence between the exact derivative of a filtered variable and the central difference derivative of the unfiltered variable (Rogallo and Moin, 1984), leading to the conclusion that the implicit numerical filter behaves like the classical box filter of width equal to twice the grid size. One obvious drawback is the inherent filter width error when the cell aspect ratio is big (Tejada-Martinez and Jansen, 2004). As pointed by Vasilyev et al. (1998), most large eddy simulations performed in complex geometries to date adopt the implicit filtering due to lack of straightforward discrete filtering operators that commute with numerical differentiation. They proposed a general class of commutative discrete filters applied to nonuniform filter widths based on a mapping of the nonuniform grid in physical space onto a uniform grid in computational space where the filtering is performed.

Determination of the Smagorinsky constant C_s

Lilly (1987) and Lesieur and Metais (1996) explained the determination of C_s based on the equilibrium hypothesis, i.e. the magnitude of production term ϵ_{sgs} is equivalent to the one of the viscous dissipation of SGS energy ϵ_ν.

$$-\tau_{ij}\widetilde{S_{ij}} = \epsilon_\nu \tag{2.21}$$

One can assume that the cutoff wavenumber in Fourier space $k_C = \pi/\Delta$ lies within the $k^{-5/3}$ inertial range spectrum $E(k) = C_K\epsilon^{2/3}k^{-5/3}$, where $C_K = 1.41$ is the Kolmogorov constant. Thus, one can adjust C_s so that the ensemble-averaged subgrid kinetic energy dissipation ϵ_ν is equivalent to ϵ (dissipation due to both resolved and subgrid scales). ϵ_ν can be determined from equation (2.13), (2.14) and equation (2.21).

The magnitude of the strain-rate tensor can be approximated as follows:

$$\left|\widetilde{S_{ij}}\right|^2 \simeq 2\int_0^{k_C} k^2 E(k)dk = \frac{3}{2}C_K\epsilon^{2/3}\left(\frac{\pi}{\Delta}\right)^{4/3} \tag{2.22}$$

One can formulate an equilibrium hypothesis to describe the inertial range dynamics (energy is generated from large-scale eddies and transfered to small scales, where the viscous dissipation takes place) as

$$\epsilon_\nu = (C_s\Delta)^2\left|\widetilde{S_{ij}}\right|^3 = \epsilon \tag{2.23}$$

Substituting equation (2.22) into equation (2.23), one can approximately determine the Smagorinsky constant,

$$C_s \simeq \frac{1}{\pi}\left(\frac{2}{3C_K}\right)^{3/4} = 0.18. \tag{2.24}$$

However, as found by Deardorff (1970) and Piomelli et al. (1988), in the presence of shear for channel flow simulations, the Smagorinsky coefficient must be reduced to $0.065 - 0.1$. Addad et al. (2003) have chosen $C_s = 0.059$ in the simulation of flow over a forward-backward facing step.

2.4.2 The Germano-Lilly dynamic model

One of the drawbacks of the standard Smagorinsky model is that the Smagorinsky constant cannot be dynamically tuned particularly in the presence of the wall

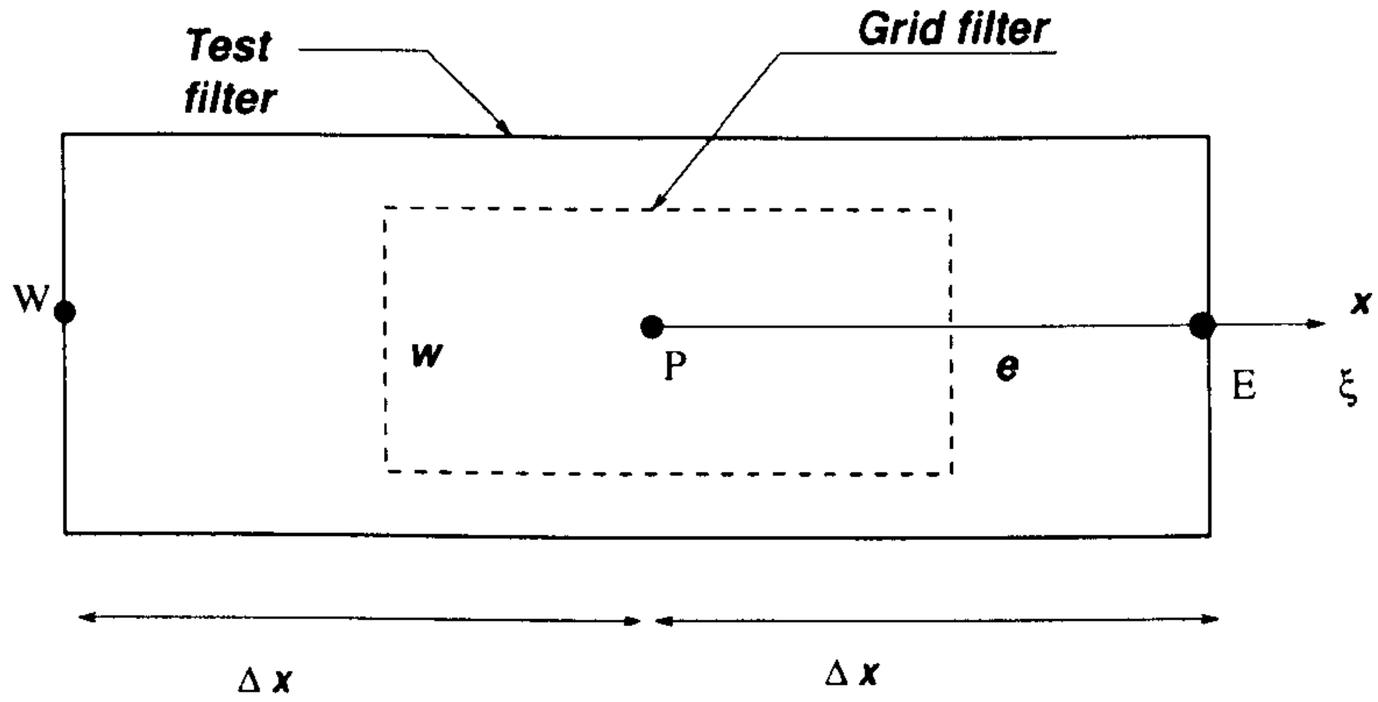

Figure 2.5: Test filtering of a grid filtered variable

boundary. By introducting a second-level filtering operation, the Smagorinsky constant can be determined dynamically using the information extracted from the smallest resolved scales. The idea of the dynamic subgrid scale model was introduced firstly by Germano et al. (1991). It often uses the Smagorinsky model as a base so that the Smagorinsky constant C_s can be determined using the information from the smallest resolved scales, i.e. C_s is dynamically tuned at each node at any time step using two levels of filtering operations, namely, the grid level filtering and the test filtering.

A simple example below can illustrate the test filtering operation (denoted by a hat $\wedge$) on a 1D structured grid. As shown in figure 2.5, normally, the test filter width is taken as twice the grid filter width, i.e. $\widehat{\Delta} = 2\Delta$. After the test filtering, a grid filtered variable (denoted by a tilde, e.g. $\widetilde{u}$) becomes

$$\begin{aligned}\widehat{\widetilde{u}} &= \frac{1}{2\Delta x}\int_W^E \widetilde{u}dx = \frac{1}{2\Delta x}\left(\int_W^P \widetilde{u}dx + \int_P^E \widetilde{u}dx\right) \\ &= \frac{1}{2\Delta x}(\widetilde{u}_w\Delta x + \widetilde{u}_e\Delta x) = \frac{1}{4}\left(\widetilde{u}_W + 2\widetilde{u}_P + \widetilde{u}_E\right)\end{aligned} \tag{2.25}$$

Similarly, a 3D test filter for a structured grid can be constructed in the same way as Zang et al. (1993) have demonstrated, by integrating over the test cells assuming a linear variation of the variables.

Equations 2.10 and 2.11 are further filtered using the filtering operation at the test level to yield the following equations:

$$\frac{\partial(\rho\widehat{\widetilde{u}}_i)}{\partial x_i} = 0, \tag{2.26}$$

$$\frac{\partial(\rho\widehat{\widetilde{u}_i})}{\partial t} + \frac{\partial(\rho\widehat{\widetilde{u}_i\ \widetilde{u}_j})}{\partial x_j} = -\frac{\partial\widehat{\widetilde{p}}}{\partial x_i} + \frac{\partial\widehat{\tau_{ij}^{sgs}}}{\partial x_j} + \frac{\partial}{\partial x_j}\left\{\mu\left(\frac{\partial\widehat{\widetilde{u}_i}}{\partial x_j} + \frac{\partial\widehat{\widetilde{u}_j}}{\partial x_i}\right)\right\}. \tag{2.27}$$

The test level subgrid scale stress is defined as

$$T_{ij}^{sgs} = -\rho\left(\widehat{\widetilde{u_i u_j}} - \widehat{\widetilde{u}}_i\ \widehat{\widetilde{u}}_j\right) \tag{2.28}$$

The Leonard stress term, L_{ij}, illustrated in figure 2.6, is obtained from equation (2.12) and (2.28), and is defined as follows:

$$L_{ij} = -\rho\left(\widehat{\widetilde{u}_i\ \widetilde{u}_j} - \widehat{\widetilde{u}}_i\ \widehat{\widetilde{u}}_j\right) = T_{ij}^{sgs} - \widehat{\tau_{ij}^{sgs}}. \tag{2.29}$$

Equation (2.27) is transformed as follows using (2.28) and (2.29),

$$\frac{\partial(\rho\widehat{\widetilde{u}_i})}{\partial t} + \frac{\partial(\rho\widehat{\widetilde{u}_i\ \widetilde{u}_j})}{\partial x_j} = -\frac{\partial\widehat{\widetilde{p}}}{\partial x_i} + \frac{\partial T_{ij}^{sgs}}{\partial x_j} + \frac{\partial}{\partial x_j}\left\{\mu\left(\frac{\partial\widehat{\widetilde{u}_i}}{\partial x_j} + \frac{\partial\widehat{\widetilde{u}_j}}{\partial x_i}\right)\right\}. \tag{2.30}$$

The eddy viscosity model used for the grid level filtering operation is

$$\tau_{ij}^{sgs} - \frac{\delta_{ij}}{3}\tau_{kk}^{sgs} = 2\rho(C_s\Delta)^2\left|\widetilde{S_{ij}}\right|\widetilde{S_{ij}} = 2C\beta_{ij}. \tag{2.31}$$

where $\beta_{ij} = \rho\Delta^2\left|\widetilde{S_{ij}}\right|\widetilde{S_{ij}}$.

Similarly, the eddy viscosity model used for the test level filtering operation is

$$T_{ij}^{sgs} - \frac{\delta_{ij}}{3}T_{kk}^{sgs} = 2\rho\left(C_s\widehat{\Delta}\right)^2\left|\widehat{\widetilde{S_{ij}}}\right|\widehat{\widetilde{S_{ij}}} = 2C\alpha_{ij}. \tag{2.32}$$

where $\alpha_{ij} = \rho\widehat{\Delta}^2\left|\widehat{\widetilde{S_{ij}}}\right|\widehat{\widetilde{S_{ij}}}$, and $C = C_s^2$ is supposed to be the common coefficient for the two filtering levels.

Substituting (2.31) and (2.32) into equation (2.29), the Leonard stress term is written as follows:

$$L_{ij} - \frac{\delta_{ij}}{3}L_{kk} = 2C\alpha_{ij} - 2\widehat{C\beta_{ij}}. \tag{2.33}$$

The Leonard tensor L_{ij} can be evaluated explicitly and equation 2.33 can be used to calculate the parameter C. However, this is an over-determined system (to obtain a single coefficient from five independent equations). Assuming C as a common coefficient so that $\widehat{C\beta_{ij}} = C\widehat{\beta_{ij}}$, Lilly (1992) proposed solving equation 2.33 in the least square sense. The error is given by

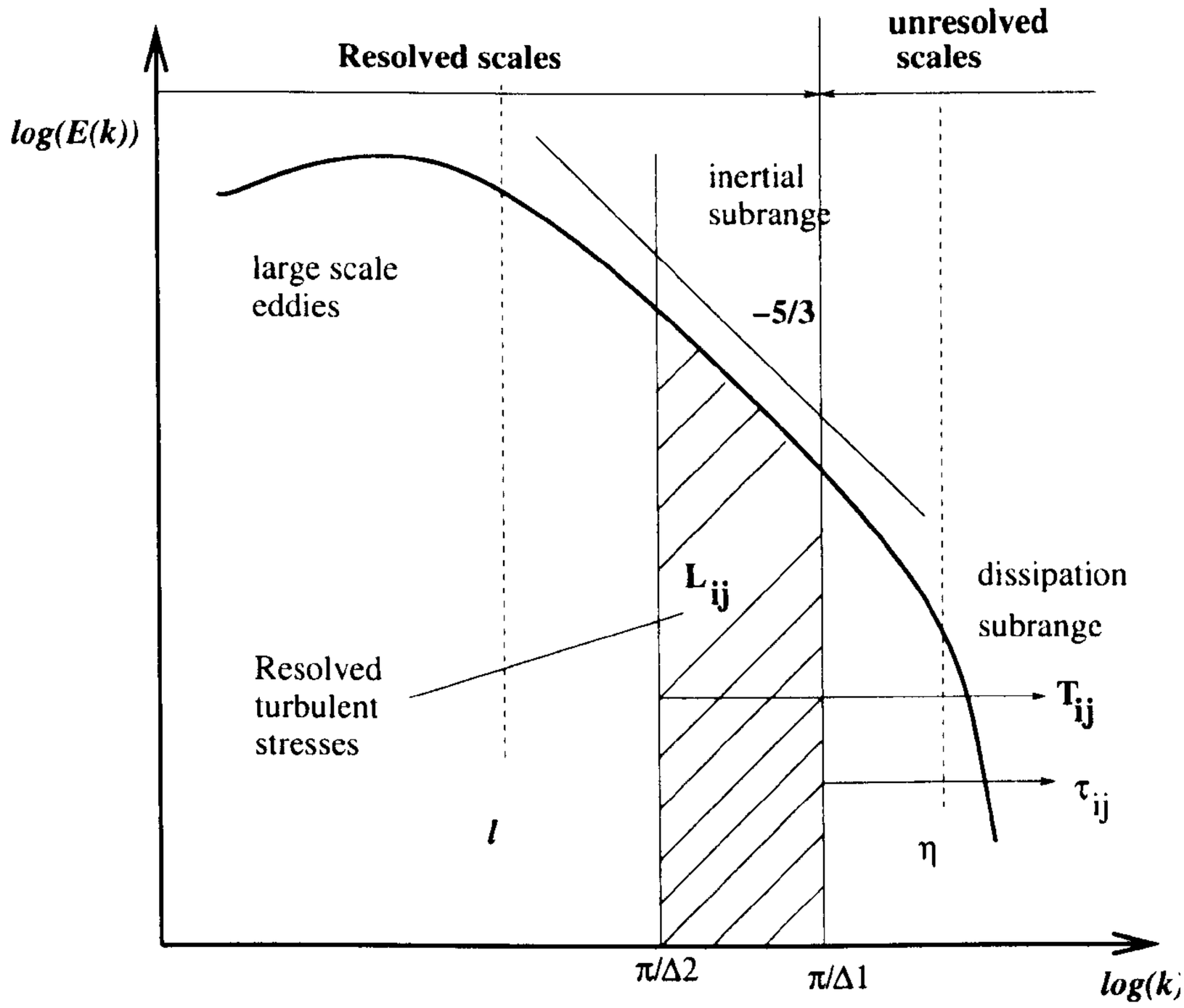

Figure 2.6: Grid-level and test-level filtering of the energy spectrum; $\Delta 1$ and $\Delta 2$ refer to the grid-level and test-level filter widths respectively.

$$Q = \left(L_{ij} - \frac{\delta_{ij}}{3} L_{kk} - 2CM_{ij} \right)^2 , \tag{2.34}$$

where

$$M_{ij} = \frac{1}{\rho} \left(\alpha_{ij} - \widehat{\beta_{ij}} \right) = \left(\widehat{\Delta}^2 \left| \widehat{\widetilde{S_{ij}}} \right| \widehat{\widetilde{S_{ij}}} - \Delta^2 \widehat{\left| \widetilde{S_{ij}} \right| \widetilde{S_{ij}}} \right) , \tag{2.35}$$

and is minimized by requiring $\frac{\partial Q}{\partial C} = 0$,which gives

$$C(\mathbf{x}, t) = \frac{1}{2} \frac{L_{ij} M_{ij}}{M_{mn} M_{mn}} \tag{2.36}$$

The numerator $L_{ij}M_{ij}$ can have both positive and negative values. This indicates that the model can account for the backscatter of the turbulent energy, in other words, the energy is allowed to transfer from small to large scales. This can happen in real flows locally and for short periods, however, for long time intervals, the time-averaged energy transfer is always from the large to the small scales. The negative viscosity that can be produced tends to cause numerical instability, and M_{ij} can become zero, which leads to no solution for the Smagorinsky constant. However, the procedure described above, is not mathematically self-

consistent since it requires a spatially-dependent coefficient to be taken out of the filtering operation as already mentioned. To overcome this problem, the coefficient is assumed to be a function of only the inhomogeneous directions. If a flow is homogeneous in x and z directions, the coefficient is written in an ensemble average form as:

$$C(y,t) = \frac{1}{2}\frac{\langle L_{ij}(\alpha_{ij} - \beta_{ij})\rangle}{\langle(\alpha_{mn} - \widehat{\beta_{mn}})(\alpha_{mn} - \widehat{\beta_{mn}})\rangle} \tag{2.37}$$

where the brackets indicate an appropriate ensemble average over the homogeneous direction.

For the classical dynamic model of Germano et al. (1991), by applying the test filtering as described, the coefficient C is determined. It is noted that a negative value of the coefficient is possible and can be viewed as modelling of backscatter. However, for the sake of stability, artificial constraints are often imposed to make the coefficient always positive. Some relaxation approaches in time have been also proposed, e.g. Breuer and Rodi (1994) suggested relaxation using the value C^n from the previous time step according to $C^{n+1} = \varepsilon C^* + (1-\varepsilon)C^n$ with $\varepsilon = 0.001$ and ε being the preliminary value determined from the standard dynamic procedure.

Yang and Ferziger (1993) are probably the first who applied the dynamic subgrid-scale model to a LES of turbulent channel flow with a square rib mounted on the bottom wall where only one homogeneous direction exists. To evaluate C_s, the spatial averaging was performed in the spanwise direction and additional averaging was employed over nine neighbouring grid points with the point for which the averaging was carried out located at the center. Jordan (2001) also extended the dynamic subgrid-scale model to compute the cross-flow over a circular cylinder at $Re_D = 3,900$ in a curvilinear coordinate where C_s was evaluated in the computational (transformed curvilinear) space. Recently, the Lagrangian ensemble proposed by Meneveau et al. (1996) has started to be used widely. A Lagrangian ensemble averaging technique is used to evaluate the eddy-viscosity coefficient C. Successful examples of this approach to simulate the flow across a circular cylinder can be found in Balaras (2004) and Piomelli et al. (2003).

Explicit filtering of nonlinear terms in the filtered equations could be used to remove the smallest scales polluted by the numerical errors (Lund and Kaltenbach, 1995). However, when the dynamic subgrid-scale model is used, the test filter width has to be consistently computed as shown by Lund (1995) and Tejada-Martinez and Jansen (2004), leading to difficult application in complex geometries.

2.4.3 Dynamic model without test filtering

In essence, the dynamic model is based on an approach for evaluating subgrid-scale (or subfilter-scale, if explicit filtering is used) model coefficients directly from information contained in the resolved turbulent flow field on a grid-level (smallest filter width) by a test filter operation and thus the model samples the turbulent stresses from a band of the smallest resolved scales (see figure 2.6) and effectively extrapolates this information to the subgrid-scale (or subfilter-scale) range. However, various approaches can be used to evaluate the grid-level and test-level filtering operations. In the following text, a method based on a truncated Taylor series expansion will be used (Chester et al., 2001).

Ghosal and Moin (1995) propose to define the filtering over an one-dimensional interval by:

$$\widetilde{f}(\xi) = \frac{1}{\Delta} \int_{-\infty}^{+\infty} G\left(\frac{\xi - \eta}{\Delta}\right) f(\eta) d\eta. \tag{2.38}$$

where Δ is the characteristic cut-off length scale.

Introducing a new variable ζ to satisfy,

$$\xi = \eta + \Delta\zeta, \tag{2.39}$$

the filtering operation in one dimension can be written as

$$\widetilde{f}(\xi) = \int_{-\infty}^{+\infty} G\left(\zeta\right) f(\eta) d\zeta. \tag{2.40}$$

We can determine a differential operator associated with the convolution filter so that the associated continuous differential operator is equivalent to the filtering operator up to a certain order. The Taylor series expansion of function $f(\eta)$ around point ξ is

$$f(\eta) = f(\xi) + \sum_{e=1}^{\infty} \frac{(-1)^e}{e!} (\Delta)^e (\zeta)^e \frac{\partial^e f(\xi)}{\partial \xi^e}. \tag{2.41}$$

Substituting equation (2.41) into (2.40) leads to

$$\widetilde{f}(\xi) = f(\xi) + \sum_{e=1}^{\infty} (\Delta)^e M_e \frac{(-1)^e}{e!} \frac{\partial^e f(\xi)}{\partial \xi^e}. \tag{2.42}$$

where M_e is e-th order moment of convolution kernel G

$$M_e = \int_{-\infty}^{+\infty} G(\zeta) \zeta^e d\zeta. \tag{2.43}$$

Moments of the convolution filter kernels				
M_n	0	2	4	6
Top-hat	1	1/12	1/80	1/448
Gaussian	1	1/12	1/48	5/576

Table 2.2: Values of the first four non-zero moments for the top-hat and Gaussian filters.

The top-hat filtering and the Gaussian filtering transformations are

$$G^{top-hat}(\zeta) = \begin{cases} 1, & \text{if } |\zeta| \leq \frac{1}{2} \\ 0, & \text{otherwise.} \end{cases} \tag{2.44}$$

$$G^{Gauss}(\zeta) = \left(\frac{6}{\pi}\right)^{1/2} exp\left(-6\zeta^2\right). \tag{2.45}$$

Substituting (2.44) and (2.45) into (2.43), the non-zero filter moments can be calculated and the results up to the sixth order as shown in table 2.2. The odd-order moments vanish because the filter convolution kernel is symmetric.

Thus, the truncated Taylor series expansion approximation for the filtered functions are

$$\widetilde{f}^{top-hat}(\xi) = f(\xi) + \frac{\Delta^2}{24}\frac{\partial^2 f(\xi)}{\partial \xi^2} + \frac{\Delta^4}{1920}\frac{\partial^4 f(\xi)}{\partial \xi^4} + O(\Delta^6). \tag{2.46}$$

$$\widetilde{f}^{Gauss}(\xi) = f(\xi) + \frac{\Delta^2}{24}\frac{\partial^2 f(\xi)}{\partial \xi^2} + \frac{\Delta^4}{1152}\frac{\partial^4 f(\xi)}{\partial \xi^4} + O(\Delta^6). \tag{2.47}$$

It can be observed up to second order, the Taylor series approximations for the two filtering functions are the same.

Substituting 2.46 into equation 2.29, the Leonard term can be approximated similarly up to the second order (Chester et al., 2001):

$$L_{ij}^t = \rho\frac{(\alpha\Delta)^2}{12}\frac{\partial \widetilde{u}_i}{\partial x_k}\frac{\partial \widetilde{u}_j}{\partial x_k}, \tag{2.48}$$

where the test filter width is $\alpha\Delta$ and α is normally taken as 2. The superscript 't' denotes terms evaluated from Taylor series.

Substituting 2.46 into equation 2.35, M_{ij} can be approximated up to the second order as follows:

$$M_{ij}^t = 2\rho\Delta^2 \left\{ \left(\left|\widetilde{S}\right| \widetilde{S_{ij}} - \alpha^2 \left|\widetilde{S}^t\right| \widetilde{S_{ij}} \right) + \frac{(\alpha\Delta)^2}{24} \left[\partial_e^2 \left(\left|\widetilde{S}\right| \widetilde{S_{ij}} \right) - \alpha^2 \left|\widetilde{S}^t\right| \partial_e^2 \widetilde{S_{ij}} \right] \right\}. \tag{2.49}$$

where $\left|\widetilde{S}^t\right|$ is the second order Taylor series approximation to $\left|\widehat{\widetilde{S}_{ij}}\right|$,

$$\left|\widetilde{S}^t\right| = \left[2 \left(\widetilde{S_{ij}} + \frac{(\alpha\Delta)^2}{24} \partial_e^2 \widetilde{S_{ij}} \right)^2 \right]^{1/2}. \tag{2.50}$$

where $\widetilde{S_{ij}} = \frac{1}{2}\left(\frac{\partial \widetilde{u_i}}{\partial x_j} + \frac{\partial \widetilde{u_j}}{\partial x_i}\right)$ and e is the index for homogeneous directions.

For a channel flow, taking the ensemble average over the x and z homogeneous directions of $L_{ij}^t M_{ij}^t$ and $M_{mn}^t M_{mn}^t$, the dynamic Smagorinsky coefficient can be obtained by minimizing the mean square error in the Germano identity $\left\langle \left[L_{ij}^t - \frac{\delta_{ij}}{3} L_{kk} - 2(C_s^t)^2 M_{ij}^t \right]^2 \right\rangle$ similarly as Lilly (1992). The resulting C_s is

$$\left(C_s^t\right)^2 = \frac{1}{2} \frac{\left\langle L_{ij}^t M_{ij}^t \right\rangle}{\left\langle M_{mn}^t M_{mn}^t \right\rangle} \tag{2.51}$$

As shown by Chester et al. (2001), this model is able to reproduce the correct near-wall behavior $C_s^2\Delta^2 \approx O(y^+)^3$ for the turbulent channel flow. In this thesis, the model is also applied to the cross-flow over a single cylinder and an inline tube array, where only the spanwise direction is homogeneous. The formulations are only slightly different from the channel flow formulation, in which the derivatives are only evaluated in the spanwise direction. Additionally, negative eddy viscosity is clipped in order to maintain a stability of the solver for the momentum and continuity equations. If there is no homogeneous direction in the flow configuration, this derivative based approach can also be applied in combination with the Lagrangian ensemble averaging operators proposed by Meneveau et al. (1996).

2.4.4 Applying the subgrid-scale model to the energy equation

Applying the filtering operation to the energy equation, we obtain

$$\frac{\partial \widetilde{\Theta}}{\partial t} + \left(\frac{\partial \widetilde{u_j \Theta}}{\partial x_j} - \widetilde{\Theta} \frac{\partial \widetilde{u_j}}{\partial x_j} \right) = \alpha \frac{\partial^2 \widetilde{\Theta}}{\partial x_j \partial x_j} \tag{2.52}$$

The eddy visocity concept is often employed to model the SGS heat flux q_j as a whole without any decomposition. Similar to the SGS stresses in the Smagorinsky model, the SGS heat fluxes are aligned with the local resolved temperature gradient (Moin et al., 1991; Cabot and Moin, 1993) as follows:

$$q_j = \widetilde{u_j}\widetilde{\Theta} - \widetilde{u_j\Theta} = \alpha_T \frac{\partial \widetilde{\Theta}}{\partial x_j} \tag{2.53}$$

Substituting equation (2.53) into equation (2.52), the filtered scalar transport equation becomes

$$\frac{\partial \widetilde{\Theta}}{\partial t} + \widetilde{u}_j \frac{\partial \widetilde{\Theta}}{\partial x_j} = (\alpha + \alpha_T) \frac{\partial^2 \widetilde{\Theta}}{\partial x_j \partial x_j} \tag{2.54}$$

The turbulent thermal diffusivity α_T is calculated from a turbulent viscosity ν_T using either the Smagorinsky subgrid-scale model or the dynamic subgrid-scale model. Therefore the diffusive term of equation (2.54) becomes $\left(\frac{\nu}{Pr_L} + \frac{\nu_T}{Pr_T}\right) \frac{\partial^2 \tilde{\Theta}}{\partial x_j \partial x_j}$, where the sgs turbulent Prandtl number is set as $Pr_T = 0.9$ (Durbin and Pettersson-Reif, 2001).

Recently, there have been some new developments on the SGS heat flux modelling, however, their application is still limited to simple geometries, like channel flow. Katopodes et al. (2000) proposed a series expansion model, which was considered better than the traditional eddy-diffusivity closure model to represent the subfilter-scale scalar transport. However, the accuracy of this model in a complex geometry, like tube bundles, is unknown due to accuracy problems in evaluating higher order expansion terms. Zhang and Chen (2000) proposed a filtered dynamic SGS model (FDSM) to model the flow field and scalar transport for indoor airflow. The FDSM model performed generally better than the standard Smagorinsky model. Peng and Davidson (2002) proposed a new non-linear SGS heat flux (GGDH) model. It was tested in a channel flow, where the GGDH model performed better than the isotropic SGS eddy-diffusivity closure model. However, it was noted that the Rayleigh number was rather low and thus the effect of SGS heat flux model is less important. In summary, all these sophisticated SGS heat flux models still need rigorous testing and further improvements in simple geometries before their application to model turbulent heat transfer around tube bundles.

2.5 Closure

In this chapter, the principles of LES were presented using the energy spectrum and the governing equations for both velocity and temperature scalar field were presented. The classical filtering operators were reviewed and the different LES formulations including the standard Smagorinsky model, the classical Germano-type dynamic model and a dynamic model without test filtering based on the truncated Taylor series expansion were described in detail. The SGS models for the scalar transport equation were also presented and discussed.

Chapter 3

NUMERICAL SOLUTION METHOD OF THE GOVERNING EQUATIONS

3.1 Introduction

In essence, any discretization process is aimed to transform one or more partial differential equations (PDEs) into one or more systems of algebraic equations. Two steps are involved in the discretization process: the discretization of the solution domain and the discretization of the equations. The first step gives a discrete description of the computational domain in time and space. In flow modelling, this step normally produces a simplification of the actual physical domain. The space is divided into a set of discrete and non-overlaping regions, called control volumes (CVs) or cells. These finite regions are limited by the domain boundaries where boundary conditions are specified. For time-dependent simulations, this step also involves the temporal discretization into a finite number of time-steps. The second step involves the transformation of the terms of the governing equations into a system of algebraic equations.

The purpose of this chapter is to describe the Finite-Volume discretization method used for solving both the Navier-Stokes and the energy equations. Firstly, the discretization approaches of the general transport equation are described for each term. This is followed by the discussion of the Rhie and Chow interpolation method as well as the PISO algorithm. Finally, the boundary conditions are described and the BICG solver is briefly introduced.

3.2 Discretization of the general transport equation

The differential form of the general transport conservation equation is

$$\underbrace{\frac{\partial(\rho\phi)}{\partial t}}_{Transient} + \underbrace{div(\rho\phi\overrightarrow{U})}_{Convection} = \underbrace{div(\Gamma_\phi \overrightarrow{grad\phi})}_{Diffusion} + \underbrace{S_\phi}_{Source} \tag{3.1}$$

where Γ_ϕ is the exchange coefficient which is equal to the viscosity in the momentum equations, and to viscosity/Pr in the temperature transport equation. The dependent variable ϕ can be U, V, W, Θ etc.

Equation 3.1 is discretized using the finite-volume method (see Patankar (1980); Ferziger and Peric (2001); Versteeg and Malalasekera (1995)). The integral form over the control volume $\Delta\Omega$ is

$$\int_{\Delta\Omega} \frac{\partial(\rho\phi)}{\partial t} d\Omega + \int_{\Delta\Omega} div(\rho\phi\overrightarrow{U}) d\Omega = \int_{\Delta\Omega} div(\Gamma \overrightarrow{grad\phi}) d\Omega + \int_{\Delta\Omega} S_\phi d\Omega \tag{3.2}$$

3.2.1 Staggered versus collocated variable arrangement

In the staggered arrangement, the pressure and other scalar variables are stored at the centroids of the control volume (CV), while, the velocities are stored at these faces. On the other hand, when the collocated arrangement is used, all variables are stored in the centre of the control volume. Throughout this thesis, the collocated arrangement is adopted considering its advantages in the implementation of higher order differencing schemes, the treatment of boundary conditions, handling of non-orthogonal grids and local grid refinement (see Peric et al. (1988) and Muzaferija and Gosman (1997) among many others).

Furthermore, Morinishi et al. (1998) showed that the staggered-arrangement methods can be made fully kinetic energy conserving when the analysis is restricted to uniform meshes, whereas the collocated-arrangement methods will always contain an energy conservation error ($O(\Delta t^m \Delta x^n)$ [1]). However, when the analysis of non-uniform meshes is considered, Felten and Lund (2001) demonstrated that the staggered-arrangement methods introduce commutation errors due to a lack of commutivity between the discrete differencing and averaging operators. This source of error does not appear in the collocated-arrangement methods. As far

[1] Typically, the pressure term has a conservation error of $O(\Delta t \cdot \Delta x^2)$ if a second order finite difference scheme is used.

as turbulent channel flow is concerned, they also concluded that the collocated-arrangement methods generally give slightly poorer results than the staggered-arrangement methods on the coarser meshes. However, the collocated-arrangement and staggered-arrangement methods produce similar results at high mesh resolution.

In the following sections, only the collocated arrangment is considered for discretization of the different terms in equation 3.1.

3.2.2 Discretization of the convection term

The convection term can be written according to the Gauss theorem as:

$$\int_{\Delta\Omega} div(\rho\phi\overrightarrow{U})d\Omega = \int_{s}(\rho\phi\overrightarrow{U}\cdot\overrightarrow{n})ds \tag{3.3}$$

where $\overrightarrow{n}$ is the unit vector normal to the surface of the volume and directed outwards in relation to the volume. The surface integral can be split into a sum of integrals over each of the faces surrounding the control volume:

$$\int_{s}(\rho\phi\overrightarrow{U}\cdot\overrightarrow{n})ds \cong \sum_{f}\rho_f(\overrightarrow{U_f}\cdot\overrightarrow{n})\phi_f S_f \tag{3.4}$$

The convective flux $F^c_{i,f} = \rho_f\cdot(\overrightarrow{U_f}\cdot\overrightarrow{n})\cdot\phi_f S_f$ in equation 3.4 is equal to the product of mass flux and the value of ϕ at the face f, i.e.

$$F^c_{i,f} = \dot{m}_f\phi_f. \tag{3.5}$$

In order to evaluate the CV face value of ϕ_f, linear interpolation is the simplest second order approximation and it is denoted as the central difference scheme (CDS). Implicit treatment of all terms would reduce the diagonal dominance of the coefficient matrix, and sometimes create convergence problems. Therefore, a deferred-correction approach suggested by Khosla and Rubin (1974) is used

$$\phi^c_f = \phi^{UDS}_f + (\phi^{CDS}_f - \phi^{UDS}_f)^{m-1} \tag{3.6}$$

The second term in the right-hand-side of the equation is evaluated explicitly using values from the previous iteration $(m-1)$. It is normally relatively small compared to the implicit term, so that the explicit treatment does not slow down the convergence significantly.

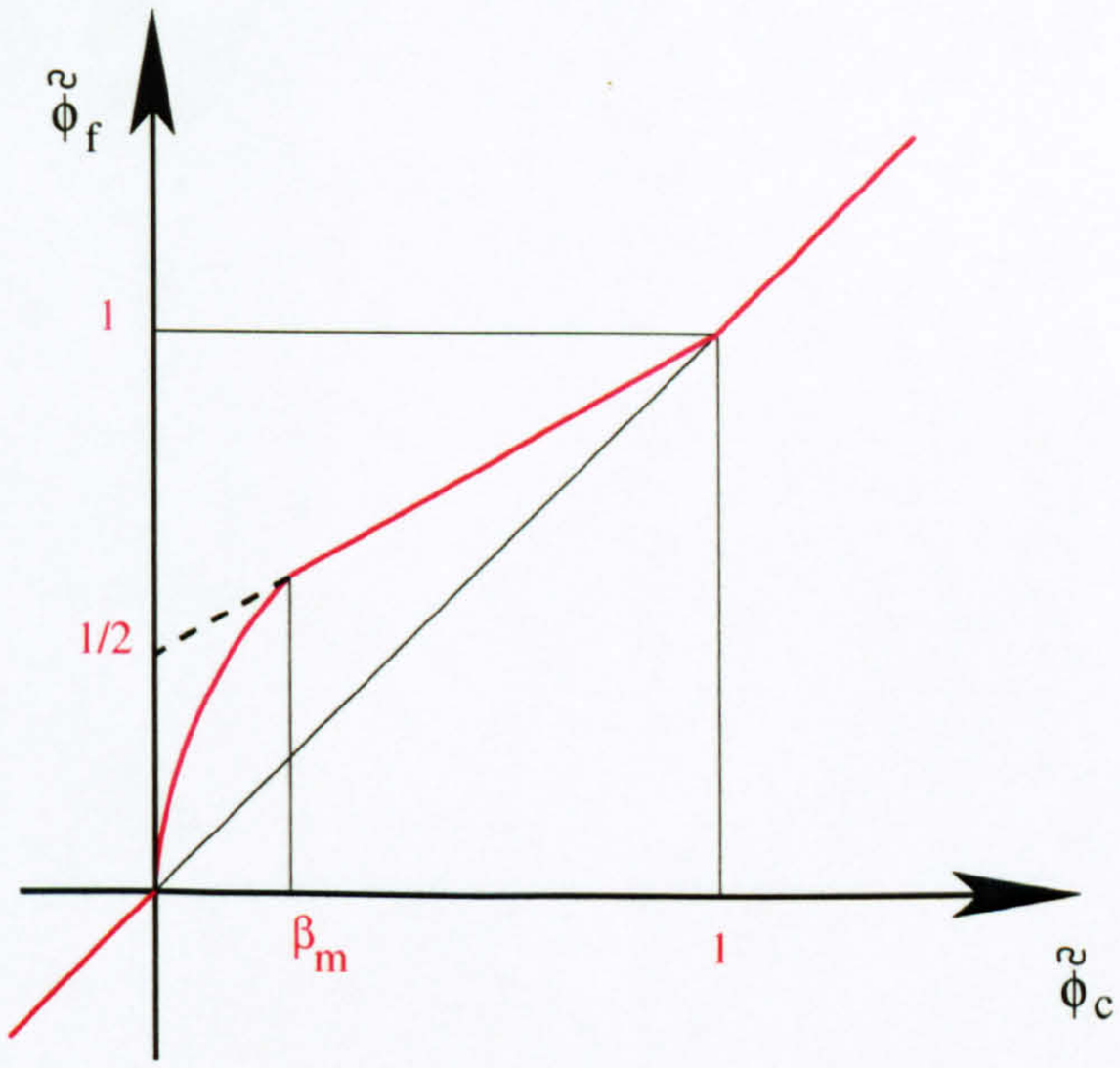

Figure 3.1: Gamma differencing scheme in the NVD diagram.

It should be noted here that the second order central difference scheme causes unphysical oscillations in the solution for convection-dominated problems, thus violating the boundedness of the solution. For this reason, the convective flux of the temperature scalar transport equation is approximated using a blended scheme called the Gamma differencing scheme, suggested by Jasak et al. (1999). The Normalised Variable Diagram (NVD) of this differencing scheme is shown in figure 3.1.

The Gamma-scheme blends the first order upwind scheme (UDS) and the second order central difference scheme (CDS). The blending factor γ is not a constant but dependent on the local normalised value at the upstream cell $\widetilde{\phi}_c$. The constant parameter $\beta_m = 1/4$ has been selected to secure a smooth transition between the UDS and CDS:

$$\gamma = \frac{\widetilde{\phi}_c}{\beta_m} \tag{3.7}$$

The Gamma differencing scheme can be described as follows according to the NVD diagram,

$$\phi_f = \begin{cases} \phi_c, & \text{if } \widetilde{\phi}_c \leq 0 \text{ or } \widetilde{\phi}_c \geq 1 \\ \phi_c + (1 - f_x)(\phi_D - \phi_c), & \text{if } \beta_m \leq \widetilde{\phi}_c \leq 1 \\ \phi_c + \gamma(1 - f_x)(\phi_D - \phi_c). & \text{if } 0 \leq \widetilde{\phi}_c \leq \beta_m \end{cases} \tag{3.8}$$

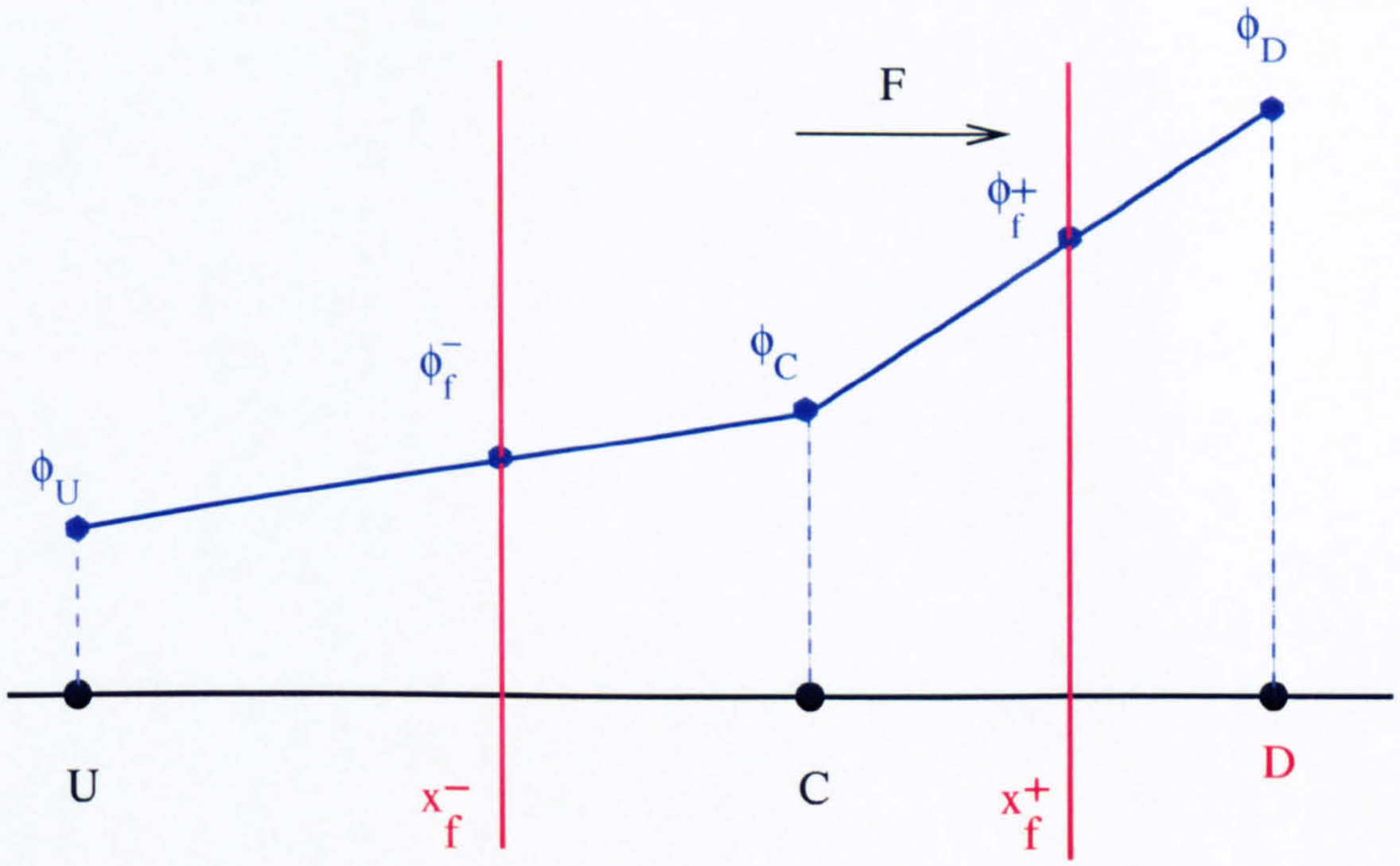

Figure 3.2: Definition of variables for the Gamma differencing scheme.

where f_x is the weighting factor and $\widetilde{\phi}_c = \frac{\phi_C - \phi_f^-}{\phi_f^+ - \phi_f^-} = 1 - \frac{\phi_D - \phi_c}{2\overrightarrow{\nabla\phi}\big|_C \cdot \vec{d}}$ as illustrated in figure 3.2. This calculation for $\widetilde{\phi}_c$ does not require addressing the far upwind node. Therefore the scheme is suitable and can be easily implemented on arbitrary unstructured meshes. In calculating the temperature convective flux, a similar deferred correction approach as shown earlier, in equation 3.6, is used.

3.2.3 Discretization of diffusion term

The diffusion term can also be approximated using Gauss theorem as follows:

$$\int_{\Delta\Omega} div(\Gamma \overrightarrow{grad\phi}) d\Omega = \int_s \Gamma \overrightarrow{grad\phi} \cdot \vec{n}\, ds \cong \sum_f \Gamma \overrightarrow{grad\phi} \cdot \vec{n}\, S_f \qquad (3.9)$$

If the grid is orthogonal, the diffusive flux shown in equation 3.9 can be evaluated using a simple central difference approximation:

$$F_e^d = \Gamma_{\phi,e} \left(\frac{\partial\phi}{\partial n}\right)_e S_e \approx \Gamma_{\phi,e} \frac{\phi_E - \phi_P}{\left|\overrightarrow{PE}\right|} S_e \qquad (3.10)$$

In the case of a non-orthogonal grid, the deferred correction approach suggested by Muzaferija (1994) is used. The diffusive flux is estimated using the deferred

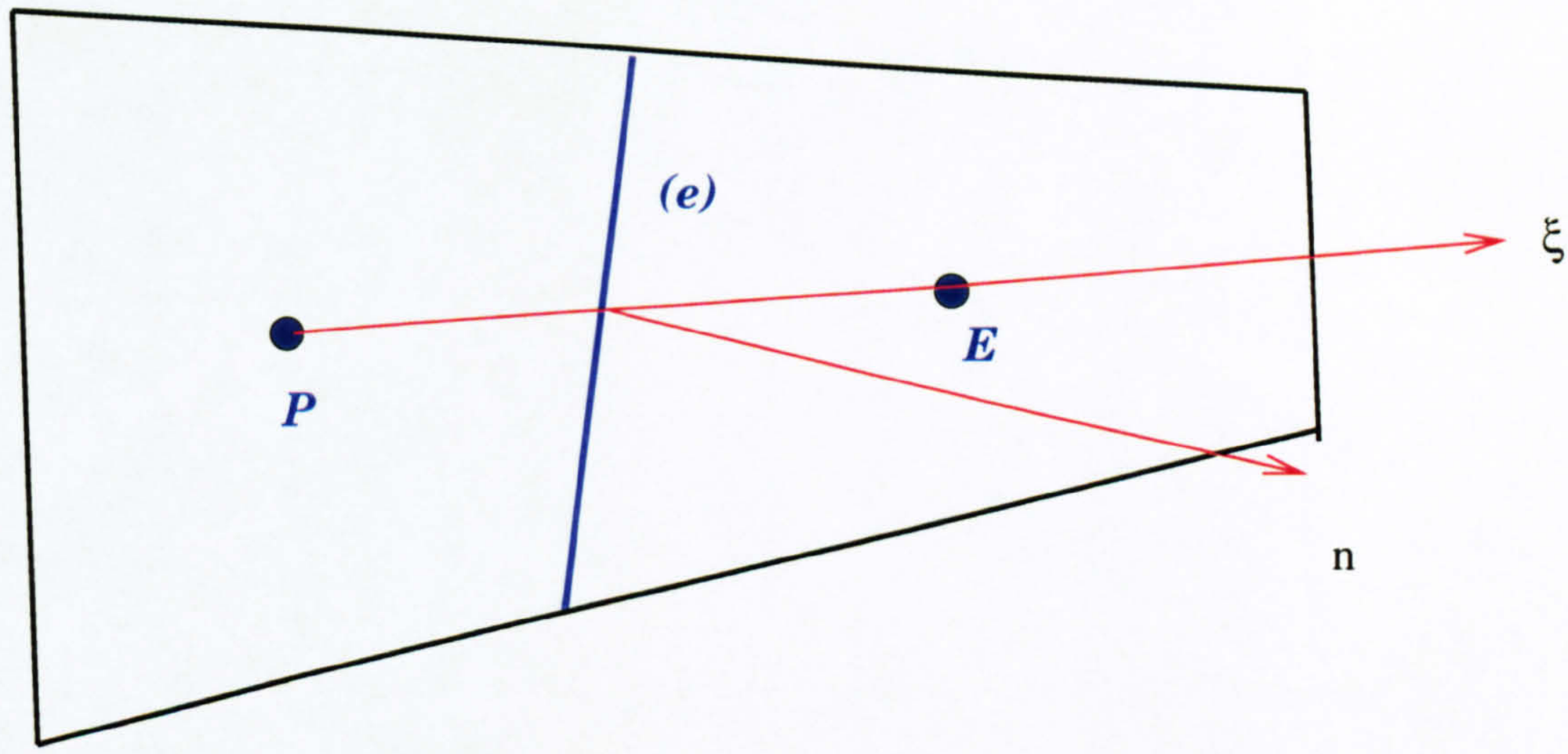

Figure 3.3: Adjacent cells P and E and definition of unit vector normal to the face (e) $\vec{n}$ and vector $\vec{\xi}$ connecting P and E.

correction approach as follows:

$$F_e^d = \Gamma_e \frac{p_E - p_P}{\left|\overrightarrow{PE}\right|} S_e + \Gamma_e S_e \left.\overrightarrow{\overrightarrow{grad\phi^{old}}}\right|_e \cdot (\vec{n} - \vec{i}_\xi) \tag{3.11}$$

The second term in the right-hand-side of the equation 3.11 is estimated using interpolated cell-center gradients in $\vec{n}$ and $\vec{\xi}$ directions (as shown in figure 3.3).

3.2.4 Discretization of source term

All terms of the original transport equation that cannot be included in the convection, diffusion or temporal terms are treated as sources. The source term $S_\phi(\phi)$ can be a general function of ϕ. It is advisable to treat the source term as "implicitly" as possible (Patankar, 1980). The source term is normally linearised as follows:

$$S_\phi(\phi) = Su + Sp\phi, \tag{3.12}$$

where Su and Sp may also depend on ϕ. For the sake of stability, Sp should be negative. Following equation 3.2, the volume integral of the source term is linearised as follows:

$$\int_{\Delta\Omega} S_\phi d\Omega = (Su + Sp \cdot \phi_P)\, \Delta\Omega_P. \tag{3.13}$$

3.2.5 Discretization of the transient term

Using the total convective and diffusive flux defined as

$$H = \rho\phi\overrightarrow{U} - \Gamma\overrightarrow{grad\phi} \tag{3.14}$$

equation 3.2 can be simplified as

$$\int_{\Delta\Omega} \frac{\partial(\rho\phi_i)}{\partial t} d\Omega = -\int_{\Delta\Omega} div(H_i) d\Omega + \int_{\Delta\Omega} S_\phi d\Omega \tag{3.15}$$

Integrating all the terms in the above equation over time results in

$$\int_{t-\Delta t}^{t}\int_{\Delta\Omega} \frac{\partial(\rho\phi_i)}{\partial t} d\Omega dt = -\int_{t-\Delta t}^{t}\int_{\Delta\Omega} div(H_i) d\Omega dt + \int_{t-\Delta t}^{t}\int_{\Delta\Omega} S_\phi d\Omega dt \tag{3.16}$$

In the present work, the Crank-Nicolson scheme is used since its combination with central difference schemes is known to keep the amplication factor always equal to one as described in Appendix B. If all the terms in the equation are divided by Δt so that the time step affects only the transient term, the final form of the above equation becomes

$$\begin{aligned}\frac{\rho\phi^{n+1}\Delta\Omega - \rho\phi^{n}\Delta\Omega}{\Delta t} = &-\frac{1}{2}\left(\int_{\Delta\Omega} div(H_i^{n+1}) d\Omega + \int_{\Delta\Omega} div(H_i^{n}) d\Omega\right) \\ &+\frac{1}{2}\left(\int_{\Delta\Omega} S_\phi^{n+1} d\Omega + \int_{\Delta\Omega} S_\phi^{n} d\Omega\right)\end{aligned} \tag{3.17}$$

3.3 Solution method of Navier-Stokes equations

Throughout this thesis, the time-advancing schemes used can be written as

$$\rho\frac{\partial\widetilde{u_i}^{n+1}}{\partial x_i} = 0, \tag{3.18}$$

$$\rho\frac{\widetilde{u}_i^{n+1}-\widetilde{u}_i^{n}}{\Delta t}+\frac{\rho}{2}\left[\frac{\partial\left(\widetilde{u}_i\widetilde{u}_j\right)^{n+1}}{\partial x_j}+\frac{\partial\left(\widetilde{u}_i\widetilde{u}_j\right)^{n}}{\partial x_j}\right]=-\frac{\partial P^{n+1}}{\partial x_i}$$
$$+\frac{\partial}{\partial x_j}\left[\frac{(\mu+\mu_t)^{n+1}}{2}\left(\frac{\partial\widetilde{u}_i}{\partial x_j}+\frac{\partial\widetilde{u}_j}{\partial x_i}\right)^{n+1}\right]$$
$$+\frac{\partial}{\partial x_j}\left[\frac{(\mu+\mu_t)^{n}}{2}\left(\frac{\partial\widetilde{u}_i}{\partial x_j}+\frac{\partial\widetilde{u}_j}{\partial x_i}\right)^{n}\right]. \tag{3.19}$$

Thus, except for the pressure term that is treated implicitly, both convection and diffusion terms are treated using the Crank-Nicolson time marching scheme. Since the collocated arrangement is used, the mass conservation equation has to be satisfied at the cell face level. Because the pressure term does not appear in the mass conservation equation, velocities and pressure must be numerically related through pressure-velocity coupling algorithms. In the following paragraphs, the Rhie and Chow interpolation method followed by the PISO algorithm (Issa, 1986) will be described.

3.3.1 Rhie and Chow interpolation method

In order to estimate the velocity components on the control volume faces from those on the cell centers, the special Rhie and Chow (1983) interpolation method is used. The weighted linear interpolation in physical space, $U_e = f_x U_E + (1 - f_x)U_P$, is not used in order to avoid non-physical oscillations in pressure. The method used here is similar to that of Lien et al. (1996). The pressure gradient evaluated directly at the cell centroids is added to the velocity field stored at the centroid of the control volumes to obtain a new velocity field U^*, i.e.

$$U_P^* = U_P + \frac{P_e - P_w}{|\overrightarrow{we}|}\left.\frac{\Delta\Omega}{A_P}\right|_P \tag{3.20}$$

$$U_E^* = U_E + \frac{P_{ee} - P_e}{\left|\overrightarrow{e(ee)}\right|}\left.\frac{\Delta\Omega}{A_P}\right|_E \tag{3.21}$$

where $|\overrightarrow{we}|$ denotes the distance between face e and w shown in figure 3.4, and P_w, P_e and P_{ee} are calculated by linear interpolation at the cell faces. The east face velocity is now calculated with the correct pressure gradient across the face subtracted from the linear average of intermediate velocities at nodes "P" and "E"

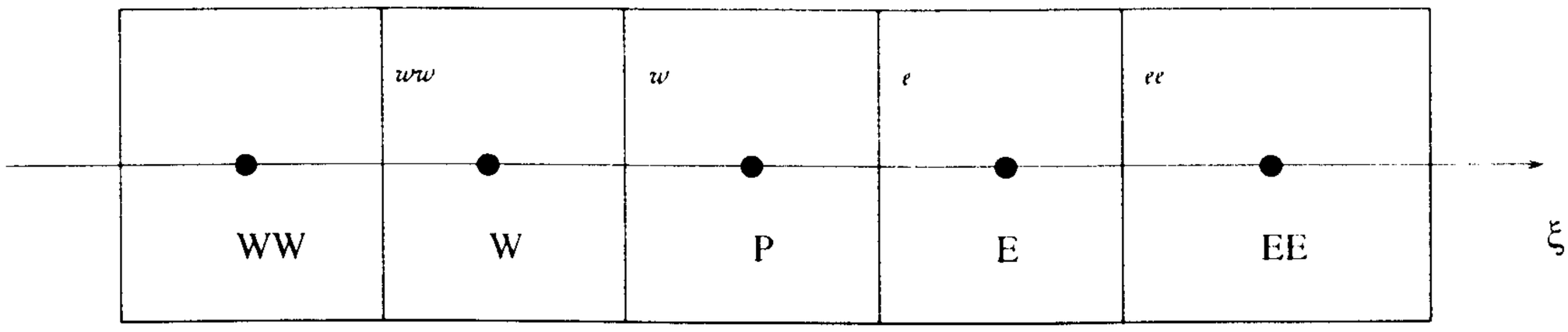

Figure 3.4: Grid nomenclature for Rhie and Chow interpolation method

as follows:

$$U_e = f_x U_E^* + (1 - f_x) U_P^* - \frac{P_E - P_P}{\left|\overrightarrow{PE}\right|} \left.\frac{\overline{\Delta\Omega}}{A_P}\right|_e \tag{3.22}$$

where f_x is the interpolation factor calculated using,

$$f_x = \frac{\left|\overrightarrow{Pe}\right|}{\left|\overrightarrow{Pe}\right| + \left|\overrightarrow{eE}\right|} \tag{3.23}$$

In order to resolve better the velocity and pressure field in the near wall region, non-uniform grids with constant expanding ratio r are oftern used. The accuracy of the Rhie and Chow interpolation method with the non-uniform grids will be analysed below.

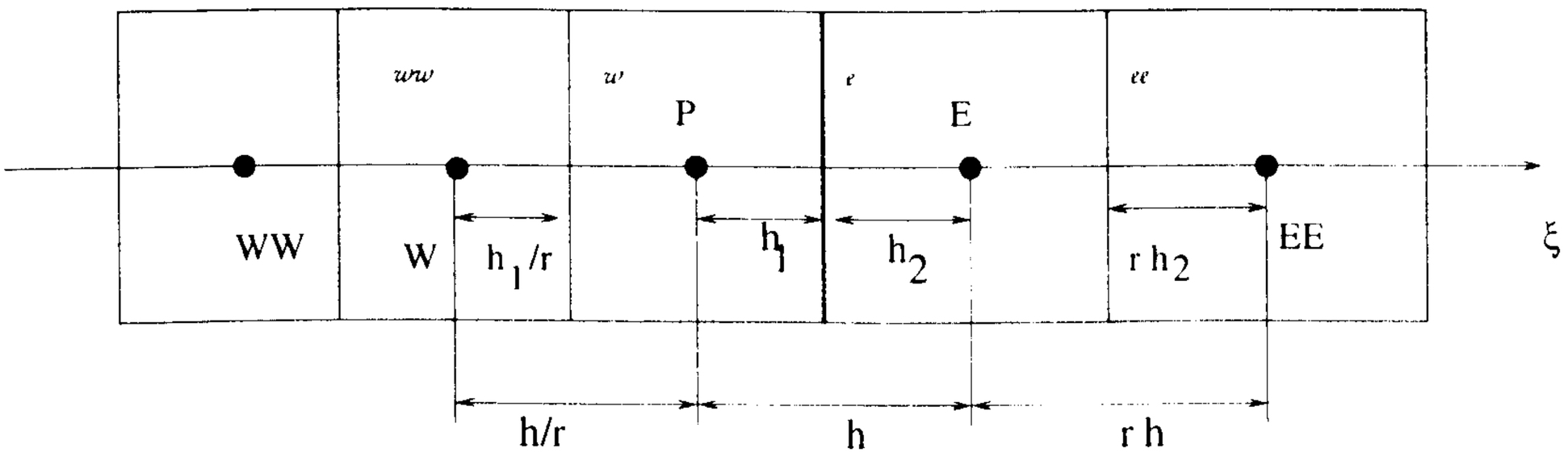

Figure 3.5: Non-uniform grid with constant ratio r.

Using Taylor series, we can express all pressure terms with respect to pressure at face (e).

$$p_E = p_e + h_2 \frac{\partial p}{\partial \xi} + \frac{h_2^2}{2} \frac{\partial^2 p}{\partial \xi^2} + \frac{h_2^3}{6} \frac{\partial^3 p}{\partial \xi^3}. \tag{3.24}$$

$$p_P = p_e - h_1 \frac{\partial p}{\partial \xi} + \frac{h_1^2}{2} \frac{\partial^2 p}{\partial \xi^2} - \frac{h_1^3}{6} \frac{\partial^3 p}{\partial \xi^3}. \tag{3.25}$$

$$p_{EE} = p_e + (rh + h_2)\frac{\partial p}{\partial \xi} + \frac{(rh + h_2)^2}{2}\frac{\partial^2 p}{\partial \xi^2} + \frac{(rh + h_2)^3}{6}\frac{\partial^3 p}{\partial \xi^3}. \tag{3.26}$$

$$p_W = p_e - (h/r + h_1)\frac{\partial p}{\partial \xi} + \frac{(h/r + h_1)^2}{2}\frac{\partial^2 p}{\partial \xi^2} - \frac{(h/r + h_1)^3}{6}\frac{\partial^3 p}{\partial \xi^3}. \tag{3.27}$$

The standard Rhie and Chow method can be expressed as

$$u^*_{i,e} = \overline{u^*_{i,e}} - \frac{\overline{\Delta\Omega}}{A_P}\left(\left.\frac{\delta p}{\delta \xi}\right|_e - \left.\overline{\frac{\delta p}{\delta \xi}}\right|_e\right). \tag{3.28}$$

According to the grid shown in figure 3.5, the following formulations are used:

$$\left.\frac{\delta p}{\delta \xi}\right|_e = \frac{p_E - p_P}{h}. \tag{3.29}$$

$$\left.\frac{\delta p}{\delta \xi}\right|_P = \frac{p_e - p_w}{2h_1} = \frac{(r-1)p_P + p_E - rp_W}{2h}. \tag{3.30}$$

$$\left.\frac{\delta p}{\delta \xi}\right|_E = \frac{p_{ee} - p_e}{2h_2} = \frac{(r-1)p_E + p_{EE} - rp_P}{2rh}. \tag{3.31}$$

Substituting p_E, p_P, p_W and p_{EE} from equations (3.29), (3.30) and (3.31) respectively using (3.24), (3.25), (3.27) and (3.26), we obtain the Taylor series expansion forms of $\left.\frac{\delta p}{\delta \xi}\right|_e$, $\left.\frac{\delta p}{\delta \xi}\right|_P$ and $\left.\frac{\delta p}{\delta \xi}\right|_E$.

$$\left.\frac{\delta p}{\delta \xi}\right|_e = \frac{\partial p}{\partial \xi} + \frac{(r-1)h}{2(r+1)}\frac{\partial^2 p}{\partial \xi^2} + \frac{(r^3+1)h^2}{6(1+r)^3}\frac{\partial^3 p}{\partial \xi^3} \tag{3.32}$$

$$\left.\frac{\delta p}{\delta \xi}\right|_P = \frac{\partial p}{\partial \xi} + \frac{(r^2-4r-1)h}{4r(r+1)}\frac{\partial^2 p}{\partial \xi^2} + \frac{(r^4-r^3+8r^2+5r+1)h^2}{12r^2(1+r)^2}\frac{\partial^3 p}{\partial \xi^3}. \tag{3.33}$$

$$\left.\frac{\delta p}{\delta \xi}\right|_E = \frac{\partial p}{\partial \xi} + \frac{(r^2+4r-1)h}{4(r+1)}\frac{\partial^2 p}{\partial \xi^2} + \frac{(r^5+6r^4+13r^3+7r^2+1)h^2}{12(1+r)^3}\frac{\partial^3 p}{\partial \xi^3}. \tag{3.34}$$

The volume-averaging form is used to evaluate $\left.\overline{\frac{\delta p}{\delta \xi}}\right|_e$

$$\left.\overline{\frac{\delta p}{\delta \xi}}\right|_e = \frac{h_2}{h}\left.\frac{\delta p}{\delta \xi}\right|_P + \frac{h_1}{h}\left.\frac{\delta p}{\delta \xi}\right|_E. \tag{3.35}$$

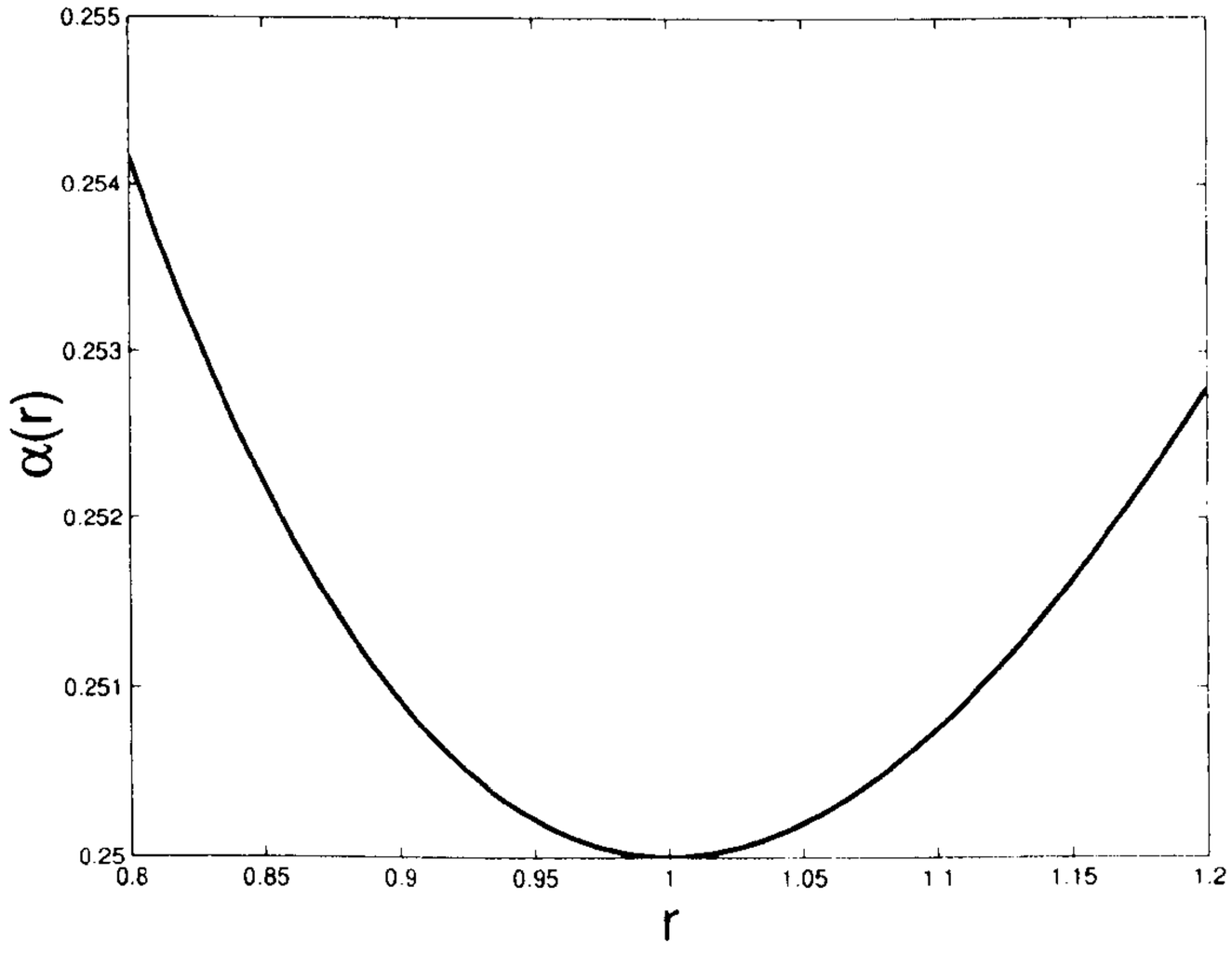

Figure 3.6: The coefficient of the second order term in the pressure gradient difference.

Substituting (3.33) and (3.34) into (3.35), the linearly interpolated term is obtained

$$\left.\overline{\frac{\delta p}{\delta \xi}}\right|_e = \frac{\partial p}{\partial \xi} + \frac{(r-1)h}{2(r+1)}\frac{\partial^2 p}{\partial \xi^2} + \frac{(r^4+5r^3+2r^2+5r+1)h^2}{12r(1+r)^2}\frac{\partial^3 p}{\partial \xi^3} \tag{3.36}$$

The difference can be evaluated using (3.32) and (3.36) as follows,

$$\left.\overline{\frac{\delta p}{\delta \xi}}\right|_e - \left.\frac{\delta p}{\delta \xi}\right|_e = \frac{(r^2+r+1)h^2}{12r}\frac{\partial^3 p}{\partial \xi^3} = \alpha(r)h^2\frac{\partial^3 p}{\partial \xi^3} \tag{3.37}$$

Thus, it has been shown that the standard Rhie-Chow interpolation method has a second-order accuracy for both uniform and non-uniform grids. The coefficient $\alpha(r)$ varies with the expansion ratio as shown in figure 3.6.

3.3.2 Pressure velocity coupling

The pressure correction equation can be obtained from the mass conservation equation. In the following, we restrict the discussion to a summary of the PISO algorithm within one time step.

1. Initial guess for velocities and pressure.

2. Solve momentum equations for new velocities using the guessed pressure: momentum will be conserved, mass will not be conserved.

3. Solve pressure correction equation for new pressure.

4. Correct velocities using new pressure.

5. Solve a second pressure correction equation for new pressure.

6. Correct velocities using new pressure: mass will be conserved, momentum will not be conserved.

7. Go to step 2 and iterate until convergence.

The detailed form of the pressure correction equation (steps 3 and 5) will not be repeated here as it can be found in standard textbooks of computational fluid dynamics (Versteeg and Malalasekera, 1995; Ferziger and Peric, 2001).

3.4 Boundary conditions

3.4.1 Inlet and outlet boundaries

The distribution of all the dependent variables, except pressure, is prescribed at the inlet boundary. For fully developed channel flow computation case, different practices are employed, which are shown in section 3.4.3. The boundary condition on pressure is a zero gradient.

The convective boundary condition $\frac{\partial \phi}{\partial t} + U_{conv} \frac{\partial \phi}{\partial x} = 0$ is used for the exit boundary, where ϕ is any physical variable convected out through the outlet and U_{conv} is the convective velocity normal to the outlet boundary. As discussed by Sohankar et al. (1998), this treatment of the exit boundary appears particularly suitable for the simulation of bluff body flow.

3.4.2 Wall boundaries

Impermeable non-slip conditions are used for all the wall boundaries. The shear stress at wall is not zero, but the normal stress is. The cylinder heated wall boundaries have specified constant heat flux q", which is normal to the wall boundary and is directed to the inner fluid cell. A zero gradient boundary condition is used for the pressure. The details of implementation of wall boundary conditions are explained by Ferziger and Peric (2001).

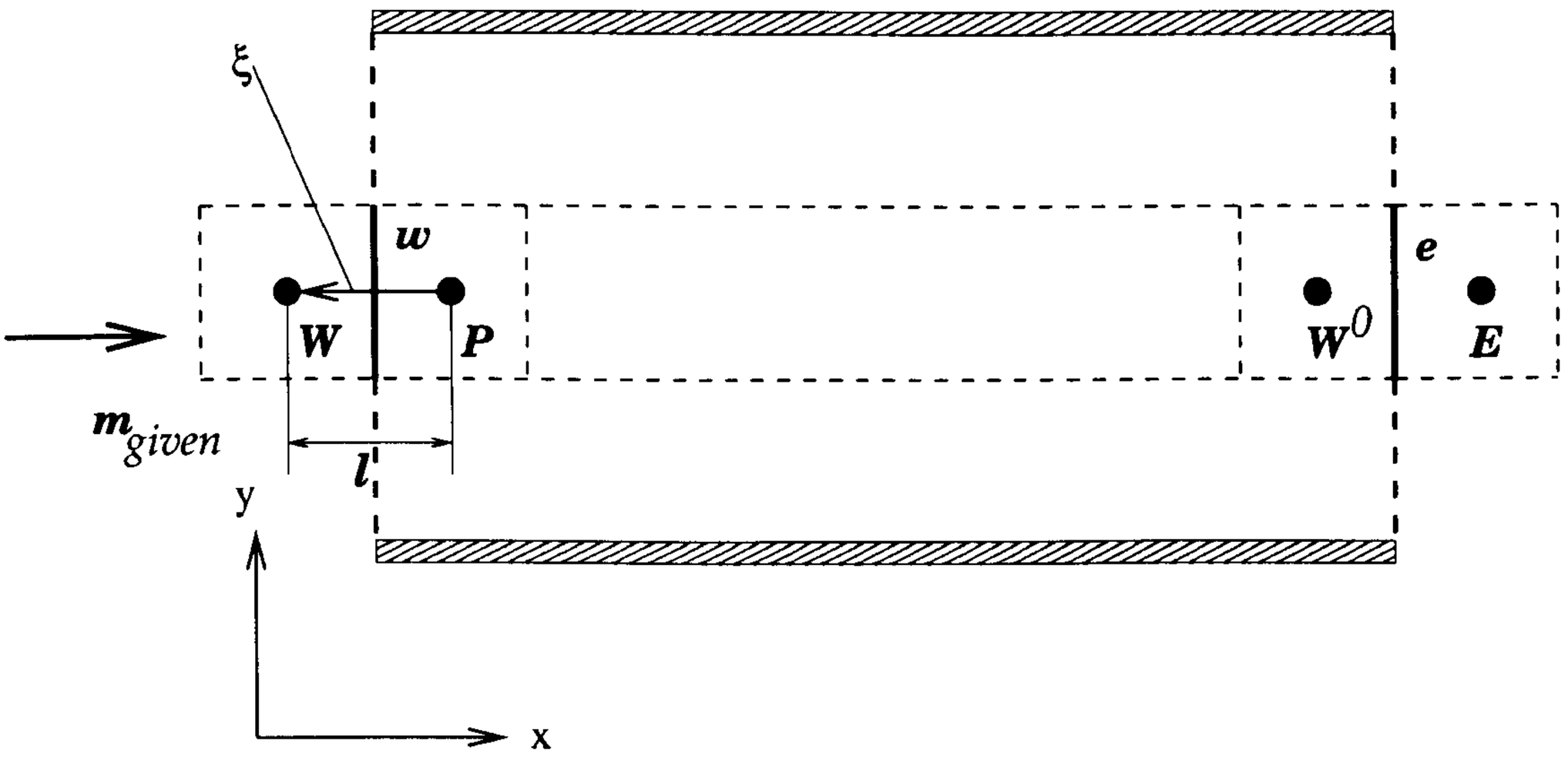

Figure 3.7: The flow domain for inlet-outlet cyclic boundaries.

3.4.3 Cyclic boundaries

Two types of cyclic boundary conditions are used, namely, normal- and inlet-outlet cyclic boundaries. Pressure and velocities are identical for normal cyclic pairs, however, due to pressure drop, the pressure for inlet-outlet boundary cyclic boundary pairs is not the same. The inlet-outlet cyclic boundary conditions are used for the simulation of the turbulent channel flow with a specified constant mass flow rate m_{given} as shown in figure 3.7.

Normal cyclic boundaries

A linear interpolation can be easily implemented for the normal cyclic boundaries using the idea of 'ficticious' cells. Introducing the weighting factor $\alpha_f = \frac{|\overrightarrow{wW}|}{l}$, the following formula can be used to calculate the variables at the 'east' and 'west' faces:

$$\phi_w = \phi_P + (1 - \alpha_f)(\phi_{W^0} - \phi_P); \quad \phi_e = \phi_w \tag{3.38}$$

Inlet outlet cyclic boundaries

For a fully developed channel flow, in order to find the correct pressure and velocity distribution, inlet-outlet cyclic boundaries must be used. Therefore, the pressure correction equation must be constructed in such a way so that the corrected velocities satisfy continuity for each cell as well as the inlet mass flow rate m_{given}.

A new variable $\Delta P'$ is introduced and is used to drive the intermediate mass flow rate to m_{given}. The pressure corrections at W and E cells as shown in figure 3.7 are related with the ones of the inner fluid cells as follows:

$$p'_E = p'_P - \Delta P'; \quad p'_W = p'_{W^0} + \Delta P' \tag{3.39}$$

Discretization of all terms in the momentum equations yields an algebraic equation for every CV at time instant $n+1$

$$A_P U_{i,P}^{n+1} = \sum_{nb} A_{nb} U_{i,nb}^{n+1} - \frac{\partial P^{n+1}}{\partial x_i} \Delta\Omega + SU_P(U_{i,nb}^{n+1}, U_{i,P}^{n+1}), \tag{3.40}$$

where coefficients A_{nb} are evaluated with velocities, diffusivities from previous time step (or iteration).

In the first corrector step of the PISO algorithm, the correction of ith component of face velocity derived from equation 3.40 for the orthogonal grid is given by:

$$u'_{i,w} = -\left.\frac{\partial p'}{\partial \xi}\right|_w \left.\frac{\overline{\Delta\Omega}}{A_P}\right|_w = -\frac{p'_W - p'_P}{\partial \xi} \left.\frac{\overline{\Delta\Omega}}{A_P}\right|_w = -\frac{p'_{W^0} + \Delta P' - p'_P}{\partial \xi} \left.\frac{\overline{\Delta\Omega}}{A_P}\right|_w \tag{3.41}$$

Similar relationship holds for 'east' face as follows:

$$u'_{i,e} = -\left.\frac{\partial p'}{\partial \xi}\right|_e \left.\frac{\overline{\Delta\Omega}}{A_P}\right|_e = -\frac{p'_E - p'_{W^0}}{\partial \xi} \left.\frac{\overline{\Delta\Omega}}{A_P}\right|_e = -\frac{p'_P - \Delta P' - p'_{W^0}}{\partial \xi} \left.\frac{\overline{\Delta\Omega}}{A_P}\right|_e \tag{3.42}$$

In order to obtain the corrected velocities that give the prescribed mass flow rate m_{given}, the following relation is required:

$$\sum_{w \ faces} \rho(u_{i,w} + u'_{i,w}) \cdot n_{i,w} S_w = -m_{given}. \tag{3.43}$$

The minus (-) sign in the right-hand-side of the above equation comes from the fact that the normal vector is directed outwards to the inlet faces.

Substituting equation 3.41 into equation 3.43, the parameter $\Delta P'$ can be esti-

mated as follows:

$$\Delta P' = \frac{-m_{given} + m_{inter} + \sum_w \rho \frac{p'_{W0} - p'_P}{l} \xi_i \left.\overline{\frac{\Delta\Omega}{A_P}}\right|_w n_{i,w} S_w}{\sum_w \rho \frac{-1}{l} \xi_i \left.\overline{\frac{\Delta\Omega}{A_P}}\right|_w n_{i,w} S_w} \approx \frac{-m_{given} + m_{inter}}{\sum_w \rho \frac{-1}{l} \xi_i \left.\overline{\frac{\Delta\Omega}{A_P}}\right|_w n_{i,w} S_w} \tag{3.44}$$

where the intermediate mass flow rate is estimated as $m_{inter} = -\sum_w \rho u_{i,w} n_{i,w} S_w$. In SIMPLE, we do not know p'_{W0} and p'_P and thus the last term in the nominator was neglected in equation 3.44.

The SIMPLE algorithm suggested by Patankar and Spalding (1972) is modified for inlet-outlet cyclic boundaries as outlined below:

1. Solve momentum equations to obtain the node velocities.

2. Calculate face velocities using the Rhie and Chow method.

3. Calculate $\Delta P'$ from equation 3.44.

4. Solve pressure correction. For fluid cells next to the inlet and outlet boundaries, the source term will be modified to include the effect of $\Delta P'$.

5. Correct pressures and internal face velocities as usually. For boundary face velocities at inlet and outlet use equation 3.41 and 3.42.

6. Go to step 1 and iterate until convergence.

3.5 Solution of the linear algebraic equations

To solve the linear system of discretized equations mentioned above, $A\Phi = Q$, the bi-conjugate gradient method (BICG) was used with incomplete LU decomposition. Details are given by Theodoropoulos (1990). Fletcher (1976) has shown that the BICG method can handle both symmetric and asymmetric matrices. The BICG method requires almost twice as much effort as the conjugate gradient method, but converges in about the same speed.

3.6 Closure

The discretization approachs for the general transport equation were dicussed for each term. The Rhie and Chow interpolation method for the collocated arrangement was described and its accuracy was analysed. A brief introduction was also provided for the PISO algorithm used to deal with the pressure-velocity coupling. The classical boundary conditions were presented at the end of the chapter. A more detailed description of the finite difference truncation and aliasing errors associated with the nonlinear term is provided in appendix A. The discretization accuracy of the transient term is illustrated using the one-dimensional inviscid linear Burgers equation in Appendix B. Finally information on the kinetic energy conservation properties of the numerical method is provided in Appendix C.

Chapter 4

LES OF TURBULENT CHANNEL FLOW

4.1 Introduction

It is believed that Deardorff (1970) presented the first LES calculation of a turbulent channel flow. The Smagorinksy constant $C_s \approx 0.094$ was used. Over the years, the Smagorinsky model has been the most widely used SGS model. Despite that, it has some notable drawbacks including (i) a case dependent model coefficient C_s; (ii) incorrect prediction of the asymptotic behaviour near a wall (in particular, the eddy viscosity near solid boundary is highly over-predicted); (iii) no provision of SGS energy backscatter to the resolved scales; and (iv) incapability in simulating transition to turbulence flow (Kleiser and Zang, 1991).

During the last 30 years, different kinds of methods have been applied for the calculation of turbulent channel flow at increasing Reynolds numbers: LES calculations including those of Moin and Kim (1982) at $Re_\tau = 640$, Kravchenko et al. (1996) and Kravchenko and Moin (1997) at $Re_\tau = 1100$ and DNS calculations including those of Kim et al. (1987) at $Re_\tau = 180$, Moser et al. (1999) at $Re_\tau = 590$ and Abe et al. (2001) at $Re_\tau = 640$. Researchers are investigating the turbulent flow and heat transfer at ever increasing Reynolds and Prandtl numbers as indicated by the DNS investigations performed by Kawamura et al. (1998, 1999).

LES has been shown to give improved predictions for many turbulent flows at medium to large Reynolds numbers compared to RANS. In contrast to RANS, where the steady or unsteady solutions are smooth, turbulent flows have broad band spectra, and most numerical methods used for robust RANS computations

[0]Part of results presented in this chapter are published in Liang and Papadakis (2003).

are inaccurate for the numerical representation of the medium to small resolved eddies in LES (Moin, 2002). LES also consumes substantially less computational resources than that required for DNS, since only the largest, most energetic scales need to be resolved. Nevertheless, if the purpose of using LES is to capture the turbulent structures, which are not availabe from RANS, sufficient grid resolution is often required (Jimenez and Moin, 1991) in contrast to DNS where the vast majority of grid points is devoted to the dissipation range (Pope, 2000).

However, many LES calculations fail in simulating the transition from laminar- to turbulent-state of a channel flow, due to either improper setting of initial conditions or low accuracy of numerical schemes in solving the momentum and the continuity equations. Physically, the small turbulent energy-containing scales generated from the walls can be 5-10 times smaller than these of a turbulent single cylinder flow at a comparable Reynolds number. The accuracy of the solution of the Navier Stokes equations is highly determined by the spatial discretization and the time advancement schemes as shown in Appendix B.

On the other hand, the conventional Smagorinsky model may also fail in simulating turbulent channel flow due to either high predicted eddy viscosity near the walls or improper tuning of the Smagorinsky constant C_s. For instance, when the resolved flow is laminar, the standard value of C_s overestimates the SGS stress and dissipation, often preventing transition to turbulence (Piomelli and Zang, 1991).

Accurate prediction of the second order Reynolds stresses requires careful treatment in controlling numerical, filtering and modelling errors (Chow and Moin, 2003). As discussed by Laurence (2002), in coarse LES calculations, typically, wall-normal fluctuations are underestimated but streamwise fluctuations are however overestimated. He attributed this to insufficient resolution of the pressure field. In the Finite-Volume context, the collocated approach introduces pressure-gradient interpolation (Rhie and Chow, 1983) leading to diffulty of kinetic energy conservation, compared to staggered arrangements (Ham et al., 2002).

Many different new developments in turbulence modelling were made recently. Fröhlich and Rodi (2002) summarised three directions for LES to develop: (i) the construction of explicit filtering. For example, Vasilyev et al. (1998) has devised filters to commute with discrete derivatives; (ii) the use and improvement of higher order energy-conserving discretization schemes (Morinishi et al., 1998; Vasilyev, 2000); and (iii) the use of higher order methods as they narrow the range of scales which are influenced by the discretization of the filtered equations. More comprehensive reviews can be found in Lesieur and Metais (1996) and Meneveau

and Katz (2000). More recently, Gullbrand and Chow (2003) concluded that (a) turbulence modelling played a more important role when the 4th order finite-difference scheme was used compared to the 2nd order scheme; and (b) explicit filtering can be used as a means to reduce the influence of the numerical errors in the high wavenumbers.

It must be pointed out here that a general drawback of the models developed for channel flow is their difficulty to be extended to unstructured complex grids. This is because more flexible grids have to be used in order to simulate flows in complex geometries, thus higher-order difference schemes can not be implemented as conveniently as for the turbulent channel flow.

To accelerate the transition from laminar to turbulent state of a channel flow, the Orr-Sommerfeld equation is solved using a fourth order finite difference scheme and the most unstable perturbation is imposed on the laminar flow solution. A good kinetic energy conserving scheme is developed through careful spatial and temporal discretizations of both the momentum and the continuity equations.

The purpose of this chapter is to validate the finite-volume collocated grid code using channel flow predictions at two different Reynolds numbers. The rest of the chapter is arranged as follows: the process of solving the Orr-Sommerfeld equation will be firstly described in the first section below. The computational conditions for the channel flow at two different Reynolds numbers will be introduced in the first part of the second section. The predicted results are compared with the available DNS data and a discussion is given at the end of the section. Finally, this chapter is summarised and the mean conclusions of the work are drawn.

4.2 Solving the Orr-Sommerfeld equation using a 4CDS

Small disturbances super-imposed to the laminar flow solution of the 2D Navier-Stokes equations of a plane Poiseuille flow lead to an eigenvalue problem described by the Orr-Sommerfeld equation with given boundary conditions. The Orr-Sommerfeld instability equation is

$$\frac{d^4\phi}{dy^4} - 2\alpha^2\frac{d^2\phi}{dy^2} + \alpha^4\phi - i\alpha Re_c\left\{(\overline{u}-C)\left(\frac{d^2\phi}{dy^2}-\alpha^2\phi\right) - \frac{d^2\overline{u}}{dy^2}\phi\right\} = 0 \qquad (4.1)$$

where ϕ is the disturbance field and C is the complex phase velocity of the disturbance, α is its streamwise wavenumber, and $Re_c = \frac{U_c\delta}{\nu}$ is Reynolds number based

on the centerline velocity U_c and channel half length δ. For more introduction about the derivation of the equation, the interested reader is referred to the book of Schmid and Henningson (2001). The laminar streamwise velocity solution is given as

$$\overline{u} = U_c \left(1 - \eta^2\right) \tag{4.2}$$

where, $\eta = y/\delta$.

Non-slip wall boundary conditions are used at the top and bottom planes $|\eta| = 1$ as

$$\phi = 0 \quad \frac{d\phi}{dy} = 0, \tag{4.3}$$

and the symmetrical boundary conditions are applied at the centerline $\eta = 0$ as

$$\frac{d\phi}{dy} = 0 \quad \frac{d^3\phi}{dy^3} = 0. \tag{4.4}$$

In particular, we use the following formulation used by Thomas (1953) in order to gain a more accurate difference equation

$$f = \phi - \frac{1}{6}\Delta y^2 \frac{d^2\phi}{dy^2} + \frac{1}{90}\Delta y^4 \frac{d^4\phi}{dy^4} \tag{4.5}$$

The Orr-Sommerfeld equation is then discretised and put into a linear system form as

$$\mathcal{A}\mathcal{F} = \mathcal{R} \tag{4.6}$$

where $\mathcal{A}$ is an $N \times N$ matrix, $\mathcal{F}$ is an $1 \times N$ matrix of f and $\mathcal{R}$ is an $1 \times N$ matrix with all elements set as zero, except for the first element which set as 1.

The Gauss-Jordan scheme with full pivoting is used to get an upper triangular matrix and obtain the solution of the linear system. The Newton method is used in order to search for a complex number C that will make the $\mathcal{A}$ matrix singular.

Given different values of the streamwise wavenumber α, we can solve the Orr-Sommerfeld equation and obtain the most unstable eigenvalue as shown in Figure (4.1). The streamwise wavenumber 0.875 gives the maximum value of αC_i for case B defined in table 4.1, therefore, this eigen-mode is chosen for obtaining the eigen-solutions.

After adjusting $\phi|_{\eta=0} = 1$ for normalization, the final eigen-solutions of the Orr-Sommerfeld equation are shown in Figures 4.2 and 4.3 for the real and imaginary

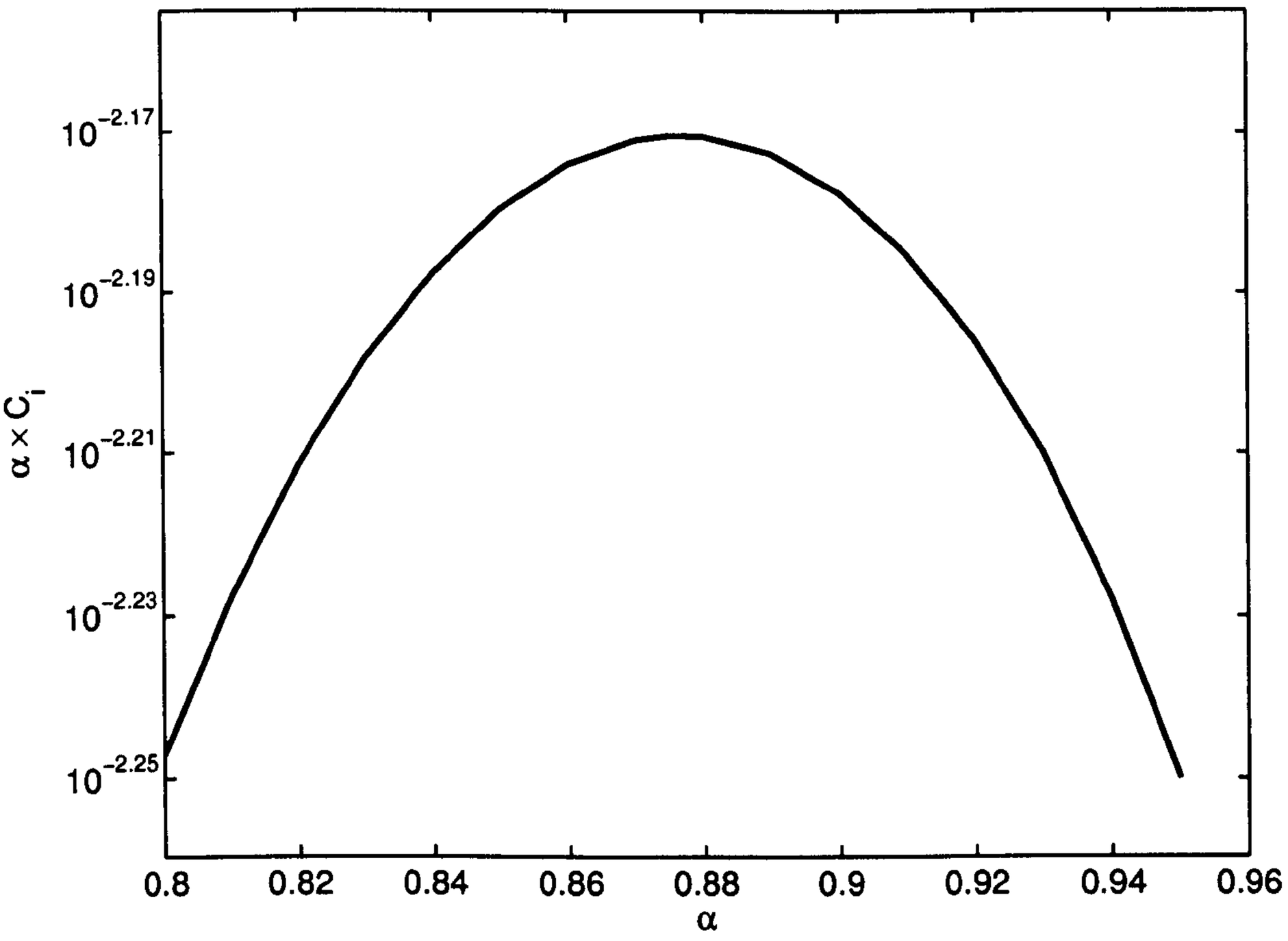

Figure 4.1: The product of the streamwise wavenumber and the imaginary part of disturbance velocity against streamwise wavenumber

parts respectively.

The streamfunction of the perturbation field is given by

$$\psi = \phi(\eta)e^{i(kx-\omega t)} \tag{4.7}$$

where $\omega = C\alpha U_c/\delta$ and $k = \alpha/\delta$.

Thus we can evaluate the velocity disturbance using the following relationships

$$u' = \frac{\partial \psi}{\partial y} = \frac{d\phi(\eta)}{dy}e^{i(kx-\omega t)} \tag{4.8}$$

$$v' = -\frac{\partial \psi}{\partial x} = -ik\phi(\eta)e^{i(kx-\omega t)} \tag{4.9}$$

The disturbance is imposed on the laminar solution of the plane Poiseuille flow as

$$u = \overline{u} + \epsilon u' \tag{4.10}$$

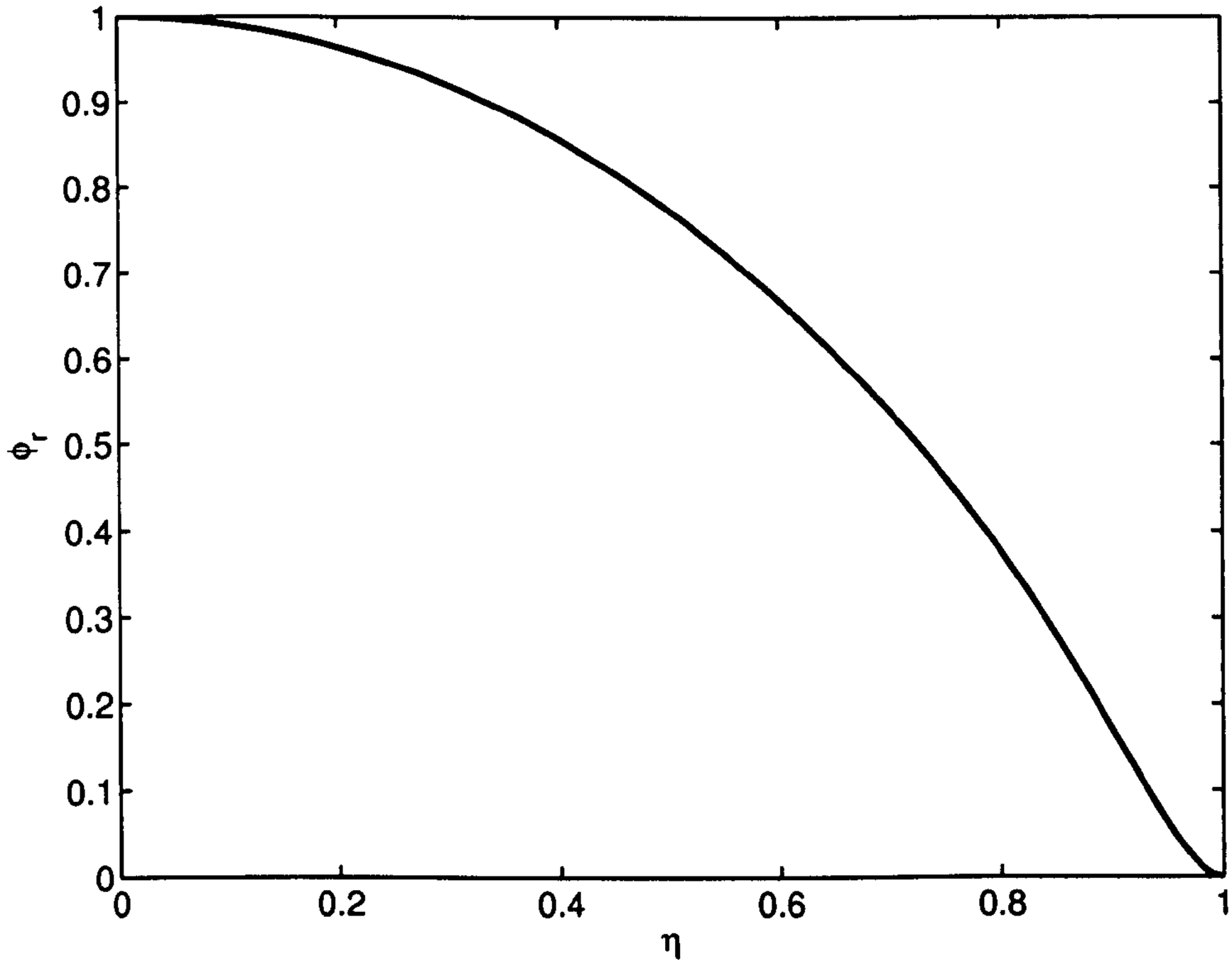

Figure 4.2: The eigen-solution of the Orr-Sommerfeld equation (real part)

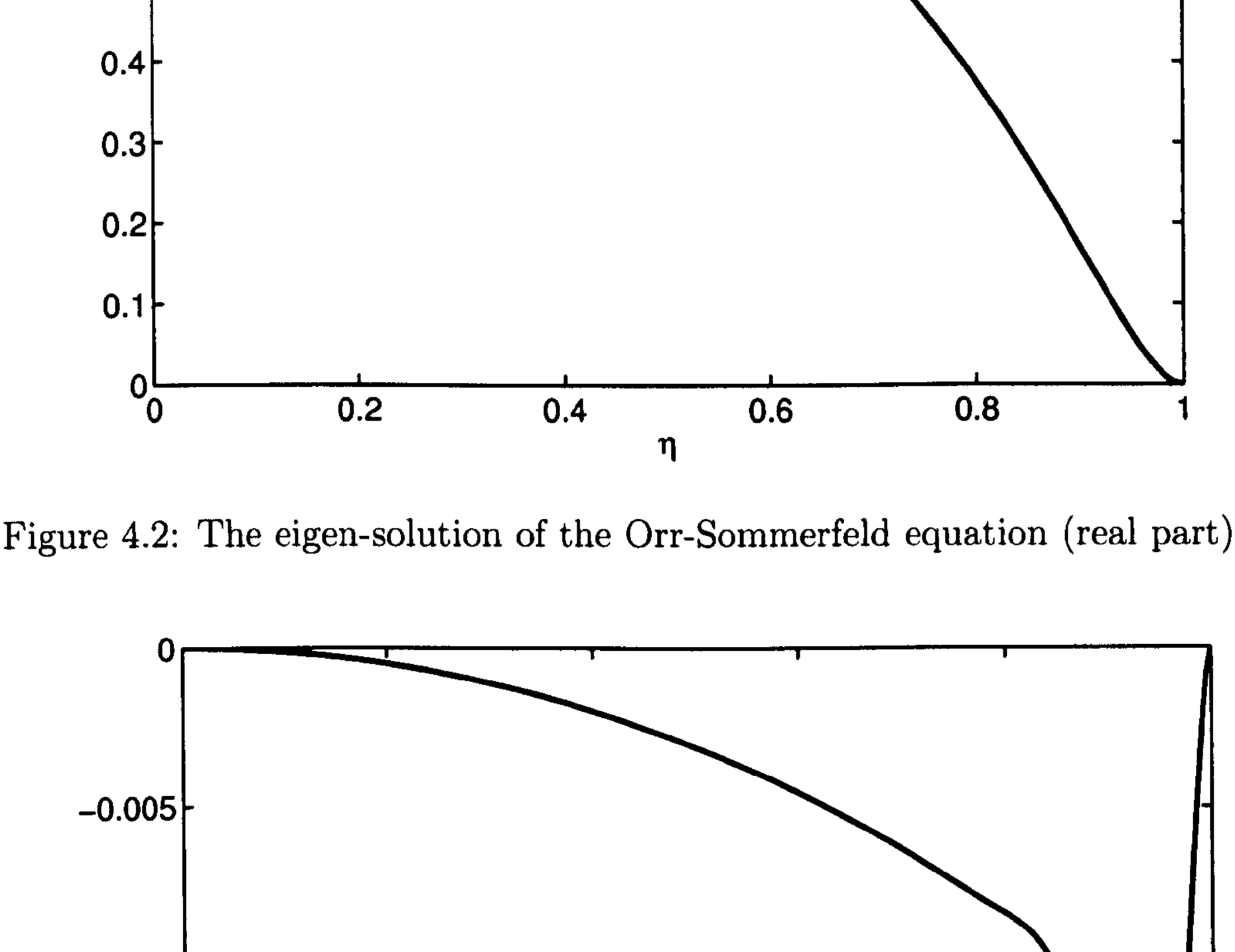

Figure 4.3: The eigen-solution of the Orr-Sommerfeld equation (imaginary part)

Figure 4.4: Contour plot of the imposed streamwise perturbation velocity field. The values are presented in m/s.

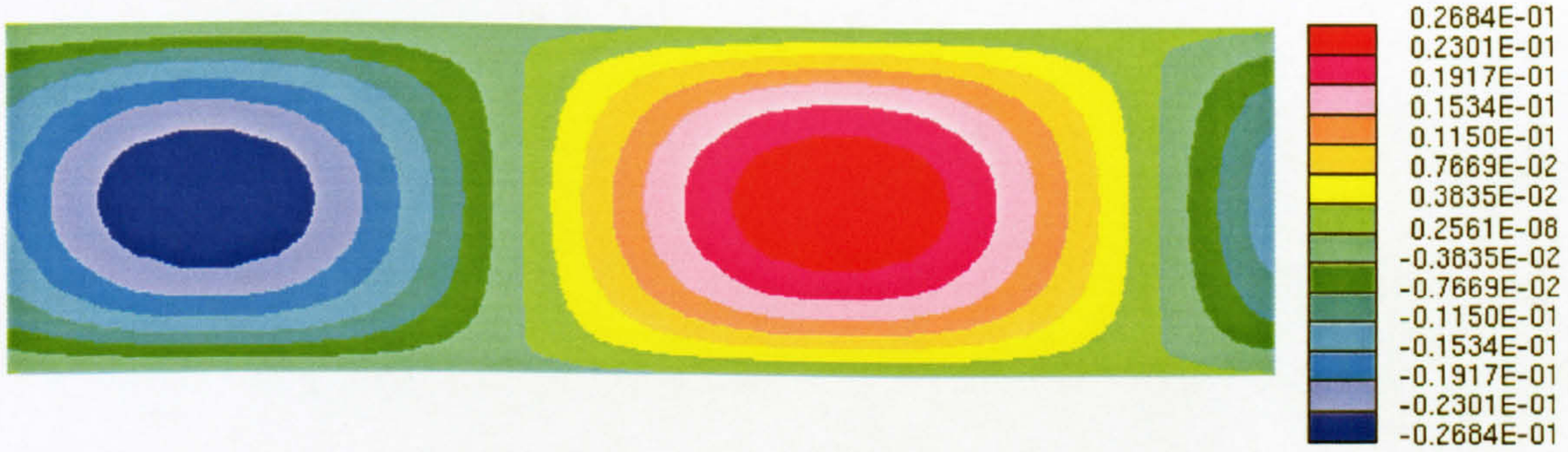

Figure 4.5: Contour plot of the imposed wall-normal perturbation velocity field. The values are presented in m/s.

$$v = \epsilon v' \tag{4.11}$$

where ϵ is a small number normally less than 1 to ensure that a small disturbance is imposed on the laminar flow solution. (ϵ is 0.5 for the present investigation). For example, the determined perturbation fields for case B at Reynolds number ($Re_c = \frac{u_\infty \cdot \delta}{\nu} = 12,960$) are shown in Figure (4.4) for $\epsilon u'$ and Figure (4.5) for $\epsilon v'$.

4.3 Modelling of Channel Flow at Two Different Reynolds numbers

4.3.1 Computational conditions

As presented by Jimenez and Moin (1991), a minimal set of structures in a channel flow are necessary in order to sustain a turbulent boundary layer and play an important dynamic role in the simulated flow. Thus the computational mesh for

Channel flow computational conditions					
Cases	Re_τ predicted	Cell Number	Mesh spacing (wall units)	Δt^+	CFL Number
A	970	$N_x = 96$	$\Delta x^+ = 77.6$	0.84	Max=0.5
		$N_y = 64$	$155.5 \geq \Delta y^+ \geq 0.71$		Mean=0.18
		$N_z = 48$	$\Delta z^+ = 31.7$		
B	680	$N_x = 88$	$\Delta x^+ = 58.8$	0.2	Max=0.16
		$N_y = 96$	$58.6 \geq \Delta y^+ \geq 1.1$		Mean=0.05
		$N_z = 64$	$\Delta z^+ = 17.7$		
FR Coarse Mesh	504	n/a	$\Delta x^+ = 62$	n/a	n/a
		$N_y = 65$	$\Delta y^+ \geq 1.8$		
		n/a	$\Delta z^+ = 30$		
FR Finer Mesh	600	n/a	$\Delta x^+ = 50$	n/a	n/a
		159	$\Delta y^+ \geq 1$		
		n/a	$\Delta z^+ = 16$		

Table 4.1: Computational conditions for the channel flow simulations. FR represents the work by Fröhlich and Rodi (2002).

the channel flow should be capable of capturing the structures responsible for the generation of the low-order statistics. The computational domain shown in figure 4.6 has the following parameters: the streamwise length $L_x = 2\pi\delta/\alpha$, the wall-normal length $L_y = 2\delta$ and the spanwise length $L_z = \delta\pi/2$.

Two cases of the channel flow were simulated with details shown in Table 4.1. The LES computations using the coarser mesh (see figure 4.7) have been presented by Liang and Papadakis (2003). The Reynolds number is based on the wall friction velocity and channel half height δ. The mesh spacings in wall units shown in the table are also evaluated using the predicted wall friction velocity. Only 64 cells are used for case A in the wall-normal direction which is close to the 65 cells used for the coarser mesh by Fröhlich and Rodi (2002) at a much smaller Reynolds number.

The finer mesh is shown in figure 4.8 for case B. Totally, 96 cells are used in the wall-normal direction with 32 cells equally spaced in the middle of the centerline region $\frac{2}{3}\delta$. It should also be noted that, for a slightly smaller Reynolds number calculation, Fröhlich and Rodi (2002) used about twice the number of cells in this direction used for case B.

The LES calculation for case B was performed using the upstream mean velocity $\overline{u} = 0.36m/s$ which is the same as the one used for the approaching flow over a single cylinder which will be presented in subsequent chapter. The wall-normal length L_y is also equivalent to the ones used for the single cylinder flow as well

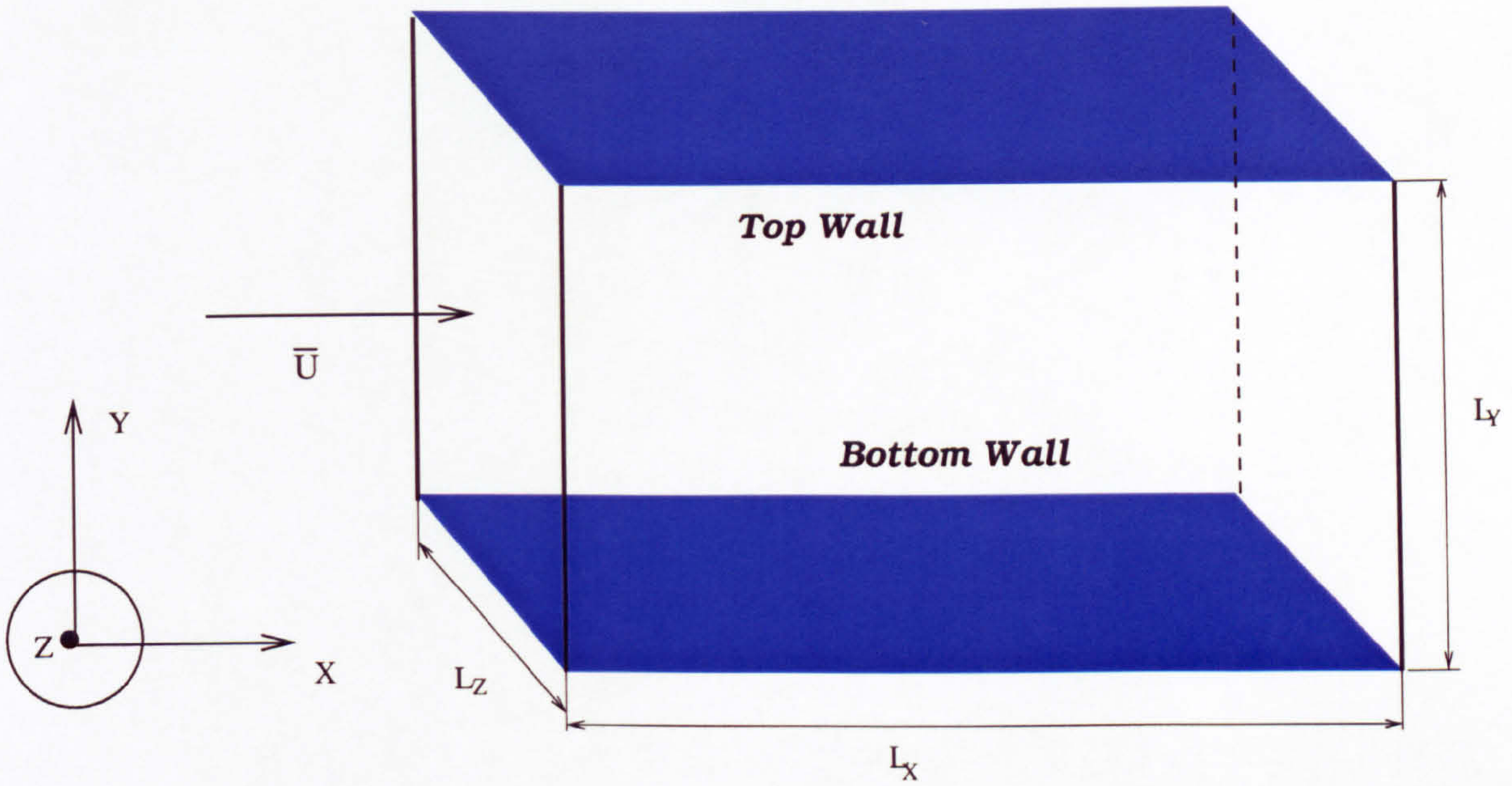

Figure 4.6: The channel flow computational domain

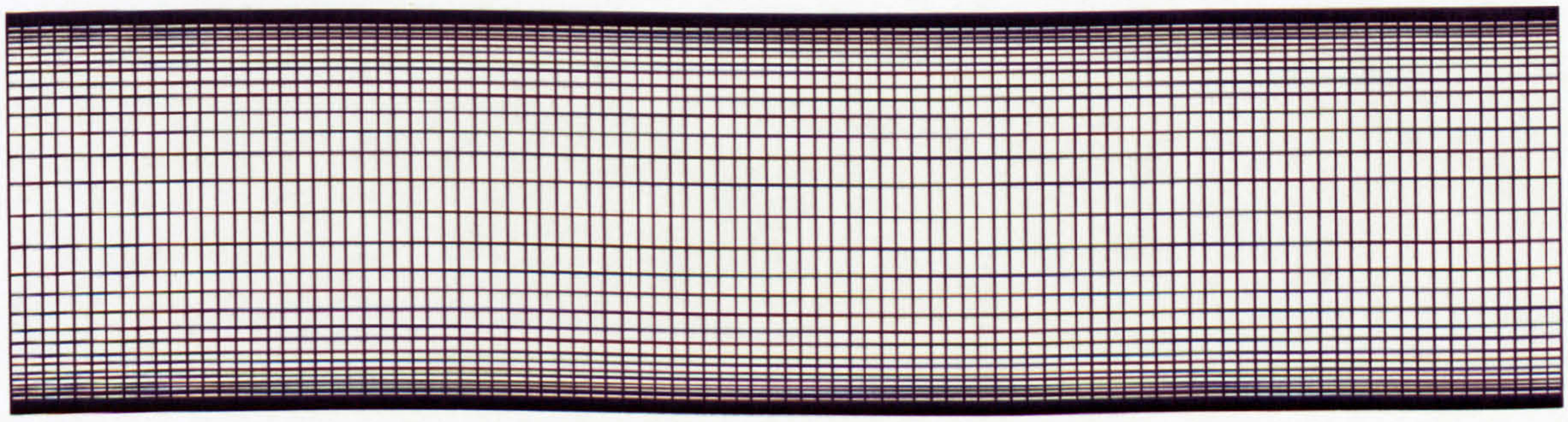

Figure 4.7: Coarser mesh used in case A (x-y view).

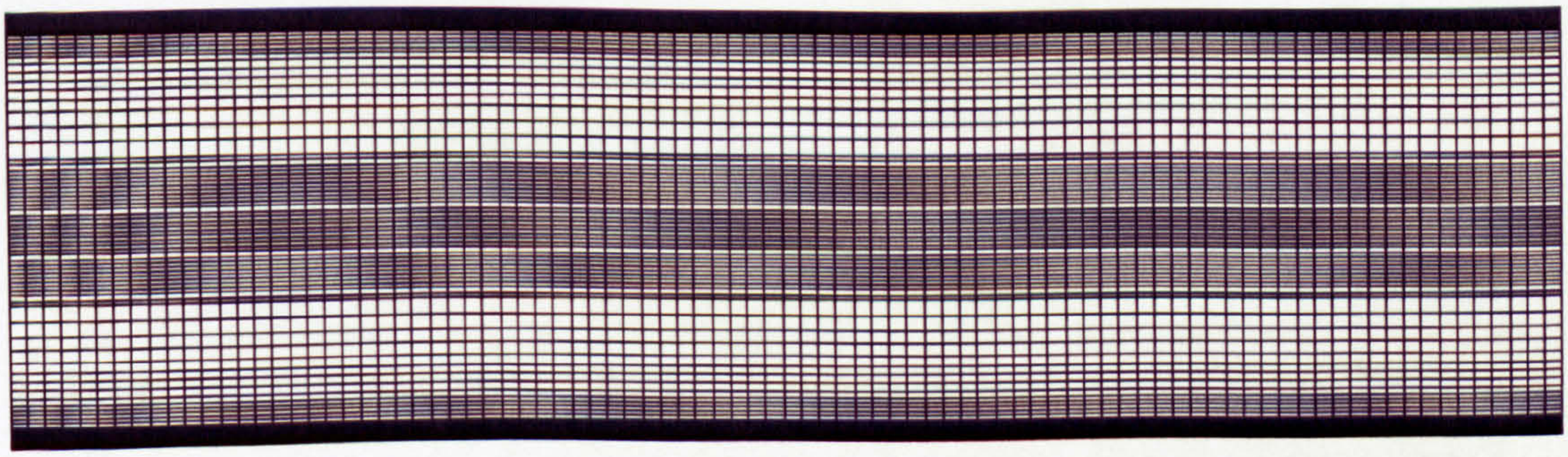

Figure 4.8: Finer mesh used in case B (x-y view).

as the flow over tube bundles which will be presented in chapters 6 and 7. An estimation of the friction velocity u_τ can be obtained by iteratively solving the following equation:

$$\overline{u} = u_\tau \left\{ \frac{1}{k} ln \frac{\delta u_\tau}{\nu} + B - \frac{1}{k} \right\} \tag{4.12}$$

where $B = 5$, $k = 0.42$ and $\delta = 0.036$. The friction velocity is determined approximately as 0.02m/s and the corresponding Reynolds number is $Re_\tau = 680$. The closest Reynolds number for which detailed DNS data are available is the one reported by Abe et al. (2001), which is equal to $Re_\tau = 650$.

This value was used to obtain the mesh spacings in wall units in order to have a check of the grid resolution and to compare with other investigators. Periodic boundary conditions are used in the streamwise and spanwise directions. The details of the implemention were discussed in chapter 3.

4.3.2 Discretization schemes and turbulence closure model

The standard Smagorinsky model is modified with the van Driest damping applied to the wall (equation 4.13) so as to damp the predicted eddy viscosity in presence of the wall:

$$\nu_T = \left(C_s \Delta (1 - e^{-y^+/25}) \right)^2 \left| \widetilde{S} \right|, \tag{4.13}$$

where the non-dimensional distance from the wall is $y^+ = (\delta - |y|)u_\tau/\nu$ taking into account the presence of two symmetrical walls on either sides of the centerline and C_s is equal to 0.065.

The Smagorinsky constant can also be evaluated as a function of time and y by the dynamic model without test filtering presented in Chapter 2. It can be used to eliminate the difficulty and ambiguity of evaluating y^+ in complex geometries which makes the van Driest damping function difficult to apply. Apart from this difficulty, the van Driest damping can not reproduce the correct asymptotic behaviour of μ_τ close to the wall (Fureby et al., 1997), and this problem can be solved by using the dynamic model.

As described in Chapter 3, the Finite Volume method applied on a collocated grid system is employed to discretize the governing equations. All terms in the momentum equation are discretized using the 2nd order central difference scheme (CDS) in space, and the 2nd order Crank-Nicolson scheme is employed to advance them in time, except for the pressure term which is treated implicitly. The PISO scheme (Issa, 1986) is used to deal with the pressure coupling between the

momentum and the continuity equations.

The discrete kinetic energy transport equation is analysed using similar operators to those used by Ham et al. (2002) as explained in appendix C. The present approach is found to be kinetic energy conserving in an uniform mesh for all terms apart from the pressure term. However, in a non-uniform mesh, the convective term is not kinetic energy conserving. An accuracy analysis of the Rhie and Chow interpolation method has proved that the method dissipates energy in both uniform and non-uniform meshes with an error which is of a second order accuracy with respect to the grid size.

4.3.3 Results and discussion

Case A

Figure 4.9 shows comparison between the results obtained using the LES method and the DNS data of Satake et al. (2003). The streamwise velocity fluctuations are over-predicted, while the wall-normal fluctuations are slightly under-estimated. However, the shear stress is very well predicted. As shown in figure 4.10, the results of the standard Smagorinsky model are very close with the ones of the dynamic model, but in the centerline region, both simulations overpredict the law of the wall formula. It is believed that this is partially attributed to the coarser resolution in the spanwise direction which underpredicts the wall friction velocity as also pointed out by Fröhlich and Rodi (2002). The underpredicted wall friction velocity can be seen from the y^+ coordinate in figure 4.9, where the maximum of y^+ only reaches 970 compared with the DNS prediction value of 1100. The under-prediction of the wall friction velocity will directly lead to the overprediction of the normalized streamwise velocity fluctuation. Lund and Kaltenbach (1995) pointed out that grid refinement can greatly improve the velocity fluctuation profiles. On the other hand, Laurence (2002) has stated that insufficient resolution of the pressure field for the collocated arrangement leads to the underestimation of wall-normal fluctuations compared to the staggered arrangement, because the former introduces pressure-gradient interpolation operations. Indeed, the staggered grid arrangments seem to be more suitable for LES, considering also their advantages in conserving the kinetic energy (Ham et al., 2002).

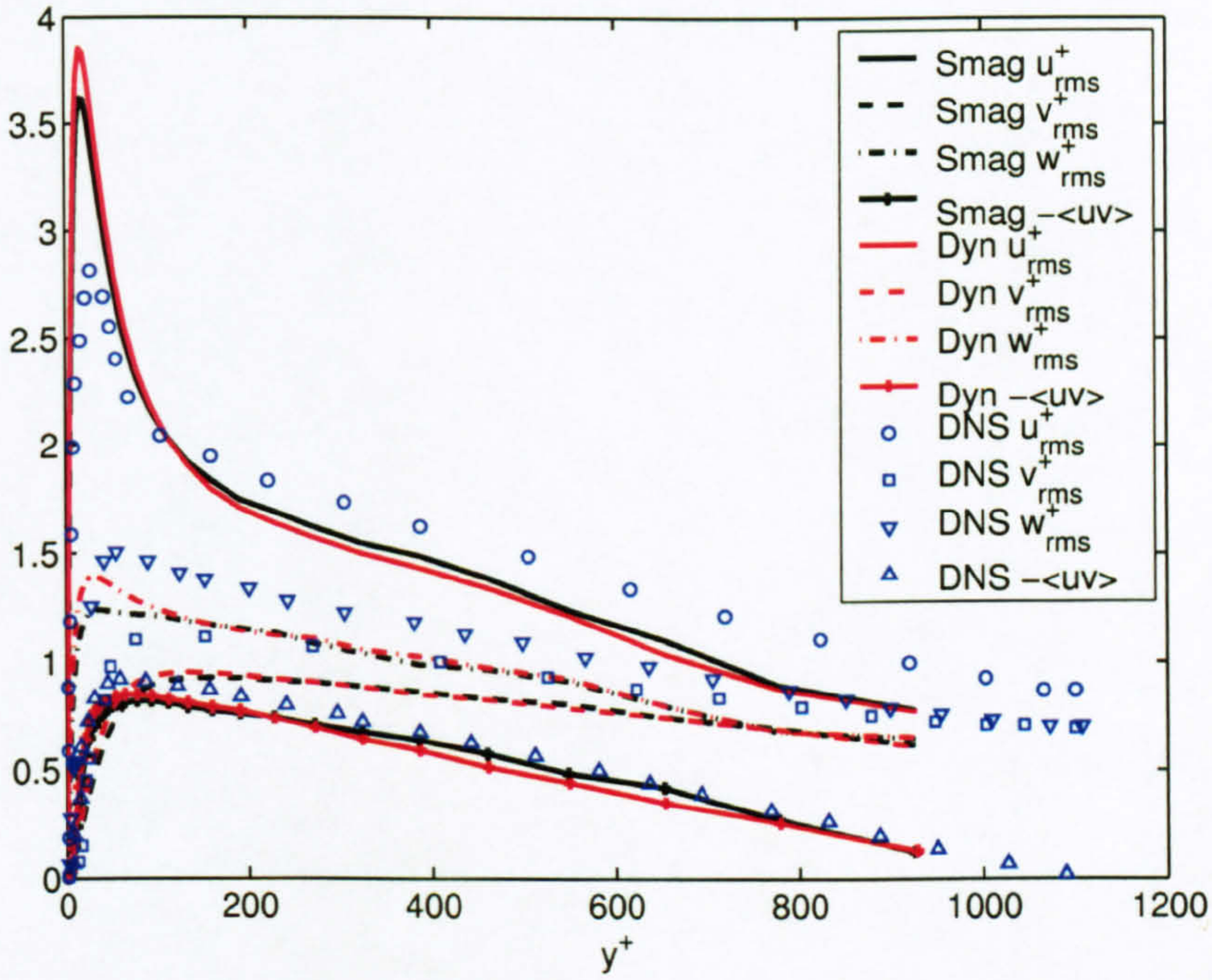

Figure 4.9: Comparison between the predicted r.m.s velocity fluctuations using the LES method against DNS data (Satake et al., 2003) for Case A.

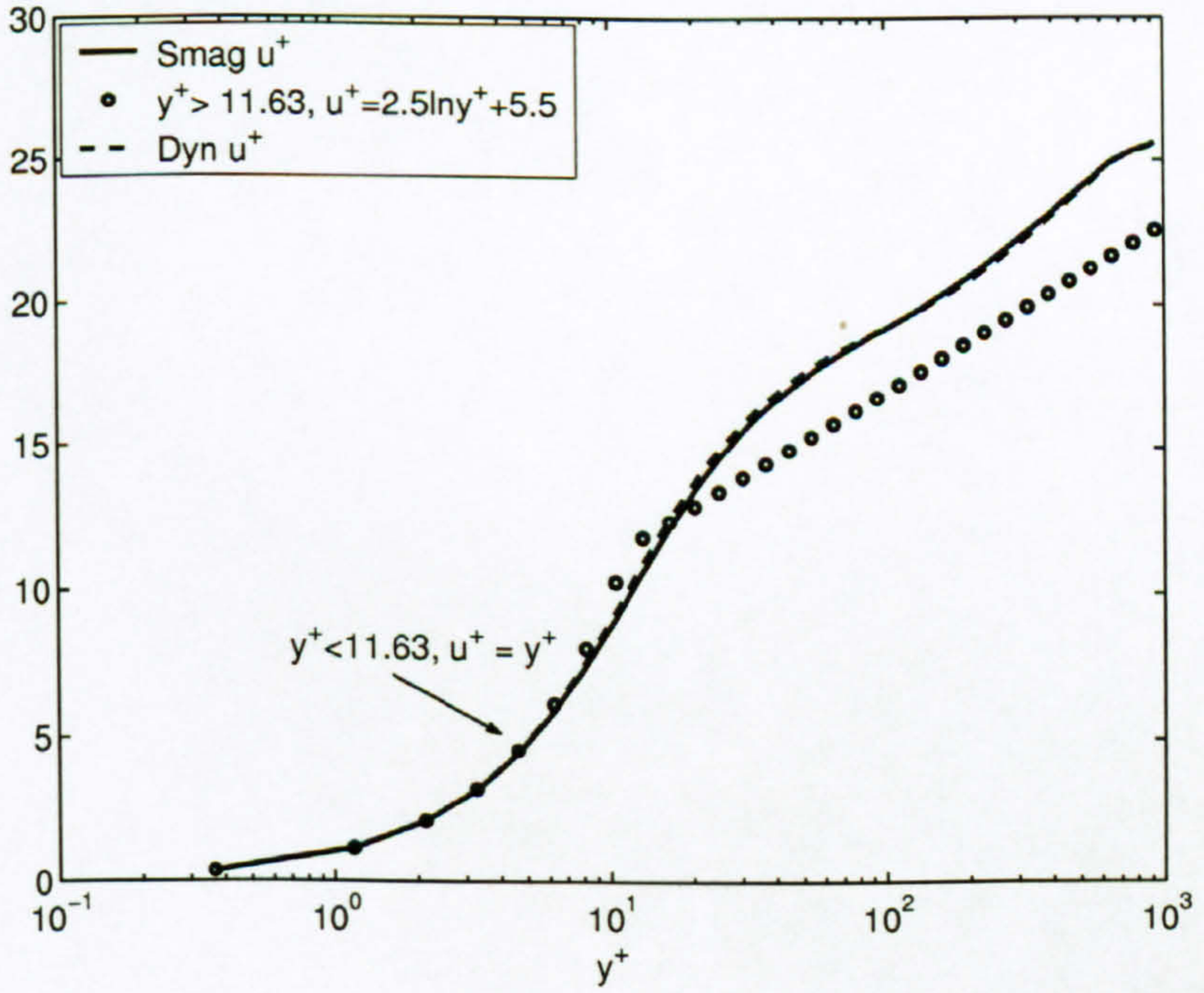

Figure 4.10: Mean velocity profiles predicted by Smagorinsky model and dynamic model against the law of the wall formula for Case A.

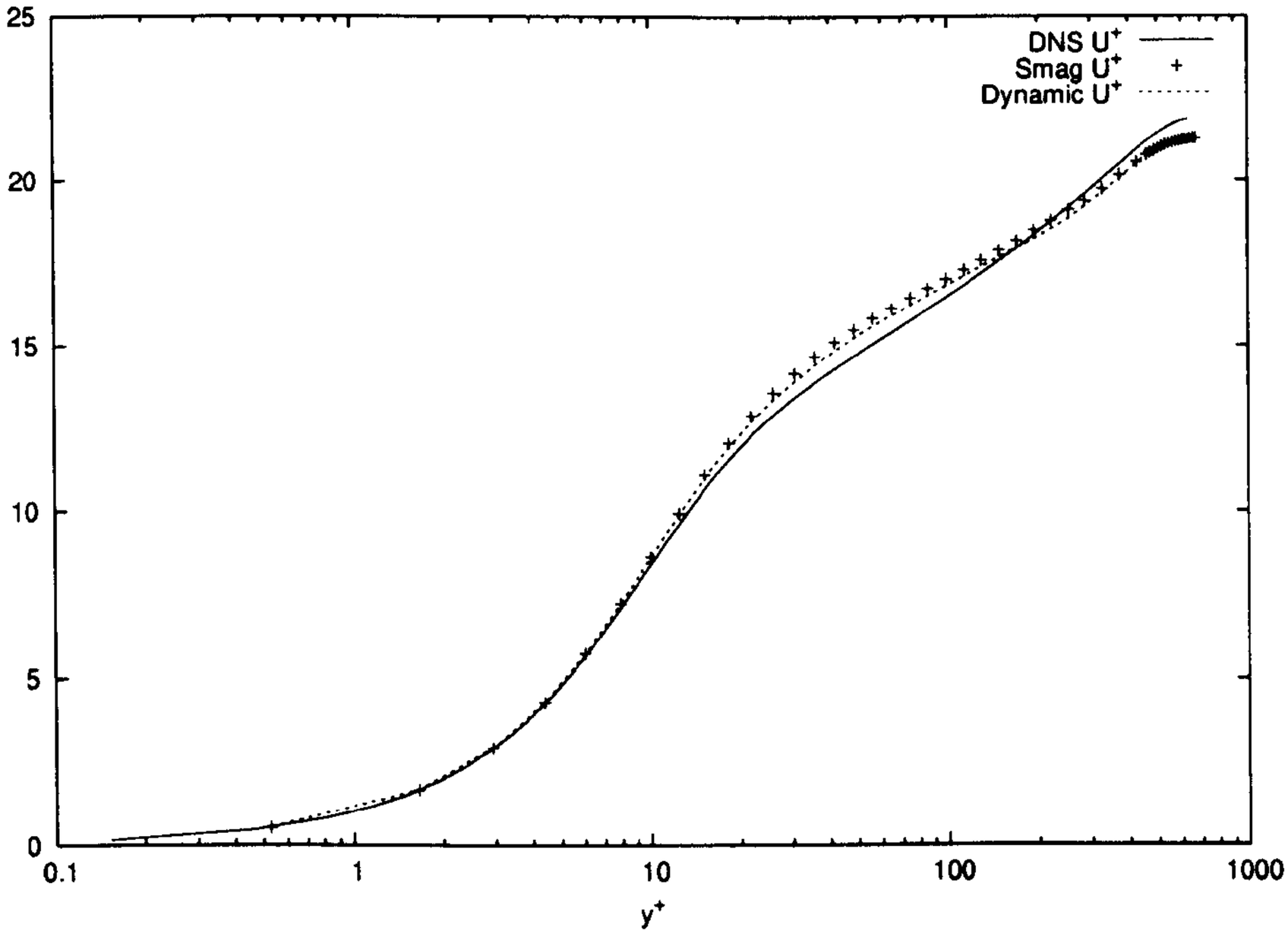

Figure 4.11: Comparison of predicted mean velocity profile of fully developed turbulent channel flow against the DNS data of Abe et al. (2001) for case B.

Case B

Case B has a lower Re_τ and the calculations are performed using a finer mesh. The friction velocity obtained using the Smagorinsky model with the van Driest damping wall function is 0.019 (and the dynamic model predicted the same value which gives $Re_\tau = 680$). The value of the predicted wall friction velocity is consistent with the value $Re_\tau = 684$ obtained using equation (4.12). The mean profiles obtained using both the Smagorinsky and the dynamic models agree well with the DNS results of Abe et al. (2001) as shown in figure 4.11. Figure 4.12 shows the variation of the Smagorinsky constant C_s^t as predicted by the dynamic model against the wall-normal distance y^+ to the wall. The value of C_s^t goes to zero close to the wall as expected. The maximum value of the coefficient 0.082 is found at the location $y^+ = 580$. Chester et al. (2001) predicted a maximum value of around 0.12 at Reynolds number $Re_\tau = 180$. This difference is possibly due to the fact that case B has a much higher Reynolds number. It is also noted that the predicted values of C_s^t in the bulk region agree quite well with the values obtained *a priori* from filtered DNS of minimal channel flow at $Re_\tau = 180$.

The root-mean-square velocity fluctuations are obtained by taking the average in the streamwise and spanwise directions. In figure 4.13 the results of the

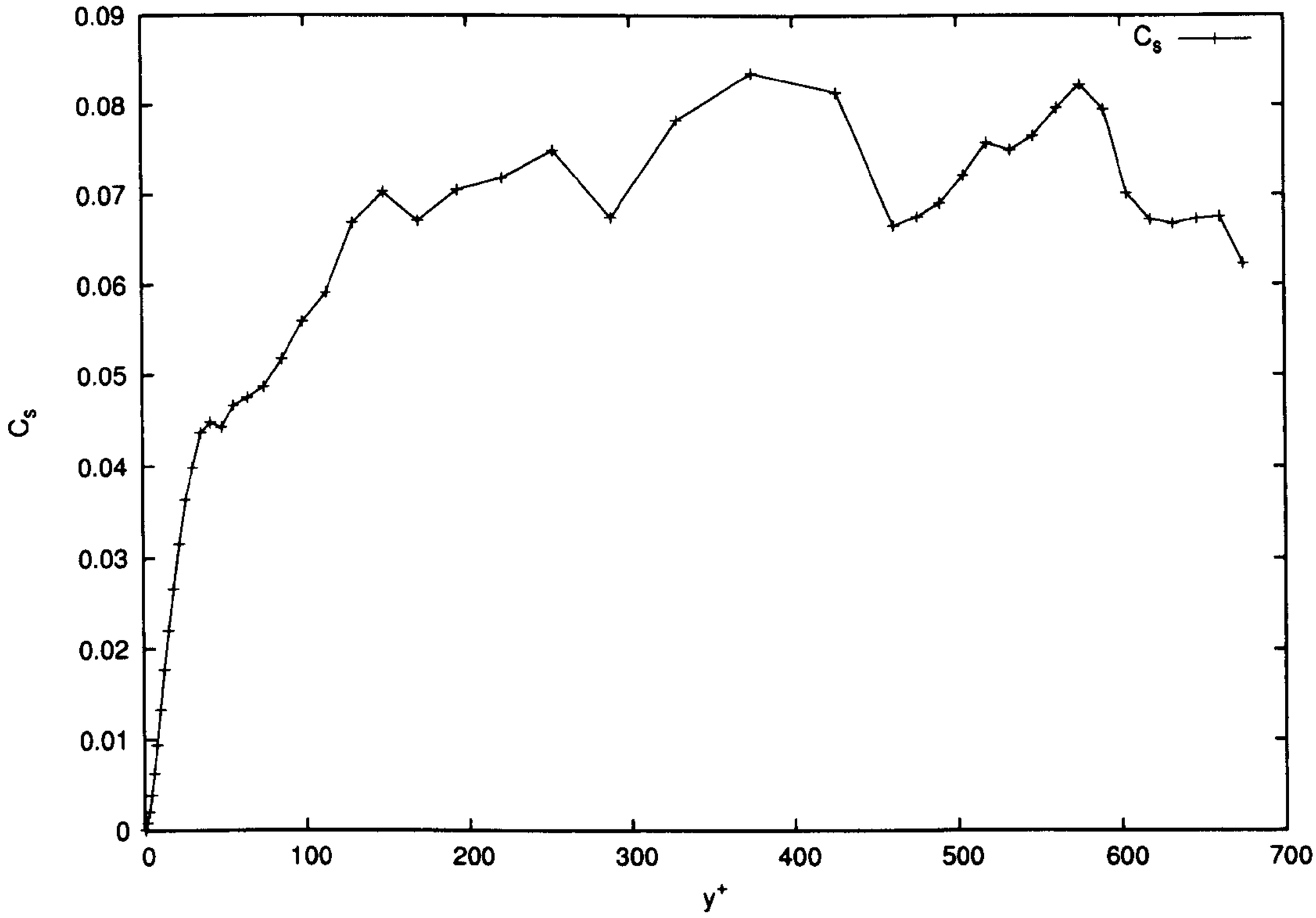

Figure 4.12: Variation of the instantaneous Smagorinsky constant predicted by the dynamic model without test filtering for Case B.

Smagorinsky model are plotted with the DNS results. It is noted that the Reynolds number of the DNS investigation is slightly smaller than the one of the LES calculation for case B, as explained earlier. The streamwise velocity fluctuations are under-estimated in the core region for case B with the finer mesh. The Reynolds stress profiles predicted are very similar to the finer mesh results obtained by Fröhlich and Rodi (2002), who observed the same discrepancy for the streamwise Reynolds stress in the core region. On the other hand, very promisingly, the spanwise velocity fluctuations and Reynolds shear stress $- < uv >$ are only slightly under-estimated and the dynamic model results agree also well with the Smagorinsky model ones. This gives a stronger basis for application of this dynamic model to more complex configurations.

One of the promising advantages of LES over RANS is that LES can model the coherent structures of the turbulence. In the near wall region, roughly from $y^+ = 8$ to 110, the flow is highly organized with regions of high- and low- speed fluid (streaks) alternating in the spanwise direction (as shown in figures 4.14 and 4.15). High-speed streaks are generated by convection of high momentum fluid toward the wall and are generally shorter than the low-speed streaks. The predicted spanwise

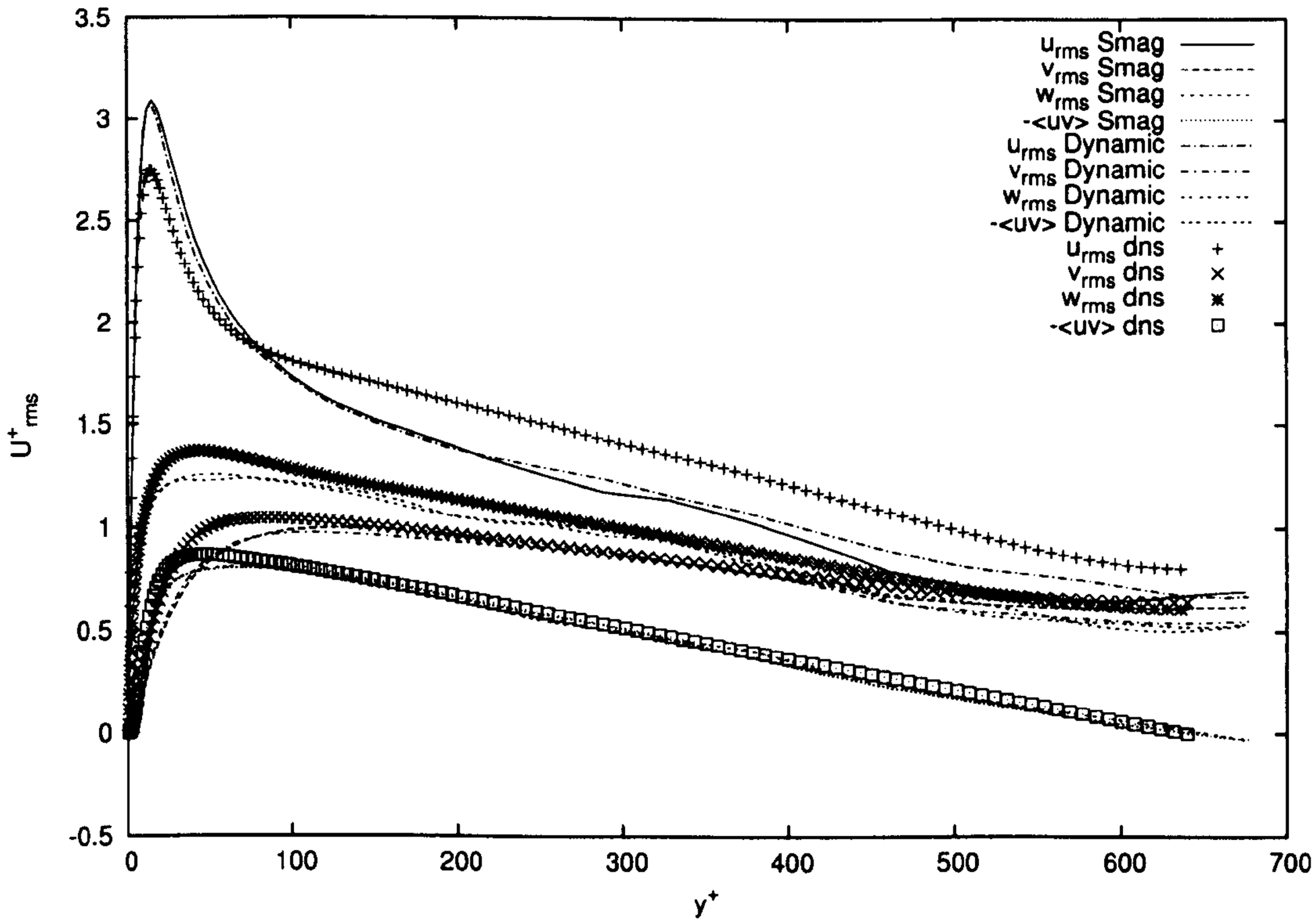

Figure 4.13: Root-mean-square velocity fluctuations normalized by the wall friction velocity for Case B.

spacing is in good agreement with the averaged spaced spanwise wavelength $\Delta z^+ \approx 100$ reported by Smith and Metzler (1983). The streamwise length of the streaks is around $\Delta x^+ = 1000$, consistently with Kim et al. (1971). Low-speed streaks act as apparent sites for the production of turbulent kinetic energy via a bursting process defined by Kim et al. (1971). During this process, individual low-speed streaks are lifted away from the wall, oscillate and then break down so that a substantial portion of the low-speed fluid is ejected away from the wall. It can also be observed that the low-speed streaks tend to merge accompanied by an increase of spanwise wavelength and a decrease of streamwise wavelength as the distance away from the wall increases.

The formation of velocity streaks is associated with the advection of the mean velocity gradient by streamwise vortices. Bulges of streamwise vortices and shear layers were also found to protrude from the boundary layer into the outer flow (see figure 4.16). The bursting process is also believed to be associated with the production of the turbulent kinetic energy close to the wall (Kim et al., 1971).

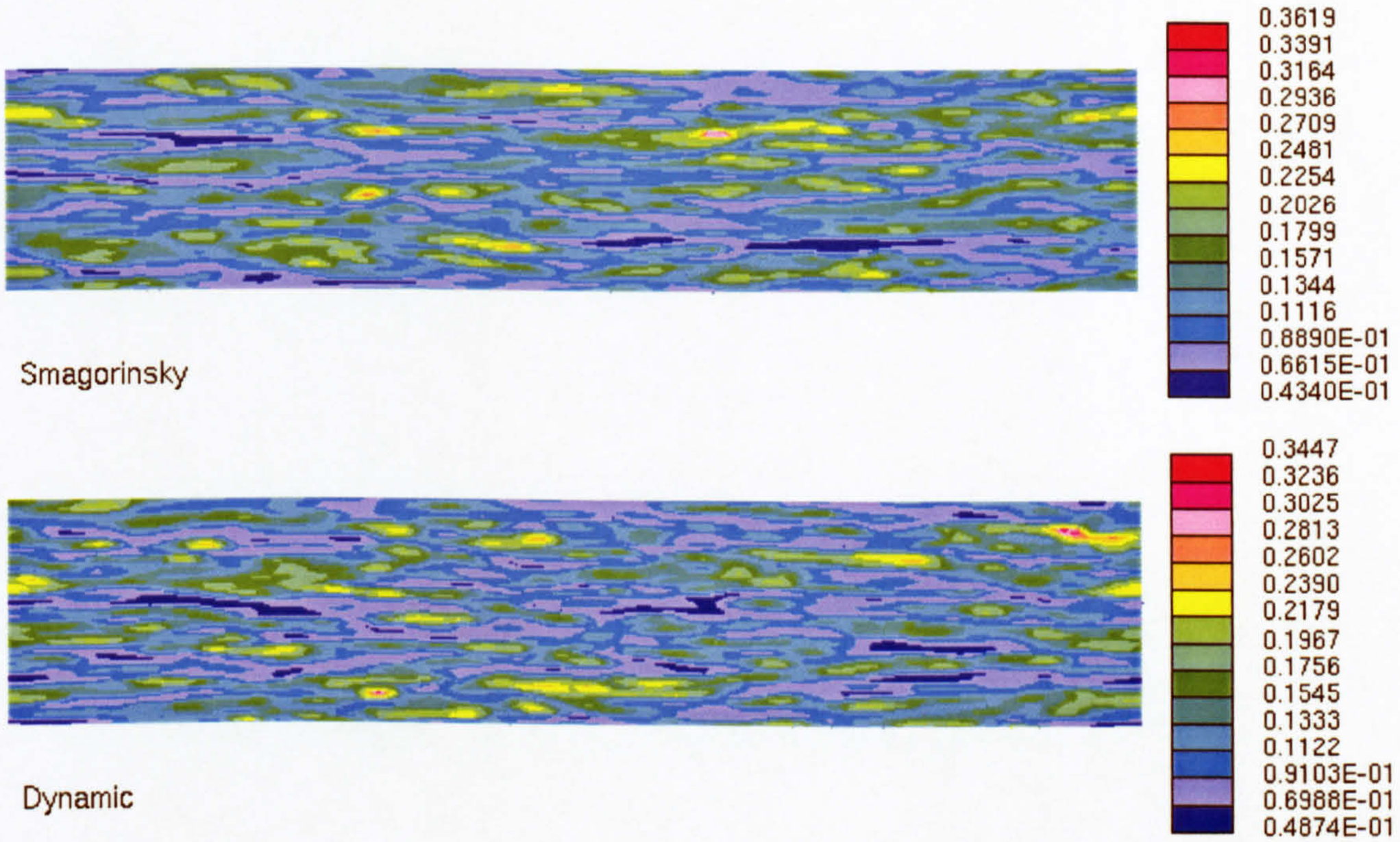

Figure 4.14: Regions of low-speed and high-speed flow field predicted by Smagorinsky and dynamic models at $y^+ = 8.4$ for Case B (x-z view). The variable shown is the instantaneous streamwise velocity u.

4.4 Closure

The chapter presented LES predictions obtained using the finite-volume collocated code with 2CDS for the turbulent flow between parallel plates for two Reynolds numbers. Calculations for two Reynolds numbers were presented. No-slip condition at the wall was used as boundary condition. The initial perturbation field of the channel flow was obtained by solving the Orr-Sommerfeld equation using a fourth-order CDS. The calculations successfully reproduced the growth of the perturbations and the transition to turbulence. The accuracy of the simulations depends heavily on the grid resolution for a particular Reynolds number. For low grid resolution, the mean velocity close to the centerline is overpredicted. For a lower Reynolds number, when resolution requirements are milder, at least for the case with mesh and discretization schemes examined in this chapter, the predictions of mean velocity significantly improve but there is still scope for improvement of the turbulent stresses. It has to be mentioned that the use of near wall LES models can significantly improve the results as Fröhlich and Rodi (2002) have demostrated. However, this approach was not examined in this thesis.

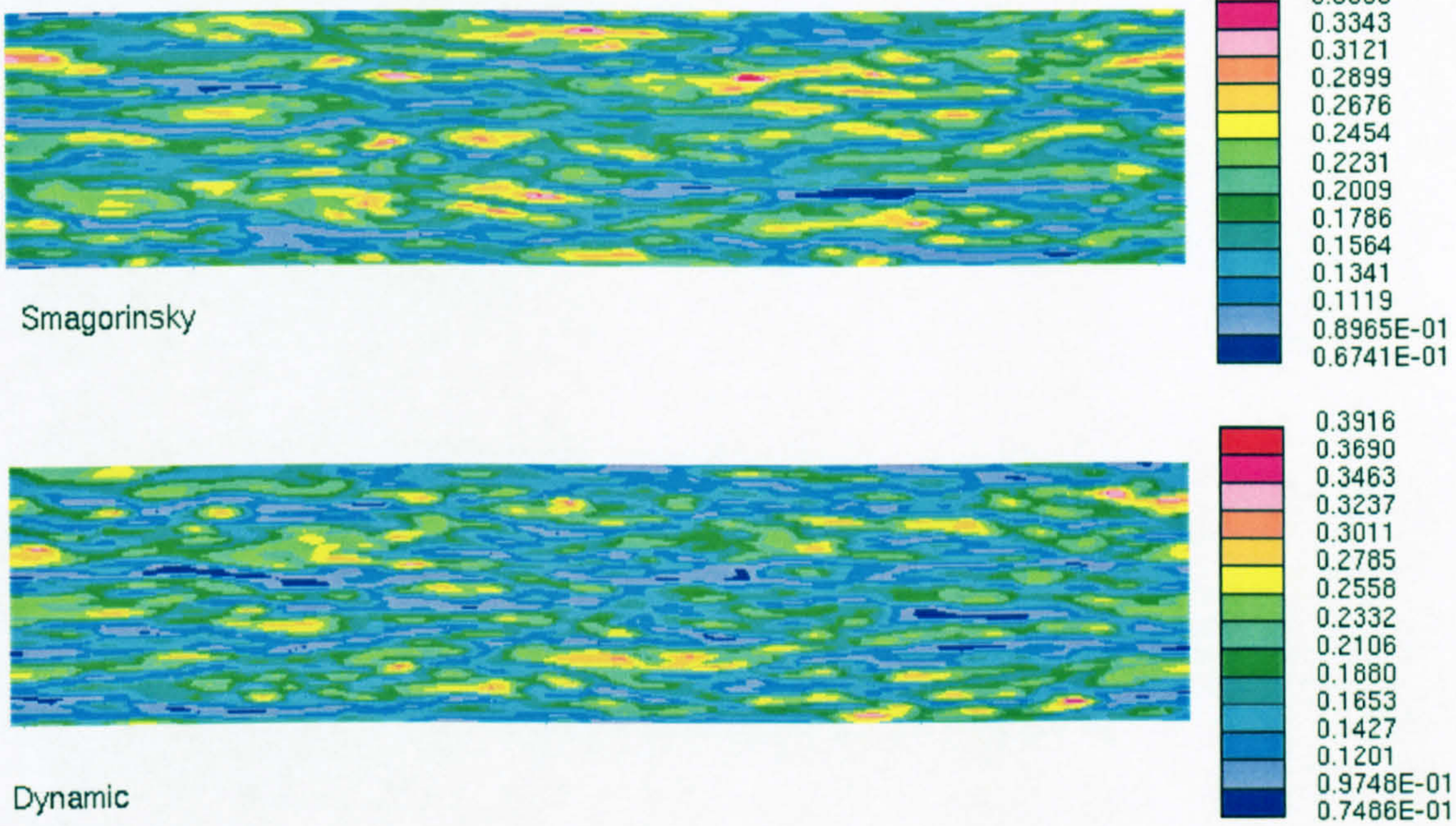

Figure 4.15: Regions of low-speed and high-speed flow field predicted by Smagorinsky and dynamic models at $y^+ = 110$ for Case B (x-z view). The variable shown is the instantaneous streamwise velocity u.

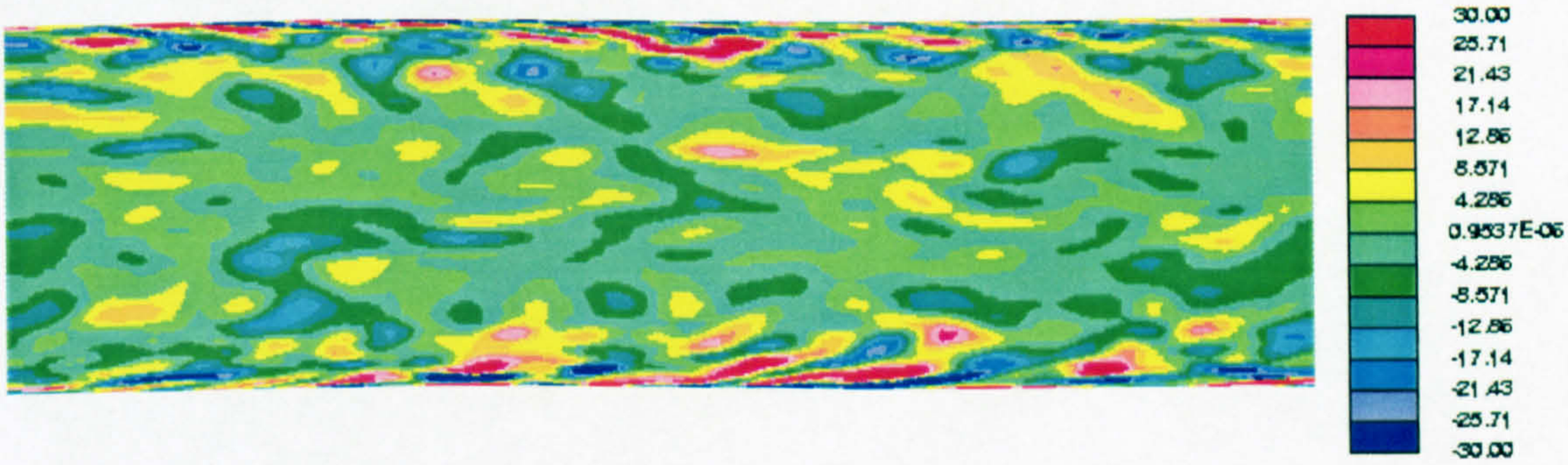

Figure 4.16: Bulges, contour plot of streamwise vorticity (x-y view).

The simulation also successfully reproduced the main dynamic feature of the flow in the near wall region, for example the low and high speed streaks as well as the turbulent bulges. It was also shown that both the dynamic and the standard Smagorinsky model with van Driest damping provide almost the same results. However the dynamic model provides the correct near-wall behaviour of the C_s coefficient. As the dynamic model does not use the distance from the wall, it is more suitable for complex geometries. The next chapter will examine the flow around a circular cylinder using both sgs models.

Chapter 5

LES OF CROSS-FLOW AND HEAT TRANSFER OVER A SINGLE CIRCULAR CYLINDER UNDER STEADY AND PULSATING CONDITIONS

5.1 Introduction

The understanding of vibrations induced by bluff body vortex shedding is of great practical importance for the design of structures such as heat exchangers, offshore platforms, power cables etc. The uniform cross flow over a circular cylinder is a classical example of bluff body flow. Although the configuration is simple, the flow is characterised by very rich and complex phenomena for the Reynolds number examined in this thesis which is in the subcritical regime: thin and attached laminar boundary layers in the front part of the cylinder, separating shear layers, development of Kelvin-Helmholtz instabilities along these layers that lead to transition, as well as small scale streamwise and spanwise vortices in the turbulent wake that interact with large scale Karman vortices. A comprehensive review of the flow characteristics for a wide range of Reynolds numbers is given by Williamson

[0]Part of the results presented in this chapter are published in Liang and Papadakis (2004*b*).

(1996). Having validated the code using turbulent channel flow test case in chapter 4, attention now is focused on the cross-flow over a circular cylinder.

During the past decade, many LES calculations have been performed for subcritical Reynolds numbers, especially at $Re_D = 3900$, mainly due to the availability of the experimental results of Lourenco and Shih (1993) and Ong and Wallace (1996). The calculations have been performed in either structured (Beaudan and Moin, 1994; Mittal and Moin, 1997; Kravchenko and Moin, 2000) or unstructured meshes (Fröhlich et al., 1998; Ma et al., 2000; Hasen and Long, 2002). Very recently, (Piomelli et al., 2003) performed LES calculations using the Lagrangian dynamic model (Meneveau et al., 1996) and the immersed boundary method (Balaras, 2004). In the aforementioned studies, the effect of grid resolution, subgrid scale model, as well as discretisation schemes for the convection terms, have been examined in great detail. There is a general consensus, for example, that low-order upwind schemes are not able to predict correctly the base suction coefficient, separation angles and the size and structure of the recirculation zone behind the cylinder. A variety of discretisation methods and numerical solution techniques have been used, for example the finite volume method, the Galerkin B-Spline or the spectral/hp method. This flow has also been used as a benchmark case to examine theoretical issues pertaining to the application of LES in general curvilinear coordinate systems. For example, Jordan (1999) examined the sequence of two spatial operations, namely coordinate transformation of the basic Cartesian form of the governing equations and filtering. He recommended to transform the full-resolution equation system first and then filter the result. In addition, grid filtering in the computational space proved to be comparatively cheaper than in the physical domain with no discernible differences in the respective damped spectral energies.

None of the aforementioned LES calculations considered the effect of inlet flow conditions, although they have a great impact on the wake flow structure. Invariably, all experiments contain some level of freestream turbulence. For the interested reader, Scholten and Murray (1998*b*,*c*) provide much information on the effect of inlet turbulence level. Prescribing time-dependent turbulent inlet flow conditions at the upstream boundary is an important and challenging task (Lund et al., 1998) but it requires a separate solution of the filtered equations in a simpler arrangement, usually between parallel flat plates. During this simulation, the instantaneous velocities in a cross-stream plane are stored and then used as inlet conditions for the simulation of the turbulent flow around the cylinder (or

any other object).

The aforementioned inlet conditions do not contain a discrete frequency i.e. the energy of the fluctuations is spread along a wide range of frequencies, which is typical of fully turbulent flows. On the other hand, there are many practical applications for which a sinusoidal wave is superimposed on a uniform mean bulk flow. For example, most biological flows in peristaltic pumps are pulsating. Pulsation also occurs in many engineering applications such as the discharge from a reciprocating pump, the flow in the intake and exhaust manifolds of an internal combustion engine, and the flow in hydraulic and pneumatic lines. It has been shown that pulsating approaching flow enhances mixing (Mackley et al., 1996), heat and mass transfer (Sung et al., 1994; Kikuchi et al., 2000) and also offers the opportunity for active flow control by tuning the frequency and amplitude of pulsation (Griffin and Hall, 1991; Papadakis and Bergeles, 2001).

Pulsating approaching cross-flow at a frequency around twice the natural vortex shedding frequency introduces the phenomenon of vortex shedding lock-on. The phenomenon is accompanied by a number of changes in the cylinder body forces and the wake flow and it is therefore expected to result in significant changes of heat transfer as well. Experimental measurements of Barbi et al. (1986), Armstrong et al. (1986, 1987) and Konstantinidis et al. (2003*a*) reveal that lock-on modifies significantly the near-wake flow structure. The numerical results of Papadakis and Bergeles (2001) have shown that lock-on leads to shorter recirculation bubble length (the minimum being at the middle of the lock-on region) and enhances heat transfer after the separation point at low Reynolds numbers. In contrast, the numerical simulations of Hall and Griffin (1993) showed longer vortex formation length due to lock-on.

Although detailed simulations of the steady flow around a single cylinder have been reported in the past as already mentioned, similar simulations for pulsating flows have yet to appear in the literature. In fact, all the simulations mentioned in the previous paragraph for pulsating approaching flows are for two-dimensional laminar flows only. However, as the Reynolds number increases, streamwise vortices form and the flow first becomes three dimensional, while instabilities appear in the laminar separating shear layers that eventually lead to transition to a turbulent wake. The interaction of the externally imposed pulsation, the separating and unsteady shear layers and the Karman vortices constitute a very interesting problem of fluid dynamics that can be tackled only using the Large Eddy Simulation technique (LES) or Direct Numerical Simulation (DNS).

Accurate prediction of the turbulent Reynolds stresses is a prerequisite for reliable simulation of the turbulent heat transfer. Recently Tiwari et al. (2003) performed a very coarse 3D finite-volume simulation of the heat transfer around a circular cylinder at Reynolds numbers of 1,000 and 1,400 confined in a rectangular channel. Only 78,000 cells were used in their simulation which most likely are not sufficient to model the cylinder wall boundary layer and 3D wake. The small aspect ratio (see the experimental investigation by Chang and Mills (2004) about the influence of aspect ratio on heat transfer) and large blockage ratio have a great influence on the cylinder wake size and structure. Thus the interplay between the effects from the channel walls and the cylinder wake makes the simulation results difficult to interpret. Their results are not quantitatively compared with any measurement, thus their accuracy can not be assessed. Gau et al. (2001) recently measured the heat transfer around a circular cylinder oscillating in the streamwise direction and they found that the highest heat transfer coefficient occurs when the oscillating frequency is twice the cylinder vortex shedding frequency. Investigation of LES heat transfer characteristics under pulsating approaching flow conditions in the streamwise direction at different frequencies is therefore considered to be a novel contribution. Quantitative comparison with Gau et al. (2001) assures that the present LES calculation gives credible agreement with the thermocouple measurements.

The aim of the present chapter is threefold. First, to analyse the effect of flow pulsation on the mean and instantaneous flow patterns. To this end, the instantaneous vortex shedding patterns are examined, the lift and drag coefficients are correlated with the observed patterns and the changes on the vortex shedding frequency are quantified. For comparative purposes, runs have also been made for a steady approaching flow in the same Reynolds number. Second, to fill the aforementioned gap in the literature and examine the suitability of LES to accurately predict pulsating approaching flow around a cylinder. To this end, the effect of grid size and subgrid-scale model on the predicted time and span averaged mean flow and turbulence quantities under pulsating approaching conditions is examined. The results are validated against detailed experimental data. Third, to investigate the effect of pulsation on the heat transfer around the cylinder.

This chapter is arranged as follows. First, the configuration and computational conditions are briefly described. Second, the ensemble-averaged mean and r.m.s velocity profiles are compared with the experimental data followed by a detailed description of the instantaneous pressure, vorticity and velocity field as well as lift

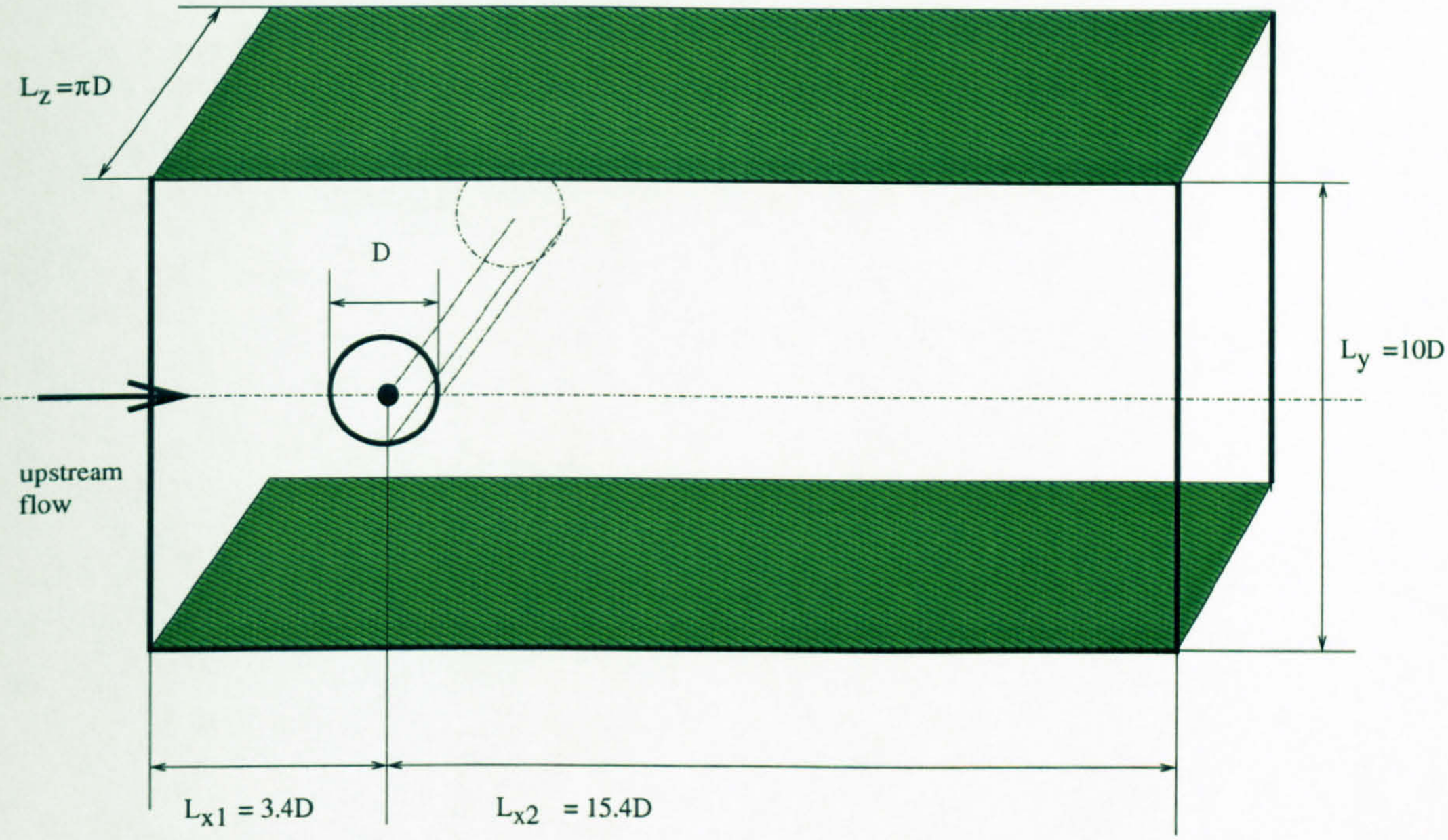

Figure 5.1: Physical configuration of the computational domain.

and drage coefficients for both steady and pulsating approaching flow conditions. Finally, heat transfer results obtained by LES using constant wall heat flux boundary condition for both steady and pulsating approaching flow cases are presented and discussed. The heat transfer results are correlated with the observed flow patterns.

5.2 Computational domain and boundary conditions

The computational domain is described in a Cartesian coordinate system (x,y,z) where the x axis is fixed as the inlet flow direction (streamwise direction), the z axis is aligned to be parallel with the cylinder axis (spanwise direction), while the y axis (transverse direction) is perpendicular to both the x and z axies. The experiments were carried out in the ECLAT stainless steel water tunnel with cross-section $72cm \times 72cm$ and the cylinder diameter is $72mm$. The same blockage ratio is used for the computational domain, which is shown in Figure 5.1. The computational inlet mean velocity is kept at $u_\infty = 0.36m/s$ which corresponds to Reynolds number $Re_D = 2580$.

As shown in figure 5.2, two meshes are used, i.e. a coarser one (294912 cells)

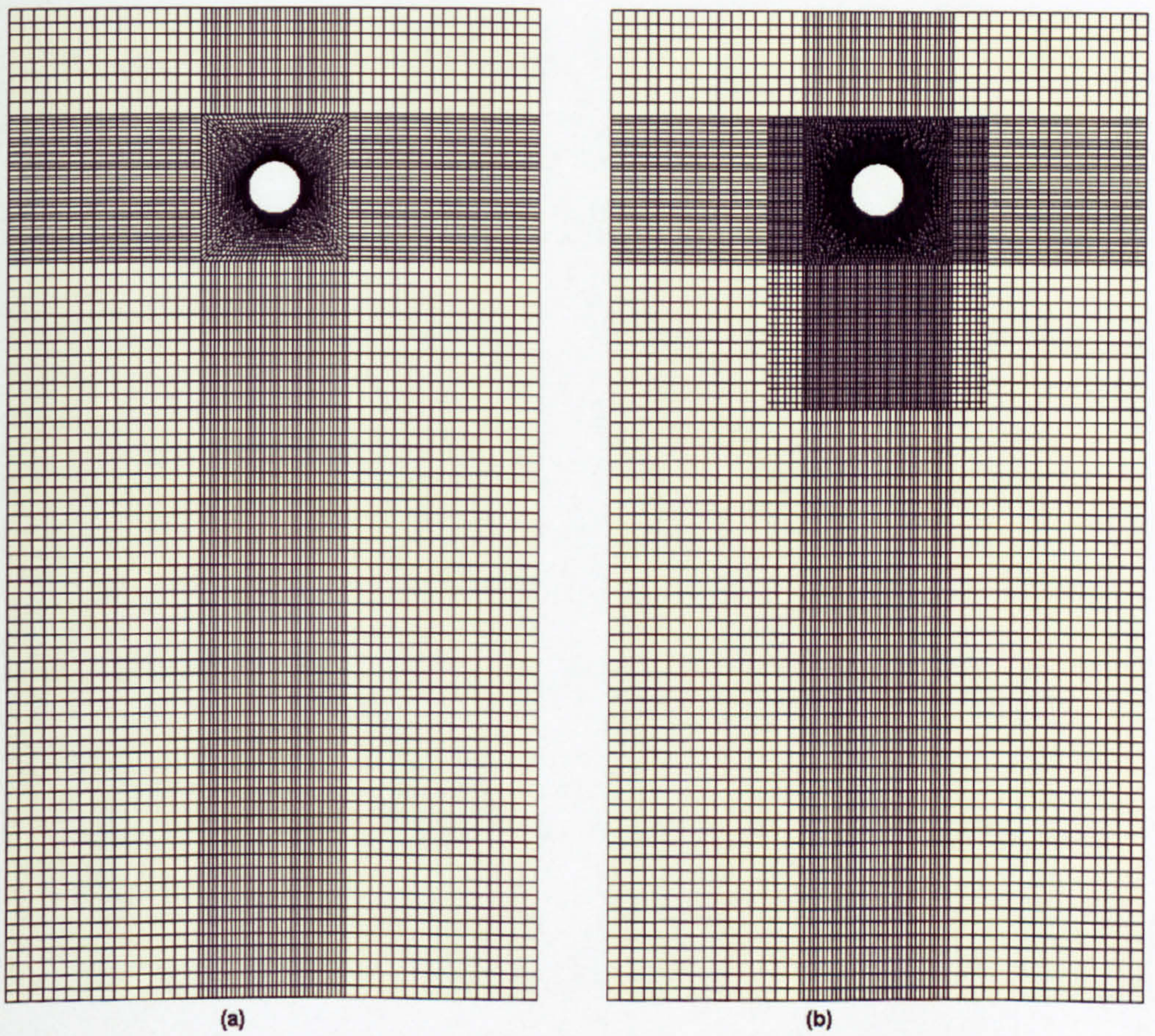

Figure 5.2: Cross section (x-y veiw) of the computational meshes used. a: coarser mesh; b: finer mesh.

and a finer one (746688 cells). Totally 128 and 256 cells are placed along the periphery of the cylinder for the coarser and the finer mesh respectively while 32 layers are used in the spanwise direction for both meshes with spanwise length $L_z = \pi D$. The finer grid is obtained from the coarser one by refining locally the cells in the near cylinder region in the radial and circumferential direction. The maximum CFL number is around 4 for the finer mesh and 2.5 for the coarser mesh, while the mean CFL number is around 0.8 for the finer mesh and 0.35 for the coarser mesh. The normalised time step size used is $\Delta T = \frac{\Delta t u_\infty}{D} = 0.025$ for all cases.

A convective boundary condition recommended by Sohankar et al. (1998) $\frac{\partial \phi}{\partial t} + U_{conv}\frac{\partial \phi}{\partial x} = 0$ is used for the exit boundary, where U_{conv} is the the exit velocity normal to the outlet boundary, and ϕ is any physical variable convected out through the outlet. For the flow fields presented in this chapter, ϕ stands for the velocity components u_i in each direction for the flow field and scalar Θ for the temperature field. Zero velocity boundary conditions are used for the top and bottom walls. Periodic boundary conditions are applied in the spanwise direction. The normal derivative for the pressure correction is set to zero at all boundaries. A constant velocity is prescribed at the inlet boundary for the steady cross-flow, and the superimposed pulsating profile is $u(t) = u_\infty + \frac{\Delta u}{2} sin(2\pi f_e t)$. The peak-to-peak amplitude used is $\Delta u = 0.1 u_\infty$ unless otherwise stated, and the pulsating frequency is $f_e = 21.6$ Hz, which gives a pulsating Strouhal number $S_e = 0.43$. In order to show the effect of different amplitudes, the value $\Delta u / u_\infty = 0.05$ is also used for case A2. Case A3 is performed at this pulsation amplitude and a pulsation frequency of 32.4Hz. Thus the effect of different pulsation frequencies on flow field and heat transfer is also examined. Table 5.1 provides an overview of the examined cases.

The Finite Volume method applied on a collocated grid system is employed to discretize the governing equations. All terms in the momentum equation are discretized using the 2nd order central difference scheme (CDS) in space and the 2nd order Crank-Nicolson scheme is employed to advance them in time, except for the pressure term which is treated implicitly as explained in chapter 3. The PISO scheme (Issa, 1986) is used to deal with the pressure coupling between the momentum and the continuity equations. The LES calculation is sensitive to the modelling of the near cylinder wall region, because the separation depends on the details of the attached boundary layer, i.e. whether it is laminar or turbulent (in the present conditions laminar). In order to avoid the resolution of the

thin boundary layers, one can use wall functions (Cabot, 1996; Templeton et al., 2002). However, this is a delicate task when the separation point is not fixed by the goemetry and is far from being settled. For the present simulations, a local refinement technique is used to obtain high resolution in the near wall region as explained above, so that direct or almost direct numerical simulation is performed in the near wall region. The van Driest damping function is often used together with the Smagorinsky model to reduce the high eddy visocity in the presence of shear and this was done in chapter 4. However, it was not used in the present investigation, because this approach lacks generality as it involves the distance of a cell centroid to the wall which is difficult to evaluate in complex geometries and also because it is well known that this particular damping function does not reproduce the correct asymptotic behaviour of the sgs viscosity close to the wall (Sagaut, 2002). Other more complicated functions have been suggested in the literature that eliminate this problem, but in the present investigation it was decided to abandon these approaches and use a dynamic model instead that not only reproduces the correct near-wall behaviour, but also evaluates dynamically the coefficient of the Smagorinsky model based on the local flow field (Chester et al., 2001). The model was described in chapter 2.

A constant heat flux boundary condition is applied for the cylinder wall boundaries. The constant heat flux per unit area is $q" = 2419W/m^2$ and the thermal conductivity is $k = 0.59W/(m \cdot K)$. A constant temperature boundary condition is applied for the top and bottom wall boundaries and inlet boundary ($T_\infty = 25^oC$). The convective exit boundary condition is also used for the temperature transport equation.

5.3 Results and discussion

In this section, the results of the simulations will be presented and discussed. More specifically, this section is focused on: the impact of grid resolution and sgs models, analysis of turbulence statistics and comparison with experiments, variation of lift and drag coefficients, interpretation of instantaneous flow patterns and finally heat transfer. LES calculations are performed for the Cases shown in Table 5.1 with the finer mesh. In order to examine the effect of grid resolution, two additional runs were performed with parameters shown in table 5.2.

Cases investigated using finer mesh						
Case	A0	B0	A1	B1	A2	A3
LES model	Dyn	Smag	Dyn	Smag	Dyn	Dyn
f_e	0	0	21.6Hz	21.6Hz	21.6Hz	32.4Hz
$\Delta u/u_\infty$	0	0	0.1	0.1	0.05	0.05
Heat Transfer	Yes	Yes	No	Yes	Yes	Yes

Table 5.1: Investigated cases using either the Smagorinsky model (cases B0 and B1) or Dynamic model (cases A0-A3).

5.3.1 Impact of grid resolution

As shown by Kravchenko and Moin (2000), insufficient grid resolution can cause early transition in the shear layers separating from the cylinder which leads to inaccurate predictions of the near-wake statistics. The impact of grid resolution was studied by comparing the results of Cases C0 and C1 with the results of Cases B0 and B1 for steady and pulsating inflow conditions respectively.

The effect of grid refinement can be seen by comparing the turbulence statistics between the results obtained by the coarser and the finer mesh. Figure 5.3 shows the time-averaged streamwise velocity for Cases C0 and B0. The grid refinement clearly improves the results and predicts a longer bubble zone, however, the grid resolution is still not adequate enough to capture the correct bubble zone reflecting the fact that further refinement, particularly in the spanwise direction, is needed. Figure 5.4 shows the time-averaged cross-wake velocity in the near wake region for cases C0 and B0. Although there is some improvement close to the cylinder, the effect of refinement is much smaller than that on the mean streamwise velocity. This grid indepence study performed using cases C0 and B0 shows that further grid refinement is necessary for simulating the steady cross-flow case. Breuer (1998) also showed that using more layers in the spanwise direction in conjunction with the Germano type dynamic model (Germano et al., 1991) can lead to correct prediction of the size of recirculation zone (see his D3 case). Figures 5.5 and 5.6 show the time-averaged streamwise and cross-stream velocity respectively in the near wake region for cases C1 and B1 (pulsating flow). The two meshes give very similar results for all examined streamwise locations for both velocity components, with slightly better predictions obtained with the finer mesh for the streamwise component. The effect of grid refinement on other turbulence quantities is similar, although supporting graphs are not shown for brevity of presentation. The resolution of the finer mesh is therefore considered adequate for the pulsating flow cases and in the

Parameters defining the resolved wake region							
Case	N_r^{eff}	N_{total}	$\Delta r_{min}/D$	N_z	f_e	$\Delta u/u_\infty$	Model
C0	128	294,912	3.5×10^{-3}	32	0	0	Smag
C1	128	294,912	3.5×10^{-3}	32	21.6Hz	0.1	Smag
B0	256	746,688	1.75×10^{-3}	32	0	0	Smag
B1	256	746,688	1.75×10^{-3}	32	21.6Hz	0.1	Smag

Table 5.2: Grid independence study using two meshes (cases C: coarser grid).

recirculation bubble length						
Case	A0	B0	A1	B1	A2	A3
L_r/D prediction	1.5	1.7	1.1	1.12	1.24	1.3
L_r/D Konstantinidis et al. (2003a)	2.1	2.1	1.05	1.05	N/A	N/A

Table 5.3: The recirculation bubble length predicted for the different cases studied.

forthcoming sections results are shown only for the finer mesh.

5.3.2 Turbulence statistics of both steady and pulsating cross-flows

Detailed PIV experimental data were provided by Konstantinidis (2004) for the steady and the pulsating cross-flow case with $f_p = 2f_n$ and $\Delta u/u_\infty = 0.1$. This made possible a detailed and direct comparison between LES simulations and experiments. Figure 5.7 shows the time-averaged streamwise velocity along the wake centerline for pulsating cases against the experimental data (Konstantinidis, 2004). Since the recirculation bubble length (l_r) is defined as the position of zero mean velocity along the wake centerline, it can be seen that both the Smagorinsky model and the dynamic model predicted longer recirculation zones compared to the experiment.

Table 5.3 shows that the Smagorinsky model calculation of case B0 predicts a recirculation bubble length $l_r = 1.7D$ which is shorter than the PIV measurement for the steady approaching cross-flow (2.1D), while for case B1 the recirculation zone predicted is 1.12D which agrees very well with the experiment for the pulsating cross-flow. The dynamic model predicts a recirculation bubble length $l_r = 1.24D$ for pulsating incoming flow with half amplitude (case A2). The detailed turbulence statistics are not shown here, but it can be seen that higher amplitude

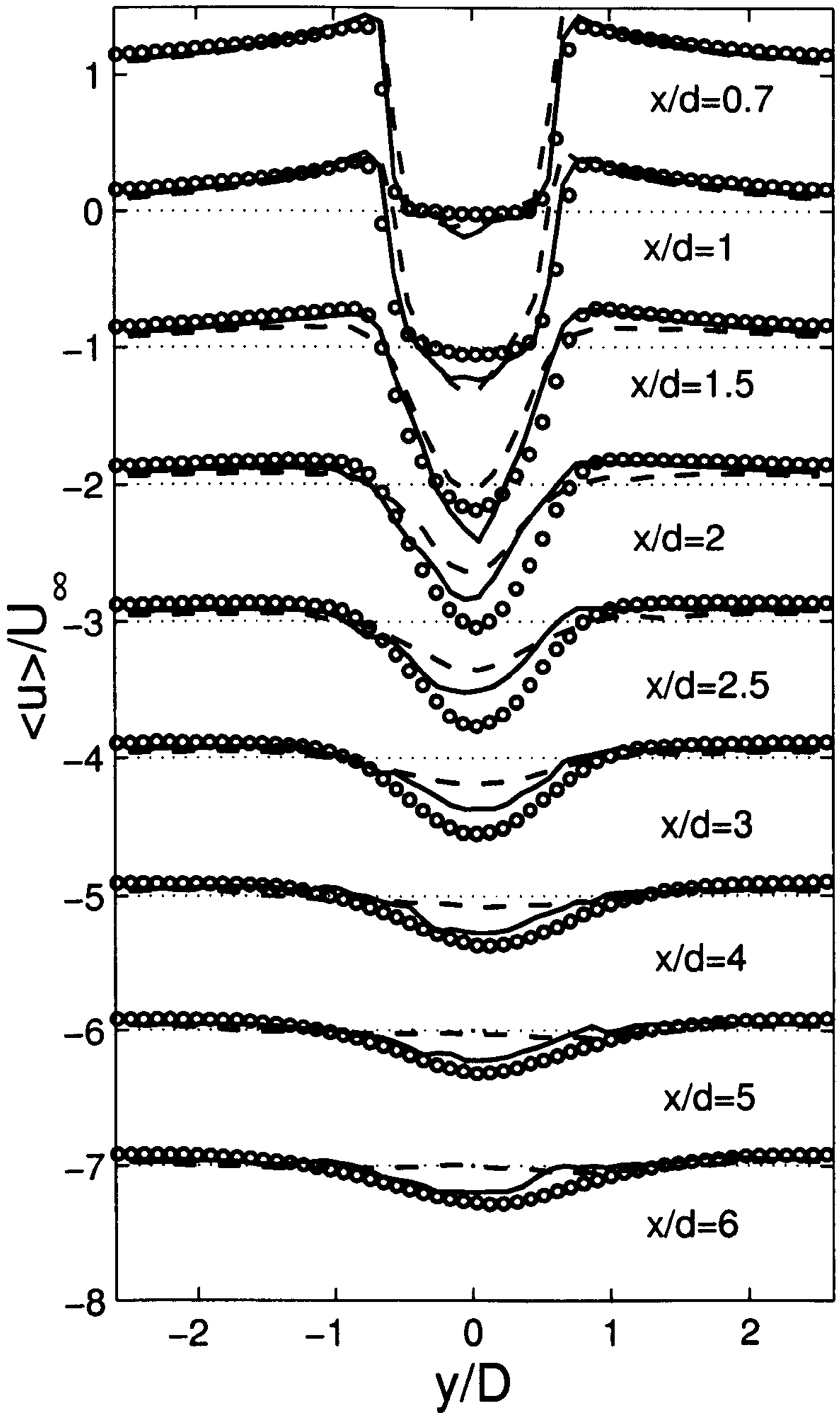

Figure 5.3: Time-averaged streamwise velocity of the steady cross-flow in the near wake, (- - - -) Case C0; (——) Case B0; (o o o o o) Experiment; For clarity of presentation, the curves at different streamwise positions are shifted and (.....) shows the zero location of each profile.

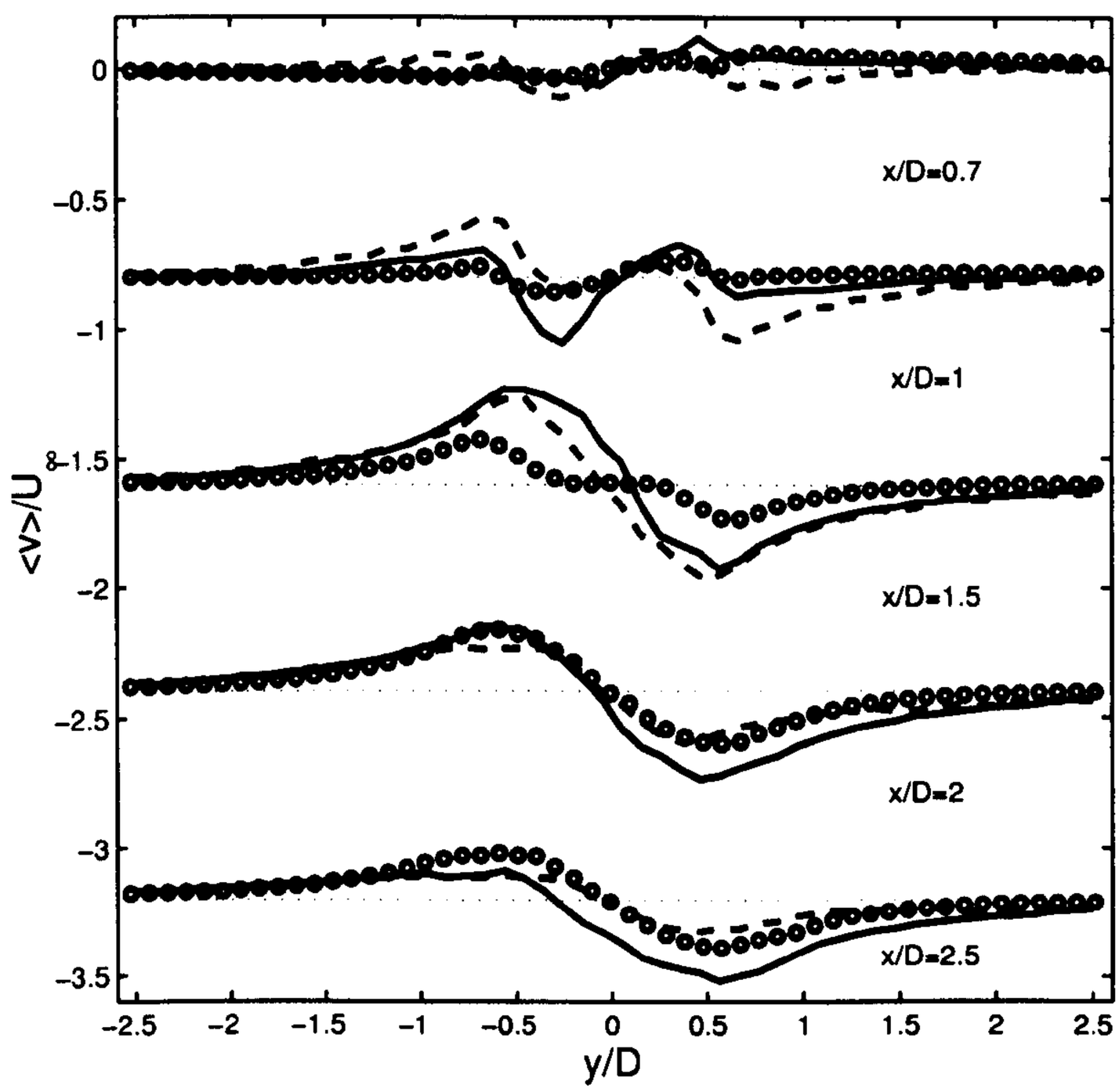

Figure 5.4: Time-averaged cross-wake velocity of the steady cross-flow in the near wake, (- - - -) Case C0; (——) Case B0; (o o o o o) Experiment; For clarity of presentation, the curves at different streamwise positions are shifted and (.....) shows the zero location of each profile.

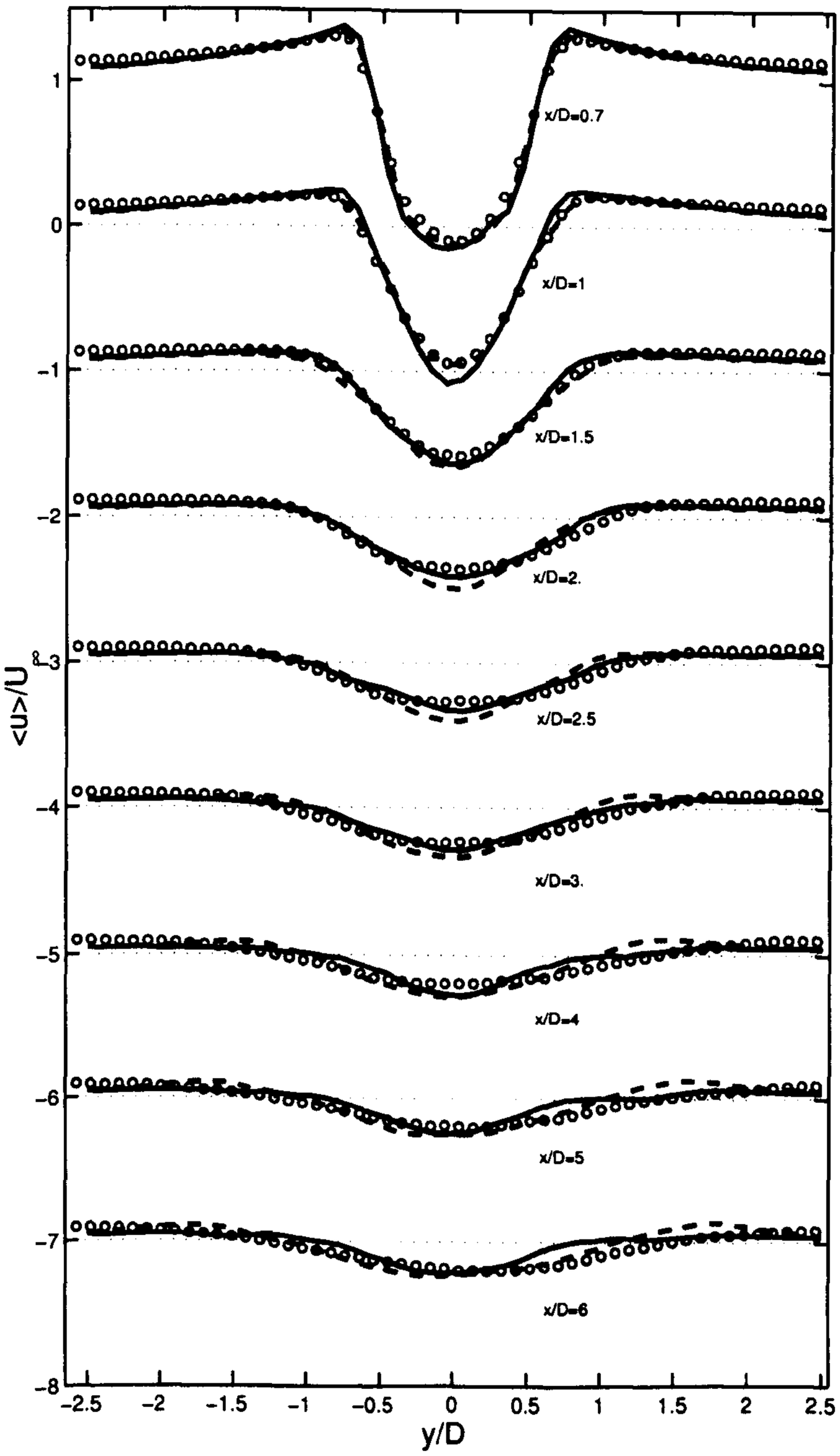

Figure 5.5: Time-averaged streamwise velocity of the pulsating cross-flow in the near wake, (- - - -) Case C1 (——) Case B1; (o o o o o) Experiment; For clarity of presentation, the curves at different streamwise positions are shifted and (.....) shows the zero location of each profile.

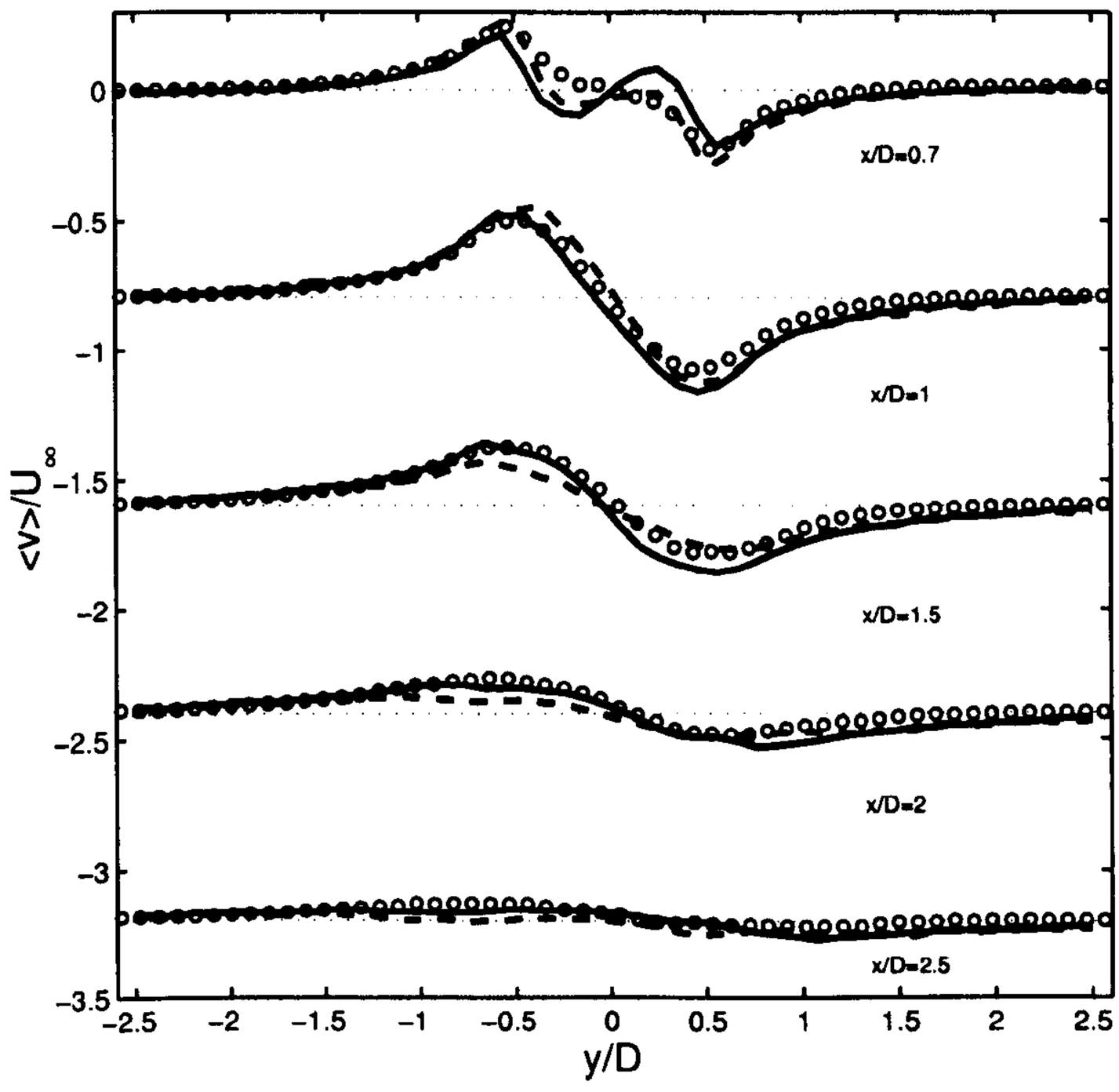

Figure 5.6: Time-averaged cross-wake velocity of the pulsating cross-flow in the near wake, (- - - -) Case C1; (——) Case B1; For clarity of presentation, the curves at different streamwise positions are shifted and (.....) shows the zero location of each profile.

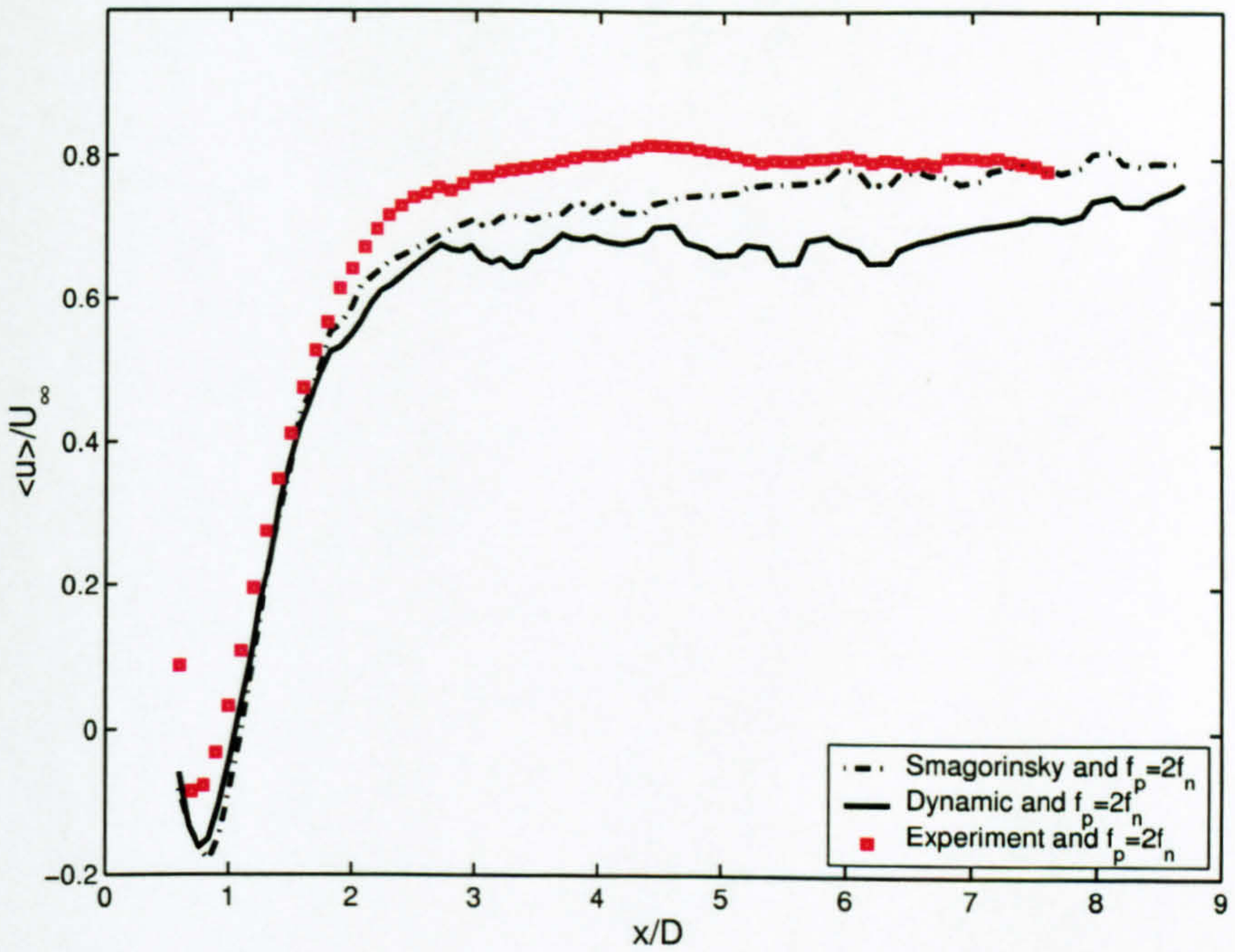

Figure 5.7: Time-averaged velocity along the wake centerline for case B1.

resulted in shorter recirculation bubble length. Nevertheless, both the pulsating cross-flow cases (either A1 or A2) result in a significantly smaller recirculation zone compared to the steady approaching flow (see also figure 5.8).

Figure 5.9 shows the normalized streamwise r.m.s velocity fluctuation along the wake centerline for cases A1 and B1. Both LES models give quite good agreement with the experiment for the pulsating cross-flow case especially in the near-wake region. The dynamic model gives slightly better prediction in the far-wake region than the standard Smagorinsky model. This may indicate that the dynamic model is more suitable for simulating the momentum transfer in the far-wake region.

Figure 5.10 shows the normalized cross-wake r.m.s velocity fluctuation along the wake centerline for both cases A1 and B1. Both LES models give excellent agreement with the experiment for the pulsating cross-flow case in both near- and far- wake region. Despite the fact that the maximum r.m.s velocity is slightly over-predicted in both cases, the location of maximum cross-wake r.m.s velocity represents accurately the length of the recirculation bubble. Gerrard (1966) has suggested the definition of vortex formation length using the location of maximum streamwise or cross-wake r.m.s velocity. As indicated by Gerrard, the transverse velocity fluctuation follows the streamwise velocity fluctuation, and both of them are good characteristic lengths for the vortex formation length. The length indi-

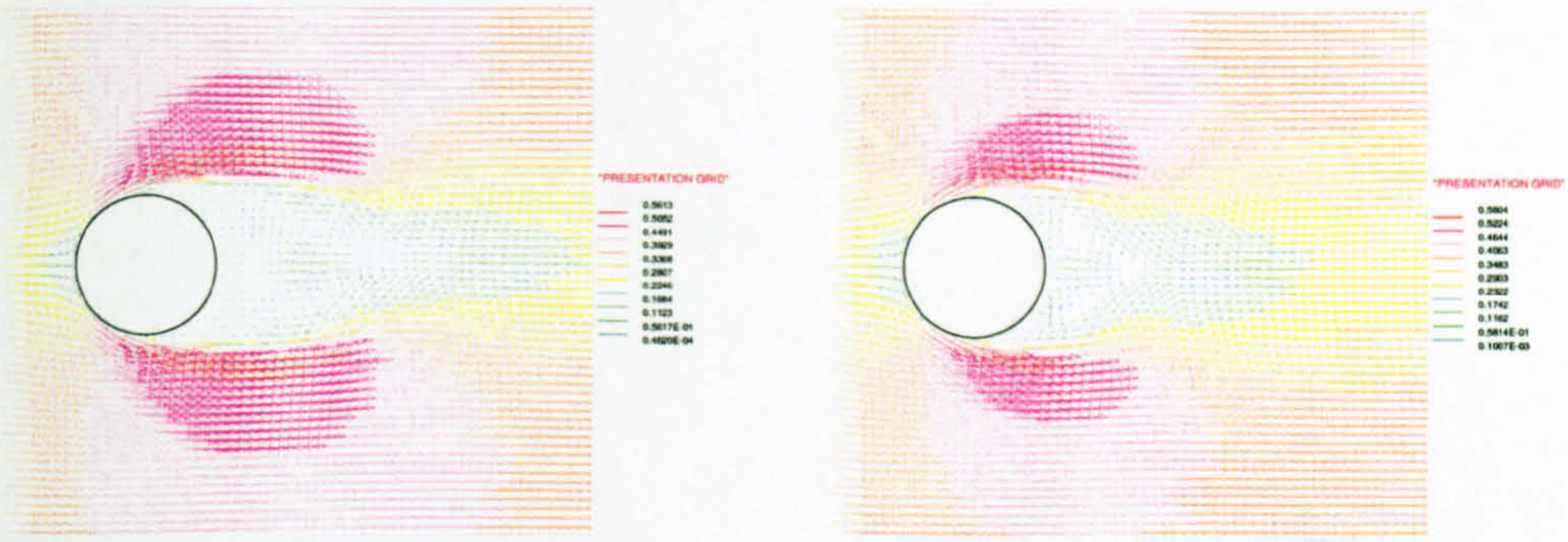

(a) Case B0 (b) Case B1

Figure 5.8: Vector plot of the ensemble-averaged velocity in a middle x-y plane of predicted by the standard Smagorinsky model for case B0 and B1 respectively.

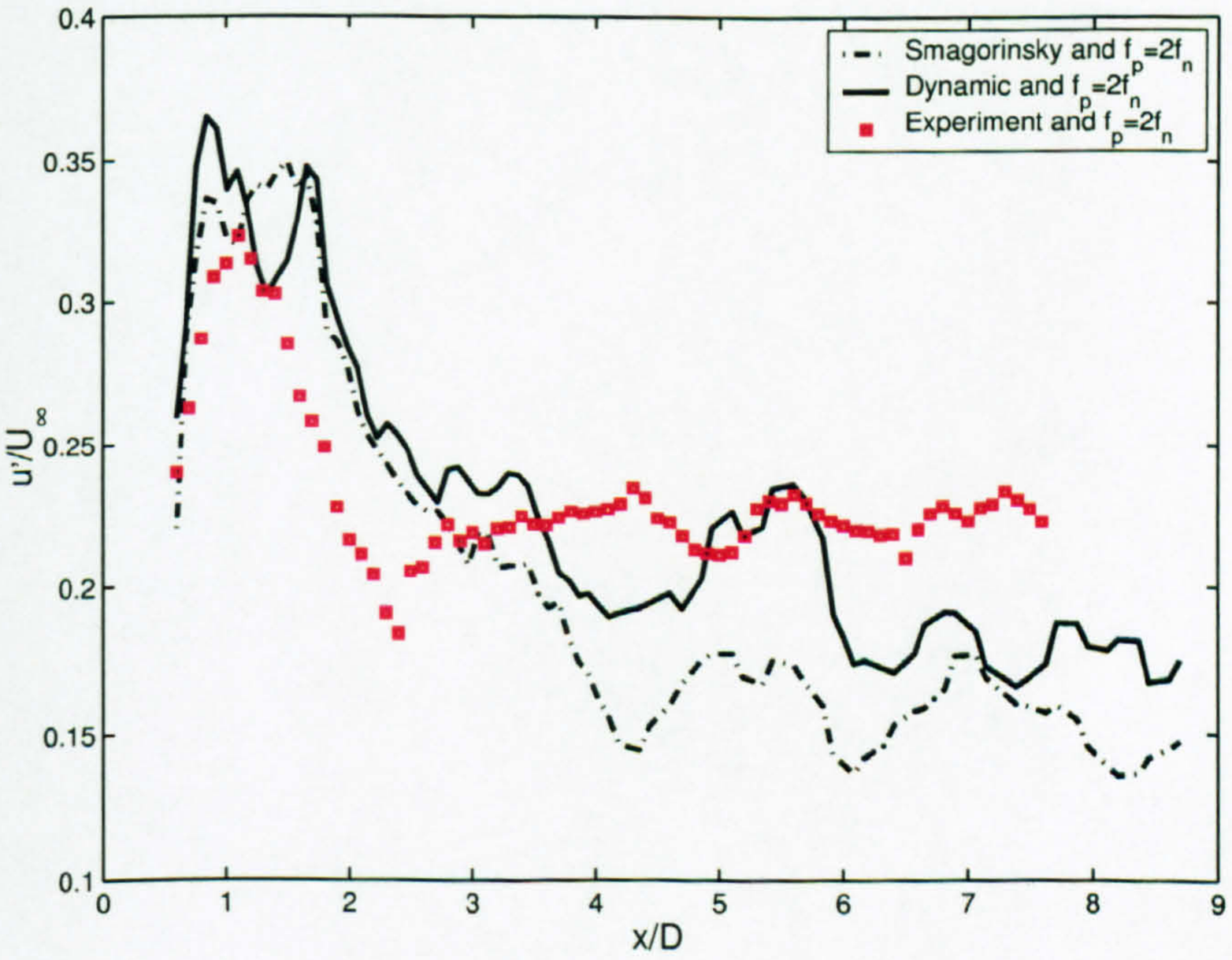

Figure 5.9: Streamwise r.m.s velocity along the centerline for cases A1 and B1.

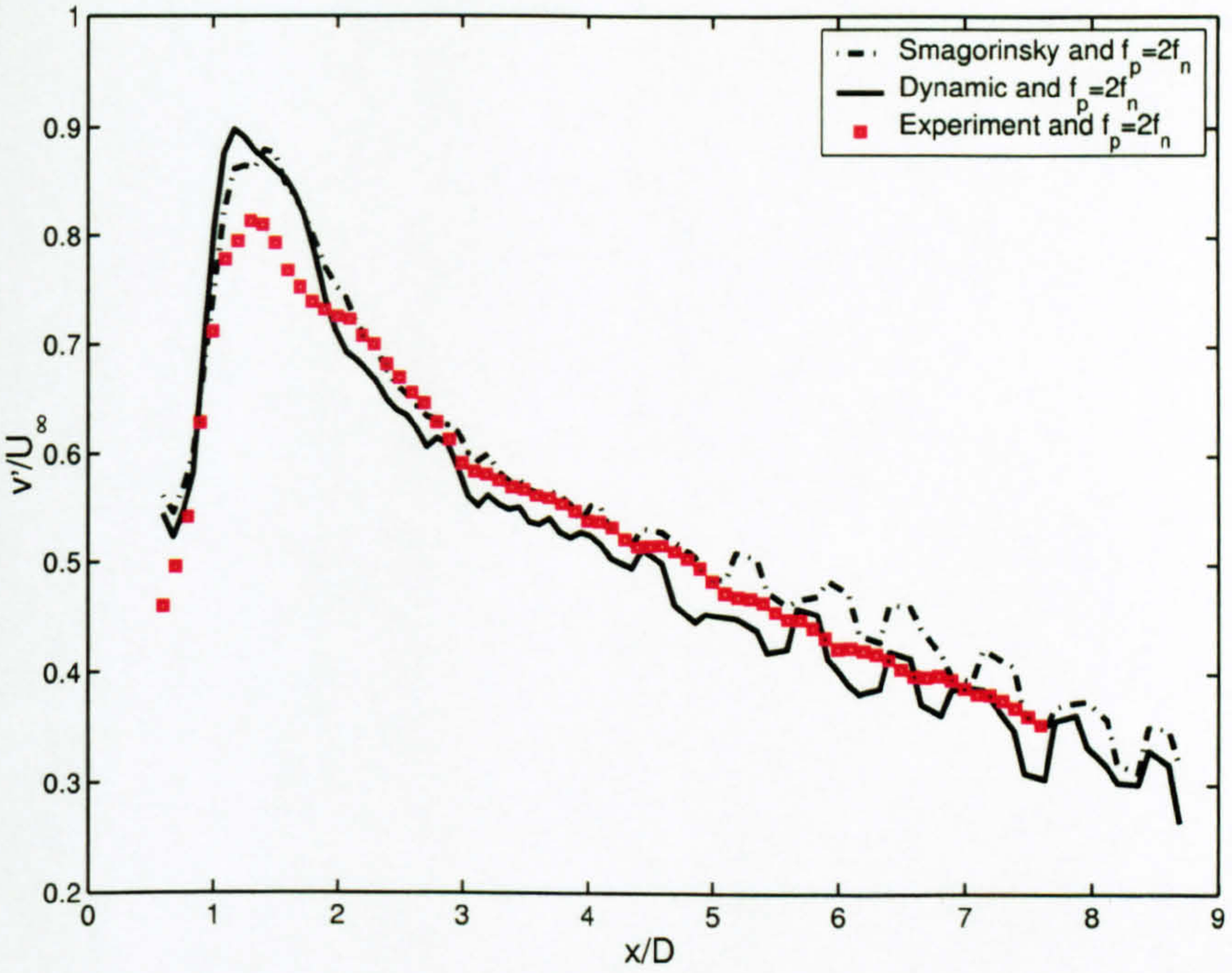

Figure 5.10: Cross-wake r.m.s velocity along the centerline for cases A1 and B1.

cated by the maximum of v' shown in figure 5.10 agrees very well with the location of zero mean streamwise velocity shown in table 5.3. Konstantinidis et al. (2003a) investigated the r.m.s streamwise velocity distributions of the cross-flow over a single cylinder with various approaching pulsating frequencies in the lock-on region and found that the position of the maximum in the streamwise velocity fluctuations moves from x/D = 1.9 to 1.15 when f_e/f_n decreases from 2.25 to 2 (referring to the middle of the lock-on region); in other words, lock-on is accompanied by a considerable decrease in the vortex formation length, and the formation length attains the minimum value at $f_e/f_n = 2$, a result which is in agreement with Armstrong et al. (1987). Due to the difficulty in measuring the streamwise velocity fluctuations in a staggered tube bundle with longitudinal and tranverse spacing ratio ($S_L/S_T = 2.1D/3.6D$), Konstantinidis (2001) measured the tranverse velocity fluctuations and found that similar phenomena occured for this tube arrangement as well.

Figure 5.11 shows normalized streamwise time-averaged velocity behind the cylinder for the steady cross-flow. Clearly, the discrepancy between the LES models and experiment reflects the shorter recirculation bubble predicted by both the standard Smagorinsky model and the dynamic model. The results shown here are the ones obtained from the finer mesh, which are more accurate than the results

obtained using the coarser mesh, as explained earlier. Thus further refinement of the mesh is needed for more accurate prediction, for instance, refinement on the spanwise direction probably should improve the results significantly, as the three-dimensionality of the steady cross-flow is high. On the other hand, it can be shown from this figure that refinement will affect more the derivative based dynamic model and hopefully make it more accurate, as evaluation of the Smagorinsky coefficient is only based on averaging of $L_{ij}M_{ij}$ and $M_{ij}M_{ij}$ along the spanwise direction. Thus sufficient resolution along the spanwise direction is crucial for the dynamic model.

Figure 5.12 shows the normalized cross-wake time-averaged velocity behind the cylinder for the steady cross-flow. In the very near wake region, both the Smagorinsky model and the dynamic model cannot accurately predict the shape and magnitude of the mean velocity. The difficulty may be due to the strongly anistropic nature of the flow in this region, as well as to insufficient grid resolution. Further downstream, away from the recirculation bubble zone, the shape and magnitude of the time-averaged cross-wake velocity are predicted very accurately. The dynamic model also performs slightly better than the Smagorinsky model in this region. Therefore, the merits or deficiencies of the dynamic model are still not clear from modelling the steady cross-flow using the current finer mesh. Further grid refinement is required to resolve fully this issue.

Figures 5.13 and 5.14 show that both the Smagorinsky and the dynamic models overpredict u_{rms} and v_{rms} in the near-wake region. This reflects the fact that the recirculation bubble length is under-predicted. In general, Ma et al. (2000) also overpredicted the v_{rms} distribution compared to the experimental results. Figure 5.15 presents the Reynolds shear stress in the near-wake region. There is a clear over-prediction at $x/D = 1.5$ and 2 where the vortex formation region ends. The agreement between the prediction and the experiment is good elsewhere.

Figure 5.16 shows the normalized time-averaged streamwise velocity behind the cylinder for pulsating cross-flow. Both LES models give surprisingly good agreement with the experiment (especially compared with Figure 5.11), suggesting that lock-on makes the wake structure more well-organized and the grid resolution is sufficient. Very small differences between the two LES models may indicate that the modelling error is less important than the discretization error given the current grid resolution and second-order schemes both in space and time. Figure 5.17 shows the normalized time-averaged cross-wake velocity behind the cylinder of the pulsating cross-flow. Both shape and magnitude are captured very well by both the

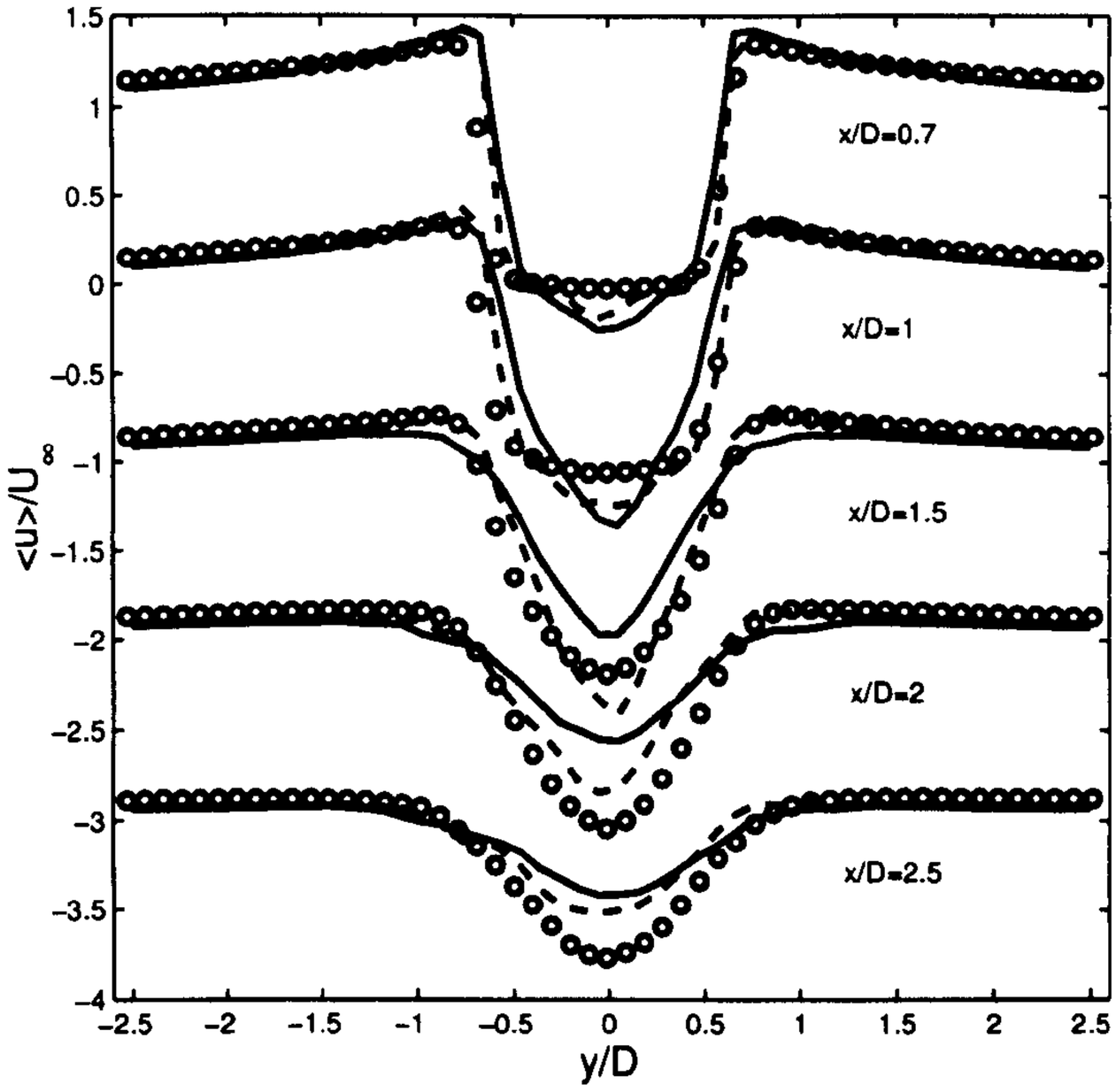

Figure 5.11: Normalized streamwise mean velocity behind the cylinder of the steady cross-flow. (——) Dynamic model; (- - - - -) Smagorinsky model; (o o o o) Experiment.

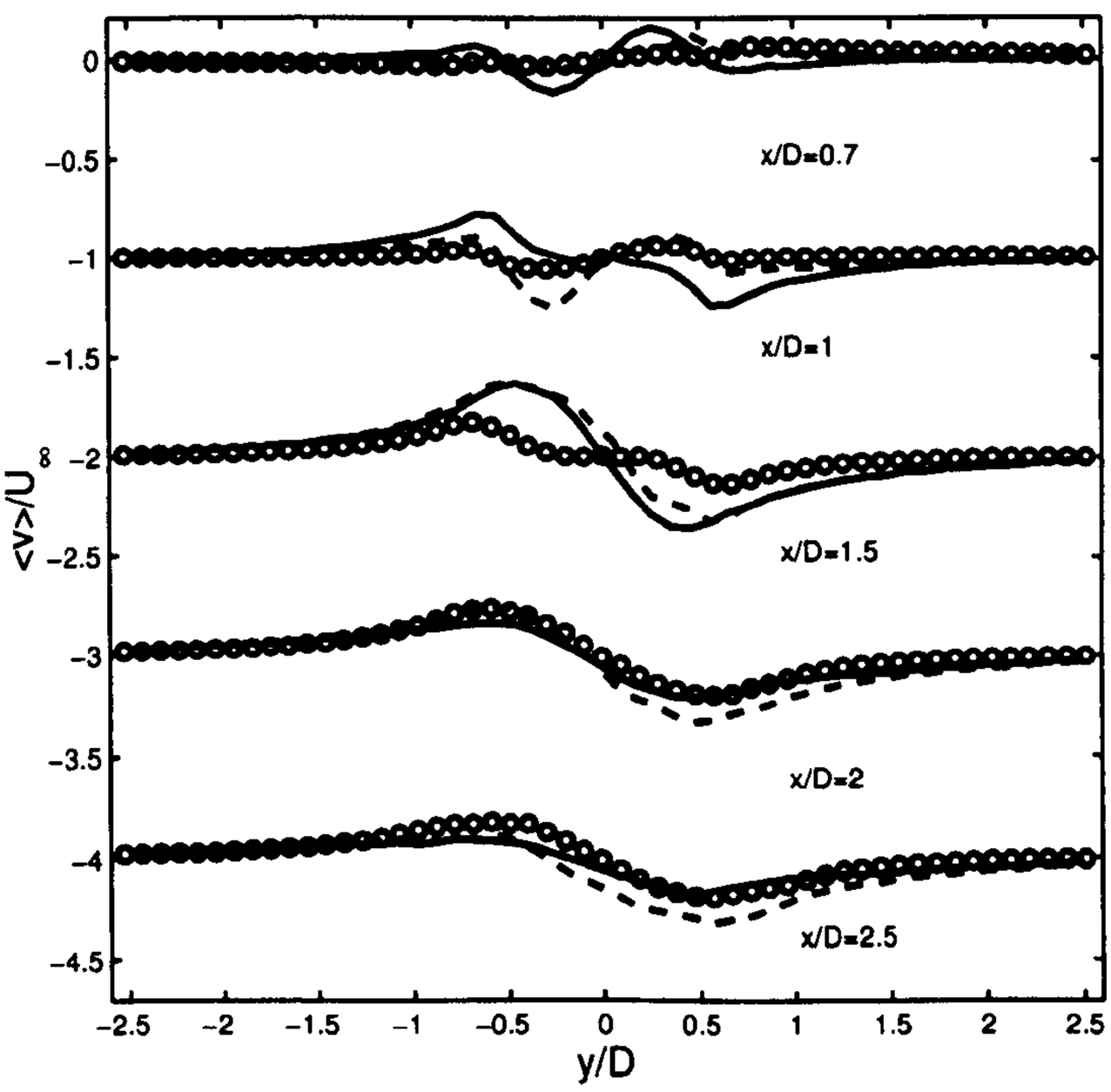

Figure 5.12: Normalized cross-wake mean velocity behind the cylinder of the steady cross-flow. (——) Dynamic model; (- - - - -) Smagorinsky model; (o o o o) Experiment.

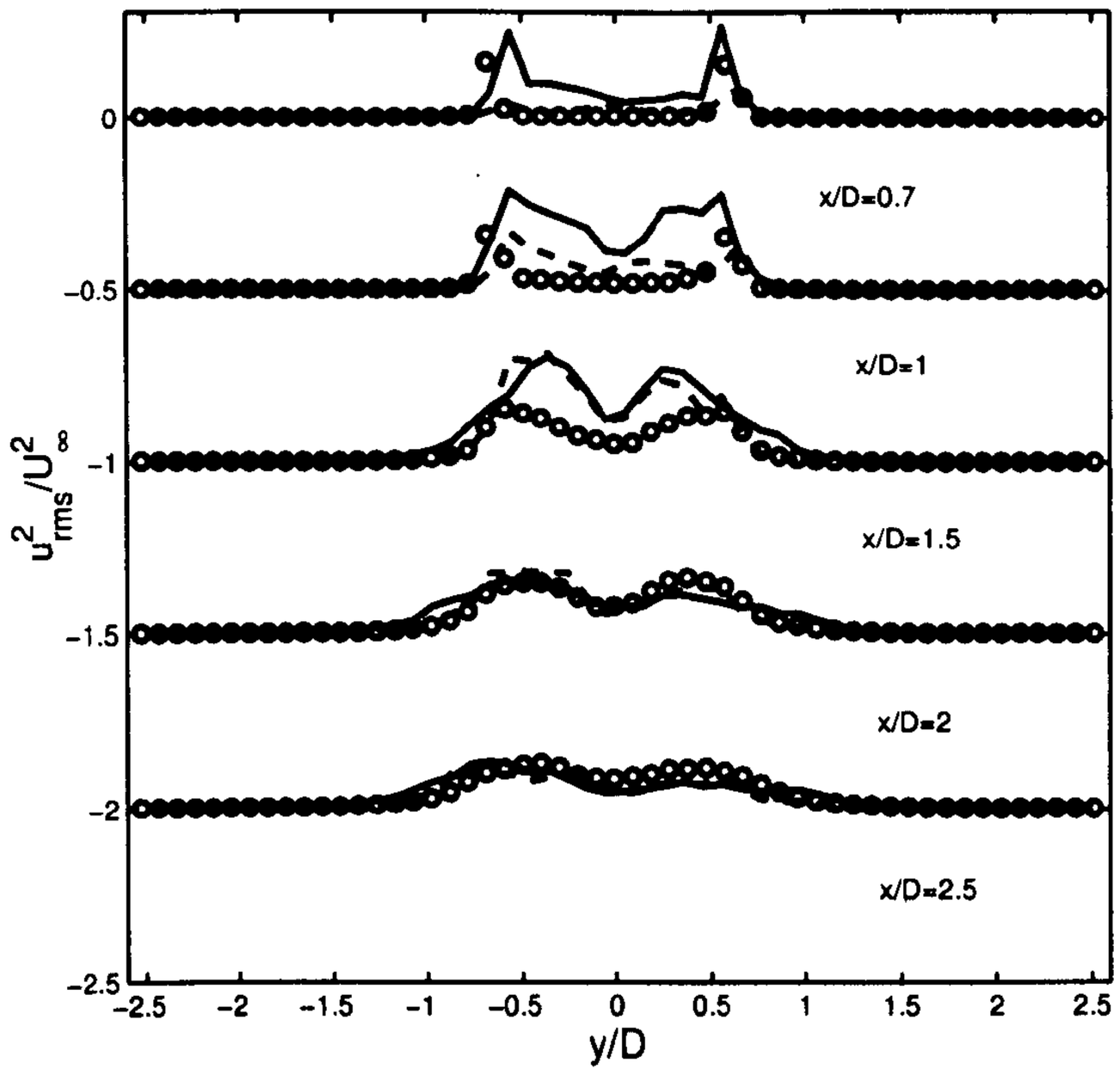

Figure 5.13: $\overline{u^2_{rms}}/u^2_\infty$ behind the cylinder of the steady cross-flow. (——) Dynamic model; (- - - - -) Smagorinsky model; (o o o o) Experiment.

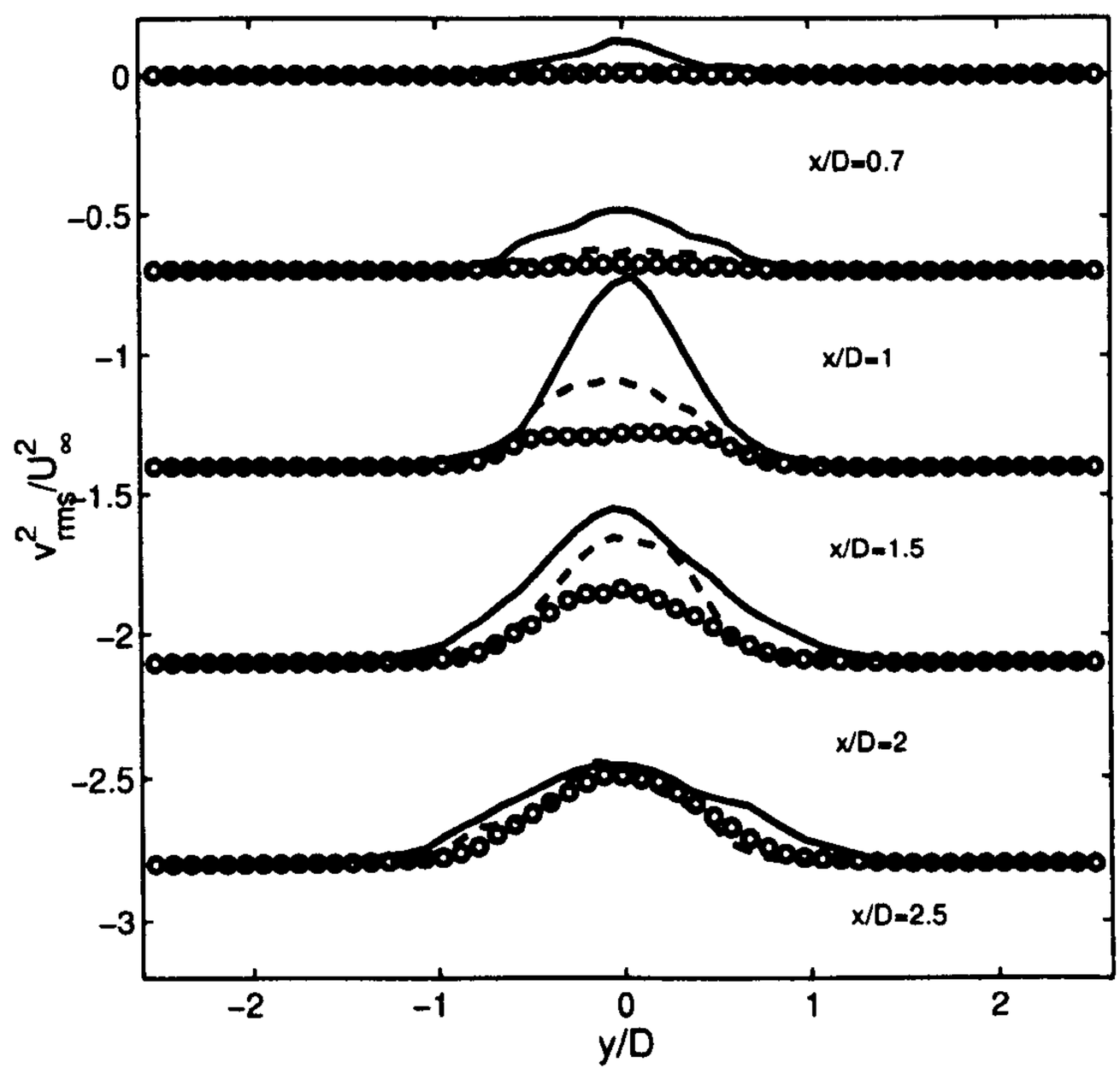

Figure 5.14: $\overline{v^2_{rms}}/u^2_\infty$ behind the cylinder of the steady cross-flow. (——) Dynamic model; (- - - - -) Smagorinsky model; (o o o o) Experiment.

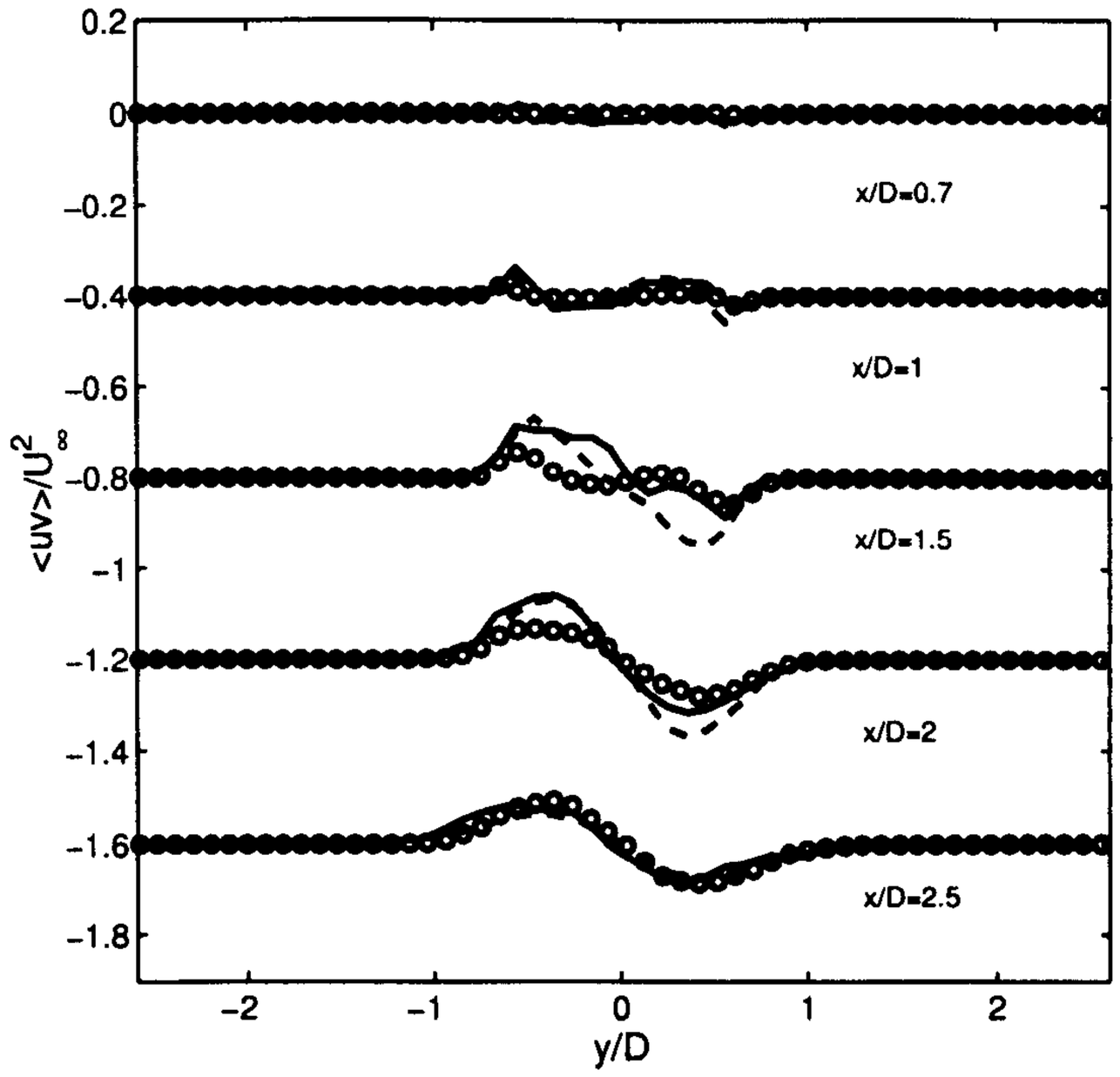

Figure 5.15: $\overline{u_{rms}v_{rms}}/u_\infty^2$ behind the cylinder of the steady cross-flow. (——) Dynamic model; (- - - - -) Smagorinsky model; (o o o o) Experiment.

LES models. Figures 5.18 and 5.19 show the normalized time-averaged streamwise and cross-wake Reynolds stress respectively, and again both models give excellent agreement with the experiment for the second-order statistics. Figure 5.20 shows the normalized time-averaged Reynolds shear stress and both LES models are successful in capturing both the shape and its magnitude.

5.3.3 Lift and drag coefficients

Having fully validated the turbulence statistics for the cylinder near-wake flow field, the lift, drag and base pressure coefficients will now be studied and compared with results from the existing literature.

The current LES calculation shows that the lift coefficient varies at the vortex shedding frequency f_n, while the drag coefficient varies at a frequency two times f_n. It can be seen from figures 5.21 and 5.22 that the average drag coefficient increases from 1.26 to 1.5 and the r.m.s of lift coefficient is also increased due to the lock-on. This is in agreement with the experiments of Barbi et al. (1986) and Armstrong et al. (1986) (where it increased from 1.28 to 1.52 as shown in table 5.4). There is a direct correlation between the drag coefficient and the length of the recirculation bubble; generally speaking, the shorter the recirculation zone,

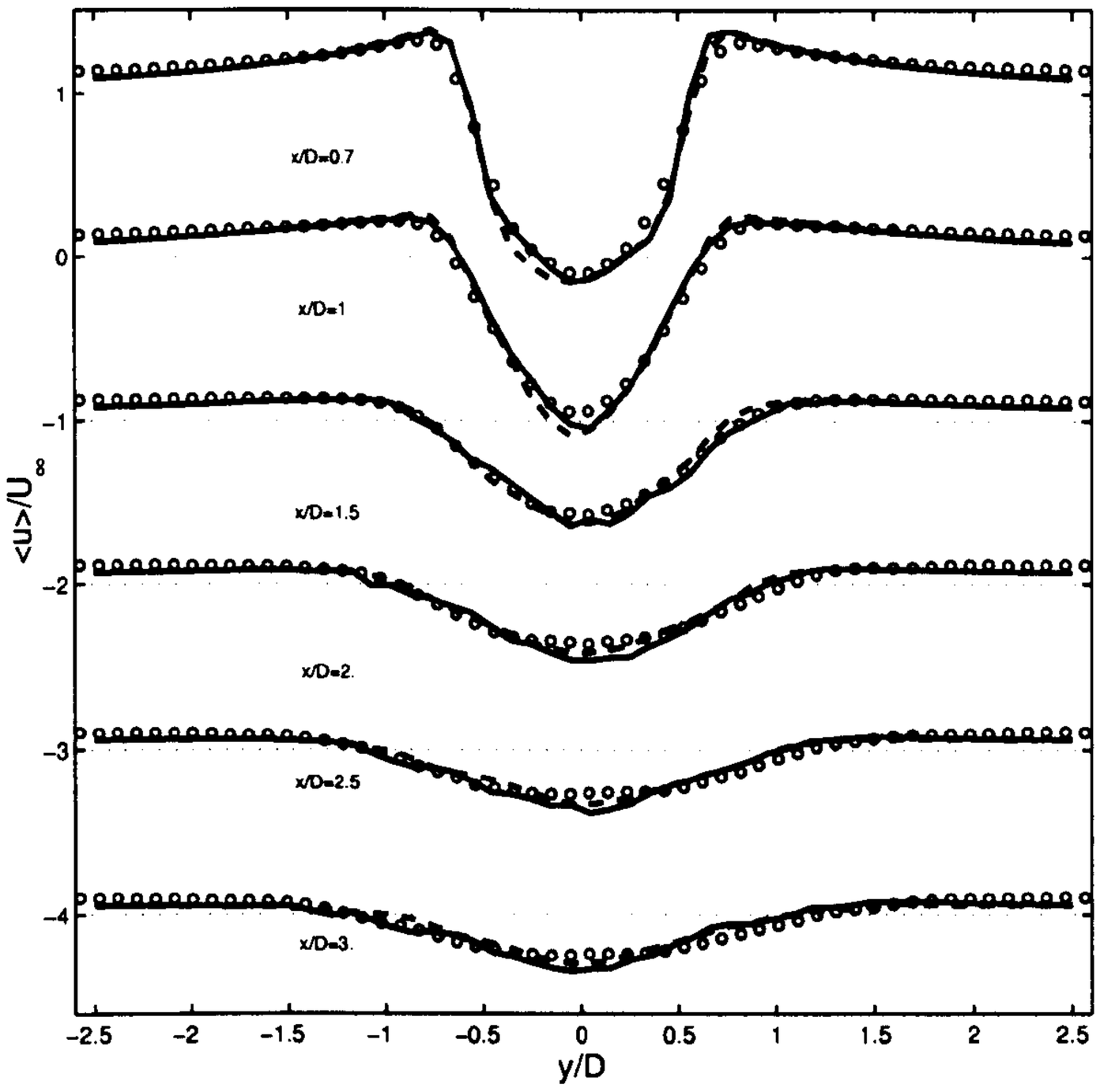

Figure 5.16: Normalized streamwise mean velocity behind the cylinder of the pulsating cross-flow. (——) Dynamic model; (- - - - -) Smagorinsky model; (o o o o) Experiment; For clarity of presentation, the curves at different streamwise positions are shifted and (.....) shows the zero location of each profile.

Wall effects on the base suction and drag coefficient				
Investigator	$-C_{pb}/C_D$ steady flow	$-C_{pb}/C_D$ pulsating flow	Aspect ratio	Blockage ratio
Armstrong et al. (1986) $Re_D = 2.15 \times 10^4$	1.44/1.28	1.85/1.52	10.9	8.4%
Williamson (1996) $Re_D = 2.15 \times 10^4$	1.1/-	-/-	∞	0
Konstantinidis et al. (2003a) $Re_D = 2.15 \times 10^3$	-/-	-/-	10	10%
Breuer (1998) $Re_D = 3.9 \times 10^3$	0.94/1.02	-/-	∞	0
Current LES	1.32/1.26	1.7/1.5	πD	10%

Table 5.4: Wall effects on base suction and drag coefficient, LES results shown here are predicted by the standard Smagorinsky model.

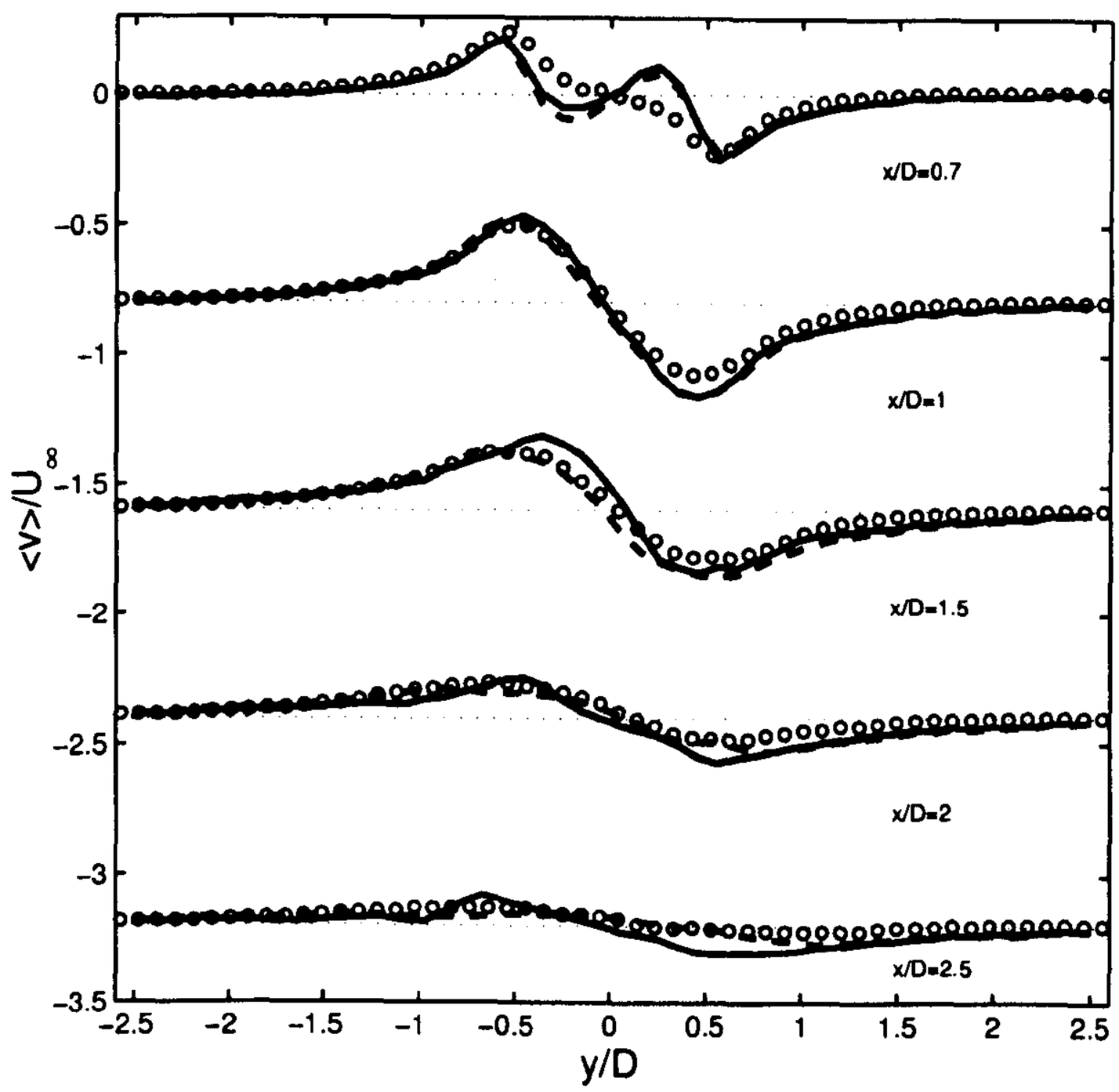

Figure 5.17: Normalized cross-wake mean velocity behind the cylinder of the pulsating cross-flow. (——) Dynamic model; (- - - - -) Smagorinsky model; (o o o o) Experiment; For clarity of presentation, the curves at different streamwise positions are shifted and (.....) shows the zero location of each profile.

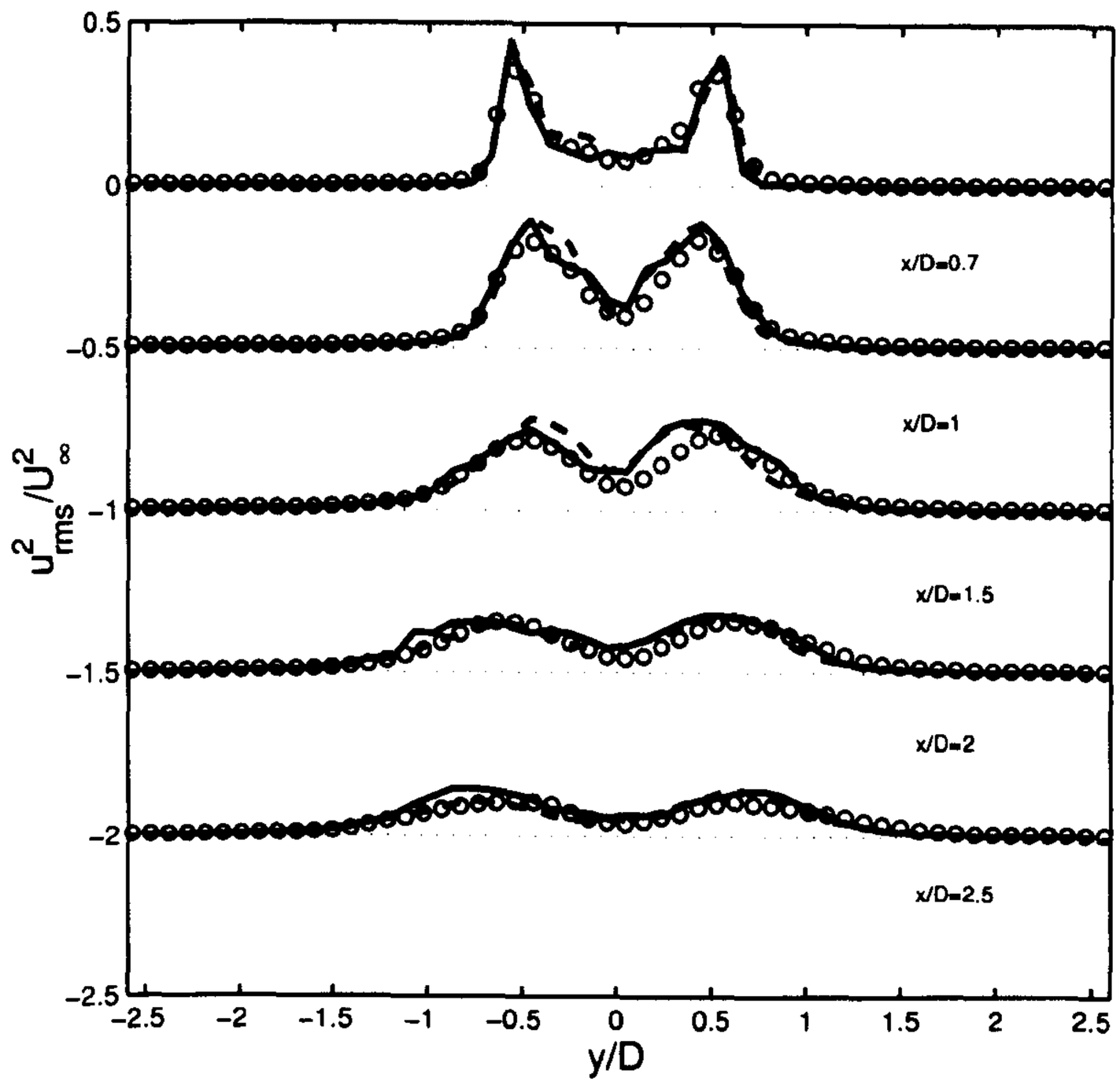

Figure 5.18: $\overline{u'u'}/u_\infty^2$ behind the cylinder of the pulsating cross-flow. (——) Dynamic model; (- - - - -) Smagorinsky model; (o o o o) Experiment; For clarity of presentation, the curves at different streamwise positions are shifted and (.....) shows the zero location of each profile.

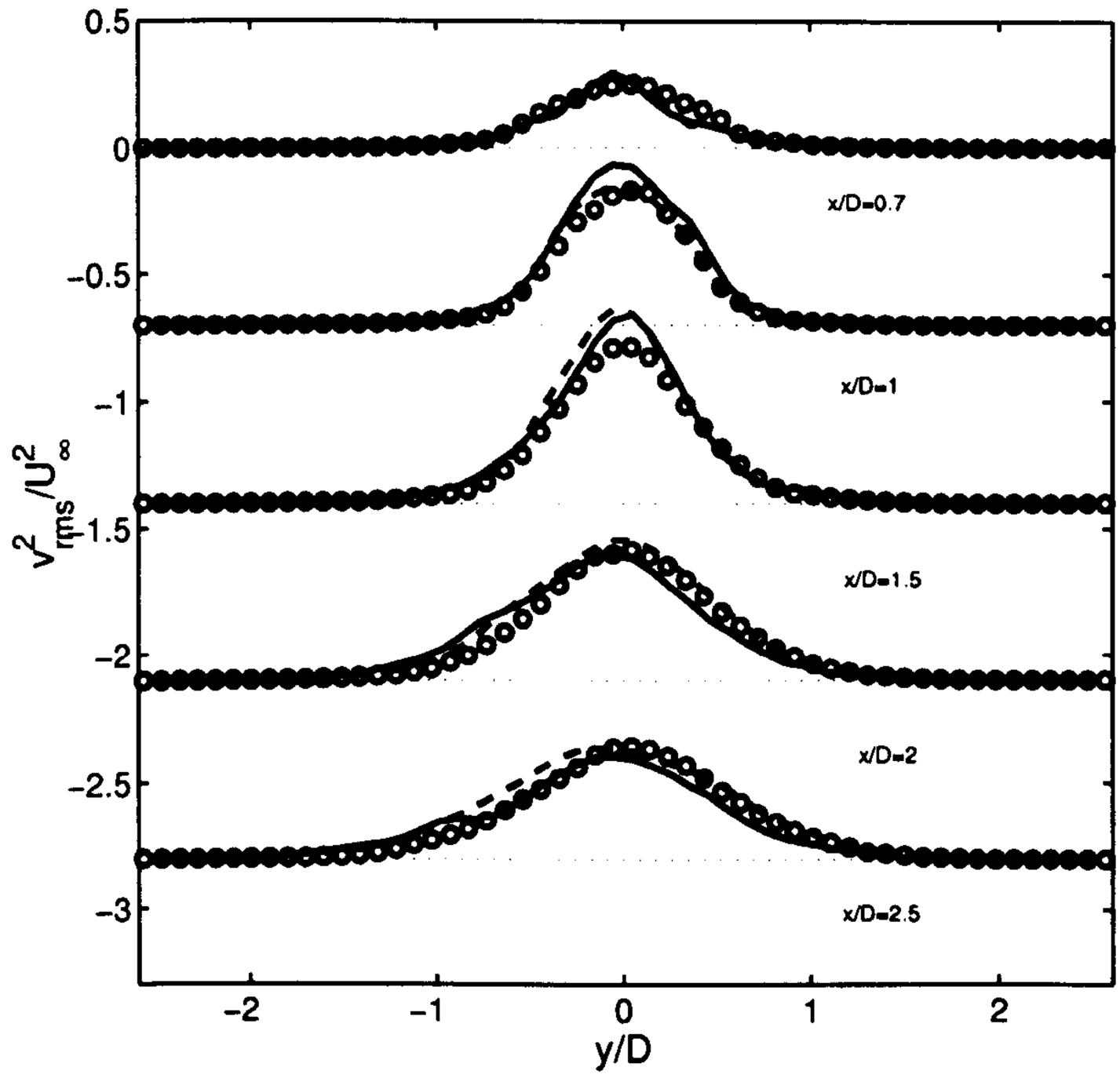

Figure 5.19: $\overline{v'v'}/u_\infty^2$ behind the cylinder of the pulsating cross-flow. (——) Dynamic model; (- - - - -) Smagorinsky model; (o o o o) Experiment; For clarity of presentation, the curves at different streamwise positions are shifted and (.....) shows the zero location of each profile.

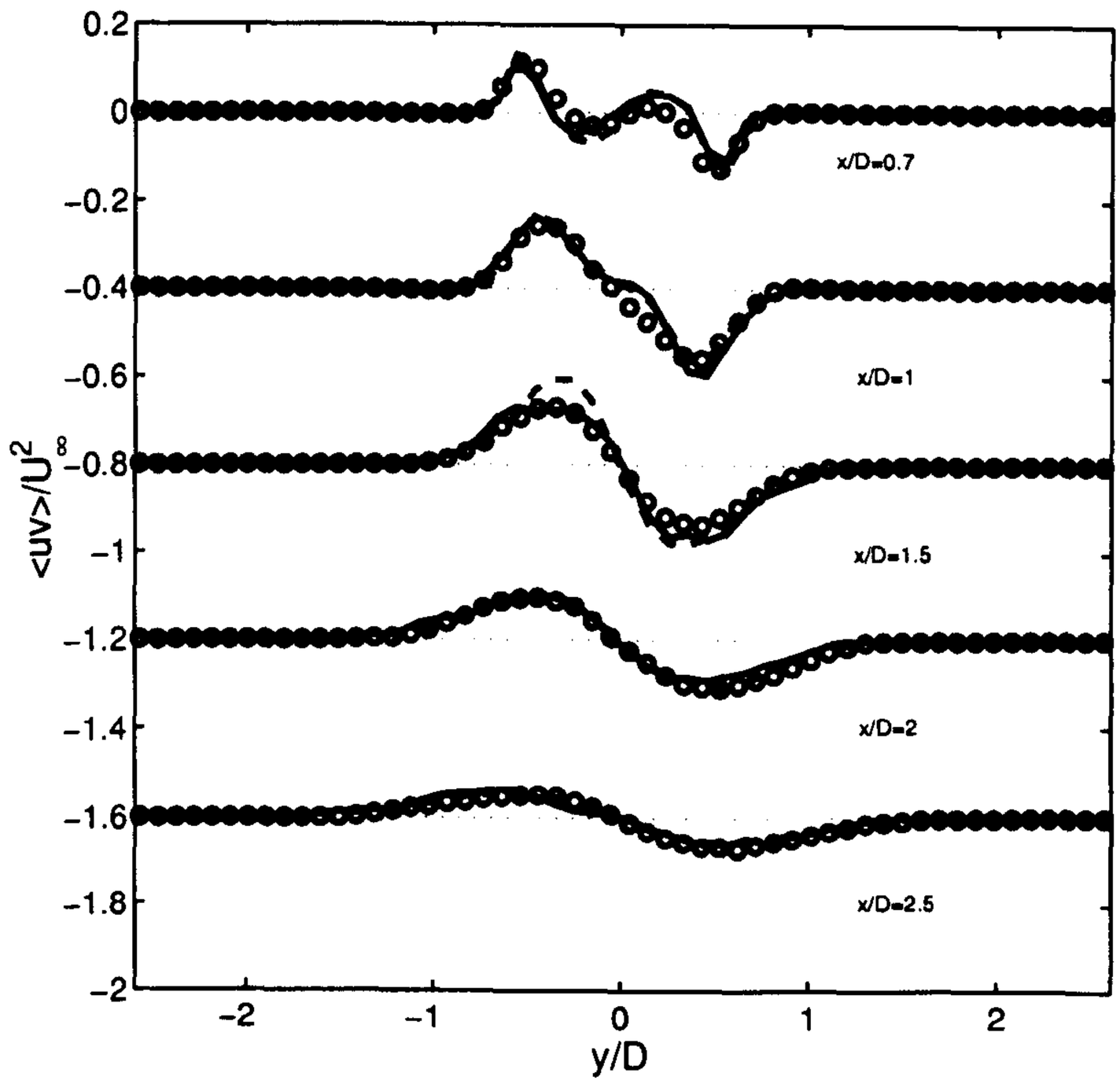

Figure 5.20: $\overline{u'v'}/u_\infty^2$ behind the cylinder of the pulsating cross-flow. (——) Dynamic model; (- - - - -) Smagorinsky model; (o o o o) Experiment. For clarity of presentation, the curves at different streamwise positions are shifted and (.....) shows the location of zero.

the higher the drag coefficient (Williamson, 1996). It can also be seen that the contribution of the viscous part on the two coefficients is very small.

Figure 5.23 shows that the base suction coefficient $-C_{pb}$ is equal to 1.32 for the steady cross-flow prediction. Hasen and Long (2002) predicted $-C_{pb} = 1.34$ for $Re_D = 3,900$ using a highly dissipative first-order upwind scheme. However, it is believed that the wall effects on the cylinder wake play a dominant role in increasing the base suction coefficient for the present case, from $-C_{pb} \simeq 0.9$ predicted by most other LES investigators (Kravchenko and Moin, 2000; Breuer, 1998) and reported by Williamson (1996). At about $Re_D = 2.15 \times 10^4$, Armstrong et al. (1986, 1987) measured the base suction coefficient of steady cross-flow to be 1.44, and that of pulsating cross-flow 1.85 as shown in table 5.4. On the contrary, Williamson (1996) reported $-C_{pb} = 1.1$ for a free cylinder, which is much smaller than the experiments of Armstrong et al. When the experimental arrangements of Konstantinidis et al. (2003*a*) and Armstrong et al. (1986, 1987) are compared, it can be seen that the wall effects of both experiments are significant, as shown in table 5.4, where the aspect ratio refers to L_z/D and blockage ratio refers to D/L_y. The LES predicted higher base suction coefficient for the pulsating cross-flow than the steady cross-flow and the trend is in good agreement with the experiments of Armstrong et al. (1986, 1987), indicating that lock-on modifies the wake structure, leading to a shorter vortex formation length and stronger vortices. Armstrong et al. (1986, 1987) report a higher base suction coefficient than the current LES, mainly due to the Reynolds number effect. The literature on turbulent cross-flow over a circular cylinder confined in a channel is very scarce so direct comparison with other data for similar Reynolds number and aspect ratio could be made. Kim et al. (2004) performed LES of turbulent cross-flow over a square cylinder confined in a channel at Reynolds number 3000. They also found that the drag coefficient increases from 1.97 in an infinite domain to 2.76 in the channel with a blockage ratio of 20%.

5.3.4 Instantaneous flow field for steady and pulsating approaching flows

Having examined the effect of grid resolution and subgrid scale model and having validated the numerical results through comparison with experimental data, the next step is the study of the instantaneous flow field. The flow field characteristics are examined with the help of pressure traces on selected points on the surface of

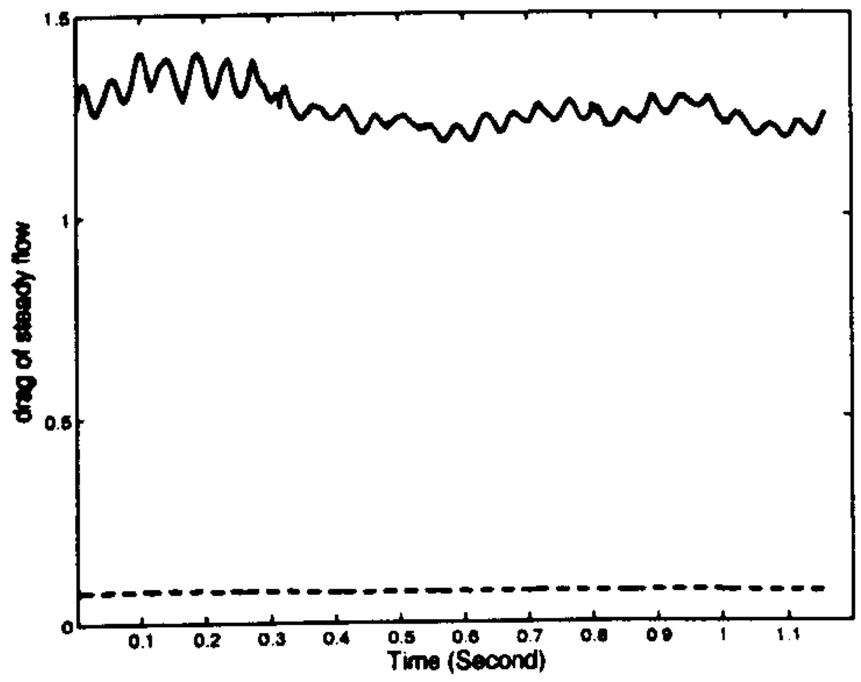

(a) Case B0

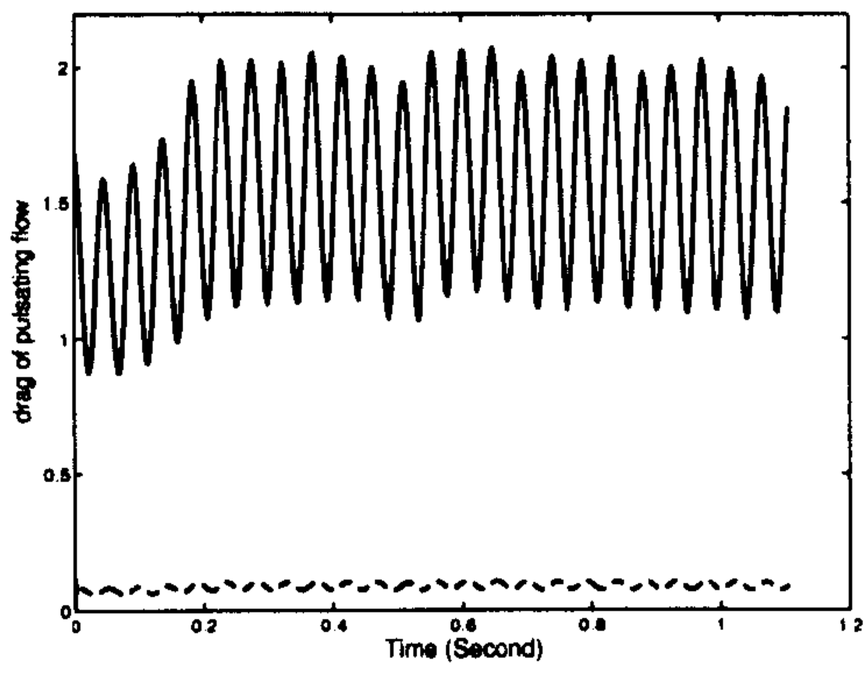

(b) Case B1

Figure 5.21: Drag coefficient predicted by the standard Smagorinsky model for cases B0 and B1. (——) Total drag; (- - - - -) viscous part.

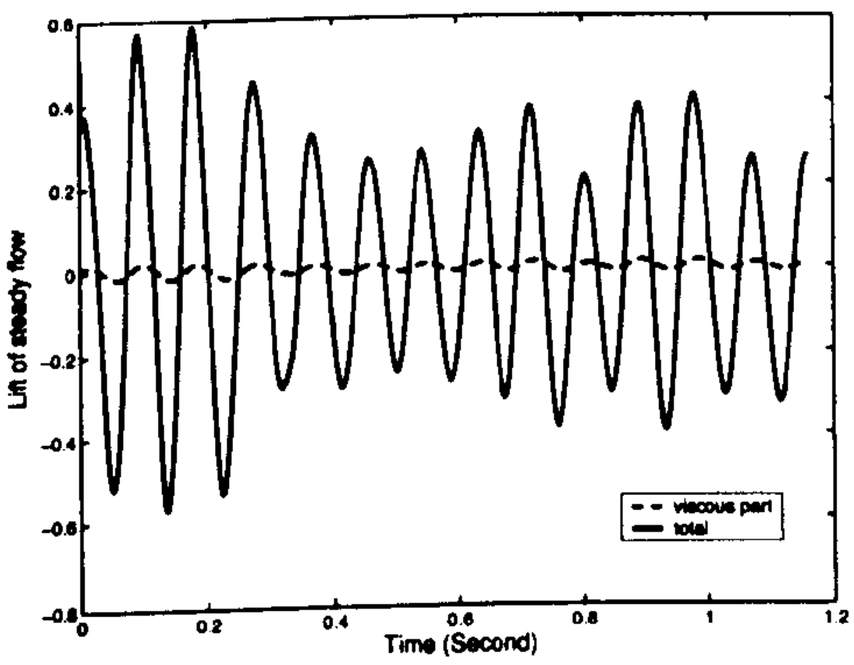

(a) Case B0

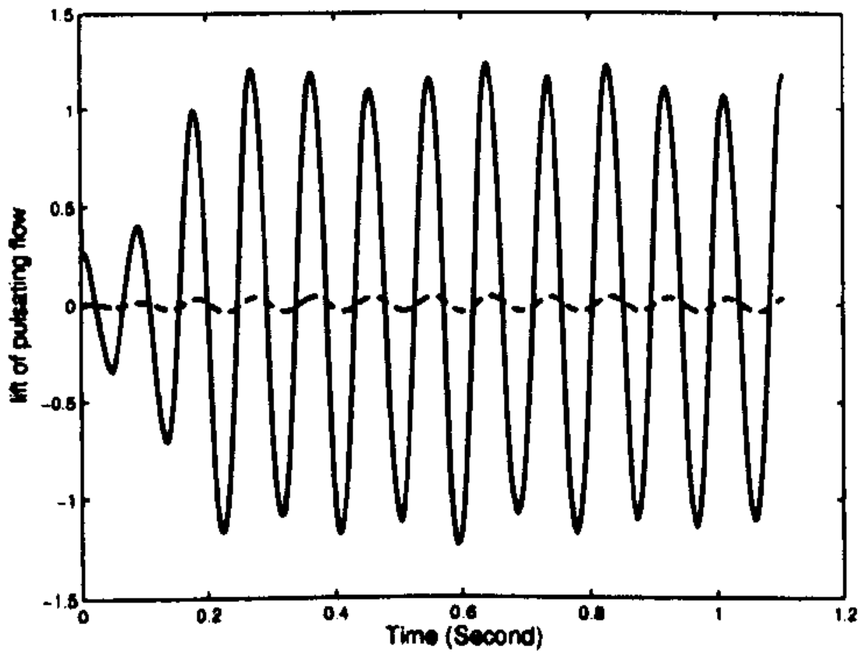

(b) Case B1

Figure 5.22: Lift coefficient predicted by the standard Smagorinsky model for cases B0 and B1.

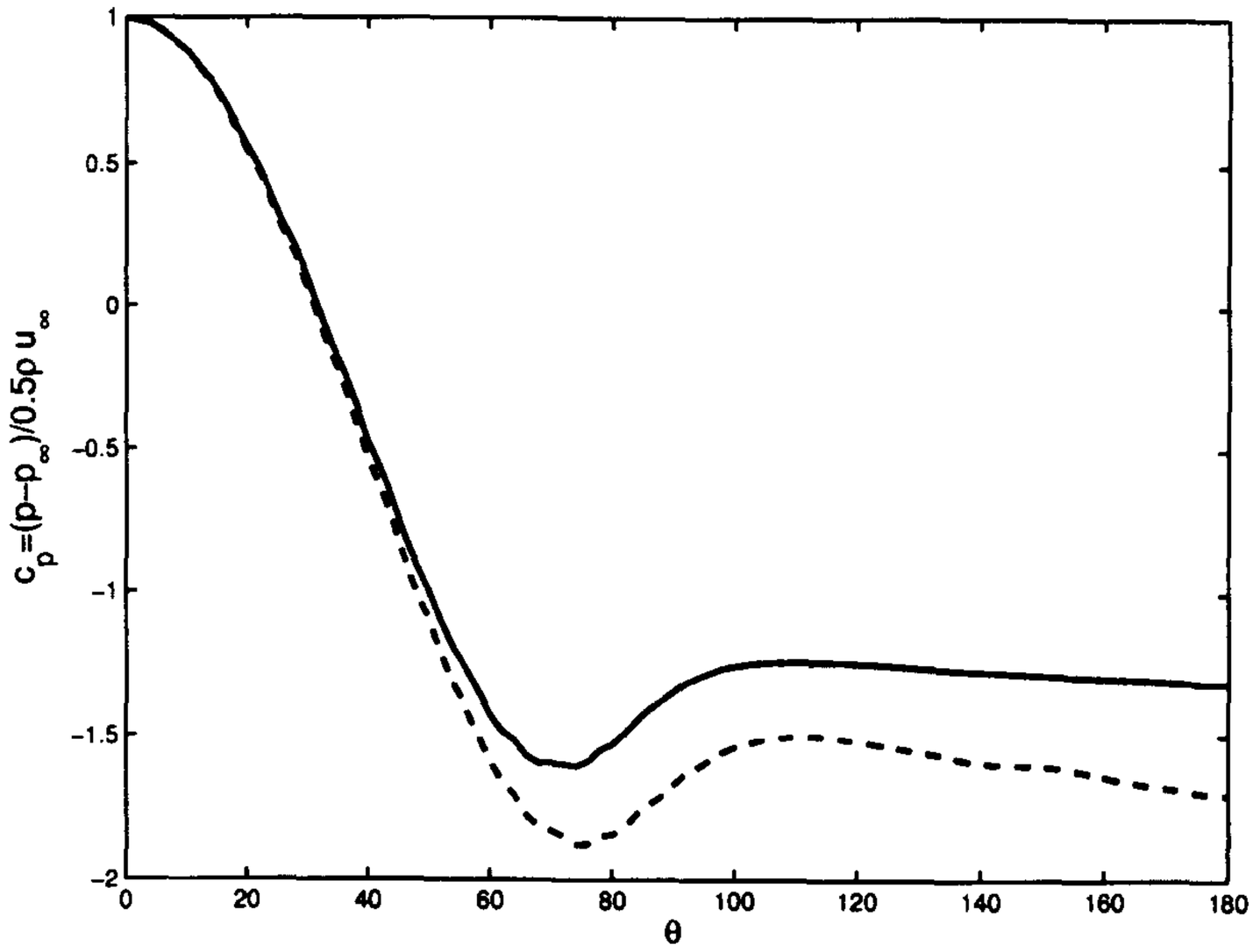

Figure 5.23: Pressure coefficient on the cylinder surface $c_p = \frac{\bar{p}-p_\infty}{\frac{1}{2}\rho u_\infty^2}$. (——) steady cross-flow and (- - - -) pulsating cross-flow. LES results here are predicted by the standard Smagorinsky model

the cylinder as well as instantaneous velocity vectors and vorticity plots. In order to understand the effect of pulsation, corresponding results are also presented for the case of steady approaching flow. The first approach, i.e. the pressure traces, is used to study the effect of pulsation upstream of the separation point while the second approach, i.e. velocity vectors and vorticity plots, is used to understand the effect of pulsation on the cylinder near wake.

The difference between the steady and pulsating approaching flows probably originates from the difference of the pressure fluctuation at the cylinder surface before the shear layer separation point. It can be seen from figure 5.24 that the pressure fluctuation at 60^o for the pulsating flow has bigger amplitude than the steady flow (note the difference on the vertical scale in the two graphs). After the separation point, for instance, at 120^o on the periphery of the cylinderm, the amplitude of pressure fluctuation for the pulsating flow is still roughly 4 times higher than that of the steady flow as shown in figure 5.25. It could be seen that the two dominant frequencies, i.e. external pulsation frequency and the locked-on vortex shedding frequency, still persist clearly.

It is not possible to compare the instantaneous velocity and vorticity patterns in the wake of the cylinder for steady and pulsating flow without some sort of a common reference signal. For the pulsating flow, the external velocity provides

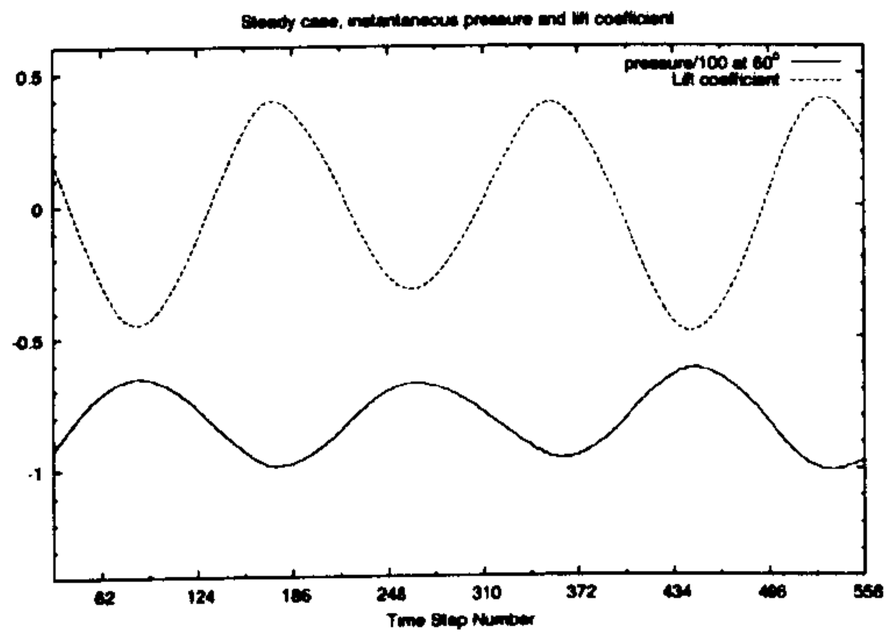

(a) Case B0

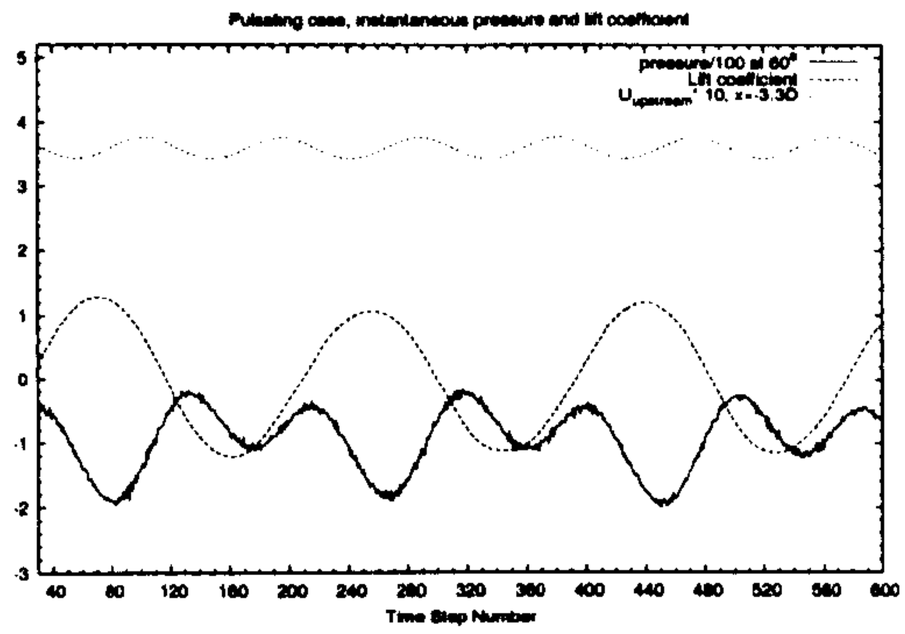

(b) Case B1

Figure 5.24: Time series of instantaneous pressure at a point 60^o on the periphery of the cylinder for cases (a) B0 and (b) B1.

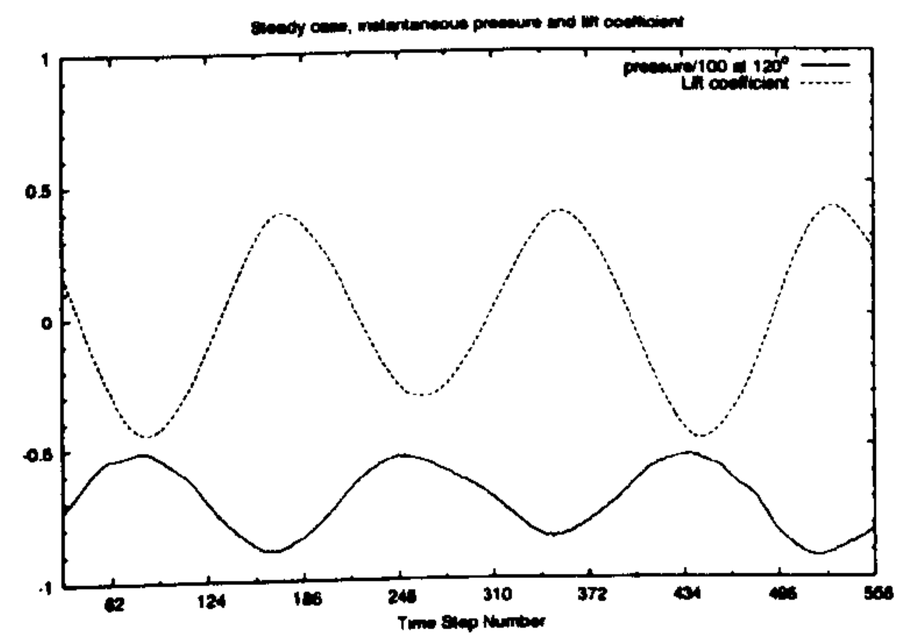

(a) Case B0

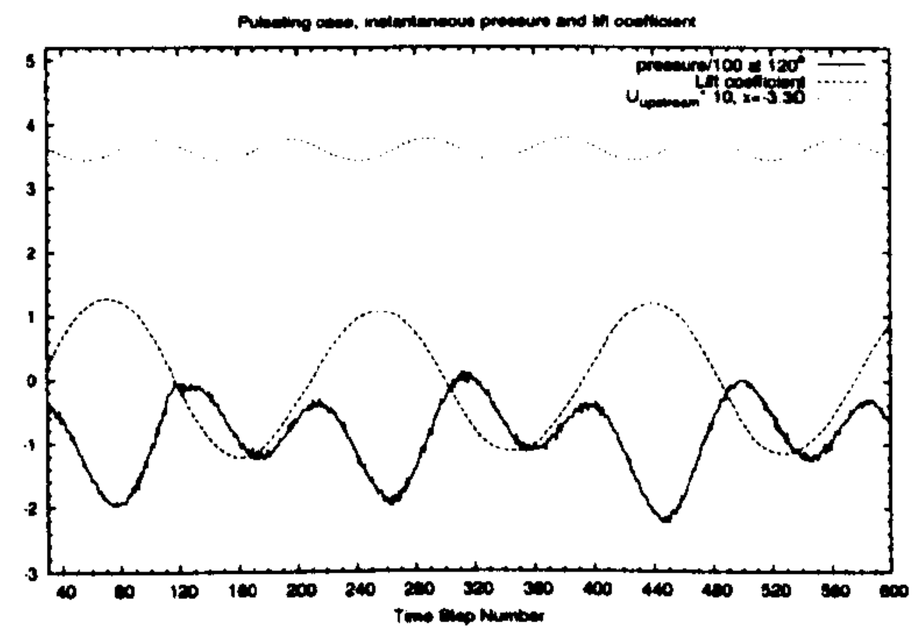

(b) Case B1

Figure 5.25: Time series of instantaneous pressure at a point 120^o on the periphery of the cylinder for cases (a) B0 and (b) B1.

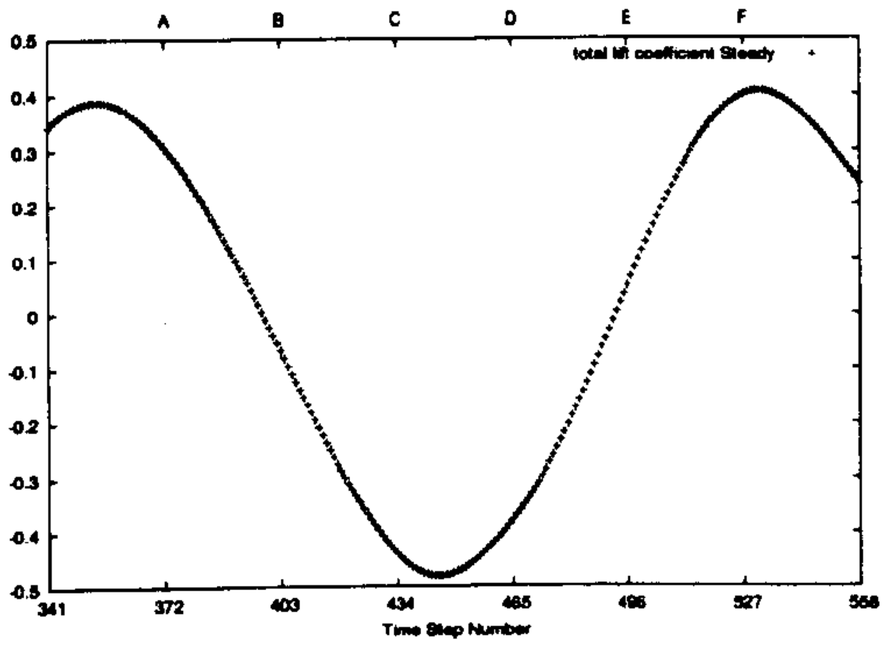

(a) Case B0

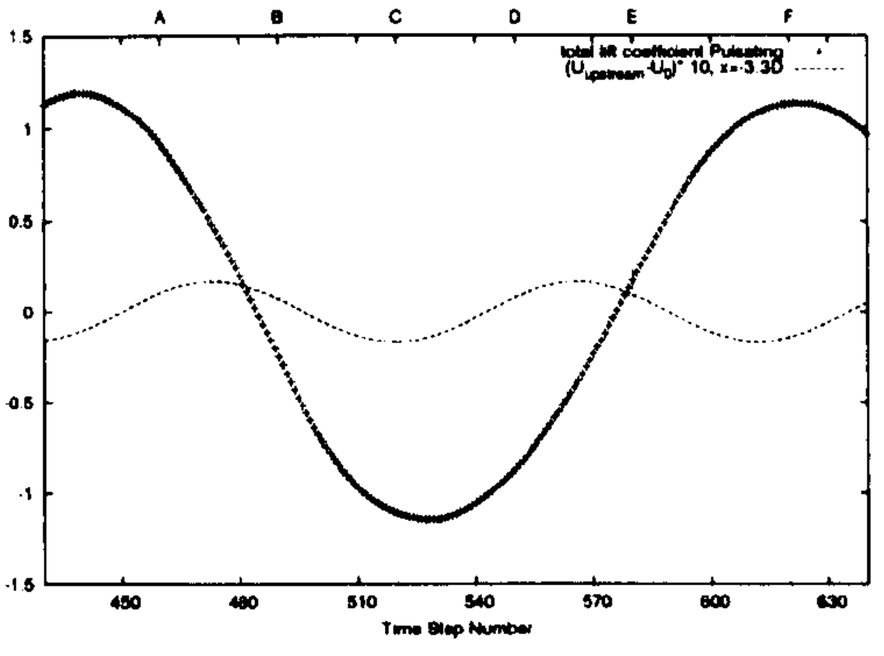

(b) Case B1

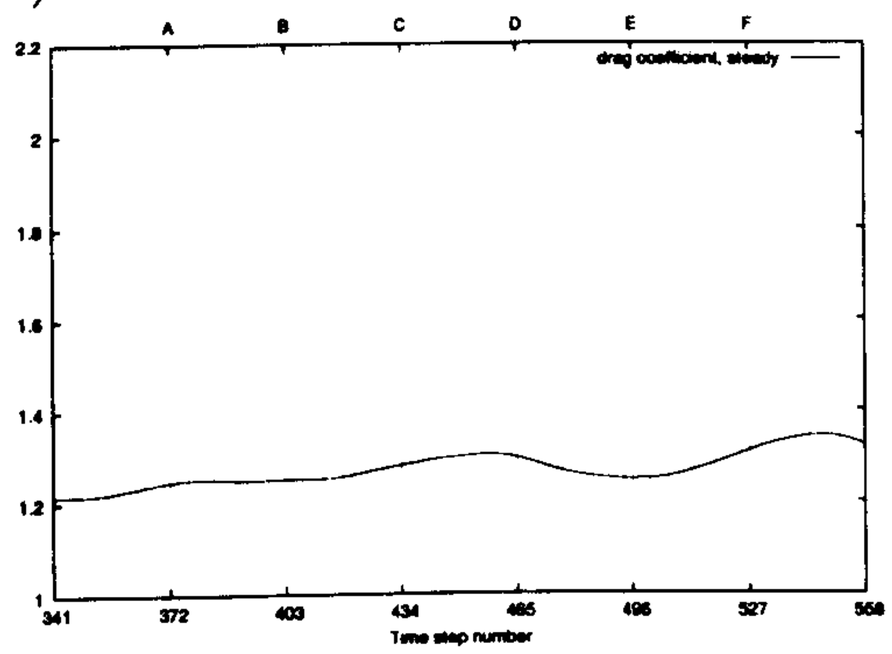

(c) Case B0

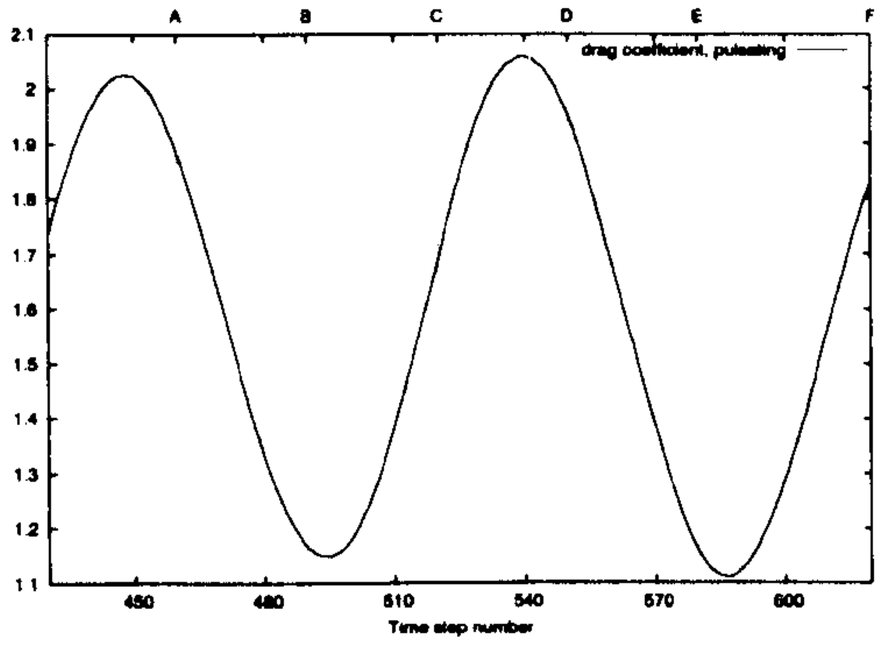

(d) Case B1

Figure 5.26: The lift (a,b) and drag (c,d) coefficients predicted for Cases B0 and B1 respectively.

such a reference, but this is absent for the steady flow. In order to compare the two flow patterns, the variation of the lift coefficient was used as a reference signal. This coefficient has also been used in the past, for example by Beaudan and Moin (1994), in order to calculate the contributions of the random and coherent components of the Reynolds stresses. In the present work, it also provides a useful common reference for comparing the instantaneous flow patterns for steady and pulsating approaching flows. Its variation with time for cases B0 and B1 is shown in figure 5.26. The six phases (A-F) for which the instantaneous flow variables have been recorded and compared are shown in the same figure as well. For figure 5.26(b), it is also possible to relate these phases to the variation of external velocity as well for pulsating case.

Before comparing the phases one by one, it is useful to examine how the instantaneous vorticity and pressure fields are related to the lift coefficient. The phase selected for comparison is Phase D, which corresponds to a lift coefficient close to the minimum. Similar conclusions can be obtained by comparing other phases as well. Figure 5.27 presents the instantaneous spanwise isovorticity and

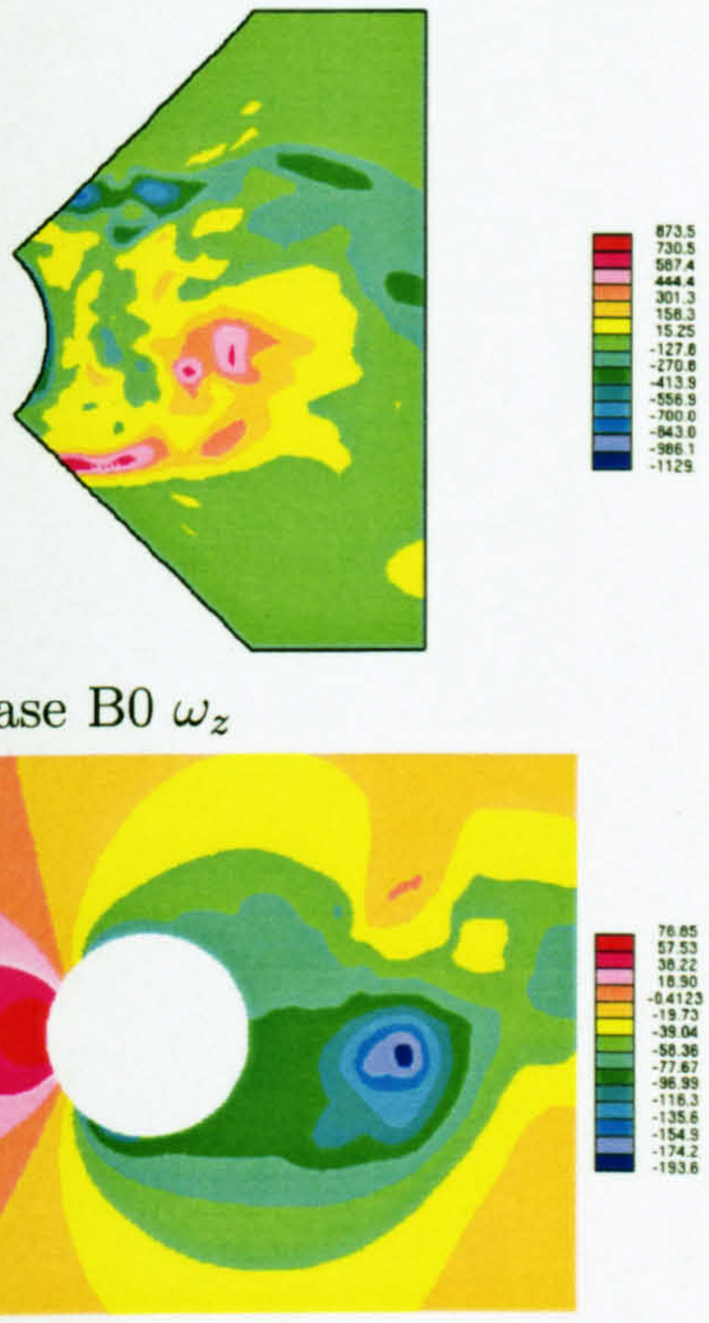

(a) Case B0 ω_z

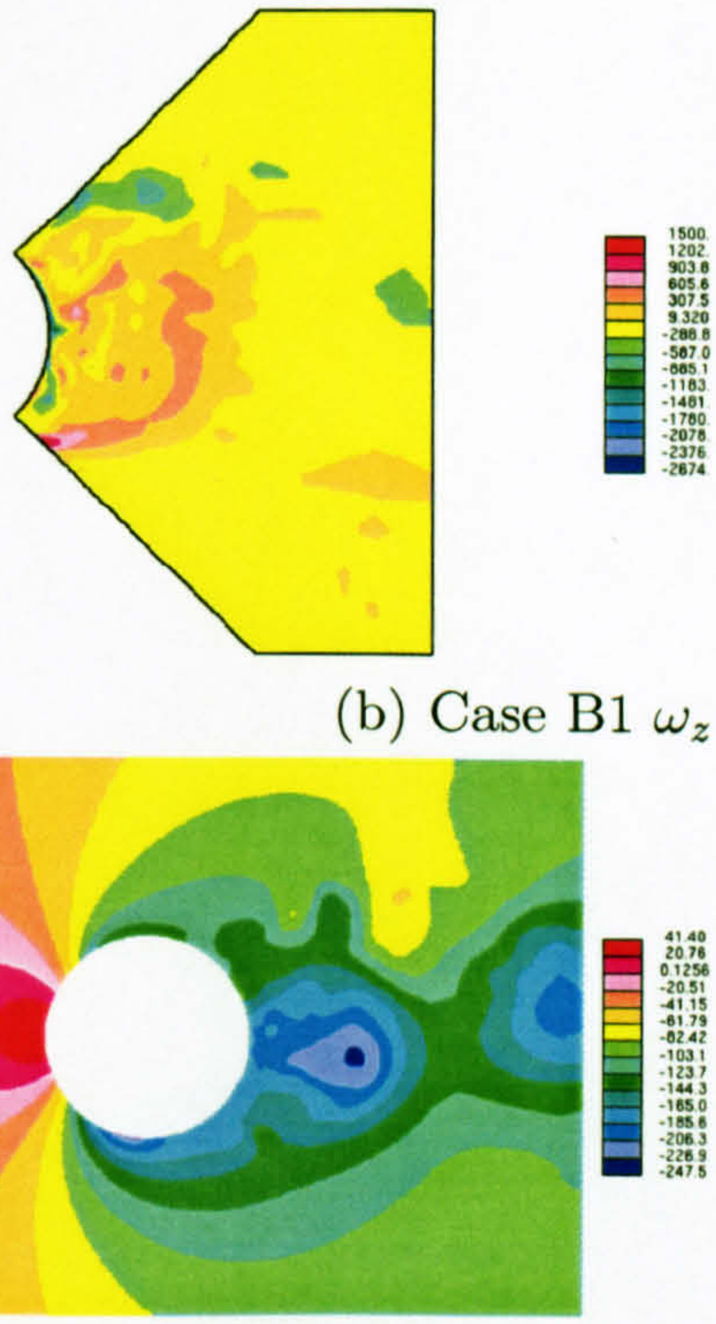

(b) Case B1 ω_z

(c) Case B0 pressure

(d) Case B1 pressure

Figure 5.27: The instantaneous spanwise vorticity and pressure for Cases B0 and B1 at phase D.

isopressure contours for cases B0 and B1. The maximum and minimum values of spanwise vorticity in the cylinder wake for the pulsating case are about twice as high compared with the steady case. It is noted that the minimum and maximum values refer only to the cells located in the near wake of the cylinder, i.e. within the square section shown in the graph. The isopressure contours correlate quite well with the isovorticity ones. For both flow cases, the emitted vortices create a low pressure region that affects the pressure field in the lower part of the cylinder. This negative pressure at the lower part of the cylinder results in a negative lift coefficient as shown in figure 5.26 for phase D. The Strouhal vortex formed by the pulsating cross-flow is also found closer to the cylinder. Consequently, the surface pressure is strongly affected by a nearby vortex. This combination results in smaller values of the lift coefficient compared with the steady approaching flow case.

Figures 5.28 and 5.29 present six snapshots for phases A-F in one shedding period for cases B0 and B1. The velocity vectors are colour coded with the local values of the spanwise vorticity in order to facilitate the identification of vorticity

in areas where the flow does not recirculate. For all graphs, the minimum and maximum values of vorticity were kept the same in order to facilitate the comparison. The graphs show that the wake behind the cylinder at this Reynolds number is extremely complicated, and apart from the dominating Karman vortices, many other smaller vortices exist that make a detailed description of the flow and vorticity patterns a very difficult task. Nevertheless, an attempt will be made to describe the broad features of the two flow patterns and pinpoint the major differences between the wakes. In phase A, which corresponds to high positive values of the lift (figure 5.26), a vortex is shed from the top part of the cylinder for both cases, but when the approaching flow is pulsating, it is located closer to the cylinder. In phase B, the vortex is convected further downstream (thus the lift becomes smaller), but for case B1 the top and bottom shear layers are much shorter and appear to start disintegrating. A rolling-up of the bottom shear layer close to the cylinder is also evident for the same phase. In phase C, the vortex from the top of the cylinder is further convected downstream and is now located close to the right end of the graph, while the process for the formation of the bottom vortex is well under way. Indeed, the shear layer of case B0 forms a vortex rotating counter-clockwise while for case B1 the roll-up of the bottom shear layer has progressed so much that the vortex is about to be released. The close proximity of this strong vortex at the bottom part of the cylinder results in a lift coefficient that is very close to its minimum value. In phase D, the bottom vortex has been released in both cases. It is this phase that was examined in the previous paragraph where it was found that the strength of the emitted vortex is higher for the pulsating case B1. The vortex is then convected downstream while the process for the formation of the upper vortex is under way (Phases E and F in figure 5.29).

From the previous description, it becomes apparent that the pulsation of the external approaching flow results in stronger vortices that are formed closer to the cylinder surface compared to the steady approaching flow and create regions of lower pressure. It is gratifying to note that this observation agrees with the result found experimentally by Armstrong et al. (1986, 1987). This also explains the observed behaviour of the lift coefficient as well as that of the drag coefficient as explained below. Figures 5.26(c) and 5.26(d) present the variation of the drag coefficient with time. Since the emitted vortices create regions of lower pressure compared to the steady case, the resulting instantaneous drag coefficient is increased (for example for phase D). Note also that the flow pulsation results in an increase in the time averaged value of the drag coefficient. Unfortunately,

measurements of the time averaged value of the drag coefficients are not available for comparison, but it is worth noting that this result again agrees with the experimental findings of Armstrong et al. (1986, 1987).

The aforementioned flow instantaneous features can explain the observed behaviour described in the previous section i.e. the smaller time-averaged recirculation zone compared to the steady approaching flow and the small influence of the subgrid scale model. As the vortices become stronger, the contribution of the coherent component of the Reynolds stress increases and thus the effect of small scale fluctuations is reduced. It is for this reason that the predictions agree well with the measurements even for the second order turbulent statistics and the results reveal that the subgrid scale model is not critical for the quality of the predictions. As previously discussed, it is noted that the dynamic Smagorinsky model could lead to worse results than the standard Smagorinsky model on a under-resolved grid for LES because the test filter operation projects the velocity onto an even coarser grid.

Attention is now turned to velocity spectra. Figure 5.30 shows the streamwise velocity spectra for cases B0 and B1 obtained from the velocity signal at the location ($x/D = 0.86$ and $y/D = 0.54$) at the top shear layer. A clear peak at 11.47 Hz is observed for the steady flow. When the external flow is pulsed at 21.6 Hz, i.e. with a frequency close to double the natural shedding frequency, the peak is moved to 10.87 Hz. This is exactly half of the external frequency i.e. the wake is locked to the external perturbation. Note also that the amplitude is increased, which suggests that more energy is carried now by the emitted vortices and the flow has become more coherent. Figure 5.31 shows that the transverse velocity spectra for case B0 and B1 obtained from the velocity time series at the same location in the shear layer. The same behaviour is apparent for the v component as well, the difference being that for this component the pulsation leads to a much higher increase in the amplitude. This is consistent with the big fluctuations that appear in the transverse direction in the instantaneous plots described earlier when the flow is pulsed. It is interesting to note a distinct frequency at 62Hz in the spectra for the steady flow which is not a harmonic of the basic shedding frequency. It is likely that this might be the Bloor frequency, associated with the Kelvin-Helmholtz instabilities that develop in the shear layers and eventually lead to transition into turbulence. Prasad and Williamson (1997) have extensively studied the development of such instabilities in the shear layer and have related the resulting frequency with the Karman shedding frequency with the expression

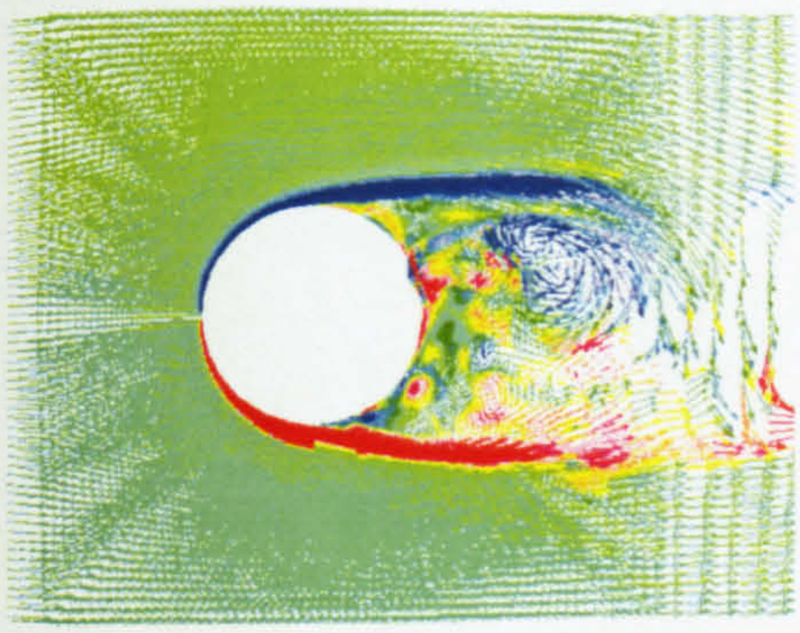

(a) Case B0, phase A

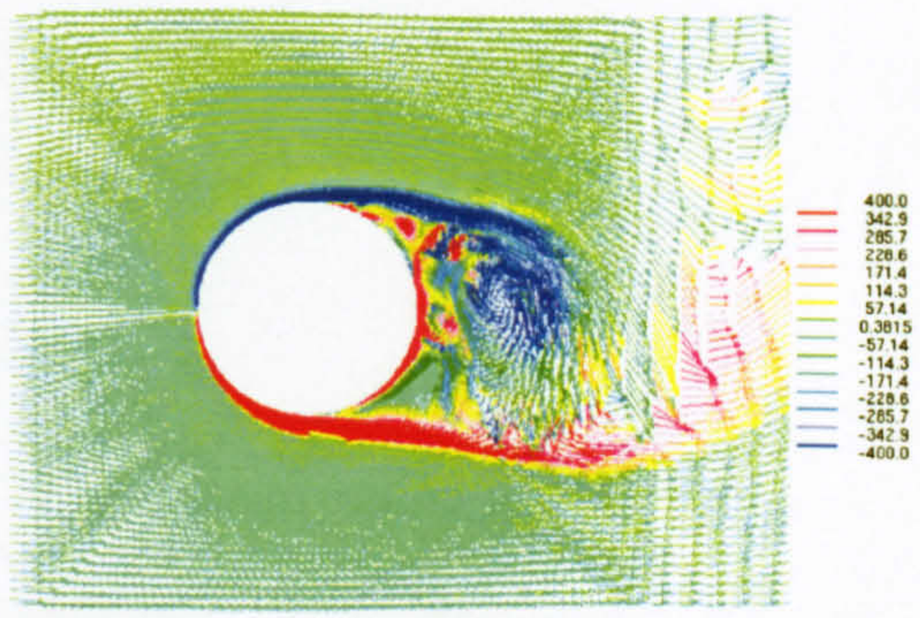

(b) Case B1, phase A

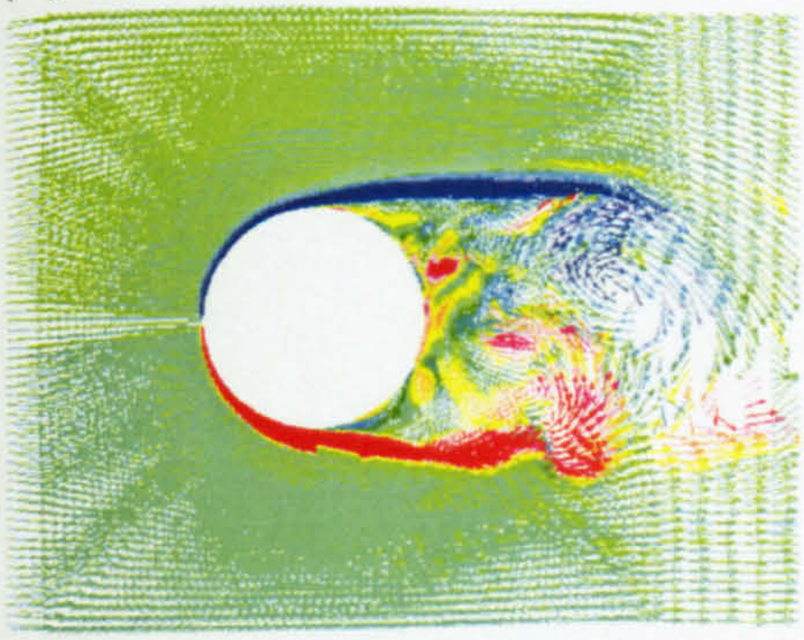

(c) Case B0, phase B

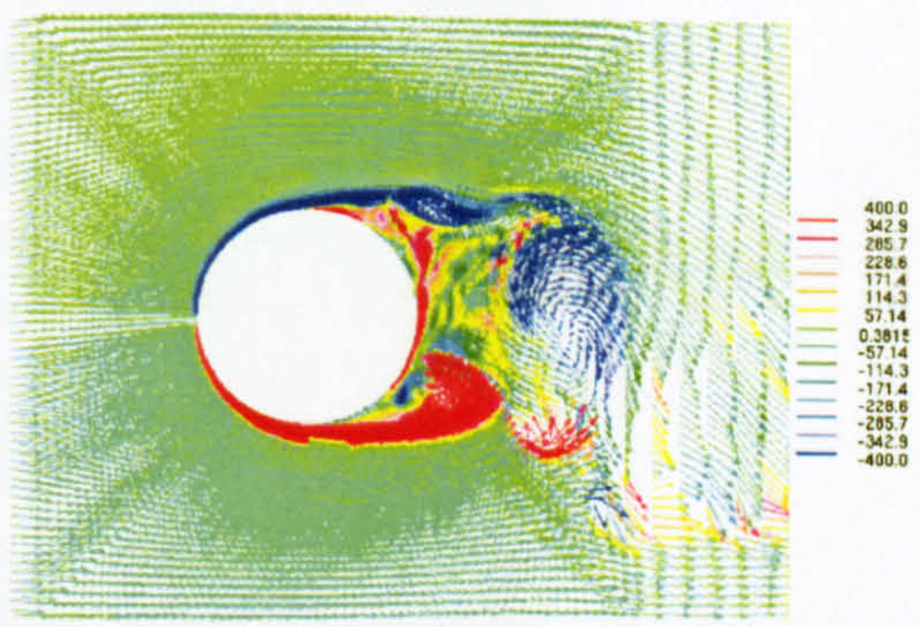

(d) Case B1, phase B

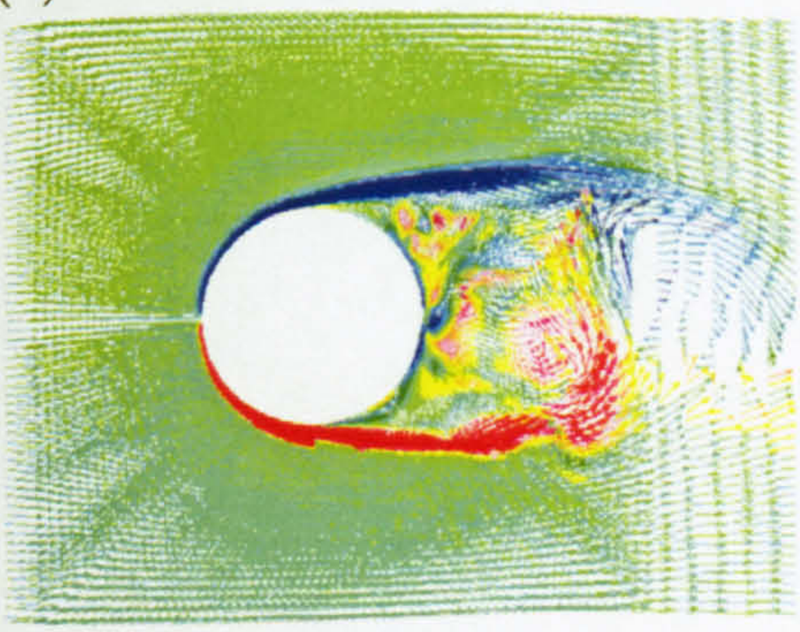

(e) Case B0, phase C

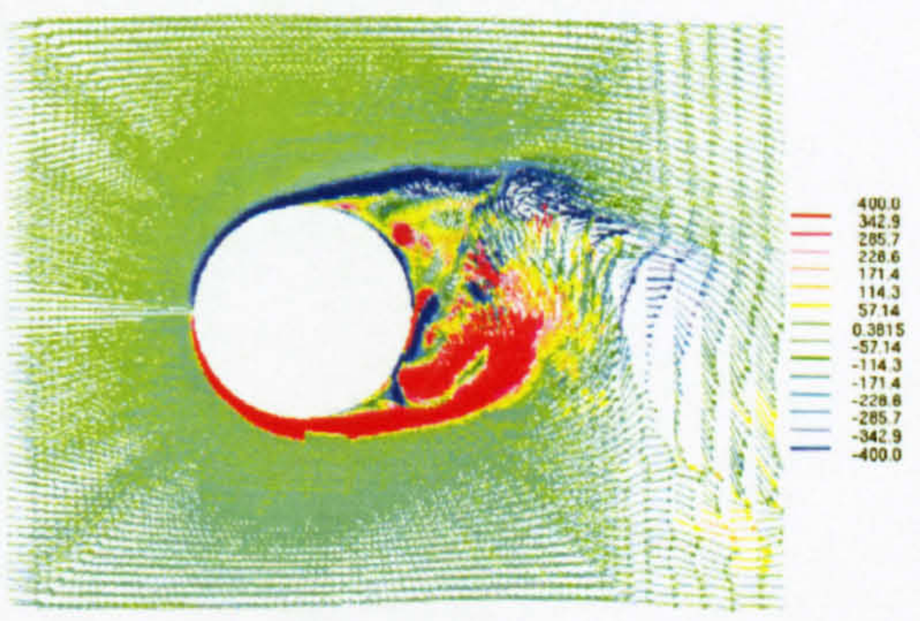

(f) Case B1, phase C

Figure 5.28: The instantaneous velocity and spanwise vorticity field predicted for Cases B0 and B1 (1).

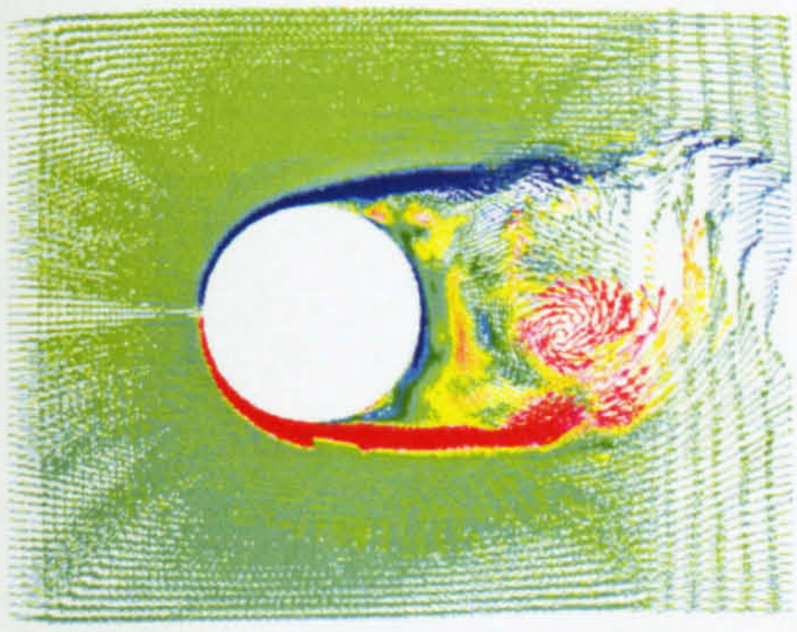

(a) Case B0, phase D

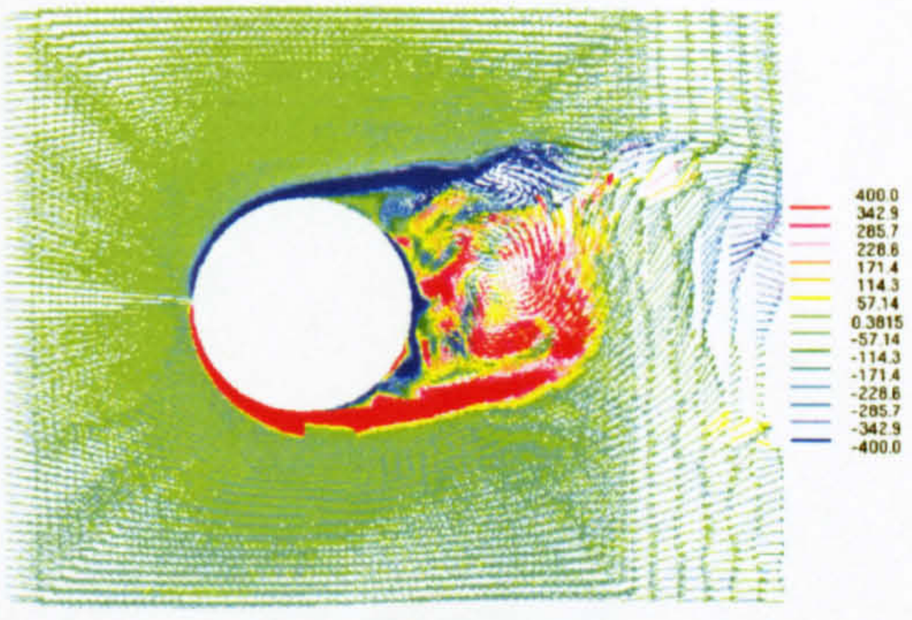

(b) Case B1, phase D

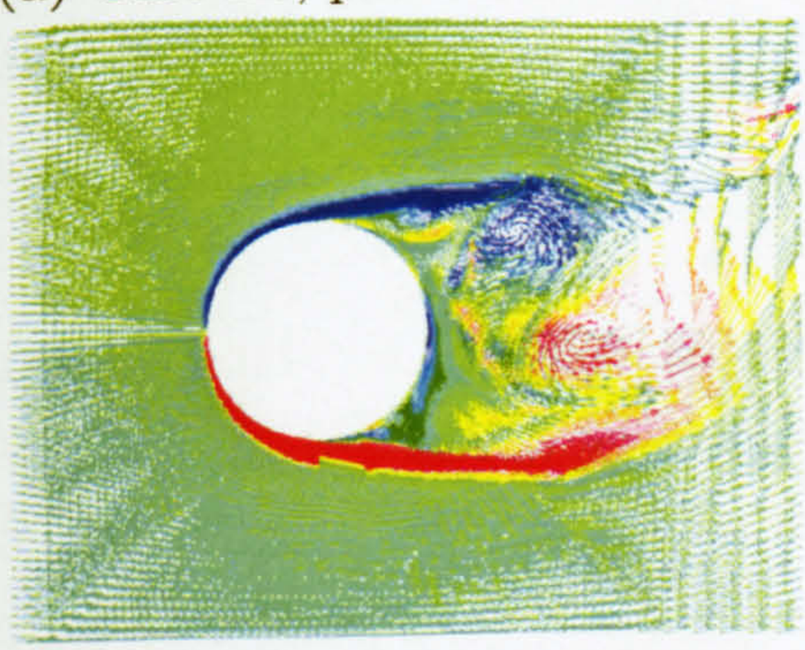

(c) Case B0, phase E

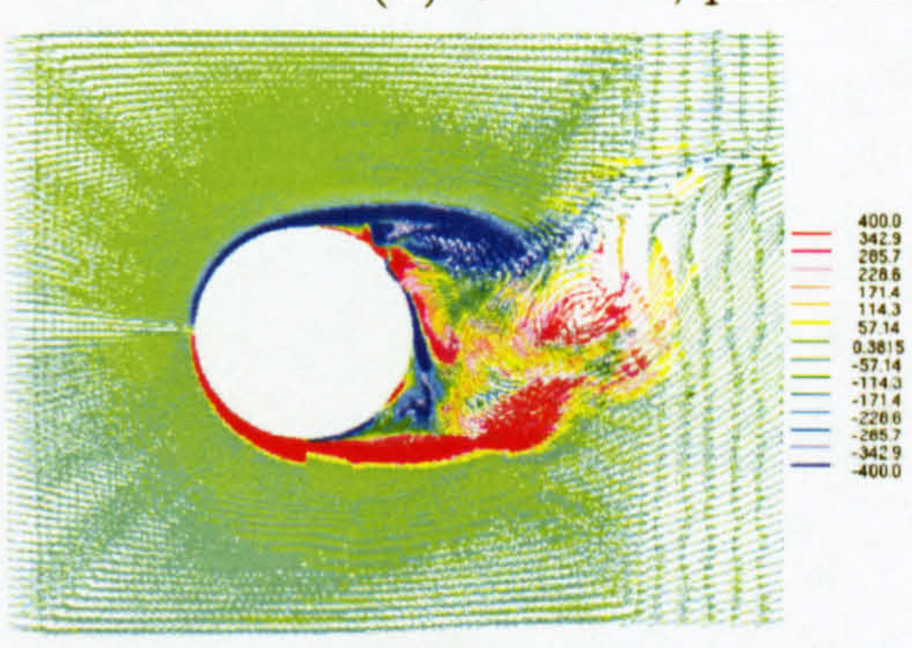

(d) Case B1, phase E

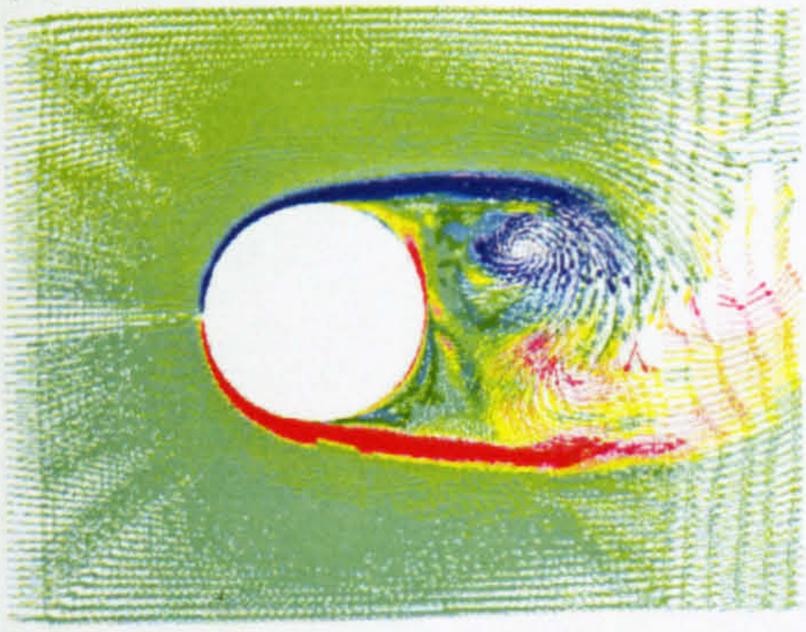

(e) Case B0, phase F

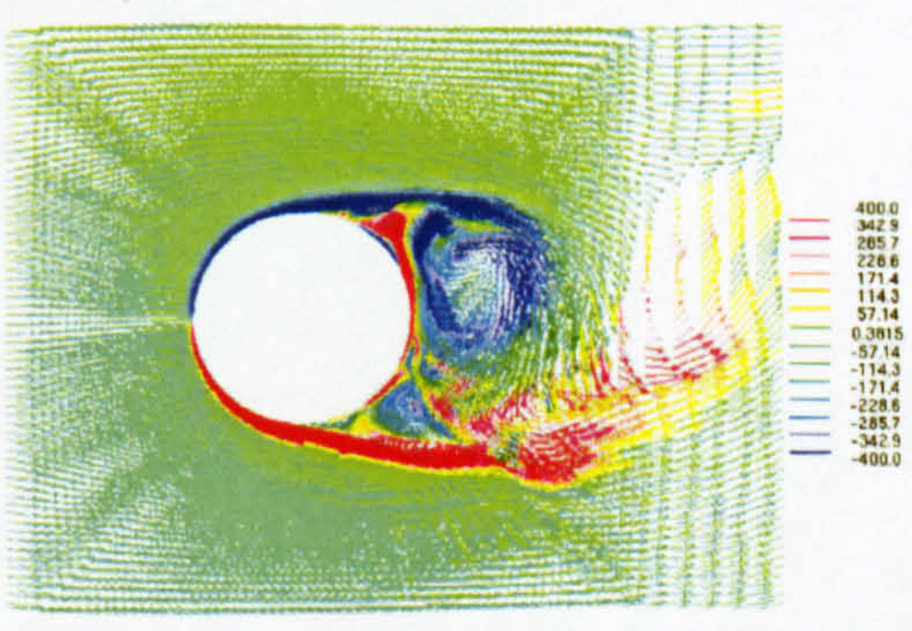

(f) Case B1, phase F

Figure 5.29: The instantaneous velocity and spanwise vorticity field predicted for Cases B0 and B1 (2).

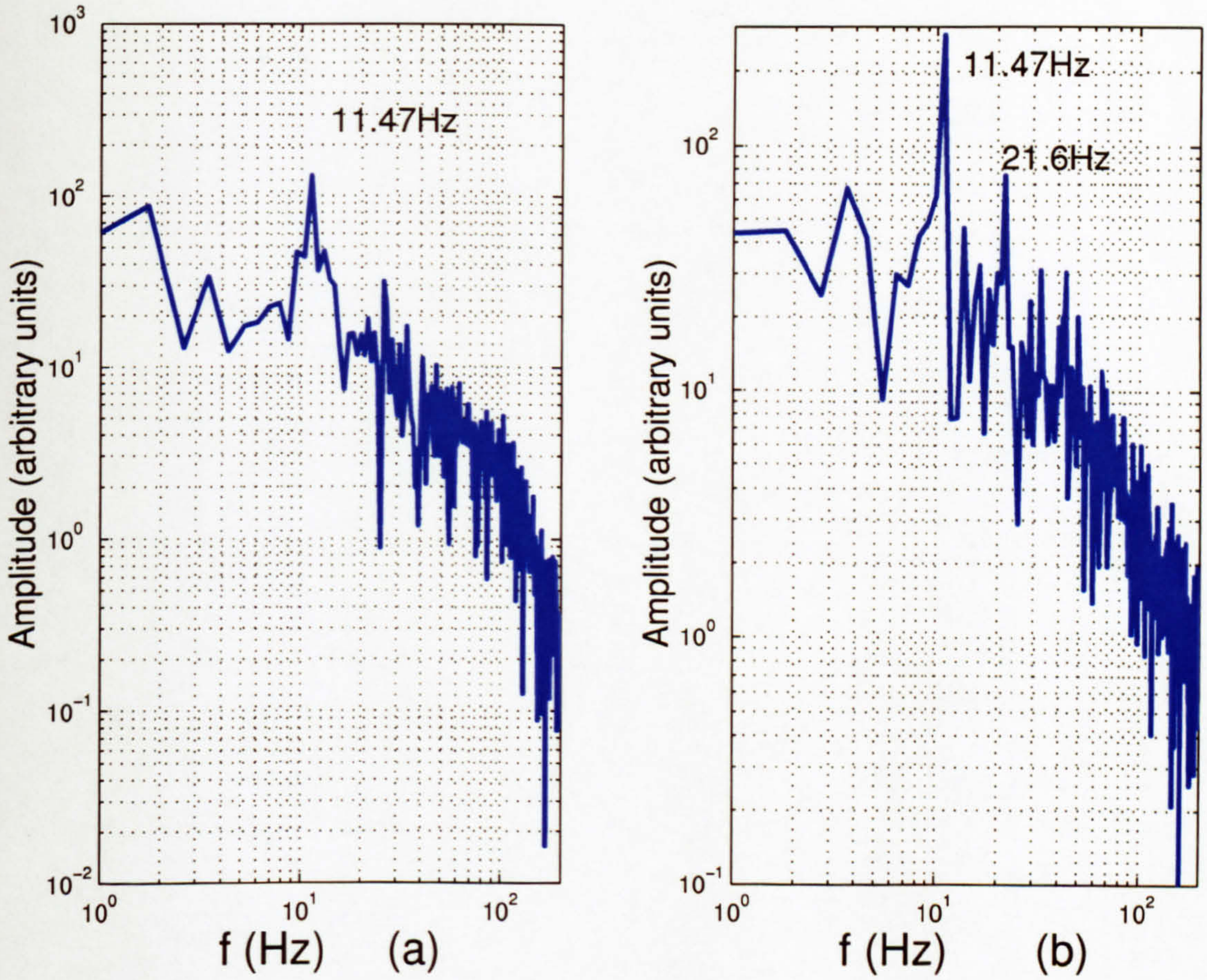

Figure 5.30: Streamwise velocity spectra for Cases B0 (a) and B1 (b) in the location $x = 0.86D$, $y = 0.54D$.

$f_{Bloor}/f_n = 0.0235 \times Re_D^{0.6742}$ which for the examined Reynolds number gives 53.8 Hz. Note that this expression has been obtained for unconfined cylinders, while in the present case the blockage ratio is 10% which leads to increased velocity outside the separating shear layers. This might explain the difference of 8Hz obtained between the expression and the results of the present simulation. It is worth noting that this frequency is less discernible for the pulsating case.

The velocity autocorrelation plots confirm the above findings. Figure 5.32(a) presents the autocorrelation of the streamwise velocity at the same location ($x/D = 0.86$ and $y/D = 0.54$). The u velocity becomes periodically correlated with peaks for case B1 higher than case B0, suggesting stronger periodic coherence for this component. The period of the autocorrelation function of the locked-on case is longer due to the small shift of the vortex shedding frequency shown in figure 5.30. Figure 5.32 (b) shows the autocorrelation of the transverse velocity. The peaks from the case B1 are now much higher than the ones from case B0.

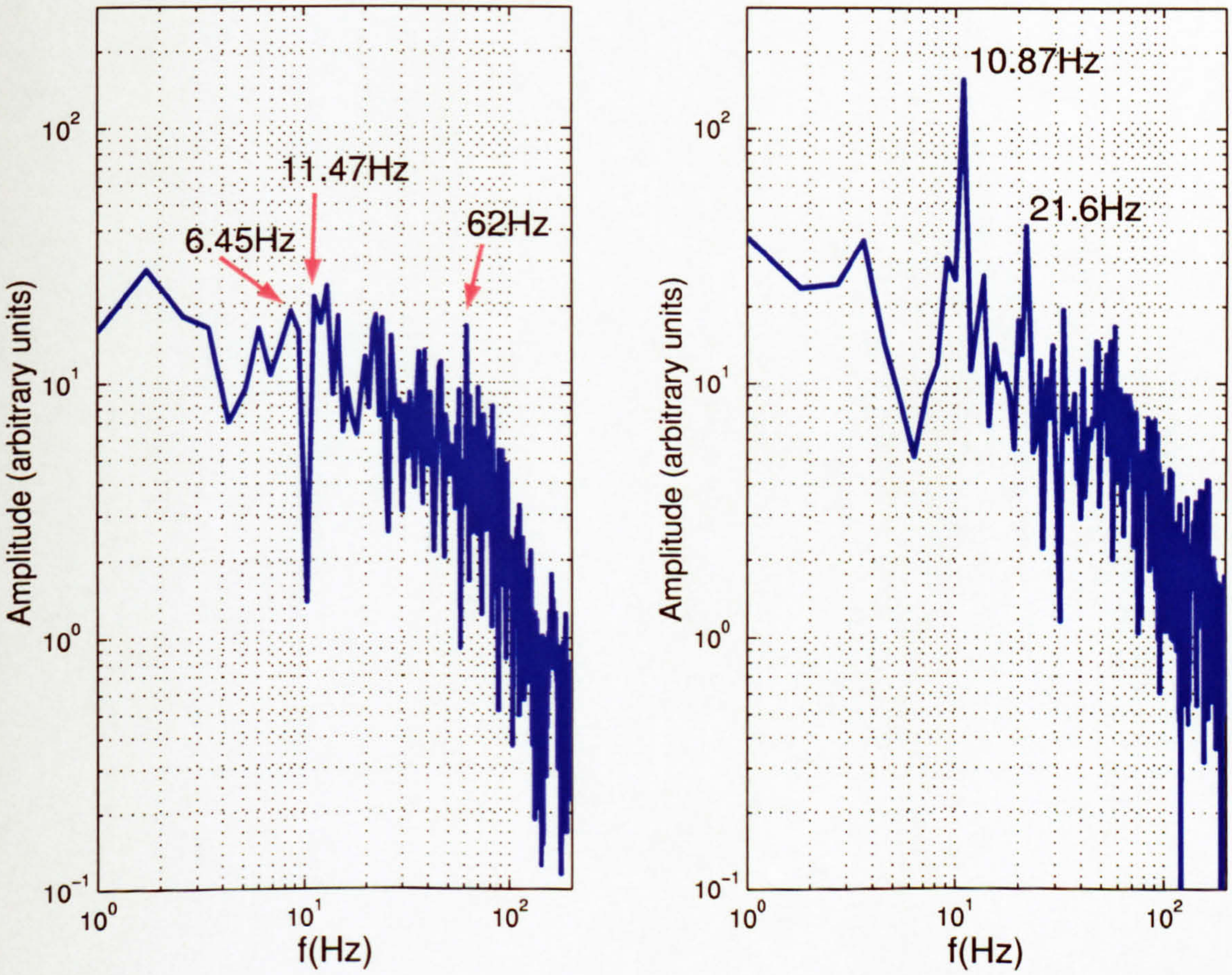

Figure 5.31: Transverse velocity spectra for Cases B0 (left) and B1 (right) in the location $x = 0.86D$, $y = 0.54D$.

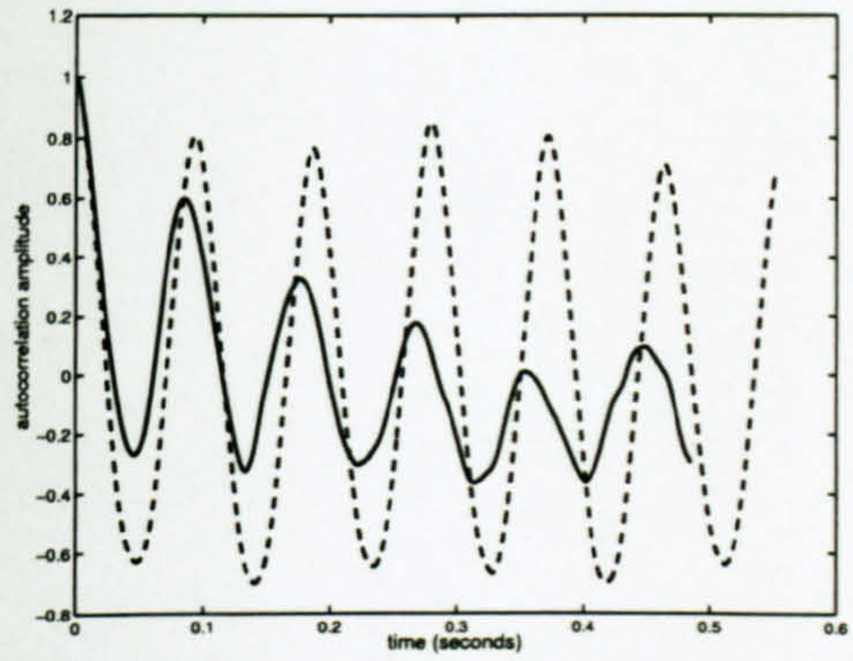

(a) u autocorrelation

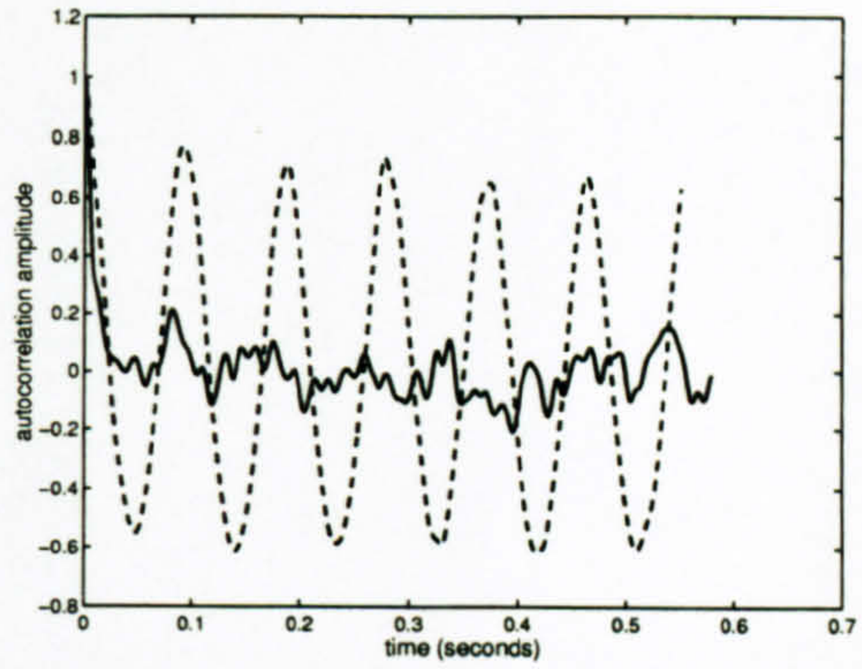

(b) v autocorrelation

Figure 5.32: Autocorrelation function of instantaneous streamwise and transverse velocity fields predicted for Cases B0 (——) and B1 (- - - - -).

The dominant vortex shedding frequency shown in the figure corresponds to the peak shown in figure 5.31. No significant peaks in the autocorrelation function of the transverse velocity are detected in case B0, indicating that the shear layer fluctuation is small in the transverse direction.

It is also instructive to evaluate the energy associated with the coherent structures by filtering off the vortex shedding peaks and directly compare the mean and r.m.s filtered velocity signals of Cases B0 and B1. Figure 5.33 shows the streamwise velocity time series at the same point ($x/D = 0.86$, $y/D = 0.54$) of the shear layer predicted by Case B0. The filtered time series is obtained using an elliptic filter available in MATLAB package after attenuation of the signal data range around the natural shedding frequency. The corresponding frequency spectra is shown in Figure (5.34). The mean square velocities of the original and filtered time series are $\overline{u'u'}/u_\infty^2 = 0.27$ and $\overline{u'_*u'_*}/u_\infty^2 = 0.135$. Thus the coherent contribution accounts for 50% of the total streamwise Reynolds stress. Figure 5.35 shows the streamwise velocity time series of the shear layer predicted by Case B1. The filtered time series is obtained using the same elliptic filter as mentioned before and the corresponding frequency spectra are shown in Figure 5.36. The mean square velocity of the original and filtered time series are $\overline{u'u'}/u_\infty^2 = 0.38$ and $\overline{u'_*u'_*}/u_\infty^2 = 0.10$. Thus the coherent contribution accounts for 74% of the total streamwise Reynolds stress at this particular point. A higher coherent contribution to the pulsating cross-flow is most likely one reason that Case B1 is much easier to model than B0.

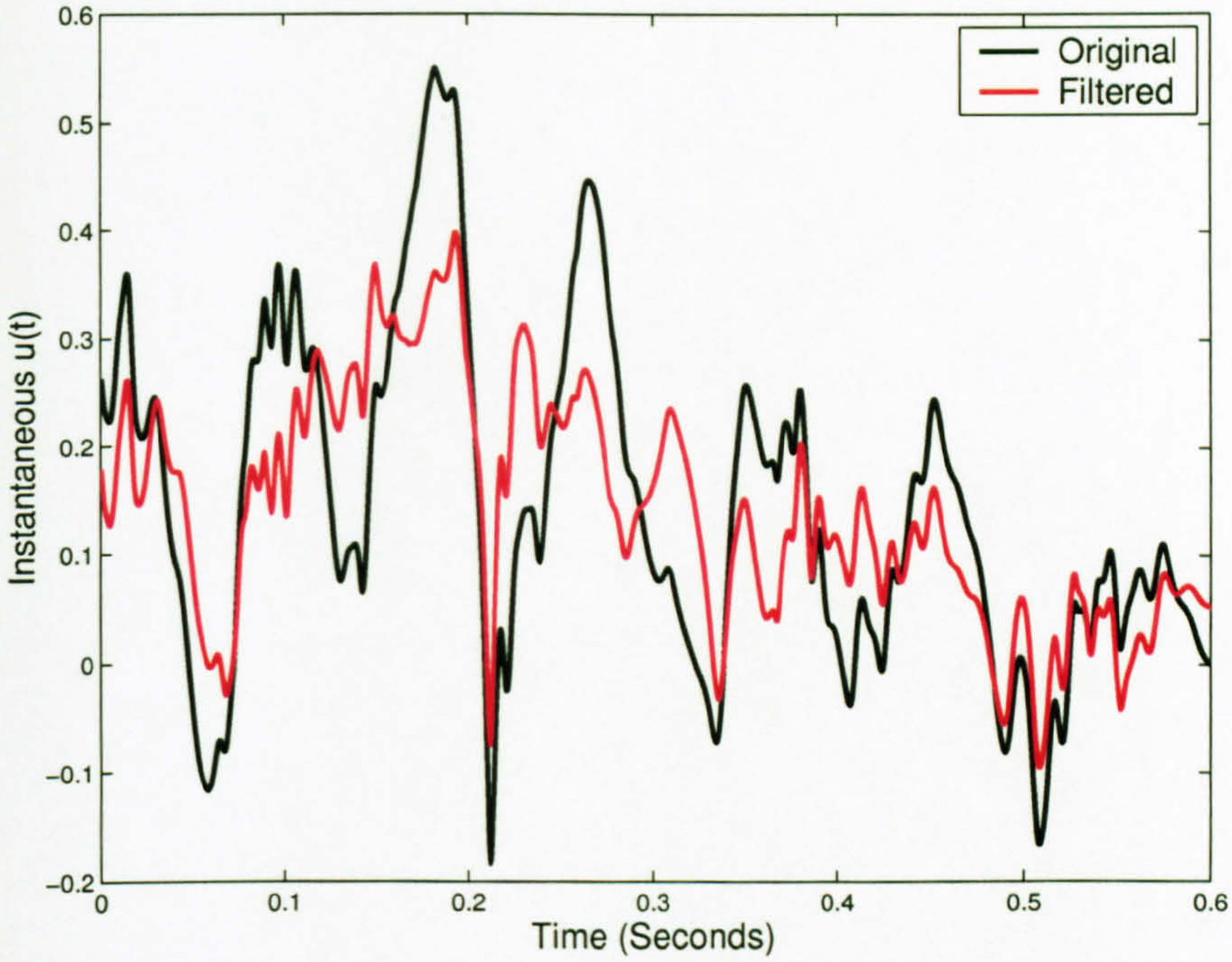

Figure 5.33: Streamwise velocity time series at a point ($x/D = 0.86$, $y/D = 0.54$) behind the cylinder of the steady cross-flow for Case B0.

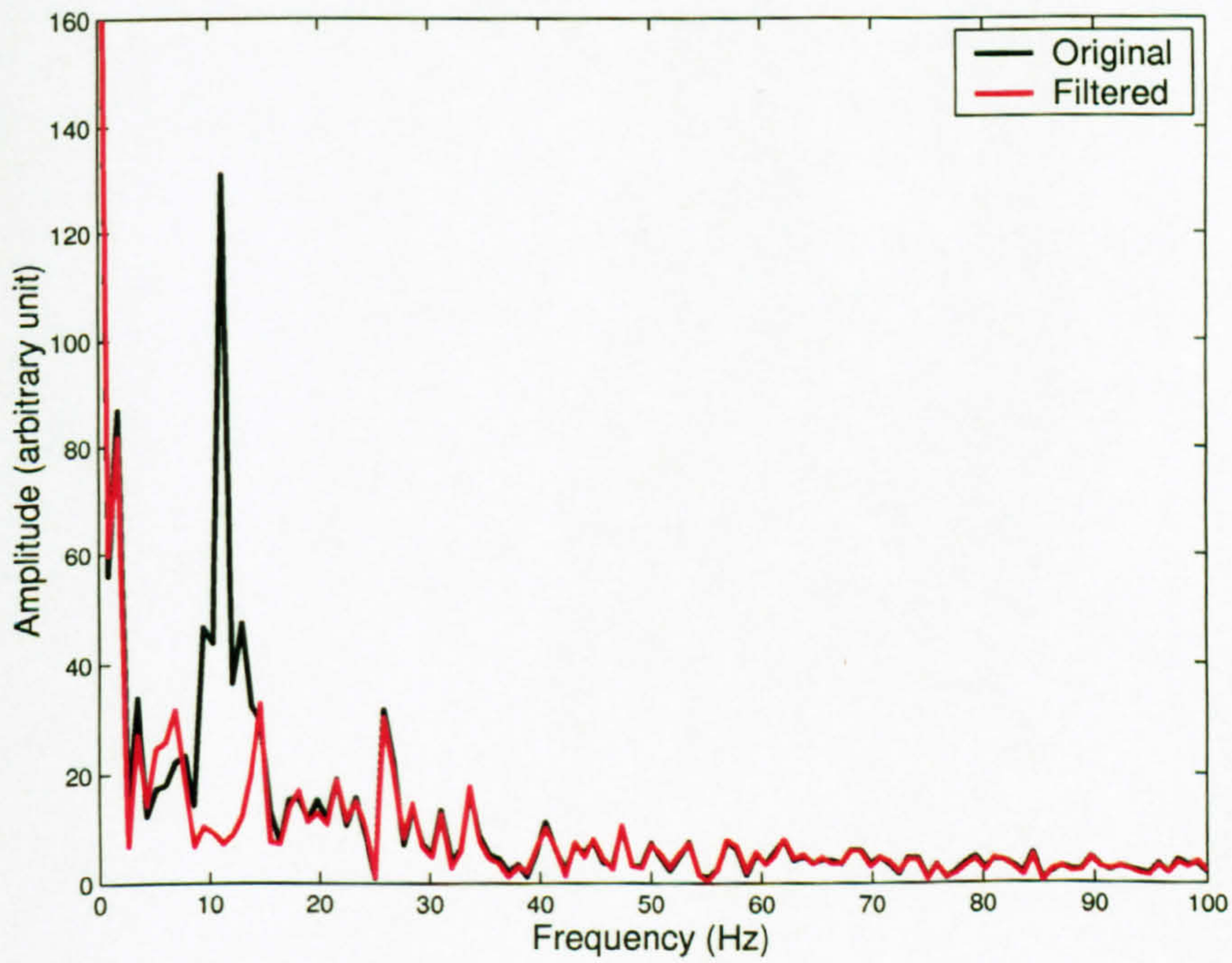

Figure 5.34: Streamwise velocity spectra at a point ($x/D = 0.86$, $y/D = 0.54$) behind the cylinder of the steady cross-flow for case B0.

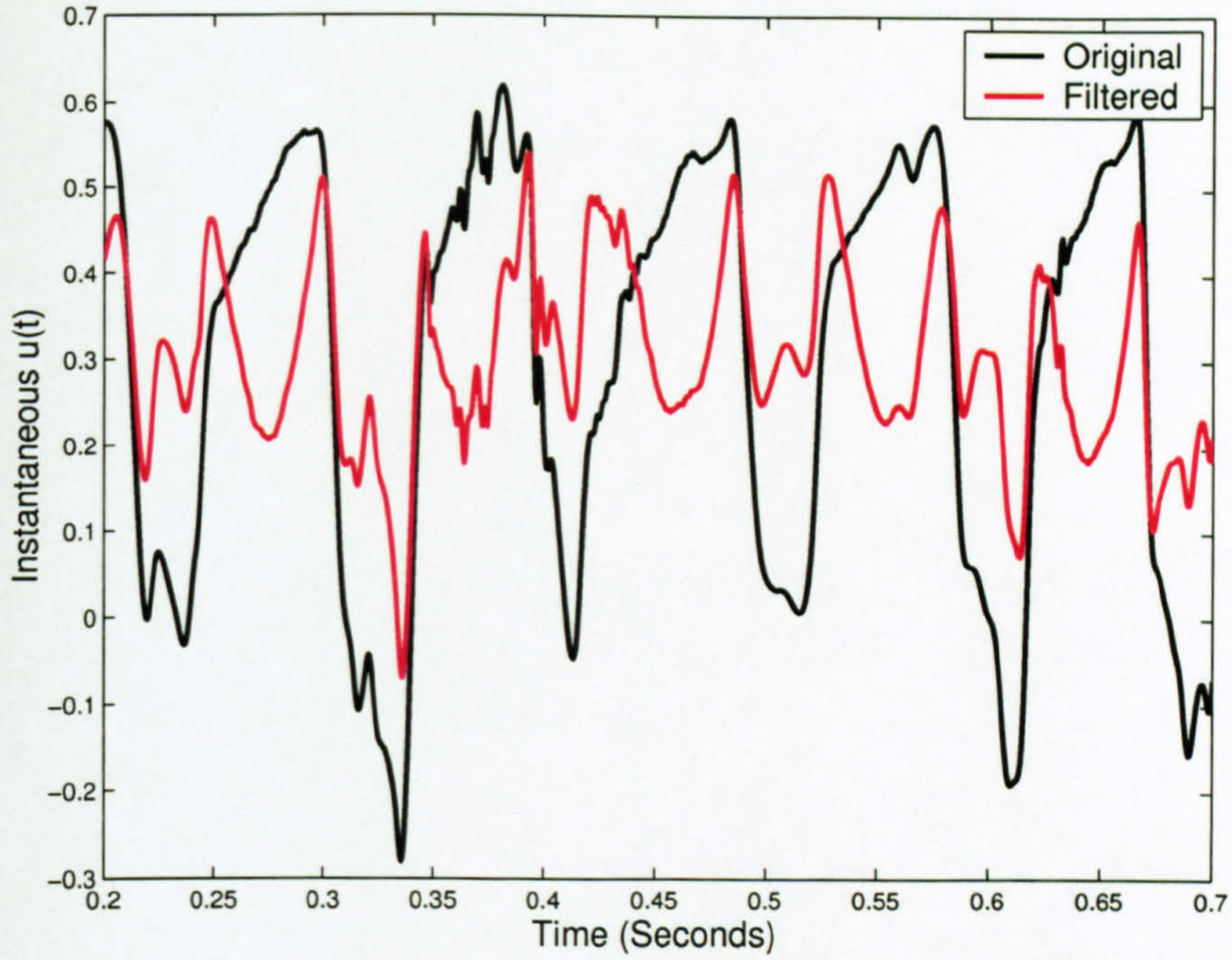

Figure 5.35: Streamwise velocity time series at a point ($x/D = 0.86$, $y/D = 0.54$) behind the cylinder of the pulsating cross-flow for case B1.

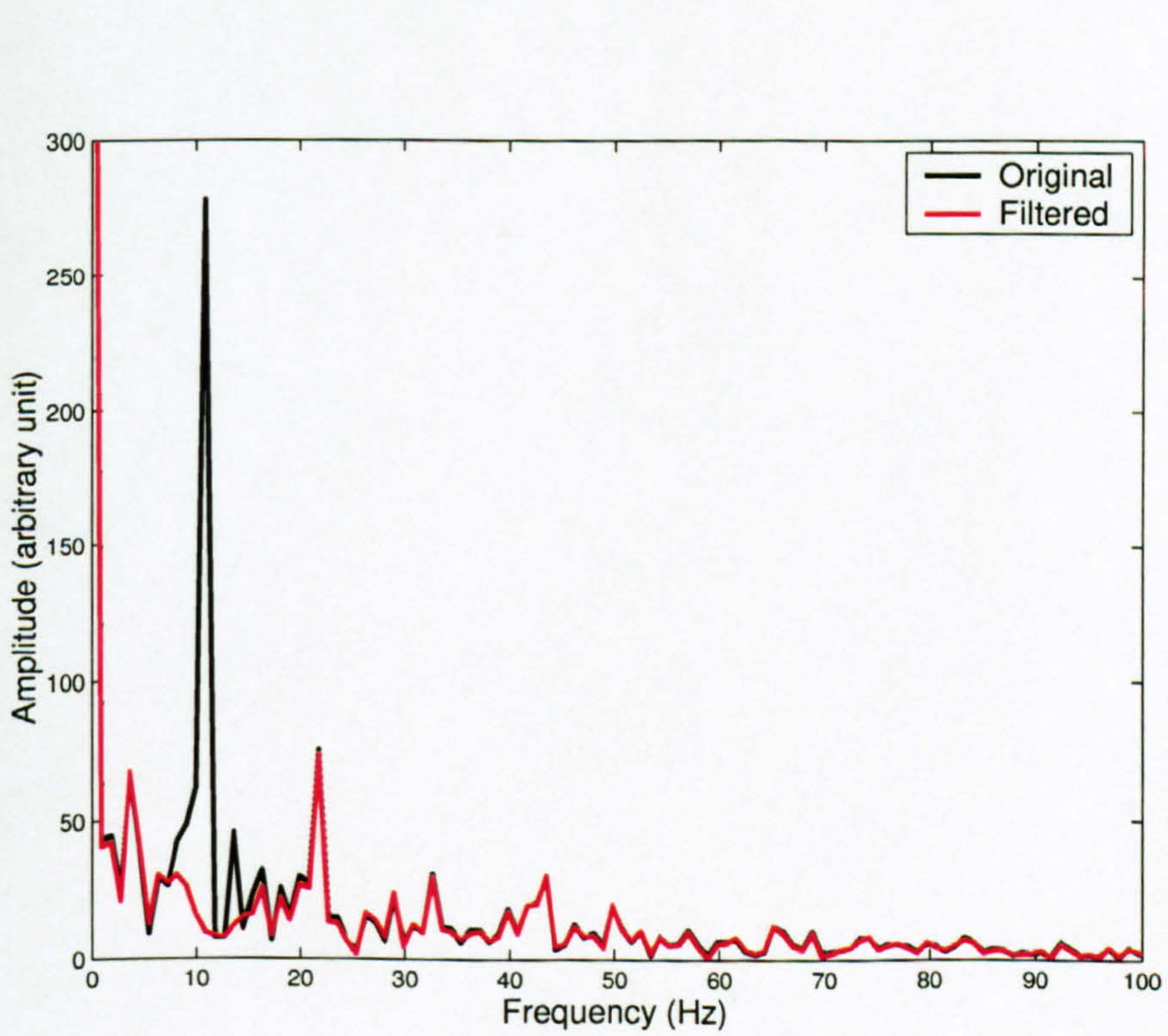

Figure 5.36: Streamwise velocity spectra at a point ($x/D = 0.86$, $y/D = 0.54$) behind the cylinder of the steady cross-flow for case B1.

5.3.5 Heat transfer

The results of the temperature field are presented first using the time-averaged local Nusselt numbers. The instantaneous isotemperature field in the near wake region is then correlated with the turbulent flow field. LES simulation of heat transfer using the dynamic model is performed for two cases, namely, the steady cross-flow case and the pulsating flow with amplitude $\Delta u/u_\infty = 0.05$. As shown in figure 5.37, the local time-averaged Nusselt number obtained by the dynamic model has reasonable agreement with the experimental result of Gau et al. (2001) and with Frossling's formula (Frossling, 1958) scaled using the value of Nusselt number at the front stagnation point. LES predicted that the Nusselt number for pulsating flow is higher than that for the steady cross-flow case only after the separation point in agreement with Sung et al. (1994). This also demonstrates that oscillating inflow has similar effect over vortex shedding synchronization as the streamwise oscillation of the cylinder presented by Gau et al. (2001).

Figure 5.38 shows the instantaneous temperature at a point at 150^o on the back surface of the cylinder. It can be seen that case B0 has a higher mean temperature leading to lower mean Nusselt number at this point which is consistent with figure 5.37. Figure 5.39 shows the instantaneous spanwise vorticity at the 150^o point on the back surface of the cylinder. It can be seen case B1 generally has higher fluctuations of the spanwise vorticity at this particular point which explains that higher heat transfer rate is associated with increased shed vorticity.

The small difference between the LES prediction and the experimental result in the laminar boundary layer region probably results from the top and bottom wall effects on the cylinder laminar boundary layer development. It may also result from the Reynolds number difference ($Re_D = 3,200$ is used by Gau et al. (2001) which is slightly higher than the present Reynolds number). The higher $\overline{Nu_\theta}$ in the near wake region after the separation point is due to the increased r.m.s velocity fluctuation as shown in figures 5.13 and 5.14 and stronger vortices.

Figures 5.40 and 5.41 present six snapshots of isotemperature contours in one vortex shedding period for cases B0 and B1. The results are recorded at the same phases as the ones shown in figure 5.26, which correspond to the instants shown in figures 5.28 and 5.29. For both steady and pulsating approaching flow cases, there is a strong correlation between the instantaneous velocity vector pattern and the temperature scalar contour pattern. It could be seen that more cool fluid is recirculated by stronger vortices at the rear of the cylinder for the pulsating approaching flow case leading to increased Nusselt number. The heated wake size

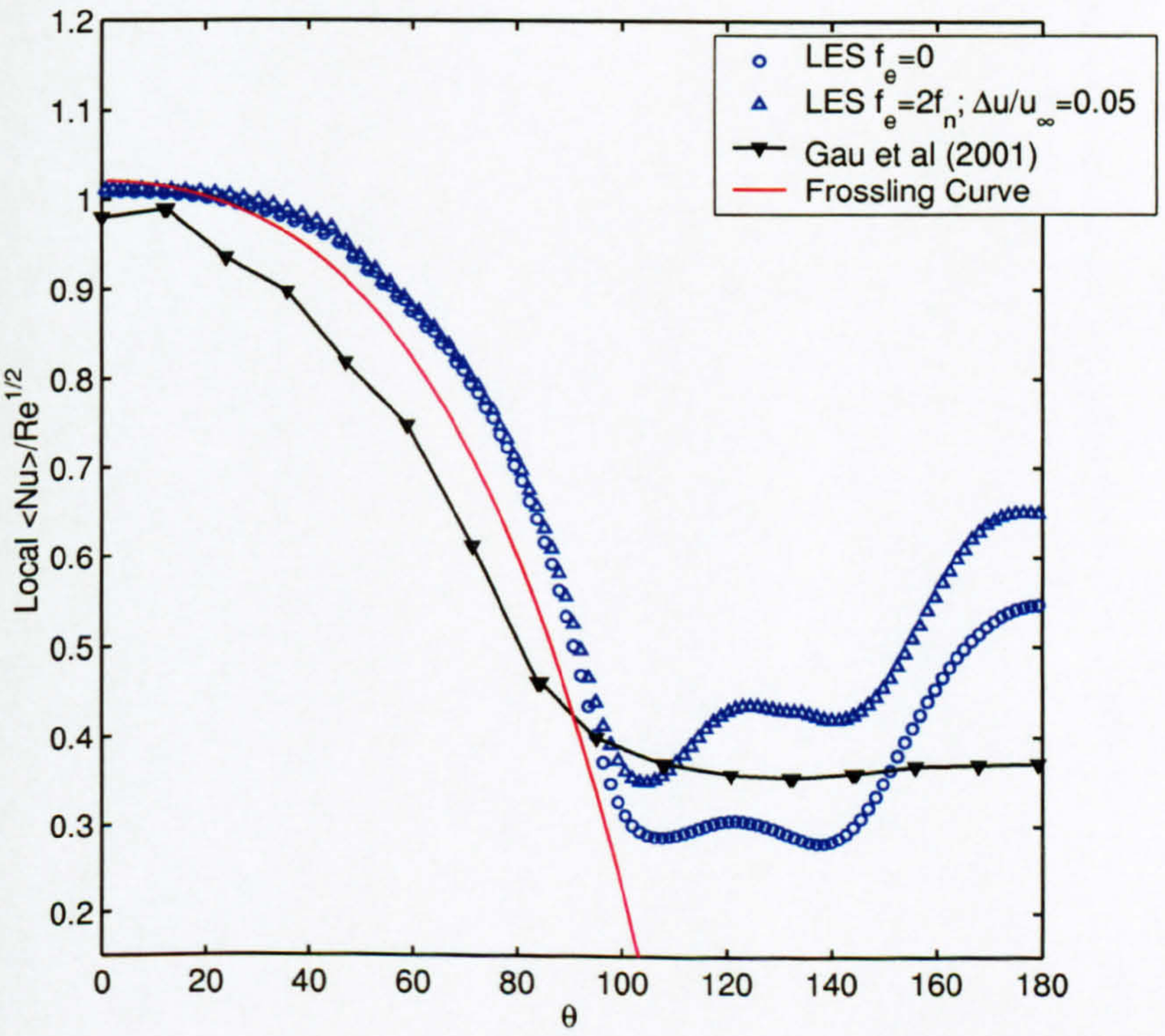

Figure 5.37: Local time-averaged Nusselt number around the cylinder for steady cross-flow and pulsating cross-flow. Experimental results represent for the steady case in Gau et al. (2001).

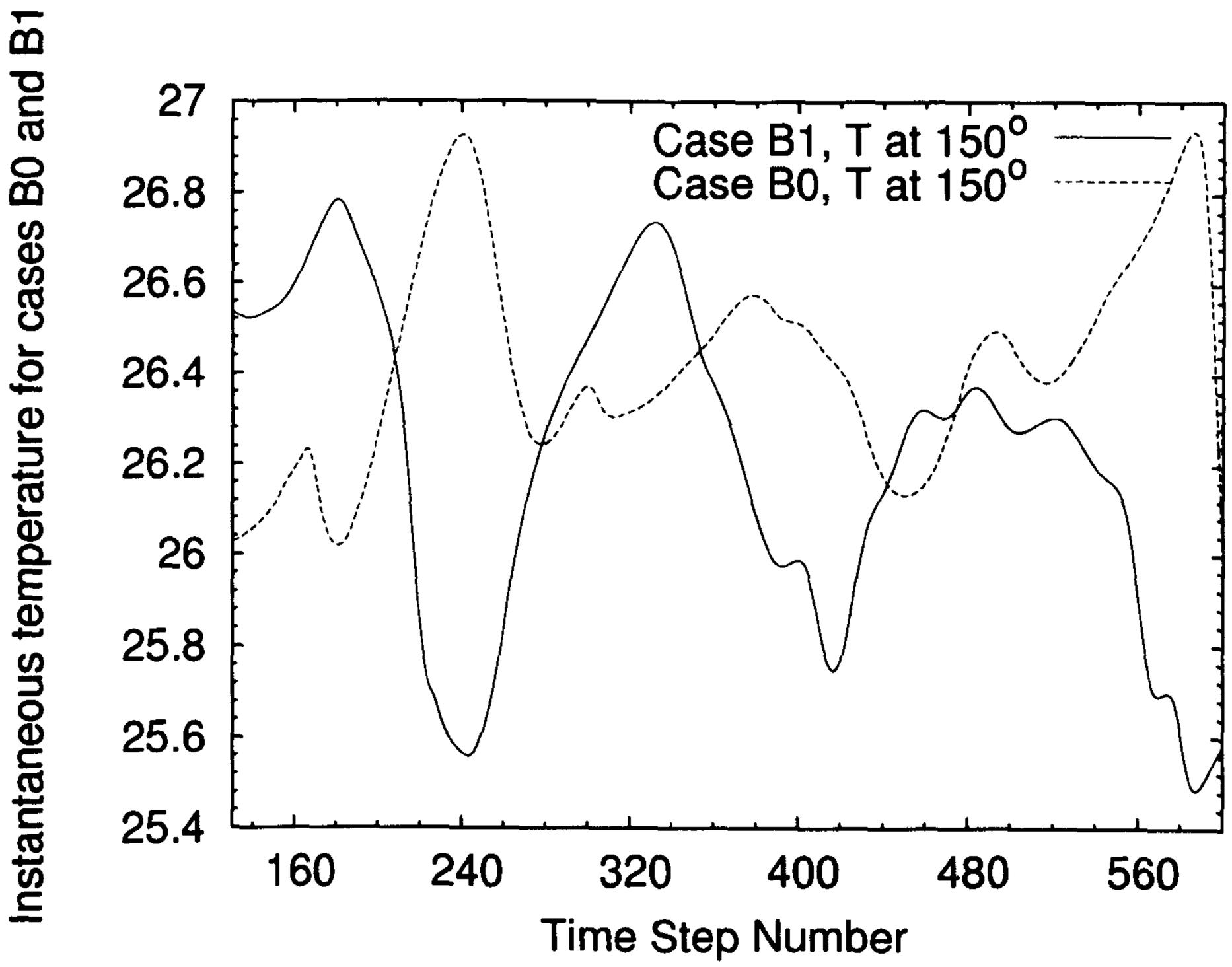

Figure 5.38: Instantaneous temperature at 150° on the cylinder surface for steady cross-flow and pulsating cross-flow.

for the pulsating case is smaller due to smaller recirculation bubble length and increased shed vorticity.

5.4 Closure

LES was performed on the 3D Finite Volume collocated unstructured mesh for the turbulent flow across a circular cylinder at Reynolds number $Re_D = 2580$ for steady and pulsating inflow condition. Good agreement was achieved between the LES results and PIV measurements especially for the pulsating flow. The dynamic model without test filtering was generally not as successful as the standard Smagorinsky model to simulate the steady cross-flow case using the current mesh. It is believed that insufficient spanwise grid resolution is the main reason. Nearly identical results were obtained for the pulsating cross-flow case ($f_e = 2f_n$ and $\Delta u/u_\infty = 0.1$) using the two models. Excellent agreement is obtained against the experimental mean flow and r.m.s velocity fields. It was found that the steady cross-flow case requires finer grid resolution, while the interplay of the modelling and the numerical error makes LES of this case more difficult to simulate. Nev-

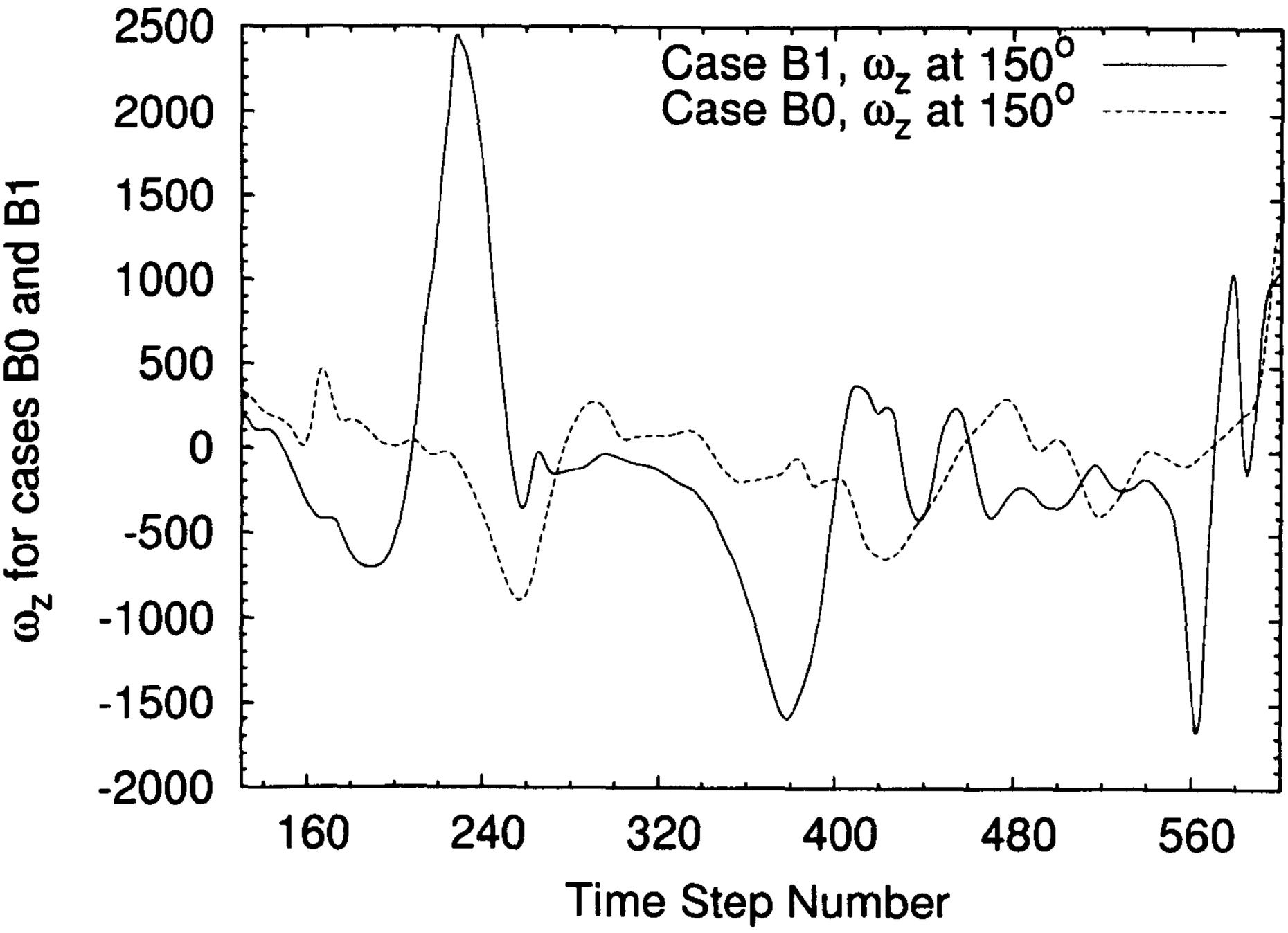

Figure 5.39: Instantaneous spanwise vorticity at 150° on the cylinder surface for steady cross-flow and pulsating cross-flow.

ertheless, the Strouhal number is in good agreement with the experiments. One reason that the pulsating flow is easier to model than the steady one is because lock-on modifies the flow wake structure leading to a shorter recirculation bubble zone. Larger contribution of the coherent part of the Reynolds stresses for the pulsating cross-flow is certainly another factor to result in better prediction by the LES models.

It has also been concluded that locked-on vortex shedding is associated with higher-amplitude surface pressure fluctuations at points both before and after the shear layer separation point. The vortex structures inside the recirculation bubble zone are more complex than the steady case. Lock-on also increases the drag, base suction and r.m.s of lift coefficient. It also leads to stronger vortices that form closer to the cylinder and a higher base suction coefficient which is associated with a shorter vortex formation length. The top and bottom walls are also believed to have a significant impact on the shorter vortex formation region, higher drag force and base suction coefficient.

The LES of the temperature scalar transport also shows good agreement with the experimental results of Gau et al. (2001). The LES predicted that at $f_e = 2f_n$,

the Nusselt number is higher than that for the steady cross-flow, demostrating that oscillating inflow has similar effect over vortex shedding synchronization as the streamwise oscillation of the cylinder. The LES models overpredict $\overline{Nu_\theta}$ in the wall surface region after the separation point for the steady cross-flow owing to the under-predicted recirculation bubble length and over-predicted r.m.s velocity fluctuations. The instantaneous temperature field was shown to have strong correlation with the velocity and vorticity field.

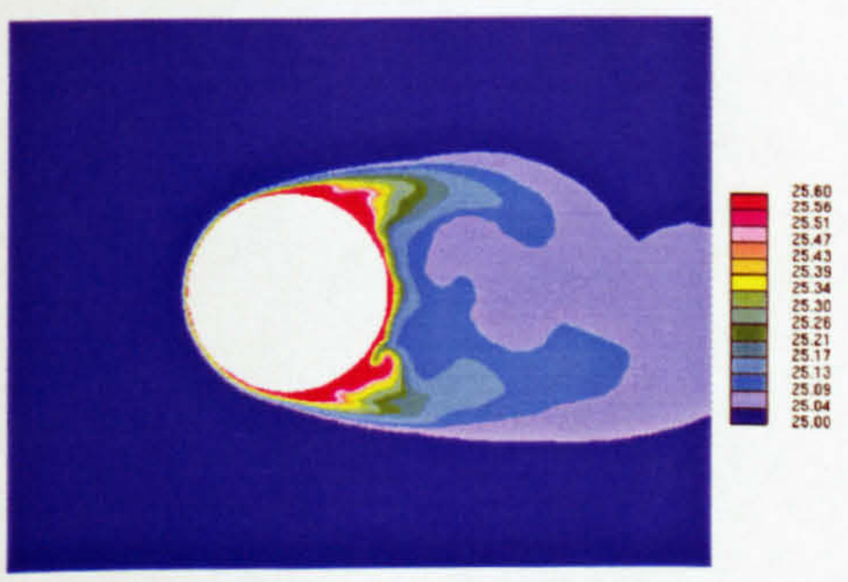

(a) Case B0, phase A

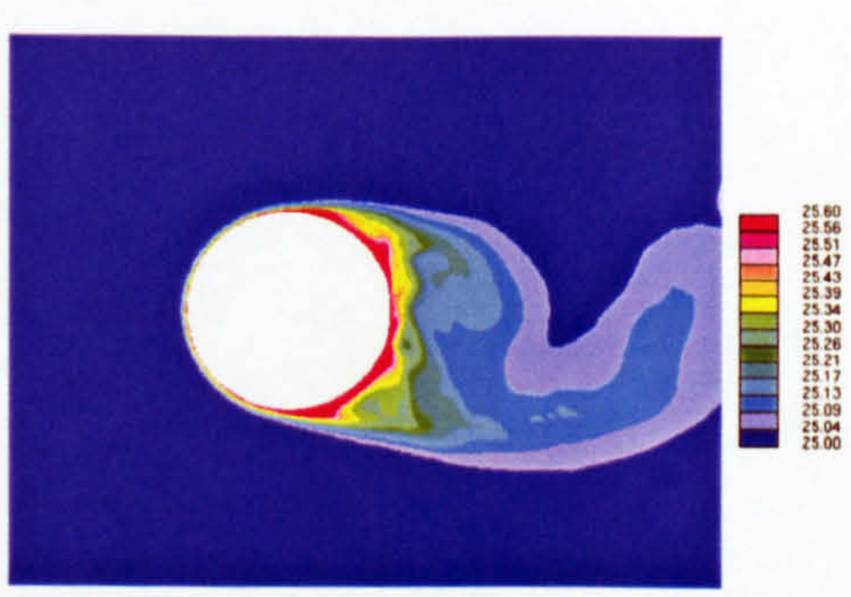

(b) Case B1, phase A

(c) Case B0, phase B

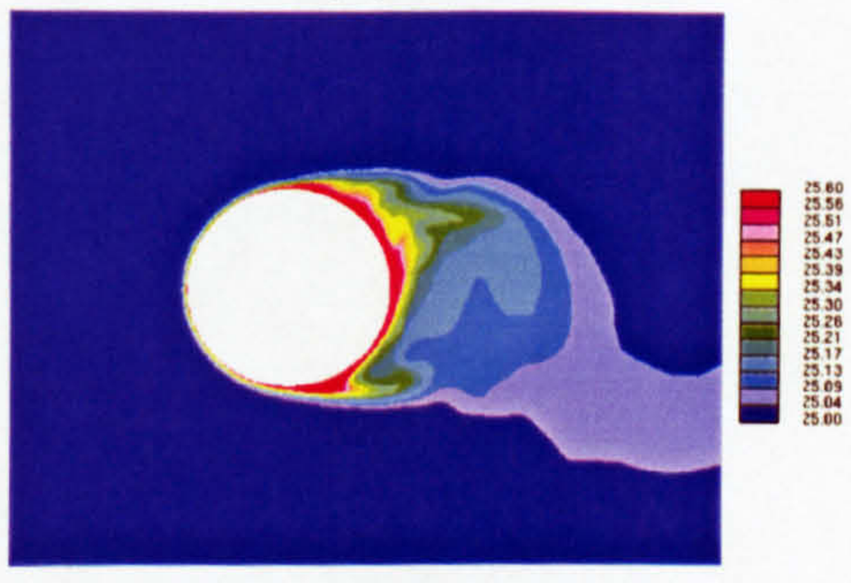

(d) Case B1, phase B

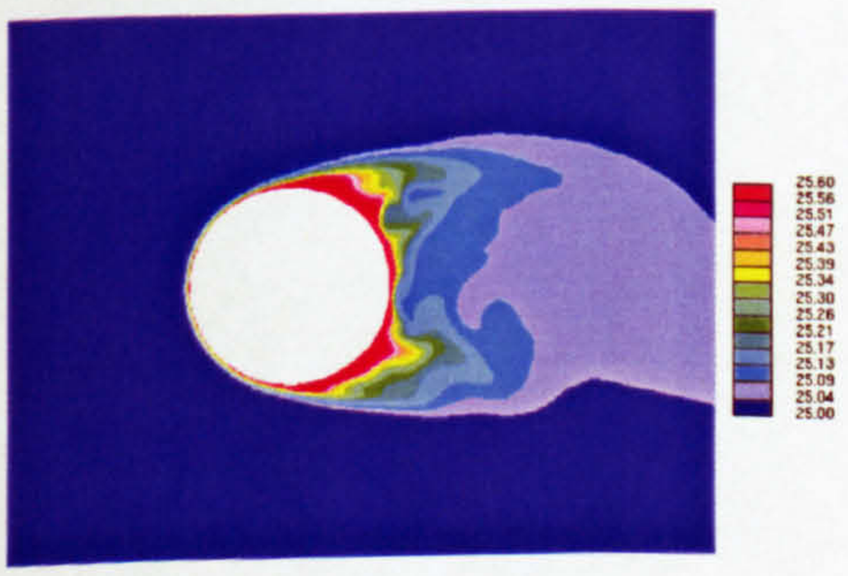

(e) Case B0, phase C

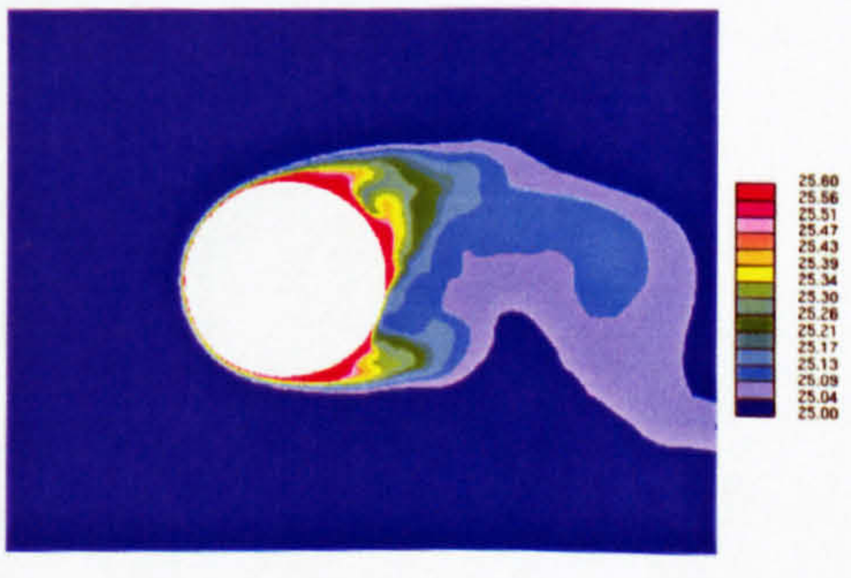

(f) Case B1, phase C

Figure 5.40: The instantaneous temperature field predicted for cases B0 and B1. The values are presented in ^oC. (1).

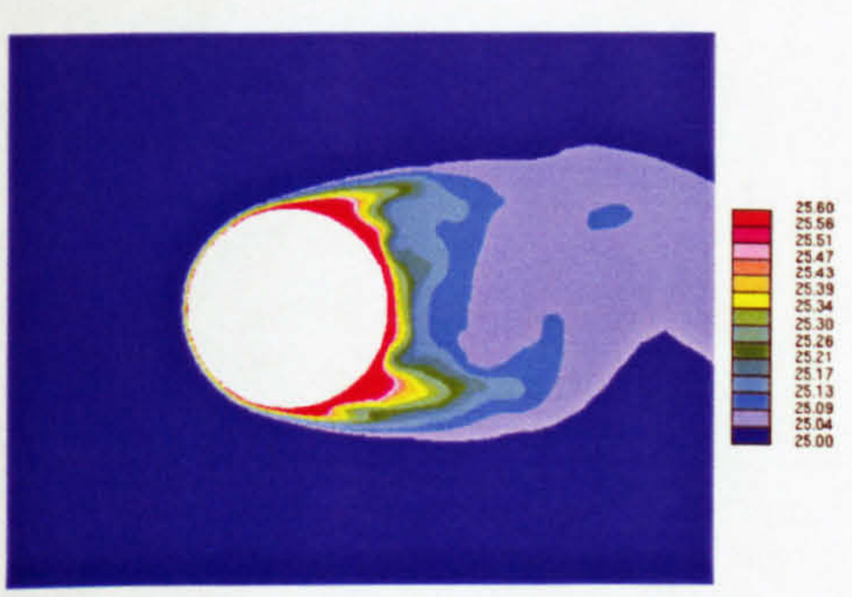

(a) Case B0, phase D

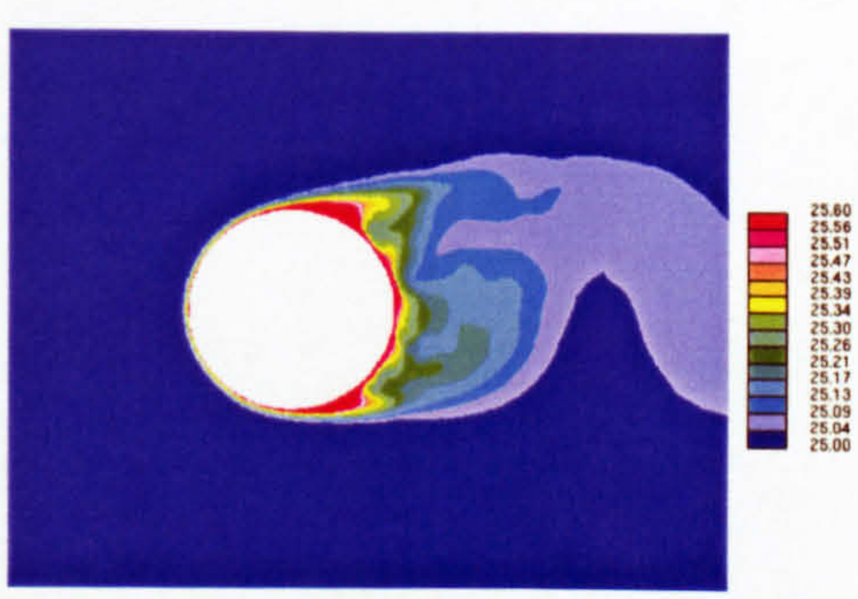

(b) Case B1, phase D

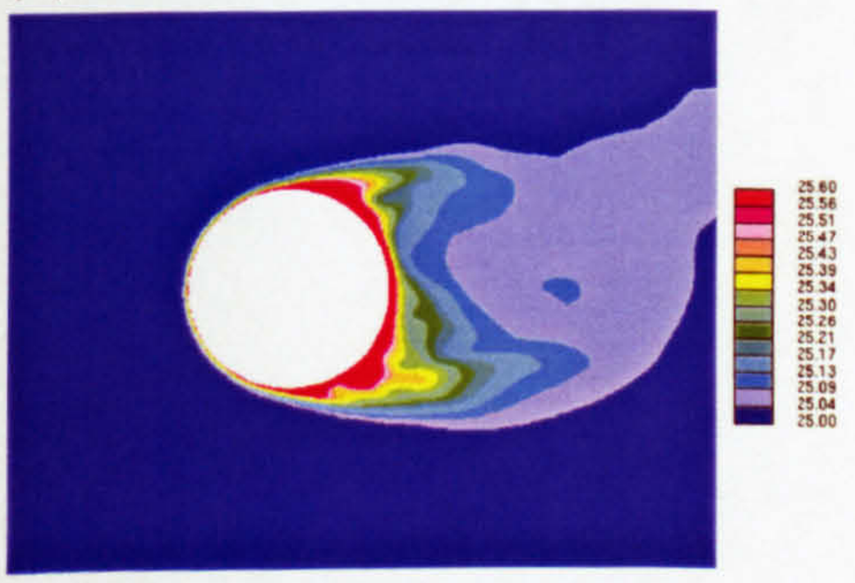

(c) Case B0, phase E

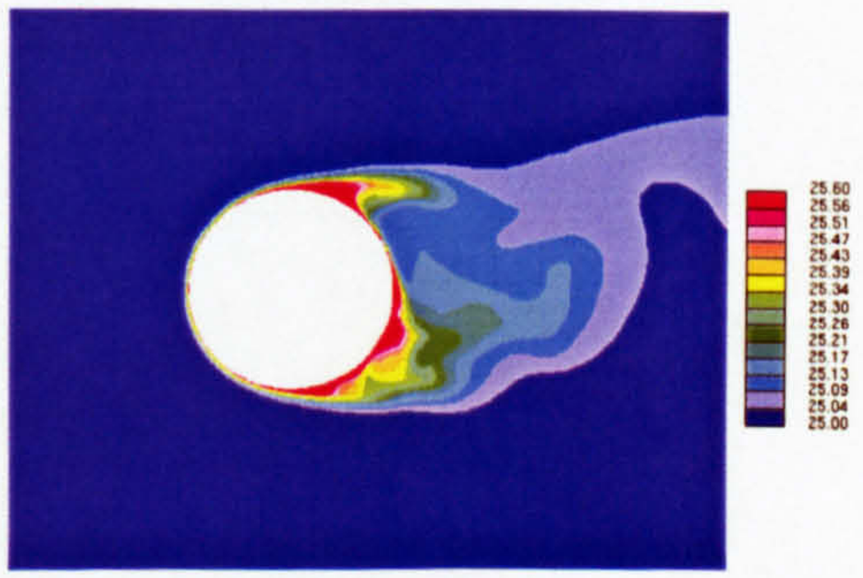

(d) Case B1, phase E

(e) Case B0, phase F

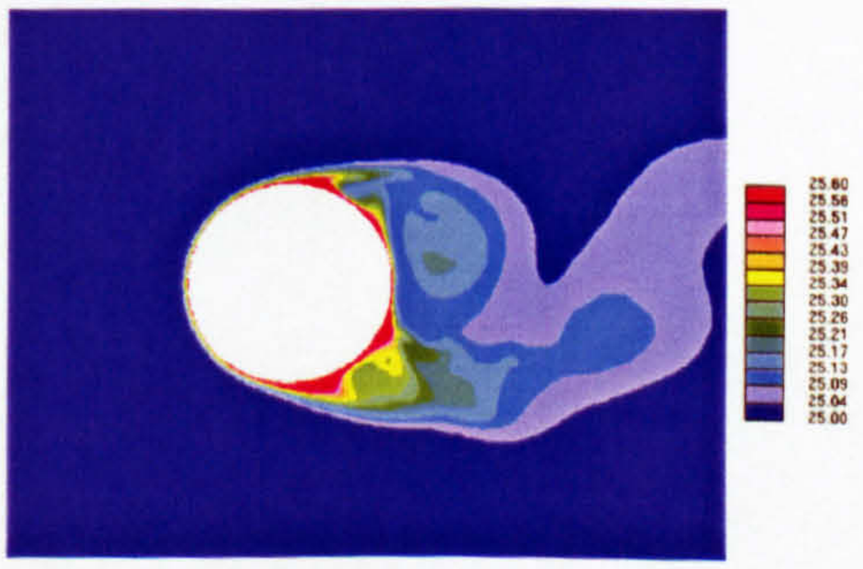

(f) Case B1, phase F

Figure 5.41: The instantaneous temperature field predicted for cases B0 and B1. The values are presented in ^oC. (2).

Chapter 6

LES OF CROSS-FLOW AND HEAT TRANSFER OVER INLINE TUBE BUNDLE

6.1 Introduction

Groups of circular cylinders arranged close to each other and immersed in cross-flow arise in a number of engineering applications, for example, heat exchanger tubes, electrical transmission lines and chimney stacks. It is well known that the flow field around several cylinders is very different from the one around a single cylinder which has been examined in detail in chapter 5. In cases where several cylinder structures are arranged inline, the flow separates from the upstream cylinder and then reattaches or rolls up in the front of the downstream cylinder. In the subcritical turbulent regime, the approaching flow over the downstream cylinder will be already turbulent and the turbulence level will have an effect on the flow and heat transfer around the downstream cylinder. On the other hand, due to the existence of the downstream cylinder, the space available for the formation of Karman vortex behind the upstream cylinder is restricted when the distance between the two cylinders is small. As a result, such flow interference may cause a change in the characteristics of the fluid forces over the cylinders.

A comprehensive investigation of interference effects on the lift and drag forces and their fluctuating components for two or three circular cylinders at a subcritical Reynolds number $Re_{bulk} = 2.7 \times 10^4$ has been presented by Kareem et al. (1998).

[0]Part of the results presented in this chapter are published in Liang and Papadakis (2004*a*) and Liang and Papadakis (2005).

The flow interference and pressure distribution of the arrangement of two cylinders in tandem has been extensively reviewed by Zdravkovich (1977, 1987). In general, there are three regimes for flow past two cylinders in tandem. This classification was reported in chapter 1 but is briefly repeated here for completeness. The first flow regime is observed when the two cylinders are in contact or in extremely close proximity. The shear layers separating from the upstream cylinder completely engulf the downstream cylinder. Thus, the two cylinders essentially behave as an extended single bluff body. The second flow regime occurs when the tube spacing is within a medium range in which a separation bubble is formed behind the upstream cylinder and reattaches on the front part of the downstream cylinder. Vortex shedding is observed behind the downstream cylinder but not the upstream one, while a steady recirculation region consisting of a pair of counter-rotating vortices exists in the gap. This regime is defined as the *reattachment regime*. The third flow regime is observed for a larger tube S_L/D spacing in which vortex shedding occurs behind both cylinders. The wake behind the downstream cylinder is called binary, because each vortex is formed by the combination of one vortex shed from the upstream cylinder and another by the downstream cylinder. Interference effects on the upstream cylinder are negligible, although wake interference continues to affect the downstream cylinder even for S_L/D larger than 50. This regime can be termed as the *two vortex streets regime*.

There is a great deal of discrepancy in the literature on the exact tube spacing that marks the transition between the *reattachment* and *two vortex streets* regimes. The lowest Reynolds number presented by Ljungkrona and Sundén (1993) for an arrangement with pitch ratio 2 was 3.3×10^3. They found that the shear layers formed big vortices behind the upstream cylinder and reattached on the front of the downstream cylinder. The vortex shedding frequency behind the downstream cylinder gave a Strouhal number 0.17. They reported that the critical spacing pitch ratio should be larger than 4. In another experimental investigation, Wu et al. (1994) have concluded that the small distance between the upstream and downstream cylinders ($S_L \leq 4D$) resulted in higher spanwise coherence and smaller Strouhal number for the vortex shedding behind the downstream rows. Mittal et al. (1997) have performed a two-dimensional finite element calculation for an arrangement with a pitch-to-diameter ratio of 2.5 at a Reynolds number of 1,000. They found that the vortex behind the upstream cylinder rolls up in front of the downstream cylinder (which can be defined as the *two vortex streets* regime). Tanida et al. (1973) found that the critical separation for the vortex shedding

occurs at the spacing of $S_L \approx 3D$ at $Re = 3,400$. This is in agreement with Ljungkrona and Sundén (1993). However, this critical spacing appears to be much higher than the two-dimensional computational results of Jester and Kallinderis (2003) and Mittal et al. (1997). On the other hand, Gu (1996) reported that the critical spacing pitch ratio could be smaller than 2.8 for supercritical flows. This discrepancy can be attributed to either a Reynolds number effect or the three-dimensionality of the flow. Another reason for this scatter of data may be the presence of a hysteretic effects[1]. The hysteresis effect is an experimentally observable feature in two cylinders in tandem as presented by Zdravkovich (1984).

For multiple-row inline tube bundle, the flow conditions are dominated by boundary layer separation effects and wake interactions. Ziada and Oengören (1993) confirmed that there is no vortex shedding behind the first row cylinder at a spacing of $S_L = 3.25D$ at the Reynolds number range $2,560 \leq Re_{gap} \leq 7,040$. Konstantinidis et al. (2000) reported that no vortex shedding exists behind the first row at a Reynolds number $Re_{gap} = 3,400$ with a streamwise tube spacing of $2.1D$. It is noted that both Ziada and Oengören (1993) and Konstantinidis et al. (2000) reported a single vortex shedding frequency in the subsequent downstream rows. It is worth mentioning that the vortex shedding in consecutive rows is 180^o out-of-phase. Castiglia et al. (2001) performed 3D LES calculations with the Smagorinsky model for the turbulent flow across an inline elliptic bundle at Reynolds number $Re_{de,g} = 10,400$ (based on the equivalent diameter of elliptic cylinders and the gap velocity) using the STAR-CD CFD package. They did not observe obvious vortex shedding phenomena behind the first two rows due to the small streamwise spacings between consecutive elliptic cylinders.

Konstantinidis et al. (2000) also found that vortex shedding lock-on resulted from the pulsating approaching flow with $f_p = 2f_n$ over the inline tube bundle. The frequency of vortex shedding is locked-on at half the pulsation frequency. In other words, there is a small shift of the peak in the velocity energy spectra between steady and pulsating flows. Behind the first two rows, the peak strength in the spectra clearly shows that the locked-on vortex shedding frequency is associated with a better organized coherent vortex structure. The intensity of the vortex shedding peak was also found to decrease gradually from row 1 to 4. Subsequently,

[1]One of the two flow regimes (*reattachment* or *two vortex streets*) persisted longer when the velocity was increased or, at the same velocity when the cylinder was displaced in one direction, and the other regime lasted longer when the opposite conditions were imposed. The hysteresis effect produced an apparent overlap of the two flow regimes although only one flow regime existed at a time.

they expected that this lock-on mode will increase the heat transfer behind the first few rows inside the inline tube bundle.

In another recent paper, Konstantinidis et al. (2003*b*) reported a symmetrical vortex formation mode behind the first cylinder row when the external pulsation frequency is around three times the vortex shedding frequency ($f_p = 3f_n$). However, this symmetric mode cannot be sustained in the downstream rows due to lack of a feedback mechanism. Therefore, this mode subsides in the downstream rows and turns to the antisymmetric shear layer instability which is the same as that of steady approaching flow.

Heat transfer inside inline tube arrays has been investigated much less than the flow field. Gowda et al. (1998) have simulated the unsteady laminar flow and heat transfer over an inline tube array at a Reynolds number of 100 using the finite element method with a maximum of 5376 elements. Aiba et al. (1982*a*) have measured the turbulent heat transfer over seven rows of cylinders at a Reynolds number ($Re_{gap} = 1.6 - 4.1 \times 10^4$) with spacings ($S_L/D \times S_T/D = 1.2 \times 1.2$ and $S_L/D \times S_T/D = 1.6 \times 1.6$). Only a few measurements were performed when pulsating approaching flow condition was imposed. VandenBerghe et al. (1983) have measured the heat transfer over a three-row inline tube array with pulsating incoming flow. They found that the external small-amplitude pulsation can increase significantly the heat transfer rate in the front of the second row cylinder.

In order to demonstrate the capability of LES to predict the vortex shedding phenomenon and heat transfer quantitatively inside the inline tube bundle and to improve the understanding of the observed flow patterns and the interaction of the cylinder wakes, several LES calculations were performed based on the configuration used by Konstantinidis et al. (2000) and these will be presented in this chapter. These simulations also elucidate the flow field patterns and help to improve understanding of the interactions of multiple cylinders. The pulsation effect on the flow characteristics and heat transfer was also investigated in detail and the results were compared with steady incoming flow and assessed against available experimental data.

The rest of this chapter is arranged as follows. First, the computational conditions for all runs performed for the inline tube array are presented. This section is then followed by a detailed description of the instantaneous flow field for different cases. The bistable regime is described using the instantaneous flow information obtained from calculations for the steady flow over the two-row bundle. A detailed comparison with experimental data for time-averaged first-order and second-order

statistics is presented next. Subsequently, the lift and drag coefficients are summarised for all cylinders. Finally, heat transfer results are presented.

6.2 Computational conditions

The configuration of Konstantinidis et al. (2000) was examined. Two meshes are used, one coarser mesh that covers all six rows i.e. the whole bundle studied in the experiments and another finer mesh that covers only the first two rows. Twice as many cells were used in-between these two rows compared to the coarser mesh. The X-Y section views of the six- and two-row inline tube bundle configurations are shown in figures 6.1 and 6.2 respectively. A convective boundary condition $\frac{\partial \phi}{\partial t} + U_c \frac{\partial \phi}{\partial x} = 0$ is used for the exit boundary, where U_c is the convective velocity normal to the outlet boundary and ϕ is any physical variable convected out through the outlet. Zero velocity boundary conditions are used for top, bottom and cylinder walls. Periodic boundary conditions are applied in the spanwise direction. The normal derivative for the pressure correction is set to zero at all boundaries. The inlet streamwise velocity profile is imposed as $u(t) = u_\infty + \frac{\Delta u}{2} sin(2\pi f_p t)$, where the approaching velocity was $u_\infty = 0.2456 m/s$ and the cylinder diameter was $D = 0.01m$. The free-stream temperature was 25K, constant wall heat flux was $q" = 2419 W/m^2$ and thermal conductivity was $k = 0.59 W/(m \cdot K)$.

Figures 6.3 and 6.4 show the meshes for the six- and two-row inline tube arrays respectively. For the latter arrangement, double the number of cells are used along the periphery of the two cylinders and in the gap region of the first and second central column cylinders. A clearer local view of the refinement can be gained by comparing figures 6.5 and 6.6. As shown in table 6.1, a total of 112 and 224 cells are placed along the periphery of each cylinder for the six-row and two-row inline tube bundles respectively. A constant expansion factor 1.2 is used for the cell spacings in the radial direction away from each cylinder wall and 20 equally-spaced planes are used in the spanwise direction for both meshes with a total spanwise length $L_z = \pi D$, which is the same as the resolution of Benhamadouche and Laurence (2003). The smallest cell spacing in the radial direction is around $\Delta r_{min}/D = 4.3 \times 10^{-3}$ or 4.2×10^{-4}, which is comparable to or better than the finest mesh used by Beaudan and Moin (1994) ($\Delta r_{min}/D = 1.25 \times 10^{-3}$) for a single cylinder at a similar Reynolds number.

As shown in table 6.2, all the calculations for the six-row inline tube array were performed with a fixed time step size of $5 \times 10^{-4} s$ which gives maximum

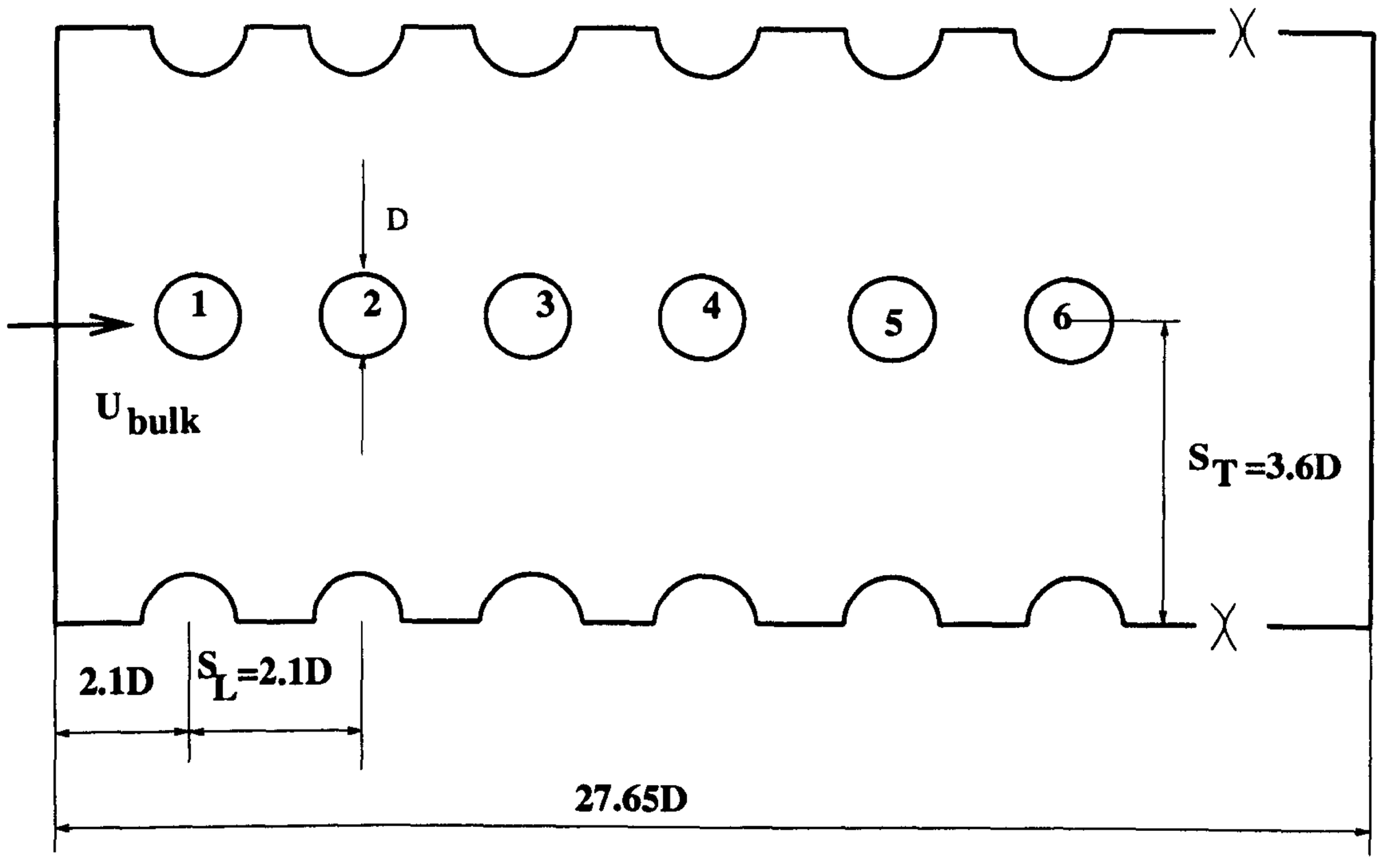

Figure 6.1: Illustration of the physical configuration of the six-row inline tube array and tube numbering.

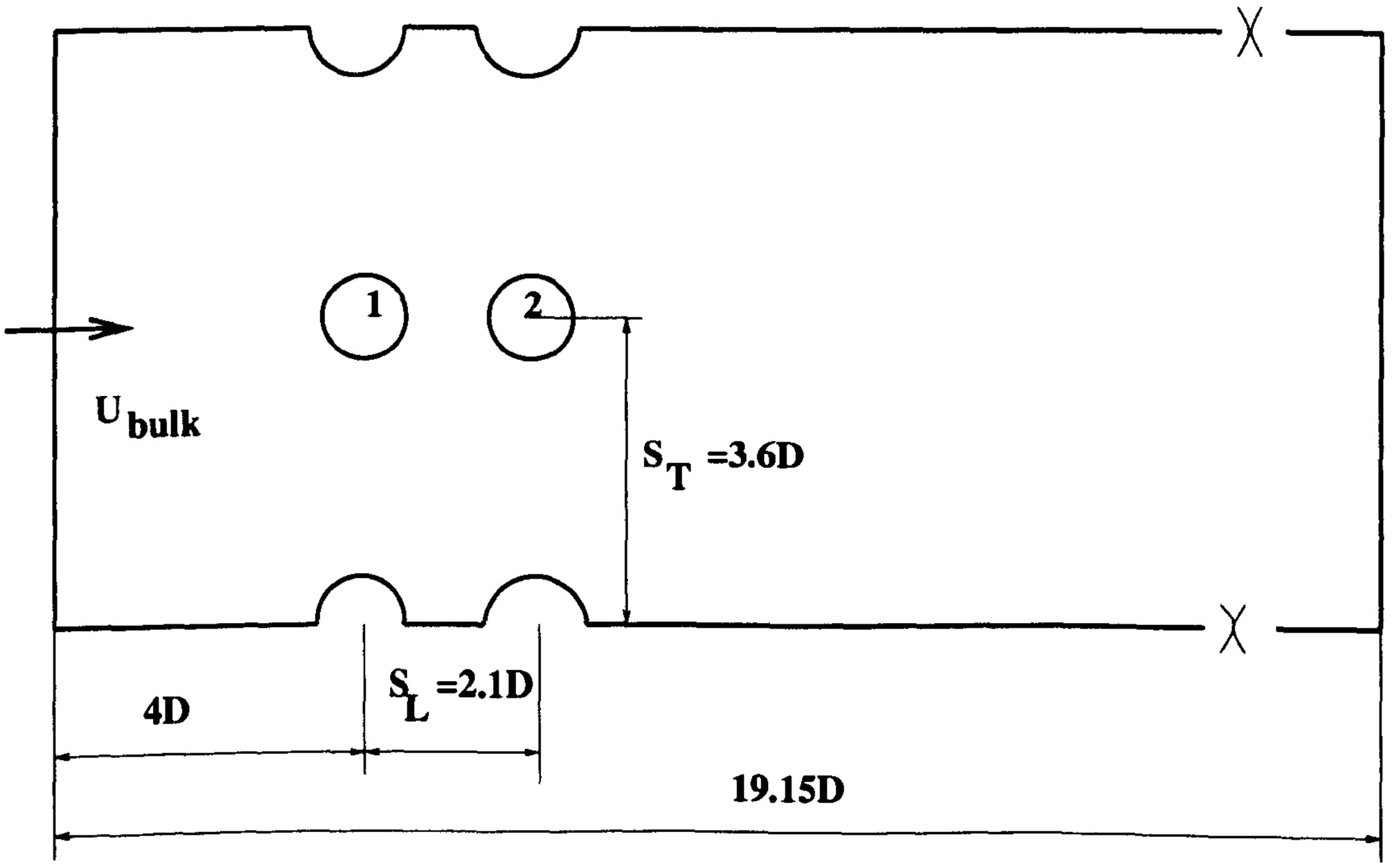

Figure 6.2: Illustration of the physical configuration of the two-row inline tube array and tube numbering.

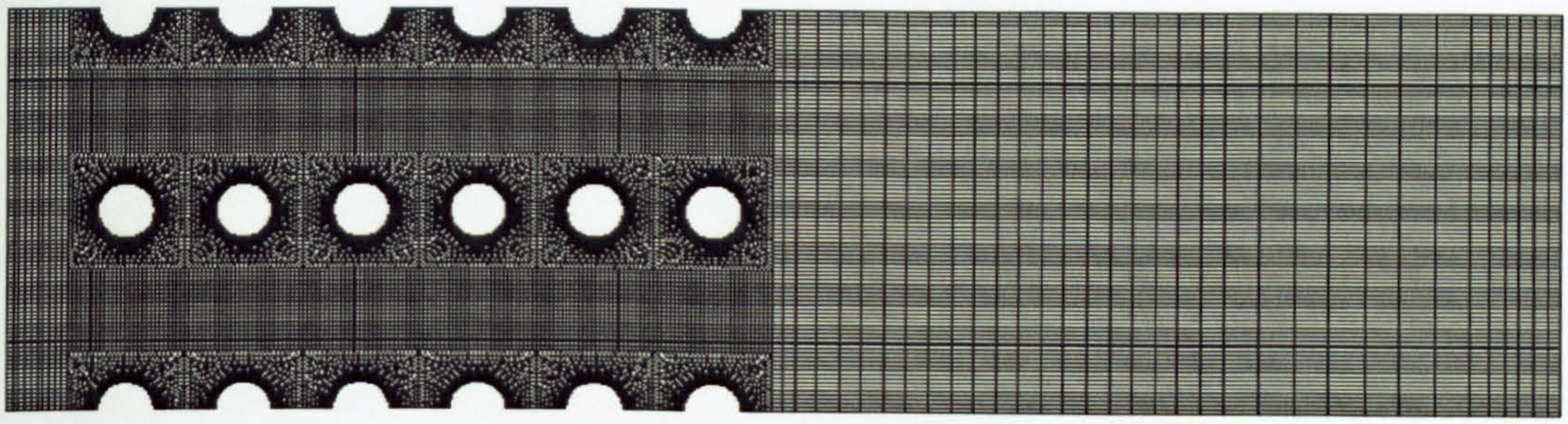

Figure 6.3: The computational mesh of the six-row inline tube bundle.

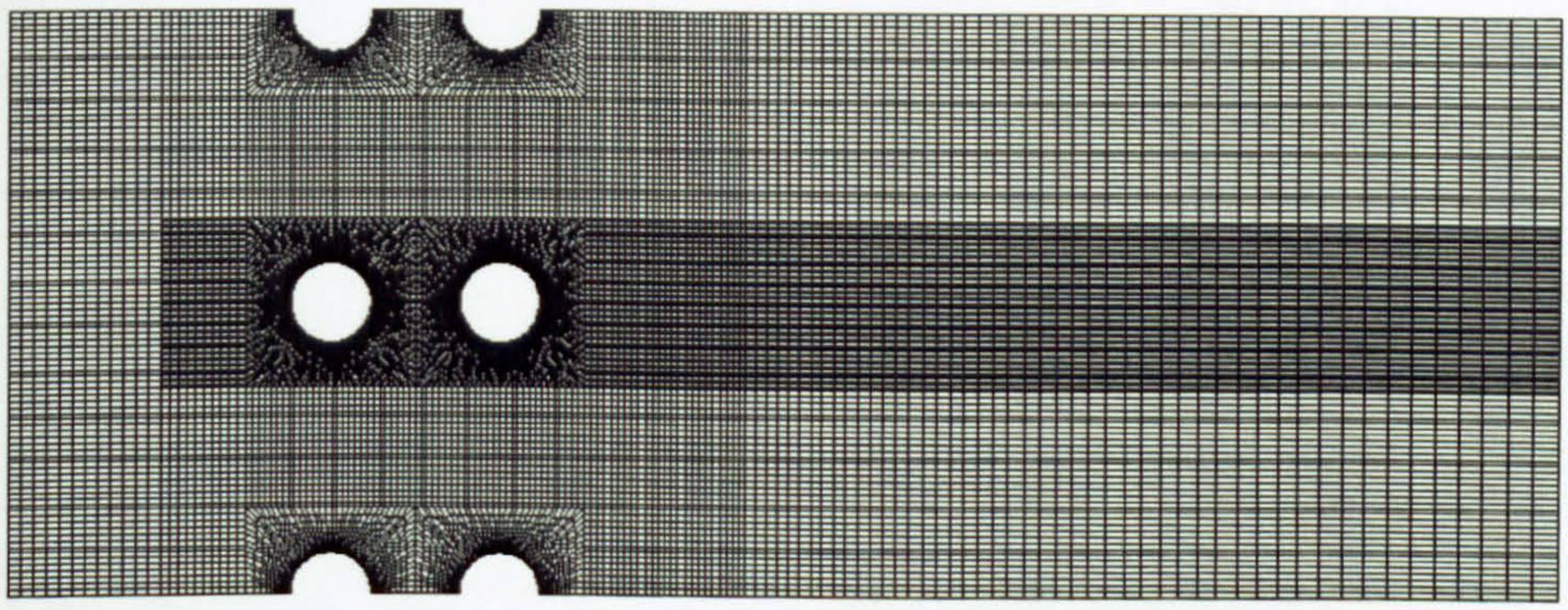

Figure 6.4: The computational mesh of the two-row inline tube bundle. The cells are locally refined in the area around and behind the middle column cylinders.

and mean CFL numbers of 2.0 and 0.29 respectively. The calculations with the refined resolution of the two-row inline tube array were performed at the same time-step size too, which gives maximum and mean CFL numbers of 1.13 and 0.18 respectively. Normally, if the flow field is started from a laminar state, the turbulent flow field will be fully developed after the time that a fluid point at the bulk velocity takes to travel from the inlet to the outlet. The calculations are then started from the fully-developed turbulent flow field and statistics are collected for more than 6 vortex shedding periods (based on the second cylinder) for all cases.

6.3 Instantaneous flow field

6.3.1 Instantaneous flow field of six-row bundle

Figure 6.7 shows the lift coefficients for the different rows for cases 2, 4 and 5. Detailed information for the whole field was stored for phases A-E shown in the same graph. Figures 6.8, 6.9 and 6.10 show the velocity pattern at one mid-section (X-Y) for 5 time instants A-E that cover slightly less than one vortex shedding

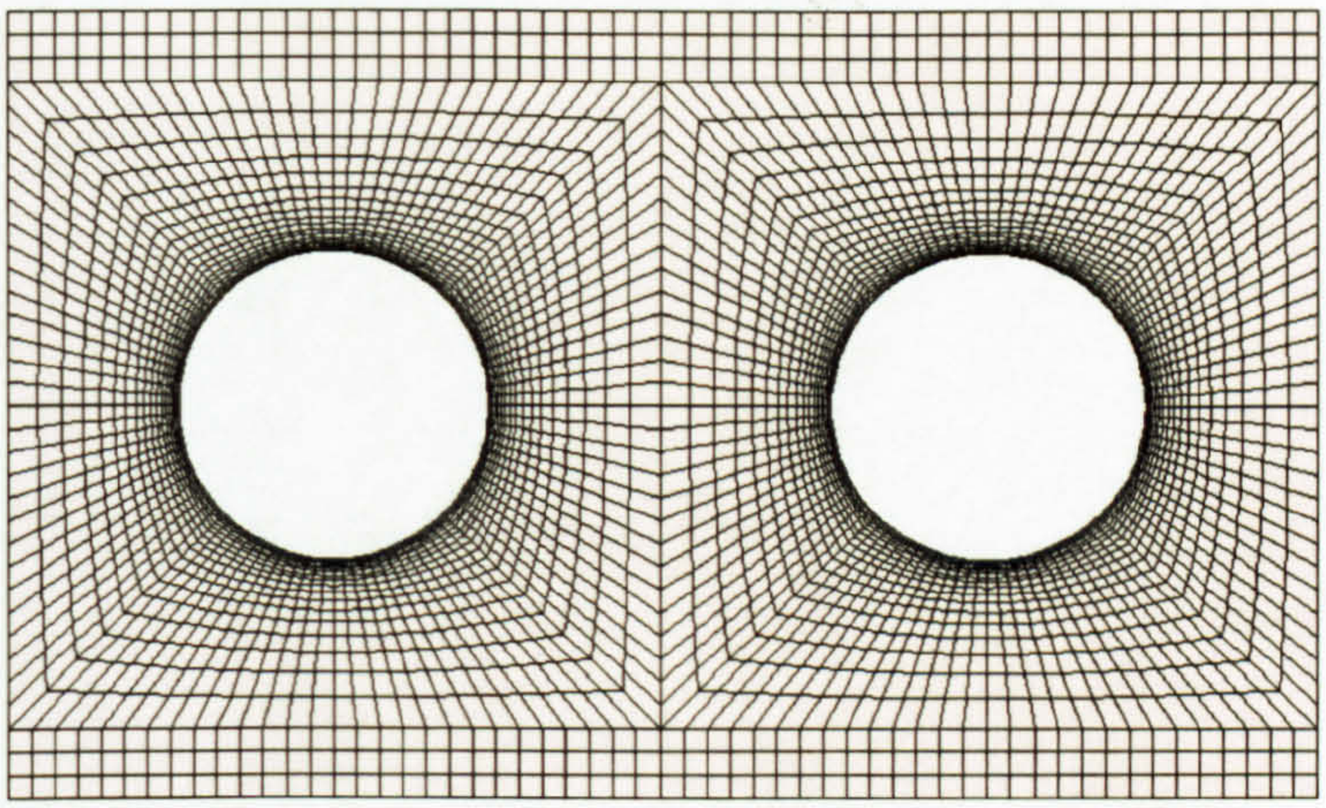

Figure 6.5: Local view of the computational mesh around the first two cylinders of the six-row inline tube bundle.

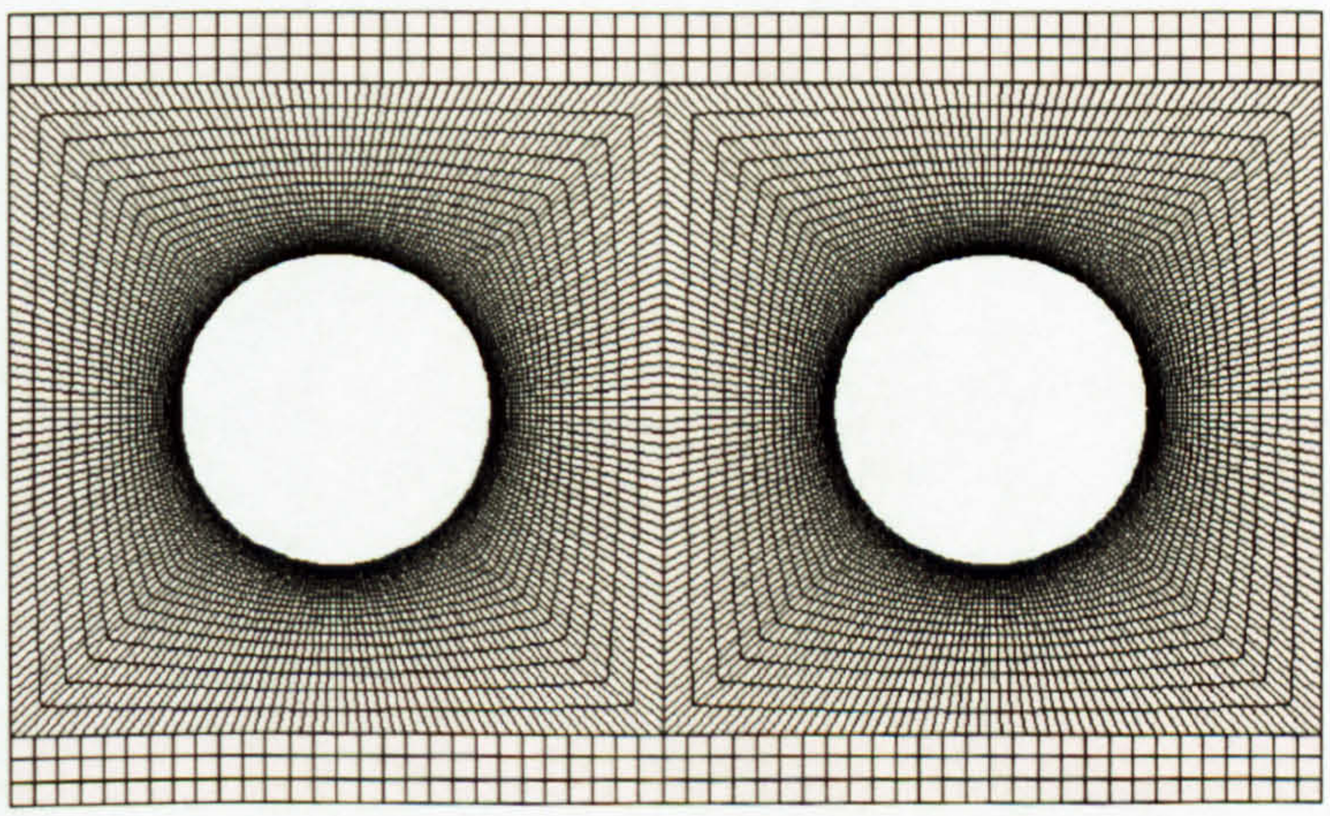

Figure 6.6: Local view of the computational mesh around the central two cylinders of the two-row inline tube bundle.

Tube bundle mesh parameters								
Type	N_r^{eff}	N_{total}	$\Delta r_{min}/D$	N_z	S_L	S_T	r_{exp}	N_{gap}
6-row Inline	112	702,720	4.3×10^{-3}	20	2.1D	3.6D	1.2	36
2-row Inline	224	674,400	4.2×10^{-4}	20	2.1D	3.6D	1.2	72

Table 6.1: Grid parameters for inline tube bundle arrangements. N_{gap} refers to the number of cells used along the streamwise direction between the first- and second-row cylinders, N_r^{eff} refers to the number of cells used along the periphery around the middle column cylinders, r_{exp} is the expansion factor in the radial direction and $\Delta r_{min}/D$ is the normalised radial thickness of the first cell on the cylinder wall.

LES cases investigated for inline tube bunbles							
Name	Arrangement	Re_{gap}	Model	f_p	$\Delta u/u_\infty$	CFL_{mean}	CFL_{max}
Case 1	Six-row inline	3,400	Smag.	0.	0	0.29	2
Case 2	Six-row inline	3,400	Dyn.	0.	0	0.29	2
Case 3	Six-row inline	3,400	Smag.	10 Hz	0.1	0.29	2
Case 4	Six-row inline	3,400	Dyn.	10 Hz	0.1	0.29	2
Case 5	Six-row inline	3,400	Dyn.	15.5 Hz	0.1	0.29	2
Case 6	Two-row inline	3,400	Smag.	0.	0	0.18	1.13
Case 7	Two-row inline	3,400	Dyn.	0.	0	0.18	1.13

Table 6.2: Investigated inline tube array cases using either standard Smagorinsky or Dynamic model.

period.

Experimental investigations by Ziada and Oengören (1992), Konstantinidis et al. (2000) and Ljungkrona and Sundén (1993) have demonstrated that there is no vortex shedding behind the first row in the intermediate spacing tube array at Reynolds number from $10^3 - 10^4$. However, as shown in figures 6.7 and 6.8, vortex shedding behind the first row is clearly predicted for case 2. This probably results from the fact that the current grid resolution is still too coarse to resolve the small scales generated by the separated shear layer of the first row. Further grid refinement over the region between the first and second cylinders will clarify this issue later. As a result of the predicted vortex shedding, the r.m.s of the lift coefficient shown in figure 6.7(a) will be overpredicted for the steady approaching flow. It is also expected that the r.m.s velocities due to the vortex shedding will be over-predicted behind the first row. The r.m.s velocity will be examined in more detail in section 6.4. As a result, the heat transfer rate will be over-predicted too. The details of heat transfer will be discussed in more detail in section 6.6. After the 2nd row the vortex shedding pattern is close to 180^o out of phase between successive rows. The correspondence between the observed vorticity pattern and lift coefficients is similar to that observed in chapter 5 for a single cylinder. For instance, the Strouhal vortex is still associated with a low pressure region which is directly linked with the lift coefficient. Nevertheless, figure 6.7(a) also shows that the locked-on ($f_p = 2f_n$) vortex shedding will give a higher r.m.s lift coefficient, suggesting stronger vortex shedding behind the first row which is consistent with the flow pattern shown in figure 6.9. It can also be noted from the same figure that the vortex shedding for case 4 has a bigger transverse amplitude behind the first and second rows than the one for case 2. This behaviour has also been observed

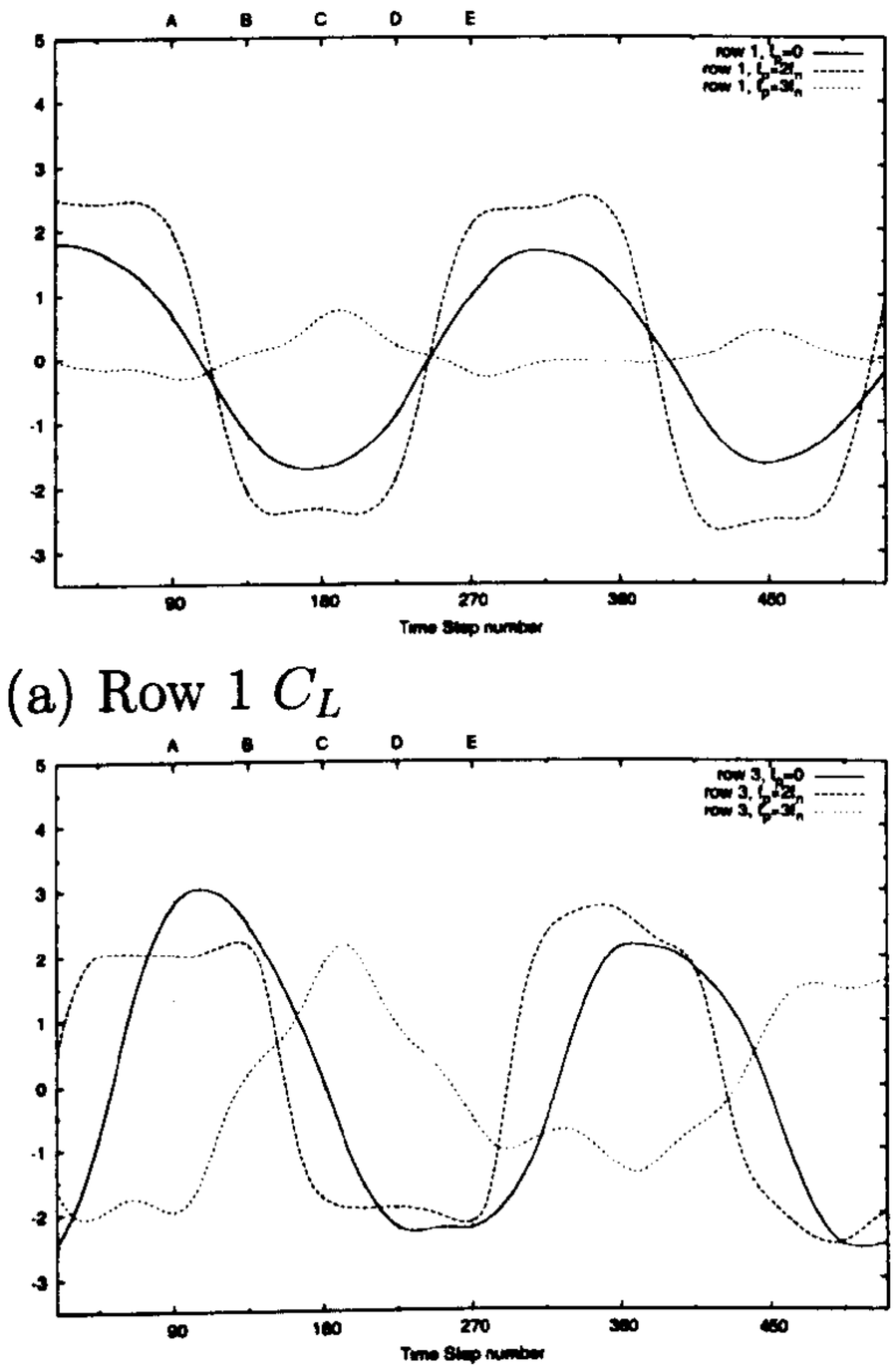

(a) Row 1 C_L

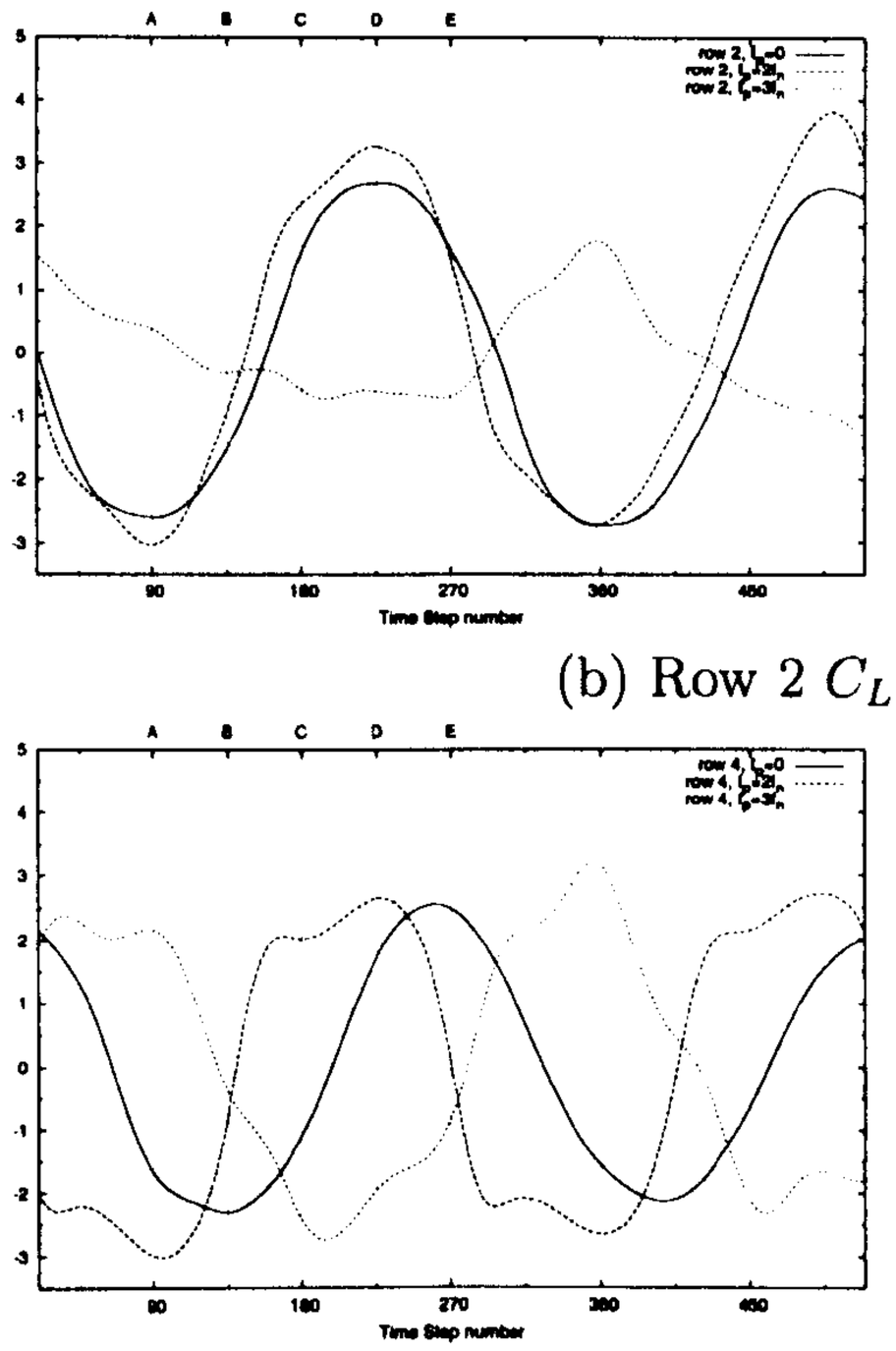

(b) Row 2 C_L

(c) Row 3 C_L

(d) Row 4 C_L

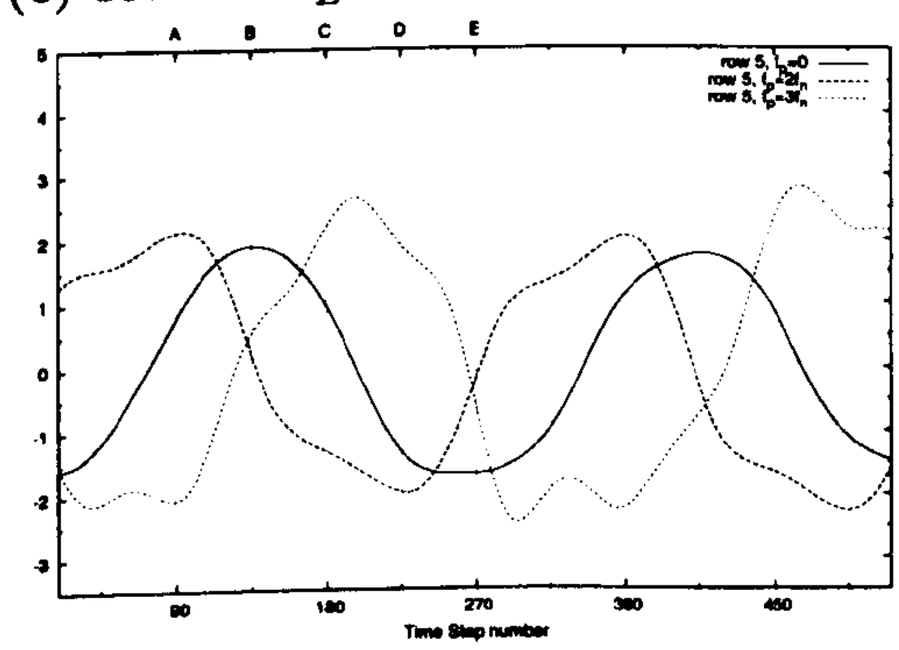

(e) Row 5 C_L

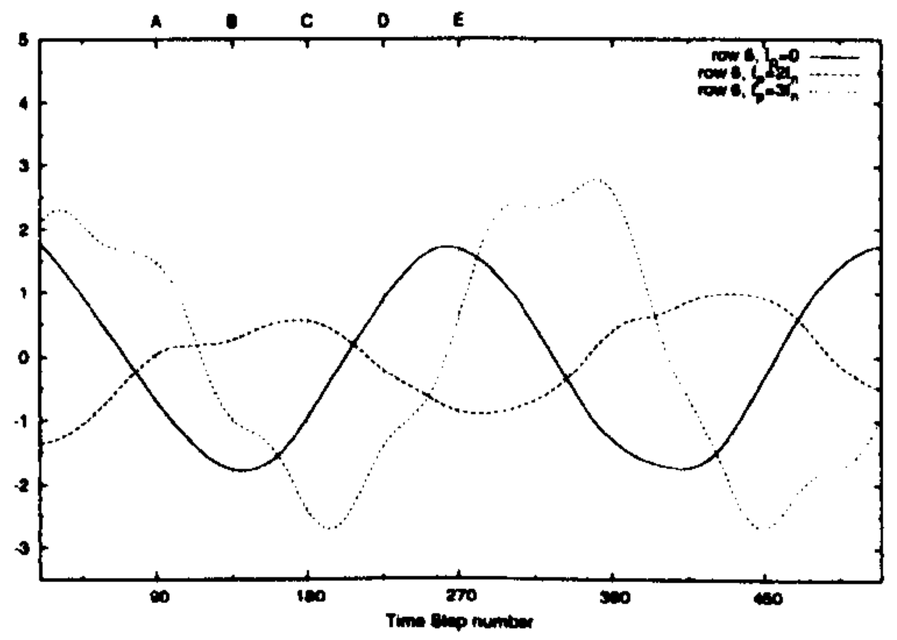

(f) Row 6 C_L

Figure 6.7: The time-dependent lift coefficients of six cylinders in the inline tube bundle with three different inlet conditions corresponding to cases 2, 4 and 5 of table 6.2.

in the previous chapter on the flow behind a single cylinder. In agreement with the flow visualization study by Konstantinidis et al. (2003*b*), a symmetrical vortex shedding pattern is predicted for case 5 as shown in figure 6.10 behind the first row when the external pulsation frequency is three times of the vortex shedding frequency ($f_p = 3f_n$). The symmetrical vortex formation mode is expected to result in a smaller r.m.s lift coefficient than the alternate vortex shedding mode (which is predicted by both cases 2 and 4) as clearly shown in figure 6.7(a). As shown in figures 6.7(b) and 6.10, the vortex shedding behind the second row appears to be weaker than the one of the alternate vortex shedding mode too. However, about the same level of r.m.s lift coefficient for the third and downstream rows is predicted for all cases, indicating the vortex shedding is not affected very much by the external pulsation and an alternate vortex shedding pattern is established.

Figure 6.11 presents the streamwise velocity spectra of one point in the shear layer behind each cylinder. The recording points are located at 1D behind the cylinder center of each row in the streamwise direction and 0.5D above in the transverse direction. The spectra reveal a distinct peak frequency at 4.93Hz which gives a Strouhal number 0.145 based on the gap velocity. The predicted Strouhal number is in a good agreement with 0.14 obtained by Konstantinidis et al. (2000). This frequency is found to persist behind each row in the inline tube array. Flow visualization of the spanwise vorticity confirms 180 degree out-of-phase alternate vortex shedding. This is, in general, in a good agreement with the observation of Konstantinidis et al. (2000). However, Konstantinidis et al. (2000) did not observe a vortex shedding frequency behind the first row because two standing vortices occupied the gap between the first and second row. On the other hand, by using a flow visualization technique, they also pointed out that intermittently, the separated shear layers do roll up before the second cylinder. This probably indicates the bistable nature of the vortex shedding behind the first cylinder. This discrepancy between the present coarser mesh prediction and experiments can be resolved by performing mesh refinement as will be demonstrated in the next section 6.3.2.

6.3.2 Instantaneous field of two-row bundle (bistable transition regime)

As far as experimental classifications are concerned, a bistable transition regime between the *reattachment* and *two vortex streets* flow regimes may be expected.

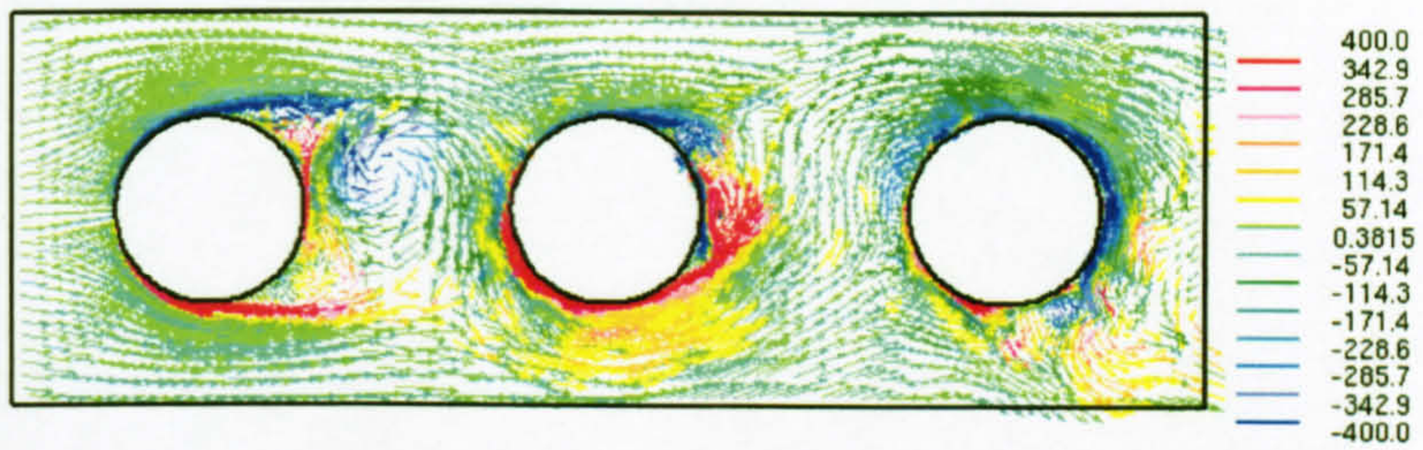

Phase A

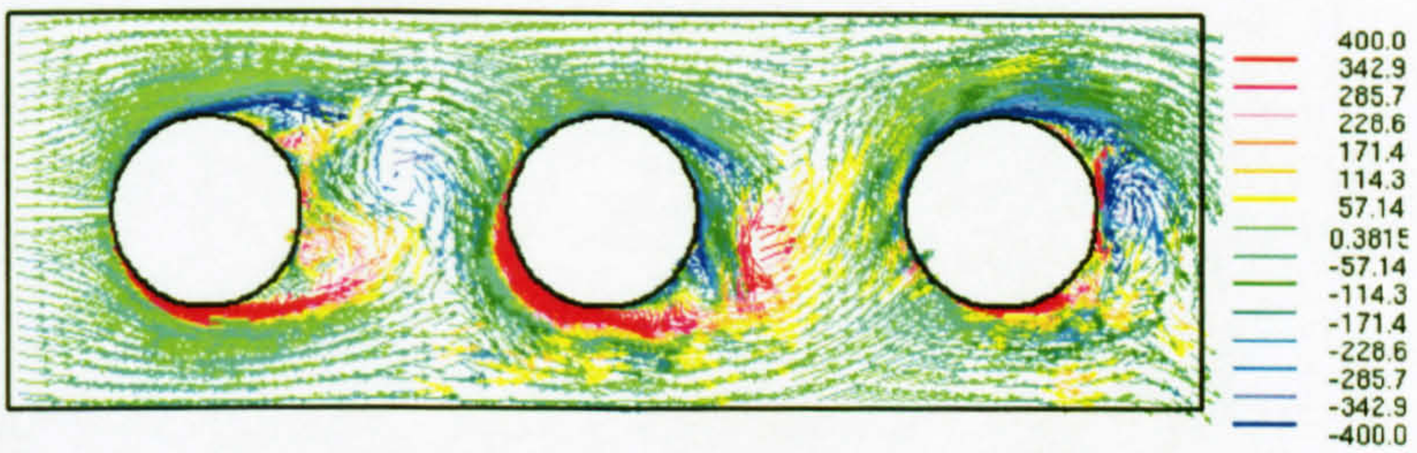

Phase B

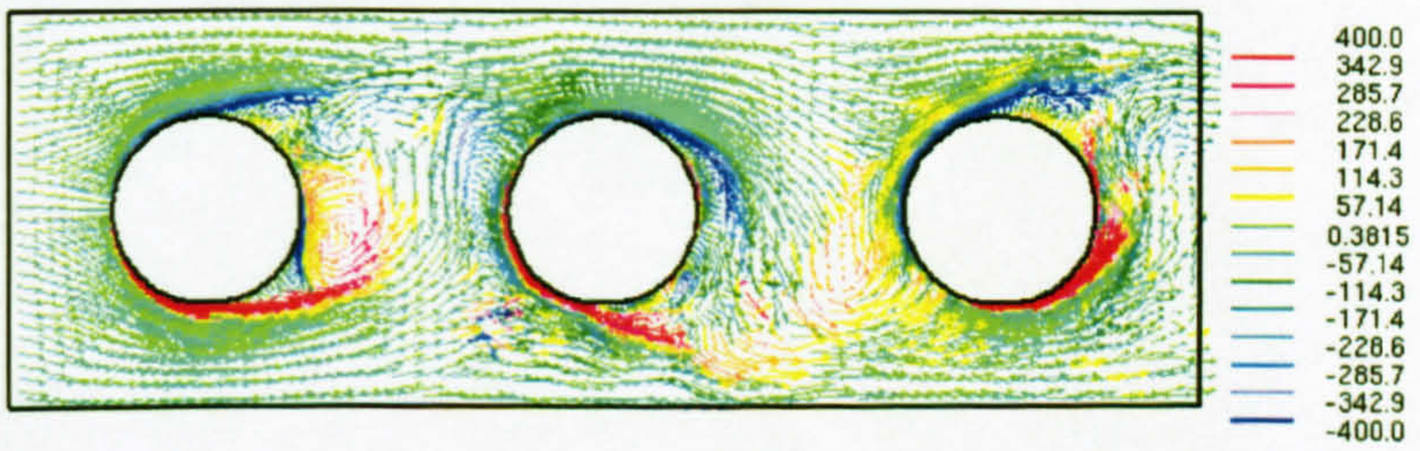

Phase C

Phase D

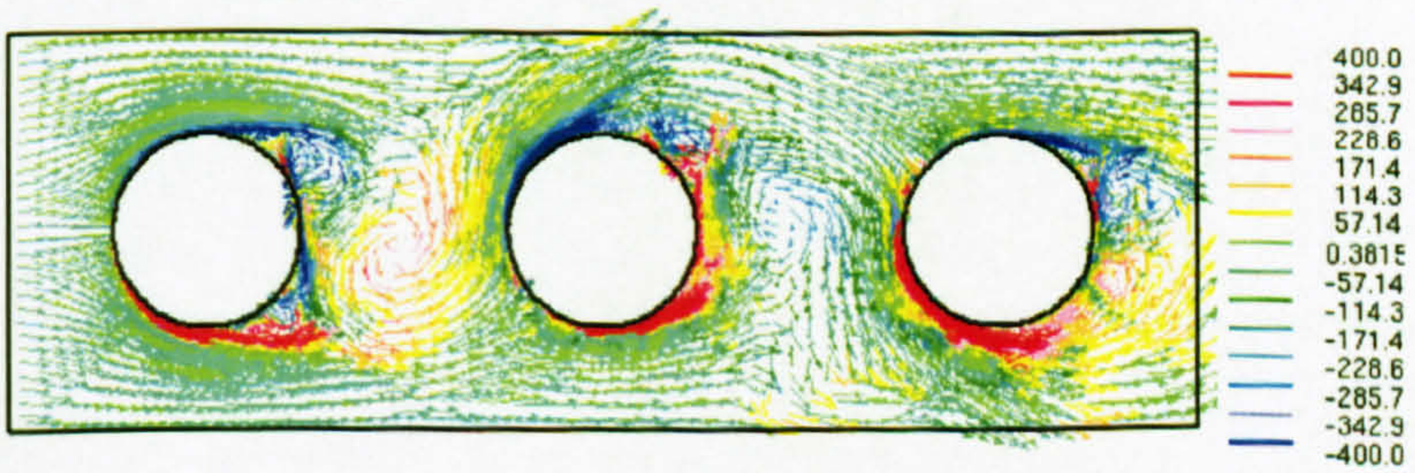

Phase E

Figure 6.8: Instantaneous velocity vectors colour-coded with the values of spanwise-vorticity of the first three cylinder rows for Case 2.

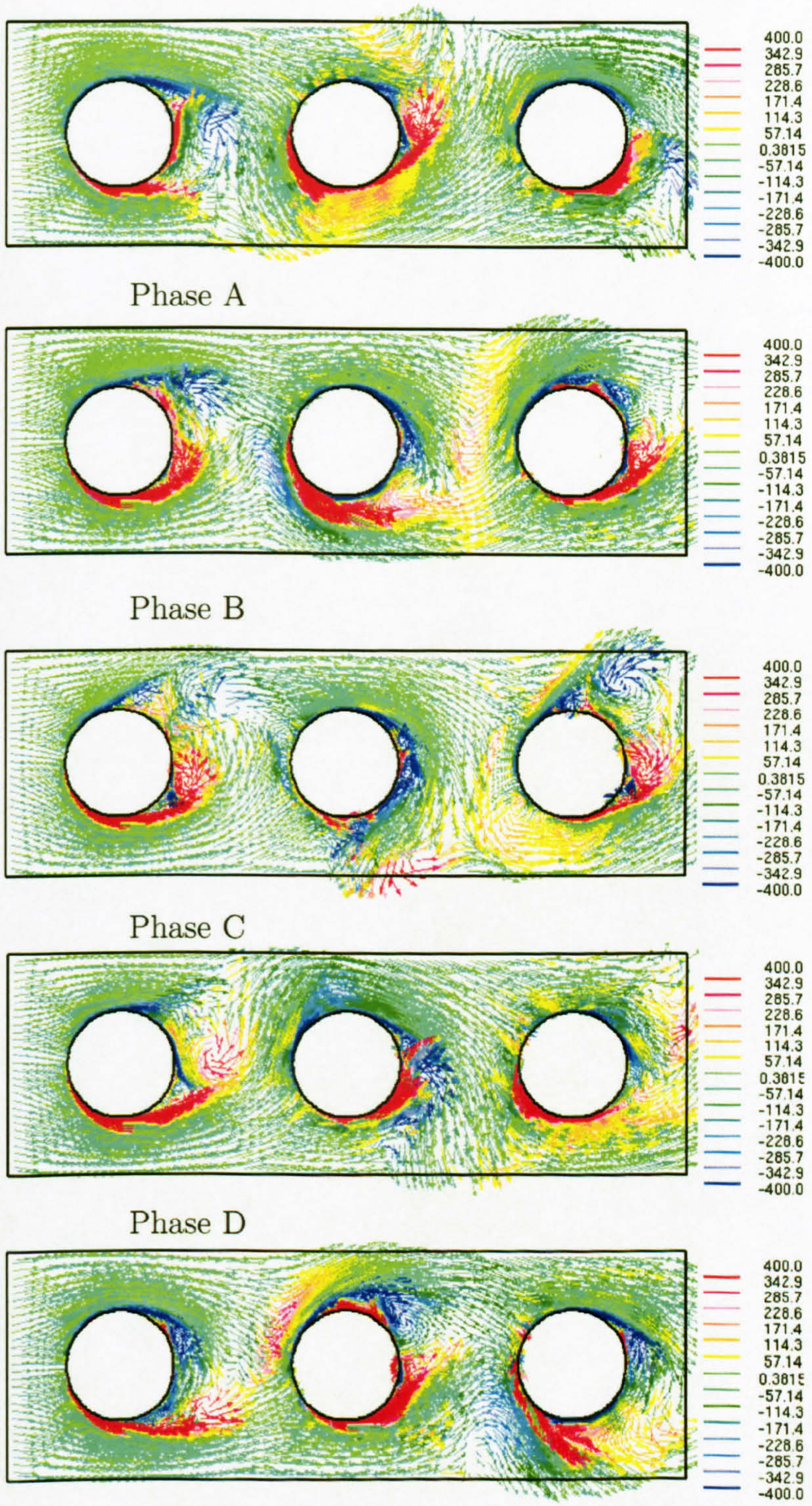

Figure 6.9: Instantaneous velocity vectors colour-coded with the values of spanwise-vorticity of the first three cylinder rows for Case 4.

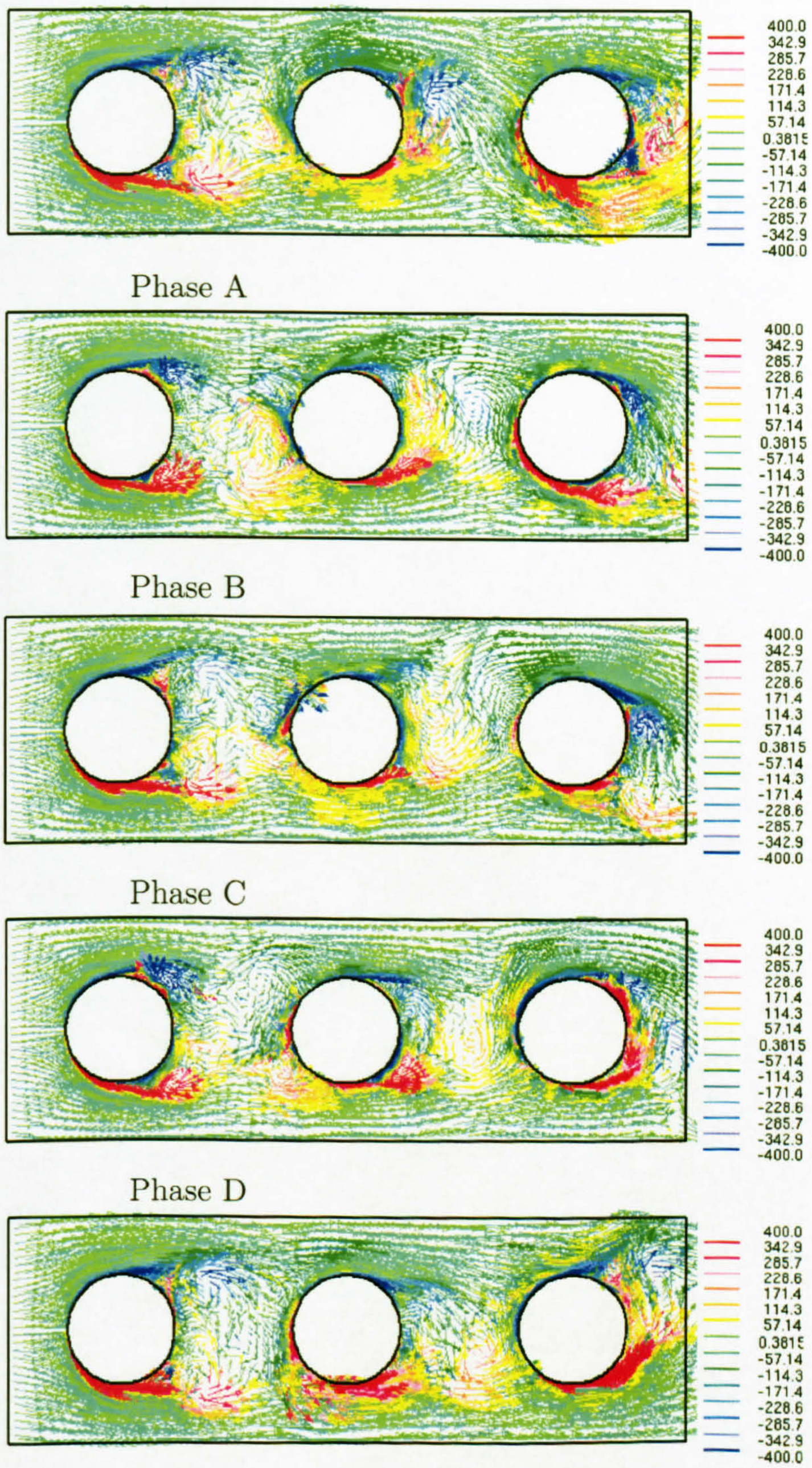

Figure 6.10: Instantaneous velocity vectors colour-coded with the values of spanwise-vorticity of the first three cylinder rows for Case 5.

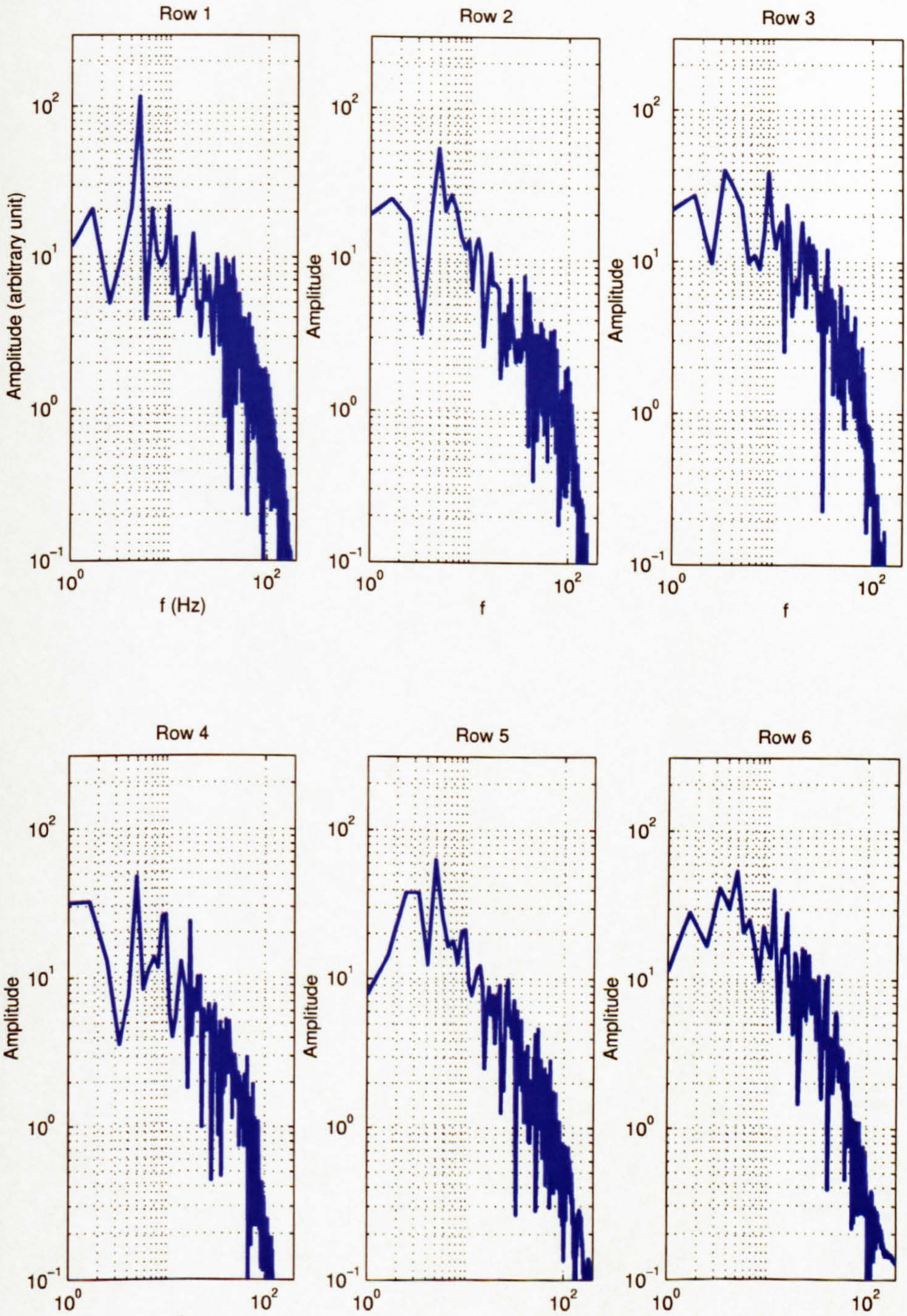

Figure 6.11: Predicted streamwise velocity spectra at one shear layer point behind each row for case 1. The peak frequency is 4.93 Hz, which is corresponding to $St_{gap} = 0.145$.

Kiya et al. (1992) observed two different vortex shedding patterns in the bistable transition regime at a Reynolds number $Re \approx 3 \times 10^4$ with tube spacings $3.47D$ and showed that the switching between the regimes occurred every $10^3 - 10^5$ vortex shedding periods when freestream turbulence was taken into account. They also pointed out that the *reattachment* regime is associated with small pressure fluctuations, while the *two vortex streets* regime is associated with violent pressure fluctuations. Ziada and Oengören (2000) observed that there are also both symmetric (similar to *reattachment* regime) and antisymmetric vortex shedding patterns between first and third rows using flow visualization in a parallel triangle array with pitch ratio 2.08 at a Reynolds number of $Re_{gap} = 1870$[2]. Therefore, it could be expected that as the Reynolds number decreases from 10^4 to 10^3, the tube spacings for the bistable transition will decrease from 3.5 to 2.1.

Jester and Kallinderis (2003) performed two-dimensional finite-element calculation for arrangements with pitch ratios of 2 and 2.15 also at a Reynolds number of 1,000. They found that the shear layers separating from the upstream cylinder always reattach on the front of the downstream cylinder when the pitch ratio is 2. However, the flow characteristics of the arrangement with pitch ratio of 2.15 can either belong to the *reattachment* or the *two vortex streets* regime, depending on the initial state.

For the present three-dimensional computation, the initial state of the flow inside the two-row inline tube array can also be very important for the vortex shedding phenomenon. If the initial state starts from a laminar flow (i.e. the same starting field used for the 6-row array), cases 6 and 7 predict a pair of well-defined counter-rotating vortices in the gap. In agreement with the simulation performed by Jester and Kallinderis (2003), the *reattachment* regime is reached. The instantaneous velocity fields at 10 time instants (A-J in figure 6.13) predicted by case 7 are shown in figure 6.14. It can be seen that there is no clear alternate vortex shedding in the gap region although there will be a small variation of the reattachment locations on the front part of the second cylinder at different time instants. It can thus be observed that by refining the mesh the reattachment regime is indeed reached. Thus the effect of mesh refinement is important. A possible explanation for this is that when the mesh is coarse the dispersive error of the second order central difference scheme triggers an instability in the gap

[2]It should be noted that the vortex shedding patterns between the first and third rows in the parallel triangle array should be similar to that of the two cylinders in tandem. The reason for this similarity lies in the fact that the parallel triangle array allows the flow to proceed along the free-flow lanes between the tube columns (see figure 1.3 in chapter 1).

between the first and second cylinder that leads to vortex shedding. When the mesh is refined the dispersive error is reduced and the flow stays at the *reattachment* regime. Ideally this should be confirmed by performing calculations for the whole bundle with refined mesh, however this was not attempted due to limitation of the present computing power. The observed flow pattern is in a good agreement with the observation by Lin et al. (2002) for the two-row bundle with spacing $S_L = 2D$. On the other hand, if the initial flow field starts from the fully developed pulsating approaching flow ($f_p = 2f_n$) field, then after roughly 10 shedding periods, the flow field is stabilized with clear vortex shedding pattern behind the first cylinder. Figure 6.15 presents the instantaneous velocity fields for the *two vortex streets* regime predicted by case 7. One can clearly see the alternate vortex shedding mode behind the first row which is about 180^o out-of-phase with the vortex shedding behind the second row. It was shown in chapter 5 that pulsation reduces the size of the recirculation bubble zone and the vortices are formed closer to the cylinder. It is thus easier to establish a stable vortex shedding pattern in the available gap between the two cylinders. When the approaching flow is switched to a steady one, this pattern persists due to the bistable nature of the flow. Figure 6.12 shows clearly the difference in the drag coefficient of the first-row cylinder between the two different regimes. The *two vortex streets* regime is associated with a higher mean and r.m.s drag coefficient than the *reattachment* regime. The fact that two stable big vortices are formed behind the first row in the *reattachment* regime gives a very small drag coefficient and r.m.s lift coefficient (as shown in figure 6.13 for the variation of lift coefficient of the upstream cylinder). It is noted that both regimes in the present two-row bundle possess a higher mean drag coefficient than the one predicted by Jester and Kallinderis (2003). This is related to the blockage effect from the top and bottom walls and the mounted half-cylinders. A similar effect on a single cylinder flow was discussed in detail in the previous chapter 5.

6.4 Time-averaged flow field

6.4.1 Steady flow

Figure 6.16 shows the time-averaged velocity field predicted for the different cases shown in table 6.2 for the six-row inline tube bundle. The standard Smagorinsky and the dynamic model produced similar results for the mean velocity field. Figure 6.8 has demonstrated that the coarser grid resolution predicts a clear vortex

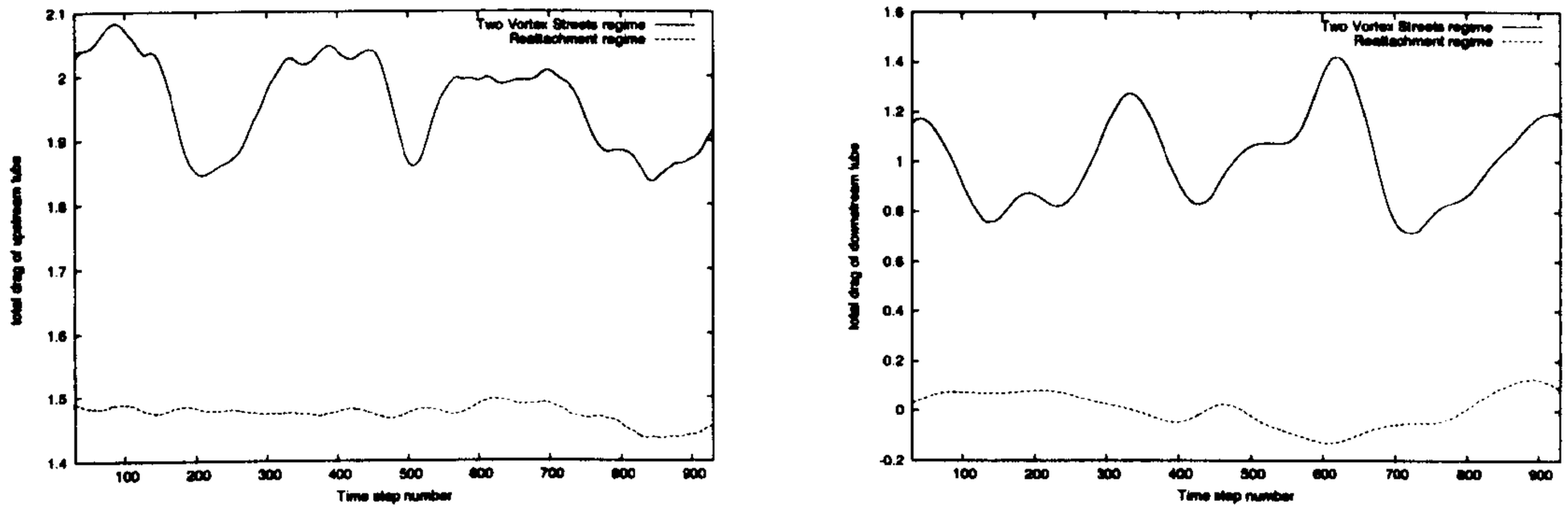

(a) upstream row C_D (b) downstream row C_D

Figure 6.12: The time-dependent drag coefficient of the two cylinders at two different vortex shedding regimes predicted by Case 7.

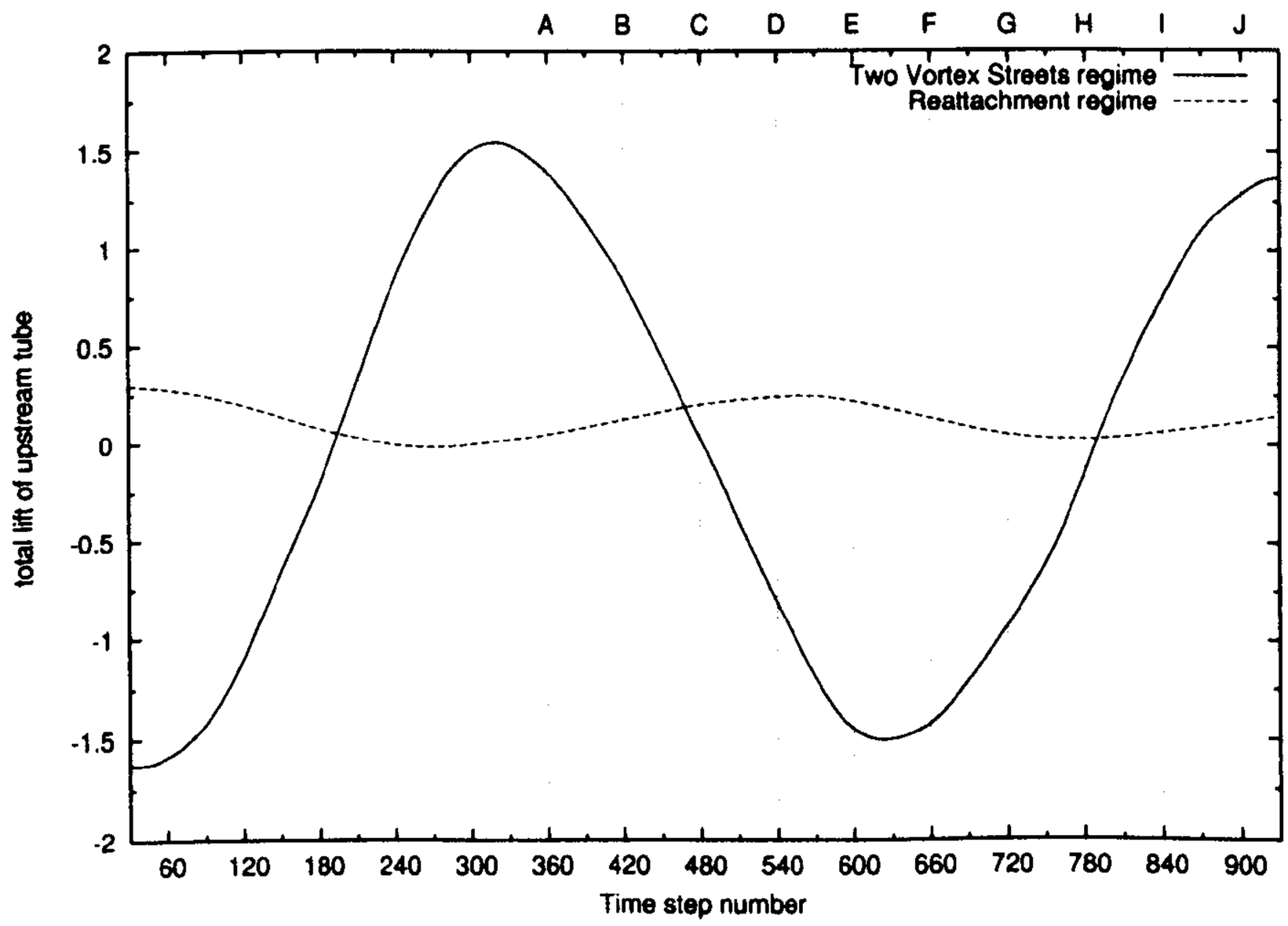

Figure 6.13: The time-dependent lift coefficient of the first-row cylinder at two different vortex shedding regimes predicted by Case 7.

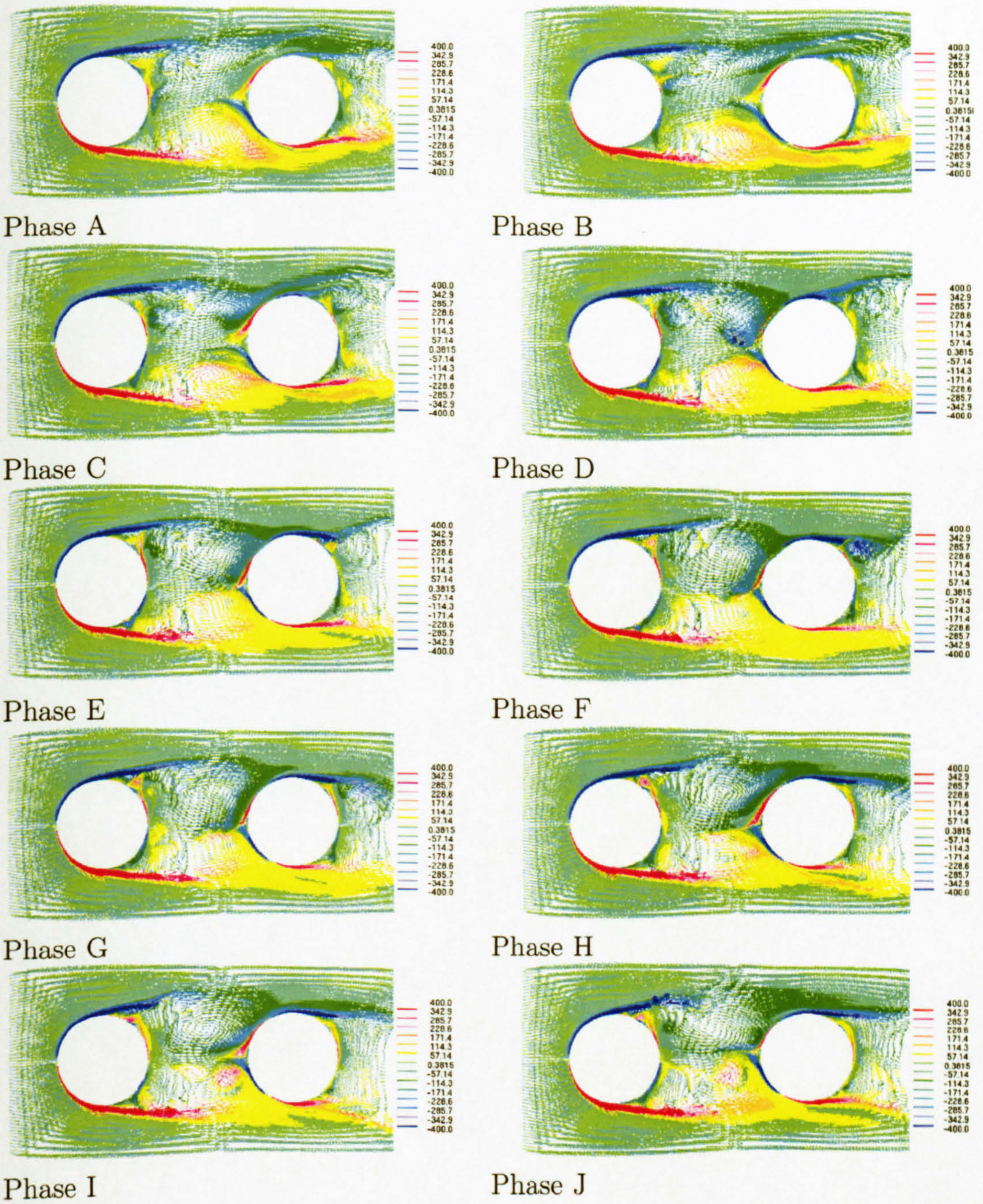

Figure 6.14: Instantaneous velocity vectors colour-coded with the values of spanwise vorticity for one shedding period in the *reattachment* regime (case 7).

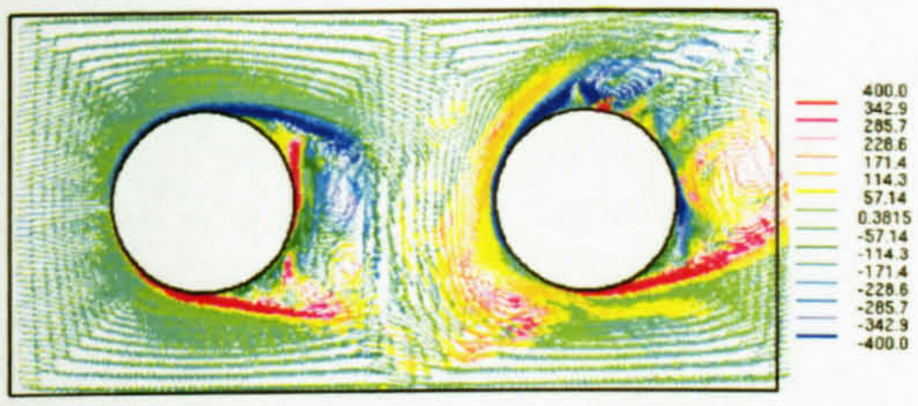

Phase A

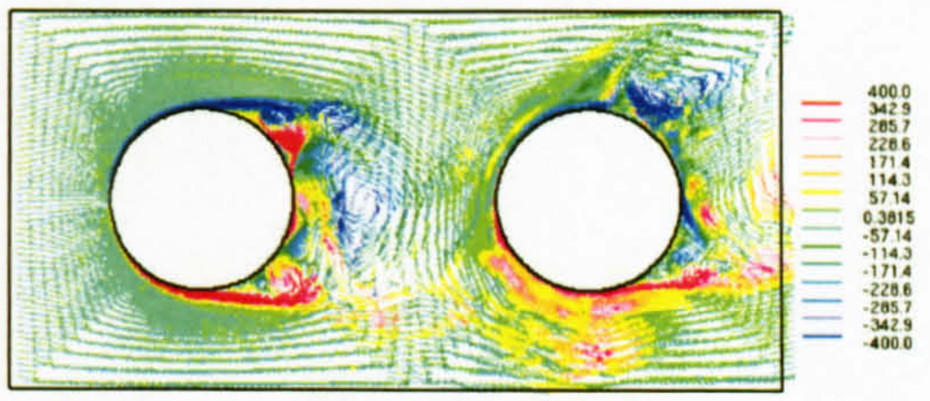

Phase B

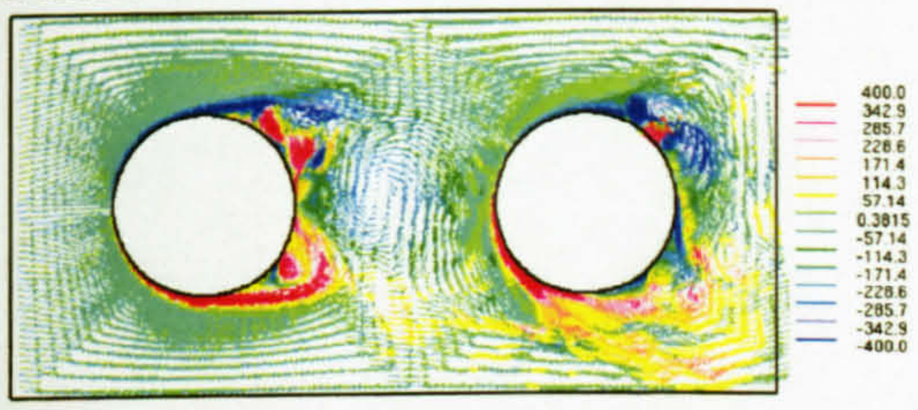

Phase C

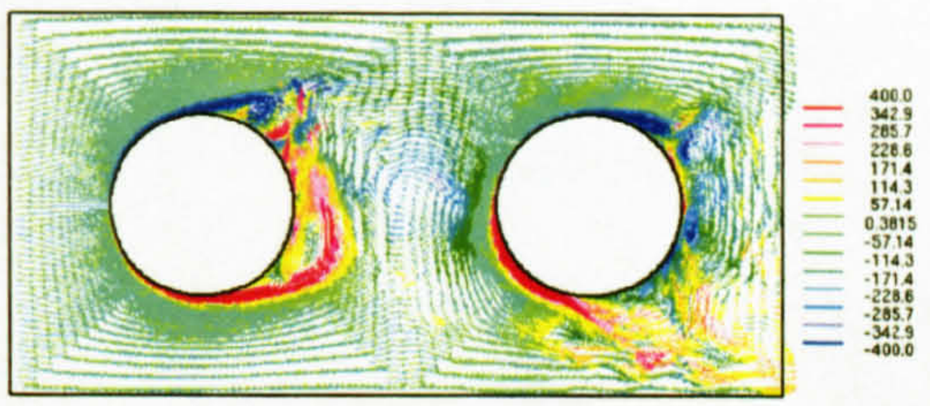

Phase D

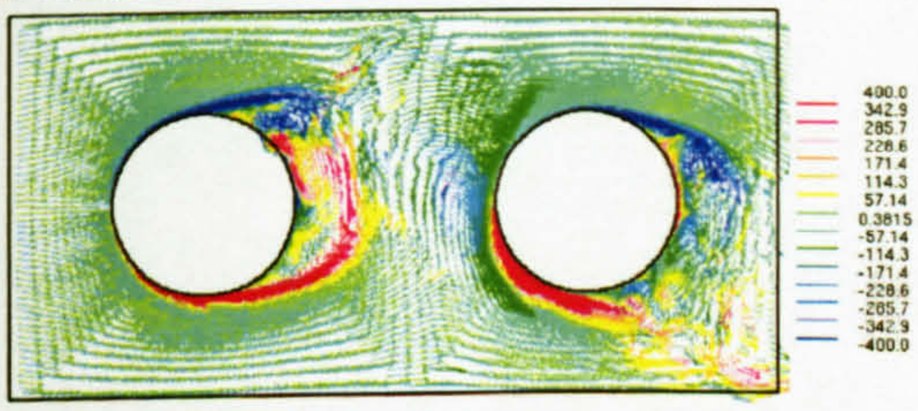

Phase E

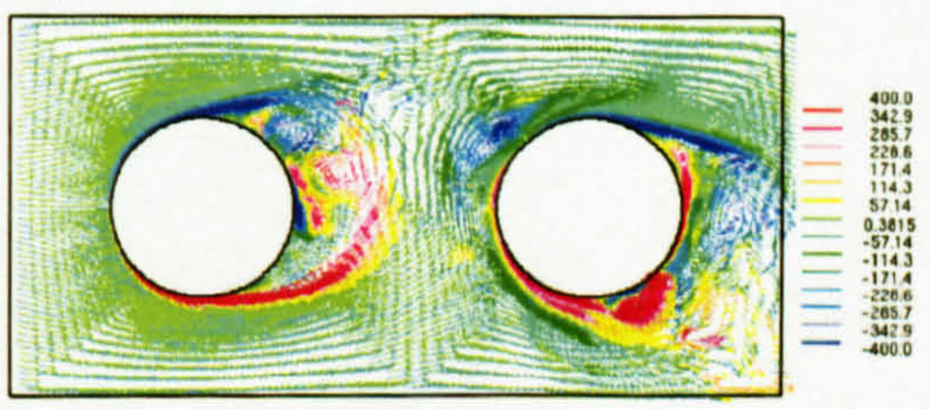

Phase F

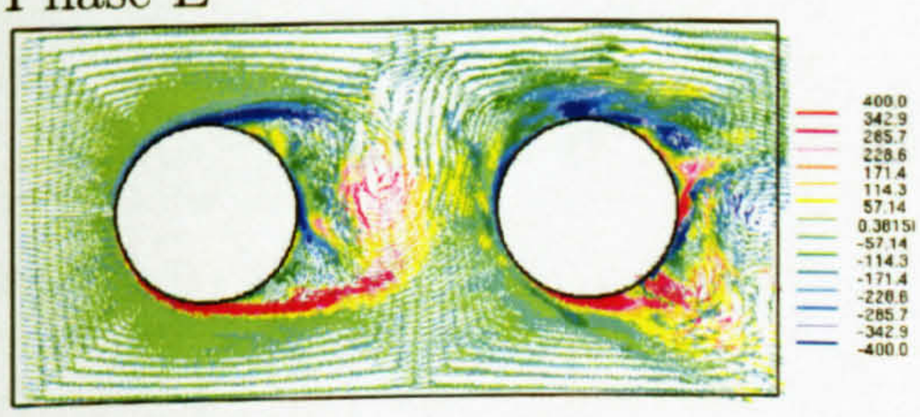

Phase G

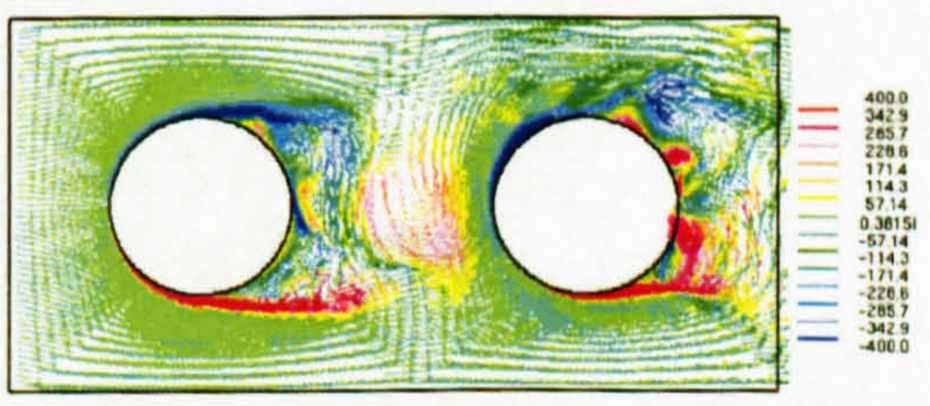

Phase H

Phase I

Phase J

Figure 6.15: Instantaneous velocity vectors colour-coded with the values of spanwise vorticity for one shedding period in the *two vortex streets* regime (case 7).

shedding pattern in the gap between the first and second row i.e. the *two vortex streets* regime. As a result, the predicted time-averaged recirculation bubble zone behind the first row as shown in figure 6.16 will be smaller than the one predicted for the *reattachment* regime.

Figure 6.17 shows a comparison between the time-averaged and the r.m.s streamwise velocity against experimental data for the steady cross-flow over the in-line tube bundle. The experimental inlet turbulence level ($u^*_{rms} = u_{rms} + 0.09$) was used to adjust the predicted r.m.s velocity. Both the Smagorinsky and the dynamic model predict good mean velocity profiles in agreement with the LDA measurements. The dynamic model predicts the mean velocity profile behind the second row cylinder slightly more accurately than the standard Smagorinsky model. The discrepancy of the mean profile behind the first row cylinder is probably because the rather coarse grid resolution predicts earlier separation and shorter recirculation bubble zone. The streamwise r.m.s velocity field behind the first row is over-predicted because of the vortex shedding as explained in the previous section. Further grid refinement is needed if higher accuracy is required. The r.m.s streamwise velocity grows slowly in the flow lane region along the streamwise direction. It is predicted that the maximum streamwise r.m.s velocity of the entire bundle exists in the separating shear layer of the second row cylinder.

Figure 6.18 shows the variation of the streamwise r.m.s velocity along the flow lane[3] of the steady cross flow over the inline tube bundle. The results of Konstantinidis et al. (2000) at $Re_{gap} = 3,100$ are plotted together with the present predictions. Both sgs models overpredict the rise of the r.m.s streamwise velocity compared to the experiment although the dynamic model predicts a slightly slower growth which is closer to the measurements. The over-prediction is partly attributed to the fact that vortex shedding is already established after the first row in the present simulation. On the other hand, the inlet r.m.s turbulence level is very close to zero in the simulations so it is bound to increase up to one level along the streamwise direction. Although the dynamic model predicts slightly better results than the Smagorinsky model, case 2 still predicts an increase of 12% which is comparable to the measurements of Ziada and Oengören (1992) with the inlet turbulence level below 0.1%. Konstantinidis et al. (2000) found that the increase of r.m.s turbulence level for the steady cross-flow is only around 3% and 5% across the bundle at Reynods numbers of 3,100 and 6,700 respectively. They also attributed

[3]The flow lane is defined as the streamwise line at a transverse location $y = 1.8D$ away from the bundle centerline.

Figure 6.16: The time-averaged mean velocity fields for the six-row inline tube array (only the first four rows are shown for clarity of presentation).

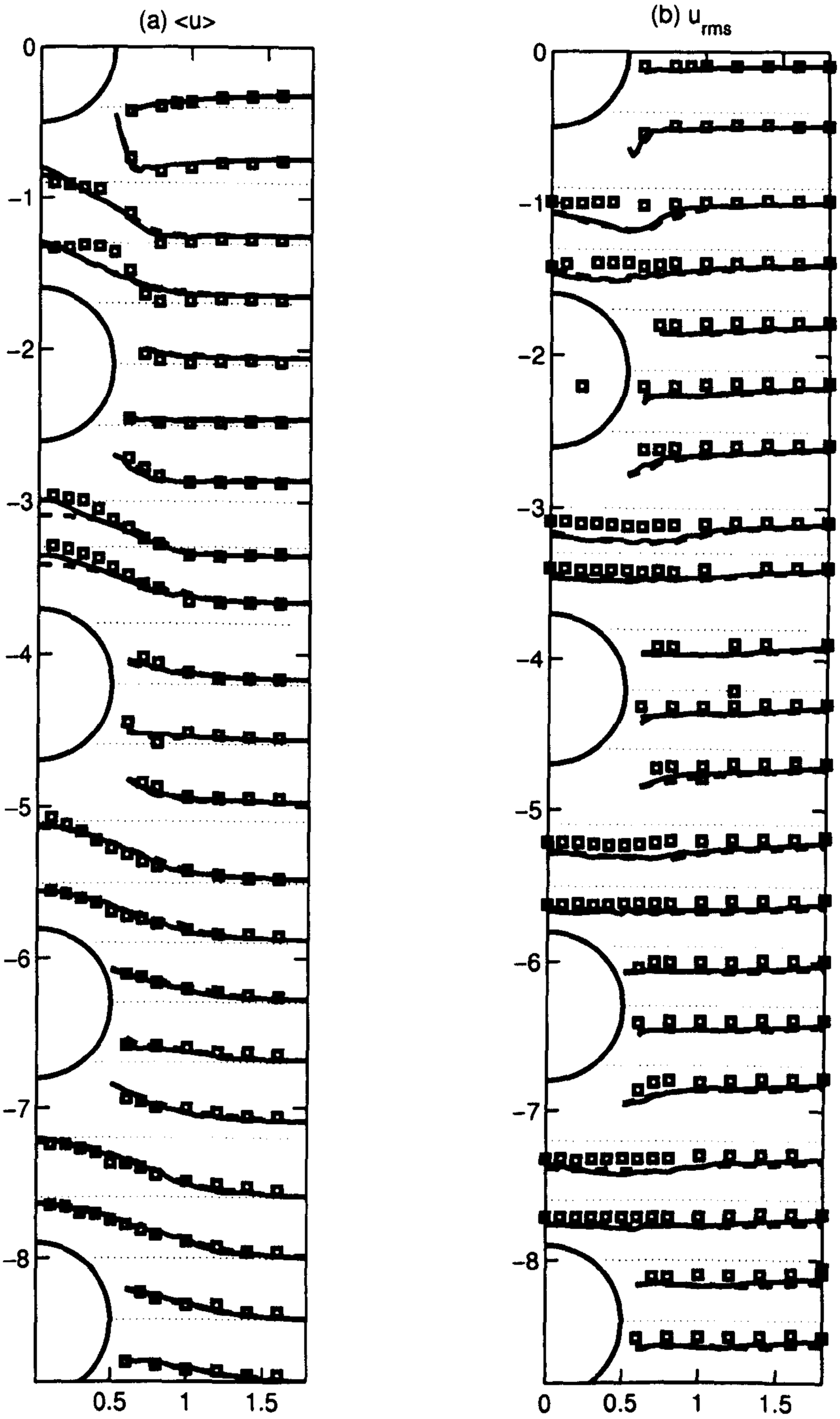

Figure 6.17: Streamwise (a) mean and (b) r.m.s velocity of the steady cross flow over the inline tube bundle. (——) Dynamic model; (- - - - -) Smagorinsky model; (□□□□□) LDA measurements

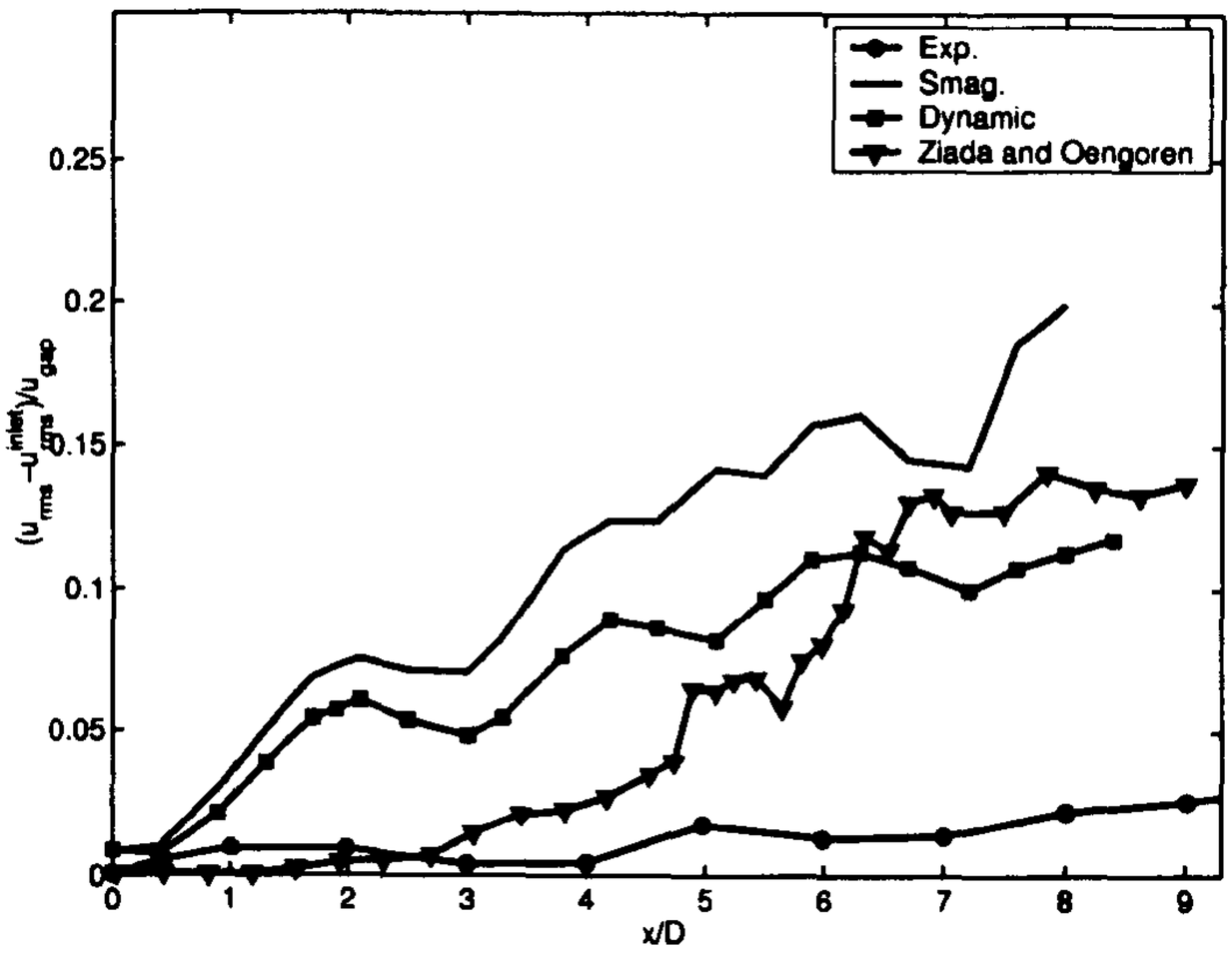

Figure 6.18: Variation of streamwise r.m.s velocity along the flow lane for the steady cross flow over the inline tube bundle for Cases 1 and 2.

the discrepancy with the results of Ziada and Oengören (1992) at $Re_{gap} = 6,800$ to the bigger transverse spacing ($S_L = 1.75D$ and $S_T = 1.95D$) which was used by these investigators and the fact that half tubes were mounted along the side walls. However, the high inlet turbulence level maybe another factor which kept the increase of the streamwise r.m.s velocity very small in Konstantinidis et al. (2000).

Figure 6.19 shows the mean velocity vectors predicted for cases 6 and 7. Both *reattachment* and *two vortex streets* regimes are shown for Case 7. The Smagorinsky model predicts a similar mean velocity pattern as the dynamic model reflecting the fact that the effect of different sgs model on the mean profiles is small. Both sgs models predicted that the two big vortices fully occupy the gap region between the first and second row. However, if the initial state was that of a fully-developed pulsating approaching flow, the two counter-rotating vortices will shrink to a narrower region, moving the mean reattachment points nearer to the front stagnation point of the second row. The instantaneous flow fields shown in figure 6.15 justify this time-averaging flow pattern.

6.4.2 Pulsatile flow

Figure 6.20 shows the streamwise r.m.s velocities along the flow lane for the locked-on pulsating cross flow over the inline tube bundle predicted by Cases 3 and 4. The dynamic model appears more suitable for the prediction of the pulsatile

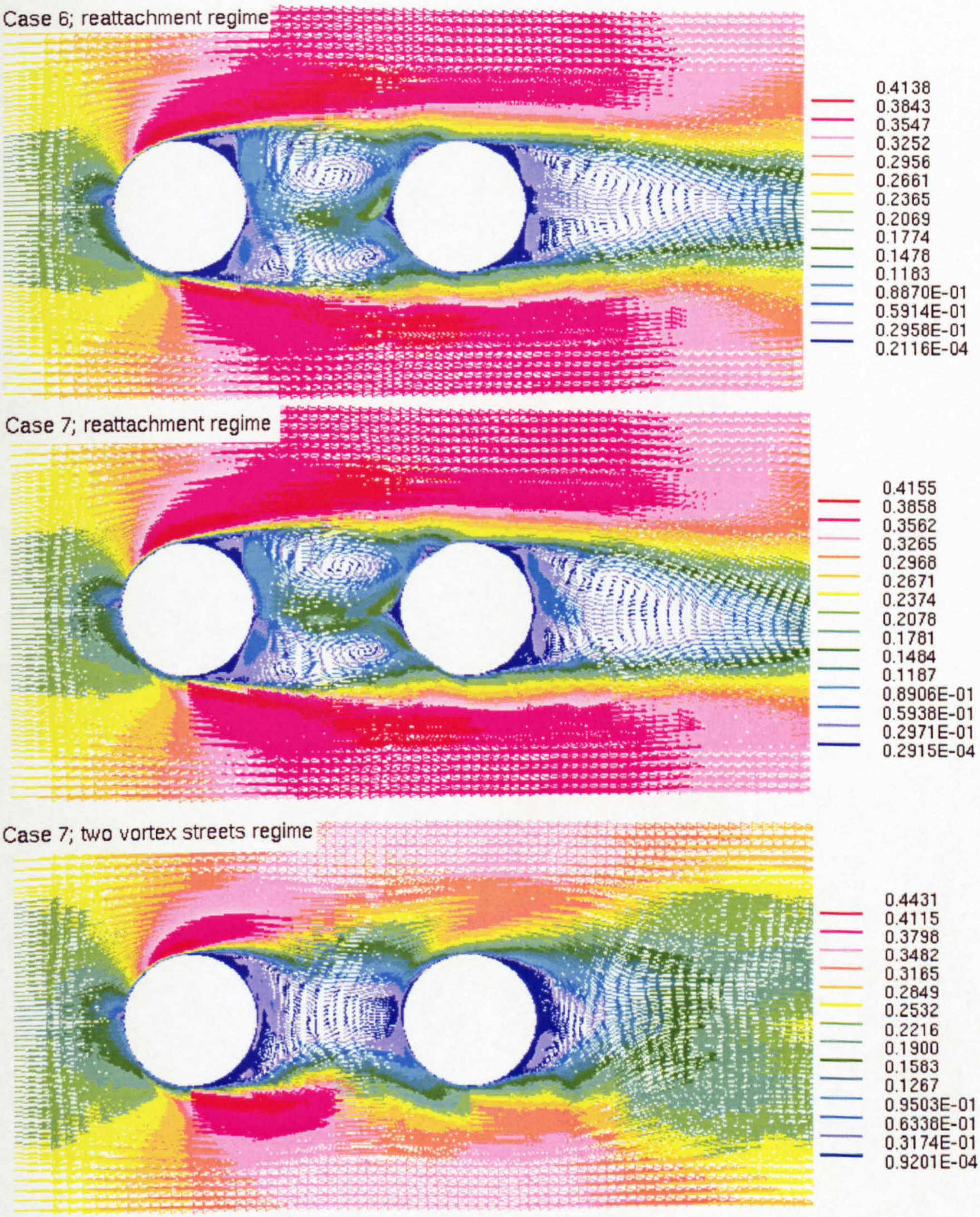

Figure 6.19: The time-averaged velocity vectors predicted for cases 6 and 7.

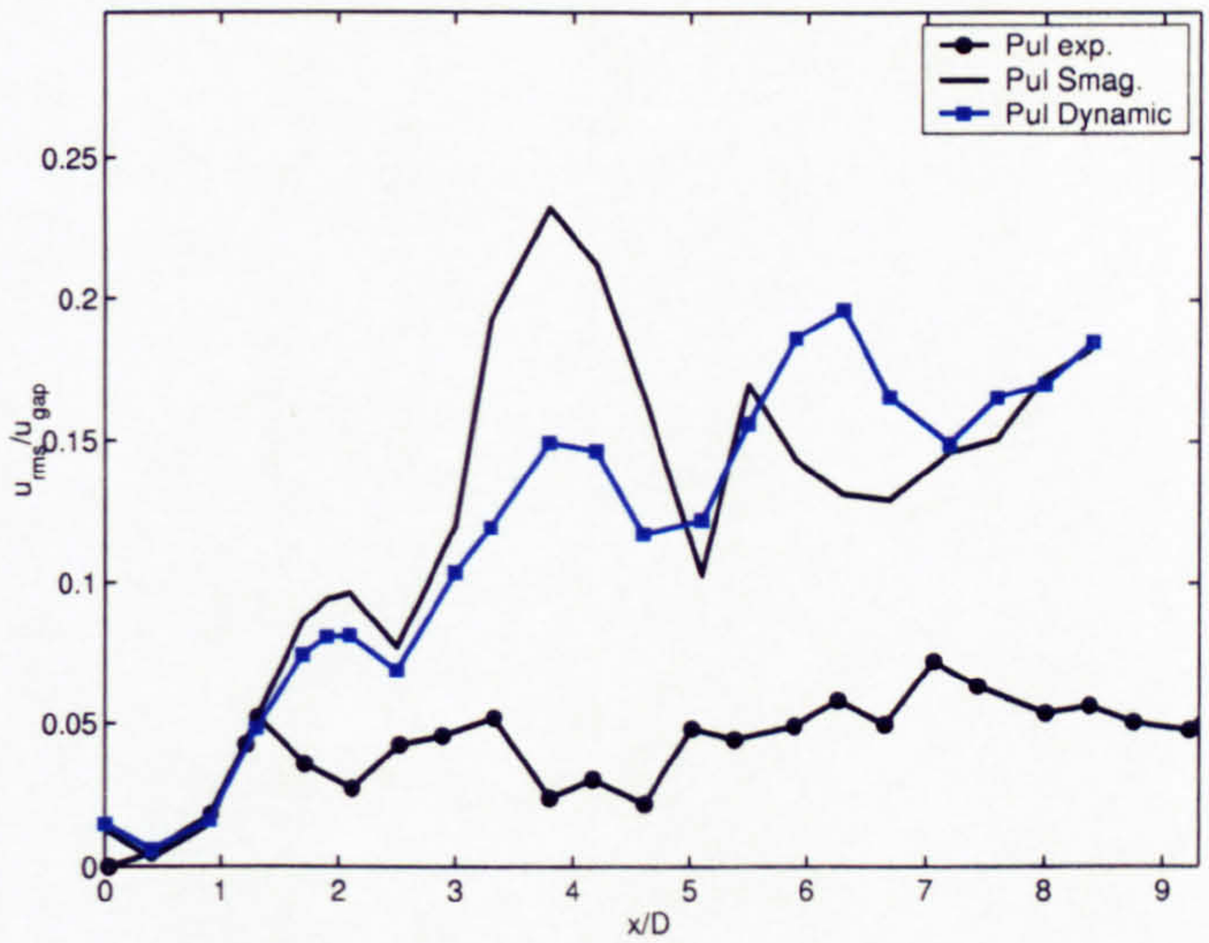

Figure 6.20: Streamwise r.m.s velocities along the flow lane of the pulsating cross flow over the inline tube bundle predicted by Case 3 and 4.

flow although both the Smagorinsky and the dynamic model overpredict the r.m.s velocity in the downstream level. This overprediction can be partially attributed to the high turbulence level at the inlet in the experiment as explained earlier. The dynamic model predicts that the maximum r.m.s velocity exists at the 4th row level, while the Smagorinsky model predicts the maximum r.m.s velocity at the 3rd row level. Nevertheless, the increase of the r.m.s velocity between the first and second row is correctly predicted.

Figure 6.21 shows a comparison between predicted and measured mean and r.m.s streamwise velocity at one mid-plane (X-Y section) of the mesh. Both the Smagorinsky and the dynamic model predict mean velocity profiles in very good agreement with the LDA measurements. The dynamic model predicts nearly identical results to the Smagorinsky model for both mean and r.m.s streamwise velocity. Behind the first cylinder, the mean velocity is slightly over-predicted at the location of $x/D = 0.8$. The inlet turbulence level of the measurement was added to the predicted r.m.s velocity field in order to have a quantitative comparison. However, this practice over-estimates the effect of the inlet turbulence on the r.m.s velocity of the cylinder wakes. It is believed that this is one of the main reasons that the predicted r.m.s velocity field shown in figure 6.21(b) is generally higher than the experimental results.

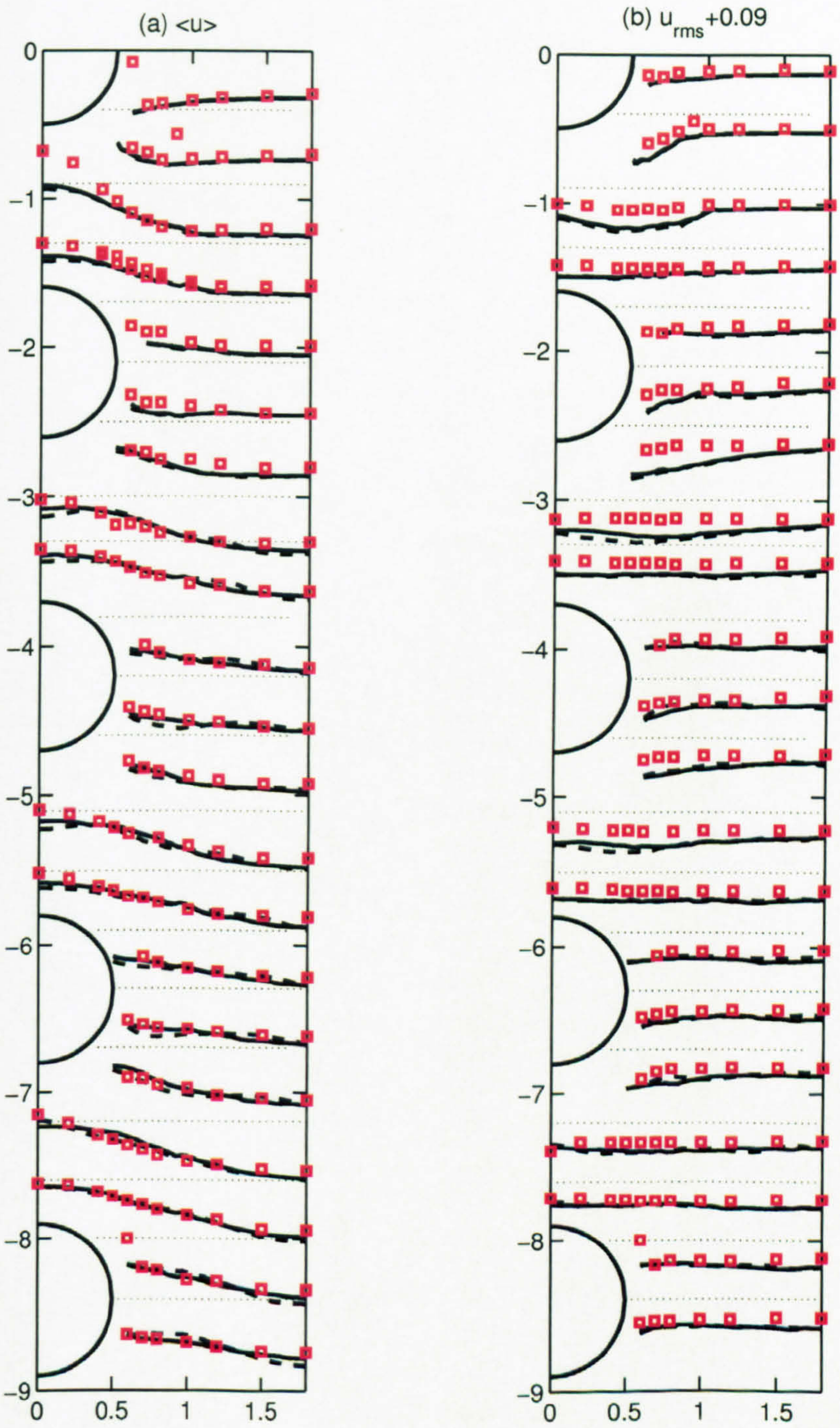

Figure 6.21: Streamwise mean and r.m.s velocity of the locked-on pulsating cross flow over the inline tube bundle. (——) Dynamic model; (- - - - -) Smagorinsky model; (□□□□□) LDA measurements.

6.5 Lift and drag coefficients

Table 6.3 summarises the lift and drag coefficients for each central row cylinder in different cases. The cylinder numbering was presented in figure 6.1. The mean lift coefficient is generally close to zero for the different cases indicating the symmetry of the flow and pressure fields.

It should be noted that case 7(b) and case 2 predict very similar lift and drag coefficients for the first row. This is due to the fact that both of them reached the alternate vortex shedding regime behind the first row. Although the coarser resolution used in case 2 is unable to sustain the *reattachment* regime, the resolution seems good enough to predict the main features of the vortex shedding behind the first row which gives nearly identical results to the *two vortex streets* regime predicted by the refined mesh. The two different regimes predict different lift and drag cofficients. The *two vortex streets* regime predicts higher mean drag and r.m.s lift coefficients which can be explained by the stronger vortex shedding existing behind the first row. The mean drag of the second row predicted by case 6 and case 7(a) is very small, which agrees with the finding by Jester and Kallinderis (2003). As predicted for case 4, the locked-on pulsating cross-flow has higher mean drag and r.m.s lift coefficients for the first two rows than case 2. In the subsequent downstream rows, case 4 predicted slightly higher drag coefficients, while the r.m.s lift coefficients are about the same level as predicted for Case 2. Although case 5 has much lower mean drag and r.m.s lift coefficients than case 4 due to the symmetrical vortex formation mode behind the first row, it exhibits higher mean drag coefficient in the subsequent downstream rows.

6.6 Heat transfer distribution

Figure 6.22 shows the local spanwise- and time-averaged Nusselt number for the first and second rows for cases 6 and 7(b). For the upstream row, the *two vortex streets* regime possesses a higher Nusselt number after the separation point due to the alternate vortex shedding mode. The results are comparable to the measurement of the steady flow heat transfer rate at Reynolds number $Re_D = 3,200$ presented by Gau et al. (2001). For the downstream row, the heat transfer rate is significantly increased in the front part by the alternate vortex shedding.

Figure 6.23 shows the spanwise- and time-averaged local Nusselt numbers predicted for cases 2, 4 and 5 for different rows in the six-row tube array. The heat

Lift and drag coefficients of the cross-flow over inline tube bundle						
Cases	Re_{gap}	Rows	Mean C_L	Mean C_D	r.m.s C_L	r.m.s C_D
Case 2	3,400	Row 1	0.007	1.95	1.18	0.08
		Row 2	0.015	0.98	1.98	0.42
		Row 3	-0.055	0.88	1.87	0.37
		Row 4	0.023	0.74	1.65	0.36
		Row 5	-0.020	0.61	1.31	0.23
		Row 6	0.006	0.75	1.26	0.21
Case 4	3,400	Row 1	0.006	2.34	2.14	0.99
		Row 2	-0.001	1.78	2.26	1.08
		Row 3	0.051	1.14	1.82	1.03
		Row 4	-0.055	0.99	1.83	0.85
		Row 5	-0.017	0.81	1.57	0.84
		Row 6	0.004	0.97	1.12	0.91
Case 5	3,400	Row 1	0.037	1.60	0.25	1.84
		Row 2	0.053	0.70	0.81	1.82
		Row 3	-0.019	1.18	1.26	1.80
		Row 4	0.012	1.21	1.86	1.76
		Row 5	-0.059	0.98	1.83	1.95
		Row 6	0	1.12	1.81	1.87
Case 6	3,400	Row 1	0.04	1.46	0.11	0.03
		Row 2	-0.06	-0.01	0.18	0.08
Case 7 (a)	3,400	Row 1	0.04	1.47	0.11	0.03
		Row 2	-0.03	0.03	0.17	0.07
Case 7 (b)	3,400	Row 1	-0.005	1.95	1.06	0.09
		Row 2	0.014	0.99	0.73	0.18

Table 6.3: Computed lift and drag coefficients for inline tube array. Case 7(a) refers to the reattachment regime, and Case 7(b) predicts the two vortex streets regime.

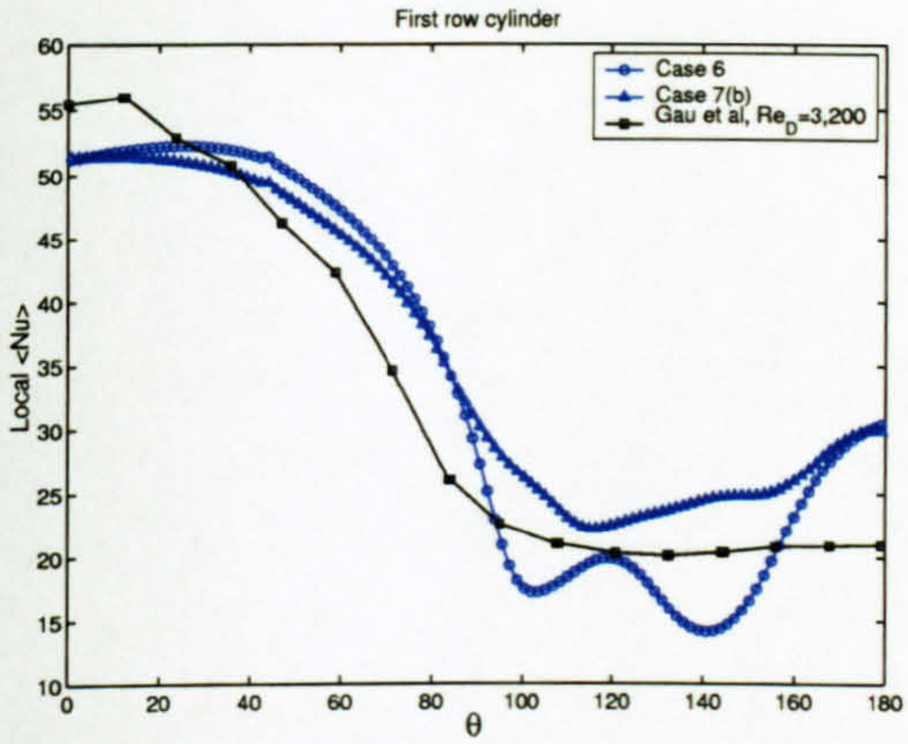

(a) upstream row local $< Nu >$

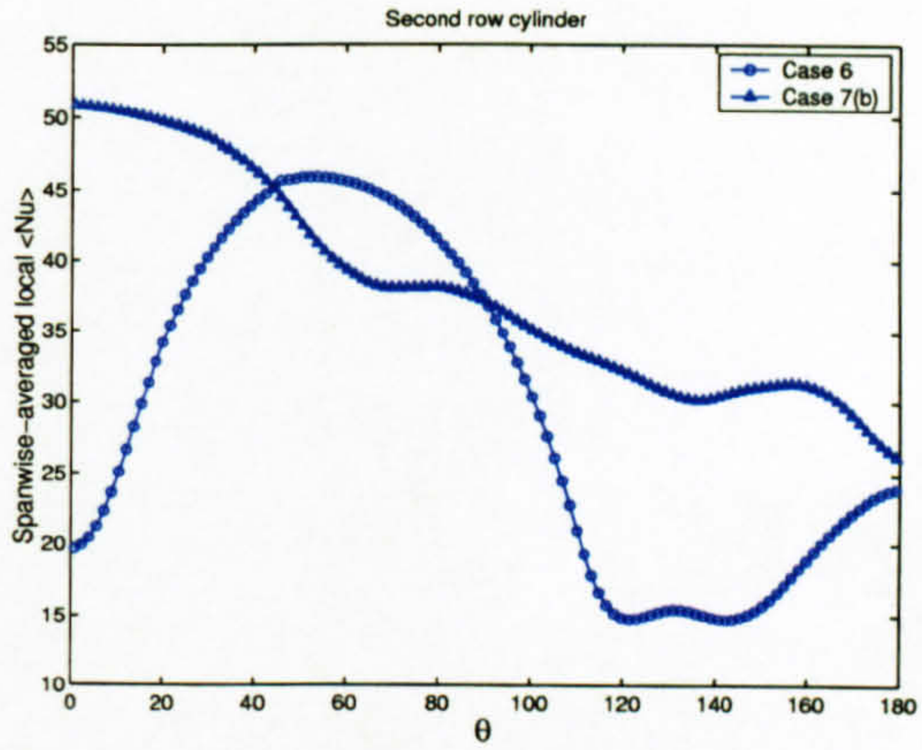

(b) downstream row $< Nu >$

Figure 6.22: The time- and spanwise-averaged local Nusselt numbers predicted for cases 6 and 7(b).

transfer rate in the front part of the second row is strongly determined by the vortex shedding in the gap between the first and second rows. Locked-on vortex shedding mode predicted for case 4 has the highest Nusselt number which explains why VandenBerghe et al. (1983) found that the external small-amplitude pulsation can increase much the heat transfer rate in front of the second cylinder. The symmetrical vortex formation mode predicted for case 5 gives a lower Nusselt number than the alternate vortex shedding mode predicted for case 2. However it should be noted that the symmetrical mode gives higher Nusselt number than the one predicted for case 6 for the front part of the second cylinder. Although the heat transfer around the third row predicted for case 5 is still smaller than the other two, the differences of the further downstream rows predicted for cases 2, 4 and 5 are relatively small, suggesting the pulsation effects on the heat transfer in the downstream rows is small. The maximum local heat transfer rate exists near to the location around 35^o for those downstream rows. In comparison, for case 6 the maximum heat transfer is located at around 55^o for the second cylinder which corresponds to the location of impingement of the separated shear layer on the front of the cylinder. Therefore, it can be concluded that alternate vortex shedding mode will have higher heat transfer rate than the reattachment mode, because the rolling-up vortex sweeps more quickly the cold fluid to the front part of the downstream cylinder. For smaller spacing inline tube bundle, the reattachment mode could exist also in front of the third row and even downstream rows. For instance, Murray (1993) measured the single-phase heat transfer over an inline tube

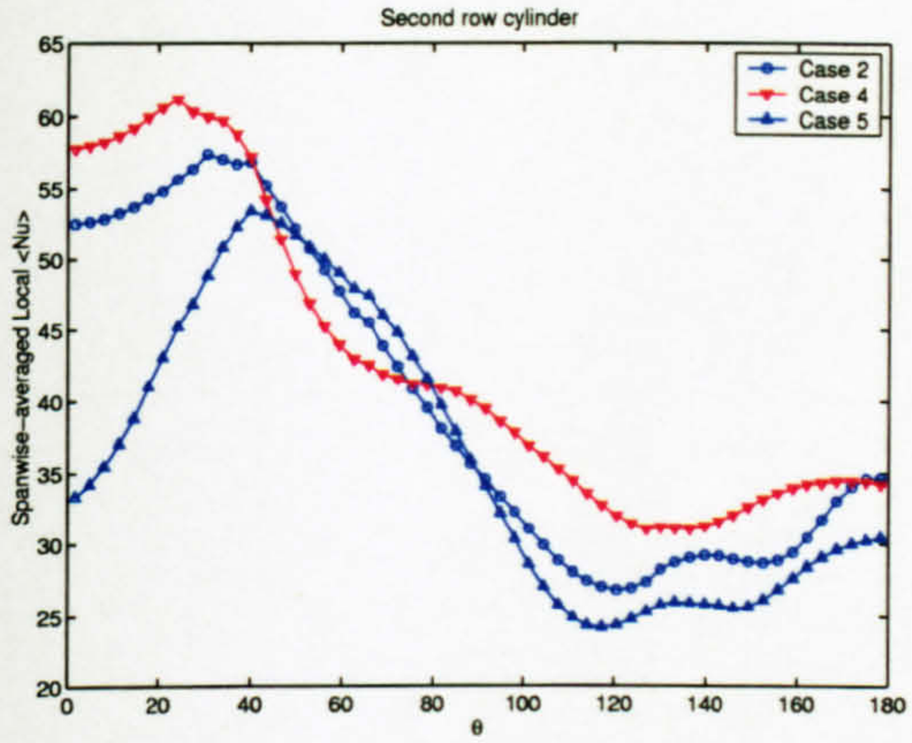

(a) row 2 local $< Nu >$

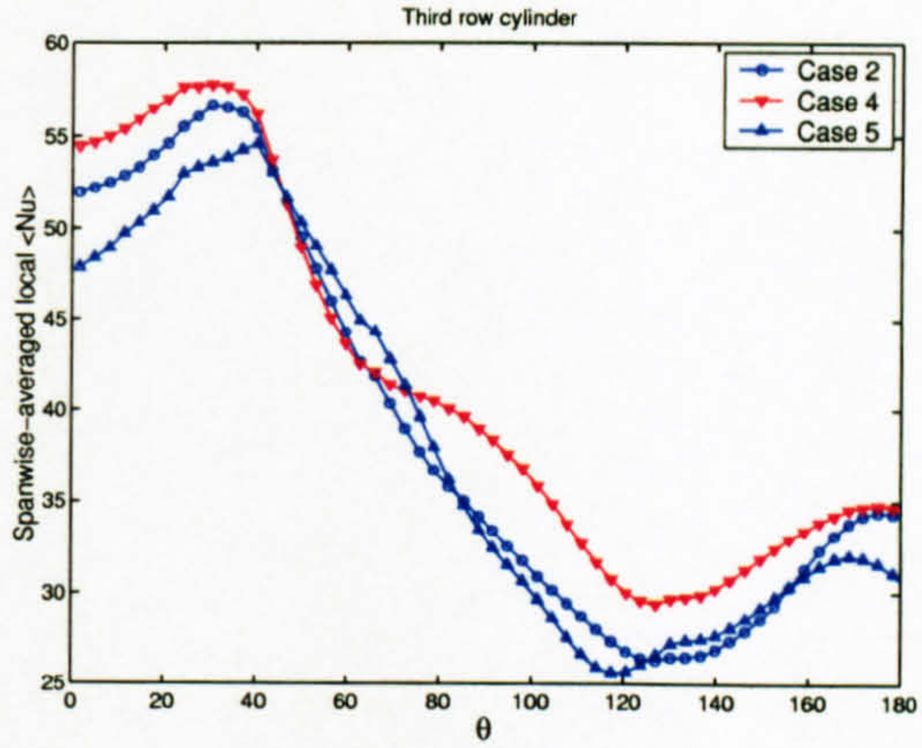

(b) row 3 local $< Nu >$

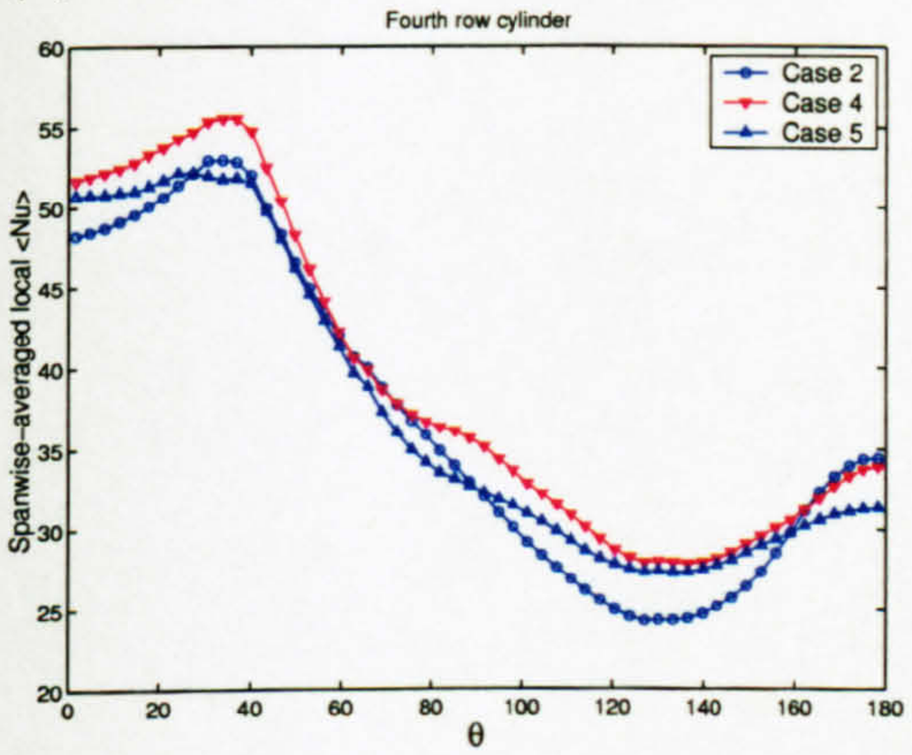

(a) row 4 local $< Nu >$

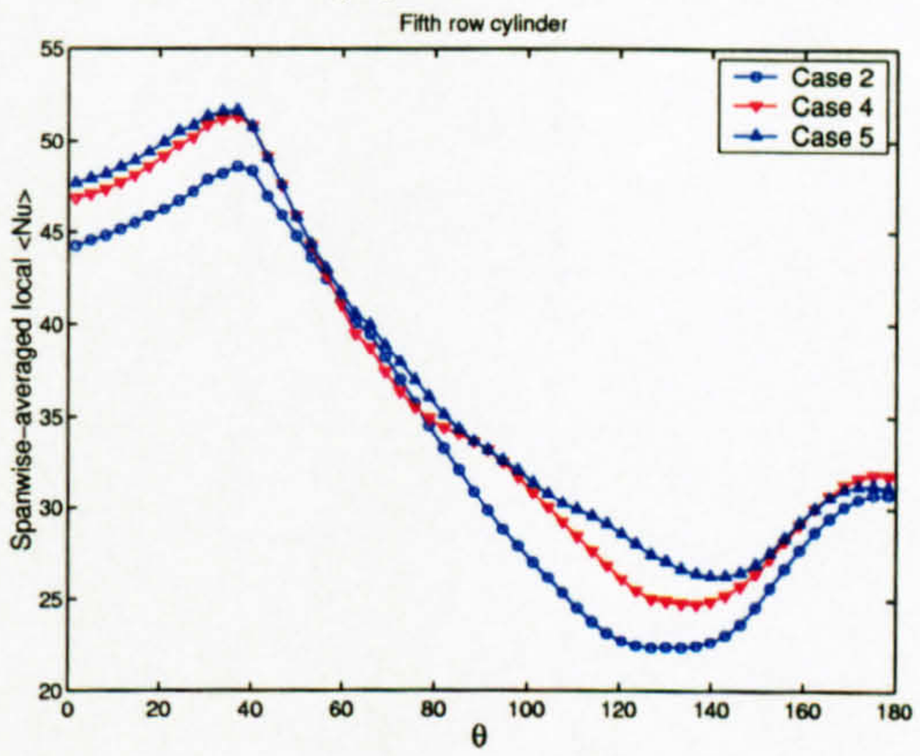

(b) row 5 local $< Nu >$

Figure 6.23: The time- and spanwise- averaged local Nusselt number predicted by Cases 2, 4 and 5.

bundle with pitch-diameter ratio 1.75 at a Reynolds number $Re_{gap} = 6,000$. She found that the heat transfer rate in the front part of the third row is still as low as the one of the second cylinder suggesting that the separated shear layers from the second cylinder reattached to the front of the third cylinder and formed two counter-rotating vortices occuping the gap between the second and third cylinders.

The instantaneous temperature field for cases 2, 4 and 5 are shown in figure 6.24, 6.25 and 6.26 respectively. The time instants correspond to the ones shown for the instantaneous velocity patterns in figures 6.8, 6.9 and 6.10 respectively. It is clear from the contours that the transverse velocity amplitude of the vortex shedding for case 4 is bigger than the one for case 2. It could be seen from figures 6.24 and 6.25 that the transverse mixing of hot and cold fluid is stronger for case 4. The instantaneous temperature pattern behind the first row for case 5 reflects the strong correlation between the symmetrical vorticity pattern and the temperature

field. The temperature pattern of case 2 also shows strong correlation with the vorticity pattern. However, there are some similarities between cases 2 and 5 for the downstream rows indicating that the heat transfer rate and the turbulence intensity level is about the same.

6.7 Closure

Several LES runs have been performed for the cross-flow over the six-row inline tube array. The results were compared in detail with the LDA measurements by Konstantinidis et al. (2000). Despite the fact that r.m.s velocities in the flow-lane region are affected by the freestream turbulence level, the overall agreement between the prediction and the measurement data in the near wake regions is satisfactory. Both the Smagorinsky model and dynamic model predict the mean velocity profile very well. Overall, the two different subgrid-scale models give very similar patterns of the mean velocity field for both steady and locked-on pulsatile cross-flow. The LES calculation also captured the symmetrical vortex formation mode when the external pulsating frequency is three times the vortex shedding frequency which is in agreement with the finding by Konstantinidis et al. (2003*b*).

The study of cross-flow over the two-row inline tube array can be viewed as a grid dependence study for the LES predictions. It can be concluded that LES calculations with coarse grid resolution predict an alternate vortex shedding behind the first row, which is different from the two standing vortices reported by the existing experimental investigations. The refined grid can predict correctly the two standing vortices provided that the initial flow field was obtained from a laminar solution. However, the present tube spacing lies in the bistable transition region, which is proved by the fact that *two vortex streets* regime is predicted if the initial flow field was provided from the fully-developed pulsatile flow.

The lift and drag coefficients as well as the heat transfer rate around the first two rows are affected a lot by the external small-amplitude pulsation. For the first row, the locked-on vortex shedding mode possesses the highest mean drag and r.m.s lift coefficients as well as the highest heat transfer rate after the separation point. For the second row, the LES calculations of the flow across a two-row inline tube bundle at the *two vortex streets* regime gives much higher mean drag coefficient as well as heat transfer rate in the front part than the *reattachment* regime. LES calculations of the flow across a six-row inline tube bundle demonstrated that the locked-on vortex shedding mode gives the highest mean drag and r.m.s lift

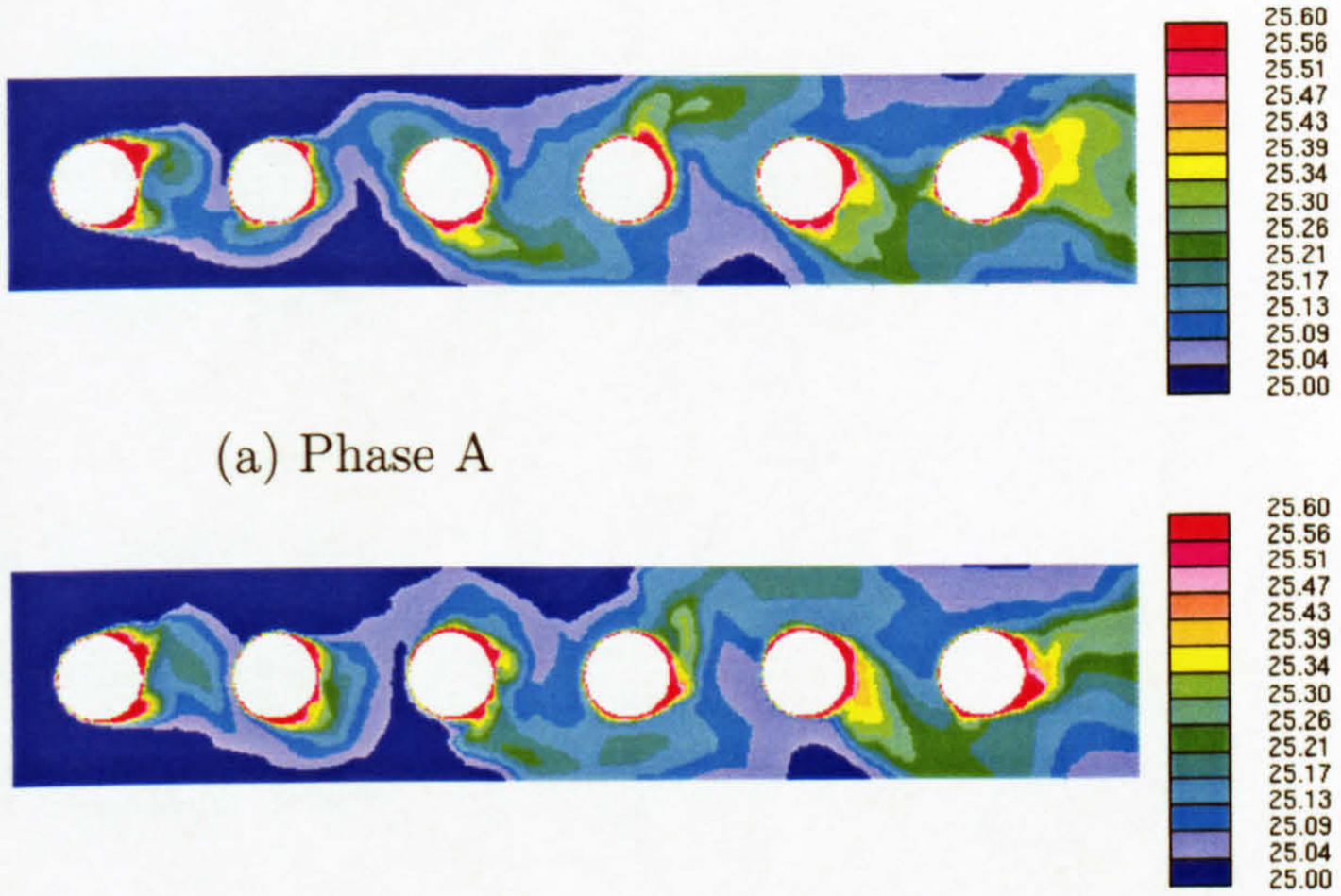

(a) Phase A

(b) Phase B

(c) Phase C

(d) Phase D

(e) Phase E

Figure 6.24: The contour of temperature field for Case 2.

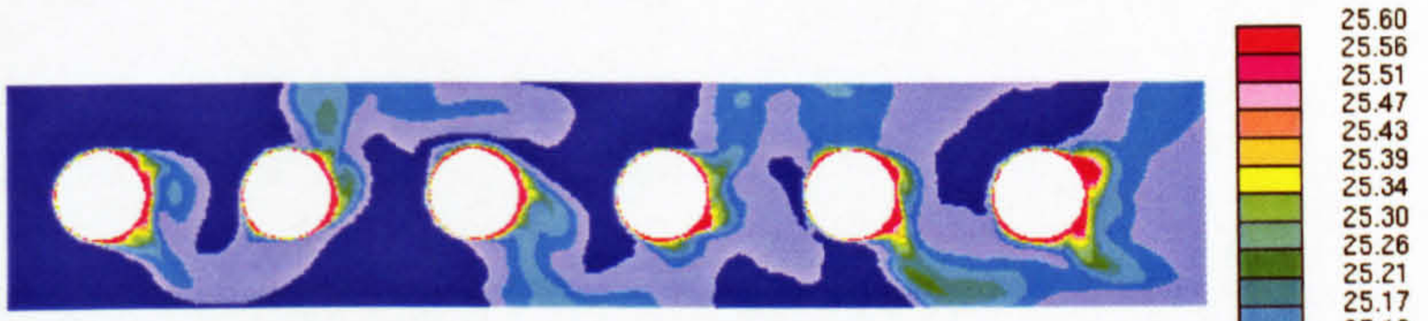

(a) Phase A

(b) Phase B

(c) Phase C

(d) Phase D

(e) Phase E

Figure 6.25: The contour of temperature field for Case 4.

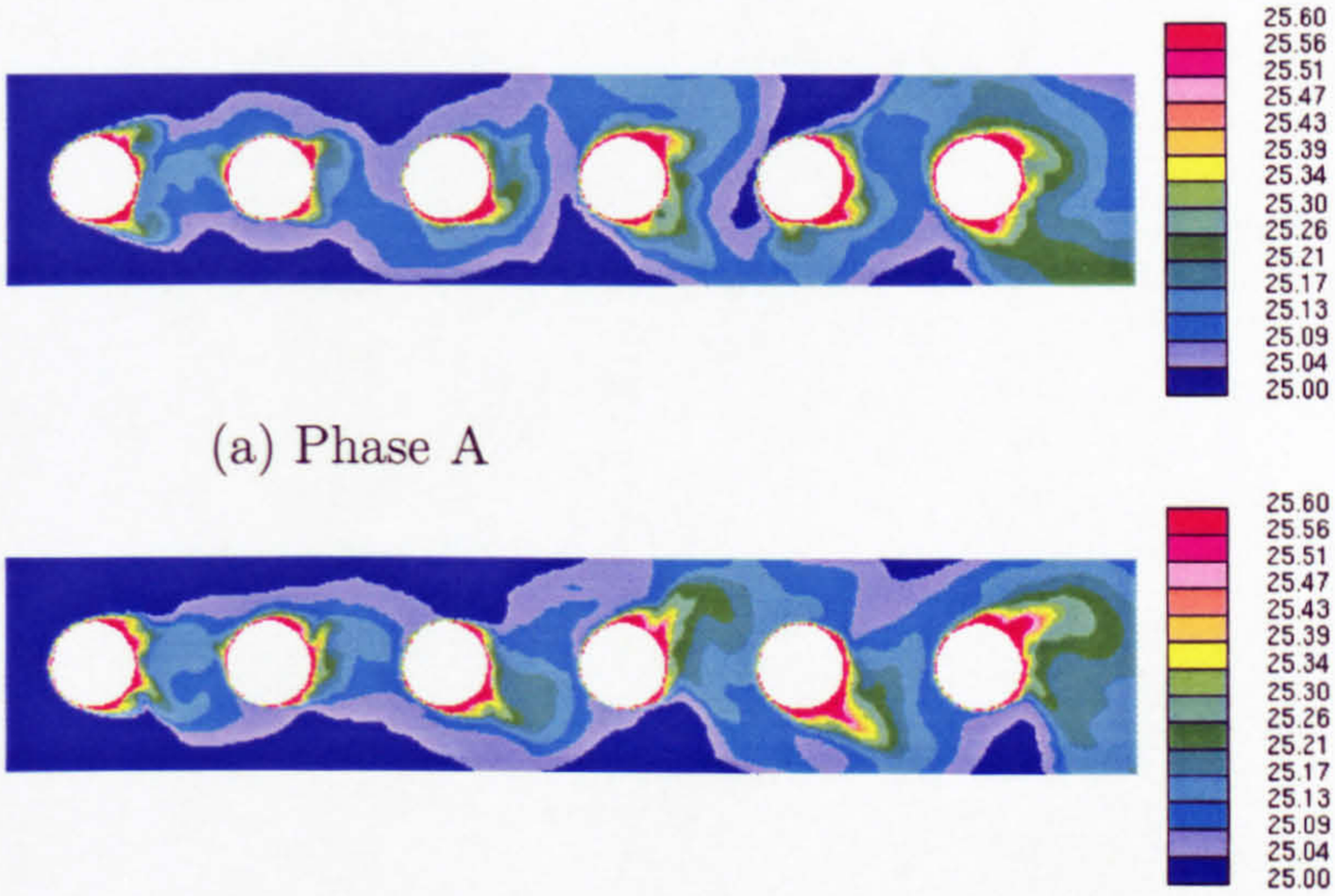

(a) Phase A

(b) Phase B

(c) Phase C

(d) Phase D

(e) Phase E

Figure 6.26: The contour of temperature field for Case 5.

coefficients for the second row as well as the highest heat transfer rate in its front part. The effect of the pulsation on the mean drag, r.m.s lift coefficients as well as the heat transfer rate for further downstream rows is relatively small.

As expected, there is a strong correlation between the vorticity and the temperature fields.

Chapter 7

LES OF TURBULENT CROSS-FLOW AND HEAT TRANSFER OVER A STAGGERED TUBE BUNDLE

7.1 Introduction

Many experimental investigations have been performed on staggered arrays due to their wide use in heat exchangers. Standard arrangements can be roughly categorized into three configurations: (1) Rotated square array, investigated by Simonin and Barcouda (1988), Weaver et al. (1993) and Price et al. (1995); (2) Normal triangular array, investigated by Polak and Weaver (1995) and Oengören and Ziada (1998); (3) Parallel triangular array, investigated by Price et al. (1995) and Ziada and Oengören (2000). The staggered array used by Balabani and Yianneskis (1996, 1997) ($S_L = 1.6D$ and $S_T = 3.6D$) is very close to a rotated square array with pitch ratio 2.41 which has been studied by Weaver et al. (1993).

Oengören and Ziada (1998) investigated the vortex shedding phenomena inside several normal-triangle tube arrays. They found three vortex shedding frequencies inside the normal triangle array with a pitch-diameter ratio of 2.08 at a Reynolds number $Re_{gap} = 26,300$, more specifically a high frequency f_{v2} associated with the first row cylinder; a low frequency f_{v1} associated with the alternate vortex shedding from the downstream row cylinder; and a third frequency f_{vd} resulting

[0]Some results shown in this chapter were published in Liang and Papadakis (2004*a*).

from the nonlinear interaction of f_{v2} and f_{v1}. They also demonstrated that the multiple frequency nature of vortex shedding behind the first few row cylinders is strongly Reynolds number dependent. For instance, if the Reynolds number decreases, the third frequency f_{vd} tends to disappear.

Mandhani et al. (2002) solved directly the two-dimensional Navier-Stokes and energy equations using a simplified outer cylindrical cell boundary based on the size of the cylinder and the porosity of the assemblage of cylinder arrays. The maximum Reynolds number investigated was $Re_D = 500$. The characteristics of heat transfer were highly related to the values of porosities employed. The effect of the actual geometrical arrangement of the array could not be correctly represented because the computational mesh was not actually representing the real physical tubes.

For the time being, RANS models are not capable of accurately producing the Reynolds stresses of the turbulent flow across a closely spaced staggered tube array. Comparing with the measurements of Simonin and Barcouda (1988), Watterson et al. (1999) have demonstrated that the $k-\epsilon$ model gives poor predictions of the Reynolds stresses in the cylinder wakes. Rollet-Miet et al. (1999) also found that RANS with the $k-\epsilon$ turbulence model predicted the mean profiles very well, but the shear stress profiles did not match well the measurement data. For a staggered tube array with larger pitch-to-diameter ratio, Bouris and Bergeles (1999) have demonstrated that a two-dimensional unsteady calculation with a subgrid scale model has the potential to predict accurately tube bundle flows where turbulence anisotropy, transitional effects and flow field periodicity are important aspects and which are difficult for traditional RANS models to capture. Rodi (1997) also pointed out that standard RANS models are incapable of predicting accurately the vortex shedding behaviour in flow around bluff bodies.

Heat transfer inside a staggered tube array has been much less investigated compared to the flow field. Aiba et al. (1982*b*) have measured the turbulent heat transfer over a 7-row cylinder normal triangle array with pitch-to-diameter ratio of 1.6. Murray and Fitzpatrick (1991) and Murray (1993) also presented some single-phase air flow heat transfer measurements around a cylinder in a normal triangle array with a pitch-to-diameter ratio equal to 2. However, their arrangements are all somewhat different from the one considered in this chapter.

The rest of this chapter is arranged as follows. First, the computational conditions for all runs performed for the staggered tube array are presented. This is followed by a detailed description of the instantaneous flow fields for the different

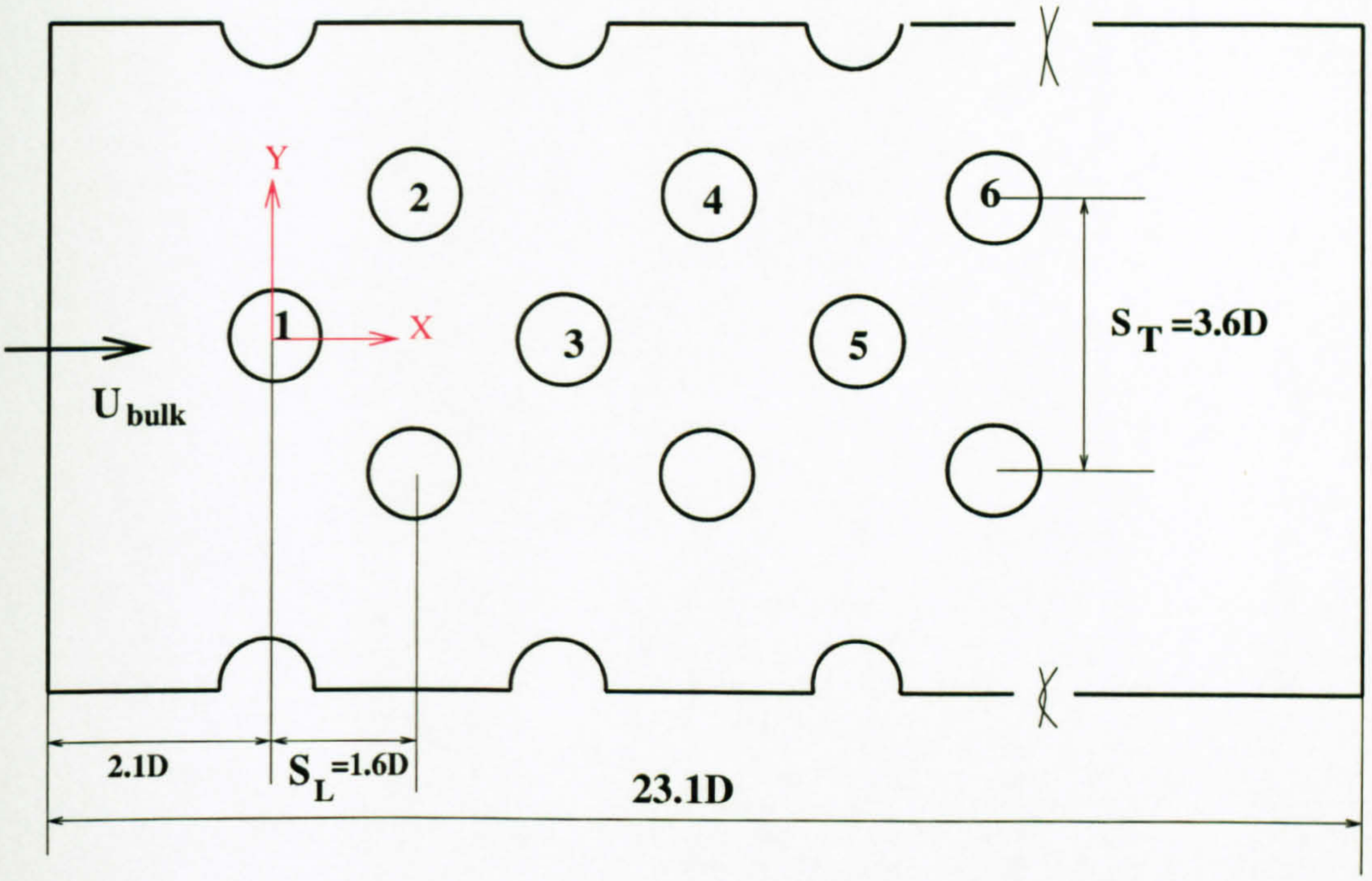

Figure 7.1: Illustration of the physical configuration of the six-row staggered tube array and tube numbering.

cases examined. The subsequent section presents the time-averaged first-order and second-order statistics together with detailed comparison with available measurement data. Subsequently, lift and drag forces are presented and discussed for all rows of cylinders. Finally, time-averaged and instantaneous heat transfer results are presented.

7.2 Computational conditions

The computational domain is described in a Cartesian coordinate system (x,y,z) where the x axis is fixed as the inlet flow condition (streamwise), the z axis is parallel to the cylinder axis (spanwise), while the y axis (transverse or cross-wake) is perpendicular to both the x and z axes. The computational domain is based on the set-up of Balabani and Yianneskis (1996) with spacings $S_L \times S_T = 1.6D \times 3.6D$. Two meshes are used; one coarse mesh which covers all the six-row cylinders in the experiments and another finer mesh which covers only the first two rows of cylinders where a double number of cells are used along the periphery of the full cylinders.

The X-Y sections of the six- and two-row staggered tube bundle configurations

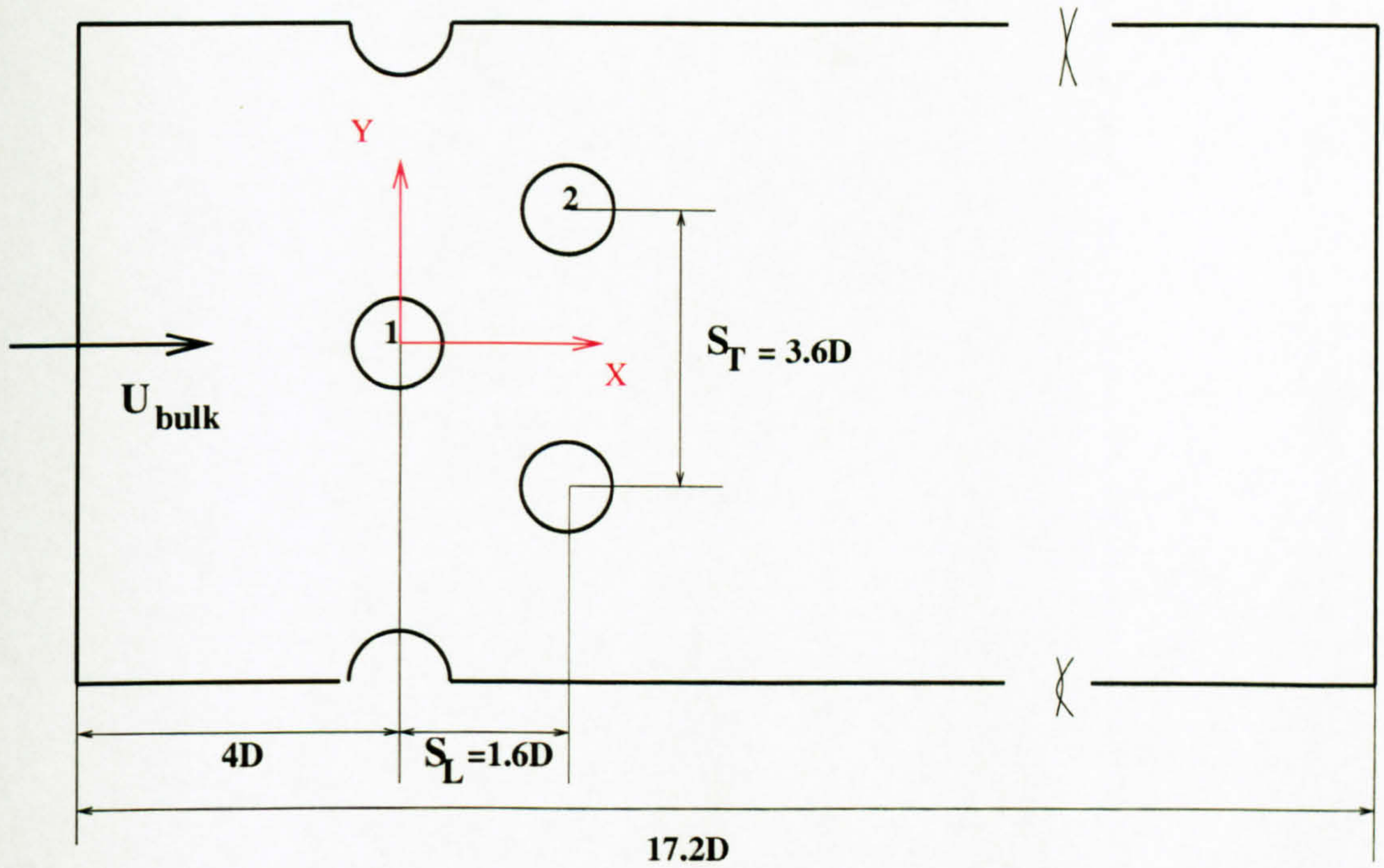

Figure 7.2: Illustration of the physical configuration of the two-row staggered tube array and tube numbering.

are shown in figures 7.1 and 7.2 respectively. Figures 7.3 and 7.5 show the meshes for the six- and two-row inline tube arrays respectively. The computational parameters for the different cases examined are summarised in tables 7.1 and 7.2. A total of 96 and 192 cells are placed along the periphery of each full cylinder for the 6-row and 2-row staggered tube bundle repectively. A closer view of the cell distribution around a full cylinder can be seen in figures 7.4 and 7.6 respectively. A constant expansion factor 1.16 is used for the cell spacings in the radial direction away from each cylinder wall. Twenty equally-spaced layers are used in the spanwise direction for both meshes with spanwise length $L_z = \pi D$ which is the same as the resolution of Benhamadouche and Laurence (2003). The smallest cell spacing in the radial direction is around $\Delta r_{min}/D = 1.8 \times 10^{-3}$, which is comparable to the finest mesh used in Beaudan and Moin (1994) ($\Delta r_{min}/D = 1.25 \times 10^{-3}$) for a single cylinder. As shown in table 7.2, the coarse mesh calculations for the six-row staggered tube array at $Re_{gap} = 8,600$ are all performed with a fixed time step size, which gives the maximum and mean CFL numbers of 2.6 and 0.27 respectively. The calculations with the refined resolution of the two-row inline tube array are performed at the same time-step size too, which gives maximum and mean CFL numbers of 2 and 0.29 respectively. Case 4 represents a run with the coarse mesh at a lower Reynolds number $Re_{gap} = 3,400$, which is identical to the one used for

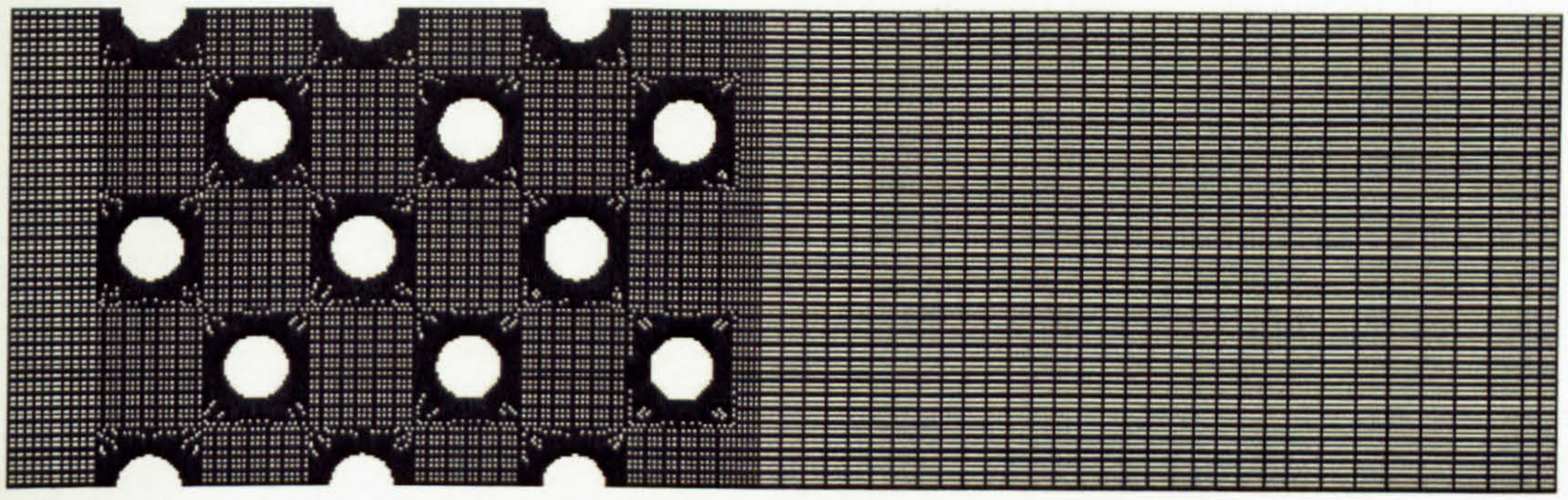

Figure 7.3: The computational mesh of the six-row staggered tube bundle.

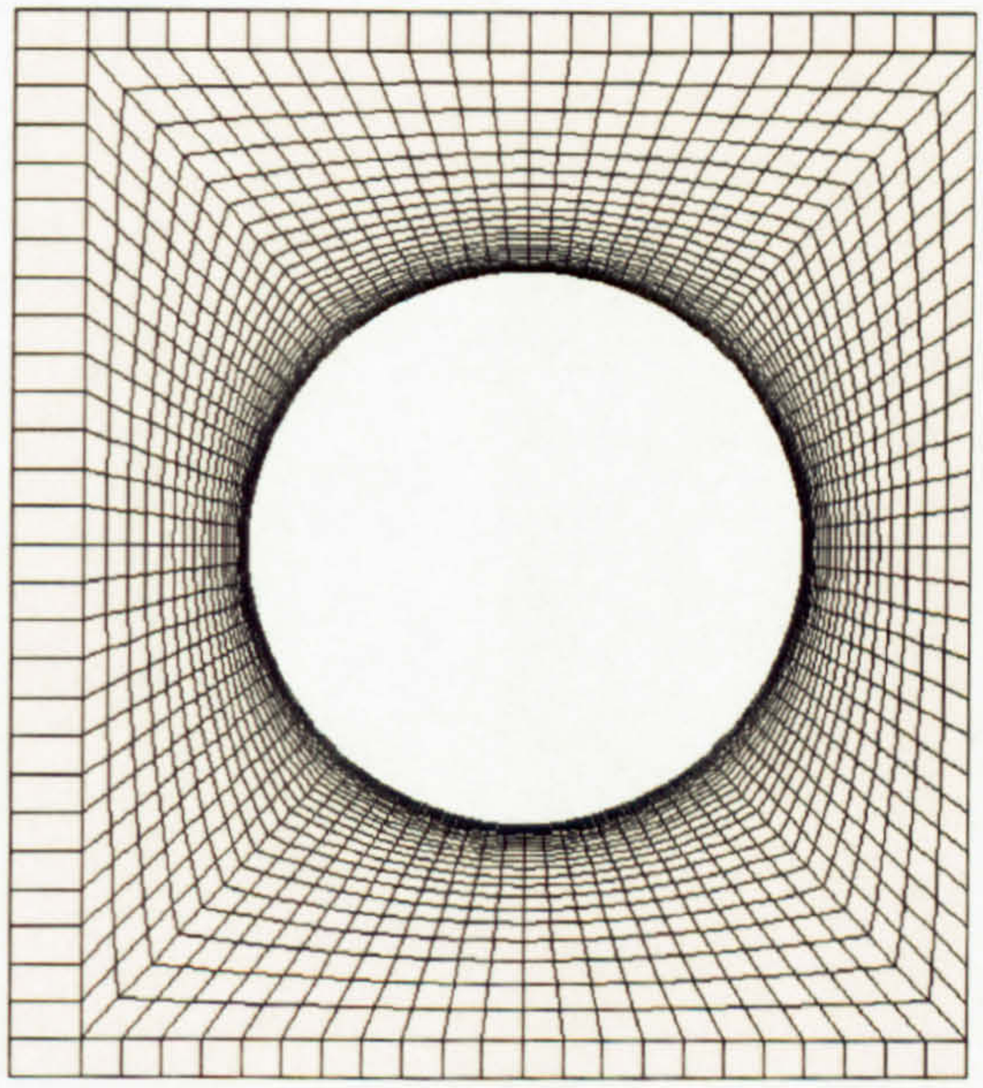

Figure 7.4: The computational grid around the first cylinder of the six-row staggered tube bundle.

the inline tube array cases shown in the previous chapter 6.

7.3 Instantaneous flow field inside the staggered tube array

The variation of lift coefficients for all rows is shown in figure 7.7. In the same figure, the four phases A-D for which the instantaneous velocity and vorticity fields were stored are also denoted. The amplitude of C_L for the first cylinder is very small because the vortex shedding fluctuates with a small amplitude in

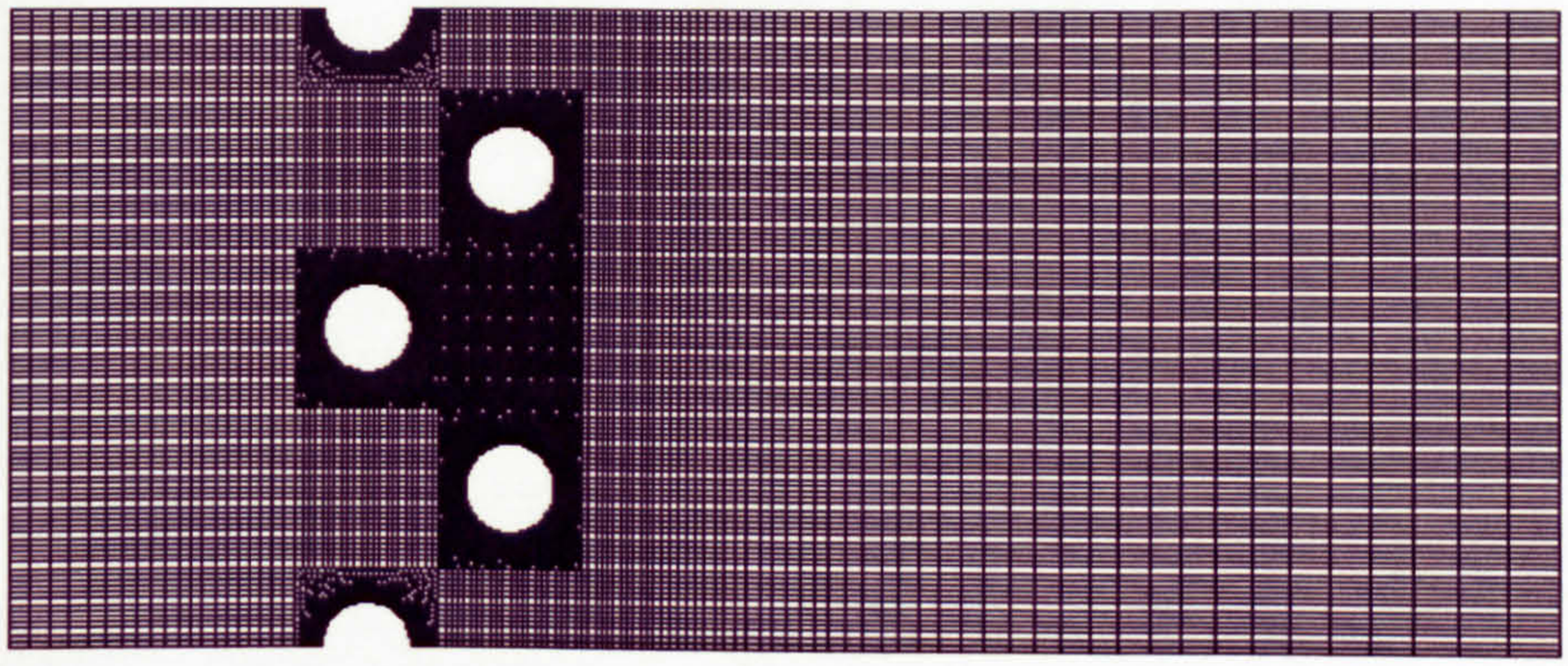

Figure 7.5: The computational mesh of the two-row staggered tube bundle. The cells are locally refined along the periphery of the full cylinders.

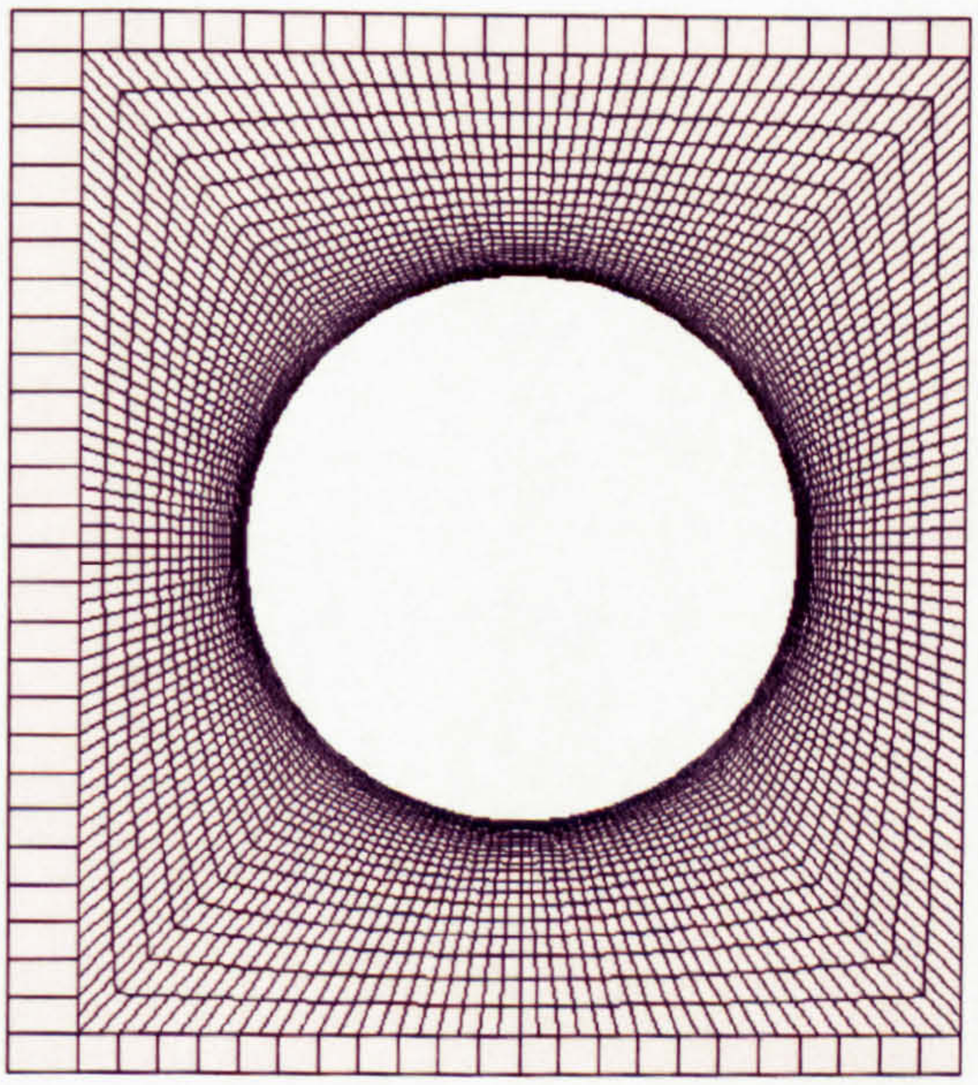

Figure 7.6: The computational grid around the first cylinder of the two-row staggered tube bundle.

Staggered tube bundle mesh parameters								
Type	N_r^{eff}	N_{total}	$\Delta r_{min}/D$	N_z	S_L	S_T	r_{exp}	N_{gap}
6-row Staggered	96	785,920	1.8×10^{-3}	20	1.6D	3.6D	1.16	36
2-row Staggered	192	550,320	1.8×10^{-3}	20	1.6D	3.6D	1.16	36

Table 7.1: Grid parameters for staggered tube bundle arrangements. N_{gap} refers to the cell numbers used along the streamwise direction between the first- and second-row cylinders, and N_r^{eff} refers to the number of cells used along the periphery of the full cylinders.

LES cases investigated for staggered tube bundle							
Name	Arrangement	Re_{gap}	Model	f_e Hz	$\Delta u/u_\infty$	CFL_{mean}	CFL_{max}
Case 1	Six-row	8,600	Smag.	0.	0	0.27	2.6
Case 2	Six-row	8,600	Smag.	27.4	0.1	0.27	2.7
Case 3	Two-row	8,600	Smag.	0.	0	0.29	2
Case 4	Six-row	3,400	Smag.	0.	0	0.25	2.2

Table 7.2: Investigated cases of staggered tube array.

the transverse direction. The amplitudes of C_L for the 2nd-5th row cylinders are roughly equal to each other. However, the one for the sixth row is smaller most likely because no further cylinder exists behind it. The velocity vectors of the last three rows (4, 5 and 6) shown in figure 7.9 are much more erratic than the first 3 rows shown in figure 7.8 due to the higher level turbulence. The approaching flow is still laminar in front of both the first and second cylinders. The vortex formation length behind the first cylinder is the longest at any time instant. The one behind the second cylinder is shorter because the local effective Reynolds number is higher (the cylinder sees the gap velocity instead of the bulk velocity). A much shorter vortex formation region is formed behind the third cylinder due to the upstream turbulence. Due to the upstream turbulence, it can be observed that the third cylinder wake has higher transverse velocity fluctuations than the first cylinder wake. There is a strong correlation between the variation of lift coefficient and the observed vorticity patterns, similar to the one observed for the single cylinder in chapter 5. For example the lift coefficient of the second cylinder reaches the minimum close to phase C and the one of the third cylinder reaches the minimum at phase B. In both cases, the minimum of lift coefficient results from a high vorticity field accompanied with a lower pressure region which is formed in the lower part of the shear layer.

Figure 7.10 shows the cross-wake velocity frequency spectra. Two frequencies are detected behind the first and the second row cylinders. The corresponding Strouhal numbers are $St^1_{gap} = 0.26$ and $St^2_{gap} = 0.35$ based on the gap velocity, or $St^1_{bulk} = 0.37$ and $St^2_{bulk} = 0.49$ based on the bulk velocity. It is noted that these figures are very close to the ones obtained by Weaver et al. (1993) (0.37 and 0.51 based on the bulk velocity) behind the first and the second row cylinders for an arrangement very similar to the one examined in this chapter. Also in agreement with Weaver et al. (1993), the higher frequency disappears in the present simulation in the rows further downstream. This results from vortex shedding at a higher

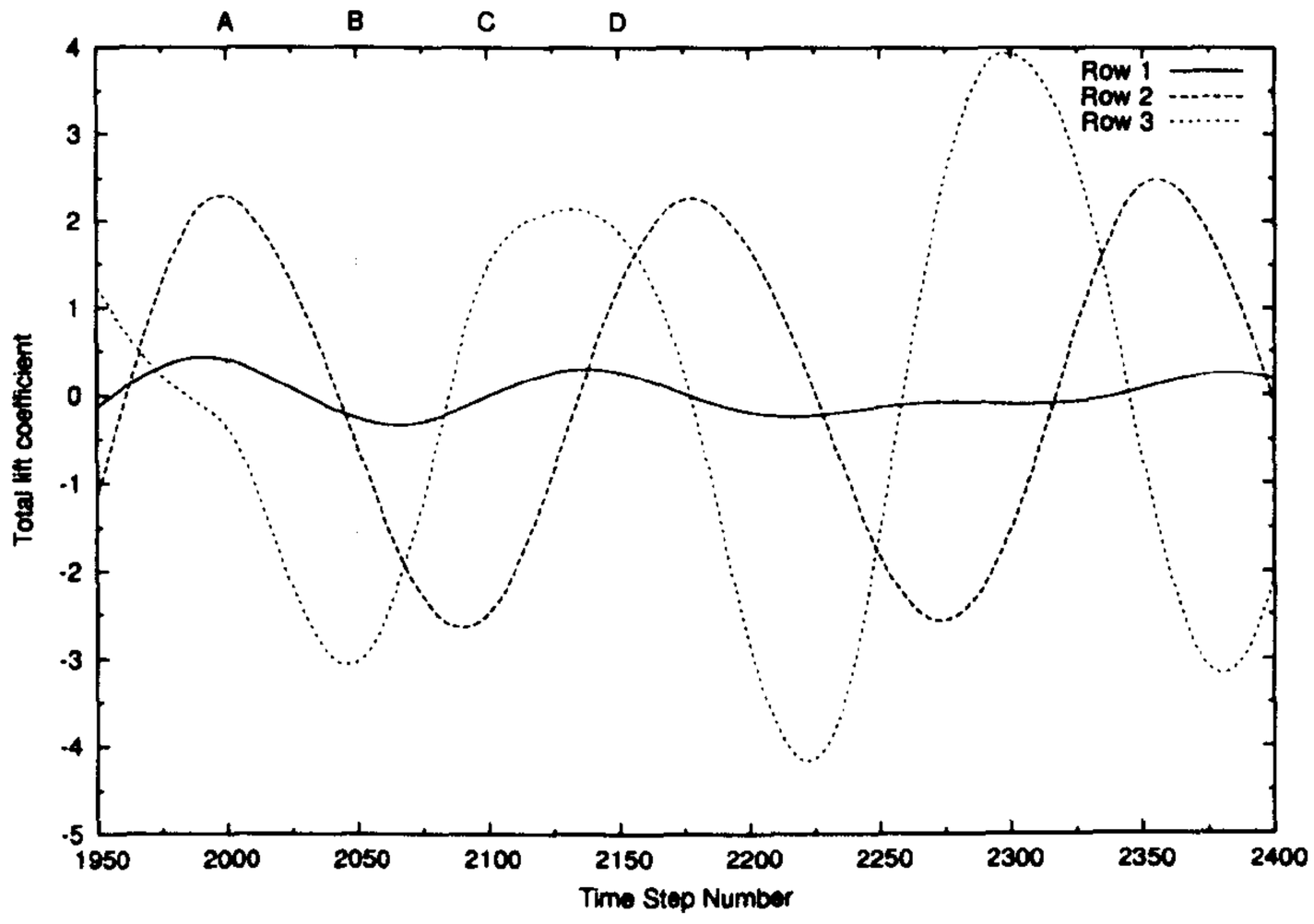

(a) 3 upstream rows

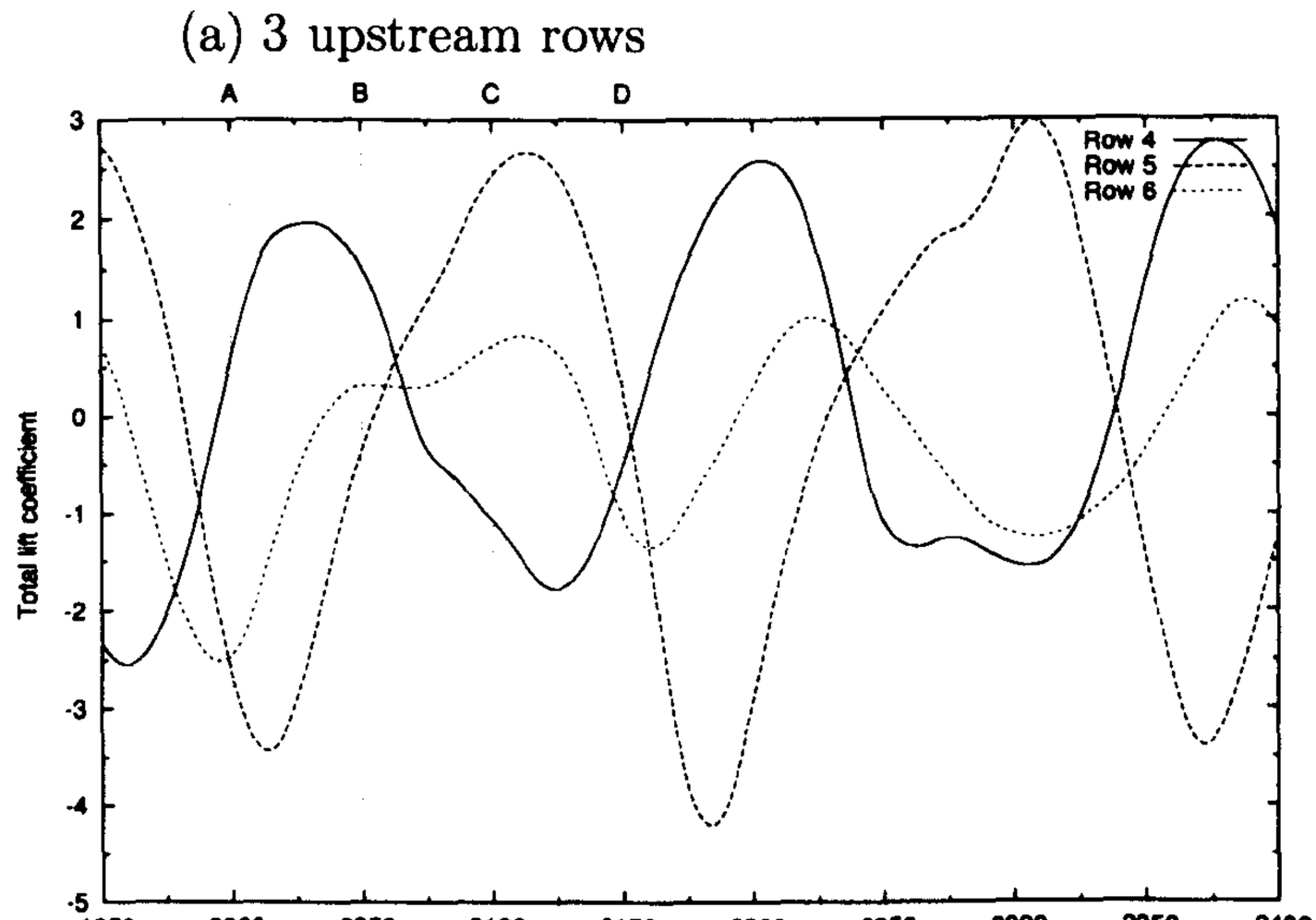

(b) 3 downstream rows

Figure 7.7: The lift coefficients for the 6-row cylinders.

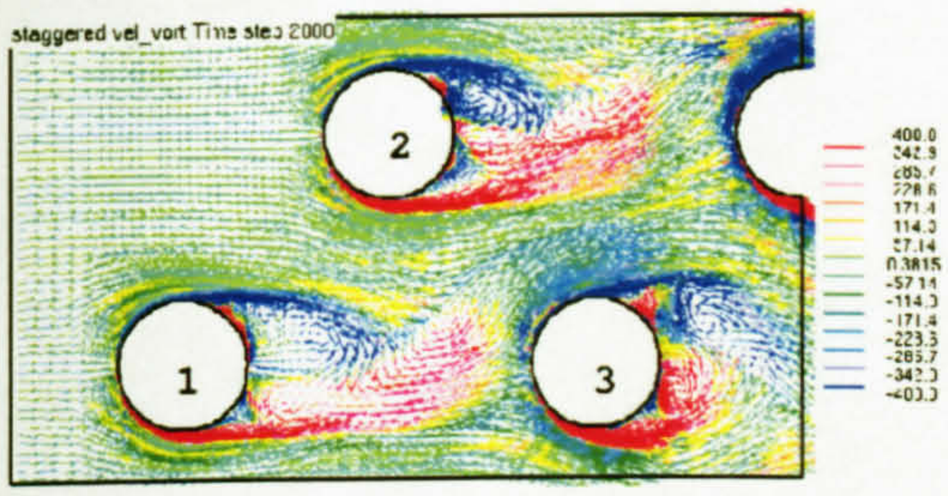

(a) Phase A

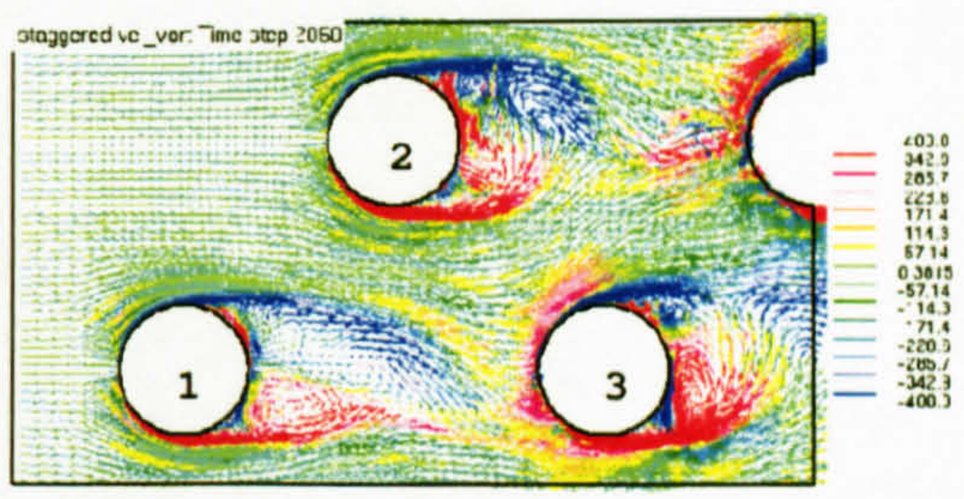

(b) Phase B

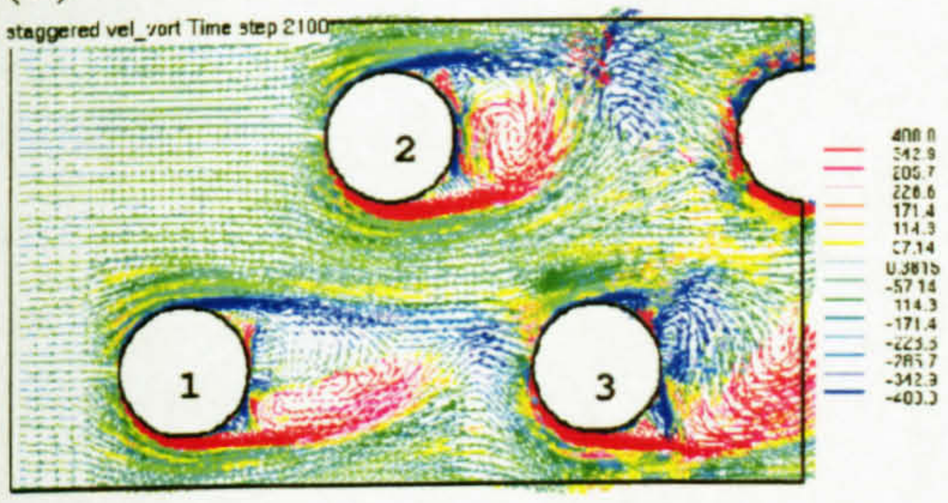

(c) Phase C

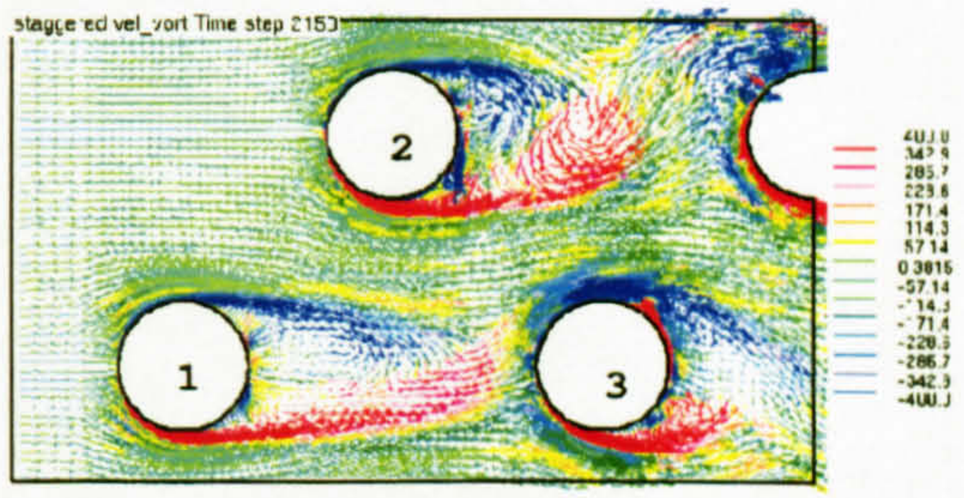

(d) Phase D

Figure 7.8: Instantaneous velocity vectors colour-coded with the values of spanwise vorticity in the six-row staggered tube array (3 upstream rows).

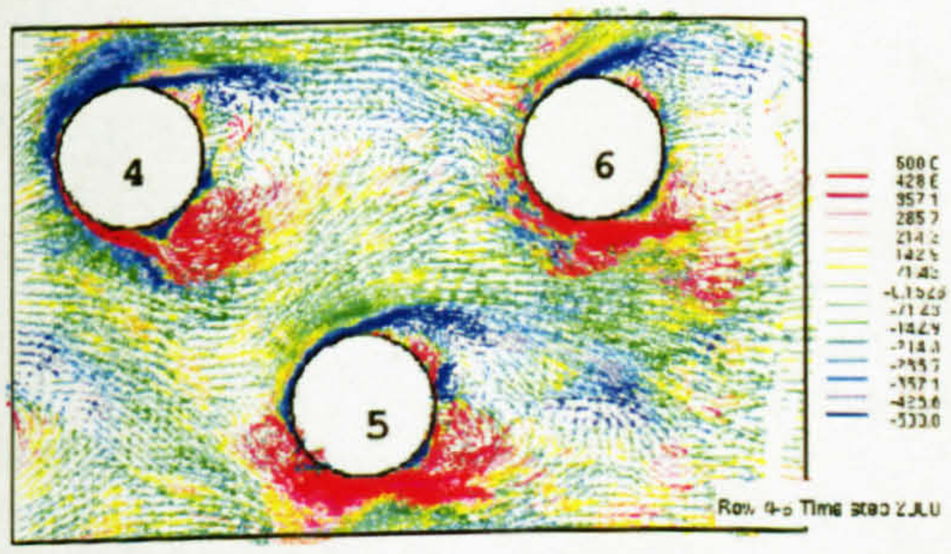

(a) Phase A

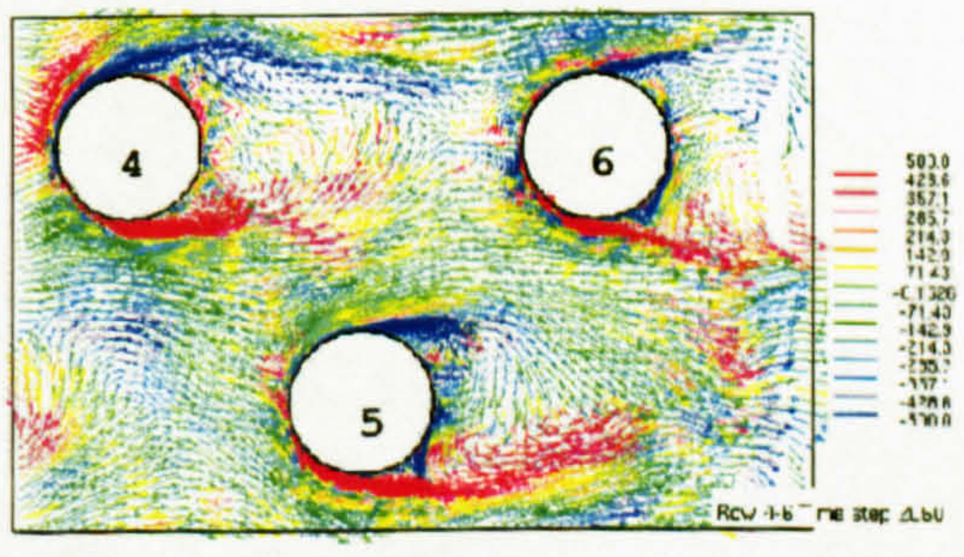

(b) Phase B

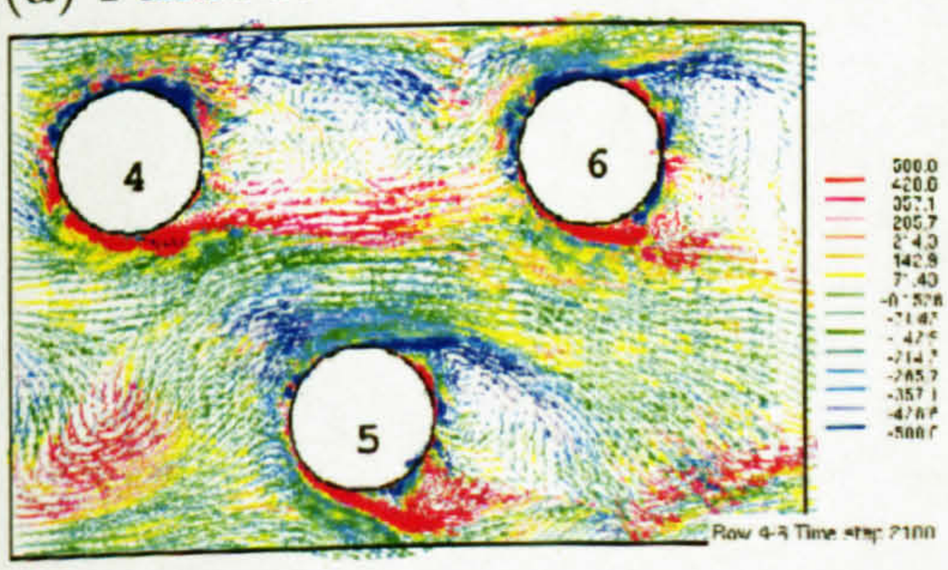

(c) Phase C

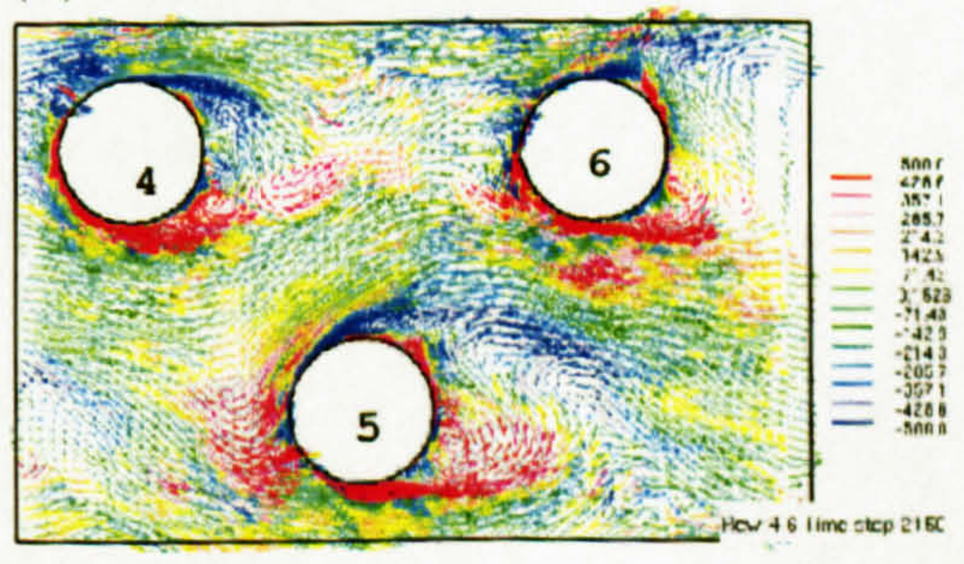

(d) Phase D

Figure 7.9: Instantaneous velocity vectors colour-coded with the values of spanwise vorticity in the six-row staggered tube array (3 downstream rows).

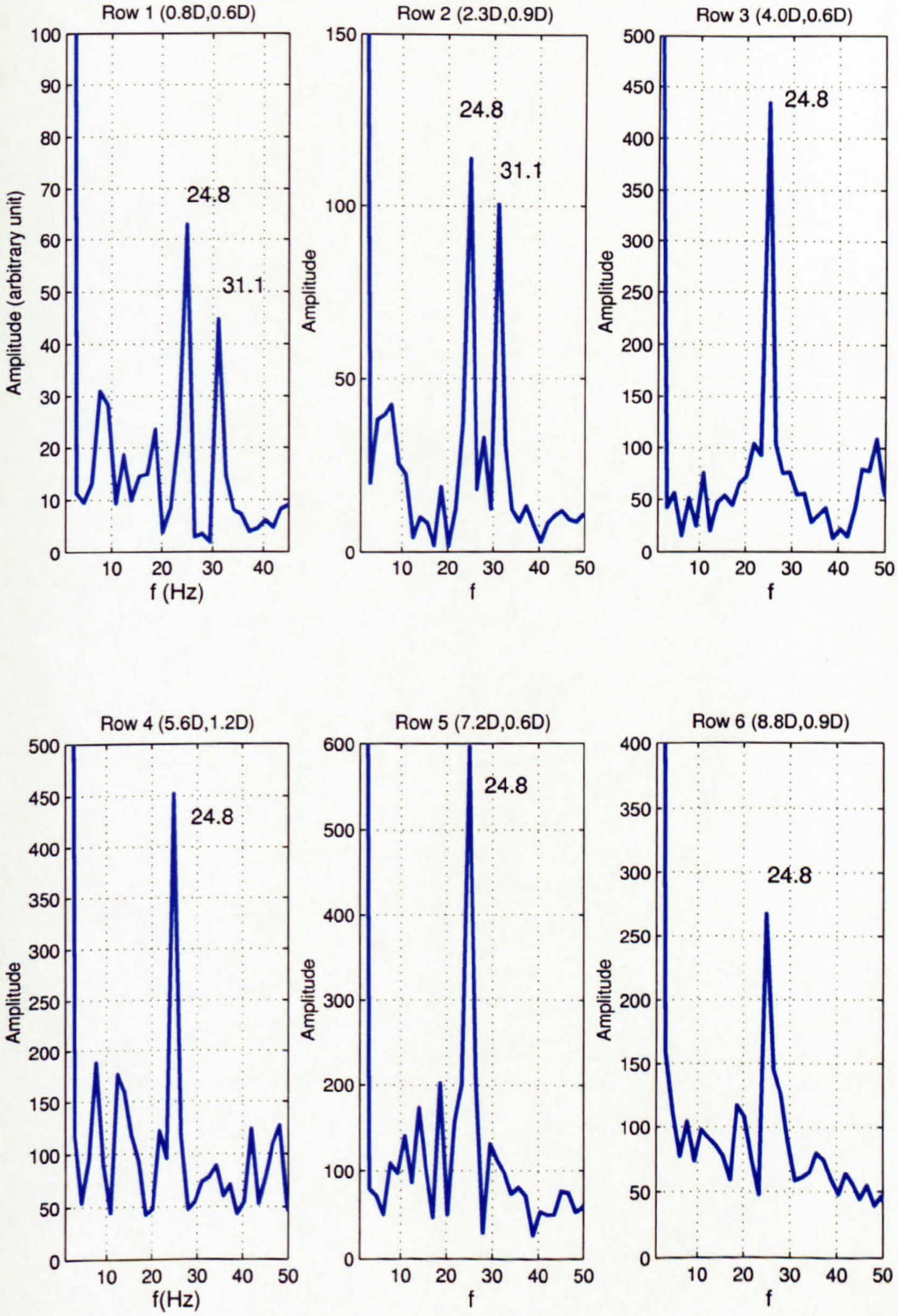

Figure 7.10: Cross-wake velocity spectra of the steady cross flow over the staggered tube bundle for case 1.

frequency from the first row and the one at a lower frequency from the second row. In fact Case 3 has justified that when further downstream cylinders are not present, the vortex shedding behind the second row has only one low frequency.

In order to show the effects of different Reynolds numbers, the standard Smagorinsky model is also used to compute the turbulent flow inside the staggered tube array at a Reynolds number of 3,400 (Case 4). Two distinct vorticity shedding frequencies (at Strouhal numbers 0.41 and 0.51) are also obtained behind the first and second rows. Only the low Strouhal frequency persists behind the third row cylinder and further downstream. The reason that Oengören and Ziada (1998) found three vortex shedding frequencies for the first two rows in a normal triangle array can thus be attributed only to the different total number of rows in the staggered tube bundle arrangement. It is also noted that the amplitudes of the peaks for the vortex shedding in the cross-wake direction behind the first cylinder are much smaller than the ones of other cylinders. This fact explains the small amplitude of instantaneous lift coefficient of the first cylinder. The highest amplitude of vortex shedding in the cross-wake direction exists behind the fifth full cylinder. It is also consistent with the amplitude of the instantaneous lift coefficient shown in figure 7.7 (b).

For Case 3, the instantaneous velocity and spanwise vorticity snapshots are obtained according to the phases of the lift coefficient shown in figure 7.11. The 8 time instants shown in figure 7.12 correspond approximately to one shedding period of the vortex behind the second row cylinder. The formation of the recirculation bubble behind the first cylinder at different phases is limited in a narrow wake region in which the transverse motion of the bubble has a very small amplitude. The cross-wake distance travelled by the recirculation bubble behind the second cylinder is clearly wider. It also indicates that transverse velocity fluctuations in this region are higher than those behind the first cylinder. The Fourier transforms of the lift coefficients shown in figure 7.11 demonstrated that the vortex shedding behind the first row cylinder has one high and one low frequency similar to the vortex shedding phenomena in the six-row tube array. However, the vortex shedding behind the second row cylinder only has only one low frequency which shows that the high frequency existing at this location in the six-row staggered tube bundle has now disappeared. The amplitude of instantaneous lift coefficient for the first cylinder predicted for case 3 is slightly higher than the one for case 1. This can be explained by the small effect of suppression of the vortex shedding received from the third cylinder which is absent in case 3.

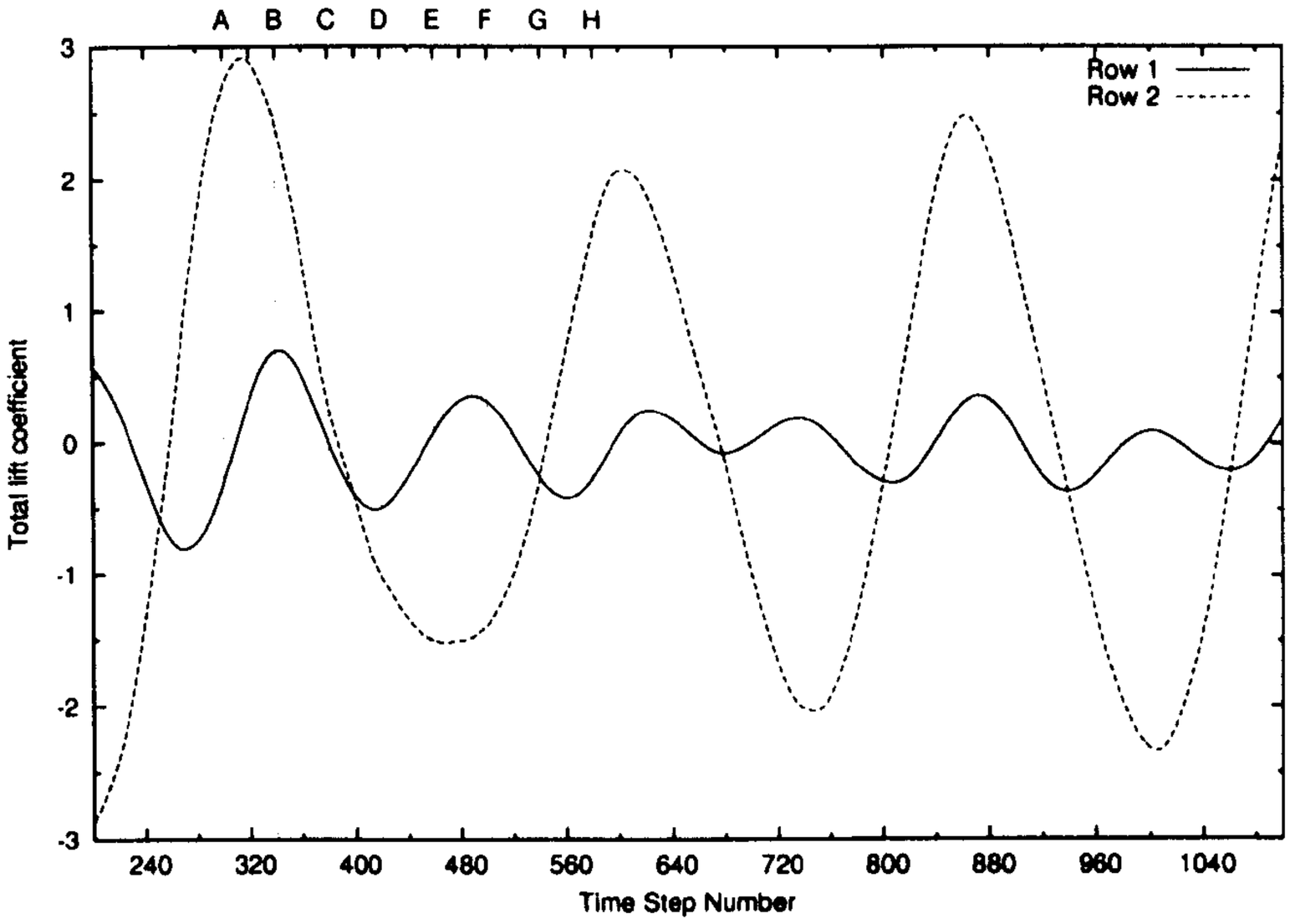

Figure 7.11: The lift coefficient for two-row cylinders of Case 3.

7.4 Time-averaged flow field inside the staggered tube array

The time-averaged flow field is obtained by averaging for more than 8 shedding periods based on the low frequency for the vortex shedding behind the first row after the turbulent flow is fully-developed for all cases presented in table 7.2. Table 7.3 summarises the sizes of recirculation bubbles obtained from the mid-plane for Cases 1, 2 and 4 as well as the measurement data presented in Balabani and Yianneskis (1996). The sizes of the first and third rows are in good agreement with the available experimental formula provided by Balabani and Yianneskis (1996).

$$l_r^1 = -0.76log(Re_{gap}) + 4.66 \tag{7.1}$$

$$l_r^3 = -0.69log(Re_{gap}) + 3.80 \tag{7.2}$$

For example, the length of the recirculation bubble for Case 1 is found to be $l_r^1 = 1.66D$ and $l_r^3 = 1.1D$ behind the first and third row cylinders respectively. They are in very good agreement with results obtained using the experimental formula (which gives $l_r^1 = 1.67D$ and $l_r^3 = 1.09D$).

Although the grid resolution on the first row cylinder is coarser than the resolution of the single cylinder simulation presented in Chapter 5, the recirculation bubble length behind the first row cylinder agrees very well with the one behind

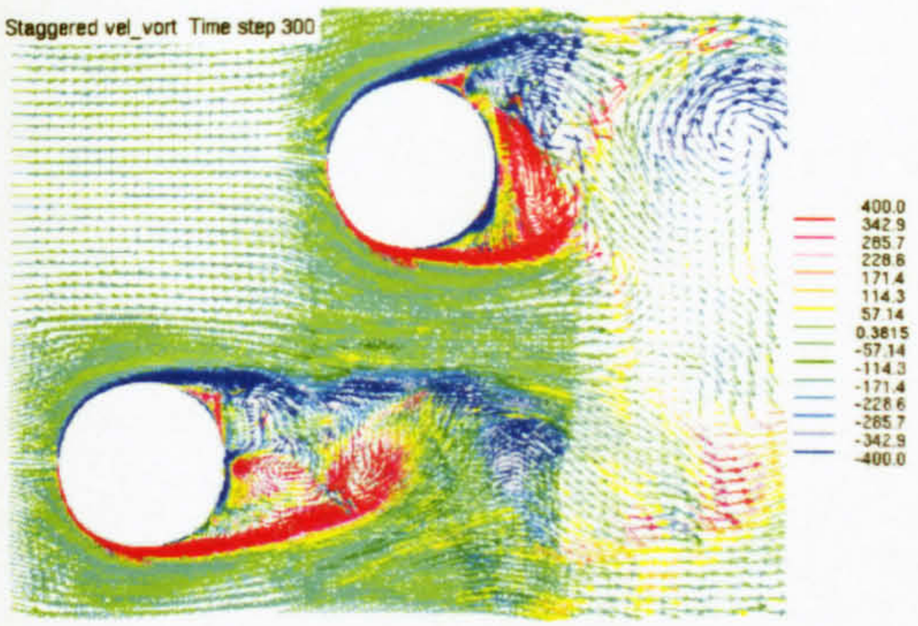

(a) Phase A

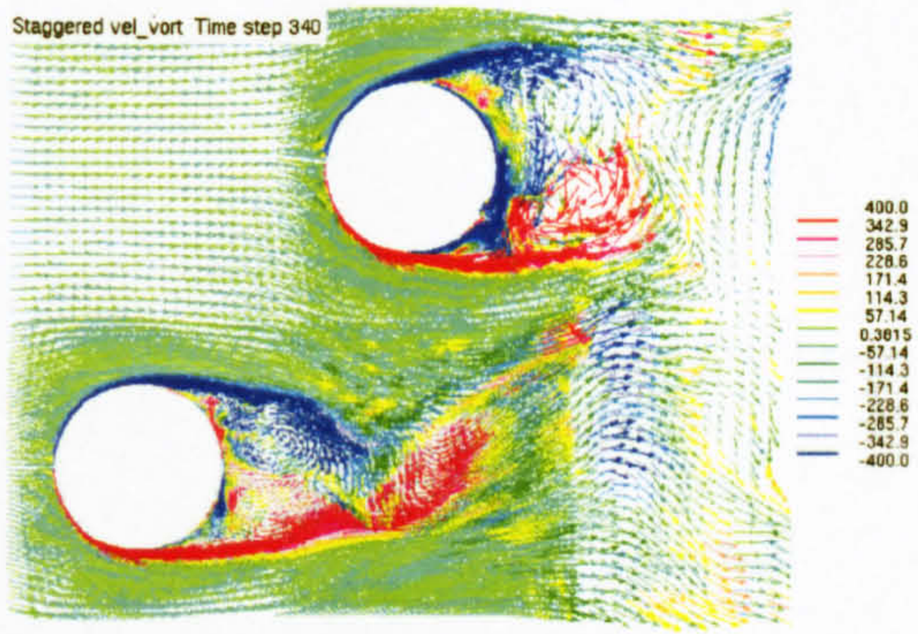

(b) Phase B

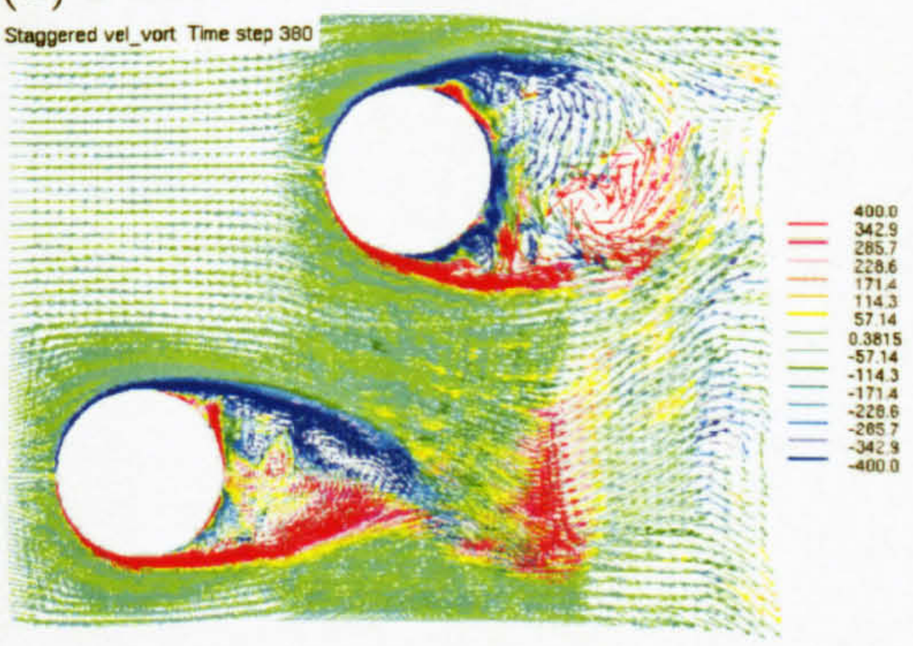

(c) Phase C

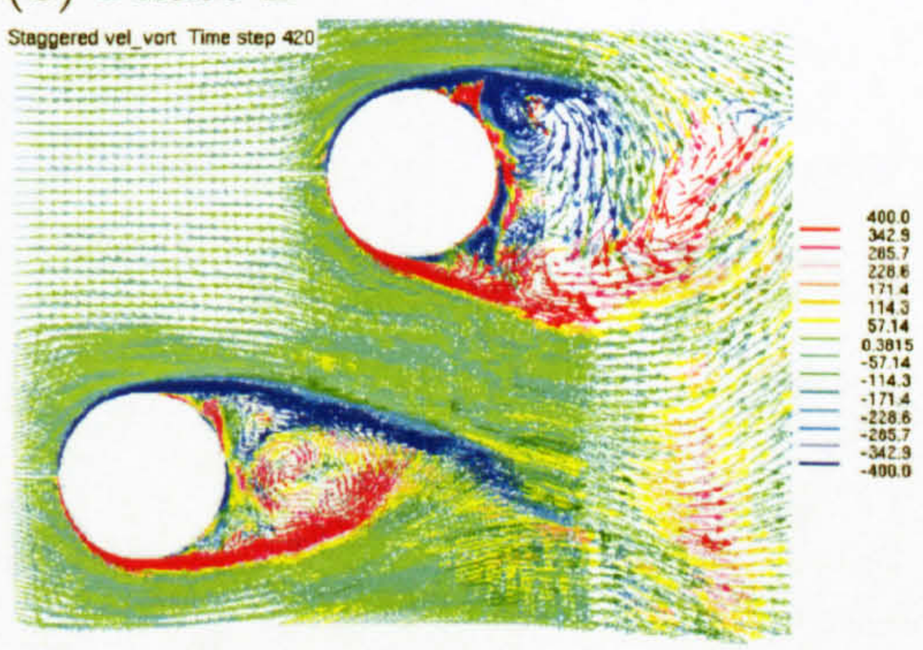

(d) Phase D

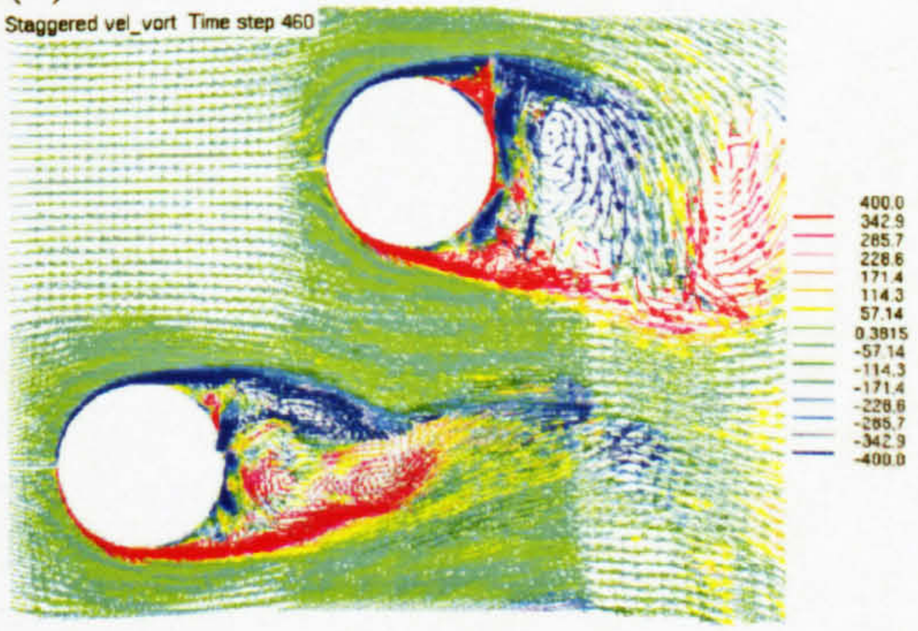

(e) Phase E

(f) Phase F

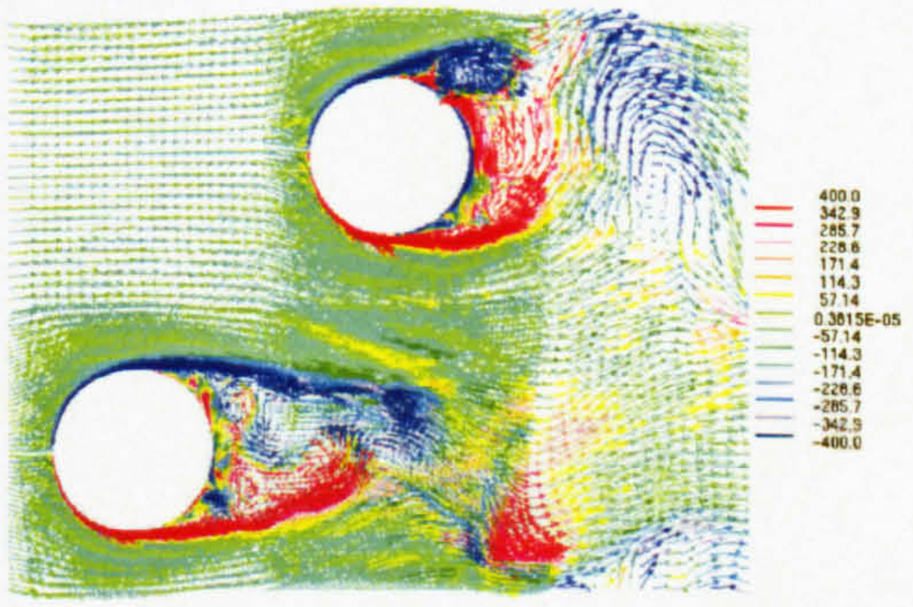

(g) Phase G

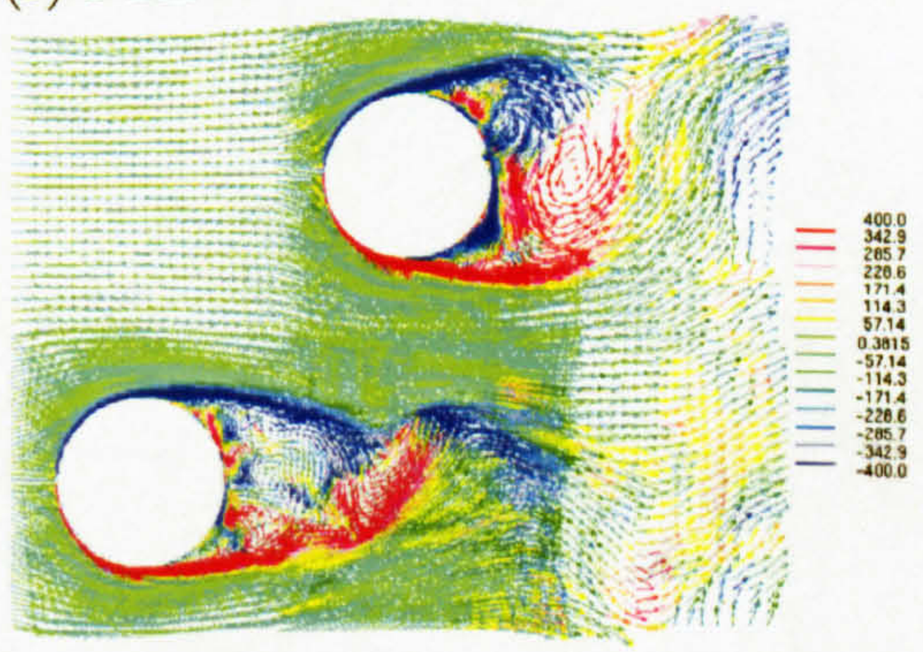

(h) Phase H

Figure 7.12: Instantaneous velocity and spanwise vorticity in the two-row staggered tube array.

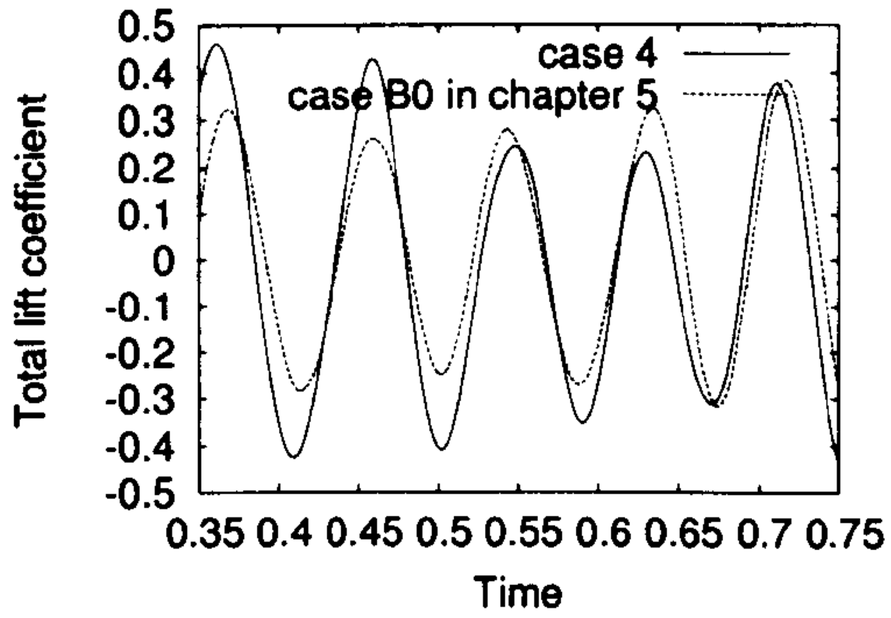

(a) Total lift coefficient

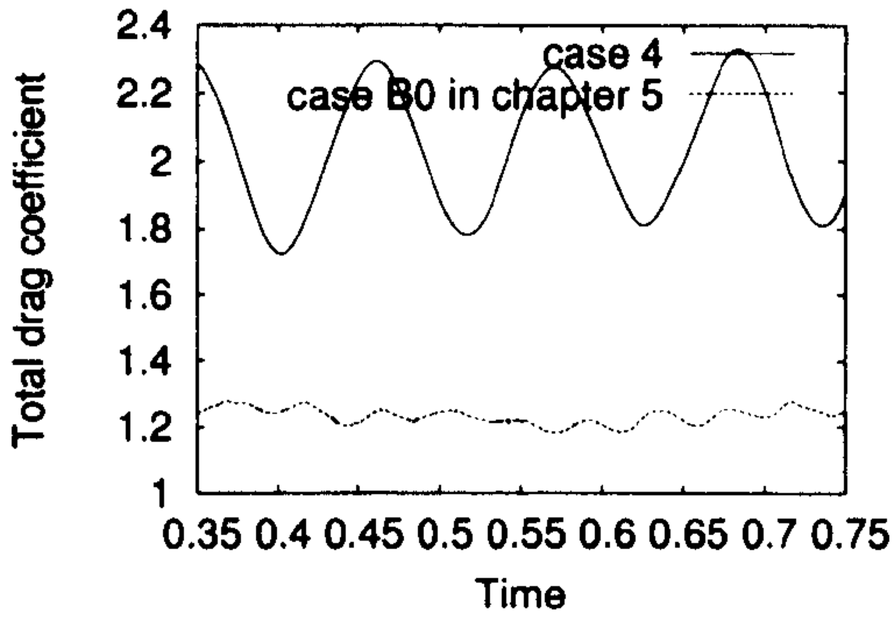

(b) Total drag coefficient

Figure 7.13: The lift and drag coefficients for case 4 investigated for a six-row tube bundle and case B0 investigated for a single cylinder.

Recirculation bubble length of the staggered tube array						
Type	Re_{gap}	row 1	row 2	row 3	row 4	row 5
LES (Case 1)	8,600	1.66D	1.24D	1.1D	1.24D	1.15D
LES (Case 2)	8,600	1.63D	1.23D	1.02D	1.16D	1.1D
LES (Case 4)	3,400	2D	1.31D	1.31D	1.24D	1.11D
Experiment	12,858	1.65D	1.6D	0.98D	0.8D	n/a
Exp. correlation	8,600	1.67D	n/a	1.09D	n/a	n/a
Exp. correlation	3,400	1.98D	n/a	1.36D	n/a	n/a

Table 7.3: Recirculation bubble length of the staggered tube array. Experimental results taken from Balabani and Yianneskis (1996).

a single cylinder at the same Reynolds number. As shown in figure 7.13, case 4 has a very similar lift coefficient as that of the single cylinder (case B0 presented in chapter 5). For the first cylinder, Case 4 has a much higher drag coefficient than that of the case B0 due to the blockage effect and the presence of the other cylinders. However, it shall be noted that there are two dominant vortex shedding frequencies behind the first cylinder in the tube bundle, despite that only one frequency is associated with the von Karman vortex shedding behind a single cylinder.

Figure 7.14 shows comparison of the predicted steamwise time-averaged mean and r.m.s velocities with the LDA measurements performed by Balabani and Yianneskis (1996). The predicted streamwise mean velocity agrees very well with the measurements. The r.m.s velocity has a very good agreement at nearly all locations with the measurement data, apart from the relatively higher discrepancy existing at the level of the first row which is probably due to the freestream turbulence

existing in the experiment.

Figure 7.15 shows the cross-wake time-averaged mean and r.m.s velocities. They are compared with the LDA measurements performed by Balabani and Yianneskis (1996). The agreement with the measurement data at all locations is very satisfactory. This clearly demonstrates that the current grid resolution is enough to predict correctly the second-order turbulence statistics for this tube bundle arrangement and Reynolds number.

7.4.1 Effect of pulsation

A 10% amplitude of pulsation with frequency 27.4Hz was imposed on the mean upstream velocity for case 2. Detailed results are not presented because the effect of pulsation on the flow pattern is small. The recirculation bubble width is nearly not altered, although the recirculation bubble length is slightly shortened. This is in agreement with the experimental findings by Konstantinidis (2001) for the staggered tube array with the same streamwise spacings. He attributed the small effect of pulsation on the flow pattern to high Reynolds number and small streamwise tube spacings. Further higher pulsation frequency could have been imposed, however, it would slow down the convergence of the algorithm significantly because the inlet mass flow rate keeps changing quickly.

7.5 Lift and drag forces of the cylinders in the staggered tube array

Figure 7.16 shows the instantaneous pressure at a point on the surface of the first row cylinder in Case 3. The amplitude of the pressure fluctuation increases as the flow develops from the front stagnation point. It can be shown that the highest amplitude of fluctuation is at 90^o, which is a location around the separation point. After the separation point, the pressure fluctuation is approximately kept at the same level.

Table 7.4 presents the lift and drag coefficients for the different rows. In particular, the r.m.s lift coefficient for the first row is much smaller than the ones for the other rows. This can be explained firstly by the small amplitude of the cross-wake velocity spectra behind the first row as shown in figure 7.10. The reason for this is that the spanwise vorticity of the Strouhal vortex formed by the shear layer of the first row is much weaker than the one of other rows too as shown in figure 7.8.

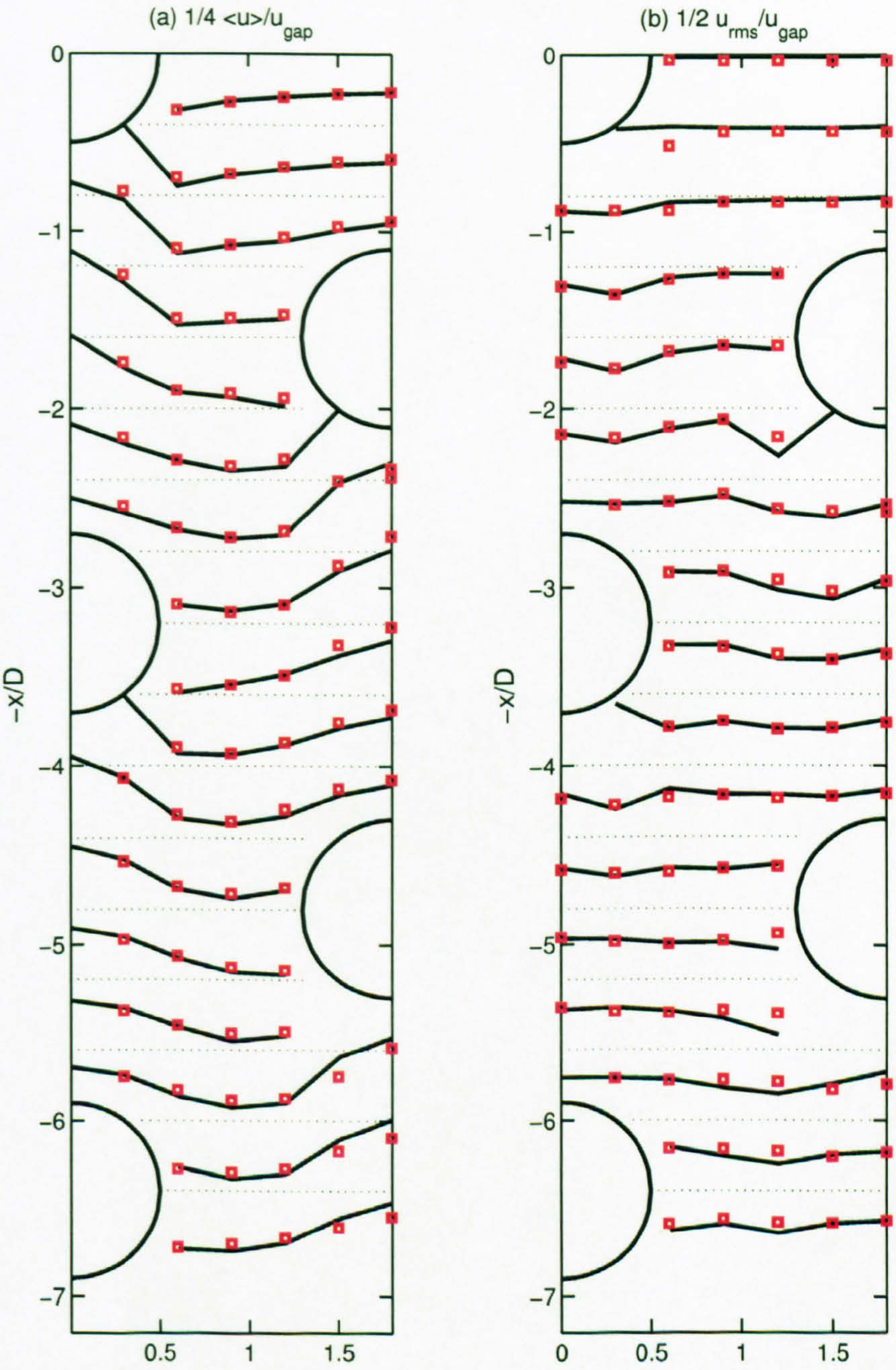

Figure 7.14: Mean and r.m.s streamwise velocity of the steady cross flow over the staggered tube bundle. (——) Smagorinsky model; (□□□□□) LDA measurement

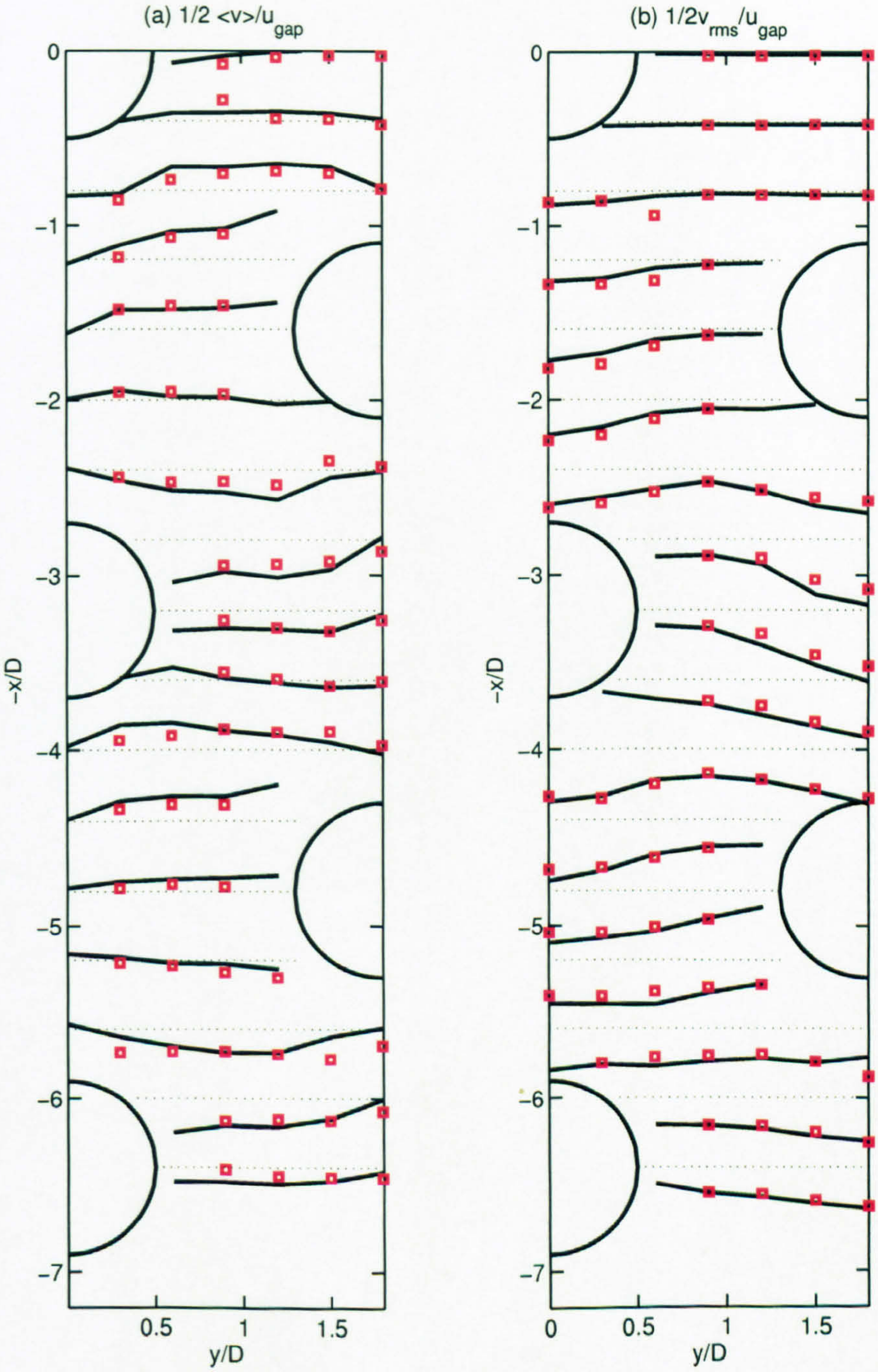

Figure 7.15: Mean and r.m.s cross-wake velocity of the steady cross flow over the staggered tube bundle. (——) Smagorinsky model; (□□□□□) LDA measurement

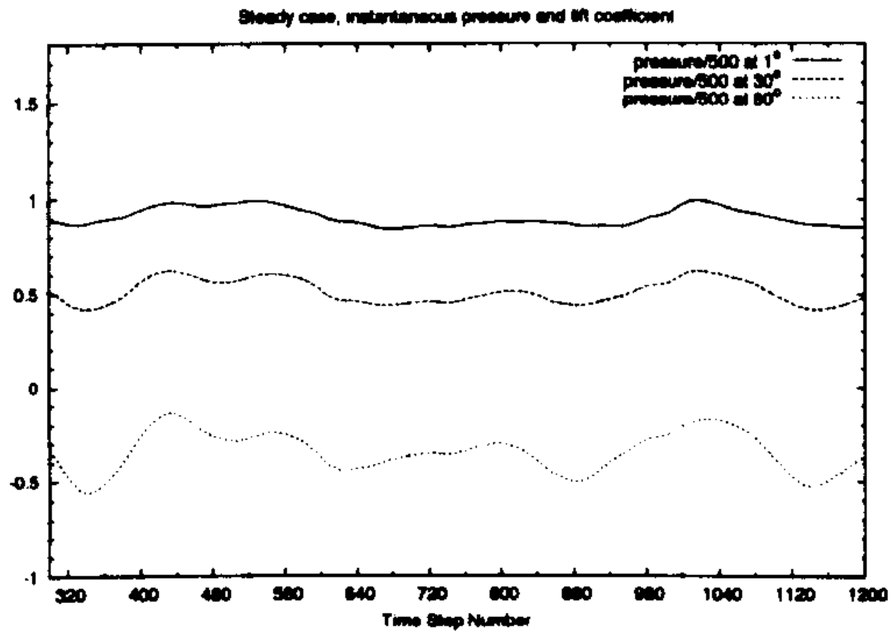

(a) Time series of pressure

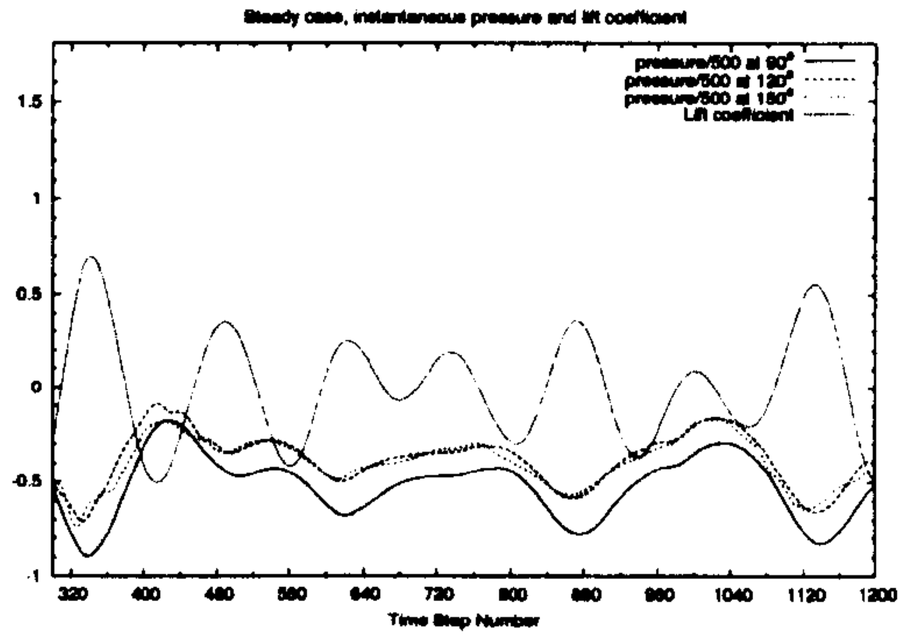

(b) Time series of pressure and C_L

Figure 7.16: The instantaneous pressure at the surface of the first row cylinder predicted for case 3.

The highest mean drag coefficient is the one for the second full cylinder predicted for case 1 and the one for the fourth cylinder predicted for case 4. However, the highest r.m.s drag coefficient is the one for the fifth full cylinder predicted for both cases 1 and 4. The mean drag coefficient of the first full cylinder predicted for both cases 1 and 4 is higher than the one for the single cylinder at the correponding Reynolds numbers respectively. This can be explained if the effect from the top and bottom half cylinders is taken into account (Lam and Fang, 1995).

7.6 Heat transfer distribution around cylinders in the staggered tube bundle

Figure 7.17 shows the time- and spanwise averaged Nusselt number distribution over the first row cylinder for Cases 1 and 3. The finer mesh predicts a similar curve to the one predicted by coarse mesh. The results are in a good agreement with the measurement data by Murray (1993) for the single-phase air flow at a comparable Reynold number $Re_{gap} = 10,000$. This reflects that the grid resolution of the coarse mesh is generally sufficient to produce the correct mean heat transfer coefficient distribution. Figure 7.17 shows that the profile at the range $0^o - 45^o$ for case 1 is fairly flat which is slightly different from the typical shape of Frossling curve (Frossling, 1958).

Figure 7.18 shows the time- and spanwise averaged Nusselt number distribution over the second row cylinder for cases 1 and 3. Case 1 has a higher Nusselt number than Case 3 after the separation point due to stronger small-scale vortex

Lift and drag coefficients of the cross-flow over staggered tube bundle						
Cases	Re_{gap}	Rows	Mean C_L	Mean C_D	r.m.s C_L	r.m.s C_D
Case 1	8,600	Row 1	-0.015	2.01	0.24	0.13
		Row 2	-0.132	2.90	1.50	0.19
		Row 3	-0.181	2.78	2.16	0.50
		Row 4	0.022	2.07	1.94	0.70
		Row 5	0.014	2.22	1.53	0.74
		Row 6	-0.127	1.74	0.91	0.29
Case 4	3,400	Row 1	-0.008	2.05	0.29	0.18
		Row 2	-0.291	2.60	1.64	0.66
		Row 3	-0.221	2.44	1.57	0.71
		Row 4	0.169	3.03	1.75	0.26
		Row 5	0.058	2.36	2.52	0.94
		Row 6	-0.237	2.01	1.42	0.54

Table 7.4: Computed lift drag coefficient for staggered tube array.

recirculation near the rear wall due to the presence of the downstream cylinders. The second row has a higher Nusselt number than the first row from the front stagnation point to the separation point because of the higher approaching velocity (i.e. the cylinder sees the gap velocity). In fact, Scholten and Murray (1998*a*) also measured the higher heat transfer rate for the front part of the second cylinder using surface mounted hot film sensor. However, they have about the same Nusselt number at the rear stagnation points for the first two rows although the recirculation bubble length behind the first row is much larger.

Figure 7.19 presents the spanwise- and time- averaged Nusselt numbers for the downstream cylinders in the 6-row arrangement. One can see that the heat transfer rate for all the rows are roughly at the same level with the rate around the fourth cylinder only slightly higher than the others. This indicates that the turbulence level saturates after the third row. This is consistent with the turbulence fluctuation levels indicated by the instantaneous velocity patterns shown in figures 7.8 and 7.9. Aiba et al. (1982*b*) measured the local Nusselt number distribution for a normal triangle tube array with pitch-to-diameter ratio of 1.6. They also found that the heat transfer rate reached the maximum at the third-row level.

The global instantaneous temperature field has a strong correlation with the vortex shedding as shown in figure 7.20. The temperature patterns at different phases follow the spanwise vorticity patterns shown in figure 7.12. At most of the time instants, the temperature near the rear stagnation point of the first cylinder is lower than the one near the rear stagnation point of the second cylinder. This

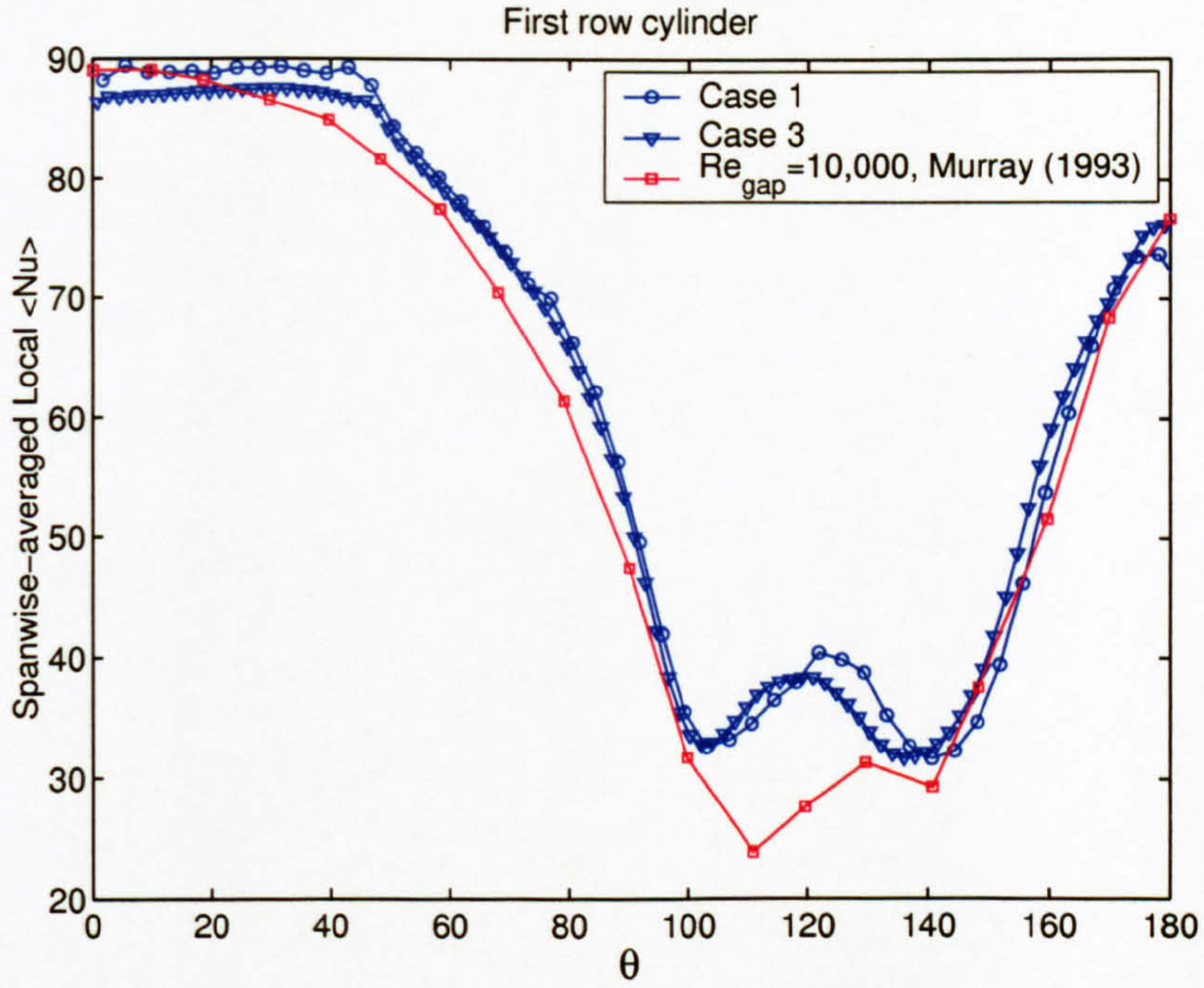

Figure 7.17: The time- and spanwise averaged Nusselt number distribution over the first row cylinder in the staggered tube array.

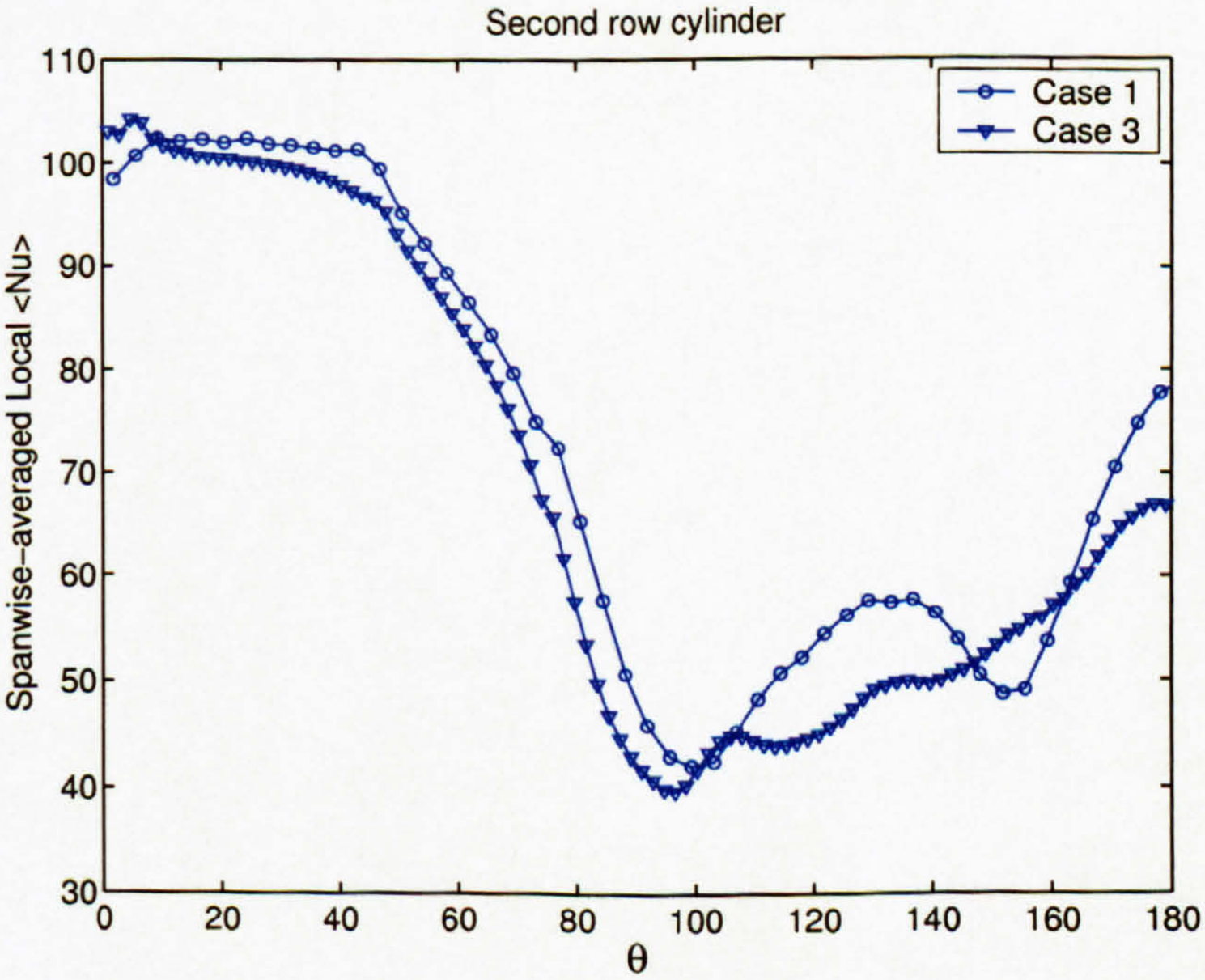

Figure 7.18: The time- and spanwise averaged Nusselt number distribution over the second row cylinder in the staggered tube array.

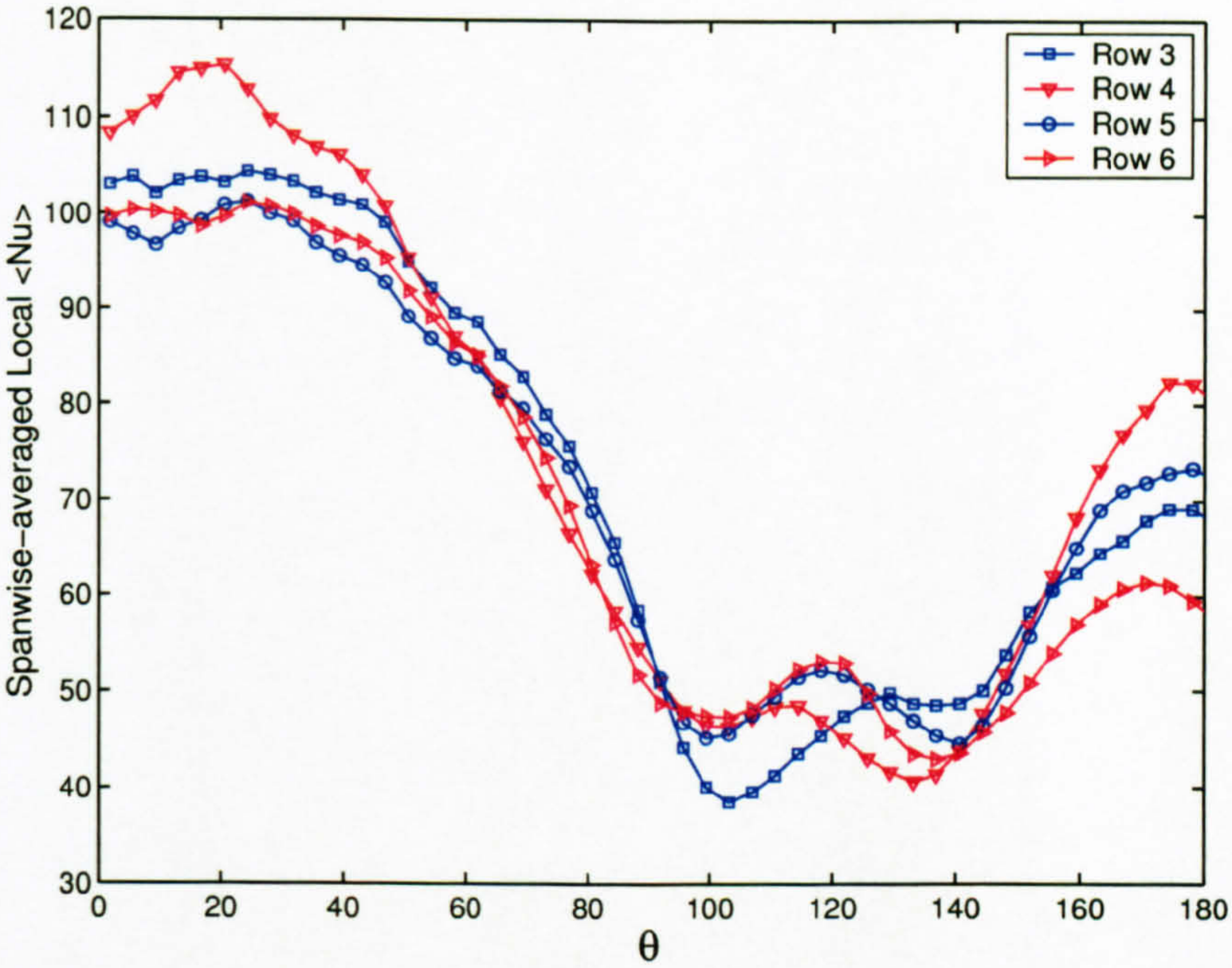

Figure 7.19: The time- and spanwise averaged Nusselt number distribution over the four downstream cylinders in the 6-row staggered tube array (Case 1).

explains why the heat transfer rate is higher for the first cylinder in this region.

7.7 Closure

LES calcuations have been performed at two Reynolds numbers $Re_{gap} = 8,600$ and $Re_{gap} = 3,400$ for a staggered tube arrangement. The basic turbulence statistics of mean and r.m.s velocities as well as recirculation bubble lengths are in very good agreement with the experimental data. A separate run with a refined grid for only two rows of cylinders confirmed that the coarser grid resolution around the first cylinder is sufficient to obtain satisfatory results.

The lift coefficient of the first cylinder in the studied 6-row staggered arrangement at $Re_{gap} = 3,400$ is similar to that of the single cylinder at $Re_D = 2,580$ studied in chapter 5. The recirculation bubble sizes of the first cylinder for the different cases studied in the staggered arrangements are about the same as the ones for the single cylinder at a comparable Reynolds number.

Two vortex shedding frequencies were detected. A high-frequency component results from the first row, and a low-frequency component form the second row and/or further downstream rows. The lift and drag coefficients were quantified for

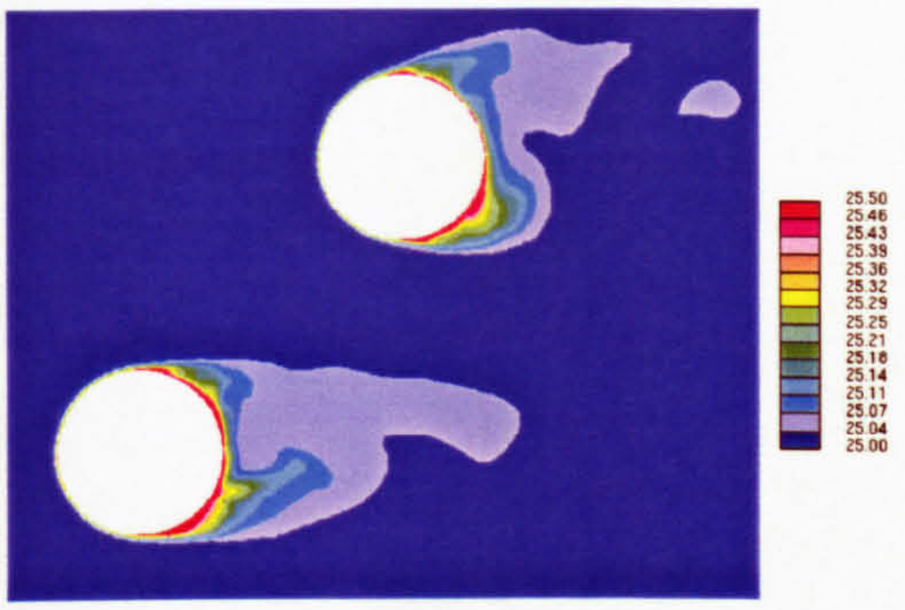

(a) Phase A

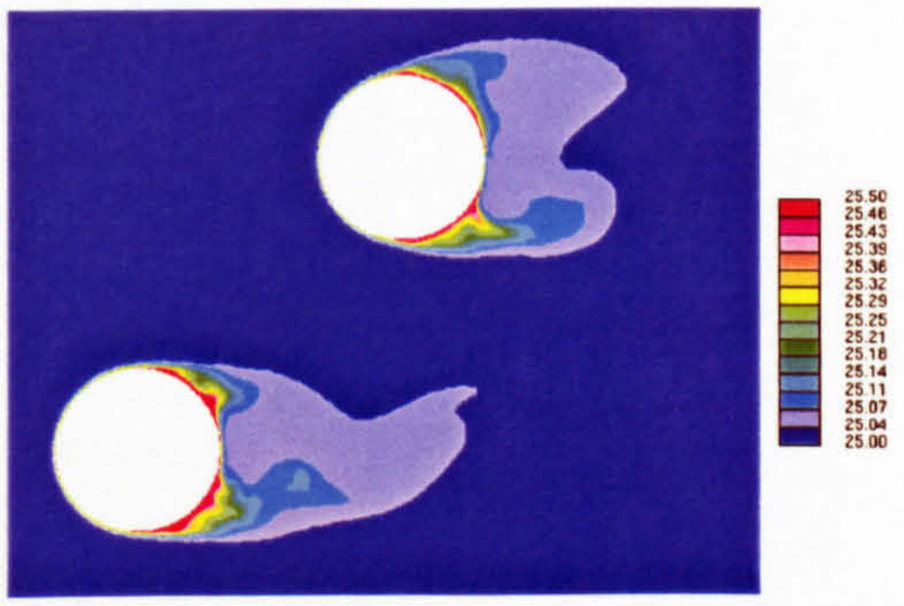

(b) Phase B

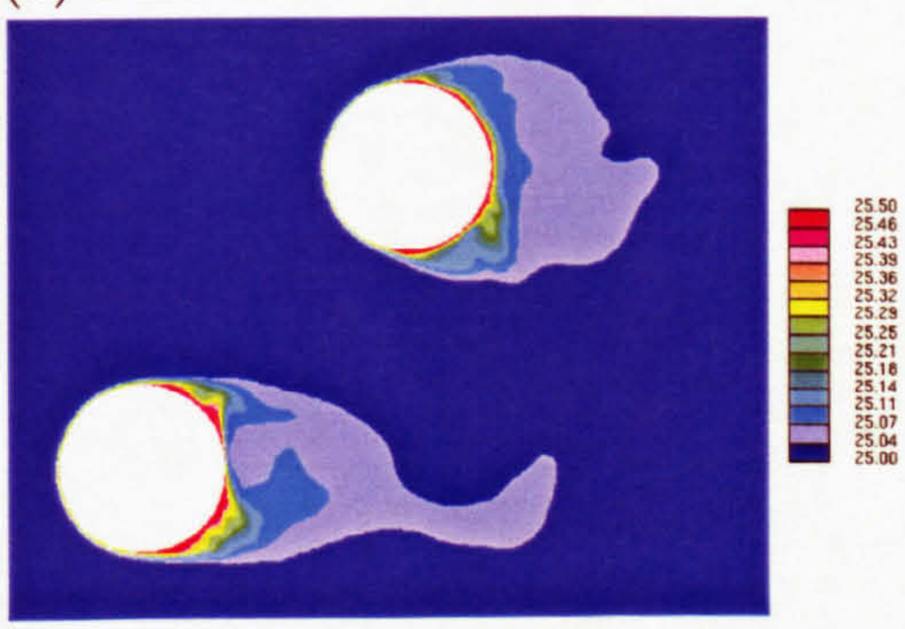

(c) Phase C

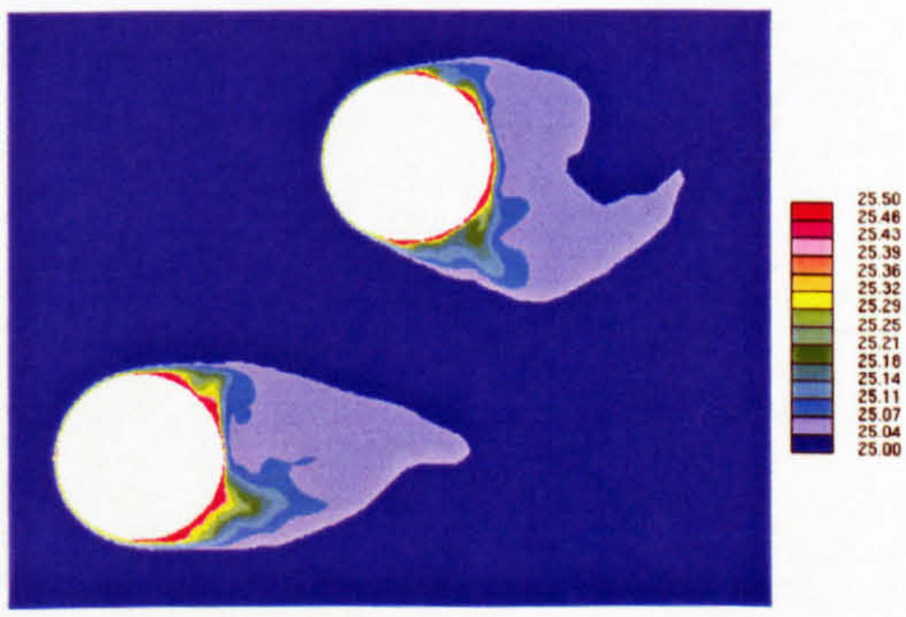

(d) Phase D

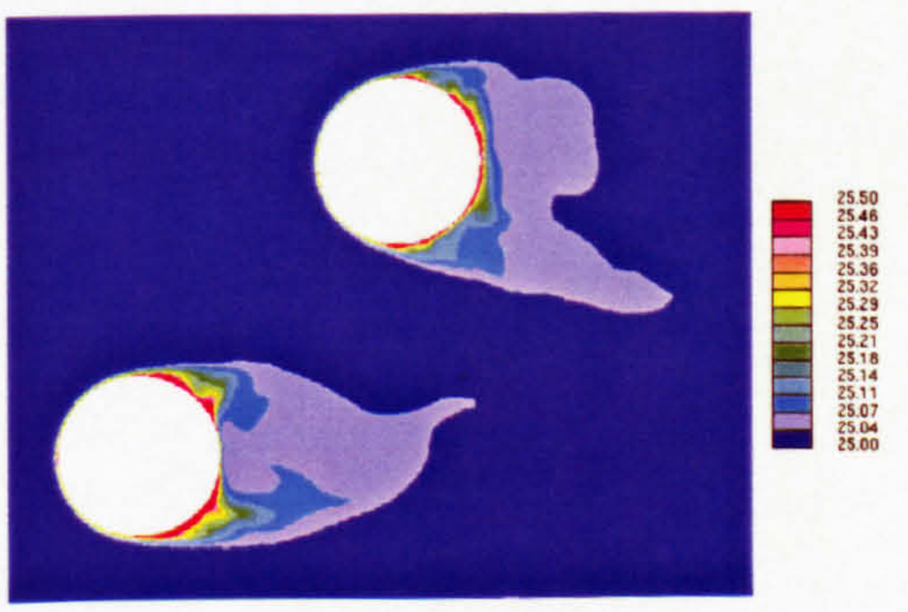

(e) Phase E

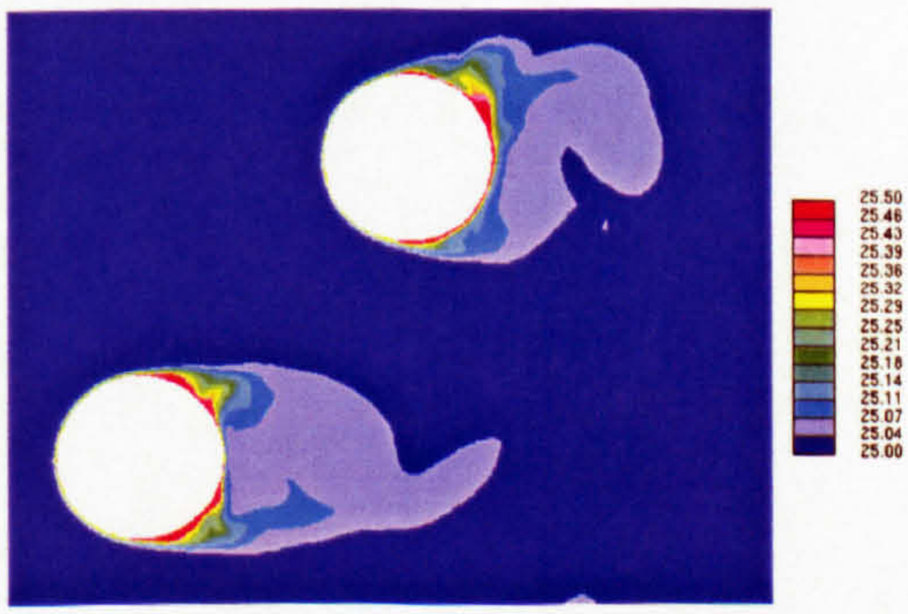

(f) Phase F

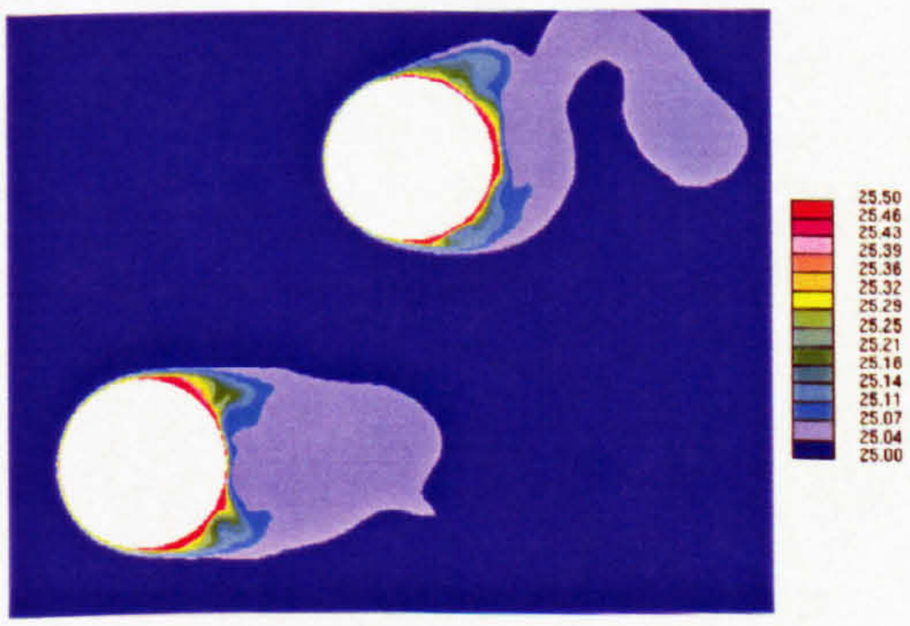

(g) Phase G

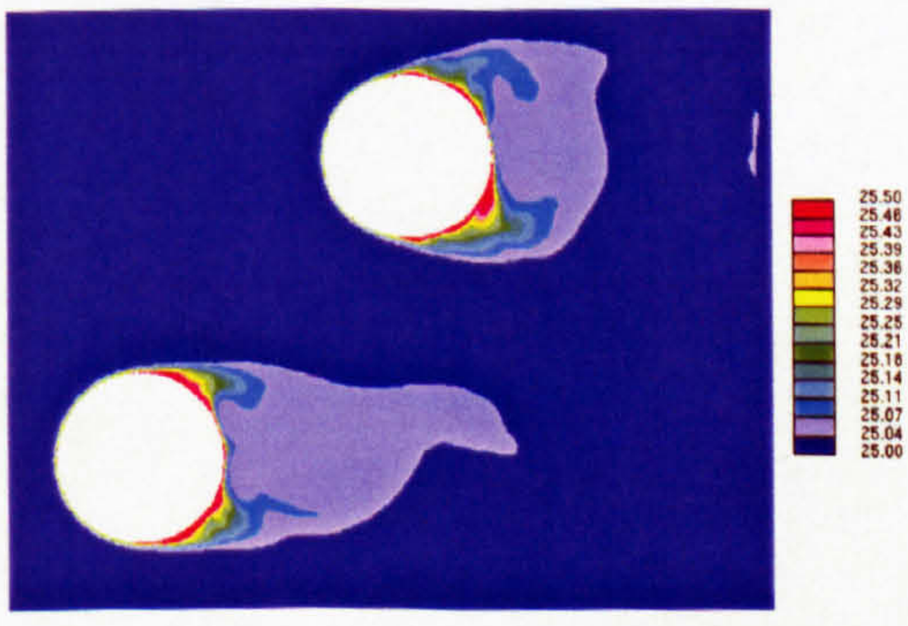

(h) Phase H

Figure 7.20: Temperature contours at 8 time instants for Case 3.

each different cylinder and the local heat transfer results were also reported. The velocity vectors colour-coded with the values of spanwise vorticity field are presented for different phases determined using the lift coefficient. The temperature field is also correlated with the vorticity field at the same time instants. The heat transfer rate in the front part ($0^o - 150^o$) of the second cylinder is higher than the one of the first cylinder. The heat transfer rate reached about the same level in the rows further downstream despite that the one for the fourth cylinder is slightly higher than the others.

Due to the relatively high Reynolds number and small streamwise tube spacings, the pulsating approaching flow has litte effect on the flow pattern at a Reynolds number $Re_{gap} = 8,600$.

Chapter 8

CONCLUDING REMARKS AND RECOMMENDATIONS FOR FUTURE WORK

8.1 The present study

The objective of this computational study was to investigate the turbulent flow characteristics and heat transfer across tube bundles using the LES technique. A three-dimensional finite volume in-house code using unstructured collocated mesh was used for the solution of the Navier-Stokes and energy equations. For the spatial discretization of the convection and diffusion terms for velocities, the second order central differencing scheme was used. For time marching, the Crank-Nicolson method was used for both convection and diffusion terms. The pressure term was treated fully-implicitly. The subgrid-scale Reynolds stress is modelled using both the standard Smagorinsky model as well as a dynamic model, for which the test-filtered quantities are obtained through a truncated Taylor series expansion.

In order to demonstrate the accuracy of the LES models and discretization practices, the developed numerical approach was validated first in a turbulent channel flow at two Reynolds numbers (based on friction velocity and channel half-height) $Re_\tau = 640$ and $1,100$. Both sgs models gave reasonably good agreement with DNS data although there is scope for improvement in the predictions especially for the turbulent stresses. A thorough and detailed validation was also performed for steady and pulsating incoming cross-flow and heat transfer over a circular cylinder. The numerical predictions were in very good agreement with PIV measurements (especially for the pulsating incoming flow) both in terms of

mean as well as turbulence quantities. For the steady approaching flow case, a prohibitively large number of cells is needed to capture the very small scale accelerating flow in the laminar boundary layer before the shear layer separation point and the laminar sublayer after the separation point. For pulsating approaching flow, the synchronized vortex shedding has higher transverse turbulence fluctuations and the contribution of coherent part of the Reynolds stresses is stronger which makes the flow easier to model more accurately. For instance, the finer mesh with around 750K cells proved to be adequate for the simulation of the turbulent wake in the locked-on state. On the other hand, it is believed that the same mesh, particularly the spanwise resolution, appeared to be insufficient to resolve the smaller-scale turbulent eddies in the wake for steady approaching flow. The effect that the locked-on vortex shedding has on the vortex formation length, Strouhal number, vortex strength as well as the lift and drag coefficients was examined in detail.

Several simulations were then performed for both inline and staggered tube bundles with focus on the vortex shedding phenomena occurring behind cylinders in different rows under different inlet flow conditions. New information regarding the interaction between separated shear layer and/or Strouhal vortex and cylinders was obtained for different rows. The lift and drag forces over each full cylinder were quantified based on time averaging for more than 5-6 vortex shedding periods. The enhancement of heat transfer by the external pulsation was also quantified via the Nusselt number distributions averaged over temporal and homogeneous directions.

The spacings for the inline and staggered tube arrays were $S_L \times S_T = 2.1D \times 3.6D$ and $S_L \times S_T = 1.6D \times 3.6D$ respectively, following the experimental studies performed by Balabani and Yianneskis (1996, 1997). The study of the inline tube array, in conjunction with other related experimental studies, in particular those of Konstantinidis et al. (2000, 2003*b*) who considered different pulsating frequencies for a similar Reynolds number, advances the understanding of the vortex shedding phenomena, heat transfer distribution as well as lift and drag forces for different row cylinders.

The study of the staggered tube array improves the understanding over the LDA measurements and flow visulizations of Balabani and Yianneskis (1996) and Weaver et al. (1993) on the vortex shedding phenomena with the identification of two frequencies, variation of lift/drag coefficients and heat transfer distributions. The knowledge gained from the simulations can be used not only to improve the

design of shell-and-tube heat exchangers and other engineering structures with similar configurations but also to provide experience for the CFD community regarding the reliability of simulations of intermediate-spacing tube bundles with multiple rows of cylinders. This experience can lead to improvement of numerical schemes and turbulence modelling techniques for industrial complex geometries.

The understanding gained from the present simulations about the global flow patterns, i.e. the flow patterns in an array as a whole, are in agreement with the main experimental findings of Konstantinidis (2001). But the simulations certainly give more extensive information on the overall flow, pressure and temperature fields, while the LDA measurements are limited over a small number of locations inside the bundles. The following section summarises the main finding and section 8.3 provides suggestions for future work.

8.2 Main findings

In this section, the main findings from the simulations of turbulent channel flow, flow around a single cylinder as well as inline and staggered tube bundles are summarised. At first, experience was gained from the simulations of simple geometries which provided robust and validated foundation for the simulations of flow around tube bundles. Those validations provided sound basis for the simulations of flow around tube bundles.

8.2.1 Simple geometries

1. The collocated grid cannot preserve kinetic energy for the pressure term due to the special interpolation practice needed to avoid a checkerboard pressure field. The Rhie and Chow method has a second order accuracy $(O(\Delta x)^2)$ for both uniform and nonuniform meshes with constant expansion ratio. Although the uniform mesh gives the smallest magnitude of the coefficient for the pressure gradient, the rise of the magnitude is not big for typical values of expansion ratios used in practical applications, demonstrating that the numerical dissipation of this special interpolation technique is not really significant.

2. A fourth order accurate central difference scheme has been implemented to solve the Orr-Sommerfeld equation and the most unstable perturbation field was superimposed to the laminar solution of channel flows. These per-

turbations have been found to speed up the transition to turbulence quite effectively.

3. In order to reduce the over-estimated eddy viscosity in the near wall region, the van Driest damping function was found to be particularly important when the standard Smagorinsky model is used for the channel flows. The dynamic model used can predict the correct near-wall behaviour and generate correctly the $C_s(y)$ profile with the right near-wall behaviour, so that the same accuracy is gained as the standard Smagorinsky model with the van Driest damping function. The low resolution grid for a high Reynolds number overpredicted the mean profile. For a lower Reynolds number, when resolution requirements are milder, the predictions of mean velocity significantly improve but there is still scope for improvement of the turbulent stresses.

4. The synchronized lock-on vortex shedding case for a single cylinder has higher transverse turbulence fluctuations and the contribution of the coherent part of the Reynolds stresses is stronger which makes the flow easier to model compared to steady approaching flow case. The dynamic and the standard Smagorinsky subgrid model produced nearly the same results for the synchronized lock-on case. On the other hand, the performance of the dynamic model was mixed compared the standard Smagorinsky model for the steady approaching flow over a single cylinder, which is in agreement with the finding of Fröhlich and Rodi (2004) for a simulation of turbulent flow over a cylinder of finite height. This is because the test filter operation projects information onto even coarser grid. Therefore, a fine resolution is needed in the homogeneous directions along which the averaging operation is performed.

5. Central differencing schemes have been proved generally more suitable for LES. The second order CDS is the best choice for the unstructured grid simulations of the flow over tube bundles. The present grid resolution is insufficient to simulate the steady approaching flow over a circular cylinder. This can be further improved by grid local refinement or even higher differencing scheme which might be difficult to apply in unstructured grid. On the other hand, for structured meshes, in order to better resolve the turbulent wake of the steady approaching flow over a single cylinder, the fourth order CDS proposed by Jordan (2003) can be used.

6. The vortex formation length was decreased while the mean drag as well as rms values of the drag and lift coefficients increased significantly under pulsating flow conditions. Heat transfer was found to increase after the seperation point, in agreement with the experimental findings of Sung et al. (1994).

8.2.2 Tube bundles

1. In this work, 3D LES calculations for both inline and staggered tube bundles with intermediate-spacings were performed. Most existing works in the literature either assume fully developed flow and use periodic conditions or report calculations in 2D which are of doubtful accuracy. On the other hand, in this study 3D calculations were performed for many rows and this type of simulation provides detailed information on the interaction of cylinder wakes. It was found that this interaction is very important for the successful simulation of interesting fluid dynamics phenomena as will be summarised later on.

2. It is believed that only 20 layers in the spanwise direction are insufficient to predict correctly the small-scale eddy structures behind the first cylinder in the intermediate-spacing inline tube array. The under-resolution in the streamwise and transverse directions of the coarser mesh also led to the prediction of a fictitious alternate vortex shedding behind the first cylinder which was not observed by Konstantinidis et al. (2000). All the simulations underpredict the recirculation bubble size between the first and second row cylinders in the inline tube bundle, although the dynamic model used gives slightly better results than the standard Smagorinsky model.

3. A finer mesh with local refinement around the first and second row cylinders captures better the eddy structures in the gap region. Two counter-rotating big vortices are predicted in the gap region and the *reattachment* regime is correctly predicted. The predicted heat transfer rate in the front part of the second cylinder is significantly smaller than that for the alternate vortex shedding mode.

4. It has been found that the streamwise tube spacing 2.1D inline arrangement at Reynolds number $Re_{gap} = 3,400$ lies in the range of the bistable transition. There are two regimes namely the *two vortex streets* regime and the

reattachment regime. The flow develops into one of the two depending on the initial flow field. The alternate vortex shedding is also associated with higher r.m.s lift coefficients and higher turbulence intensity in the wake of the first cylinder.

5. When the computational grid is under-resolved for the turbulent flow field in the six-row inline tube bundle, the development of turbulence level in the flow lane along the streamwise direction will be amplified by the alternate vortex shedding behind the first cylinder and the heat transfer rate is also over-predicted in the rear part of the first cylinder and the front part of the second cylinder. Nevertheless, a single vortex shedding frequency has been correctly simulated for different cylinder rows. The vortex shedding in the adjacent rows was predicted to be 180^o out-of-phase.

6. The same grid used for the steady approaching flow over the six-row inline tube bundle has been found to give better predictions for the pulsating approaching flow case when the external frequency is twice that of the natural vortex shedding than the prediction of the steady approaching flow case. The pulsating approaching flow with synchroinized lock-on was found to produce the best mixing effect and resulted in the highest heat transfer rate for the first two cylinders.

7. The symmetrical vortex formation is correctly predicted when the pulsating frequency is three times that of the natural vortex shedding. The predicted heat transfer rate in the front part of the second cylinder for this case is lower than that for the cases with alternate vortex shedding behind the first cylinder. The heat transfer rates for the third and further downstream cylinders are not affected much by the external pulsation.

8. The simulation of the flow over a staggered tube array gives results in very good agreement with the experimental data. The recirculation bubble size behind the first cylinder has been predicted accurately by the standard Smagorinsky model. The bubble size is equivalent to the one of the single circular cylinder at the same Reynolds number.

9. The inlet turbulence level has a smaller effect on the turbulence levels in the downstream cylinders inside the staggered tube array than in the inline one. The high frequency associated with the first cylinder and the low

frequency associated with the second cylinder were correctly predicted in a good agreement with the experimental results of Weaver et al. (1993).

8.3 Recommendations for future work

The conclusions drawn from the present study provide an important background for extending the applicability of the methodology employed in simulating cross-flows over tube bundle as well as fluid induced vibrations to optimize the design of heat exchangers. On the other hand, tube bundle structures provide a good platform to validate and improve the development of both RANS and LES models. Some recommendations for future investigations are given below:

The present study considered only one inline and one staggered tube array configuration. Clearly, similar investigations should be extended to a wider variety of tube spacings for both inline and staggered arrangements in order to understand better the performance of LES models in capturing the size of recirculation bubbles and the location of reattachment points in different intermediate-spacing tube arrays.

For the inline tube array, the flow field in-between the first and second row cylinders is important for the development of the overall turbulence levels across the whole bundle. Local refinement over this region in the spanwise direction will help to quantify more accurately the three-dimensional effect of pulsation on the flow field and heat transfer over the rear part of the first row cylinder and the front part of the second row cylinder. The effect of different inlet turbulence levels on the flow and heat transfer characteristics should be examined.

For the staggered tube array, pulsation tends to have little effect on the recirculation bubble size behind different cylinders because of the close streamwise spacing and the high Reynolds number. The experimental work of Konstantinidis et al. (2002) was concerned with a staggered array with streamwise spacing $S_L = 2.1D$ at a lower Reynolds number around 2,300. Their more recent experimental work (Konstantinidis et al., 2004) reported phase-averaged results which could provide a good basis for the validation of further LES calculations of the flow around this staggered array.

Recently, an ever increasing research effort is being devoted to the investigation of numerical error and its separation from the subgrid-stress modelling error for bluff body flows. For instance, Nakayama and Vengadesan (2002) computed the flow around a square cylinder using both central and upwind-biased

finite-differencing schemes of various orders of accuracy, computational grids with different resolution, with conventional and dynamic eddy viscosity subgrid scale models, but with the same calculation procedures in other aspects such as pressure iteration and time advancing methods. Park et al. (2004) studied both central and upwind-biased compact difference schemes for the flow around a circular cylinder at Reynolds number 3,900. A detailed investigation of different differencing schemes for the steady and pulsating approaching flow across a single circular cylinder will provide more information on their predictive capabilities. Subsequently, a similar investigation should be performed for the flow over both the inline and staggered tube bundles.

Detailed information on lift and drag coefficients has been reported for single and multiple cylinder arrays. A natural extension of the present simulations is to simulate the flow-induced vibration of one or more tubes taking into account the flow-structure coupling and fluid-elastic effects. For instance, Longatte et al. (2003) have performed a pioneering 3D simulation of cross-flows in an inline tube bundle with a flexible tube.

Recently, Wallin and Johansson (2000) proposed an explicit algebraic Reynolds stress turbulence model (EARSM) where the production to dissipation ratio is obtained as a solution to a nonlinear algebraic relation. The applicability of this new anistropic RANS turbulence model for the flow around tube bundles may help draw new conclusions about unsteady RANS in simulating this particular flow.

The effect of solid particles in suspension or fouling on the heat transfer characteristics of tube bundles in cross-flows is of significance for the design of heat exchangers (Murray, 1993). Bouris et al. (2001) have performed a two-dimensional simulation using a subgrid scale model for the particle deposition rates in the cross-flows over both inline and staggered tube bundles. Three-dimensional LES simulation for the particle deposition rates should be carried out to produce more accurate results since the turbulent Reynolds stresses are better predicted than the 2D simulation. Also the interaction of 3D vortices with particles of different sizes would be a very interesting phenomenon to study.

Appendix A

Truncation and Aliasing Errors

A.1 Modified wavenumber

Two primary coupled components, namely, truncation error and the error associated with the nonlinearity of the governing equations, are created by the discrete spatial and temporal discretization. Truncation errors result from the discrete approximation of the first or second order derivatives in the governing equations by finite differences. A concept called a 'modified wavenumber' is often used to assess the spectral distribution of the truncation errors in the context of LES simulation. For instance, an approximation of the first derivative of a function $u(x)$ is

$$\frac{\delta u}{\delta x} = \frac{du}{dx} + truncation\ errors. \tag{A.1}$$

In Fourier space, equation A.1 can be written as

$$\widehat{\frac{\delta u}{\delta x}} = ik'(k)\widehat{u}, \tag{A.2}$$

where $k'(k)$ is a modified wavenumber and $\widehat{u}$ indicates the Fourier transform of u. The modified wavenumbers for the second- and fourth-order central differencing schemes for the first order derivative are

$$k'(k) = \frac{sin(k\Delta x)}{\Delta x}, \tag{A.3}$$

and

$$k'(k) = \frac{sin(k\Delta x)(4 - cos(k\Delta x))}{3\Delta x} \tag{A.4}$$

respectively.

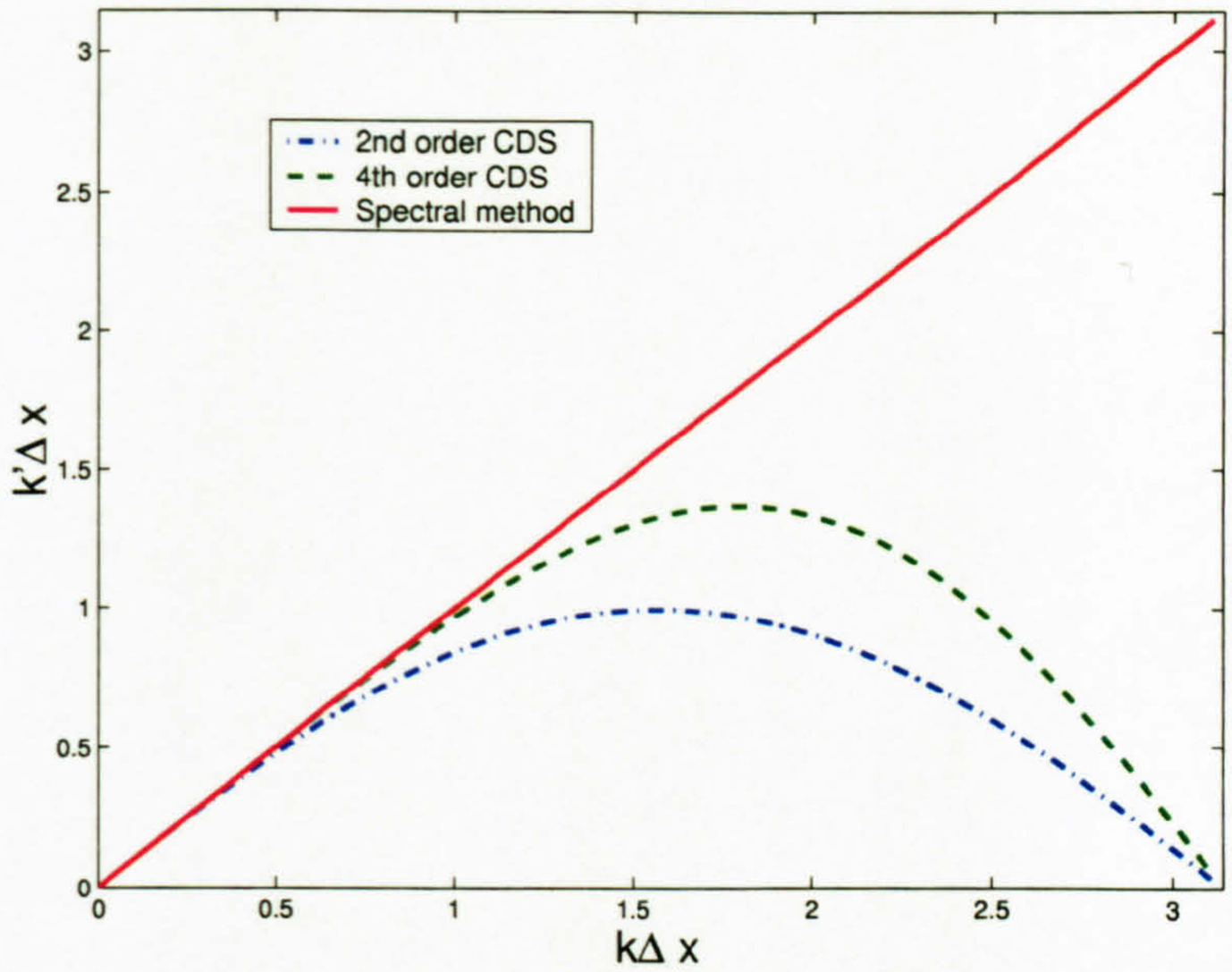

Figure A.1: *Modified* wave numbers

As shown in figure A.1, the spectral method gives an exact representation of the first derivative up to the grid resolution level. Both 2nd- and 4th-order central finite difference schemes give large errors at high wavenumbers, although the 4th-order central differencing scheme gives always better approximation than the 2nd-order one. In other words, all finite difference (or finite volume) methods have low modified wavenumbers near the grid cutoff point. The smaller the turbulent scales are, the bigger is the wavenumber to be resolved. Consequently, very fine grid resolution is normally required by even higher order central difference discretizations to capture these scales.

The smaller scales also have larger levels of aliasing error (Moin and Mahesh, 1998). Aliasing error is associated with the computation of the nonlinear convection term by taking products in physical space on a discrete lattice. By evaluating this term discretely, higher frequency components, beyond the grid wavenumber cutoff, are incorrectly "aliased" to wavenumbers that are resolved. As shown by Ghosal (1996) and Chow and Moin (2003), the aliasing errors have an adverse effect over the subgrid scale force modelling because they are concentrated in the high wavenumber range of the energy spectrum, while it is in this range that scale-invariance information is extracted in order to construct the LES models.

In the following paragraphs, the different forms of the convection term will be presented and the aliasing errors will be illustrated using simple one-dimensional analysis.

A.2 Forms of convective derivative

The nonlinear convective terms in the Navier-Stokes equation can be expressed using four analytically, but not numerically, equivalent formulations:

Divergence (or conservative) form,

$$N_i^d = \frac{\partial u_i u_j}{\partial x_j} \tag{A.5}$$

Convective (or advective) form,

$$N_i^c = u_j \frac{\partial u_i}{\partial x_j} \tag{A.6}$$

Skew-symmetric (or Arakawa [1]) form,

$$N_i^s = \frac{1}{2}\frac{\partial u_i u_j}{\partial u_j} + \frac{1}{2} u_j \frac{\partial u_i}{\partial x_j} \tag{A.7}$$

Rotational form,

$$N_i^r = u_j \left(\frac{\partial u_i}{\partial x_j} - \frac{\partial u_j}{\partial x_i} \right) + \frac{1}{2}\frac{\partial u_j u_j}{\partial x_i} \tag{A.8}$$

Horiuti (1987) performed numerical simulation of turbulent channel flow using a finite difference scheme with the skew-symmetric form and the rotational form. He attributed the worse performance of the rotational form to large truncation errors in the vicinity of the wall. Zang (1991) performed similar numerical simulation using these two forms of turbulent channel flow using spectral method with or without dealiasing treatment. He concluded that the worse performance of the rotational form was due to higher aliasing errors. Blaisdell et al. (1996), Kravchenko and Moin (1997) and Park et al. (2004) have proved that the skew-symmetric form has the smallest aliasing error and there is little difference between the results of aliased and dealiased simulations. On the other hand, the rotational form has the largest aliasing error.

A.3 Forms of aliasing errors

Aliasing errors appear when two functions are multiplied in a discrete space. We consider a uniform grid of $N+1$ points x_i, $i = 0, 1, ..., N$ in physical space and

[1] By following Arakawa (1966), Jordan (2003) denoted the skew-symmetric form as the Arakawa form.

$x \in [0, L]$ with $L = 2\pi$ for simplicity. Fourier expansions of two periodic discrete functions f and g can be obtained as:

$$f_j = \sum_{n=-N/2}^{N/2-1} \widehat{f}_n e^{i(2\pi/N)jn} \quad and \quad g_j = \sum_{m=-N/2}^{N/2-1} \widehat{g}_m e^{i(2\pi/N)jm} \tag{A.9}$$

where $\widehat{f}$ indicates the Fourier transform of function f. The Fourier coefficient of the product of these two discrete functions $w_j = f_j g_j$ (no summation on j) can be obtained as follows:

$$\widehat{w}_k = \sum_{n+m=k} \widehat{f}_n \widehat{g}_m + \sum_{n+m=k\pm N} \widehat{f}_n \widehat{g}_m \tag{A.10}$$

The second term in the right-hand side of equation A.10 is the aliasing error. Clearly, the contribution of aliasing errors is larger at higher wavenumbers.

Numerical approximation will also modify the aliasing errors of the derivatives of products when the aliasing errors are multiplied by modified wavenumbers. Therefore, the aliasing errors are multiplied by high wavenumbers in spectral methods. In contrast, low wavenumbers are multiplied with the aliasing errors in finite difference methods since the modified wavenumber decreases to zero at high wavenumber.

In order to perform one-dimensional analysis by Fourier transforming of the four different forms of convective derivative, the two functions $u(x)$ and $v(x)$ are defined on a one-dimensional domain $0 \leq x \leq \pi$ and projected onto discrete and uniform grid points $x_i (i = 0, 1, ..., N)$. They are also assumed to have the Fourier coefficients $\widehat{u} = \widehat{v} = \sqrt{E(k)}$, where $\sqrt{E(k)}$ is the von Karman spectrum (which is a good representation of high Reynolds number turbulence spectrum) defined as below

$$E^{high}(k) = \frac{a(k/k_p)^4}{\{b + (k/k_p)^2\}^{17/6}} \tag{A.11}$$

where $a = 2.683$, $b = 0.417$ and $k_p = 1$.

We obtain the following Fourier coefficients of the nonlinear terms.

$$\widehat{N}_1^d = ik'(k) \sum_{n+m=k} \widehat{u}_n \widehat{v}_m + ik'(k) \sum_{n+m=k\pm N} \widehat{u}_n \widehat{v}_m \tag{A.12}$$

$$\widehat{N}_1^c = \sum_{n+m=k} (ik'(m)\widehat{u}_n\widehat{v}_m + ik'(n)\widehat{u}_n\widehat{v}_m) + \sum_{n+m=k\pm N} (ik'(m)\widehat{u}_n\widehat{v}_m + ik'(n)\widehat{u}_n\widehat{v}_m) \tag{A.13}$$

$$\widehat{N}_1^s = \frac{1}{2}\widehat{N}_i^d + \frac{1}{2}\widehat{N}_i^c \tag{A.14}$$

where the second terms in $\widehat{N}_1^d$ and $\widehat{N}_1^c$ are the aliasing errors. One can see that unless the identity $k'(n+m) = k'(n) + k'(m)$ holds, $\widehat{N}_1^d$ and $\widehat{N}_1^c$ are not the same even if the aliasing errors are removed.

If aliasing errors are denoted as $E_i^{alias}(k)$, the PSD of the aliasing errors can be defined as $\varepsilon_i^{alias}(k) = (2\pi/L)E_i^{alias}(k) \cdot E_i^{alias*}(k)$. Since upwind scheme gives modified wavenumber as $k' = k_r + ik_i$ with $(k_r, k_i \in R)$, the PSD of the aliasing error for the divergence form (which is the form used in the present in-house code) is

$$\varepsilon_i^{alias}(k) = (k_r^2 + k_i^2)\left(\sum_{n+m=k\pm N} \sqrt{E(n)E(m)}\right)^2. \tag{A.15}$$

It can be seen from A.15 that the imaginary part of the modified wavenumber increases the PSD of the aliasing error. The aliasing error of the first order upwind scheme is larger than that of the second order central difference scheme because the two schemes have the same real part of modified wavenumber.

The skew-symmetrical form $\widehat{N}_1^s$ has the smallest aliasing errors because aliasing errors of divergence form $\widehat{N}_1^d$ and convective form $\widehat{N}_1^c$ have opposite signs (Kravchenko and Moin, 1997; Fedioun et al., 2001). One-dimensional analysis on the aliasing error and conservation property (Zang, 1991; Blaisdell et al., 1996; Kravchenko and Moin, 1997) also suggested that the use of the skew-symmetric form gives the least aliasing error. However, Fedioun et al. (2001) proposed that high-order central difference schemes shall be used in conjunction with the convective form N_i^c in order to minimize the aliasing errors for isotropic turbulence test. Park et al. (2004) confirmed that the skew-symmetric form combined with 4th-order central difference (COM4) gives the least aliasing error as well as trunction error compared with other forms.

Appendix B

Accuracy analysis of 1D advection equation

The von Neumann analysis can be used to illustrate the effect of time advancement and spatial discretisation on the error at different scales. Several temporal and spatial discretization schemes can be applied to solve the one dimension inviscid linear Burgers equation:

$$\frac{\partial u}{\partial t} + c\frac{\partial u}{\partial x} = 0 \tag{B.1}$$

Assuming $u(x,t) = A_0 e^{\alpha t} e^{ikx}$, the following relationship can be obtained,

$$\alpha = -ick; \quad u_{j+1}^{n+1} = u_j^{n+1} \cdot e^{ik\Delta x}; \quad u_{j-1}^{n+1} = u_j^{n+1} \cdot e^{-ik\Delta x}. \tag{B.2}$$

If the CFL number is defined as $\gamma = \frac{c\Delta t}{\Delta x}$ and the phase angle as $\theta = k\Delta x$, the amplification factor of the exact solution of equation B.1 is

$$G_{exact} = \frac{u_j^{n+1}}{u_j^n} = \frac{u(x, t+\Delta t)}{u(x,t)} = e^{-i\gamma\theta} \tag{B.3}$$

It is obvious that the magnitude of the exact solution is equal to 1. This indicates that the analytical solution has zero numerical dissipation.

The exact phase angle is

$$\Psi_{an} = -\gamma\theta \tag{B.4}$$

After the equation is discretized, the complex amplification factor will be a

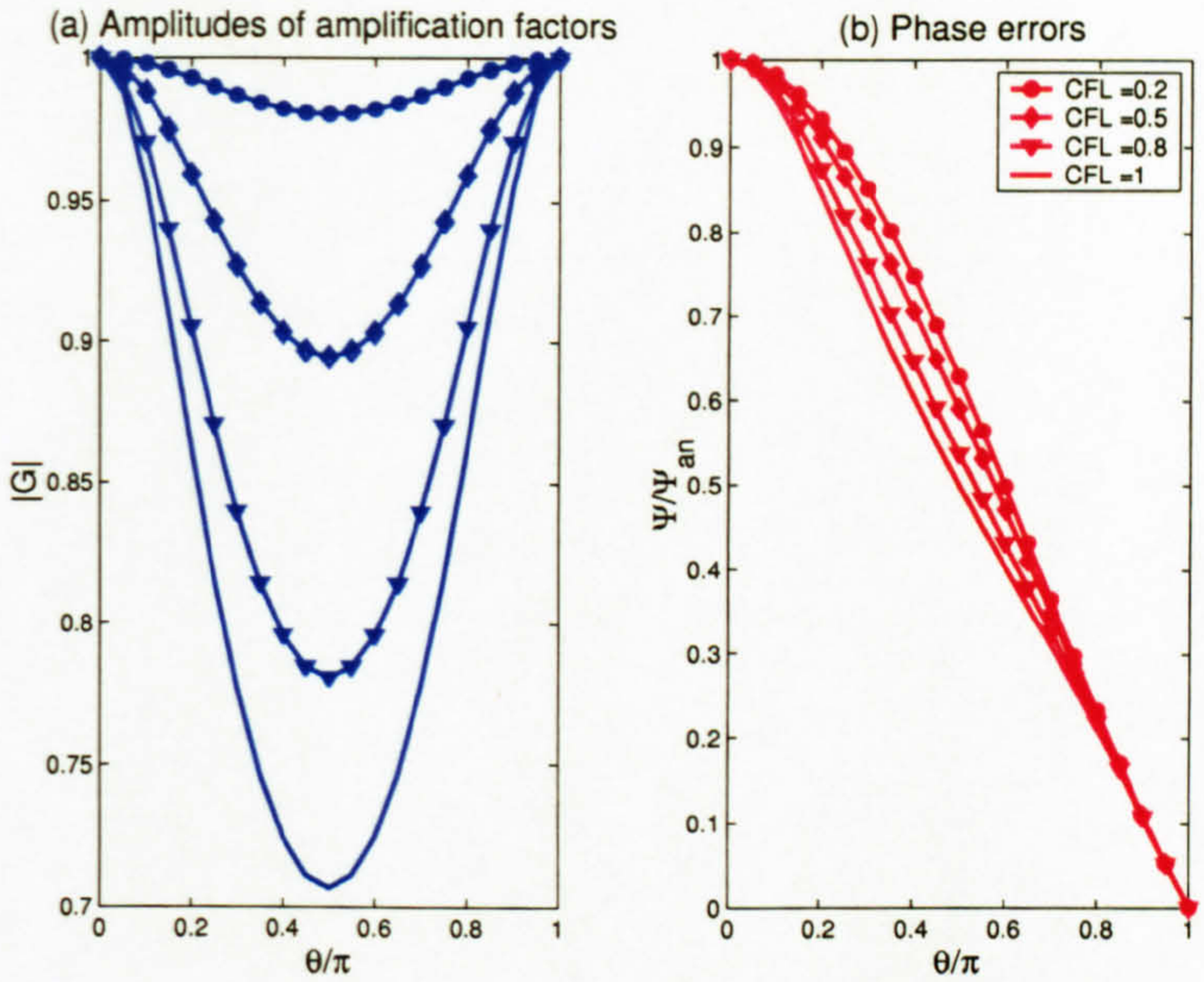

Figure B.1: $|G|$ and Ψ/Ψ_{an} when the first order Euler implicit and the second order CDS are used for the 1D wave equation

function of $\theta' = k'\Delta x$ and γ. The magnitude (or amplitude) of G is calculated as

$$|G| = \left(Real(G)^2 + Imag(G)^2\right)^{1/2} \tag{B.5}$$

and the phase error of G is calculated as follows:

$$\frac{\Psi}{\Psi_{an}} = \frac{tan^{-1}\left(Imag(G)/Real(G)\right)}{-\gamma\theta} \tag{B.6}$$

where $\frac{\Psi}{-k\Delta t}$ represents the numerical propagation speed.

Table B summarises the discrete forms of the inviscid linear Burgers equation and amplification factors for three different time-marching schemes combined with two central differencing schemes.

As shown in separate figures, the amplitudes of amplification factors and the phase errors are plotted as a function of $k\Delta x$ and γ. Figure B.1 shows the amplitudes of the amplification factors and the phase errors when the first order implicit Euler scheme is used for time marching and the 2CDS for the spatial discretization. The smaller γ is, the nearer is the amplitude of the amplification factors to 1. The phase errors are also smaller with smaller CFL number γ.

If 4CDS is used for spatial discretization with the first order implicit Euler scheme as shown in figure B.2, the amplitudes of the amplication factors are re-

von Neumann analysis of inviscid Burgers equation			
Time Scheme	Space Scheme	Discrete form of the equation	Amplification Factor G
1st order Euler implicit	2nd order CDS	$\frac{u_j^{n+1}-u_j^n}{\Delta t}+c\frac{u_{j+1}^{n+1}-u_{j-1}^{n+1}}{2\Delta x}=0$	$\frac{1}{1+i\gamma sin\theta}$
	4th order CDS	$\frac{u_j^{n+1}-u_j^n}{\Delta t}+c\frac{-u_{j+2}^{n+1}+8u_{i+1}^{n+1}-8u_{i-1}^{n+1}+u_{j-2}^{n+1}}{12\Delta x}=0$	$\frac{1}{1+i\frac{\gamma}{6}(-sin2\theta+8sin\theta)}$
2nd order Euler implicit	2nd order CDS	$\frac{3u_j^{n+1}-4u_j^n+u_j^{n-1}}{2\Delta t}+c\frac{u_{j+1}^{n+1}-u_{j-1}^{n+1}}{2\Delta x}=0$	$\frac{4\pm\sqrt{16-4(3+2i\gamma sin\theta)}}{6+4i\gamma sin\theta}$
	4th order CDS	$\frac{3u_j^{n+1}-4u_j^n+u_j^{n-1}}{2\Delta t}+c\frac{-u_{j+2}^{n+1}+8u_{i+1}^{n+1}-8u_{i-1}^{n+1}+u_{j-2}^{n+1}}{12\Delta x}=0$	$\frac{4\pm\sqrt{16-4\left[3+i\frac{\gamma}{3}(8sin\theta-sin2\theta)\right]}}{6+i\frac{2\gamma}{3}(8sin\theta-sin2\theta)}$
2nd order Crank-Nicolson	2nd order CDS	$\frac{u_j^{n+1}-u_j^n}{\Delta t}+\frac{c}{2}\left(\frac{u_{j+1}^{n+1}-u_{j-1}^{n+1}}{2\Delta x}+\frac{u_{j+1}^n-u_{j-1}^n}{2\Delta x}\right)=0$	$\frac{2-i\gamma sin\theta}{2+i\gamma sin\theta}$
	4th order CDS	$\frac{u_j^{n+1}-u_j^n}{\Delta t}+\frac{c}{2}\left(\frac{-u_{j+2}^{n+1}+8u_{i+1}^{n+1}-8u_{i-1}^{n+1}+u_{j-2}^{n+1}}{12\Delta x}+\frac{-u_{j+2}^n+8u_{i+1}^n-8u_{i-1}^n+u_{j-2}^n}{12\Delta x}\right)=0$	$\frac{1-i\frac{\gamma}{12}(-sin2\theta+8sin\theta)}{1+i\frac{\gamma}{12}(-sin2\theta+8sin\theta)}$

Table B.1: Algebraic (discretised) schemes for the 1D wave equation $\frac{\partial u}{\partial t}+c\frac{\partial u}{\partial x}=0$ and associated amplification factors.

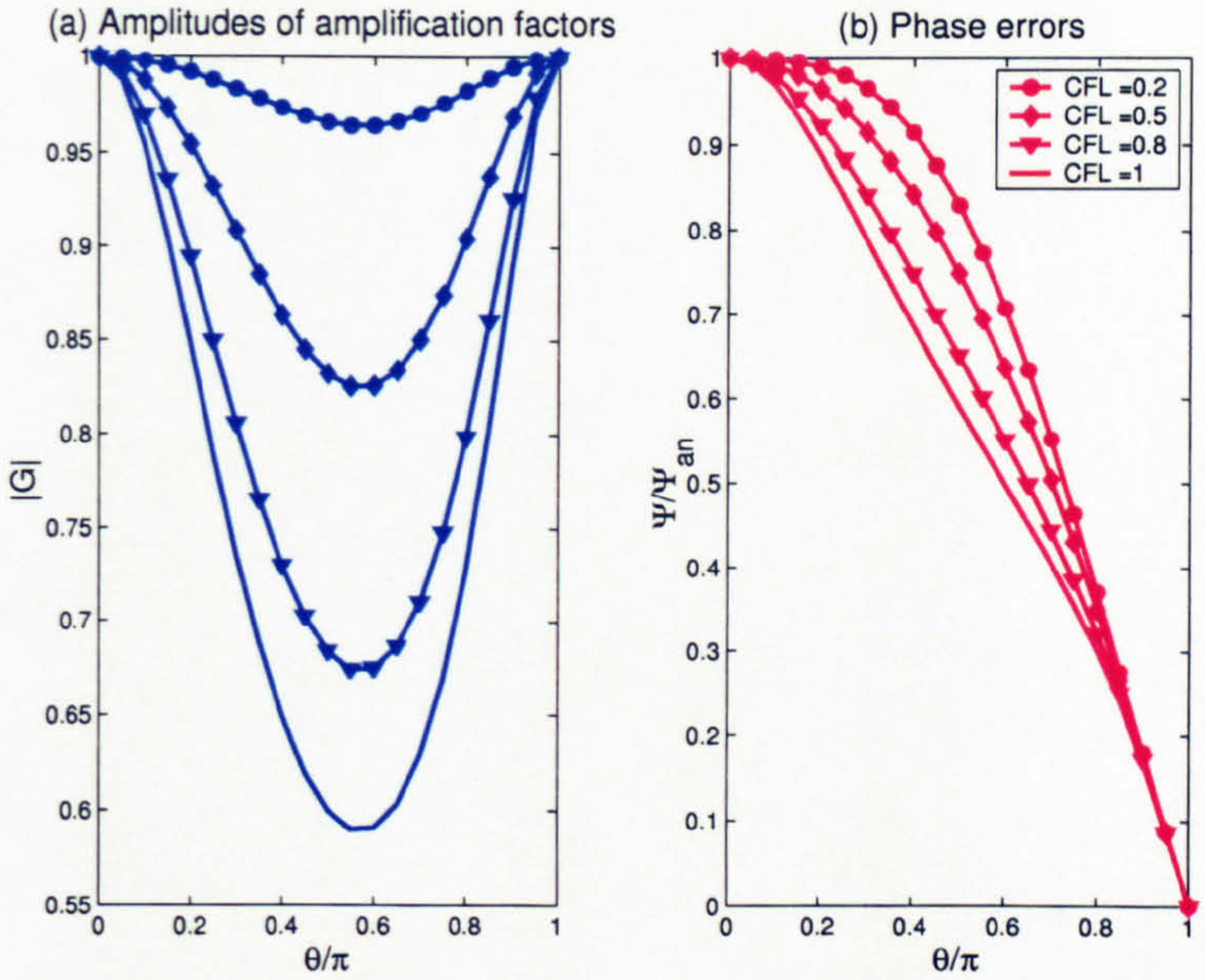

Figure B.2: $|G|$ and Ψ/Ψ_{an} when the first order Euler implicit and the 4th order CDS are used for the 1D wave equation

duced more than the 2CDS, despite that the phase errors are much improved in the low wavenumber range.

Figure B.3 shows the amplitudes of amplification factors and the phase errors when the second order implicit Euler time-marching scheme and 2CDS for spatial discretization are used. The amplitudes of the amplification factors are much closer to 1 compared with the first order implicit Euler scheme, while the phase errors are nearly identical to those with the first order implicit Euler scheme.

Figure B.4 shows the amplitudes of amplification factors and the phase errors when the second order implicit Euler time-marching scheme and 4CDS for spatial discretization are used. The amplitudes of the amplification factors are much closer to 1 compared with the first order implicit Euler scheme. However, they are slightly further away from 1 compared with the previous scheme. Nevertheless, the phase errors are much reduced due to the higher order spatial discretization scheme used.

Figure B.5 shows the amplitudes of amplification factors and the phase errors when the Crank and Nicolson (1947) scheme is used for time marching and the 2CDS is used for spatial discretization. One can see that the amplification factors are always equal to 1 for different CFL numbers γ. The effect of different CFL numbers on the phase errors is also very small.

If the 2nd order Crank-Nicolson time marching scheme is used with the 4CDS

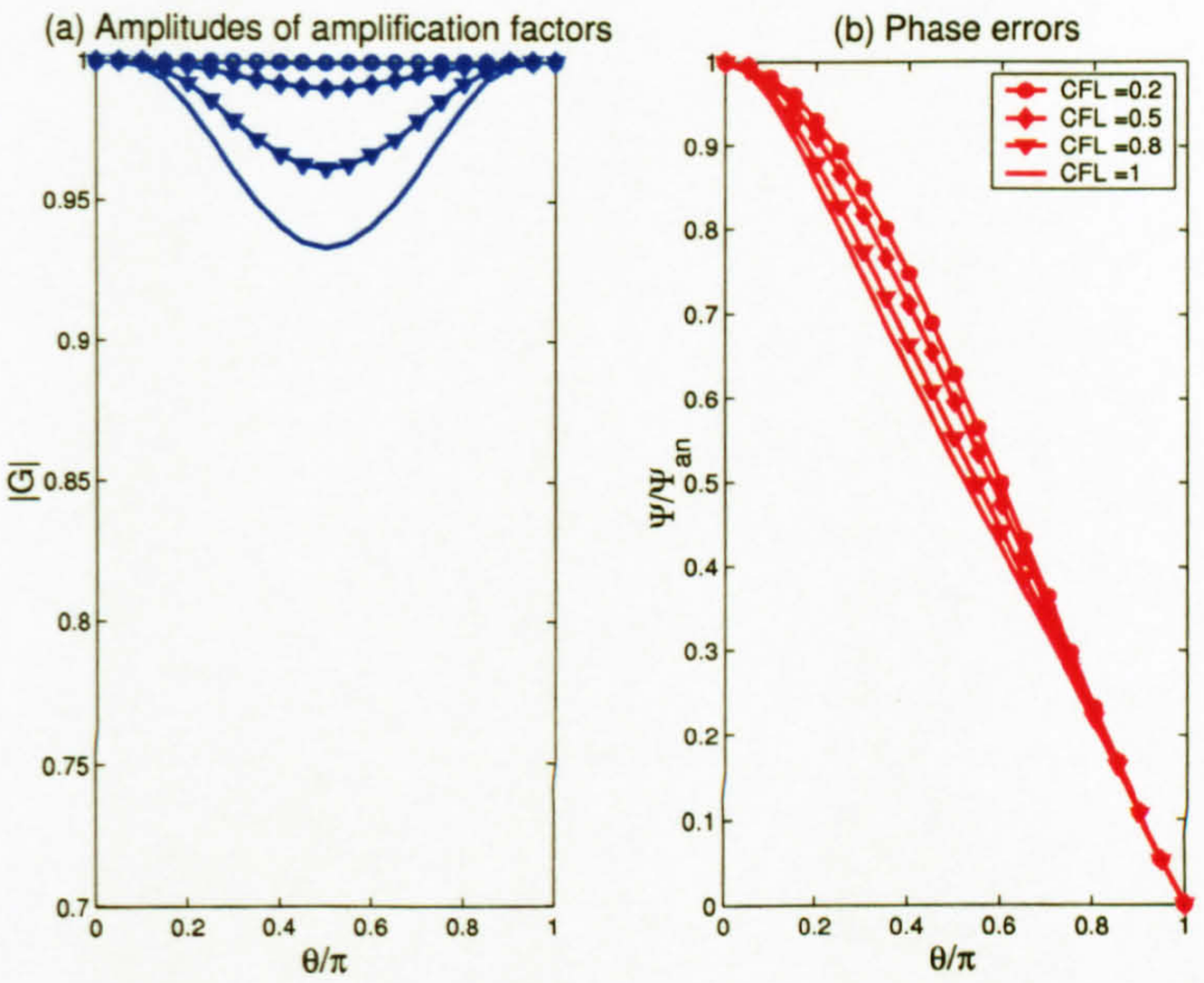

Figure B.3: $|G|$ and Ψ/Ψ_{an} when the 2nd order implicit scheme and the 2nd order CDS are used for the 1D wave equation

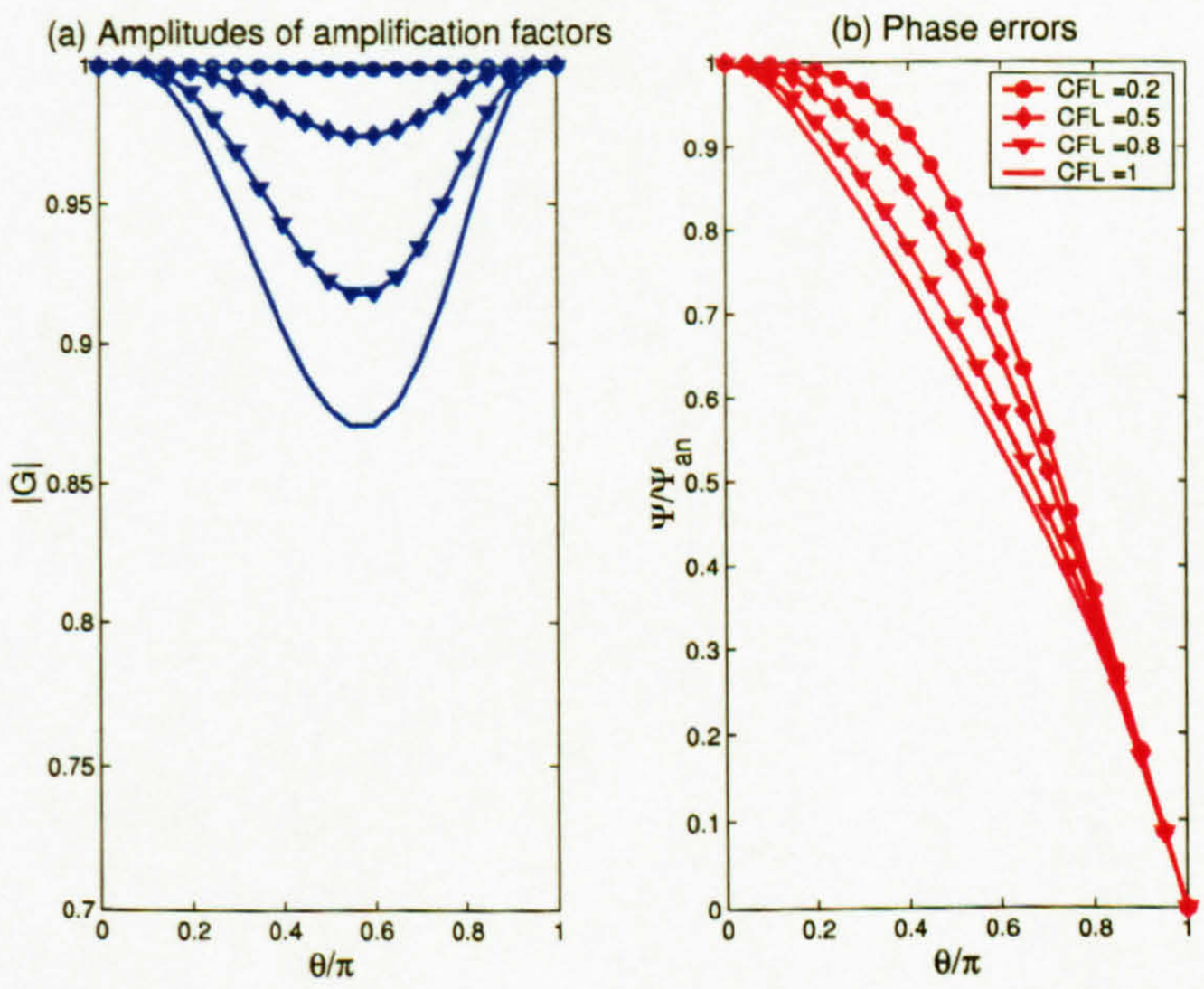

Figure B.4: $|G|$ and Ψ/Ψ_{an} when the 2nd order implicit scheme and the 4th order CDS are used for the 1D wave equation

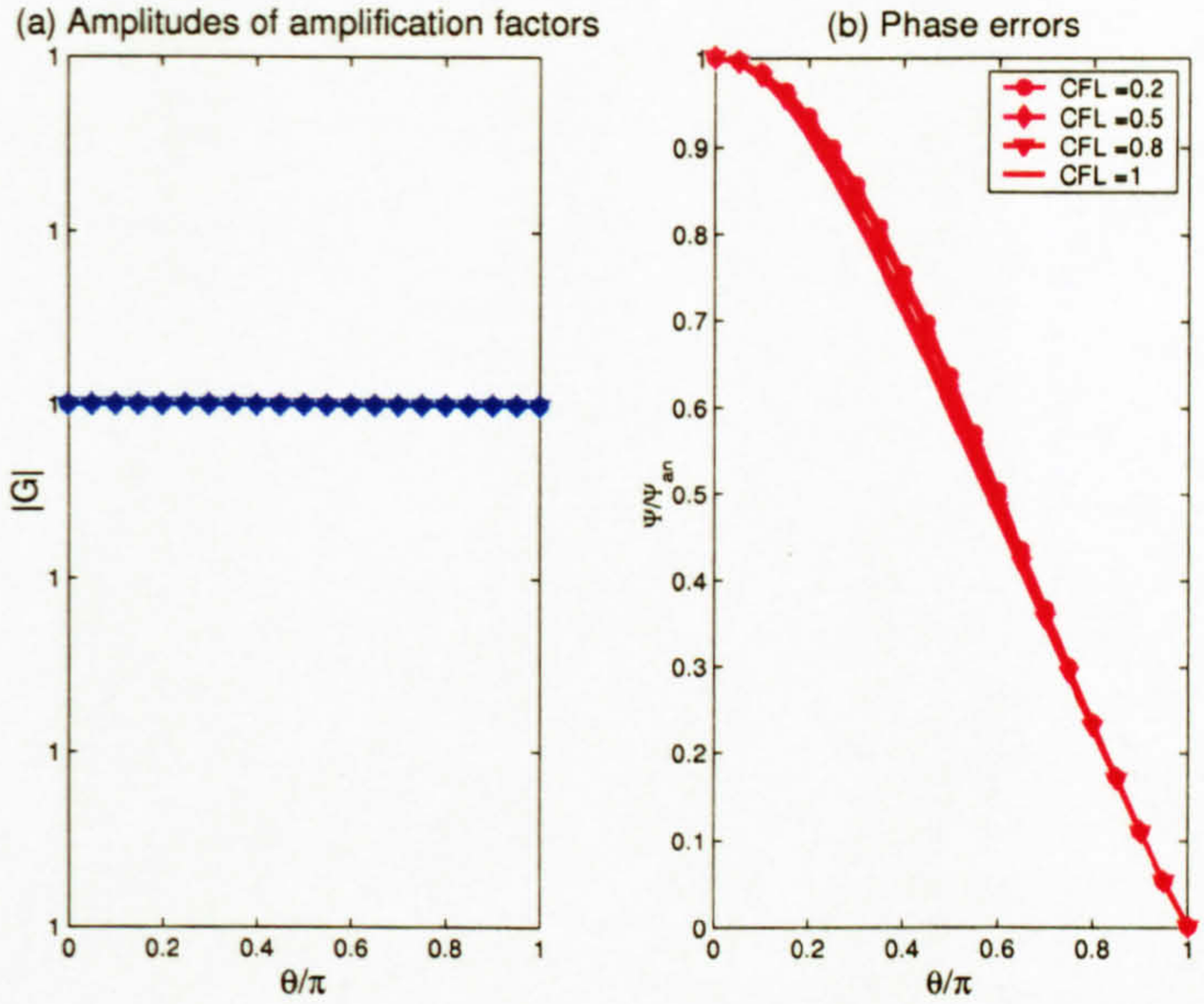

Figure B.5: $|G|$ and Ψ/Ψ_{an} when the Crank-Nicolson scheme and the 2nd order CDS are used for the 1D wave equation

for spatial discretization as shown in figure B.6, the amplitudes of the amplification factors are still preserved as 1 for different CFL numbers. The phase errors are much reduced at the low wavenumber range compared with the 2CDS.

From the above, it can be seen that the Crank-Nicolson time-advancing scheme combined with the 2nd- or 4th- order central differencing scheme could retain the amplitude of amplification factor always equal to 1. Generally, the 4th order CDS always gives lower phase errors than the 2nd order CDS. The Crank-Nicolson combined with 4th order CDS appears to be the best combination to control phase errors. However, all central difference schemes give high phase errors (lagging) at high wavenumbers.

Since the 2CDS is easier to implement in a fully unstructured code, it was used in all calculations in this thesis along with the Crank-Nicolson time advancing scheme.

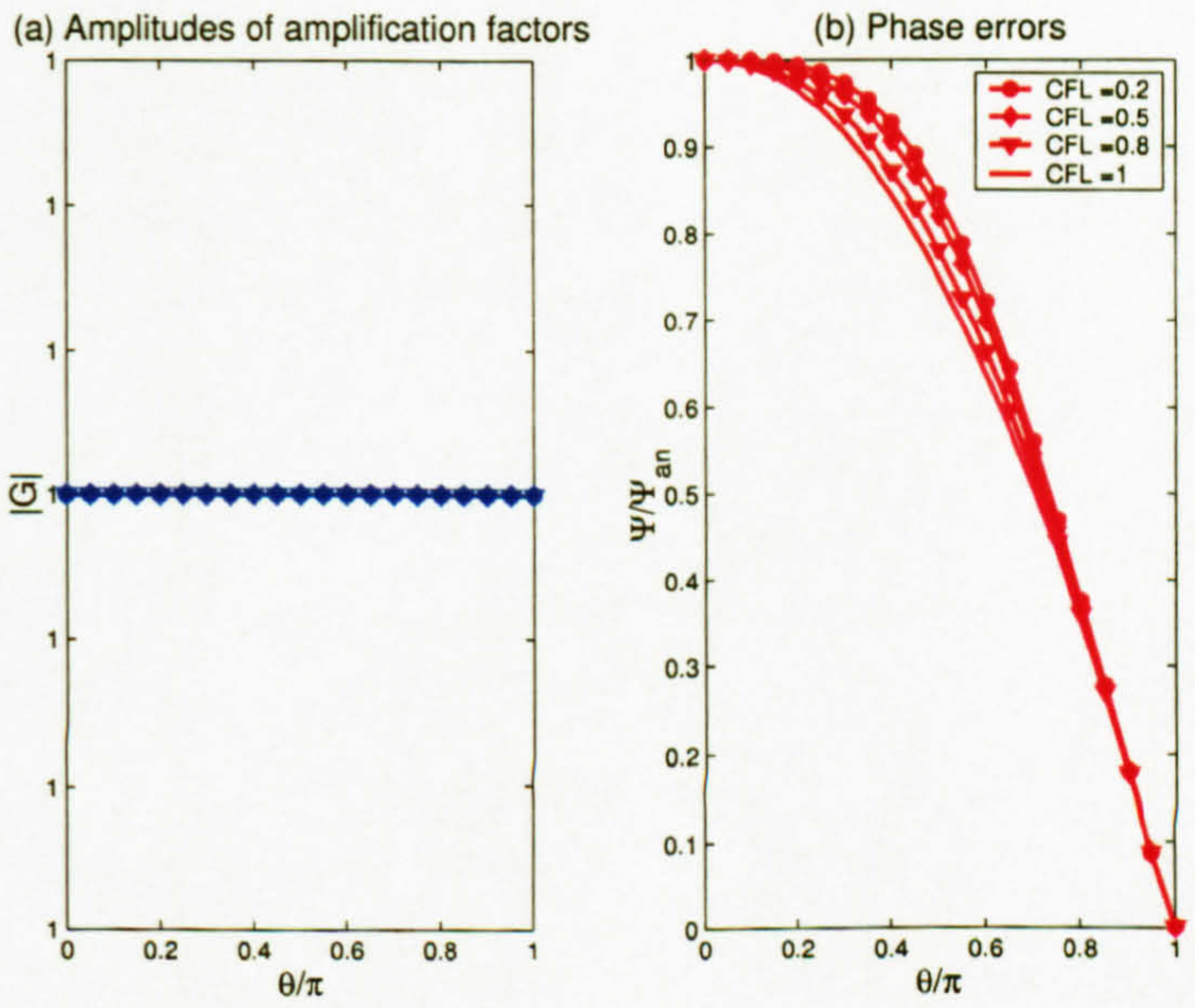

Figure B.6: $|G|$ and Ψ/Ψ_{an} when the Crank-Nicolson scheme and the 4th order CDS are used for the 1D wave equation

Appendix C

Kinetic Energy Conservation

In this chapter, the discrete approximations are analysed in order to check their kinetic energy conservation property. The notations of the discrete and averaging operators follow Morinishi et al. (1998) and Ham et al. (2002).

Three basic operators are used to derive all other operators in Morinishi et al. (1998), and they are extended to include the temporal dimension as follows:

$$\left.\frac{\delta_1 \phi}{\delta_1 x_j}\right|_{x_1,x_2,x_3,n} = \frac{\phi^n_{x_{j+1/2}} - \phi^n_{x_{j-1/2}}}{x_{j+1/2} - x_{j-1/2}}, \tag{C.1}$$

$$\left.\overline{\phi}^{1x_j}\right|_{x_1,x_2,x_3,n} = \frac{\phi^n_{x_{j+1/2}} + \phi^n_{x_{j-1/2}}}{2}, \tag{C.2}$$

$$\left.\widetilde{\phi\psi}^{1x_j}\right|_{x_1,x_2,x_3,n} = \frac{1}{2}\phi^n_{x_{j+1/2}}\psi^n_{x_{j-1/2}} + \frac{1}{2}\psi^n_{x_{j+1/2}}\phi^n_{x_{j-1/2}}. \tag{C.3}$$

Because the cell centroid is the geometric center of the cell, the physical space and mesh can be described in terms of the face locations as follows:

$$x_j = \frac{1}{2}(x_{j+1/2} + x_{j-1/2}). \tag{C.4}$$

The following relations used by Morinishi et al. (1998) are valid for uniform grids, however, they are not applicable to non-uniform meshes

$$\left.\frac{\delta_1 \widetilde{\phi\psi}^{1x_j}}{\delta_1 x_j}\right|_{x_1,x_2,x_3,n} = \phi\frac{\delta_2 \psi}{\delta_2 x_j} + \psi\frac{\delta_2 \phi}{\delta_2 x_j}, \tag{C.5}$$

$$\frac{\delta_2 \phi}{\delta_2 x_j} = \frac{\delta_1 \overline{\phi}^{1x_j}}{\delta_1 x_j}, \tag{C.6}$$

$$\frac{\delta_1 \overline{\phi}^{1x_j}}{\delta_1 x_j} = \overline{\frac{\delta_1 \phi}{\delta_1 x_j}}^{1x_j} . \tag{C.7}$$

Vasilyev (2000) points out that the commutation error between the discrete differencing and averaging operators destroys the kinetic energy conservation property for the non-uniform mesh. The commutation error exists due to the fact that

$$\frac{\delta_1 \overline{\phi}^{1x_j}}{\delta_1 x_j} = \frac{\phi_{x_{j+1}} - \phi_{x_{j-1}}}{2(x_{j+1/2} - x_{j-1/2})}, \tag{C.8}$$

and

$$\overline{\frac{\delta_1 \phi}{\delta_1 x_j}}^{1x_j} = \frac{\phi_{x_{j+1}} - \phi_{x_j}}{x_{j+3/2} - x_{j-1/2}} + \frac{\phi_{x_j} - \phi_{x_{j-1}}}{x_{j+1/2} - x_{j-3/2}}. \tag{C.9}$$

are not identical.

The following operators used by Morinishi et al. (1998) are proved to be commutable for both the uniform and non-uniform grids:

$$[\widetilde{(\phi\psi)\psi}]^{1x_j} = \overline{\phi}^{1x_j}[\widetilde{\psi\psi}^{1x_j}], \tag{C.10}$$

$$\overline{\phi}^{1x_j}\overline{\psi}^{1x_j} = \frac{1}{2}\overline{\phi\psi}^{1x_j} + \frac{1}{2}\widetilde{\phi\psi}^{1x_j}, \tag{C.11}$$

$$\overline{\psi\frac{\delta_1\phi}{\delta_1 x_j}}^{1x_j} = \frac{\delta_1\psi\overline{\phi}^{1x_j}}{\delta_1 x_j} - \phi\frac{\delta_1\psi}{\delta_1 x_j}, \tag{C.12}$$

$$\phi\frac{\delta_1\psi\overline{\phi}^{1x_j}}{\delta_1 x_j} = \frac{1}{2}\frac{\delta_1\psi\widetilde{\phi\phi}^{1x_j}}{\delta_1 x_j} + \frac{1}{2}\phi\phi\frac{\delta_1\psi}{\delta_1 x_j}. \tag{C.13}$$

The following two operators are defined for discrete differencing and averaging in the temporal dimension as follows, if everything is evaluated at $(x_i, x_j, x_k, n+1/2)$:

$$\left.\frac{\delta_1\phi}{\delta_1 t}\right|_{x_1,x_2,x_3,n+1/2} = \frac{\phi^{n+1} - \phi^n}{\Delta t}, \tag{C.14}$$

$$\left.\overline{\phi}^{1t}\right|_{x_1,x_2,x_3,n+1/2} = \frac{\phi^{n+1} + \phi^n}{2}. \tag{C.15}$$

To produce the kinetic energy conservative scheme, Ham et al. (2002) provide two weighted averaging operators as follows:

$$\overline{\phi}^{1\hat{x}_j}\Big|_{x_1,x_2,x_3,n+1/2} = \frac{(x_j - x_{j-1/2})\phi_{x_{j+1/2}} + (x_{j+1/2} - x_j)\phi_{x_{j-1/2}}}{x_{j+1/2} - x_{j-1/2}}, \tag{C.16}$$

$$\overline{\phi}^{1\check{x}_j}\Big|_{x_1,x_2,x_3,n+1/2} = \frac{(x_{j+1/2} - x_j)\phi_{x_{j+1/2}} + (x_j - x_{j-1/2})\phi_{x_{j-1/2}}}{x_{j+1/2} - x_{j-1/2}}. \tag{C.17}$$

Because the temporal dimension is uniform, the following discrete differencing and averaging operators are commutable:

$$\frac{\delta_1\overline{\phi}^{1x_j}}{\delta_1 t}\Big|_{x_1,x_2,x_3,n+1/2} = \overline{\frac{\delta_1\phi}{\delta_1 t}}^{1x_j}\Big|_{x_1,x_2,x_3,n+1/2}, \tag{C.18}$$

$$\frac{\delta_1\overline{\phi}^{1t}}{\delta_1 x_j}\Big|_{x_1,x_2,x_3,n+1/2} = \overline{\frac{\delta_1\phi}{\delta_1 x_j}}^{1t}\Big|_{x_1,x_2,x_3,n+1/2}. \tag{C.19}$$

It is proved that the following operators are commutable for both uniform and non-uniform grids, if they are evaluated at the cell-centered location and the staggered location respectively.

$$\frac{\delta_1\overline{\phi}^{1\hat{x}_j}}{\delta_1 x_j}\Big|_{x_1,x_2,x_3,n+1/2} = \overline{\frac{\delta_1\phi}{\delta_1 x_j}}^{1\hat{x}_j}\Big|_{x_1,x_2,x_3,n+1/2} = \overline{\frac{\delta_1\phi}{\delta_1 x_j}}^{1x_j}\Big|_{x_1,x_2,x_3,n+1/2}, \tag{C.20}$$

$$\frac{\delta_1\overline{\psi}^{1\check{x}_j}}{\delta_1 x_j}\Big|_{x_{j+1/2},n+1/2} = \overline{\frac{\delta_1\psi}{\delta_1 x_j}}^{1\check{x}_j}\Big|_{x_{j+1/2},n+1/2} = \frac{\delta_1\overline{\psi}^{1x_j}}{\delta_1 x_j}\Big|_{x_{j+1/2},n+1/2} = \frac{\psi_{x_{j+3/2}} - \psi_{x_{j-1/2}}}{x_{j+3/2} - x_{j-1/2}}. \tag{C.21}$$

The averaged form of kinetic energy transport equation presented in Ham et al. (2002) for staggered grid is

$$\overline{\overline{u_j}^{1t}\left(\frac{\delta_1 u_j}{\delta_1 t} + \frac{\delta_1\overline{\overline{u_i}^{1t}}^{1\check{x}_j}\overline{\overline{u_j}^{1t}}^{1x_i}}{\delta_1 x_i} + \frac{\delta_1 p}{\delta_1 x_j}\right)}^{1x_j} = 0. \tag{C.22}$$

where the viscous term is not included.

The temporal term is written as follows:

$$(Time.)|_{staggered} = \overline{u_j}^{1t}\frac{\delta_1 u_j^{n+1/2}}{\delta_1 t}^{1x_j} = \frac{\delta_1 \overline{u_j^{n+1/2} u_j^{n+1/2}}^{1x_j}}{\delta_1 t}. \quad \text{(C.23)}$$

The convective term is written using C.13 and C.21 as follows:

$$(Conv.)|_{staggered} = \overline{u_j}^{1t}\left(\frac{\delta_1 \overline{u_i}^{1t^{1\check{x}_j}} \overline{u_j}^{1t^{1x_i}}}{\delta_1 x_i}\right)^{1x_j} = \frac{1}{2}\frac{\delta_1 \overline{u_i}^{1t^{1\check{x}_j}} \widetilde{\overline{u_j}^{1t}\overline{u_j}^{1t}}^{1x_i}}{\delta_1 x_i}^{1x_j} + \frac{1}{2}\overline{u_j}^{1t}\overline{u_j}^{1t}\frac{\delta_1 \overline{u_i}^{1t^{1\check{x}_j}}}{\delta_1 x_i}^{1} \quad \text{(C.24)}$$

The pressure term is written using C.12 and C.20 as follows:

$$(Pres.)|_{staggered} = \overline{u_j}^{1t}\frac{\delta_1 p}{\delta_1 x_j}^{1x_j} = \frac{\delta_1 \overline{u_j}^{1t}\overline{p}^{1x_j}}{\delta_1 x_j} - p\frac{\delta_1 \overline{u_j}^{1t}}{\delta_1 x_j} = \frac{\delta_1 \overline{u_j}^{1t}\overline{p}^{1\hat{x}_j}}{\delta_1 x_j} - p\frac{\delta_1 u_j}{\delta_1 x_j}^{1t}. \quad \text{(C.25)}$$

The continuity equation in the staggered grids is satisfied, so that the last term in C.24 and the last term in C.25 vanish. The kinetic energy is conserved for this scheme.

The present in-house code uses the collocated grids, where the velocities and pressure are located at the cell centroids. The special interpolation proposed by Rhie and Chow (1983) is used to obtain the face flux velocity. Details of 1D analysis for the numerical accuracy of the interpolation for uniform and non-uniform mesh with a constant expansion ratio have been described in chapter 3. The face velocity is

$$F_j|_{x_{j+1/2},n+1/2} = \overline{u_j^*}^{1\hat{x}_j} - \frac{\overline{\Delta\Omega}^{1\hat{x}_j}}{Ap}\left(\left.\frac{\delta_1 p}{\delta_1 x_j}\right|_{x_{j+1/2},n+1/2} - \left.\frac{\overline{\delta_2 p}^{1\hat{x}_j}}{\delta_2 x_j}\right|_{x_{j+1/2},n+1/2}\right). \quad \text{(C.26)}$$

Ignoring the viscous term, the kinetic energy transport equation is written for the collocated grids as follows:

$$\overline{u_j}^{1t}\left(\frac{\delta_1 u_j}{\delta_1 t} + \frac{\delta_1 \overline{F_i}^{1t^{1\hat{x}_j}} \overline{u_j}^{1t^{1x_i}}}{\delta_1 x_i} + \frac{\overline{\delta_1 p}^{1x_j}}{\delta_1 x_j}\right) = 0. \quad \text{(C.27)}$$

The temporal term is written as follows:

$$(Time.)|_{collocated} = \overline{u_j}^{1t} \frac{\delta_1 u_j^{n+1/2}}{\delta_1 t} = \frac{\delta_1 \frac{u_j^{n+1/2} u_j^{n+1/2}}{2}}{\delta_1 t}. \tag{C.28}$$

The convective term is written as follows:

$$(Conv.)|_{collocated} = \overline{u_j}^{1t} \left(\frac{\delta_1 \overline{\overline{F_i}^{1t}}^{1\hat{x}_j} \overline{\overline{u_j}^{1t}}^{1x_i}}{\delta_1 x_i} \right) = \frac{1}{2} \frac{\delta_1 \overline{\overline{F_i}^{1t}}^{1\hat{x}_j} \widetilde{\overline{u_j}^{1t} \overline{u_j}^{1t}}^{1x_i}}{\delta_1 x_i} + \frac{1}{2} \overline{u_j}^{1t} \overline{u_j}^{1t} \frac{\overline{\delta_1 \overline{F_i}^{1t}}^{1\hat{x}_j}}{\delta_1 x_i}. \tag{C.29}$$

Morinishi et al. (1998) discretises the pressure of the kinetic energy transport equation for the uniform mesh using equation C.5 transformation. It is noted that for the Finite Difference scheme, Vasilyev (2000) uses a Jocobian tranformation to extend C.5 into non-uniform grids. The pressure term is described only for the uniform mesh below.

$$(Pres.)|_{collocated} = \overline{u_j}^{1t} \frac{\delta_2 p}{\delta_2 x_j} = \frac{\widetilde{\delta_1 \overline{u_j}^{1t} p}^{1x_j}}{\delta_1 x_j} - p \frac{\delta_2 \overline{u_j}^{1t}}{\delta_2 x_j} = \frac{\widetilde{\delta_1 \overline{u_j}^{1t} p}^{1x_j}}{\delta_1 x_j} - p^{n+1} \frac{\overline{\delta_1 \overline{u_j}^{1t}}^{1x_j}}{\delta_1 x_j} \tag{C.30}$$

The continuity equation for the collocated grids is

$$\frac{\delta_1 F_j}{\delta_1 x_j} = 0. \tag{C.31}$$

Because equation C.31 is satisfied, the last term of the convective term in C.29 vanishes. Kim and Choi (2000) have also shown the conservative property of the convective term by using a fractional step method to obtain a divergence-free face-normal velocity in order to calculate the convective term in the next step. However, if the Rhie and Chow method is used, there is a conservation error for the pressure term C.30 because the last term of C.30 is not divergence zero.

The following discrete operators are written in the form of Taylor series expansion

$$\frac{\delta_1 p}{\delta_1 x_j} \simeq \frac{\partial p}{\partial x_j} + \frac{h^2}{24} \frac{\partial^3 p}{\partial^3 x_j}, \tag{C.32}$$

$$\overline{\frac{\delta_2 p}{\delta_2 x_j}}^{1\hat{x}_j} \simeq \frac{\partial p}{\partial x_j} + \frac{7h^2}{24} \frac{\partial^3 p}{\partial^3 x_j}. \tag{C.33}$$

where h is the grid size.

It can shown that the difference of the discrete pressure term is

$$\overline{\frac{\delta_2 p}{\delta_2 x_j}}^{1\hat{x}_j} - \frac{\delta_1 p}{\delta_1 x_j} \simeq \frac{h^2}{4}\frac{\partial^3 p}{\partial^3 x_j}. \tag{C.34}$$

Taking the discrete operation of C.26, we obtain that:

$$\frac{\delta_1 F_j}{\delta_1 x_j} = \frac{\delta_1 \overline{u_j^*}^{1\hat{x}_j}}{\delta_1 x_j} - \frac{\delta_1\left[\overline{\frac{\Delta\Omega}{Ap}}^{1\hat{x}_j}\left(\frac{\delta_1 p}{\delta_1 x_j}\Big|_{x_{j+1/2},n+1/2} - \overline{\frac{\delta_2 p}{\delta_2 x_j}}^{1\hat{x}_j}\right)\right]}{\delta_1 x_j}. \tag{C.35}$$

If uniform grids are used, equation C.35 can be written using C.6 as follows:

$$\frac{\delta_1 F_j}{\delta_1 x_j} = \frac{\delta_2 u_j^*}{\delta_2 x_j} - \frac{\delta_1\left[\overline{\frac{\Delta\Omega}{Ap}}^{1\hat{x}_j}\left(\frac{\delta_1 p}{\delta_1 x_j}\Big|_{x_{j+1/2},n+1/2} - \overline{\frac{\delta_2 p}{\delta_2 x_j}}^{1\hat{x}_j}\right)\right]}{\delta_1 x_j}. \tag{C.36}$$

The conservation error of the pressure term is written for the uniform grids as follows:

$$\frac{\delta_2 \overline{u_j}^{1t}}{\delta_2 x_j} - \frac{\delta_1 F_j}{\delta_1 x_j} = \frac{\delta_1\left[\overline{\frac{\Delta\Omega}{Ap}}^{1\hat{x}_j}\left(\frac{\delta_1 p}{\delta_1 x_j} - \overline{\frac{\delta_2 p}{\delta_2 x_j}}^{1\hat{x}_j}\right)\right]}{\delta_1 x_j}. \tag{C.37}$$

As reported in chapter 3, the order of the conservation error for non-uniform meshes is also $O(\Delta x^2 \Delta t)$.

Bibliography

Abe, H., Kawamura, H., Matsuo, Y. (2001) Direct numerical simulation of a fully developed turbulent channel flow with respect to reynolds number dependence. ASME J. Fluids Eng. 123: 382–393.

Addad, Y., Laurence, D., Talotte, C., Jacob, M. C. (2003) Large eddy simulation of a forward-backward facing step for acoustic source identification. Int. J. of Heat and Fluid Flow 24: 562–571.

Aiba, S., Tsuchida, H., Ota, T. (1982*a*) Heat transfer around tubes in in-line tube banks. Bulletin of the JSME 25: 919–926.

Aiba, S., Tsuchida, H., Ota, T. (1982*b*) Heat transfer around tubes in staggered tube banks. Bulletin of the JSME 25: 927–933.

Arakawa, A. (1966) Computational design for long-term numerical integration of the equations of fluid motion: two-dimensional incompressible flow, part i. J. Comput. Phys. 1: 119–143.

Arie, H., Kiya, M., Moriya, M., Mori, H. (1983) Pressure fluctuations on the surface of two circular cylinders in tandem arrangement. ASME J. Fluids Eng. 105: 161–167.

Armstrong, B. J., Barnes, F. H., Grant, I. (1986) The effect of a perturbation on the flow over a bluff cylinder. Physics of Fluids 29: 2095–2102.

Armstrong, B. J., Barnes, F. H., Grant, I. (1987) A comparison of the structure of the wake behind a circular cylinder in steady flow with that in a perturbed flow. Physics of Fluids 30: 19–26.

Balabani, S., Yianneskis, M. (1996) An experimental study of the mean flow and turbulence structure of cross-flow over tube bundles. Proc. of ImechE, Part C, J. Mech. Eng. Science 210: 317–331.

Balabani, S., Yianneskis, M. (1997) Vortex shedding and turbulence scales in staggered tube bundle flows. Canadian Journal of Chemical Engineering 75 (5): 823–831.

Balaras, E. (2004) Modeling complex boundaries using an external force field on fixed cartesian grids in large-eddy simulations. Computers and Fluids 33: 375–404.

Barbi, C., Favier, D. P., Maresca, C. A., Telionis, D. P. (1986) Vortex shedding and lock-on of a circular cylinder in oscillatory flow. Journal of Fluid Mechanics 170: 527–544.

Barsamian, H. R., Hassan, Y. A. (1997) Large eddy simulation of turbulent crossflow in tube bundles. Nuclear Engineering and Design Journal 172: 103–122.

Beale, S. B., Spalding, D. B. (1999) A numerical study of unsteady fluid flow in inline and staggered tube banks. Journal of Fluids and Structures 13: 723–754.

Beaudan, P., Moin, P. (1994) Numerical experiments on the flow past a circular cylinder at a subcritical reynolds number. *Tech. Rep.* TF-62. Thermosciences Division, Department of Mechanical Engineering, Stanford University.

Benhamadouche, S., Laurence, D. (2003) Les, coarse les and transient rans comparisons on the flow across a tube bundle. Internatianl Journal of Heat and Fluid Flow 24: 470–479.

Blaisdell, G. A., Spyropoulos, E. T., Qin, J. H. (1996) The effect of the formulation of nonlinear terms on aliasing errors in spectral methods. Applied Numerical Mathematics 21: 207–219.

Bloor, M. S. (1964) The transition to turbulence in a wake of a circular cylinder. Journal of Fluid Mechanics 19: 290–304.

Bouris, D., Bergeles, G. (1997) Numerical calculation of the effect of deposit formation on heat exchanger efficiency. International Journal of Heat and Mass Transfer 40: 4073–4084.

Bouris, D., Bergeles, G. (1999) Two dimensional time dependent simulation of the subcritical flow in a staggered tube bundle using a subgrid scale model. International Journal of Heat and Fluid Flow 20: 105–114.

Bouris, D., Papadakis, G., Bergeles, G. (2001) Numerical evaluation of alternate tube configurations for particle deposition rate in heat exchanger tube bundles. International Journal of Heat and Fluid Flow 22: 525–536.

Breuer, M. (1998) Numerical and modeling influences on large eddy simulations for the flow past a circular cylinder. International Journal of Heat and Fluid Flow 19: 512–521.

Breuer, M., Rodi, W. (1994) Large eddy simulation of turbulent flow through a square duct and 180 degree bend. In *Fluid Mech. and Its Appl.* (ed. P.R. Voke, R. Kleiser & J.P. Chollet), , vol. 26. Kluwer Academic.

Butterworth, D., Guy, A. R., Welkey, J. J. (1996) Design and applications of twisted tube exchangers. In *Advances in industrial heat transfer*. IChemE.

Buyruk, E., Johnson, M. W., Owen, I. (1998) Numerical and experimental study of flow and heat transfer around a tube in cross-flow at low reynolds number. International Journal of Heat and Fluid Flow 19: 223–232.

Cabot, W. (1996) Near-wall models in large eddy simulations of flow behind a backward facing step. In *Annual Research Briefs*, pp. 199–210. Center for Turbulence Research, Stanford.

Cabot, W., Moin, P. (1993) Large eddy simulation of scalar transport with the dynamic subgrid scale model. In *Large eddy simulation of complex engineering and geophysical flows* (ed. Galperin, B. & Orszag, A. S.), pp. 142–158. Cambridge University Press.

Cantwell, B., Coles, D. (1983) An experimental study of entrainment and transport in turbulent near wake of a circular cylinder. Journal of Fluid Mechanics 136: 321–374.

Castiglia, D., Papadakis, G., Balabani, S., Yianneskis, M. (2001) An experimental and numerical study of the flow past elliptic cylinder arrays. Proc. of IMechE, J. of Mech. Eng. Sci., Part C 215: 1287–1301.

Chang, B. H., Mills, A. F. (2004) Effect of aspect ratio on forced convection heat transfer from cylinders. Int. Journal of Heat and Mass Transfer 47: 1289–1296.

Chapman, D. R. (1979) Computational aerodynamics development and outlook. AIAA J. 17: 1293–1313.

Chester, S., Charlette, F., Meneveau, C. (2001) Dynamic turbulence model for large eddy simulations without test filtering:quantifying the accuracy of taylor series approximations. Theor. and Comput. Fluid Dyn. 15: 165–181.

Chow, F. K., Moin, P. (2003) A further study of numerical errors in large eddy simulations. Journal of Comput. Phys. 184: 366–380.

Crank, J., Nicolson, P. (1947) A practical method for numerical evaluation of solutions of partial differential equations of the heat conduction type. Proc. Camb. Phil. Soc. 43: 50–67.

Deardorff, J. W. (1970) A numerical study of three-dimensional turbulent channel flow at large reynolds numbers. Journal of Fluid Mechanics 41: 453–480.

Durbin, P. A., Pettersson-Reif, B. (2001) *Statistical theory and modeling for turbulent flow*. John Wiley.

Fedioun, I., Lardjane, N., Gökalp, I. (2001) Revisiting numerical errors in direct and large eddy simulations of turbulence: physical and spectral spaces analysis. Journal of Computational Physics 174: 816–851.

Felten, F. N., Lund, T. S. (2001) Critical comparison of the collocated and staggered grid arrangements for incompressible turbulence flows. In *3rd AFOSR Int. Conference on Direct Numerical Simulation and Large Eddy Simulation*. University of Texas at Arlington.

Ferziger, J. H., Peric, M. (2001) *Computational Methods for Fluid Dynamics*. Springer.

Fletcher, R. (1976) Conjugate gradient methods for indefinite systems. Lecture Notes in Mathematics 506: 773–789.

Fröhlich, J., Rodi, W. (2002) Introduction to large eddy simulation of turbulent flows. In *Closure Strategies for Turbulent and Transitional Flows* (ed. B. E. Launder & N. D. Sandham). Cambridge University Press.

Fröhlich, J., Rodi, W. (2004) Les of the flow around a circular cylinder of finite height. Int. J. of Heat and Fluid Flow 25: 537–548.

Fröhlich, J., Rodi, W., Kessler, P., Bertoglio, J. P., Laurence, D. (1998) Large eddy simulation of flow around circular cylinder on structured and unstructured grids. In *Notes on Numerical Fluid Mechanics* (ed. E. H. Hirshel), pp. 319–338. Vieweg.

Frossling, N. (1958) Evaporation, heat transfer, and velocity distribution in two-dimensional and rotationally symmetrical laminar boundary-layer flow. NACA Technical Memorandum 1432.

Fureby, C., Gosman, A. *D.*, *Tabor*, G., Weller, H. G., Sandham, N., Wolfshtein, M. (1997) Large eddy simulation of turbulent channel flows. Proceedings of Turbulent Shear Flow 11 3: 28–31.

Gau, C., Wu, J. M., Liang, C. Y. (1999) Heat transfer enhancement and vortex flow structure over a heated cylinder oscillating in the cross-flow. ASME Journal of Heat Transfer 121: 789–795.

Gau, C., Wu, S. X., Su, H. S. (2001) Synchronization of vortex shedding and heat transfer enhancement over a heated cylinder oscillating with small amplitude in streamwise direction. ASME Journal of Heat Transfer 123: 1139–1148.

Germano, M., Piomelli, U., Moin, P., Cabot, W. H. (1991) A dynamic subgrid scale eddy viscosity model. Physics of Fluids 3(7): 1760–1765.

Gerrard, J. H. (1966) The mechanics of the formation region of vortices behind bluff bodies. Journal of Fluid Mechanics 25: 401–413.

Ghosal, S. (1996) An analysis of numerical errors in large-eddy simulation of turbulence. Journal of Comput. Physics 125: 187–206.

Ghosal, S., Moin, P. (1995) The basic equations for the large eddy simulation of turbulent flows in complex geometry. Journal of Comput. Physics 118: 24–37.

Gowda, Y. T. K., Patnaik, B. S. V. P., Narayana, P. A. A., Seetharamu, K. N. (1998) Finite element simulation of transient laminar flow and heat transfer past an in-line tube bank. Int. Journal of Heat and Fluid Flow 19: 49–55.

Griffin, O. M., Hall, M. S. (1991) Vortex shedding lock-on and flow control in bluff body wakes — review. ASME Journal of Fluids and Engineering 113: 526–544.

Grover, L. K., Weaver, D. S. (1978*a*) Cross-flow induced vibrations in a tube bank– turbulent buffeting and fluid elastic instability. Journal of Sound and Vibration 59: 277–294.

Grover, L. K., Weaver, D. S. (1978*b*) Cross-flow induced vibrations in a tube bank– vortex shedding. Journal of Sound and Vibration 59: 263–276.

Gu, Z. F. (1996) On interference between two circular cylinders at supercritical reynolds numbers. Journal of Wind Engineering and Industrial Aerodynamics 62: 175–190.

Gullbrand, J., Chow, F. K. (2003) The effect of numerical errors and turbulence models in large-eddy simulation of channel flow, with and without explicit filtering. Journal of Fluid Mechanics 495: 323–341.

Gundappa, M., Diller, T. E. (1991) The effects of free-stream turbulence and flow pulsation on heat transfer from a cylinder in cross-flow. ASME Journal of Heat Transfer 113: 766–769.

Hall, S. E., Griffin, O. M. (1993) Vortex shedding and lock-on in a perturbed flow. ASME Journal of Fluids and Engineering 115: 283–291.

Ham, F. E., Lien, F. S., Strong, A. B. (2002) A fully conservative second-order finite difference scheme for incompressible flow on nonuniform grids. Journal of Computational Physics 177: 117–133.

Hasen, R. P., Long, L. N. (2002) Large eddy simulation of a circular cylinder on unstructured grids. In *AIAA paper*.

Hassan, Y. A., Barsamian, H. R. (1999) Turbulence simulation in tube bundle geometries using the dynamic subgrid-scale model. Nuclear Technology Journal 128: 58–74.

Hassan, Y. A., Barsamian, H. R. (2001) New-wall modeling for complex flows using the large eddy simulation technique in curvilinear coordinates. Int. J. of Heat and Mass Transfer 44: 4009–4026.

Hassan, Y. A., Barsamian, H. R. (2004) Tube bundle flows with the large eddy simulation technique in curvilinear coordinates. Int. J. of Heat and Mass Transfer 47: 3057–3071.

Hassan, Y. A., Ibrahim, W. A. (1997) Turbulence prediction in two-dimensional bundle flows using large eddy simulation. Nuclear Technology Journal 119: 11–28.

Horiuti, K. (1987) Comparison of conservative and rotational forms in large eddy simulation of turbulent channel flow. J. Comput. Phys. 71: 343–370.

Issa, R. I. (1986) Solution of the implicitly discretized fluid flow equations by operator splitting. Journal of Computational Physics 62: 40–65.

Jasak, H., Weller, H. G., Gosman, A. D. (1999) High resolution nvd differencing scheme for arbitrarily unstructured meshes. Int. J. Numer. Meth. Fluids 31: 431–449.

Jester, W., Kallinderis, Y. (2003) Numerical study of incompressible flow about fixed cylinder pairs. Journal of Fluids and Structures 17: 561–577.

Jimenez, J., Moin, P. (1991) The minimal flow unit in near-wall turbulence. J. Fluid Mech. 225: 213–233.

Jordan, S. A. (1999) A large-eddy simulation methodology in generalized curvilinear coordinates. Journal of Comput. Physics 148: 322–340.

Jordan, S. A. (2001) Dynamic subgrid-scale modeling for large eddy simulations in complex topologies. ASME Journal of Fluids Engineering 123: 619–627.

Jordan, S. A. (2003) Resolving turbulent wakes. ASME Journal of Fluids Engineering 125: 823–834.

Kakac, S., Liu, H. (1997) *Heat exchangers: selction, rating and thermal design.* CRC Press.

Kareem, A., Kijewski, T., Lu, P. C. (1998) Investigation of interference effects for a group of finite cylinders. Journal of Wind Engineering and Industrial Aerodynamics 77&78: 503–520.

Karniadakis, G. (1988) Numerical simulation of forced convection heat transfer from a cylinder in crossflow. Int. J. Heat and Mass Flow 31: 107–118.

Karniadakis, G., Mikic, B., Patera, A. (1986) Unstready heat transfer from a cylinder in cross flow: a direct numerical simulation. In *Proceeding of 8th International Heat Transfer Conference*. San Francisco, California.

Katopodes, F. V., Street, R. L., Ferziger, J. H. (2000) Subfilter-scale scalar transport for large-eddy simulation. In *14th Symposium on Boundary Layers and Turbulence*, pp. 472–475. American Meteorological Society.

Kawamura, H., Abe, H., Matsuo, Y. (1999) Dns of turbulent heat transfer in channel flow with respect to reynolds and prandtl number effects. J. Heat and Fluid Flow 20: 196–207.

Kawamura, H., Ohsaka, K., Abe, H., Yamamoto, K. (1998) Dns of turbulent heat transfer in channel flow with low to medium-high prandtl number fluid. J. Heat and Fluid Flow 19: 482–491.

Khosla, P. K., Rubin, S. G. (1974) A diagonally dominant second-order accurate implicit scheme. Computers and Fluids 2: 207–209.

Kikuchi, Y., Suzuki, H., Kitagawa, M., Ikeya, K. (2000) Effect of pulsating strouhal number on heat transfer around a heated cylinder in pulsating cross-flow. JSME International Journal 43: 250–257.

Kim, D., Choi, H. (2000) A second-order time-accurate finite volume method for unsteady incompressible flow on hybrid unstructured grids. J. Compt. Phys. 162: 411–428.

Kim, D. H., Yang, K. S., Senda, M. (2004) *Large eddy* simulation of turbulent flow past a square cylinder confined in a channel. Computers and Fluids 33: 81–96.

Kim, H. T., Kline, S. J., Reynolds, W. C. (1971) The production of turbulence near a smooth wall in a turbulent boundary layer. J. of Fluid Mech. 50: 133–160.

Kim, J., Kim, D., Choi, H. (2001) An immersed-boundary finite volume method for simulations of flow in complex geometries. J. Comput. Phys. 171: 132–150.

Kim, J., Moin, P., Moser, R. (1987) Turbulence statistics in fully developed turbulent channel flow at low reynolds number. J. of Fluid Mech. 177: 133–166.

Kiya, M., Mochizuki, O., Ido, Y., Suzuki, T., Arai, T. (1992) Flip-flopping flow around two bluff bodies in tandem arrangement. In *Bluff-Body Wakes, Dynamics and Instabilities* (ed. Eckelmann, H., Graham, J. M. R., Huerre, P. & Monkewitz, P. A.), pp. 15–18. Springer, Berlin.

Kleiser, L., Zang, T. A. (1991) Numerical simulation of transition in wall-bounded shear flows. Annual Review of Fluid Mechanics 23: 495–537.

Kline, S. J., Reynolds, W. C., Schraub, F. A., Runstadler, P. W. (1967) The structure of turbulent boundary layer. Journal of Fluid Mechanics 30: 733–741.

Kondjoyan, A., Daudin, J. D. (1995) Effects of free stream turbulence intensity on heat and mass transfers at the surface of a circular cylinder and an elliptic cylinder, axis ratio 4. Int. J. Heat Mass Transfer 38: 1735–1749.

Konstantinidis, E. (2001) Pulsating flow in cylinder arrays. PhD Thesis, King's College London, University of London.

Konstantinidis, E. (2004) Piv of the steady and pulsating crossflow over a single cylinder. Private Communication .

Konstantinidis, E., Balabani, S., Yianneskis, M. (2002) A study of vortex shedding in a staggered tube array for steady and pulsating flow. ASME J. of Fluids Engineering 124: 737–746.

Konstantinidis, E., Balabani, S., Yianneskis, M. (2003*a*) The effect of flow perturbations on the near wake characteristics of a circular cylinder. Journal of Fluids and Structures 18: 367–386.

Konstantinidis, E., Balabani, S., Yianneskis, M. (2003*b*) Relationship between vortex shedding and heat transfer: implications for tube bundles in cross-flow. Transactions of the Institution of Chemical Engineering, Part A, Chemical Engineering Research and Design 81: 695–699.

Konstantinidis, E., Balabani, S., Yianneskis, M. (2004) Phase-average mean flow and turbulence structure in a staggered cylinder array subjected to pulsating cross-flow. ASME Journal of Fluids Engineering 126: 323–336.

Konstantinidis, E., Castiglia, D., Balabani, S., Yianneskis, M. (2000) On the flow and vortex shedding characteristics of an inline tube bundle in steady and pulsating crossflow. Transactions of the Institution of Chemical Engineering, Part A, Chemical Engineering Research and Design 78(8): 1129–1138.

Krall, K. M., Eckert, E. R. G. (1973) Local heat transfer around a cylinder at a low reynolds number. ASME Journal of Heat Transfer 95: 273–275.

Kravchenko, A., Moin, P., Moser, R. (1996) Zonal embedded grids for numerical simulations of wall-bounded turbulence flows. J. of Comput. Phys. 127: 412–423.

Kravchenko, A. G., Moin, P. (1997) On the effect of numerical error in large eddy simulation of turbulent flows. J. of Comput. Phys. 131: 310–322.

Kravchenko, A. G., Moin, P. (2000) Numerical studies of flow over a circular cylinder at $re_D = 3900$. Physics of Fluids 12: 403–417.

Lam, K., Fang, X. (1995) The effect of interference of four equispaced cylinders in cross flow on pressure and force coefficients. Journal of Fluids and Structures 9: 195–274.

Laurence, D. (2002) Large eddy simulation of industrial flows? In *In Closure Strategies for Turbulent and Transitional Flows* (ed. B. Launder & N. Sandham), pp. 392–406. Cambridge University Press.

Lesieur, M., Metais, O. (1996) New trends in large-eddy simulations of turbulence. Annual Review of Fluid Mech. 28: 45–82.

Liang, C., Papadakis, G. (2003) A study of kinetic energy conserving scheme using finite volume collocated grid for large eddy simulations of a channel flow. In *Fourth International Conference on Fluid Mechanics*. Dalian, China.

Liang, C., Papadakis, G. (2004*a*) Large eddy simulation of cross flow over inline and staggered tube bundles. In *Proceedings of the 8th international conference on Fluid-Induced Vibration*, , vol. 1, pp. 247–252. Paris, France.

Liang, C., Papadakis, G. (2004*b*) Large eddy simulation of pulsating cross flow over a circular cylinder in subcritical reynolds number. Under preparation .

Liang, C., Papadakis, G. (2005) Study of the effect of pulsation on the flow field and heat tranfer over inline cylinder array using les. In *Proceedings of ETMM-6*, to be published. Italy.

Lien, F. S., Chen, W. L., Leschziner, M. A. (1996) A multi-block implementation of non-orthogonal collocated finite-volume algorithm for complex turbulent flows. Int. J. Num. Meth. Fluids 23: 567–588.

Lilly, D. K. (1987) Helicity. In *Lecture Notes on Turbulence* (ed. J. R. Herring & J. C. McWilliams), pp. 171–218. Singapore, World Scientific.

Lilly, D. K. (1992) A proposed modification of the germano subgrid scale closure method. Physics of Fluids 4: 633–635.

Lin, J. C., Vorobieff, P., Rockwell, D. (1995) Three-dimensional patterns of streamwise vorticity of the turbulent near-wake of a cylinder. Journal of Fluids and Structures 9: 231–234.

Lin, J. C., Yang, P., Rockwell, D. (2002) Flow past two cylinders in tandem: Instantaneous and averaged flow structure. Journal of Fluids and Structures 16: 1059–1071.

Liu, S., Fu, S. (2002) Regimes of vortex shedding from an in-line oscillating cylinder in uniform flow. Acta Mechanica Sinica 18: 1–9.

Ljungkrona, L., Norberg, C., Sundén, B. (1991) Free-stream turbulence and tube spacing effect on surface pressure fluctuations for two tubes in an inline arrangement. Journal of Fluids and Structures 5: 701–727.

Ljungkrona, L., Sundén, B. (1993) Flow visualization and surface pressure measurement on two tubes in an inline arrangement. Experimental Thermal and Fluid Science 6: 15–27.

Longatte, E., Bendjeddou, Z., Souli, M. (2003) Methods for numerical study of tube bundle vibrations in cross-flows. Journal of Fluids and Structures 18: 513–528.

Lourenco, M., Shih, C. (1993) Characteristics of the plane turbulent near wake of a circular cylinder. a particle image velocimetry study. Private communication in Beaudan and Moin (1994).

Lund, T. S. (1995) On the use of discrete filters for large-eddy simulation. Annual research briefs. Center for Turbulence Research, Stanford University.

Lund, T. S., Kaltenbach, H. J. (1995) Experiments with explicit filtering for les using a finite-difference method. Annual research briefs. Center for Turbulence Research, Stanford University.

Lund, T. S., Wu, X., Squires, K. D. (1998) Generation of turbulent inflow data for spatially-developing boundary layer simulations. J. of Comput. Physics 140: 233–258.

Ma, X., Karamanos, G. S., Karniadakis, G. E. (2000) Dynamics and low-dimensionality of a turbulent near wake. Journal *of Fluid Mechanics* 410: 29–65.

Mackley, M. R., Stonestreet, P., Roberts, E. P. L., Ni, X. (1996) Residence time distribution enhancement in reactors using oscillatory flow. Transactions of IChemE: Chemical Engineering Research and Design 74: 541–545.

Mandhani, V. K., Chhabra, R. P., Eswaran, V. (2002) Forced convection heat transfer in tube banks in cross flow. Chemical Engineering Science 57: 379–391.

Mathey, M., Fröhlich, J., Rodi, W. (1999) Les of heat transfer in turbulent flow over a wall-mounted matrix of cubes. In *Direct and Large-Eddy Simulations III* (ed. P. Voke, N. D. Sandham & R. Kleiser), pp. 51–62. Kluwer.

Meneveau, C., Katz, J. (2000) Scale-invariance and turbulence models for large-eddy simulation. Annual Review of Fluid Mech. 32: 1–32.

Meneveau, C., Lund, T. S., Cabot, W. H. (1996) A lagrangian dynamic subgrid-scale model of turbulence. J. Fluid Mech. 319: 353–385.

Mittal, R. (1995) Large-eddy simulation of flow past a circular cylinder. Annual Research Briefs, Center for Turbulence Research, Stanford .

Mittal, R. (1996) Progress on les of flow past a circular cylinder. Annual Research Briefs, Center for Turbulence Research, Stanford .

Mittal, R., Moin, P. (1997) Suitability of upwind-biased finite-difference schemes for large-eddy simulation of turbulent flow. AIAA J. 35: 1415–1418.

Mittal, S., Kumar, V., Raghuvanshi, A. (1997) Unsteady incompressible flows past two cylinders in tandem and staggered arrangements. Int. Journal for Numerical Methods in Fluids 25: 1315–1344.

Moin, P. (2002) Advances in large eddy simulation methodology for complex flows. International Journal of Heat and Fluid Flow 23: 710–720.

Moin, P., Kim, J. (1982) Numerical investigation of turbulent channel flow. J. of Fluid Mech. 118: 341–377.

Moin, P., Mahesh, K. (1998) Direct numerical simulation: a tool in turbulence research. Annu. Rev. Fluid Mech. 30: 539–578.

Moin, P., Squires, W., Cabot, W., Lee, S. (1991) A dynamic subgrid scale model for compressible turbulence and scalar transport. Physics of Fluids 3: 2746–2757.

Moretti, P. M. (1993) Flow-induced vibrations in arrays of cylinders. Annual Review Fluid Mechanics 25: 99–114.

Morinishi, Y., Lund, T. S., Vasilyev, O. V., Moin, P. (1998) Fully conservative higher order finite difference schemes for incompressible flow. Journal of Computational Physics 143: 90–124.

Moser, R. D., Kim, J., Mansour, N. N. (1999) Direct numerical simulation of turbuent channel flow up to $re_\tau = 590$. Physics of Fluids 11: 943–945.

Murray, D. B. (1993) A comparison of heat transfer in staggered and inline tube banks with a gas-particle crossflow. ASME Journal of Heat Transfer 6: 177–185.

Murray, D. B., Fitzpatrick, J. A. (1991) Heat transfer in a staggered tube array for a gas-solid suspension flow. ASME Journal of Heat Transfer 113: 865–873.

Muzaferija, S. (1994) Adaptive finite volume method for flow predictions using unstructured meshes and multigrid approach. PhD Thesis, Imperial College London, University of London.

Muzaferija, S., Gosman, D. (1997) Finite-volume cfd procedure and adaptive error control strategy for grids of arbitrary topology. Journal of computational physics 138: 766–787.

Nakayama, A., Vengadesan, S. N. (2002) On the influence of numerical schemes and subgrid-stress models on large eddy simulation of turbulent flow past a square cylinder. International Journal for Numerical Methods in Fluids 38: 227–253.

Nishimura, S., Itoh, H., Miyashita, H. (1993) The influence of tube layout on flow and mass transfer characteristics in tube banks in the transitional flow regime. Int. Journal of Heat and Mass Transfer 36: 553–563.

Norberg, C. (1987) Effects of reynolds number and low-intensity free stream turbulence on the flow around a circular cylinder. In *Publ. 87/2, Applied Thermodynamics and Fluid Mechanics*. Charlmers University, Sweden.

Norberg, C. (1998) Ldv-measurements in the near wake of a circular cylinder. In *Advances in Understanding of Bluff Body Wakes and Vortex Induced Vibration*. Washington DC.

Oengören, A., Ziada, S. (1998) An in-depth study of vortex shedding, acoustic resonance and turbulent forces in normal triangle tube arrays. Journal of Fluids and Structures 12: 717–758.

Okajima, A. (1979) Flows around two tandem circular cylinders in very high reynolds numbers. Bulletin of the JSME 22: 501–511.

Ong, L., Wallace, J. (1996) The velocity field of the turbulent very near wake of a circular cylinder. Experiment in Fluids 20: 441–453.

Owen, P. (1965) Buffeting excitation of boiler tube vibration. Journal of Mechanical Engineering Science 7: 431–439.

Païdoussis, M. (1981) Fluidelastic vibration of cylinder arrays in axial and cross-flow: state of the art. Journal of Sound and Vibration 76: 329–360.

Païdoussis, M. P. (1983) A review of flow-induced vibrations in reactors and reactor components. Nuclear Engineering and Design 74: 31–60.

Papadakis, G., Bergeles, G. (2001) Numerical simulation of flow and heat transfer around a cylinder with pulsating approaching flow. Proceedings of IMechE, Journal of Mechnical Engineering Science, Part C 215: 105–119.

Park, H. G., Gharib, M. (2001) Experimental study of heat convection from stationary and oscillating circular cylinder in cross flow. ASME Journal of Heat Transfer 123: 51–62.

Park, N., Yoo, J. Y., Choi, H. (2004) Discretization errors in large eddy simulation: on the suitability of centered and upwind-biased compact difference schemes. J. Comput. Phys. 198: 580–616.

Patankar, S. V. (1980) *Numerical Heat Transfer and Fluid Flow*. McGraw-Hill, New York.

Patankar, S. V., Spalding, D. B. (1972) A calculation procedure for heat, mass and momentum transfer in three-dimensional parabolic flows. International Journal of Heat and Mass Transfer 15: 1787–1806.

Peng, S. H., Davidson, L. (2002) On a subgrid-scale heat flux model for large eddy simulation of turbulent thermal flow. Internatinal Journal of Heat and Mass Transfer 45: 1393–1405.

Peric, M., Kessler, R., Scheuerer, G. (1988) Comparison of finite-volume numerical methods with staggered and colocated grids. Computers and Fluids 16: 389–403.

Piomelli, U. (1997) Large-eddy and direct simulation of turbulent flows. von Karman Institute for Fluid Dynamics Lecture Series: Introduction to the Modelling of Turbulence.

Piomelli, U., Choudhari, M. M., Ovchinnikov, V., Balaras, E. (2003) Numerical simulations of wake/boundary-layer interactions. AIAA Paper 2003-0975.

Piomelli, U., Moin, P., Ferziger, J. H. (1988) Model consistency in large eddy simulation of turbulent channel flows. Physics of Fluids 31: 1884–1891.

Piomelli, U., Zang, T. A. (1991) Large eddy simulation of transitional channel flow. Comput. Phys. Commun. 65: 224–230.

Polak, D. R., Weaver, D. S. (1995) Vortex shedding in normal triangular tube arrays. Journal of Fluids and Structures 9: 1–17.

Pope, S. B. (2000) *Turbulent flows*. Cambridge University Press.

Prasad, A., Williamson, C. H. K. (1997) The instability of a shear layer separating from a bluff body. Journal of Fluid Mechanics 333: 370–402.

Price, J. S., Païdoussis, M. P., Mark, B. (1995) Flow visulisation of the interstitial cross-flow through parallel triangular and rotated square arrays of cylinders. Journal of Sound and Vibration 181: 85–98.

Reynolds, W. C. (1976) Computation of turbulent flows. Annual Review of Fluid Mechanics 8: 183–208.

Rhie, C. M., Chow, W. L. (1983) Numerical study of the turbulent flow past an airfoil with trailing edge separation. AIAA Journal 21: 1525–1532.

Rodi, W. (1997) Comparison of les and rans calculation of the flow around bluff bodies. J. Wind Eng. Indus. Aerodyne. 69-71: 55–75.

Rogallo, R. S., Moin, P. (1984) Numerical simulation of turbulent flows. Annual Review of Fluid Mechanics 16: 99–137.

Rollet-Miet, P., Laurence, D., Ferziger, J. H. (1999) Les and rans of turbulent flow in tube bundles. Int. J. Heat Fluid Flow 20: 241–254.

Sagaut, P. (2002) *Large eddy simulation for incompressible flows: an introductioin*. Springer.

Sanitjai, S., Goldstein, R. J. (2001) Effect of free stream turbulence on local mass transfer from a circular cylinder. International Journal of Heat and Mass Transfer 44: 2863–2875.

Sarghini, F., Piomelli, U., Balaras, E. (1999) Scale-similar models for large-eddy simulations. Physics of Fluids 11: 1596–1607.

Satake, S., Kunugi, T., Takase, K., Ose, Y., Naito, N. (2003) Large scale structures of turbulent shear flow via dns. Lecture Notes in Computer Science 2858: 468–475.

Schmid, P. J., Henningson, D. S. (2001) *Stability and transition in shear flows*. Springer Verlag.

Scholten, J. W., Murray, D. B. (1998*a*) Heat transfer and velocity fluctuations in a staggered tube array. Int. J. of Heat and Fluid Flow 19: 233–244.

Scholten, J. W., Murray, D. B. (1998*b*) Unsteady heat transfer and velocity of a cylinder in cross flow - i. low freestream turbulence. Int. J. of Heat and Mass Transfer 41: 1139–1148.

Scholten, J. W., Murray, D. B. (1998*c*) Unsteady heat transfer and velocity of a cylinder in cross flow - ii. high freestream turbulence. Int. J. of Heat and Mass Transfer 41: 1149–1156.

Scotti, A., Meneveau, C., Fatica, M. (1997) Dynamic smagorinsky model on anisotropic grids. Physics of Fluids 9: 1856–1858.

Scotti, A., Meneveau, C., Lilly, D. K. (1993) Generalized smagorinsky model for anisotropic grids. Physics of Fluids 5: 2306–2308.

Simonin, O., Barcouda, M. (1988) Measurements and prediction of turbulent flow entering a staggered tube bundle. In *Proceedings of Fourth International Symposium on Applications of laser anemometry to fluid mechanics*.

Smagorinsky, J. (1963) General circulation experiments with the primitive equations. i. the basic experiment. Monthly Weather Review 91: 99–164.

Smith, C. R., Metzler, S. P. (1983) The characteristics of low speed streaks in the near wall region of a turbulent boundary layer. Journal of Fluid Mech. 129: 27–54.

Sohankar, A., Norberg, C., Davidson, L. (1998) Low-reynolds flow around a square cylinder at incidence: Study of blockage, onset of vortex shedding and outlet boundary condition. Int. J. Numer. Meth. Fluids 26: 39–56.

Sumner, D., Price, S. J., Païdoussis, M. P. (2000) Flow-pattern identification for 2 staggered circular cylinders in cross-flow. Journal of Fluid Mechanics 411: 263–303.

Sung, H. J., Hwang, K. S., Hyun, J. M. (1994) Experimental study on mass-transfer from a circular cylinder in pulsating flow. International Journal of Heat and Mass Transfer 37: 2203–2210.

Sweeney, C., Meskell, C. (2003) Fast numerical simulation of vortex shedding in tube arrays using a discrete vortex method. Journal of Fluids and Structures 18: 501–512.

Tanida, Y., Okajima, A., Watanabe, Y. (1973) Stability of a circular cylinder oscillating in uniform flow or in wake. Journal of Fluid Mechanics 41: 769–784.

Tejada-Martinez, A. E., Jansen, K. E. (2004) A dynamic smagorinsky model with dynamic determination of the filter width ratio. Physics of Fluids 16: 2514–2528.

Templeton, J., Wang, M., Moin, P. (2002) Towards les wall models using optimization technique. Annual Research Briefs, CTR, Stanford pp. 189–200.

Theodoropoulos, T. (1990) Prediction of 3d engine flow on unstructured meshes. PhD Thesis, Imperial College London, University of London.

Thomas, L. H. (1953) The stability of plane poiseuille flow. Phys. Rev. 91: 780–783.

Tiselj, I., Pogrebnyak, E., Li, C., Mosyak, A., Hetsroni, G. (2001) Effect of wall boundary condition on scalar transfer in a fully developed turbulent flume. Physics of Fluids 13: 1028–1039.

Tiwari, S., Biswas, G., Prasad, P. L. N., Basu, S. (2003) Numerical prediction of flow and heat transfer in a rectangular channel with a built-in circular tube. ASME Journal of Heat Transfer 125: 413–421.

Tutar, M., Holdo, A. E. (2000) Large eddy simulation of a smooth circular cylinder oscillating normal to a uniform flow. ASME Journal of Fluids Engineering 122: 694–702.

Unal, M., Rockwell, D. (1988) On vortex shedding from a cylinder. part 1. the initial instability. Journal of Fluid Mechanics 190: 491–512.

VandenBerghe, T. M., Dhaubhadel, M. N., Diller, T. E., Telionis, D. P. (1983) pulsating flow and heat transfer over multiple cylinders. In *Proc Symp on Non-Linear Problems in Energy Engineering*, pp. 240–247. CONF-830413.

Vasilyev, O. V. (2000) High order finite difference schemes on non-uniform meshes with good conservation properties. Journal of Computational Physics 157: 746–761.

Vasilyev, O. V., Lund, T. S., Moin, P. (1998) A general class of commutative filters for les in complex geometries. Journal of Computational Physics 146: 82–104.

Versteeg, H. K., Malalasekera, W. (1995) *An introduction to computational fluid dynamics. The Finite Volume Method.* Longman, London.

Wallin, S., Johansson, A. V. (2000) An explicit algebraic reynolds stress model for incompressible and compressible turbulent flows. Journal of Fluid Mechanics 403: 89–132.

Wang, Z. J., Zhou, Y., Wang, X. W., Jin, W. (2003) A fiber-optic bragg grating sensor for simultaneous static and dynamic temperature measurement on a heated cylinder in cross-flow. Int. J. of Heat and Mass Transfer 46: 2983–2992.

Watterson, J. K., Dawes, W. N., Savill, A. M., White, A. J. (1999) Predicting turbulent flow in a staggered tube bundle. International Journal of Heat and Fluid Flow 20: 581–591.

Weaver, D., Abd-Rabbo, A. (1985) A flow visulization study of a square array of tubes in water cross-flow. ASME Journal of Fluids Engineering 107: 354–363.

Weaver, D. S., Fitzpartick, J. A. (1988) A review of crossflow induced vibrations in heat exchanger tube arrays. Journal of Fluids and Structures 2: 73–93.

Weaver, D. S., Lian, H. Y., Huang, X. Y. (1993) Vortex shedding in rotated square arrays. Journal of Fluids and Structures 7: 107–121.

Wei, T., Smith, C. R. (1986) Secondary vortices in the wake of circular cylinders. Journal of Fluid Mechanics 169: 513–533.

Williamson, C. H. K. (1996) Vortex dynamics in the cylinder wake. Annual Review of Fluid Mechanics 28: 477–539.

Wu, J., Welch, L. W., Welsh, M. C., Sheridan, J., Walker, G. J. (1994) Spanwise wake structures of a circular cylinder and two circular cylinders in tandem. Exp. Thermal and Fluid Science 9: 299–308.

Yang, K. S., Ferziger, J. H. (1993) Large eddy simulation of turbulent obstacle flow using a dynamic subgrid-scale model. AIAA Journal 31: 1406–1413.

Zang, T. A. (1991) On the rotational and skew-symmetric forms for incompressible flow simulations. Applied Numerical Mathematics 7: 27–40.

Zang, Y., Street, R. L., Koseff, J. R. (1993) A dynamic mixed subgrid-scale model and its application to turbulent recirculating flows. Physics of Fluids 5: 3186–3196.

Zdravkovich, M. M. (1977) Review of flow interference between two circular cylinders in various arrangements. ASME Journal of Fluids Engineering 99: 618–633.

Zdravkovich, M. M. (1984) Classifications of flow-induced oscillations of two parallel circular cylinders in various arrangements. ASME Symposium on Flow-induced vibrations 2: 1–18.

Zdravkovich, M. M. (1987) The effects of interference between circular cylinders in cross flow. Journal of Fluids and Structures 1: 239–261.

Zdravkovich, M. M. (1997) *Flow around circular cylinders*. Oxford University Press.

Zhang, W., Chen, Q. (2000) Large eddy simulation of indoor airflow with a filtered dynamic subgrid scale model. Int. Journal of Heat and Mass Transfer 43: 3219–3231.

Ziada, S., Oengören, A. (1992) Vorticity shedding and acoustic resonance in an inline tube bundle. part i: vorticity shedding. Journal of Fluids and Structures 6: 271–292.

Ziada, S., Oengören, A. (1993) Vortex shedding in an inline tube bundle with large tube spacings. Journal of Fluids and Structures 7: 661–687.

Ziada, S., Oengören, A. (2000) Flow periodicity and acoustic resonance in parallel triangle tube bundles. Journal of Fluids and Structures 14: 197–219.